Measurement of the Proton Recoil Spectrum in Neutron Beta Decay with the Spectrometer *a*SPECT: Study of Systematic Effects

Dissertation
zur Erlangung des Grades
"Doktor der Naturwissenschaften"
am Fachbereich Physik, Mathematik und Informatik
der Johannes Gutenberg-Universität
in Mainz

vorgelegt von
Dipl.-Math. Gertrud Emilie Konrad
geboren in Worms

Mainz, im August 2011

Dean:

First referee:
Second referee:

Oral examination: 24 January, 2012

D77

Properly speaking, such work is never finished;
one must declare it so when,
according to time and circumstances,
one has done one's best.

J. W. von Goethe, Italian Journey
Caserta, 16 March 1787

Abstract

Free neutron decay, $\mathrm{n} \rightarrow \mathrm{pe}\overline{\nu}_{\mathrm{e}}$, is the simplest nuclear beta decay, well described as a purely left-handed, vector minus axial-vector interaction within the framework of the Standard Model (SM) of elementary particles and fields. Due to its highly precise theoretical description, neutron beta decay data can be used to test certain extensions to the SM. Possible extensions require, e.g., new symmetry concepts like left-right symmetry, new particles, leptoquarks, supersymmetry, or the like. Precision measurements of observables in neutron beta decay address important open questions of particle physics and cosmology, and are generally complementary to direct searches for new physics beyond the SM in high-energy physics.

In this doctoral thesis, a measurement of the proton recoil spectrum with the neutron decay spectrometer aSPECT is described. From the proton spectrum the antineutrino-electron angular correlation coefficient a can be derived. In our first beam time at the Forschungs-Neutronenquelle Heinz Maier-Leibnitz in Munich, Germany (2005-2006), background instabilities due to particle trapping and the electronic noise level of the proton detector prevented us from presenting a new value for a. In the latest beam time at the Institut Laue-Langevin (ILL) in Grenoble, France (2007-2008), the trapped particle background has been reduced sufficiently and the electronic noise problem has essentially been solved. For the first time, a silicon drift detector was used. As a result of the data analysis, we identified and fixed a problem in the detector electronics which caused a significant systematic error. The target figure of the latest beam time was a new value for a with a total relative error well below the present literature value of 4 %. A statistical accuracy of about 1.4 % was reached, but we could only set upper limits on the correction of the problem in the detector electronics, which are too high to determine a meaningful result. The present doctoral thesis focused on the investigation of several different systematic effects. With the knowledge of the systematic effects gained in this thesis, we are now able to improve the aSPECT spectrometer to perform a 1 % measurement of a in a further beam time at the ILL.

Zusammenfassung

Der Zerfall des freien Neutrons, n → $\mathrm{pe}\overline{\nu}_{\mathrm{e}}$, ist der einfachste Kernbetazerfall. Dieser wird im Rahmen des Standardmodells (SM) der Elementarteilchenphysik gut als eine rein linkshändige Vektor-Minus-Axialvektor-Wechselwirkung beschrieben. Aufgrund seiner äußerst präzisen theoretischen Beschreibung können Neutronenbetazerfallsdaten für Tests bestimmter Erweiterungen des SMs verwendet werden. Mögliche Erweiterungen erfordern, z.B., neue Symmetriekonzepte wie Links-Rechts-Symmetrie, neue Teilchen, Leptoquarks, Supersymmetrie, oder ähnliches. Präzisionsmessungen von Observablen im Neutronenbetazerfall beschäftigen sich mit wichtigen offenen Fragen der Teilchenphysik und Kosmologie und sind im Allgemeinen komplementär zur direkten Suche nach neuer Physik jenseits des SMs in der Hochenergiephysik.

In dieser Doktorarbeit wird eine Messung des Protonenrückstoßspektrums mit dem Neutronenzerfallsspektrometer *a*SPECT beschrieben. Aus dem Protonenspektrum lässt sich der Antineutrino-Elektron Winkelkorrelationskoeffizient a ableiten. Bei unserer ersten Strahlzeit an der Forschungs-Neutronenquelle Heinz Maier-Leibnitz in München, Deutschland (2005-2006), haben uns Untergrundinstabilitäten, verursacht durch gespeicherte Teilchen und den elektronischen Rauschpegel des Protonendetektors, daran gehindert, einen neuen Wert für a zu präsentieren. Bei der letzten Strahlzeit am Institut Laue-Langevin (ILL) in Grenoble, Frankreich (2007-2008), wurde der Untergrund aufgrund von gespeicherten Teilchen ausreichend reduziert und das Problem des elektronischen Rauschens im Wesentlichen gelöst. Zum ersten Mal wurde ein Siliziumdriftdetektor verwendet. Als Ergebnis der Datenanalyse haben wir ein Problem in der Detektorelektronik identifiziert und behoben, welches einen signifikanten systematischen Fehler verursacht hat. Die Zielgröße der letzten Strahlzeit war ein neuer Wert für a mit einem relativen Gesamtfehler von weniger als dem gegenwärtigen Literaturwert von 4 %. Zwar wurde eine statistische Genauigkeit von rund 1.4 % erreicht, allerdings konnten wir für die Korrektur des Problems in der Detektorelektronik nur Obergrenzen festlegen, welche zu hoch sind, um ein aussagekräftiges Ergebnis zu bestimmen. Im Mittelpunkt der vorliegenden Doktorarbeit stand die Untersuchung von mehreren verschiedenen systematischen Effekten. Mit den Erkenntnissen über die systematischen Effekte, die in dieser Arbeit gewonnen wurden, sind wir in der Lage, das *a*SPECT Spektrometer zu verbessern, um eine 1 % Messung von a in einer weiteren Strahlzeit am ILL durchzuführen.

Publications

Some ideas and figures presented in this thesis have appeared previously in the following publications:

- G. Konrad *et al.*, Design of an Anti-Magnetic Screen for the Neutron Decay Spectrometer *a*SPECT, in *Proceedings of the European Comsol Conference, Grenoble, France, 2007*, p. 241-245 (2007) [1]
- Report for the TRAPSPEC JRA-11 in EURONS on task T-J11-1 (Simulations and calculations), 2008 [2]
- Report for the TRAPSPEC JRA-11 in EURONS on task T-J11-8 (Neutron decay retardation spectrometer), 2008 [3]
- Measurement of the Proton Spectrum in free Neutron Decay, ILL Experimental Report, 2009 [4]
- G. Konrad *et al.*, The Proton Spectrum in Neutron Beta Decay: Latest Results with the *a*SPECT Spectrometer, in *Proceedings of the eighteenth Particles and Nuclei International Conference, Eilat, Israel, 2008*, Nucl. Phys. A **827**, 529c-531c (2009) [5]
- G. Konrad *et al.*, Impact of Neutron Decay Experiments on non-Standard Model Physics, in *Proceedings of the 5th International BEYOND 2010 Conference, Cape Town, South Africa, 2010*, World Scientific, Singapore, ISBN 978-981-4340-85-4, p. 660-672, 2011, and arXiv:1007.3027v2 (2010) [6]
- G. Konrad *et al.*, Neutron Decay with PERC: a Progress Report, in *Proceedings of the 5th European Conference on Neutron Scattering, Prague, Czech Republic, 2011*, J. Phys.: Conf. Series, accepted (2011) [7]

Contents

List of Figures

List of Tables

Chapter 1

Introduction

"In 1932, [James] Chadwick made a fundamental discovery in the domain of nuclear science: he proved the existence of *neutrons* - elementary particles devoid of any electrical charge [8]. In contrast with the helium nuclei (alpha rays) which are charged, and therefore repelled by the considerable electrical forces present in the nuclei of heavy atoms, this new tool in atomic disintegration need not overcome any electric barrier and is capable of penetrating and splitting the nuclei of even the heaviest elements. Chadwick in this way prepared the way towards the fission of uranium 235 and towards the creation of the atomic bomb. For this epoch-making discovery he was awarded the Hughes Medal of the Royal Society in 1932, and subsequently the Nobel Prize for Physics in 1935.", from *Nobel Lectures, Physics 1922-1941* [9].

The present thesis deals with the decay of free neutrons. A neutron (n) is a little more massive than the proton (p), by $\Delta = m_\mathrm{n} - m_\mathrm{p} = 1293.333(33)\,\mathrm{keV/c^2}$, and in free space it decays weakly into a proton, an electron (e), and an electron-antineutrino ($\bar{\nu}_\mathrm{e}$):

$$\mathrm{n} \quad \xrightarrow{\tau_\mathrm{n}} \quad \mathrm{p} + \mathrm{e}^- + \bar{\nu}_\mathrm{e} + Q, \tag{1.1}$$

with a mean lifetime of $\tau_\mathrm{n} = (881.5 \pm 1.5)\,\mathrm{s}$ [10]. Here, the released energy is given by $Q = (m_\mathrm{n} - m_\mathrm{p} - m_\mathrm{e} - m_\nu)\cdot c^2 = 782.334(33)\,\mathrm{keV}$ [10]. At the quark level, one of the down quarks in the neutron decays to an up quark, emitting a virtual W gauge boson, which further decays into an electron and an electron-antineutrino (see Fig. 2.1). As the simplest nuclear beta decay, the free neutron provides an excellent framework for the study of the structure and nature of the weak interaction.

The Standard Model (SM) of elementary particles and fields is the mathematical theory that describes the weak, electromagnetic, and strong interactions between leptons and quarks: In 1960, Sheldon Glashow developed a theory which unifies the weak and the electromagnetic interactions [11]. In 1967, Steven Weinberg and Abdus Salam, incorporated the Higgs mechanism[1] into Glashow's electroweak theory [13, 14] (see also [15]). The Glashow-Salam-Weinberg (GSW) theory, along with QCD[2], constitute the SM. In 1973, the weak neutral currents have been discovered in the Gargamelle[3] bubble chamber at CERN [16]. Then, the GSW theory became widely accepted, and Glashow, Salam, and Weinberg shared the 1979 Nobel Prize in Physics for their contributions to the theory.

---

[1] The Higgs mechanism refers to the generation of masses for the $W^\pm$ and Z weak gauge bosons through electroweak symmetry breaking [12]. Currently, experiments at the Large Hadron Collider at CERN are searching for Higgs bosons.

[2] Quantum Chromodynamics (QCD) is a theory of the strong interaction.

[3] Gargamelle was a bubble chamber principally designed for the detection at CERN of neutrinos.

The SM has successfully explained a large number of experimental results and precisely predicted a wide variety of phenomena. So far, it is the most successful theory of particle physics. However, it is not a complete theory of all four fundamental forces, because it does not incorporate general relativity. Physics beyond the SM attempts to explain the deficiencies of the SM, such as the origin of mass, the strong CP problem, the hierarchy problem, neutrino oscillations (and their non-zero masses), matter-antimatter asymmetry, and the origins of dark matter and dark energy. Theories beyond the SM include various extensions of the SM through supersymmetry (SUSY), such as the Minimal Supersymmetric Standard Model (MSSM), or entirely novel explanations, such as string theory and extra dimensions.

High-precision measurements of observables in neutron beta decay address a number of questions which are at the forefront of particle physics [17–19], and are generally complementary to direct searches in high-energy physics. Main emphasis lies on the search for new physics beyond the SM. Possible extensions require new symmetry concepts like left-right symmetry, fundamental fermion compositeness, new particles, leptoquarks, supersymmetry, supergravity, or many more [20, 21]. Free neutron decay is therefore a very active field, with a number of new measurements underway worldwide. For recent reviews see Refs. [18, 19, 22, 23]. With high-precision measurements of angular correlations several symmetry tests based on neutron beta decay data become competitive, cf. Sec. 2.3 and Ref. [6].

In the modern form of the SM, the differential decay rate of neutrons can be written as [24]:

$$\begin{aligned} \mathrm{d}^3\Gamma &= \frac{1}{(2\pi)^5}\frac{G_\mathrm{F}^2|V_\mathrm{ud}|^2}{2} p_\mathrm{e}E_\mathrm{e}\left(E_0-E_\mathrm{e}\right)^2 \mathrm{d}E_\mathrm{e}\mathrm{d}\Omega_\mathrm{e}\mathrm{d}\Omega_\nu \times \\ & \xi\left[1 + a\frac{\mathbf{p}_\mathrm{e}\cdot\mathbf{p}_\nu}{E_\mathrm{e}E_\nu} + b\frac{m_\mathrm{e}}{E_\mathrm{e}} + \frac{\langle\mathbf{s}_\mathrm{n}\rangle}{s_\mathrm{n}}\left(A\frac{\mathbf{p}_\mathrm{e}}{E_\mathrm{e}} + B\frac{\mathbf{p}_\nu}{E_\nu} + \dots\right)\right]. \end{aligned} \tag{1.2}$$

Here, G_F is the Fermi weak coupling constant, V_ud is the upper left element of the Cabibbo-Kobayashi-Maskawa (CKM) quark-mixing matrix [25, 26], $\mathbf{p}_\mathrm{e}$, $\mathbf{p}_\nu$, E_e, and E_ν are the electron (neutrino) momenta and total energies, respectively, E_0 is the electron spectrum endpoint total energy, m_e is the electron mass, $\mathbf{s}_\mathrm{n}$ is the neutron spin, and the Ω_i denote solid angles. Quantity ξ is a factor inversely proportional to the neutron decay rate, a, A, and B are the angular correlation coefficients, while b is the Fierz interference term. The neutrino-electron correlation coefficient a and the Fierz term b are measurable in decays of unpolarized neutrons, while the beta and neutrino asymmetry parameters A and B require polarized neutrons. A non-vanishing Fierz term b would indicate the existence of left-handed scalar and tensor interactions.

Another observable is C, the proton asymmetry relative to the neutron spin [27, 28]:

$$C = -x_C(A+B), \tag{1.3}$$

where $x_C = 0.27484$ is a kinematical factor[4].

The present status on the angular correlation coefficients a, A, B, and C, the Fierz term b, and the neutron lifetime τ_n is summarized in Ref. [19]. According to the Particle Data Group's (PDG) 2011 review [10], the relative errors on a, A, B, and C are 4 %, 0.9 %, 0.3 %, and 1.1 %, respectively. Recently, three beta asymmetry experiments have

---

[4] Note that we define the proton asymmetry C with the opposite sign compared to [27]. This retains the convention that a positive asymmetry indicates more particles to be emitted in the spin direction.

completed their analyses, namely UCNA [29], PERKEO II [30][5], and PERKEO III [32]. The PERKEO III collaboration improved the uncertainty on A by about a factor of 5 compared to the PDG 2011 average [32] (preliminary). For the non-SM parameter b only an upper limit has been derived.

Within the framework of the SM, neutron beta decay is described as a purely left-handed, V−A interaction. Then, $b = 0$ and the correlation coefficients a, A, B, and C depend only on the ratio $\lambda = L_{\mathrm{A}}/L_{\mathrm{V}}$ of the weak axial-vector ($L_{\mathrm{A}}G_{\mathrm{F}}V_{\mathrm{ud}}$) to the vector ($L_{\mathrm{V}}G_{\mathrm{F}}V_{\mathrm{ud}}$) coupling constant:

$$a = \frac{1-|\lambda|^2}{1+3\,|\lambda|^2}, \quad A = -2\frac{|\lambda|^2+\lambda}{1+3\,|\lambda|^2}, \quad B = 2\frac{|\lambda|^2-\lambda}{1+3\,|\lambda|^2}, \quad \text{and} \quad C = x_C\frac{4\lambda}{1+3\,|\lambda|^2}. \tag{1.4}$$

Near the value $\lambda = -1.27$, the sensitivities of a, A, B, and C to λ are[6]:

$$\frac{\mathrm{d}a}{\mathrm{d}\lambda} = 0.298, \qquad \frac{\mathrm{d}A}{\mathrm{d}\lambda} = 0.374, \qquad \frac{\mathrm{d}B}{\mathrm{d}\lambda} = 0.076, \qquad \text{and} \qquad \frac{\mathrm{d}C}{\mathrm{d}\lambda} = -0.124. \tag{1.5}$$

The size of the weak coupling constants is important for applications in cosmology (e.g., primordial nucleosynthesis), astronomy (e.g., solar physics), and particle physics (e.g., neutrino detectors, neutrino scattering) [18, 19, 22]. The value of λ can be determined from several independent neutron decay observables, each with different sensitivity to non-SM physics. Comparing the various values of λ therefore provides an important test of the validity of the SM.

The neutron lifetime τ_{n} is inversely proportional to $|V_{\mathrm{ud}}|^2(1+3|\lambda|^2)$ [35]. Hence, independent measurements of τ_{n} and of an observable sensitive to λ allow the determination of $|V_{\mathrm{ud}}|$. Along with $|V_{\mathrm{us}}|$ and $|V_{\mathrm{ub}}|$ from K-meson and B-meson decays, respectively, the unitarity of the CKM matrix is tested [10, 36], which in turn is a test of self-consistency of the SM. Presently, $|V_{\mathrm{ud}}|$ cannot be determined reliably from neutron decay data because of very inconsistent experimental results for the neutron lifetime [10] (see also Sec. 2.2.1).

At present, the values of λ with the smallest quoted errors come from measurements of the beta asymmetry parameter A. Unfortunately, the measurements of A with the lowest quoted errors are in disagreement with earlier experiments, as can be seen from Fig. 1.1. The origin of this discrepancy is unknown, although large corrections (in the 15 − 30 % range) had to be made for, e.g., neutron polarization [37–39]. One of the most serious problems when working with polarized neutrons is the accurate knowledge of the average neutron beam polarization, where presently the error is on the 10^{-3} level [44]. A different approach to determine λ, which does not require polarized neutrons, is to measure the neutrino-electron correlation coefficient a. A measurement of a is independent of possible unknown errors in A and has entirely different systematics. However, previous measurements of a have been limited by systematic uncertainties to 5 % [40, 41], and since the late 1970s there have been no essential improvements. In addition, a precise comparison of a and A can set strict limits on possible conserved-vector-current violation and second class currents in neutron beta decay [45]. Hence, there is a great interest in improving the uncertainty in a to less than 1 %.

The neutron decay spectrometer *a*SPECT [46] has been built to perform precise measurements of the correlation coefficients a [47] and C [48], by measuring the proton recoil

---

[5] Publication of the result of the last PERKEO II run [31] is underway.

[6] Please note that in Refs. [33, 34] the sensitivities of a, A, and B are misstated with negative sign.

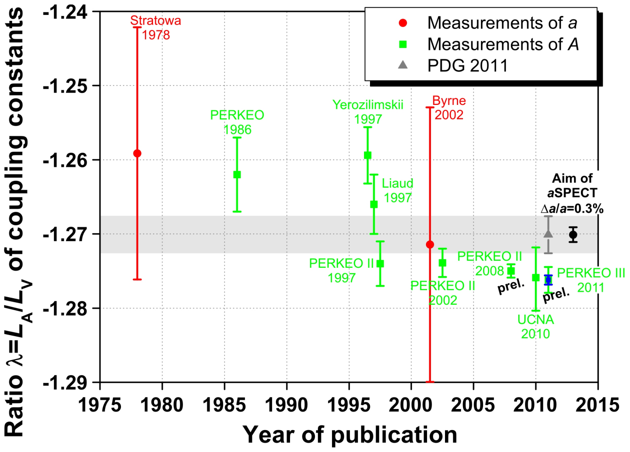

Figure 1.1: Ratio $\lambda = L_\mathrm{A}/L_\mathrm{V}$ of the weak axial-vector to the vector coupling constant, derived from measurements of correlations a (red circles, [40, 41]) and A (green squares, [18, 29, 32, 37–39, 42, 43]). In the case of PERKEO III, the error bar includes the total uncertainty of the measurement (blue square) together with the still blinded corrections (polarization, magnetic mirror effect). The black circle rightmost shows how a 0.3 % measurement of a would contribute to the determination of λ. For comparison, the grey bar represents the Particle Data Group's (PDG) 2011 average [10], where only the measurements of the correlation A are used, except for the latest results of PERKEO II and III.

spectrum in the decay of unpolarized or polarized neutrons, respectively. Since it is hard to detect the neutrino, we infer a from the shape of the proton recoil spectrum. We aim to improve the uncertainty in a and C to 0.3 % [47] and 0.1 % [48], respectively. Figure 1.1 shows how a 0.3 % measurement of a would contribute to the determination of λ.

In our first beam time at the Forschungsneutronenquelle Heinz Maier-Leibnitz in Munich, Germany, background instabilities due to particle trapping and the electronic noise level of the proton detector had prevented us from presenting a new value for a from this beam time [33, 49]. In the latest beam time at the Institut Laue-Langevin (ILL) in Grenoble, France, the trapped particle background has been reduced sufficiently and the electronic noise problem has essentially been solved [5, 50]. For the first time, a silicon drift detector was used [51]. As a result of the data analysis, we identified and fixed a problem in the detector electronics which caused a significant systematic error. The present thesis focused on the theoretical and experimental investigation of several different systematic effects. For details on the raw data analysis, the reader is referred to the theses of M. Simson [52] and M. Borg [34]. Details on detector and electronics tests and measurements of the neutron beam profile can be found in Refs. [34, 52], respectively. Measurements of the magnetic field and the development of an online nuclear magnetic resonance system are presented in the thesis of F. Ayala Guardia [53].

In Chap. 2, the theoretical basics, searches for physics beyond the SM, and previous and competing projects are presented. The measurement principles and systematics and the experimental set-up of aSPECT are described in Chap. 3. In Chaps. 4 and 5, the measurements at the ILL and the data analysis are discussed. Investigations of the patch effect, in order to improve the aSPECT spectrometer, are presented in Chap. 6. In Chap. 7, the results of the present thesis are discussed. The Apps. A to C contain additional information about the Kelvin probe samples, the design of a magnetic field return, and the new facility PERC.

Chapter 2

Neutron Beta Decay

Our understanding of the neutron has improved considerably through its description within the framework of the Standard Model (SM) of elementary particles and fields. The neutron consists of three quarks: two down quarks (d) and an up quark (u). It is stable under the strong and electromagnetic interactions, but unstable under the weak interaction: Through the emission of a virtual W gauge boson, a down quark can decay into an up quark, as shown in Fig. 2.1.

Neutron decay experiments provide one of the most sensitive means for determining the weak vector ($L_{\mathrm{V}}G_{\mathrm{F}}V_{\mathrm{ud}}$) and axial-vector ($L_{\mathrm{A}}G_{\mathrm{F}}V_{\mathrm{ud}}$) coupling constants, and the element V_{ud} of the Cabibbo-Kobayashi-Maskawa (CKM) quark-mixing matrix. Here G_{F} is the Fermi weak coupling constant. The value of L_{V} is important for testing the conserved vector current (CVC) hypothesis. The size of the weak coupling constants is important for applications in cosmology, astronomy, and particle physics [18, 19, 22].

In the framework of the SM, the CVC hypothesis requires $L_{\mathrm{V}} = 1$ for zero momentum transfer. Therefore, neutron beta decay is described by two parameters only, $\lambda = L_{\mathrm{A}}/L_{\mathrm{V}}$ and V_{ud}. The neutron lifetime τ_{n} is inversely proportional to Eq. (2.36) $|V_{\mathrm{ud}}|^2(1+3|\lambda|^2)$. Hence, independent measurements of τ_{n} and of an observable sensitive to λ, allow the determination of V_{ud}. The value of λ can be determined from several independent neutron decay observables, introduced in Sec. 2.1.4. Each observable brings a different sensitivity to non-SM physics, such that comparing the various values of λ provides an important test of the validity of the SM. Of particular interest in this context is the search for scalar and tensor interactions, discussed in Secs. 2.1.6 and 2.3. These interactions can be caused, e.g., by leptoquarks or charged Higgs bosons [20]. There are a number of other extensions of the SM. In Secs. 2.1.6 and 2.3.1 we discuss a particular kind of V+A interactions, the manifest left-right symmetric (MLRS) models, with the $SU(2)_{\mathrm{L}} \times SU(2)_{\mathrm{R}} \times U(1)_{\mathrm{B-L}}$ gauge group and right-handed charged current, approximately realized with a minimal Higgs sector.

After a short theoretical introduction to neutron beta decay, tests of and searches for physics beyond the SM in neutron decay are presented in this chapter. These searches have already been presented in Ref. [6]. I will closely follow the description therein and update the current status. The main emphasis of aSPECT and in particular of this thesis lies on the determination of the neutrino-electron angular correlation coefficient a. Hence, we also introduce the measurable parameters and spectra of neutron beta decay. Finally, we will discuss previous measurements of a and upcoming neutron decay experiments.

For more details on neutron physics and the theory of electroweak interaction, the reader is referred to recent reviews [18, 19, 54] and standard textbooks [17, 55–57].

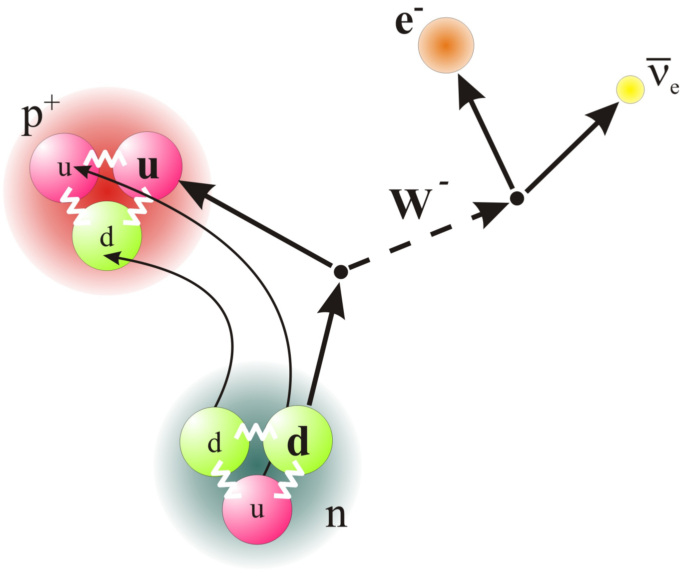

Figure 2.1: Neutron decay at the quark level: One of the down quarks (d, green) in the neutron (n) decays to an up quark (u, red), through the emission of a virtual W gauge boson, which further decays into an electron (e) and an electron-antineutrino ($\bar{\nu}_\mathrm{e}$). The gluons (Gauge bosons that participate in the strong interaction between quarks in QCD, white) hold the quarks together to form protons (p) and neutrons.

2.1 Theory of Neutron Beta Decay

Neutron beta decay is described by the weak interaction. The weak interaction, in turn, is described by the SM of elementary particles and fields.

2.1.1 The Standard Model

The SM claims that the matter in the Universe consists of elementary fermions, interacting through fields they cause. The particles related with the interaction fields are the gauge bosons. Regarding the interaction fields, the SM excludes from consideration general relativity.

The spin-1 gauge bosons of the weak interaction fields between fermions are the charged $W^\pm$ and the neutral Z bosons. The gauge boson of the electromagnetic interaction field between electrically charged fermions are the massless photons (γ's). And the postulated 8 gauge bosons of the strong interaction field are the gluons.

Two types of elementary spin-$\frac{1}{2}$ fermions are distinguished: 6 leptons and 6 quarks. Leptons interact only through the electromagnetic interaction, provided that they are charged, and the weak interaction. Quarks interact through all three fundamental forces included in the SM.

The Higgs mechanism refers to the generation of masses for the $W^\pm$ and Z weak gauge bosons through electroweak symmetry breaking [12]. The existence of the spin-0 Higgs boson is postulated to resolve inconsistencies in theoretical physics. So far, the Higgs boson is the only SM particle which has not been observed experimentally. Present experiments suggest a Higgs mass of $(115 - 200)\,\mathrm{GeV/c^2}$ [10] (more exact, the DØ collaboration [58]).

Although the SM is theoretically self-consistent, it has several deficiencies like the strong $\mathcal{CP}$ problem. In 1964, James Cronin and Val Fitch discovered $\mathcal{CP}$ violation in the decays of neutral K-mesons. This discovery earned both the 1980 Nobel Prize in Physics, as it showed that weak interaction violates not only the charge-conjugation symmetry $\mathcal{C}$ between particles and antiparticles and the parity $\mathcal{P}$, but also their combination. Parity violation was suggested in 1956 by Tsung-Dao Lee and Chen Ning Yang [59] and shortly after demonstrated by Chien-Shiung Wu [60] in the beta decay of ^{60}Co, earning Yang and Lee the 1957 Nobel Prize in Physics. The $\mathcal{CP}$ violation is incorporated in the SM by including a complex phase in the CKM matrix, describing quark mixing (see also the following section). In such theory, a necessary condition for the appearance of the complex phase is the presence of at least three quarks generations. The strong $\mathcal{CP}$ problem, in turn, is the question why quantum chromodynamic (QCD) does not seem to break the $\mathcal{CP}$ symmetry.

There are a number of attempts to explain the deficiencies of the SM; a brief overview is given in Chap. 1. In Secs. 2.1.6 and 2.3, we discuss extensions of the SM addressing these deficiencies. We note that the strong $\mathcal{CP}$ problem may also be solved within a theory of quantum gravity.

For an historical overview of the theory of the SM, the reader is referred to standard textbooks; a brief historical overview is found in Chap. 1.

2.1.2 Weak Interaction in the SM

For daily life, weak interactions are most noticeable in nuclear beta decay and in the p-p chain reaction[1] that dominates the energy generation in the sun. Beta decay also makes radiocarbon dating possible, as ^{14}C decays through the weak interaction to ^{14}N.

A neutron, e.g., is a little more massive than a proton, but it cannot decay into a proton without changing the flavor[2] of one of its two down quarks into up. Neither the electromagnetic nor the strong interaction permit flavor changing, so this must be carried out by the weak force. In fact, a down quark in the neutron can change into an up quark through the emission of a virtual W gauge boson, which, in turn, decays into an electron and an electron-antineutrino. Figure 2.1 shows an (illustrated) Feynman diagram of neutron beta decay.

The weak force was first described, in the 1930s, by Enrico Fermi's theory of a contact four-fermion (vector) interaction [61], in which the hadronic and leptonic currents interact at one vertex. In 1936, his theory was extended by George Gamow and Edward Teller to describe transitions which required the introduction of other possible (scalar) Lorentz invariants[3] [62]. In 1958, George Sudarshan and Robert Marshak [63], and also independently Richard Feynman and Murray Gell-Mann [64], incorporated the assumption of maximal parity violation into the theory, and determined the correct tensor structure (vector minus axial vector, V−A) of the four-fermion interaction. The Hamiltonian of the V−A theory has the form of a current-current interaction[4]

$$\mathcal{H}_{\mathrm{V-A}} = \frac{G_{\mathrm{F}}}{\sqrt{2}} J_\mu^\dagger \cdot J^\mu + \mathrm{h.c.}, \tag{2.1}$$

---

[1] The proton-proton chain reaction is one of several fusion reactions by which stars convert ^{1}H to (^{2}D and then) ^{4}He. The primary alternative is the CNO cycle.

[2] There are six types, also known as flavors, of quarks: up, down, charm, strange, top, and bottom.

[3] Quantities that do not change due to a Lorentz transformation, i.e., quantities that are independent of the inertial frame.

[4] In Eq.(2.1) the h.c. stands for the hermitian conjugate.

where G_F is the Fermi weak coupling constant. The current J_μ contains a hadronic and a leptonic contribution

$$J_\mu = J_\mu^\mathrm{had} + J_\mu^\mathrm{lep}. \tag{2.2}$$

The strength of Fermi's interaction is given by the Fermi weak coupling constant G_F, evaluated from the muon lifetime [10]. In modern terms [57]:

$$\frac{G_\mathrm{F}}{(\hbar c)^3} = \frac{g^2}{4\sqrt{2}m_\mathrm{W}^2} = \frac{e^2}{4\sqrt{2}m_\mathrm{W}^2 \sin^2\theta_\mathrm{W}} = 1.16637(1) \times 10^{-5}\mathrm{GeV}^{-2}, \tag{2.3}$$

where g is the coupling constant of the weak interaction, e is the electron charge, m_W is the mass of the W gauge boson, and θ_W is the Weinberg angle[5]. Due to the large mass of the gauge boson, weak decay is much more unlikely than electromagnetic or strong decay, and hence occurs less rapidly. For example, a free neutron lives about 15 minutes (see also Sec. 2.2.1).

The relative strength of the weak interaction in pure leptonic, in semileptonic, and in pure hadronic processes are not identical. This has been incorporated into the theory with the mechanism of quark mixing: In 1963, Nicola Cabibbo introduced the Cabibbo angle, θ_C, [25] to preserve the universality of the weak interaction. In his theory, the weak eigenstates of the quarks are postulated to differ from the eigenstates of the electromagnetic and strong interaction, which define the mass eigenstates. In 1973, Makoto Kobayashi and Toshihide Maskawa showed that $\mathcal{CP}$ violation in the weak interaction required more than two generations of particles [26], effectively predicting the existence of a then unknown third generation. In 2008, Kobayashi and Maskawa shared one half of the Nobel Prize in Physics for their work. In the case of the three quark families, the mixing is expressed by the Cabibbo-Kobayashi-Maskawa (CKM) matrix [25, 26]:

$$\begin{pmatrix} |d'\rangle \\ |s'\rangle \\ |b'\rangle \end{pmatrix} = \begin{pmatrix} V_\mathrm{ud} & V_\mathrm{us} & V_\mathrm{ub} \\ V_\mathrm{cd} & V_\mathrm{cs} & V_\mathrm{cb} \\ V_\mathrm{td} & V_\mathrm{ts} & V_\mathrm{tb} \end{pmatrix} \begin{pmatrix} |d\rangle \\ |s\rangle \\ |b\rangle \end{pmatrix}. \tag{2.4}$$

Here, the primes $'$ denote the weak eigenstates. For nuclear beta decay, we have

$$d' \approx V_\mathrm{ud} d = \cos\theta_\mathrm{C} d. \tag{2.5}$$

Hence, the weak interaction of the down quark introduces the matrix element V_ud into the amplitude of the hadronic current. We note that the normalization of states requires the CKM matrix to be unitary. The present status on the matrix elements and the unitarity of the CKM matrix is summarized in the Particle Data Group's (PDG) 2011 review [10] (see also Sec. 2.2.3).

Selection Rules

Beta transitions are classified in allowed and forbidden[6] decays. Allowed decays correspond to transitions in which the electron and neutrino do not carry any orbital angular

---

[5] The Weinberg angle or weak mixing angle is a parameter in the Weinberg-Salam theory. It is the angle by which spontaneous symmetry breaking rotates the original W^0 and B^0 vector boson plane, generating the Z^0 boson, and the photon (γ).

[6] Forbidden does not mean that they do not occur in nature.

momentum. Their selection rules are:

$$\Delta J = J_\mathrm{i} - J_\mathrm{f} = 0, \pm 1, \quad \text{no} \quad 0 \rightarrow 0 \tag{2.6}$$

$$\pi_\mathrm{i}\pi_\mathrm{f} = +1, \tag{2.7}$$

where J_i, J_f, π_i, and π_f are the spin and parity of the initial (i) and final (f) state of the nucleus, respectively. The parity does not change in such a transition.

The allowed transitions are subdivided into Fermi and Gamow-Teller decays. A transition mediated by the vector component does not change the spin of the nucleus (the spin of electron and antineutrino couple to a total spin $S = 0$) and is called Fermi decay. For a transition mediated by the axial-vector component the spins of electron and neutrino couple to $S = 1$; such a transition is called Gamow-Teller decay.

In the case of $J_\mathrm{i}^{\pi_\mathrm{i}} = J_\mathrm{f}^{\pi_\mathrm{f}}$, the decaying nucleon ends up in the same state where it originated, e.g., in the decay of ^{14}O to ^{14}N. Decays of this type are called superallowed decays (see also Secs. 2.2 and 2.3).

2.1.3 Neutron Beta Decay in the SM

Fermi's golden rule states that the transition rate Γ, i.e., the inverse of the lifetime, from an initial to a final state is given by

$$\Gamma = \frac{2\pi}{\hbar}|\mathcal{M}_\mathrm{fi}|^2\rho, \tag{2.8}$$

where $\mathcal{M}_\mathrm{fi}$ is the matrix element describing the interaction and ρ is the phase-space density of the final states. The matrix element $\mathcal{M}_\mathrm{fi}$ describing neutron beta decay can be constructed as a four-fermion interaction composed of hadronic and leptonic matrix elements. Assuming that vector (V), axial-vector (A), scalar (S), and tensor (T) currents are involved, the decay matrix element can be written as a sum of left-handed[7] (LH) and right-handed (RH) matrix elements:[8]

$$\mathcal{M}_\mathrm{fi} = \frac{2G_\mathrm{F}V_\mathrm{ud}}{\sqrt{2}} \sum_{j\in\{\mathrm{V,A,S,T}\}} L_j\langle \mathrm{p}|\Gamma_j|\mathrm{n}\rangle\langle \mathrm{e}^-|\Gamma_j\frac{1-\gamma_5}{2}|\nu_\mathrm{e}\rangle + R_j\langle \mathrm{p}|\Gamma_j|\mathrm{n}\rangle\langle \mathrm{e}^-|\Gamma_j\frac{1+\gamma_5}{2}|\nu_\mathrm{e}\rangle, \tag{2.9}$$

where the four types of currents are defined by the operators:

$$\Gamma_\mathrm{V} = \gamma_\mu, \quad \Gamma_\mathrm{A} = i\gamma_\mu\gamma_5, \quad \Gamma_\mathrm{S} = 1, \quad \text{and} \quad \Gamma_\mathrm{T} = \frac{i[\gamma_\mu, \gamma_\nu]}{2\sqrt{2}}. \tag{2.10}$$

Here, the γ_μ are the Dirac (gamma) matrices. The coupling constants to left-handed and right-handed neutrinos are denoted by L_j and R_j, respectively. This parametrization was introduced in Ref. [27] in order to highlight the handedness of the neutrino in the participating V,A,S,T currents. The L_j and R_j coupling constants are linear combinations of the coupling constants, C_j and C'_j, which were defined in earlier work [59]:

$$C_j = \frac{G_\mathrm{F}V_\mathrm{ud}}{\sqrt{2}}(L_j + R_j), \quad C'_j = \frac{G_\mathrm{F}V_\mathrm{ud}}{\sqrt{2}}(L_j - R_j), \quad \text{for} \quad j = \mathrm{V,\ A,\ S,\ T}. \tag{2.11}$$

---

[7] The helicity $h = \frac{\vec{\mathbf{s}}}{s} \cdot \frac{\vec{\mathbf{p}}}{p}$ of a particle is right-handed if the direction of its spin $\vec{\mathbf{s}}$ is the same as the direction of its motion $\vec{\mathbf{p}}$ ($h = +1$). It is left-handed if the directions of spin and motion are opposite ($h = -1$).

[8] In Eq. (2.9) $\frac{1-\gamma_5}{2}$ and $\frac{1+\gamma_5}{2}$ are the operators that project the neutrino field to its left-handed and right-handed part, respectively.

We emphasize that Eq. (2.9) is not the most general Hamiltonian that one can construct. In addition to V,A,S,T currents, Lee and Yang [59] allowed the possibility of pseudo-scalar (P) currents, with operator $\Gamma_\mathrm{P} = \gamma_5$. This yields ten possible couplings under the assumption that all are real (up to an overall common phase) and 20 couplings if each is allowed an imaginary component. In the latter case, time-reversal invariance, $\mathcal{T}$, may be violated. In the non-relativistic limit, the pseudo-scalar hadronic current, $\langle \mathrm{p}|\Gamma_\mathrm{P}|\mathrm{n}\rangle$, vanishes [62], therefore we neglect the pseudo-scalar term in our calculations. In addition, we neglect effects of $\mathcal{T}$ violation, i.e., we consider the remaining 8 couplings to be real.

In our tests of the SM and searches for physics beyond the SM (cf. Secs. 2.2 and 2.3), we are mainly interested in coupling constant ratios. We choose $G_\mathrm{F}V_\mathrm{ud}$ as a free parameter, therefore we are allowed to define $L_\mathrm{V} \overset{\mathrm{def}}{=} 1$ (CVC). In the SM, the only non-vanishing coupling constants are $L_\mathrm{V} = 1$ and $L_\mathrm{A} = \lambda$. In more general models, other coupling constants appear.

2.1.4 Measurable Parameters in Neutron Beta Decay

In neutron decay experiments the outgoing spins are usually not observed. Summing over these spin quantities, and neglecting the neutrino masses, one can evaluate the triple differential decay rate to be [24][9]:

$$\begin{aligned} \mathrm{d}^3\Gamma &= \frac{1}{(2\pi)^5}\frac{G_\mathrm{F}^2|V_\mathrm{ud}|^2}{2} p_\mathrm{e}E_\mathrm{e}\left(E_0-E_\mathrm{e}\right)^2 \mathrm{d}E_\mathrm{e}\mathrm{d}\Omega_\mathrm{e}\mathrm{d}\Omega_\nu \qquad (2.12)\\ &\quad \times\xi\left[1 + a\frac{\mathbf{p}_\mathrm{e}\cdot\mathbf{p}_\nu}{E_\mathrm{e}E_\nu} + b\frac{m_\mathrm{e}}{E_\mathrm{e}} + \frac{\langle\mathbf{s}_\mathrm{n}\rangle}{s_\mathrm{n}}\left(A\frac{\mathbf{p}_\mathrm{e}}{E_\mathrm{e}} + B\frac{\mathbf{p}_\nu}{E_\nu} + D\frac{\mathbf{p}_\mathrm{e}\times\mathbf{p}_\nu}{E_\mathrm{e}E_\nu}\right)\right], \end{aligned}$$

where[10] [27]:

$$\begin{aligned} \xi &= |L_\mathrm{V}|^2 + 3|L_\mathrm{A}|^2 + |L_\mathrm{S}|^2 + 3|L_\mathrm{T}|^2 + |R_\mathrm{V}|^2 + 3|R_\mathrm{A}|^2 + |R_\mathrm{S}|^2 + 3|R_\mathrm{T}|^2, && (2.13)\\ \xi a &= |L_\mathrm{V}|^2 - |L_\mathrm{A}|^2 - |L_\mathrm{S}|^2 + |L_\mathrm{T}|^2 + |R_\mathrm{V}|^2 - |R_\mathrm{A}|^2 - |R_\mathrm{S}|^2 + |R_\mathrm{T}|^2, && (2.14)\\ \xi b &= 2\Re(L_\mathrm{S}L_\mathrm{V}^* + 3L_\mathrm{A}L_\mathrm{T}^* + R_\mathrm{S}R_\mathrm{V}^* + 3R_\mathrm{A}R_\mathrm{T}^*), && (2.15)\\ \xi A &= 2\Re(-|L_\mathrm{A}|^2 - L_\mathrm{V}L_\mathrm{A}^* + |L_\mathrm{T}|^2 + L_\mathrm{S}L_\mathrm{T}^* + |R_\mathrm{A}|^2 + R_\mathrm{V}R_\mathrm{A}^* - |R_\mathrm{T}|^2 - R_\mathrm{S}R_\mathrm{T}^*), && \\ & && (2.16)\\ B &= B_0 + b_\nu\frac{m_\mathrm{e}}{E_\mathrm{e}}, \quad \text{with} && (2.17)\\ \xi B_0 &= 2\Re(|L_\mathrm{A}|^2 - L_\mathrm{V}L_\mathrm{A}^* + |L_\mathrm{T}|^2 - L_\mathrm{S}L_\mathrm{T}^* - |R_\mathrm{A}|^2 + R_\mathrm{V}R_\mathrm{A}^* - |R_\mathrm{T}|^2 + R_\mathrm{S}R_\mathrm{T}^*), && \\ & && (2.18)\\ \xi b_\nu &= 2\Re(-L_\mathrm{S}L_\mathrm{A}^* - L_\mathrm{V}L_\mathrm{T}^* + 2L_\mathrm{A}L_\mathrm{T}^* + R_\mathrm{S}R_\mathrm{A}^* + R_\mathrm{V}R_\mathrm{T}^* - 2R_\mathrm{A}R_\mathrm{T}^*), \quad \text{and} && (2.19)\\ \xi D &= 2\Im(L_\mathrm{S}L_\mathrm{T}^* - L_\mathrm{V}L_\mathrm{A}^* + R_\mathrm{S}R_\mathrm{T}^* - R_\mathrm{V}R_\mathrm{A}^*). && (2.20) \end{aligned}$$

Here $\mathbf{p}_\mathrm{e}$, $\mathbf{p}_\nu$, E_e, and E_ν are the electron (neutrino) momenta and total energies, respectively, E_0 is the maximum electron total energy, m_e the electron mass, $\mathbf{s}_n$ the neutron spin, and the Ω_i denote solid angles. Quantities a, A, B, and D are the angular correlation coefficients, while b is the Fierz interference term. The latter, and the neutrino-electron correlation coefficient a, are measurable in decays of unpolarized neutrons, while the A and

---

[9] In the modern form of the Standard Model.

[10] Please note that, here, we neglect Coulomb corrections of order α compared to Ref.[65].

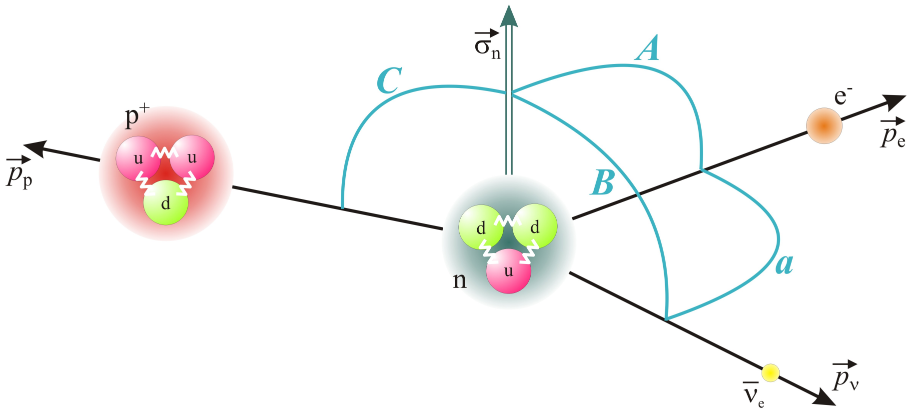

Figure 2.2: Illustration of the angular correlation coefficients a, A, B, and C. The neutron spin (green) divides the space into two hemispheres. In this example, proton and electron are emitted into the same hemisphere. The neutrino is restricted to the opposite hemisphere due to momentum conservation. The parameter a relates the electron to the neutrino momentum.

B, the beta and neutrino asymmetry parameters, respectively, require polarized neutrons (see Fig. 2.2). b_ν is another Fierz-like parameter, similar to b. We note that a, A, B_0, and D are sensitive to non-SM couplings only in second order, while b and b_ν depend in first order on L_S and L_T. A non-zero Fierz term b would indicate the existence of LH S and T interactions. A non-vanishing triple correlation coefficient D would violate $\mathcal{T}$ invariance. The most sensitive measurement of $D = (-0.96 \pm 1.89 \pm 1.01) \times 10^{-4}$ in nuclear beta decay has been conducted in the beta decay of polarized neutrons [66] (see also [67]).

If the electron spin $\mathbf{s}_\mathrm{e}$ is observed more correlation coefficients like N and R appear in the differential decay rate of neutrons [24]:

$$\begin{aligned} \mathrm{d}^2\Gamma &= \frac{1}{(2\pi)^4}\frac{G_\mathrm{F}^2|V_\mathrm{ud}|^2}{2} p_\mathrm{e}E_\mathrm{e}\left(E_0 - E_\mathrm{e}\right)^2 \mathrm{d}E_\mathrm{e}\mathrm{d}\Omega_\mathrm{e} \qquad (2.21)\\ &\times\xi\left[1 + b\frac{m_\mathrm{e}}{E_\mathrm{e}} + A\frac{\langle\mathbf{s}_\mathrm{n}\rangle}{s_\mathrm{n}}\frac{\mathbf{p}_\mathrm{e}}{E_\mathrm{e}} + \mathbf{s}_\mathrm{e}\left(N\frac{\langle\mathbf{s}_\mathrm{n}\rangle}{s_\mathrm{n}} + R\frac{\langle\mathbf{s}_\mathrm{n}\rangle}{s_\mathrm{n}} \times \frac{\mathbf{p}_\mathrm{e}}{E_\mathrm{e}} + \ldots\right)\right], \end{aligned}$$

where [27, 65]:

$$\begin{aligned} \xi N &= 2\Re(L_S L_A^* + L_V L_T^* + 2L_T L_A^* + R_S R_A^* + R_V R_T^* + 2R_T R_A^*) \qquad (2.22)\\ &+\frac{m_e}{E_e}\cdot 2\Re(|L_A|^2 + L_V L_A^* + |L_T|^2 + L_S L_T^* + |R_A|^2 + R_V R_A^* + |R_T|^2 + R_S R_T^*),\\ \xi R &= 2\Im(L_S L_A^* - L_V L_T^* + 2L_T L_A^* - R_S R_A^* + R_V R_T^* - 2R_T R_A^*) \qquad (2.23)\\ &+\alpha\frac{m_e}{p_e}\cdot 2\Re(|L_A|^2 + L_V L_A^* - |L_T|^2 - L_S L_T^* - |R_A|^2 - R_V R_A^* + |R_T|^2 + R_S R_T^*). \end{aligned}$$

Here, the neutrino momentum was averaged over. We note that N and R depend linearly on S and T couplings. First experimental values for $N = 0.065 \pm 0.012 \pm 0.004$ and $R = 0.006 \pm 0.012 \pm 0.005$ have been presented in [68, 69].

Another observable is C, the proton asymmetry relative to the neutron spin. Observables related to the proton do not appear in Eq. (2.13). However, the proton is kinematically coupled to the other decay products. Neglecting recoil-order effects and radiative corrections, the proton asymmetry parameter C is expressed by [27]:

$$C = -x_C(A + B_0) - x'_C b_\nu, \tag{2.24}$$

where $x_C = 0.27484$ and $x'_C = 0.1978$ are kinematical factors[11].

The Angular Correlation Coefficients in the Standard Model

Within the framework of the SM, neutron beta decay is described as a purely left-handed, V−A interaction. Then, the Fierz terms $b = 0$ and $b_\nu = 0$. If we permit the possibility of $\mathcal{T}$ violation, the correlation coefficients a, A, B, C, D, N, and R depend only on the ratio $\lambda = L_\mathrm{A}/L_\mathrm{V}$ of the weak axial-vector to the vector coupling constant and the phase angle ϕ between them:

$$\begin{aligned}
a &= \frac{1-|\lambda|^2}{1+3\,|\lambda|^2}, && (2.25)\\
A &= -2\frac{|\lambda|^2+|\lambda|\cos\phi}{1+3|\lambda|^2}, && (2.26)\\
B &= 2\frac{|\lambda|^2-|\lambda|\cos\phi}{1+3|\lambda|^2}, && (2.27)\\
C &= 4x_C\frac{|\lambda|\cos\phi}{1+3|\lambda|^2}, && (2.28)\\
D &= 2\frac{|\lambda|\sin\phi}{1+3|\lambda|^2}, && (2.29)\\
N &= \frac{m_\mathrm{e}}{E_\mathrm{e}}\cdot 2\frac{|\lambda|^2+|\lambda|\cos\phi}{1+3|\lambda|^2} = -\frac{m_\mathrm{e}}{E_\mathrm{e}}\cdot A, \quad \text{and} && (2.30)\\
R &= \alpha\frac{m_\mathrm{e}}{p_\mathrm{e}}\cdot 2\frac{|\lambda|^2+|\lambda|\cos\phi}{1+3|\lambda|^2} = -\alpha\frac{m_\mathrm{e}}{p_\mathrm{e}}\cdot A, && (2.31)
\end{aligned}$$

where α is the fine structure constant. If however $\mathcal{T}$ invariance is assumed, $\Im\lambda = 0$ and the triple correlation coefficient $D = 0$, and the expressions Eqs. (2.26) to (2.28) for A, B, and C reduce to the familiar expressions Eq. (1.4). When Coulomb corrections are neglected, the triple correlation coefficient $R = 0$.

The Neutron Lifetime

The neutron lifetime τ_n can be derived from the ratio $r_{\mathcal{F}t}$ of the $\mathcal{F}t^{0^+\to 0^+}$ values in superallowed $0^+ \to 0^+$ nuclear beta decays to the equivalent quantity in neutron decay, $\mathcal{F}t^\mathrm{n}$:

$$r_{\mathcal{F}t} = \frac{\mathcal{F}t^{0^+\to 0^+}}{\mathcal{F}t^\mathrm{n}} = \frac{\mathcal{F}t^{0^+\to 0^+}}{f^\mathrm{n}t(1+\delta'_R)} = \frac{\mathcal{F}t^{0^+\to 0^+}}{f_R\ln(2)}\cdot\tau_\mathrm{n}^{-1}, \tag{2.32}$$

where

$$f^\mathrm{n} = \frac{1}{{m_\mathrm{e}}^5}\int\limits_{m_\mathrm{e}}^{E_0} \mathrm{d}E_\mathrm{e}\,F(1,E_\mathrm{e})\,p_\mathrm{e}E_\mathrm{e}\,(E_0-E_\mathrm{e})^2\,[1+R_0(E_\mathrm{e})] = 1.6887 \tag{2.33}$$

---

[11] Please note that we define C with the opposite sign compared to Refs. [27, 28] to adhere to the convention that a positive asymmetry indicates that more particles are emitted in the direction of spin.

is a statistical phase-space factor [36]. The factor f^{n} includes a correction for the Coulomb attraction of the final states known as the Fermi function Eq. (2.52) $F\left(Z, E_{\mathrm{e}}\right)$[12] as well as smaller recoil corrections Eq. (2.56) $R_0(E_{\mathrm{e}})$. The nucleus-dependent (outer) radiative correction δ_R', and $\mathcal{O}(\alpha^2)$ corrections [35, 70, 71], change f^{n} by $\sim 1.5\,\%$ to $f_R = 1.71385(34)$[13]. The corrections implicitly assume the validity of the V−A theory [73]. The dependence of $r_{\mathcal{F}t}$ on the coupling constants L_j and R_j is given in Ref. [27]:

$$r_{\mathcal{F}t} = \frac{\xi}{\xi_{\mathrm{F}}}, \tag{2.34}$$

where[14]

$$\xi_{\mathrm{F}} = 2(|L_{\mathrm{V}}|^2 + |L_{\mathrm{S}}|^2 + |R_{\mathrm{V}}|^2 + |R_{\mathrm{S}}|^2). \tag{2.35}$$

Within the framework of the SM, the matrix element $|V_{\mathrm{ud}}|$ can be determined from the neutron decay rate Γ respectively the neutron lifetime τ_{n} and λ [35, 36]:

$$\begin{aligned} \tau_{\mathrm{n}}^{-1} &= \Gamma = \int \mathrm{d}^3\Gamma = \frac{m_{\mathrm{e}}^5 c^4}{2\pi^3\hbar^7}(|L_{\mathrm{V}}|^2 + 3|L_{\mathrm{A}}|^2) f^{\mathrm{n}}(1+\delta_R')(1+\Delta_R^{\mathrm{V}}) \\ &= \frac{|V_{\mathrm{ud}}|^2\left(1+3|\lambda|^2\right)}{(4908.7 \pm 1.9)\mathrm{s}}, \end{aligned} \tag{2.36}$$

where $\Delta_R^{\mathrm{V}} = 2.361(38)\%$ considers the inner (nucleus-independent) radiative correction [76].

The present status on the correlation coefficients a, A, B, C, D, N, and R, the Fierz terms b and b_ν, and the neutron lifetime τ_n is summarized in Ref. [19] (see also Sec. 2.2.1). For D and R and the non-SM parameters b and b_ν only upper limits have been measured.

In the following, we assume $\mathcal{T}$ invariance and therefore $D = 0$. In addition, we disregard the recent results for N and R [68, 69], as they lack the precision to have an impact on our analysis.

2.1.5 The Proton and Lepton Spectra

The main emphasis of aSPECT and in particular of this thesis is on the determination of the angular correlation coefficient a. For unpolarized neutron decay, we rewrite the differential decay rate Eq. (2.13):

$$\mathrm{d}^3\Gamma \propto 1 + a\beta\cos\theta_{\mathrm{e}\nu} + b\frac{m_{\mathrm{e}}}{E_{\mathrm{e}}}, \tag{2.37}$$

where $\beta = \frac{v_{\mathrm{e}}}{c}$ is the electron's velocity in units of the velocity of light and $\theta_{\mathrm{e}\nu}$ is the angle between the directions of the electron and the electron-antineutrino. As discussed earlier

---

[12] For neutron, and generally nuclear, decays Z denotes the atomic number of the daughter nucleus, i.e., $Z = 1$ for neutron beta decay.

[13] The most recently published value of $f_R = 1.71335(15)$ [72] used $f^{\mathrm{n}} = 1.6886$, and did not include the corrections by Marciano and Sirlin [35]. Applying the Towner and Hardy prescription for splitting the radiative corrections [71] increases the uncertainty in f_R slightly, to reproduce Eq. (18) in Ref. [35].

[14] Compared with Ref. [74], here, the factor 2 in Eq. (2.35) considers the nuclear matrix element $\mathcal{M}_{\mathrm{F}}$ (see also [75]). For superallowed Fermi beta decay transitions between spin $J^\pi = 0^+$, isospin $T = 1$, states, the Fermi matrix element becomes $|\mathcal{M}_{\mathrm{F}}|^2 = |\mathcal{M}_{\mathrm{F}}^0|^2(1-\delta_C^{\mathrm{V}})$, with $\mathcal{M}_{\mathrm{F}}^0 = \sqrt{2}$. Here, δ_C^{V} is the isospin-symmetry-breaking correction.

in Chap. 1, the neutrino is hard to detect. Thus, a must be inferred from the electron and proton momenta instead. One approach is to measure the angular correlation between both momenta and to derive the correlation coefficient a from it via momentum conservation. An alternative approach is to infer a from the shape of the proton recoil spectrum.

The Proton Recoil Spectrum

Nachtmann calculated relativistic corrections to the recoil spectrum in neutron beta decay [77][15]. Based on his description of the proton recoil spectrum, Dawber *et al.* showed that the spectrum is linearly dependent on the correlation coefficient a [79]:

$$w_{\mathrm{p},[\mathrm{Nac68}]}(T_\mathrm{p}) \quad \propto \quad g_1(T_\mathrm{p}) + a \cdot g_2(T_\mathrm{p}), \tag{2.38}$$

where $T_\mathrm{p} = E_\mathrm{p} - m_\mathrm{p}$ is the proton kinetic energy. Neglecting Coulomb[16] and radiative corrections, the functions g_1 and g_2 are expressed by [79]:

$$g_1(T) = \left(1 - \frac{x^2}{\sigma(T)}\right)^2 \sqrt{1-\sigma(T)} \left[4\left(1 + \frac{x^2}{\sigma(T)}\right) - \frac{4}{3}\frac{\sigma(T) - x^2}{\sigma(T)}(1-\sigma(T))\right], \tag{2.39}$$

$$g_2(T) = \left(1 - \frac{x^2}{\sigma(T)}\right)^2 \sqrt{1-\sigma(T)} \left[4\left(1 + \frac{x^2}{\sigma(T)} - 2\sigma(T)\right) - \frac{4}{3}\frac{\sigma(T) - x^2}{\sigma(T)}(1-\sigma(T))\right], \tag{2.40}$$

where

$$\sigma(T) = 1 - 2Tm_\mathrm{n}/\Delta^2, \tag{2.41}$$

$$x = m_\mathrm{e}/\Delta, \quad \text{and} \quad \Delta = m_\mathrm{n} - m_\mathrm{p} \overset{[10]}{=} 1293.333(33)\mathrm{keV/c}^2. \tag{2.42}$$

Here, m_n and m_p are the masses of the neutron and proton, respectively.

Figure 2.3 shows the influence of the correlation coefficient a on the proton recoil spectrum. With the recommended value for $a = -0.103$ [10], this is about a 10 % effect.

A positive neutrino-electron correlation a increases the average proton momentum and shifts the spectral shape to favor higher energy. A negative correlation a has the opposite effect. This means that we simply measure the shape of $w_{\mathrm{p},[\mathrm{Nac68}]}(T)$ and fit it to determine a. This method has the advantage of requiring the detection of only one particle per decay, that comes along with a larger event rate. Neutron beam densities are typically low and the neutron lifetime is long (≈ 15 min [10]), so a larger event rate is important for high statistical precision. Thus, this has been the favored method in past experiments.

On the other hand, this method presents significant challenges. The maximum proton kinetic energy is only ≈ 751 eV (cf. Eq. (2.46)), so decay protons must be accelerated to much higher energy to be detected, typically to about (10 − 30) keV. Then, the proton energy must be precisely measured prior to acceleration. This can be done by means of an electrostatic filter or by time-of-flight (TOF) measurement. In both cases only one component of the proton's velocity is measured and its total energy must be inferred. Experience has shown that controlling the measurement systematics presents by far the greatest challenge, cf. Sec. 2.4.1. Amongst others, electric fields and space charges must

---

[15] A sign error in this formula was found by C. Habeck [78]. In the last line of Eq. (4.5) in Ref. [77] the expression $\sigma + x^2$ should be changed to $\sigma - x^2$.

[16] The Coulomb correction $F(E_\mathrm{e})$ to the electron energy spectrum is discussed in the following section.

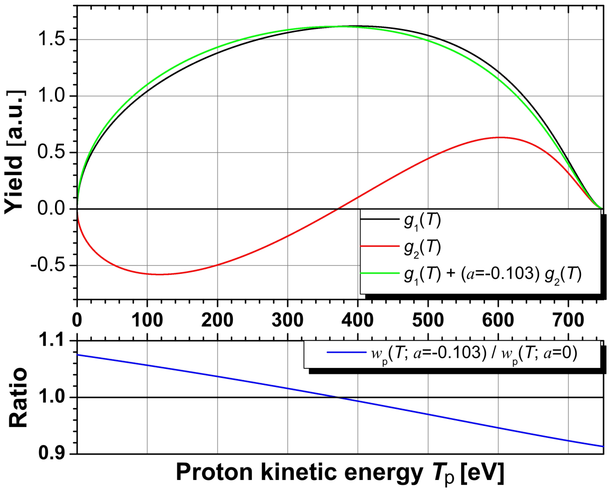

Figure 2.3: The theoretical proton recoil spectrum Eq. (2.38) in neutron beta decay. Top: The green line is the prediction from the SM with the recommended value for $a = -0.103$ [10], the black line shows how a deviation from that ($a = 0$) would look like. For elucidation of the influence of the correlation a on the proton spectrum $w_{\mathrm{p,[Nac68]}}(T_{\mathrm{p}})$, the red line shows the function $g_2(T_{\mathrm{p}})$ from Eq. (2.40). Bottom: The blue line shows the ratio $w_{\mathrm{p,[Nac68]}}(T_{\mathrm{p}}; a = -0.103)/w_{\mathrm{p,[Nac68]}}(T_{\mathrm{p}}; a = 0)$, to illustrate the dependence of $w_{\mathrm{p,[Nac68]}}(T_{\mathrm{p}})$ on a.

be carefully controlled and proton scattering from residual gas molecules must be avoided, in order not to distort the proton recoil spectrum (discussed in greater detail in Sec. 3.4 and Chap. 6).

For most of the investigations of systematic effects, the above description of the proton recoil spectrum is sufficient. On the other hand, most of the Monte Carlo (MC) simulations were performed in the infinite nucleon mass (INM) approximation[17] [27] (see also the following section), including the Coulomb correction to the electron energy spectrum.

For the analysis of measurement data, a more suitable description of the spectrum is mandatory [74], denoted as

$$w_{\mathrm{p,C},\alpha}(E_{\mathrm{p}}) = w_{\mathrm{p,C}}(E_{\mathrm{p}}) \cdot [1 + 0.01 r_{\mathrm{C}}(y)]\,[1 + 0.01 r_{\rho} + 0.01 r_{\mathrm{p}}(y)]\,. \tag{2.43}$$

This description comprises [74] (cf. Eqs. (3.1) to (3.12) in Ref. [74])

- the proton spectrum $w_{\mathrm{p,C}}(E_{\mathrm{p}})$, including the $\hat{F}(E_{\mathrm{e}}, E_{\mathrm{p}}) = 1 + \frac{\pi\alpha}{\beta}$ approximation[18],
- the higher-order Coulomb correction $r_{\mathrm{C}}(y)$ to the proton energy spectrum,
- the model-independent order-α correction $r_{\rho} = 1.505$ to the total decay rate, and
- the radiative correction $r_{\mathrm{p}}(y)$ to the proton energy spectrum,

---

[17] In the INM approximation $m_{\mathrm{n}} \to \infty$, $m_{\mathrm{p}} \to \infty$ limit, with $m_{\mathrm{n}} - m_{\mathrm{p}}$ equal to the finite, true value. In this case only the longitudinal momentum components (the $\mathbf{p}_{\nu}\mathbf{s}_{\mathrm{n}}$, $\mathbf{p}_{\mathrm{e}}\mathbf{s}_{\mathrm{n}}$, $\mathbf{p}_{\mathrm{p}}\mathbf{s}_{\mathrm{n}}$ projections) are constrained by the integration region, and we can integrate over ϕ_{e} and ϕ_{ν}. As input for our MC simulations, we have used $m_{\mathrm{n}} = 1\,\mathrm{MeV/c}^2$.

[18] In the $\hat{F}(E_{\mathrm{e}}, E_{\mathrm{p}})$ Coulomb correction, we take into account the proton energy dependence of the proton recoil.

with

$$E_\mathrm{p} = m_\mathrm{p} + (E_\mathrm{p,max} - m_\mathrm{p})y. \tag{2.44}$$

Here and in the following, we assume w.l.o.g. $c = 1$ and massless neutrinos ($m_\nu = 0$). Then,

$$E_\mathrm{p,max} = m_\mathrm{p} + \frac{\Delta^2 - m_\mathrm{e}^2}{2m_\mathrm{n}} \overset{[10]}{=} 938.272764(23)\mathrm{MeV}^2, \tag{2.45}$$

i.e.,

$$T_\mathrm{p,max} = E_\mathrm{p,max} - m_\mathrm{p} \overset{[10]}{=} 751(33)\mathrm{eV}^2. \tag{2.46}$$

The corrections r_C and r_p are tabulated in Tables III and IV in Ref. [74], and are linearly extrapolated to the proton energy regime.

To fit MC simulated data, we have used an approximation of $w_\mathrm{p,C}(E_\mathrm{p})$ as given in [74] (cf. Eq. (3.12) in Ref. [74]), only including the $\hat{F}(E_\mathrm{e}, E_\mathrm{p})$ approximation. The relative effect of this method on the correlation coefficient a is smaller than 0.1 % (see also Fig. 2.5b).

The Lepton Spectra

Using Fermi's golden rule Eq. (2.8), the decay probability of neutrons is:

$$\mathrm{d}\Gamma(E_\mathrm{e}) = \frac{2\pi}{\hbar}|\mathcal{M}_\mathrm{fi}|^2 \mathrm{d}\rho_\mathrm{e}(E_\mathrm{e}), \tag{2.47}$$

where the electron energy spectrum is given by

$$\mathrm{d}\rho_\mathrm{e}(E_\mathrm{e}) = w_\mathrm{e}(E_\mathrm{e})\mathrm{d}E_\mathrm{e}, \tag{2.48}$$

with

$$w_\mathrm{e}(E_\mathrm{e}) = \frac{(4\pi)^2}{(2\pi\hbar)^6} F(1, E_\mathrm{e}) \sqrt{E_\mathrm{e}^2 - m_\mathrm{e}^2} E_\mathrm{e} \left(E_0 - E_\mathrm{e}\right)^2 \left[1 + \delta_R(E_\mathrm{e})\right] \left[1 + R_0(E_\mathrm{e})\right]. \tag{2.49}$$

Here,

$$E_0 \overset{\mathrm{def}}{=} E_\mathrm{e,max} = \Delta - \frac{\Delta^2 - m_\mathrm{e}^2}{2m_\mathrm{n}} \overset{[10]}{=} 1292.582(32)\mathrm{keV}^2, \tag{2.50}$$

i.e.,

$$T_\mathrm{e,max} = E_\mathrm{e,max} - m_\mathrm{e} \overset{[10]}{=} 781.583(32)\mathrm{keV}^2. \tag{2.51}$$

Equation (2.49) includes (cf., e.g., [80])

- the Coulomb correction by the Fermi function[19] [70] (see also [81])

$$F(Z, E_\mathrm{e}) = \frac{2\pi\eta}{1 - \exp(-2\pi\eta)}, \quad \text{with} \quad \eta = \pm\frac{Z\alpha}{\beta}, \tag{2.52}$$

---

[19] Here Z is the atomic number of the daughter nucleus and the $-$ sign refers to nuclear decays with positron emission.

- the outer radiative correction [73]

$$\begin{aligned} \delta_R(E_\mathrm{e}) \quad = \quad & \frac{\alpha}{2\pi}\left[3\ln\frac{m_\mathrm{p}}{m_\mathrm{e}}-\frac{3}{4}\right. \\ & +4\left(\frac{\operatorname{arctanh}\beta}{\beta}-1\right)\left(\frac{E_0-E_\mathrm{e}}{3E_\mathrm{e}}-\frac{3}{2}+\ln\frac{2\left(E_0-E_\mathrm{e}\right)}{m_\mathrm{e}}\right) \\ & +\frac{4}{\beta}L\left(\frac{2\beta}{1+\beta}\right) \\ & \left.+\frac{\operatorname{arctanh}\beta}{\beta}\left(2\left(1+\beta^2\right)+\frac{\left(E_0-E_\mathrm{e}\right)^2}{6E_\mathrm{e}^2}-4\operatorname{arctanh}\beta\right)\right], \end{aligned} \tag{2.53}$$

with the Spence's function $L(z)=-\mathrm{Li}_2(z)$, where Li_2 is the dilogarithm, i.e.:

$$L(z)=\int_0^z dt\frac{\ln|1-t|}{t}, \tag{2.54}$$

- and the recoil correction [70, 74]

$$\begin{aligned} R_0(E_\mathrm{e}) \quad = \quad & \frac{1}{1+3\lambda^2}\left[2\frac{E_\mathrm{e}}{m_\mathrm{n}}+\lambda^2\left(10\frac{E_\mathrm{e}}{m_\mathrm{n}}-2\frac{m_\mathrm{e}^2}{m_\mathrm{n}E_\mathrm{e}}-2\frac{E_0}{m_\mathrm{n}}\right)\right. \\ & \left.+\lambda\left(1+2\kappa\right)\left(-4\frac{E_\mathrm{e}}{m_\mathrm{n}}+2\frac{m_\mathrm{e}^2}{m_\mathrm{n}E_\mathrm{e}}+2\frac{E_0}{m_\mathrm{n}}\right)\right], \end{aligned} \tag{2.55}$$

where $\kappa=\frac{f_2}{f_1'}\approx\frac{\mu_\mathrm{p}-\mu_\mathrm{n}}{2}\approx 1.85$ [70] is the weak magnetism form factor.

In the INM approximation, we only include the Coulomb correction to the electron energy spectrum, with the approximation of Eq.(2.52) [74]:

$$F(1,E_\mathrm{e})\approx 1+\frac{\pi\alpha}{\beta}+\alpha^2\left(\frac{11}{4}-\gamma_E-\ln\left(2\beta E_\mathrm{e}R\right)+\frac{\pi^2}{3\beta^2}\right), \tag{2.56}$$

where

$$R\approx 1\,\mathrm{fm}\approx\frac{0.01}{4m_\mathrm{e}}\quad\text{and}\quad\gamma_E\approx 0.5772. \tag{2.57}$$

The electron energy spectrum in the INM approximation is shown in Fig. 2.4a.

In analogy to Eq. (2.48), the electron-antineutrino energy spectrum can be written as:

$$\mathrm{d}\rho_\nu(E_\nu)=\frac{(4\pi)^2}{(2\pi\hbar)^6}\sqrt{\left(E_{\nu,\mathrm{max}}+m_\mathrm{e}-E_\nu\right)^2-m_\mathrm{e}^2}\left(E_{\nu,\mathrm{max}}+m_\mathrm{e}-E_\nu\right)E_\nu^2\mathrm{d}E_\nu, \tag{2.58}$$

where

$$T_{\nu,\mathrm{max}}\equiv E_{\nu,\mathrm{max}}=\Delta-\frac{m_\mathrm{p}}{m_\mathrm{n}}m_\mathrm{e}-\frac{\Delta^2+m_\mathrm{e}^2}{2m_\mathrm{n}}\overset{[10]}{=}782.008(33)\mathrm{keV}^2. \tag{2.59}$$

The electron-antineutrino spectrum in the INM approximation is shown in Fig. 2.4b. Figure 2.5a shows the influence of the Coulomb correction Eq. (2.56), in the INM

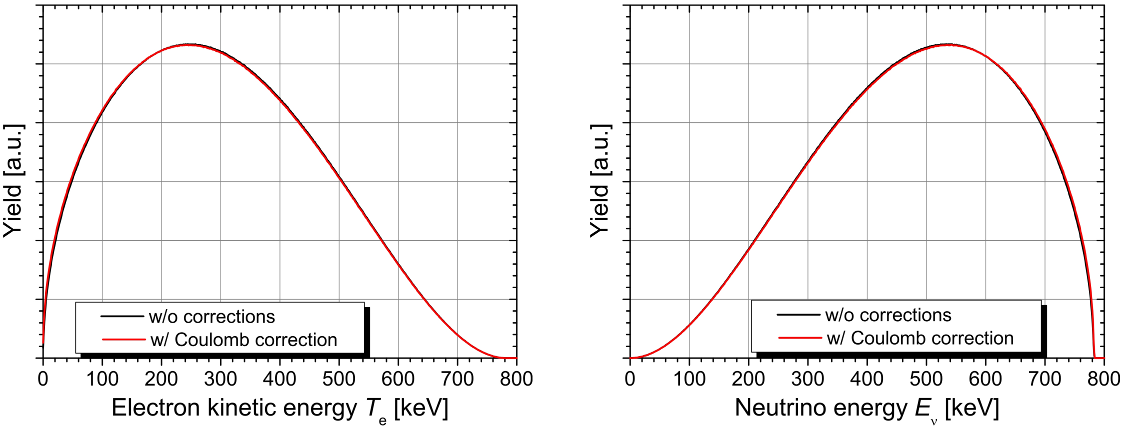

(a) (b)

Figure 2.4: The theoretical (a) electron and (b) electron-antineutrino energy spectra in neutron beta decay, in the INM approximation. The comparison between the black and the red line shows the influence of the Coulomb correction Eq. (2.56) on the lepton spectra, see also Fig. 2.5a. For details see the text. Input data for the MC simulation: Number of generated events $= 10^9$ and $a = -0.105$ (derived from $\lambda = -1.2701(25)$ [10]).

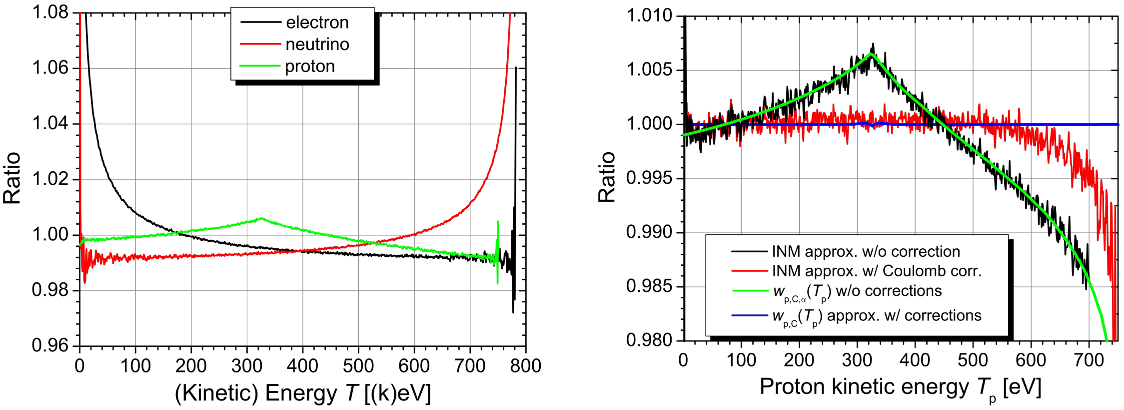

(a) (b)

Figure 2.5: Influence of several corrections on the proton and lepton energy spectra: (a) The ratios $w(T; \text{w/ } F(1, E_e)$ from Eq. (2.56)$)/w(T; \text{w/o } F(1, E_e))$ show the influence of the Coulomb correction Eq. (2.56), in the INM approximation, on the lepton and proton energy spectra. (b) The ratios $w_{p,C,\alpha}(T_p)/w_p(T_p)$ show the influence of several approximations and/or corrections on the proton recoil spectrum Eq. (2.43). The comparison between the black, the red, and the blue line shows that the higher-order Coulomb correction $r_C(y)$, the model-independent order-α correction r_ρ, and the radiative correction $r_p(y)$ have a rather small impact on the proton recoil spectrum, primarily at high proton kinetic energies. For reference, the comparison between the black and the green line shows the uncertainty resulting from the MC simulation. For details see the text. Input data for the MC simulation (in INM approximation): Number of generated events $= 10^9$ and $a = -0.105$ (derived from $\lambda = -1.2701(25)$ [10]).

approximation, on the lepton and proton spectra. With the recommended value for $\lambda = -1.2701(25)$ [10], this is about a 1 % effect. For reference, Fig. 2.5b shows the influence of several approximations and corrections on the proton recoil spectrum Eq. (2.43). As one can see, the higher-order Coulomb correction $r_{\mathrm{C}}(y)$, the model-independent order-α correction r_ρ, and the radiative correction $r_{\mathrm{p}}(y)$ (for details see the previous section) have a rather small impact on the proton recoil spectrum and primarily at higher proton kinetic energies.

2.1.6 Extensions of the Standard Model

There are a number of extensions to the SM. The question, which theory is the right one, can only be settled by experiments. Therefore, the search for physics beyond the SM is one of the most active areas both in theoretical and experimental physics. Of particular interest in the context of this thesis are the search for S and T interactions and for RH currents.

The V$-$A description of neutron beta decay omits S and T interactions as described by Eq. (2.9). Two possible models of these non-SM interactions can be tested using neutron decay observables:

Left-Handed S and T Interactions

In the LH S and T model, non-vanishing Fierz interference terms b and b_ν appear. The remaining free parameters are L_{V}, L_{A}, L_{S}, and L_{T}. The dependence of a, b, A, B_0, b_ν, and C on these parameters follows from Eqs. (2.13) to (2.19), and (2.24):

$$
\begin{aligned}
a &= \frac{L_{\mathrm{V}}^2 - L_{\mathrm{A}}^2 - L_{\mathrm{S}}^2 + L_{\mathrm{T}}^2}{L_{\mathrm{V}}^2 + 3L_{\mathrm{A}}^2 + L_{\mathrm{S}}^2 + 3L_{\mathrm{T}}^2} = \frac{1 - \lambda^2 - x^2 + \lambda^2 y^2}{1 + 3\lambda^2 + x^2 + 3\lambda^2 y^2}, && (2.60)\\
b &= 2\frac{L_{\mathrm{V}} L_{\mathrm{S}} + 3L_{\mathrm{A}} L_{\mathrm{T}}}{L_{\mathrm{V}}^2 + 3L_{\mathrm{A}}^2 + L_{\mathrm{S}}^2 + 3L_{\mathrm{T}}^2} = 2\frac{x + 3\lambda^2 y}{1 + 3\lambda^2 + x^2 + 3\lambda^2 y^2}, && (2.61)\\
A &= -2\frac{L_{\mathrm{A}}^2 + L_{\mathrm{V}} L_{\mathrm{A}} - L_{\mathrm{S}} L_{\mathrm{T}} - L_{\mathrm{T}}^2}{L_{\mathrm{V}}^2 + 3L_{\mathrm{A}}^2 + L_{\mathrm{S}}^2 + 3L_{\mathrm{T}}^2} = -2\frac{\lambda^2 + \lambda - \lambda x y - \lambda^2 y^2}{1 + 3\lambda^2 + x^2 + 3\lambda^2 y^2}, && (2.62)\\
B_0 &= 2\frac{L_{\mathrm{A}}^2 - L_{\mathrm{V}} L_{\mathrm{A}} - L_{\mathrm{S}} L_{\mathrm{T}} + L_{\mathrm{T}}^2}{L_{\mathrm{V}}^2 + 3L_{\mathrm{A}}^2 + L_{\mathrm{S}}^2 + 3L_{\mathrm{T}}^2} = 2\frac{\lambda^2 - \lambda - \lambda x y + \lambda^2 y^2}{1 + 3\lambda^2 + x^2 + 3\lambda^2 y^2}, \quad \text{and} && (2.63)\\
b_\nu &= -2\frac{L_{\mathrm{V}} L_{\mathrm{T}} + L_{\mathrm{A}} L_{\mathrm{S}} - 2L_{\mathrm{A}} L_{\mathrm{T}}}{L_{\mathrm{V}}^2 + 3L_{\mathrm{A}}^2 + L_{\mathrm{S}}^2 + 3L_{\mathrm{T}}^2} = -2\frac{\lambda y + x - 2\lambda^2 y}{1 + 3\lambda^2 + x^2 + 3\lambda^2 y^2}, && (2.64)\\
C &= 4x_C \frac{L_{\mathrm{V}} L_{\mathrm{A}} - L_{\mathrm{T}}^2}{L_{\mathrm{V}}^2 + 3L_{\mathrm{A}}^2 + L_{\mathrm{S}}^2 + 3L_{\mathrm{T}}^2} = 4x_C \frac{\lambda - \lambda^2 y^2}{1 + 3\lambda^2 + x^2 + 3\lambda^2 y^2}, && (2.65)
\end{aligned}
$$

where the neutron decay observables[20] are expressed by three free parameters:

$$\lambda = \frac{L_{\mathrm{A}}}{L_{\mathrm{V}}}, \quad x = \frac{L_{\mathrm{S}}}{L_{\mathrm{V}}}, \quad \text{and} \quad y = \frac{L_{\mathrm{T}}}{L_{\mathrm{A}}}. \tag{2.66}$$

The direct determination of b through beta spectrum shape measurement is the most sensitive way to constrain the size of the non-SM currents. The experiments discussed in Sec. 2.2.1 measure the correlation coefficients from the electron spectra and asymmetries, respectively. The published results on a, A, B, and C assume $b = b_\nu = 0$. To make use

---

[20] Please note that, here, we omit the neutron lifetime τ_{n}, since otherwise we would have to determine the possible influence of the Fierz term in Fermi decays, b_{F}, on the $\mathcal{F}t^{0^+\to 0^+}$ values. A combined analysis of neutron and superallowed $0^+ \to 0^+$ nuclear beta decays is found in Sec. 2.3.2.

of measured values of a in a scenario involving a non-zero value for the Fierz term b, we rewrite Eq. (2.13) for unpolarized neutron decay:

$$d^3\Gamma \propto \left(1 + a\frac{\mathbf{p}_\mathrm{e}\cdot\mathbf{p}_\nu}{E_\mathrm{e}E_\nu} + b\frac{m_\mathrm{e}}{E_\mathrm{e}}\right) \approx \left(1 + bm_\mathrm{e}\left\langle E_\mathrm{e}^{-1}\right\rangle\right)\left(1 + \frac{a}{1 + bm_\mathrm{e}\left\langle E_\mathrm{e}^{-1}\right\rangle}\frac{\mathbf{p}_\mathrm{e}\cdot\mathbf{p}_\nu}{E_\mathrm{e}E_\nu}\right). \tag{2.67}$$

The value quoted for a is then taken as a measurement of $\bar{a}$, defined through

$$\bar{a} = \frac{a}{1 + bm_\mathrm{e}\left\langle E_\mathrm{e}^{-1}\right\rangle}. \tag{2.68}$$

Here $\langle\cdot\rangle$ denotes the weighted average over the part $[E_{\mathrm{e},1}, E_{\mathrm{e},2}]$ of the beta spectrum Eq. (2.49) observed in the particular experiment

$$\left\langle E_\mathrm{e}^{-1}\right\rangle = \frac{1}{f}\int_{E_{\mathrm{e},1}}^{E_{\mathrm{e},2}} dE_\mathrm{e}F(1, E_\mathrm{e})p_\mathrm{e}\left(E_0 - E_\mathrm{e}\right)^2\left[1 + \delta_R(E_\mathrm{e})\right]\left[1 + R_0(E_\mathrm{e})\right], \tag{2.69}$$

where the statistical rate function f is given by:

$$f = \int_{m_\mathrm{e}}^{E_0} dE_\mathrm{e}w_\mathrm{e}(E_\mathrm{e}). \tag{2.70}$$

This procedure has been also applied in Refs. [17, 27, 76]. Reported experimental values of A, B, and C are interpreted as measurements of

$$\bar{A} = \frac{A}{1 + bm_\mathrm{e}\left\langle E_\mathrm{e}^{-1}\right\rangle}, \quad \bar{B} = \frac{B_0 + b_\nu m_\mathrm{e}\left\langle E_\mathrm{e}^{-1}\right\rangle}{1 + bm_\mathrm{e}\left\langle E_\mathrm{e}^{-1}\right\rangle}, \quad \bar{C} = \frac{-x_C(A + B_0) - x'_C b_\nu}{1 + bm_\mathrm{e}\left\langle E_\mathrm{e}^{-1}\right\rangle}, \tag{2.71}$$

assuming integration over all electrons. This procedure is not perfect. The presence of a Fierz term b might influence systematic uncertainties. For example, the background estimate in PERKEO II assumes the SM dependence of the measured count rate asymmetry on E_e. The term $m_\mathrm{e}\left\langle E_\mathrm{e}^{-1}\right\rangle$ depends on the part of the electron spectrum used in each experiment.

Right-Handed S and T Interactions

In the RH S and T model, the Fierz terms b and b_ν are zero [17]. The remaining free parameters are L_V, L_A, R_S, and R_T. The dependence of a, A, B, C, and τ_n on these parameters follows from Eqs. (2.13) to (2.17), (2.24), and (2.32) and (2.34):

$$\begin{aligned}
a &= \frac{L_\mathrm{V}^2 - L_\mathrm{A}^2 - R_\mathrm{S}^2 + R_\mathrm{T}^2}{L_\mathrm{V}^2 + 3L_\mathrm{A}^2 + R_\mathrm{S}^2 + 3R_\mathrm{T}^2} = \frac{1 - \lambda^2 - x^2 + \lambda^2y^2}{1 + 3\lambda^2 + x^2 + 3\lambda^2y^2}, && (2.72)\\
A &= -2\frac{L_\mathrm{A}^2 + L_\mathrm{V}L_\mathrm{A} + R_\mathrm{S}R_\mathrm{T} + R_\mathrm{T}^2}{L_\mathrm{V}^2 + 3L_\mathrm{A}^2 + R_\mathrm{S}^2 + 3R_\mathrm{T}^2} = -2\frac{\lambda^2 + \lambda + \lambda xy + \lambda^2y^2}{1 + 3\lambda^2 + x^2 + 3\lambda^2y^2}, && (2.73)\\
B &= 2\frac{L_\mathrm{A}^2 - L_\mathrm{V}L_\mathrm{A} + R_\mathrm{S}R_\mathrm{T} - R_\mathrm{T}^2}{L_\mathrm{V}^2 + 3L_\mathrm{A}^2 + R_\mathrm{S}^2 + 3R_\mathrm{T}^2} = 2\frac{\lambda^2 - \lambda + \lambda xy - \lambda^2y^2}{1 + 3\lambda^2 + x^2 + 3\lambda^2y^2}, && (2.74)\\
C &= 4x_C\frac{L_\mathrm{V}L_\mathrm{A} + R_\mathrm{T}^2}{L_\mathrm{V}^2 + 3L_\mathrm{A}^2 + R_\mathrm{S}^2 + 3R_\mathrm{T}^2} = 4x_C\frac{\lambda + \lambda^2y^2}{1 + 3\lambda^2 + x^2 + 3\lambda^2y^2}, \quad \text{and} && (2.75)\\
\tau_\mathrm{n} &= \frac{\mathcal{F}t^{0^+\to0^+}}{f_R\ln(2)}\frac{2(L_\mathrm{V}^2 + R_\mathrm{S}^2)}{L_\mathrm{V}^2 + 3L_\mathrm{A}^2 + R_\mathrm{S}^2 + 3R_\mathrm{T}^2} = \frac{\mathcal{F}t^{0^+\to0^+}}{f_R\ln(2)}\frac{2(1 + x^2)}{1 + 3\lambda^2 + x^2 + 3\lambda^2y^2}, && (2.76)
\end{aligned}$$

where the neutron decay observables are expressed by three free parameters:

$$\lambda = \frac{L_\mathrm{A}}{L_\mathrm{V}}, \quad x = \frac{R_\mathrm{S}}{L_\mathrm{V}}, \quad \text{and} \quad y = \frac{R_\mathrm{T}}{L_\mathrm{A}}. \tag{2.77}$$

Left-Right Symmetric Models

An electrically charged gauge boson outside the SM is generically denoted W'. The most attractive candidate for W' is the W_{R} gauge boson associated with the left-right symmetric models [82, 83], which seek to provide a spontaneous origin for parity violation in weak interactions. W_{L} and W_{R} may mix due to spontaneous symmetry breaking. The physical mass eigenstates are denoted as

$$\begin{aligned} W_1 &= W_{\mathrm{L}} \cos\zeta - W_{\mathrm{R}} \sin\zeta \quad \text{and} && (2.78) \\ W_2 &= W_{\mathrm{L}} \sin\zeta + W_{\mathrm{R}} \cos\zeta, && (2.79) \end{aligned}$$

where W_1 is the familiar W boson and ζ is the mixing angle between the two mass eigenstates. In the manifest left-right symmetric (MLRS) model, there are only three free parameters, the mass ratio $\delta = m_1^2/m_2^2$, ζ, and λ'. Here, $m_1 = 80.398(23)\,\mathrm{GeV/c^2}$ [10] and m_2 denote the masses of W_1 and W_2, respectively. Since $L_{\mathrm{V}} = 1$ (CVC) and $L_{\mathrm{S}} = L_{\mathrm{T}} = R_{\mathrm{S}} = R_{\mathrm{T}} = 0$, the coupling constants L_{A}, R_{V}, and R_{A} depend on δ, ζ, and λ' as described in Refs. [27, 84, 85][21],[22]:

$$\begin{aligned} L_{\mathrm{A}} &= \lambda' = \lambda \cdot \frac{(1+\tan\zeta) - \delta\tan\zeta(1-\tan\zeta)}{(1-\tan\zeta) + \delta\tan\zeta(1+\tan\zeta)} \approx \lambda(1+2\zeta), && (2.80) \\ R_{\mathrm{V}} &= \frac{\delta(1+\tan\zeta) - \tan\zeta(1-\tan\zeta)}{(1-\tan\zeta) + \delta\tan\zeta(1+\tan\zeta)} \approx \delta - \zeta, \quad \text{and} && (2.81) \\ R_{\mathrm{A}} &= \lambda' \cdot \frac{\delta(1-\tan\zeta) + \tan\zeta(1+\tan\zeta)}{(1+\tan\zeta) - \delta\tan\zeta(1-\tan\zeta)} \approx \lambda(1+2\zeta)(\delta+\zeta). && (2.82) \end{aligned}$$

The dependence of a, A, B, C, and τ_{n} on δ, ζ, and λ' follows from their respective dependence on L_{V}, L_{A}, R_{V}, and R_{A}:

$$\begin{aligned} a &= \frac{L_{\mathrm{V}}^2 - L_{\mathrm{A}}^2 + R_{\mathrm{V}}^2 - R_{\mathrm{A}}^2}{L_{\mathrm{V}}^2 + 3L_{\mathrm{A}}^2 + R_{\mathrm{V}}^2 + 3R_{\mathrm{A}}^2} = \frac{1 - \lambda'^2 + R_{\mathrm{V}}^2 - R_{\mathrm{A}}^2}{1 + 3\lambda'^2 + R_{\mathrm{V}}^2 + 3R_{\mathrm{A}}^2}, && (2.83) \\ A &= -2\frac{L_{\mathrm{A}}^2 + L_{\mathrm{V}}L_{\mathrm{A}} - R_{\mathrm{A}}^2 - R_{\mathrm{V}}R_{\mathrm{A}}}{L_{\mathrm{V}}^2 + 3L_{\mathrm{A}}^2 + R_{\mathrm{V}}^2 + 3R_{\mathrm{A}}^2} = -2\frac{\lambda'^2 + \lambda' - R_{\mathrm{A}}^2 - R_{\mathrm{V}}R_{\mathrm{A}}}{1 + 3\lambda'^2 + R_{\mathrm{V}}^2 + 3R_{\mathrm{A}}^2}, && (2.84) \\ B &= 2\frac{L_{\mathrm{A}}^2 - L_{\mathrm{V}}L_{\mathrm{A}} - R_{\mathrm{A}}^2 + R_{\mathrm{V}}R_{\mathrm{A}}}{L_{\mathrm{V}}^2 + 3L_{\mathrm{A}}^2 + R_{\mathrm{V}}^2 + 3R_{\mathrm{A}}^2} = 2\frac{\lambda'^2 - \lambda' - R_{\mathrm{A}}^2 + R_{\mathrm{V}}R_{\mathrm{A}}}{1 + 3\lambda'^2 + R_{\mathrm{V}}^2 + 3R_{\mathrm{A}}^2}, && (2.85) \\ C &= 4x_C\frac{L_{\mathrm{V}}L_{\mathrm{A}} - R_{\mathrm{V}}R_{\mathrm{A}}}{L_{\mathrm{V}}^2 + 3L_{\mathrm{A}}^2 + R_{\mathrm{V}}^2 + 3R_{\mathrm{A}}^2} = 4x_C\frac{\lambda' - R_{\mathrm{V}}R_{\mathrm{A}}}{1 + 3\lambda'^2 + R_{\mathrm{V}}^2 + 3R_{\mathrm{A}}^2}, \quad \text{and} && (2.86) \\ \tau_{\mathrm{n}} &= \frac{\mathcal{F}t^{0^+\to0^+}}{f_R \ln(2)} \cdot \frac{2(L_{\mathrm{V}}^2 + R_{\mathrm{V}}^2)}{L_{\mathrm{V}}^2 + 3L_{\mathrm{A}}^2 + R_{\mathrm{V}}^2 + 3R_{\mathrm{A}}^2} = \frac{\mathcal{F}t^{0^+\to0^+}}{f_R \ln(2)} \cdot \frac{2(1 + R_{\mathrm{V}}^2)}{1 + 3\lambda'^2 + R_{\mathrm{V}}^2 + 3R_{\mathrm{A}}^2}. && (2.87) \end{aligned}$$

So far, there is no experimental evidence of a W_{R} weak gauge boson. Hence W_{R} and W_2 are expected to be very massive particles. In the case of W_{R} couplings to RH quarks, the limit $M_{W_{\mathrm{R}}} > 2.5\,\mathrm{TeV}$ from $K_L - K_S$ mixing [87] is severe[23]. The SM is included in

---

[21] A sign error in R_{V} in Ref. [85] was found by H. Mest [32]: In the numerator of Eq. (2.81) the expression $\tan\zeta(1+\tan\zeta)$ should be changed to $\tan\zeta(1-\tan\zeta)$.

[22] Please note that we, such as [27], express R_{A} with a prefactor λ' compared to Refs. [32, 85, 86]. This retains the definition $L_{\mathrm{V}} = 1$ (CVC).

[23] There are also W_{R} contributions to the neutron electric dipole moment (nEDM). The combined constraints from K_L decay and the nEDM ($d_{\mathrm{n}} < 2.9 \times 10^{-26}\,\mathrm{e\,cm}$ [88]) yield a bound of $M_{W_{\mathrm{R}}} > (2-6)\,\mathrm{TeV}$ [87].

the MLRS model when no mixing occurs ($\zeta = 0$) and the W_2 boson is infinitely heavy. Then, $\delta = 0$ and $\lambda = \lambda'$.

The experimentally determined values for the angular correlation coefficients and the neutron lifetime can be used to test the SM as well to search for evidence of possible extensions to it. This is done in the following sections, applying the results of the measurements introduced in Sec. 2.2.1.

2.2 Tests of the Standard Model

As discussed earlier in Chap. 1 the angular correlation coefficients overdetermine the V−A description of neutron beta decay. Therefore, one can test the validity and consistency of its SM description. Before doing so, we have to analyze the currently available data on neutron decay.

2.2.1 Experimental Data

In Secs. 2.2 and 2.3, we present results of least-squares fits, using recent experimental data as well as target uncertainties for planned experiments on neutron decay. The various observables O_i, for $i = 1, \dots, N$, depend non-linearly on a set of M parameters p_i, for $i = 1, \dots, M$. Given the theoretical expressions of the observables $\Theta_i(\mathbf{p})$ one defines the figure-of-merit function χ^2 which is minimized to determine the best-fit parameters by

$$\chi^2 = \sum_{i=1}^{N} \left[\frac{O_i - \Theta_i(\mathbf{p})}{\sigma_i} \right]^2 , \tag{2.88}$$

where O_i is the measured value and σ_i is the corresponding (1σ) experimental error. The fit parameters $\mathbf{p}$ are defined below as $|V_{\mathrm{ud}}|$, ratios of the different couplings L_j and R_j respectively the MLRS couplings δ, ζ, and λ'. The principle of non-linear χ^2 minimization is discussed, e.g., in Ref. [89]. Figures 2.6a to 2.10b show the present and expected future limits from neutron decay, respectively. The confidence regions in 2 dimensions, or confidence intervals in 1 dimension, are defined as in Ref. [90].

Present Limits

We first analyze the presently available data on neutron decay. As input for our study we used:

$$a = -0.103(4) \quad \text{and} \quad B = 0.9807(30), \tag{2.89}$$

both from Ref. [10], as well as

$$\mathcal{F}t^{0^+ \to 0^+} = 3071.81(83)\,\mathrm{s} \tag{2.90}$$

as the average value for superallowed $0^+ \to 0^+$ nuclear beta decays, the so-called superallowed Fermi transitions (SAF) (from Ref. [76]). We used our own averages for τ_{n} and A, as follows.

The most recent results[24] of Serebrov *et al.* [93], $\tau_\mathrm{n} = 878.5(8)\,\mathrm{s}$, and Pichlmaier *et al.* [94], $\tau_\mathrm{n} = (880.7 \pm 1.8)\,\mathrm{s}$, were not included in the PDG 2010 average [95]. We preferred not to exclude the measurement by Serebrov *et al.* without being convinced that it is wrong, and include it in our average to obtain

$$\tau_\mathrm{n} = (881.8 \pm 1.4)\mathrm{s}. \tag{2.91}$$

Our average includes a scale factor of 2.5, as we obtain $\chi^2 = 45$ for 7 degrees of freedom. The statistical probability for such a high χ^2 is 1.5×10^{-7}. If our average were the true value of the neutron lifetime τ_n, both the result of Serebrov *et al.* and the PDG 2010 average would deviate at the $(2-3)\,\sigma$ level. We note that in the 2011 partial update web version of the PDG 2010 review [10], a new average[25] is given, $\tau_\mathrm{n} = (881.5 \pm 1.5)\,\mathrm{s}$, in close agreement with our average Eq. (2.91).

Two beta asymmetry experiments have completed their analyses since the PDG 2010 review, namely UCNA [29] and PERKEO II [30][26]. The UCNA collaboration has published $A = -0.11966(89)^{+0.00123}_{-0.00140}$ [29][27]. The last PERKEO II run has yielded a preliminary value of $A = -0.1198(5)$ [97]. We include these two results in our average, and obtain

$$A = -0.1186(9), \tag{2.92}$$

which includes a scale factor of 2.3 based on $\chi^2 = 28$ for 5 degrees of freedom. The statistical probability for such a high χ^2 is 5×10^{-5}, not much better than in the case of τ_n. We note that in the 2011 partial update web version of the PDG 2010 review, a new average is given, $A = -0.1176(11)$, in agreement with our average Eq. 2.92.

Hence, we find that the relative errors are about 4 % in a, 0.9 % in A, and 0.3 % in B. We will not use $C = -0.2377(26)$ [10] in the analysis of present results, since the PERKEO II results for B and C are derived from the same data set.

Future Limits

About a dozen new instruments are currently planned or under construction. For recent reviews see Refs. [18, 19, 22, 23]. We will discuss a future scenario which assumes the following improvements in precision in a couple of years.

- $\Delta a/a = 0.1\,\%$: Measurements of the neutrino-electron correlation coefficient a with the aSPECT, aCORN [98], Nab [99], and PERC experiments are projected or underway (for details see Sec. 2.4.2 and App. C).
- $\Delta b = 3 \times 10^{-3}$: Measurements of the Fierz interference term b in neutron decay are planned by the Nab [99], UCNb [100], and PERC collaborations.
- $\Delta A/A = 3 \times 10^{-4}$: Measurements of the beta asymmetry parameter A with PERKEO III [32, 101], UCNA [102], abBA [103], and PERC [104] are almost analyzed, planned, or underway.

---

[24] We note that a recent experiment [91] measured the neutron lifetime with a magneto-gravitational trap. Ezhov reported [92] at the 7th International Workshop "Ultracold and Cold Neutrons. Physics and Sources." a neutron lifetime of $\tau_\mathrm{n} = (878.2 \pm 1.9)\,\mathrm{s}$, which is in excellent agreement with the result of Serebrov *et al.* We disregard the result, as it is not published yet.

[25] The new PDG 2011 average includes the result of Serebrov *et al.*, as Pichlmaier *et al.* obtained a value closer to the value of Serebrov *et al.*.

[26] Publication of the result of the last PERKEO II run [31] is underway.

[27] In the analysis of present results we will use the previously published value $A = -0.1138(46)(21)$ [96].

- $\Delta B/B = 0.1\,\%$: The abBA [103] and UCNB [105] collaborations intend to measure the neutrino asymmetry parameter B. PERC is also exploring a measurement of B.
- $\Delta C/C = 0.1\,\%$: The *a*SPECT [48] and PANDA [106] collaborations plan measurements of the proton asymmetry parameter C; PERC may follow suit as well.
- $\Delta\tau_\mathrm{n} = 0.8\,\mathrm{s}$: Measurements of the neutron lifetime τ_n with beam experiments [107, 108], material bottles [109, 110], and magnetic storage experiments [91, 111–114] are planned or underway.

Our assumptions about future uncertainties for a, A, B, and C reflect the goal accuracies in the proposals, while for τ_n we only assume the present discrepancy to be resolved. Our assumed $\Delta\tau_\mathrm{n}$ corresponds to the best uncertainty claimed in a previous experiment [93].

Our scenario "future limits" assumes that the SM holds and connects the different observables. We used $a = -0.10588$, $b = 0$, $B = 0.98728$, $C = -0.23875$, and $\tau_\mathrm{n} = 882.2\,\mathrm{s}$ derived from $A = -0.1186$ and $\mathcal{F}t^{0^+\to 0^+} = 3071.81\,\mathrm{s}$. These values agree with the present measurements within $2\,\sigma$.

2.2.2 Test of the V−A Description

A useful model-independent test of the self-consistency of the SM is derived in Ref. [115]. Based on the expressions for a, A, and B from Eq. (1.4), one can construct two equations:

$$F_1 \overset{\mathrm{def}}{=} 1 + A - B - a \equiv 0 \quad \text{and} \tag{2.93}$$

$$F_2 \overset{\mathrm{def}}{=} aB - A - A^2 \equiv 0\,. \tag{2.94}$$

The PDG 2011 review for the correlation coefficients [10] yields:

$$F_1 = 0.0047(51) \quad \text{and} \quad F_2 = 0.0028(40), \tag{2.95}$$

where the uncertainties in F_1 and F_2

$$\Delta F_1 = \sqrt{(\Delta a)^2 + (\Delta A)^2 + (\Delta B)^2} \quad \text{and} \tag{2.96}$$

$$\Delta F_2 = \sqrt{(B\Delta a)^2 + ((1+2A)\,\Delta A)^2 + (a\Delta B)^2} \tag{2.97}$$

are dominated by the poor knowledge of a. From our present limits in Sec. 2.2.1 we derive an improved test of the self-consistency of the SM:

$$F_1 = 0.0037(51) \quad \text{and} \quad F_2 = 0.0035(40). \tag{2.98}$$

Our values are consistent with the V−A theory, but even a small improvement in a would considerably improve the precision of this comparison. New neutron decay experiments (cf. Sec. 2.2.1) could lead to accuracies of

$$\Delta F_1 = 0.001 \quad \text{and} \quad \Delta F_2 = 0.00015, \tag{2.99}$$

which would make this comparison much more useful.

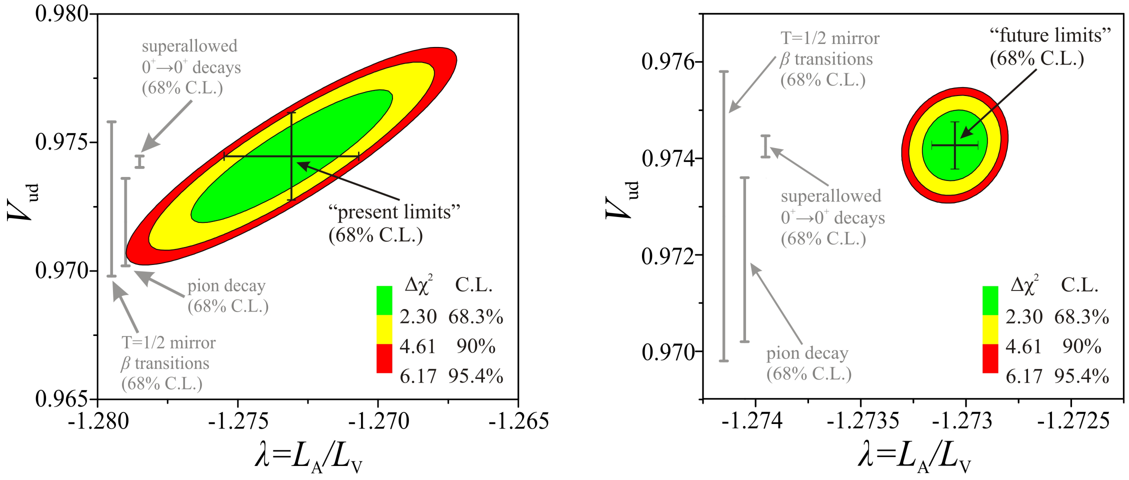

(a) (b)

Figure 2.6: Determination of $|V_{\mathrm{ud}}|$ and $\lambda = L_{\mathrm{A}}/L_{\mathrm{V}}$: (a) Present limits from a, A, B, and τ_{n} in neutron decay. (b) Future limits from neutron decay, assuming improved and independent measurements of a, A, B, C, and τ_{n}. Analogous limits for $|V_{\mathrm{ud}}|$ from superallowed $0^+ \to 0^+$ nuclear beta decays, pion decays, and $T = 1/2$ mirror decays are indicated. For details see the text. All bars correspond to single parameter limits.

2.2.3 Unitarity of the CKM Matrix and Determination of $|V_{\mathrm{ud}}|$ and λ

At present, the most accurate value of $|V_{\mathrm{ud}}|$ is derived from measurements of superallowed $0^+ \to 0^+$ nuclear beta decays (SAF) [10, 75]:

$$|V_{\mathrm{ud}}| = 0.97425(22). \tag{2.100}$$

Combined with measurements of $|V_{\mathrm{us}}|$ and $|V_{\mathrm{ub}}|$ from kaon decays and semileptonic decay of B-mesons [10], respectively, this leads to the currently most precise test of the unitarity of the CKM matrix [10, 36, 75]:

$$\Delta \overset{\mathrm{def}}{=} 1 - |V_{\mathrm{ud}}|^2 - |V_{\mathrm{us}}|^2 - |V_{\mathrm{ub}}|^2 = (1 \pm 6) \times 10^{-4}. \tag{2.101}$$

However, the extraction of V_{ud} involves calculations of radiative and nuclear structure corrections for the Fermi transition in nuclei. Even though these calculations have been done with high precision [76, 116] (and references therein), questions concerning these corrections have been raised [117–120]. In view of the intrinsic theoretical complexity of nuclear beta decays, it is highly desirable to derive the limits from neutron beta decay, with at least comparable precision, as they are independent of nuclear structure. Unfortunately, a disturbing inconsistency persists within the neutron decay data (cf. [10], Fig. 1.1, and Sec. 2.2.1).

Figure 2.6a shows the present limits from neutron decay. Free parameters $|V_{\mathrm{ud}}|$ and $\lambda = L_{\mathrm{A}}/L_{\mathrm{V}}$ where fitted to the observables a, A, B, τ_{n}. Additionally, to take into account uncertainties in radiative corrections, we fitted the denominator of Eq. (2.36) to a 'data point' (4908.7 ± 1.9) s. The contours around the minimum correspond to the three levels of constant χ^2: $\chi^2_{\mathrm{min}} + 2.3$, $\chi^2_{\mathrm{min}} + 4.61$, and $\chi^2_{\mathrm{min}} + 6.17$, respectively, where χ^2_{min} is the value of χ^2 at the minimum. The allowed regions for $|V_{\mathrm{ud}}|$ and λ, to 68.3%, 90 %, and

95.4 % C.L., are obtained by varying all three parameters around the minimum. At the $1\,\sigma$ confidence level, we find

$$|V_{\mathrm{ud}}| = 0.9745(17) \quad \text{and} \quad \lambda = -1.2731(24). \tag{2.102}$$

Hence, $|V_{\mathrm{ud}}|$ is in agreement with, but less accurate than SAF beta decays. The confidence interval for a single parameter is obtained by varying the values of the other two parameters around the minimum. Here, the $1\,\sigma$ and $2\,\sigma$ confidence intervals correspond to the two levels of constant χ^2: $\chi^2_{\mathrm{min}} + 1$ and $\chi^2_{\mathrm{min}} + 2^2$, respectively. Along with $|V_{\mathrm{us}}| = 0.2252(9)$ and $|V_{\mathrm{ub}}| = 3.89(44) \times 10^{-3}$ from the PDG 2011 review [10], our test of the unitarity of the CKM matrix yields:

$$\Delta = (-4 \pm 33) \times 10^{-4}, \tag{2.103}$$

in good agreement with the SM expectation, but also less sensitive than SAF beta decays.

Figure 2.6b demonstrates the sensitivity of our future scenario. New neutron decay experiments could considerably improve the accuracies of $|V_{\mathrm{ud}}|$ and λ to

$$\Delta|V_{\mathrm{ud}}| = 0.00049 \quad \text{and} \quad \Delta\lambda = 0.00011, \tag{2.104}$$

both at the $1\,\sigma$ confidence level. To further improve the accuracy of $|V_{\mathrm{ud}}|$ (and Δ) to, e.g., $|V_{\mathrm{ud}}| = 0.00021$, competitive to SAF beta decays, one would have to measure the neutron lifetime τ_{n} with a precision of $\Delta\tau_{\mathrm{n}} = 0.1\,\mathrm{s}$. Nevertheless, the precision in $|V_{\mathrm{ud}}|$ extracted from neutron decay experiments would mainly be limited by radiative corrections, similar to the extraction of $|V_{\mathrm{ud}}|$ from SAF beta decays. In particular, an update of the theoretical corrections would be required.

Recent studies of $T = 1/2$ nuclear mirror transitions [121] have reached a precision in $|V_{\mathrm{ud}}|$ competitive to neutron decays, as can be seen from Fig 2.6a. In Figs. 2.6 we also show the limits from pion beta decay measurements [122], namely from the rare decay mode $\pi^+ \to \pi^0 + \mathrm{e}^+ + \nu_{\mathrm{e}}$. As a pure vector transition, theoretical uncertainties in the determination of $|V_{\mathrm{ud}}|$ from pion beta decay are very small. The difficulty in measuring the pion decay rate is due to the small branching ratio of $\mathcal{O}(10^{-8})$. Higher counting statistics would be required to make this approach competitive with SAF beta decays.

2.3 Searches for Physics Beyond the Standard Model

Our fits are not conclusive if all 8 coupling constants L_j and R_j, for j =V,A,S,T, are treated as free parameters. We are more interested in restricted analyses presented below. Experiments quote a, A, B, and C after applying (small) theoretical corrections for recoil and radiative effects; we neglect any dependence on non-SM physics in these corrections.

We note that in Ref. [49], citing this thesis, the influence of improved measurements of the neutrino-electron correlation coefficient a on non-SM physics is extremely overestimated. The figures given in Ref. [49] reflect how much the area of the 95 % contours could change due to an improved measurement of a. Hence, these figures are inconclusive.

We further note that limits similar to those presented below were derived by Dubbers and Schmidt [19], using a slightly different neutron and nuclear data set. First, Dubbers and Schmidt included the proton asymmetry parameter C in their analysis of present results, by using for the neutrino asymmetry parameter B only the value of Serebrov *et al.* [123, 124]. Secondly, in the search for LH S and T currents, they included the ratio

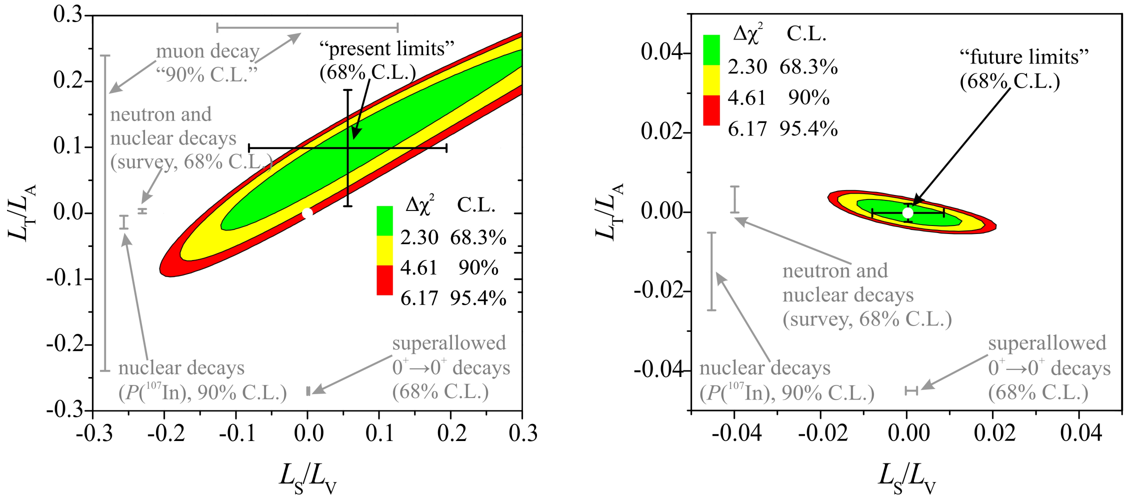

(a) (b)

Figure 2.7: Left-handed scalar and tensor currents: (a) Present limits from neutron decay (only a, A, and B). The SM values are at the origin (white) of the plot. Analogous limits extracted from muon decays are indicated. (b) Future limits from neutron decay, assuming improved and independent measurements of a, b, A, B, and C. Analogous limits extracted from muon decays are not indicated since they exceed the scale of the plot. Other limits are discussed in the text. All bars correspond to single parameter limits.

$r_{\mathcal{F}t}$ in their analysis, using the average $\mathcal{F}t^{0^+\to 0^+}$ value for SAF decays (see Sec. 2.3.2 for details). Additionally, they also derived limits for the Fierz interference terms b and b_ν, both consistent with the SM prediction.

2.3.1 Constraints from Neutron Decay Alone

Left-Handed Scalar and Tensor Currents

Addition of LH S and T currents to the SM leaves $L_\mathrm{V} = 1$, $L_\mathrm{A} = \lambda$, L_S, and L_T as the non-vanishing parameters. Non-zero Fierz terms b and b_ν appear in this model. Figure 2.7a shows the current limits from neutron decay.

Free parameters λ, $L_\mathrm{S}/L_\mathrm{V}$, and $L_\mathrm{T}/L_\mathrm{A}$ were fitted to the observables $\bar{a}$, $\bar{A}$, $\bar{B}$, and b and $\bar{C}$ in case of our future scenario (see Sec. 2.1.6 for details). We have used the following values for $m_\mathrm{e}\left\langle E_\mathrm{e}^{-1}\right\rangle$ in our study (cf. Sec. 2.1.6): $m_\mathrm{e}\left\langle E_\mathrm{e}^{-1}\right\rangle = 0.5393$ for $\bar{A}$, dominated by PERKEO II [43], $m_\mathrm{e}\left\langle E_\mathrm{e}^{-1}\right\rangle = 0.6108$ for $\bar{B}$, dominated by Serebrov *et al.* [123, 124] and PERKEO II [125], and the mean value $m_\mathrm{e}\left\langle E_\mathrm{e}^{-1}\right\rangle = 0.6556$, taken over the whole beta spectrum, for $\bar{a}$ and $\bar{C}$. The 68.3 % C.L.s are

$$\lambda = -1.322(48), \quad L_\mathrm{S}/L_\mathrm{V} = 0.099(88), \quad \text{and} \quad L_\mathrm{T}/L_\mathrm{A} = 0.056(138). \tag{2.105}$$

Unlike the following sections, here we omit the neutron lifetime τ_n, since otherwise we would have to determine the possible influence of the Fierz term in Fermi decays, b_F, on the $\mathcal{F}t^{0^+\to 0^+}$ values. A combined analysis of neutron and SAF beta decays is found in Sec. 2.3.2.

Figure 2.7b presents the impact of projected measurements in our future scenario. For comparison, a recent combined analysis of nuclear and neutron physics data [17] finds

$$L_\mathrm{S}/L_\mathrm{V} = 0.0013(13) \quad \text{and} \quad L_\mathrm{T}/L_\mathrm{A} = 0.0036(33), \tag{2.106}$$

with $1\,\sigma$ statistical errors. It includes the determination of the Fierz term b_F from superallowed beta decays, updated in Ref. [76], which sets a limit on L_S that is hard to improve with neutron beta decay alone. As in the recent survey of Severijns *et al.* [17], we do not include the limits on tensor couplings obtained [126] from a measurement of the Fierz term b_GT in the forbidden Gamow-Teller decay of ^{22}Na, due to its large $\log ft(=7.5)$ value. Neutron decay has the potential to improve the best remaining nuclear limit on L_T as provided by a measurement of the longitudinal polarization of positrons emitted by polarized ^{107}In nuclei ($\log ft = 5.6$) [127, 128][28],[29]. Limits from neutron beta decay are independent of nuclear structure. The stringent limit on L_T in the combined analysis of nuclear and neutron decay data [17] stems mainly from measurements of τ_n and B in neutron beta decay. New neutron decay experiments alone could lead to uncertainties of

$$\Delta(L_\mathrm{T}/L_\mathrm{A}) = 0.0023 \quad \text{and} \quad \Delta(L_\mathrm{S}/L_\mathrm{V}) = 0.0083, \tag{2.107}$$

both at the $1\,\sigma$ confidence level. Then, the precision in $\Delta(L_\mathrm{T}/L_\mathrm{A})$ would be competitive with the combined analysis of neutron and nuclear physics data [17]. We note that supersymmetric (SUSY) contributions to the SM can be discovered at this level of precision, as discussed in Ref. [131].

Right-Handed Scalar and Tensor Currents

Adding the RH S and T currents to the SM yields $L_\mathrm{V} = 1$, $L_\mathrm{A} = \lambda$, R_S, and R_T as the remaining non-zero parameters. The observables depend only quadratically on R_S and R_T, i.e., the possible limits are less sensitive than those obtained for LH S, T currents. Figure 2.8a shows the present limits from neutron beta decay. A similar analysis of this scenario was recently published in Ref. [132] (see also Ref. [30]).

Free parameters λ, $R_\mathrm{S}/L_\mathrm{V}$, and $R_\mathrm{T}/L_\mathrm{A}$ were fitted to the observables a, A, B, τ_n, and C, in case of our future scenario. Additionally, to take into account uncertainties in the $\mathcal{F}t$ values and in radiative corrections, we fitted $\mathcal{F}t^{0^+\to 0^+}$ and f_R to 'data points' 3071.81(83) s and 1.71385(34), respectively. The 68.3 % C.L.s are

$$\lambda = -1.2727(37), \quad R_\mathrm{S}/L_\mathrm{V} = 0.000(87), \quad \text{and} \quad R_\mathrm{T}/L_\mathrm{A} = 0.000(78). \tag{2.108}$$

The Fierz interference terms b and b_ν are zero in this model. Hence, measurements of b (or b_F in SAF beta decays) can invalidate the model, but not determine its parameters. Figure 2.8b shows the projected improvement in our future scenario. The gray ellipse stems from a recent survey of the state of the art in nuclear and neutron beta decays [17].

---

[28] Please note that in Figs. 1 and 2 in Ref. [6] the limit from Ref. [127, 128] was by mistake shifted to higher $L_\mathrm{T}/L_\mathrm{A}$ values.

[29] We note that recent experiments [129, 130] measured the beta asymmetry parameter A in Gamow-Teller decays of polarized ^{114}In ($\log ft = 4.5$) and ^{60}Co nuclei ($\log ft = 7.5$). Wauters *et al.* reported limits on possible T currents and W_R bosons:

- ^{114}In [129]: $L_\mathrm{T}/L_\mathrm{A} = +0.029(55)$ and $m_2 > 230\,\mathrm{GeV/c^2}$ (both 90 % C.L.),
- ^{60}Co [130]: $L_\mathrm{T}/L_\mathrm{A} = -0.038(28)$ and $m_2 > 245\,\mathrm{GeV/c^2}$ (both 90 % C.L.).

We do not show these limits, as they are inferior to the limits presented in Ref. [127, 128].

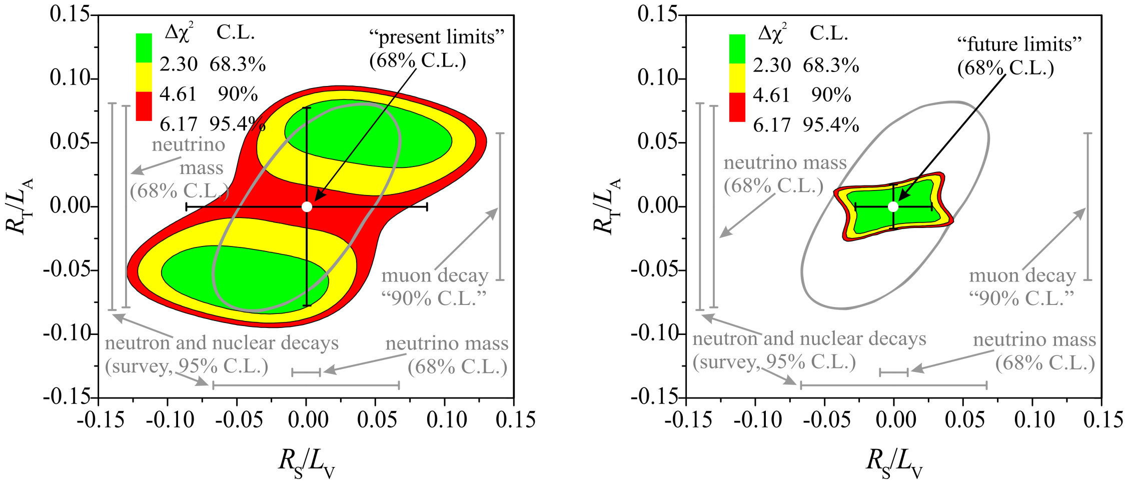

(a) (b)

Figure 2.8: Limits on right-handed scalar and tensor currents: (a) Current limits from a, A, B, and τ_n in neutron decay. (b) Projected future limits from neutron decay, assuming improved measurements of a, A, B, C, and τ_n. The SM prediction is at plot origin (white). As a comparison, we show limits from a survey of nuclear and neutron beta decays [17], and limits from muon decays and neutrino mass measurements. The gray ellipse is the present 86.5 % contour from Ref. [17]. The muon limit on R_S/L_V is larger than the scale of the plot. For details see the text.

New neutron decay experiments alone could considerably improve the limits on RH S and T currents, to

$$\Delta(R_S/L_V) = 0.0275 \quad \text{and} \quad \Delta(R_T/L_A) = 0.0173, \tag{2.109}$$

with $1\,\sigma$ statistical error.

Hypothetical W' Bosons

Addition of RH V and A currents to the SM leaves δ, ζ, and λ' as the non-vanishing parameters. Figure 2.9a shows the current limits from neutron beta decay. The fit parameters δ, ζ, λ', $\mathcal{F}t^{0^+\to0^+}$, and f_R, were fitted to the observables a, A, B, τ_n, and C, in case of our future scenario. At the $1\,\sigma$ confidence level, we find

$$\begin{aligned} \lambda' &= -1.2916(87), \quad \zeta = -0.080(84), \\ \delta &< 0.071, \quad \text{and hence} \quad m_2 > 302\,\text{GeV/c}^2. \end{aligned} \tag{2.110}$$

Measurements of the polarized observables, i.e., the electron, neutrino, or proton asymmetries, lead to important restrictions, but are at present inferior to limits on the mixing angle ζ from μ decays [134]. They are also inferior to limits on the mass m_2 from direct searches for extra W bosons [10]. Comparison of beta decay limits with high energy data is possible in our minimal MLRS model. For example, the comparison with W' searches at Tevatron [136] assumes a RH CKM matrix identical to the LH one and identical couplings. In more general scenarios the limits are complementary to each other since they probe different combinations of the RH parameters [137].

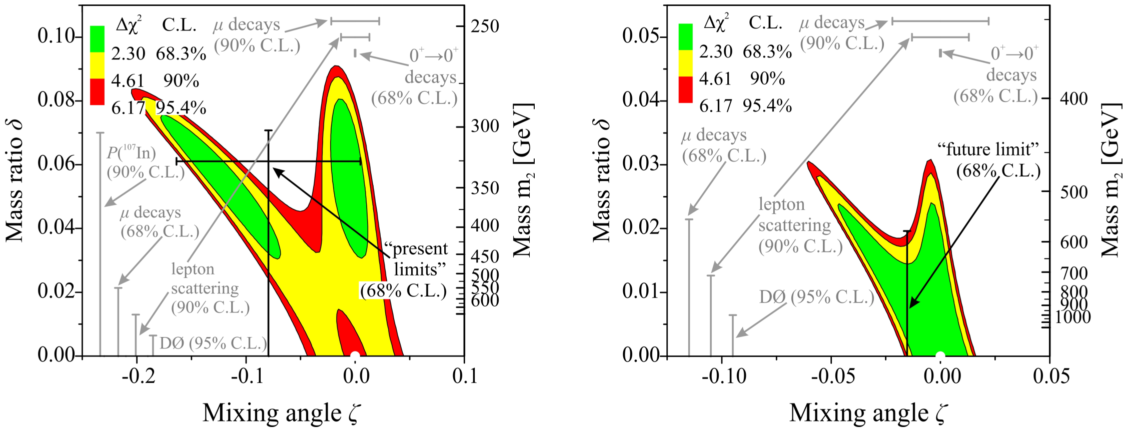

(a) (b)

Figure 2.9: Limits on hypothetical W' bosons: (a) Present limits from a, A, B, and τ_n in neutron decay. (b) Future limits from neutron decay, assuming improved measurements of a, A, B, C, and τ_n. The SM values are at the origin (white) of the plot. As a comparison, we show analogous limits from nuclear decays [127, 128], muon decays [133, 134], lepton scattering (deep inelastic ν-hadron, ν-e scattering, and e-hadron interactions) [135], and a direct search at DØ [136]. The value of $|V_\mathrm{ud}|$ from superallowed $0^+ \to 0^+$ nuclear beta decays was used to set a limit on ζ, assuming that the CKM matrix for left-handed quarks is strictly unitary (see Ref. [76]). Limits from kaon and B-meson mixing and the neutron EDM ($M_{W_\mathrm{R}} > (2-6)\,\mathrm{TeV/c^2}$) [87] are not shown.

Figure 2.9b presents the improvement from planned measurements in our future scenario. The χ^2 minimization converges to a single minimum at mass $m_2 = \infty$; with $\chi^2 = 0$, i.e., the mixing angle ζ is not defined at this minimum. The 68.3 % C.L.s are

$$\delta < 0.0196, \quad \text{which yields} \quad m_2 > 574\,\mathrm{GeV/c^2}. \tag{2.111}$$

In the mass range > 1 TeV, not excluded by collider experiments, we would improve the limit on ζ from μ decays slightly.

We emphasize that all presented RH coupling limits (R_S, R_T, δ, and ζ) assume that the RH (Majorana) neutrinos are light ($m \ll 1\,\mathrm{MeV}$). The RH interactions are kinematically weakened by the masses of the predominantly RH neutrinos, if these masses are not much smaller than the electron endpoint energy in neutron decay (782 keV). If both the W boson and neutrino left-right mixing angles were zero, and if the RH neutrino masses were above 782 keV, RH corrections to neutron decay observables would be completely absent.

2.3.2 Left-Handed Coupling Constraints from a Combined Analysis of Neutron and Nuclear Decays

Adding the LH S and T currents to the SM yields $L_\mathrm{V} = 1$, $L_\mathrm{A} = \lambda$, L_S, and L_T as the remaining non-zero parameters. As discussed earlier, non-vanishing Fierz interference terms b and b_ν appear in this model. Unlike Sec. 2.3.1 and Figs. 2.7, here, we include the neutron lifetime τ_n in our analysis, as the neutron lifetime is sensitive to the Fierz term, and the comparison of different nuclei shows that the effect of L_S on $\mathcal{F}t^{0^+\to 0^+}$ is very small.

To make use of measured values of τ_n in a scenario involving a non-zero value for the Fierz term b, we rewrite Eqs. (2.32) and (2.34) in analogy to Eq. (2.68)[30,31]

$$\overline{\mathcal{F}t^{0^+\to 0^+}} = \frac{\mathcal{F}t^{0^+\to 0^+}}{1+b_\mathrm{F}\gamma\left\langle W^{-1}\right\rangle} \quad \text{and} \tag{2.115}$$

$$\overline{\tau_\mathrm{n}} = \frac{\tau_\mathrm{n}}{1+bm_\mathrm{e}\left\langle E_\mathrm{e}^{-1}\right\rangle}, \tag{2.116}$$

where [27, 76] (see also [75])

$$\xi_\mathrm{F}\mathcal{F}t^{0^+\to 0^+} = \frac{K}{G_\mathrm{F}^2|V_\mathrm{ud}|^2\left(1+\Delta_R^\mathrm{V}\right)} \quad \text{and} \tag{2.117}$$

$$\xi\tau_\mathrm{n} = \frac{K}{f_R\ln(2)G_\mathrm{F}^2|V_\mathrm{ud}|^2\left(1+\Delta_R^\mathrm{V}\right)}, \tag{2.118}$$

with[32,33]

$$\xi_\mathrm{F}b_\mathrm{F} = \pm 4\Re(L_\mathrm{S}L_\mathrm{V}^* + R_\mathrm{S}R_\mathrm{V}^*), \tag{2.119}$$

$$\gamma = \sqrt{1-(\alpha Z)^2}, \quad \text{and} \tag{2.120}$$

$$\frac{K}{(\hbar c)^6} = \frac{2\pi\hbar\ln 2}{(m_\mathrm{e}c^2)^5} = 8120.2787(11)\times 10^{-10}\,\mathrm{GeV}^{-4}\,\mathrm{s}. \tag{2.121}$$

Here b_F is the Fierz term in Fermi decays. For ξ and ξ_F see Eqs. (2.13) and (2.35),

---

[30] Please note that, here, $\overline{\mathcal{F}t^{0^+\to 0^+}}$ does not denote the average value for SAF beta decays from Ref. [76].

[31] In Eq. (2.122) $\langle\cdot\rangle$ denotes the weighted average over the part of the electron/positron spectrum observed in the particular experiment [138] (see also Eq. (2.69))

$$\left\langle W^{-1}\right\rangle = \frac{1}{\tilde{f}}\int_1^{W_0} dW F(\pm Z,W)S(\pm Z,W)p(W_0-W)^2, \tag{2.112}$$

with the statistical rate function $\tilde{f}$

$$\tilde{f} = \int_1^{W_0} dW F(\pm Z,W)S(\pm Z,W)pW(W_0-W)^2, \tag{2.113}$$

where, to appropriate order $(\alpha Z)^3$ for our present concern, [70]

$$\begin{aligned} F(\pm Z,W) \approx\ & 1\pm\frac{\pi}{\beta}\alpha Z + \left(\frac{11}{4}-\gamma_E-\ln(2pR)+\frac{\pi^2}{3\beta^2}\right)(\alpha Z)^2 \\ & \pm\pi\beta\left(\frac{11}{4}-\gamma_E-\ln(2pR)\right)(\alpha Z)^3 . \end{aligned} \tag{2.114}$$

Here, $W = E/m_\mathrm{e}$ is the total electron/positron energy E in electron rest-mass units, W_0 its maximum value, and $p=\sqrt{W^2-1}$ its momentum. In calculating the $\gamma\left\langle W^{-1}\right\rangle$ values, we put the shape-correction function $S(\pm Z,W)$ to unity (compare Ref. [116]).

[32] The $-$ sign in Eq. (2.119) refers to nuclear decays with positron emission.

[33] Compared with Ref. [74], here, the factor 4 in Eq. (2.119) considers the nuclear matrix element $\mathcal{M}_\mathrm{F}$ (see also Fn. 14 and Ref. [76]).

Table 2.1: $\mathcal{F}t$ values of superallowed beta decays [76] used in our study. The $\gamma\left\langle W^{-1}\right\rangle$ values have been derived from the decay transition energies, Q_{EC}, summarized in [76].

Parent nucleus, $T_z=-1$			^{10}C	^{14}O	^{22}Mg	^{34}Ar
$\mathcal{F}t$	[s]		3076.7 ± 4.6	3071.5 ± 3.3	3078.0 ± 7.4	3069.6 ± 8.5
Q_{EC}	[keV/c^2]		1907.87(11)	2831.24(23)	4124.55(28)	6062.98(48)
$\gamma\left\langle W^{-1}\right\rangle$			0.6185	0.4375	0.3072	0.2106
Parent nucleus, $T_z=0$			^{26}Al^m	^{34}Cl	^{38}K^m	^{42}Sc
$\mathcal{F}t$	[s]		3072.4 ± 1.4	3070.6 ± 2.1	3072.5 ± 2.4	3072.4 ± 2.7
Q_{EC}	[keV/c^2]		4232.66(12)	5491.64(23)	6044.40(11)	6426.28(30)
$\gamma\left\langle W^{-1}\right\rangle$			0.2993	0.2321	0.2110	0.1982
		^{46}V	^{50}Mn	^{54}Co	^{62}Ga	^{74}Rb
		3073.3 ± 2.7	3070.9 ± 2.8	3069.9 ± 3.3	3071.5 ± 7.2	3078 ± 13
		7052.49(16)	7634.45(7)	8244.37(28)	9181.07(54)	10417.3 ± 4.4
		0.1805	0.1665	0.1538	0.1373	0.1192

respectively. This results in

$$\begin{aligned}
\overline{\mathcal{F}t^{0^+\to 0^+}} &= \frac{K}{G_{\mathrm{F}}^2|V_{\mathrm{ud}}|^2\left(1+\Delta_R^{\mathrm{V}}\right)} \cdot \frac{1}{2\left(L_{\mathrm{V}}^2+L_{\mathrm{S}}^2 \pm 2L_{\mathrm{V}}L_{\mathrm{S}}\gamma\left\langle W^{-1}\right\rangle\right)} && (2.122)\\
&= \frac{K}{G_{\mathrm{F}}^2|V_{\mathrm{ud}}|^2\left(1+\Delta_R^{\mathrm{V}}\right)} \cdot \frac{1}{2\left(1+x^2 \pm 2x\gamma\left\langle W^{-1}\right\rangle\right)} \qquad \text{and}\\
\overline{\tau_{\mathrm{n}}} &= \frac{K}{f_R \ln(2) G_{\mathrm{F}}^2|V_{\mathrm{ud}}|^2\left(1+\Delta_R^{\mathrm{V}}\right)} && (2.123)\\
&\quad\times \frac{1}{L_{\mathrm{V}}^2+3L_{\mathrm{A}}^2+L_{\mathrm{S}}^2+3L_{\mathrm{T}}^2+2\left(L_{\mathrm{V}}L_{\mathrm{S}}+3L_{\mathrm{A}}L_{\mathrm{T}}\right)m_{\mathrm{e}}\left\langle E_{\mathrm{e}}^{-1}\right\rangle}\\
&= \frac{K}{f_R \ln(2) G_{\mathrm{F}}^2|V_{\mathrm{ud}}|^2\left(1+\Delta_R^{\mathrm{V}}\right)}\\
&\quad\times \frac{1}{1+3\lambda^2+x^2+3\lambda^2y^2+2\left(x+3\lambda^2 y\right)m_{\mathrm{e}}\left\langle E_{\mathrm{e}}^{-1}\right\rangle}.
\end{aligned}$$

Eq. (2.122) considers the possible influence of the Fierz term b_{F} on the $\mathcal{F}t^{0^+\to 0^+}$ values. This method is not perfect either. We emphasize that the denominator $1+b_{\mathrm{F}}\gamma\left\langle W^{-1}\right\rangle$ is different for every nuclei. In our study, we have used for $\gamma\left\langle W^{-1}\right\rangle$ the values given in Table 2.1, where the rows give the measured parent nucleus, the experimental $\mathcal{F}t^{0^+\to 0^+}$ values, and the derived mean values for $\gamma\left\langle W^{-1}\right\rangle$. We used the experimental data of the 13 most precise results of Ref. [76] only. The $\gamma\left\langle W^{-1}\right\rangle$ values are derived from the decay transition energies, Q_{EC}. For nuclear decays with positron emission[34], the energy W_0 relates to the Q_{EC} values listed in Table 2.1 via [139]:

$$W_0 = \frac{Q_{\mathrm{EC}}}{m_{\mathrm{e}}} - 1. \tag{2.124}$$

---

[34] Currently, 13 transitions with positron emission, ranging from ^{10}C to ^{74}Rb, have been measured with high precision.

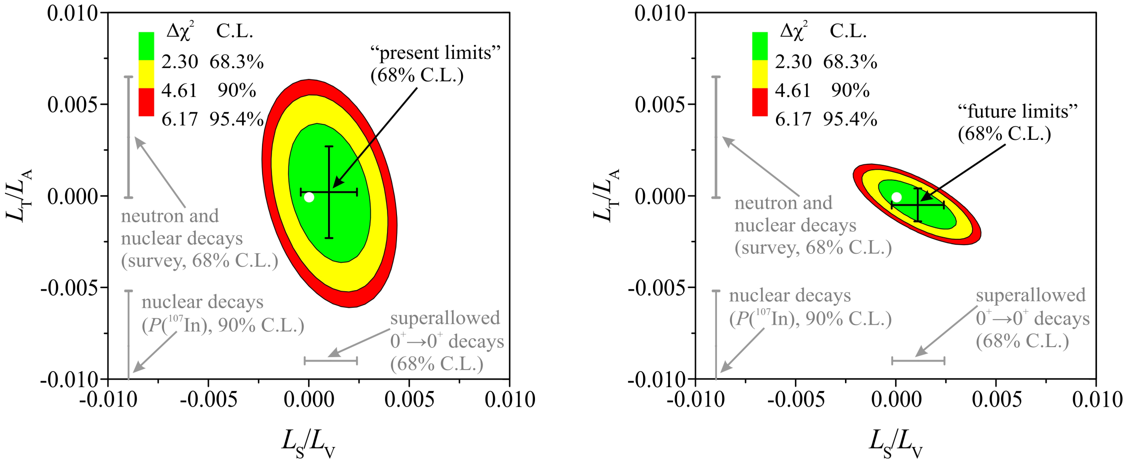

(a) (b)

Figure 2.10: Left-handed scalar and tensor currents: (a) Current limits (only a, A, B, and $\tau_{\rm n}$). (b) Projected future limits, assuming improved measurements of a, b, A, B, C, and $\tau_{\rm n}$. The SM prediction is at plot origin (white). Other limits are discussed in Sec. 2.3.1. All bars correspond to single parameter limits. Please note the different scale compared to Fig. 2.7.

We note that Eqs. (2.122) and (2.123) both depend on the element $V_{\rm ud}$ of the CKM matrix. Hence, we obtain $|V_{\rm ud}|$ as further non-vanishing parameter in this model.

Figure 2.10a shows the present limits. Free parameters λ, $L_{\rm S}/L_{\rm V}$, $L_{\rm T}/L_{\rm A}$, and $|V_{\rm ud}|$ were fitted to the observables $\bar{a}$, $\bar{A}$, $\bar{B}$, $\overline{\tau_{\rm n}}$, $\overline{\mathcal{F}t^{0^+\to 0^+}}$ (for ^{10}C to ^{74}Rb), and b and $\bar{C}$, in case of our future scenario. Additionally[35], to take into account uncertainties in radiative corrections, we fitted $\Delta_R^{\rm V}$ and f_R to 'data points' 2.361(38) % and 1.71385(34). We find

$$\begin{aligned} \lambda &= -1.2729(18), \quad |V_{\rm ud}| = 0.9745(4), \\ L_{\rm S}/L_{\rm V} &= 0.0010(14), \quad \text{and} \quad L_{\rm T}/L_{\rm A} = 0.0002(25), \end{aligned} \tag{2.125}$$

with $1\,\sigma$ statistical error.

Figure 2.10b presents the impact of projected measurements in our future scenario. New neutron decay experiments, combined with SAF decay measurements, could lead to uncertainties of

$$\Delta(L_{\rm S}/L_{\rm V}) = 0.0013 \quad \text{and} \quad \Delta(L_{\rm T}/L_{\rm A}) = 0.0009, \tag{2.126}$$

both at the $1\,\sigma$ confidence level. Hence, neutron beta decay has the potential to considerably improve the limit on LH T currents as provided by the recent survey of Severijns *et al.* [17].

In summary, new physics may be within reach of precision measurements in neutron beta decay in the near future.

2.3.3 Limits from Other Fields

The search for physics beyond the SM is one of the most active areas in experimental physics. Here, we only give an overview of experiments which also search for RH currents or for S and T interactions. For a collection of recent results see Ref. [140].

---

[35] Here, we omit the uncertainties in the physical constants $\hbar$, c, $m_{\rm e}$, and $G_{\rm F}/(\hbar c)^2$.

Constraints from Muon and Pion Decays

Muon decay provides arguably the theoretically cleanest limits on non-(V−A) weak interaction couplings [10, 141]. Muon decay involves operators that are different from the ones encountered in neutron, and generally hadronic, decays. However, in certain models (e.g., the SUSY extensions discussed in Ref. [131], or in the MLRS), the muon and neutron decay derived limits become comparable [142]. In order to illustrate the relative sensitivities of the muon and neutron sectors, we have attempted to translate the muon limits from Refs. [10] and [141] into corresponding neutron observables such as $L_{\mathrm{S}}/L_{\mathrm{V}}$, $L_{\mathrm{T}}/L_{\mathrm{A}}$, and $R_{\mathrm{T}}/R_{\mathrm{A}}$. In doing so we neglected possible differences in SUSY contributions to muon and quark decays, making the comparison merely illustrative. These limits are plotted in Figs. 2.7 to 2.10, as appropriate, showing that neutron decay experiments at their current and projected future sensitivity are not only complementary, but also competitive to the muon sector.

Limits similar to the ones discussed in Sec. 2.3.3 can be extracted from pion decays (added complexity of heavier meson decays limits their sensitivity). The presence of a tensor interaction would manifest itself both in the Fierz interference term in beta decays (e.g., of the neutron) and in a non-zero value of the tensor form factor, F_{T}, for the pion. The latter was hinted at for well over a decade, but was recently found to be constrained to $-5.2 \times 10^{-4} < F_{\mathrm{T}} < 4.0 \times 10^{-4}$ with 90 % C.L. [143]. While values for b in neutron beta decay and for the pion form factor F_{T} are not directly comparable, in certain simple scenarios they would be of the same order [144]. Thus, finding a non-zero value for b in neutron beta decay at the level of $\mathcal{O}(10^{-3})$ would be extremely interesting. Similarly, the $\pi \to \mathrm{e} + \nu$ decay ($\pi_{\mathrm{e}2}$) offers a very sensitive means to study non-(V−A) weak couplings, primarily through a pseudoscalar term in the amplitude. Alternatively, the $\pi_{\mathrm{e}2}$ decay provides the most sensitive test of lepton universality. Thus, new measurements in neutron decay would complement the results of precision experiments in the pion sector, such as PIBETA [145] and PEN [146].

Right-Handed Coupling Constraints from Neutrinoless Double Beta Decay and Neutrino Mass

The most natural mechanism of neutrinoless double beta decay ($\beta\beta0\nu$) is through virtual electron-neutrino exchange between the two neutron decay vertices. The LH and RH ν_{e} may mix with mass eigenstate Majorana neutrinos N_i [147]:

$$\nu_{\mathrm{eL}} = \sum_{i=1}^{6} U_{\mathrm{e}i} \frac{1-\gamma_5}{2} N_i \quad \text{and} \quad \nu_{\mathrm{eR}} = \sum_{i=1}^{6} V_{\mathrm{e}i} \frac{1+\gamma_5}{2} N_i, \tag{2.127}$$

where $U_{\mathrm{e}i}$ and $V_{\mathrm{e}i}$ denote elements of the LH and RH mixing matrices, respectively.

The $\beta\beta0\nu$ decay amplitude with the virtual neutrino propagator has two parts [148]. If the SM LH V−A coupling combines with LH coupling terms (LL interference), the amplitude contribution is proportional to the Majorana neutrino masses (weighted with the $U_{\mathrm{e}i}^2$ factors). Since from neutrino oscillations we have rather small lower limits for these masses (40 meV for the heaviest LH neutrino [149]), we get only weak constraints for the non-SM LH couplings. On the other hand, if the SM LH V−A coupling combines with RH non-SM terms (LR interference), the amplitude is proportional to the virtual neutrino momentum (instead of the neutrino mass); and since the momentum can be quite large we get constraints for the RH non-SM couplings. The latter part of the $\beta\beta0\nu$ decay amplitude is proportional to the effective RH couplings $\tilde{R}_j = R_j\varepsilon$, for j =V,A,S,T, where [147, 150]

$$\varepsilon = \sum_{i=1}^{6}{}^{(\text{light})} U_{\text{e}i} V_{\text{e}i}. \tag{2.128}$$

Here, "light" implies that the sum is over the light-mass neutrinos with $m_i < 10\,\text{MeV}$ only.

According to Ref. [147] there are three different scenarios:

D: all neutrinos are light Dirac particles
$\Longrightarrow$ no constraints for non-SM couplings, because $\varepsilon = 0$.

M-I: all neutrinos are light ($< 1\,\text{MeV}$) Majorana particles
$\Longrightarrow$ no constraints for non-SM couplings, because $\varepsilon = 0$ from orthogonality condition.

M-II: both light ($<$ MeV) and heavy ($>$ GeV) Majorana neutrinos exist
$\Longrightarrow$ constraints for non-SM couplings: $\varepsilon \neq 0$, because heavy neutrinos are missing from the sum; ε is on the order of the unknown, likely small, mixing angle θ_{LR} between LH and RH neutrinos.

In the M-II scenario there are stringent constraints for the effective RH V,A,S,T couplings: $|\tilde{R}_j| < 10^{-8}$ [148]. These effective couplings are proportional to $\varepsilon \sim \theta_{\text{LR}}$ [147, 150]. Since ε depends on specific neutrino mixing models, it is not possible to give model independent limits for the R_j couplings based on $\beta\beta0\nu$ decay data. We have already mentioned in Sec. 2.3.1 that for the heavy RH (Majorana) neutrinos the RH observables in neutron decay are kinematically weakened or for special cases completely suppressed.

Assuming 1 TeV effective RH neutrino mass scale within M-II, one obtains $|\zeta| < 4.7 \times 10^{-3}$ and $m_2 > 1.1\,\text{TeV}$ [150]. For a larger RH neutrino mass scale these constraints become weaker.

In Ref. [151] Klapdor-Kleingrothaus *et al.* argued that $\beta\beta0\nu$ decay occurs in nature. If further experiments confirm this observation, one can be sure that the neutrinos are Majorana particles.

The RH couplings can contribute to neutrino mass through loop effects, leading to constraints on the RH coupling constants from neutrino mass limits [152]. Using the absolute neutrino mass limit $m(\nu_{\text{e}}) < 2.2\,\text{eV}$ from the Troitsk and Mainz tritium decay experiments [153, 154], one obtains the $1\,\sigma$ limits:

$$|R_{\text{S}}| < 0.01, \quad |R_{\text{T}}| < 0.1, \quad \text{and} \quad |R_{\text{V}} - R_{\text{A}}| < 0.1. \tag{2.129}$$

With the $m(\nu_{\text{e}}) < 0.22\,\text{eV}$ model dependent limit from cosmology[36] [156], the above coupling constant limits become 10 times more restrictive. An intermediate neutrino mass upper limit in the order of $(0.5 - 0.6)\,\text{eV}$ comes from $\beta\beta0\nu$ decay [151] and from other cosmology analysis [157].

2.4 Previous and Competing Measurements of *a*

2.4.1 Previous Measurements

Previous experiments have obtained consistent measurements of the neutrino-electron correlation coefficient a with $5\,\%$ accuracy. As discussed earlier in Chap. 1 and Sec. 2.1.5, the

---

[36] The sensitivity of the KATRIN experiment [155] is similar.

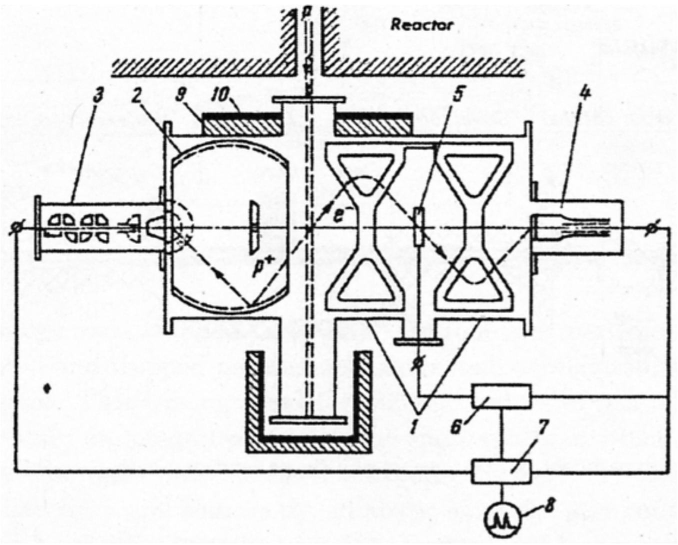

Figure 2.11: The apparatus of Grigor'ev *et al.*: 1-double toroidal spectrometer, 2-ellipsoidal proton mirror, 3-electron multiplier (proton detector), 4-photomultiplier (electron detector), 5-Geiger counter, 6-double coincidence trigger circuit, 7-camera control, 8-oscilloscope, 9-boron carbide neutron absorber, 10-lead shield. Figure from Ref. [158].

determination of a is more difficult than measurements of the beta asymmetry parameter A, since the neutrino is hard to detect and low-energy ($T < 752\,\mathrm{eV}$) recoil protons have to be detected instead.

The Measurement of GRIGOR'EV *et al.* at the ITER Research Reactor

The first important measurement of a was carried out at the ITER research reactor in the Soviet Union in 1967 by Grigor'ev *et al.* [158]. A scheme of the apparatus is shown in Fig. 2.11. The proton recoil spectrum was measured in coincidence at a fixed electron energy, in order to reduce backgrounds. The proton energy was measured by TOF through a focusing ellipsoidal electrostatic mirror. Electron and proton events coincident within a $5.5\,\mu\mathrm{s}$ time window triggered a camera that photographed the oscilloscope traces of both signals. The result was

$$a = -0.091(39), \tag{2.130}$$

with a relative error of 43 % dominated by counting statistics. At that time, the experiment of Grigor'ev *et al.* gave the best determination of $|\lambda| = 1.22(8)$.[37]

The Measurement of STRATOWA *et al.* at the Research Center Seibersdorf

The first precision measurement of the parameter a was conducted at the ASTRA reactor in Vienna by Stratowa *et al.* [40]. The set-up is schematically shown in Fig. 2.12. Stratowa *et al.* measured a from the shape of the proton recoil spectrum. The neutron decay volume was in-pile near the core of the reactor. A throughgoing beam tube was used, with no direct view to the reactor core or onto the moderator, to reduce background. Decay protons,

---

[37] According to Eq. (2.25), a can determine the magnitude but not the sign of λ.

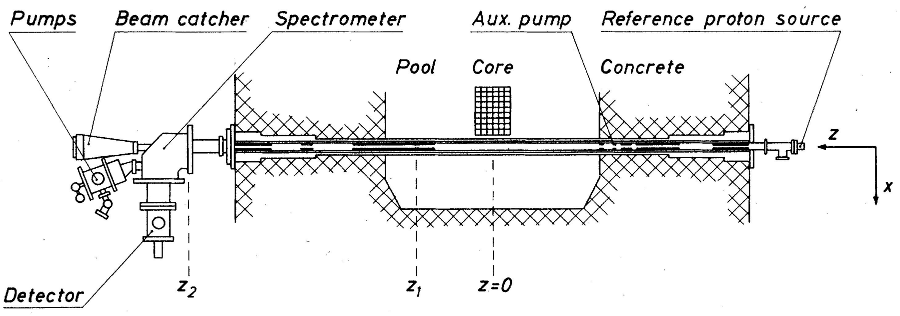

Figure 2.12: The experiment of Stratowa *et al.*. The neutron decay volume was in-pile near the core of the reactor. Decay protons emerging from the beam hole were analyzed in a spherical electrostatic spectrometer. Figure taken from Ref. [40].

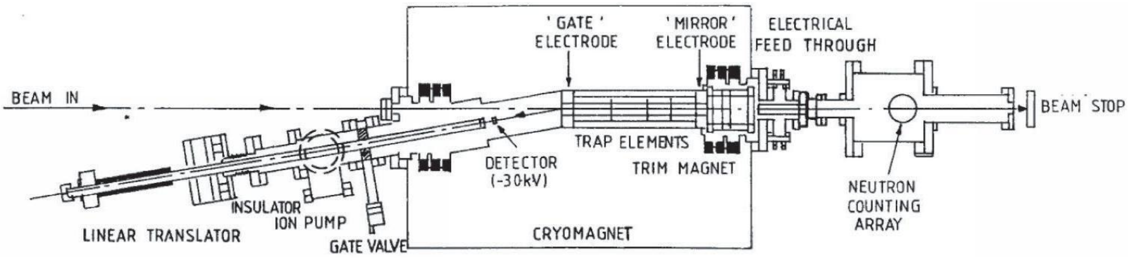

Figure 2.13: The experiment of Byrne *et al.*. A cold neutron beam passed through the center of a quasi-Penning trap. The decay protons emerged from a high to a low magnetic field region. Their energy was measured by means of a superimposed electric field. Figure taken from Ref. [41].

accepted only when their momentum was almost parallel to the tube, were analyzed in a spherical electrostatic spectrometer. The experiment achieved a proton count rate of $89\,\mathrm{s}^{-1}$, and the result was

$$a = -0.1017(51), \tag{2.131}$$

with a 5 % relative error dominated by systematic effects, especially the proton detector energy calibration, corrections for the thermal neutron motion, and proton scattering from residual gas. A result that was not surpassed for two decades.

The Measurement of Byrne *et al.* at the Institut Laue-Langevin

The second and latest precision measurement of a was performed at the Institut Laue-Langevin (ILL) in Grenoble by Byrne *et al.* [41, 159], with an apparatus converted from a previous neutron lifetime experiment [160]. A sketch of the experiment is shown in Fig. 2.13. The angular correlation coefficient a was extracted from the integral proton spectrum (for details see the measurement principles of the aSPECT spectrometer in Sec. 3.1). A cold[38] neutron beam passed through the center of a quasi-Penning trap. The decay protons emerged from a high to a low magnetic field region. In this way, their

---

[38] Free neutrons are classified according to their kinetic energy. Cold neutrons have an energy from $0.5\,\mu$eV to $0.025\,$eV, whereas, e.g., fast neutrons from fusion reactions have an energy $> 1\,$MeV.

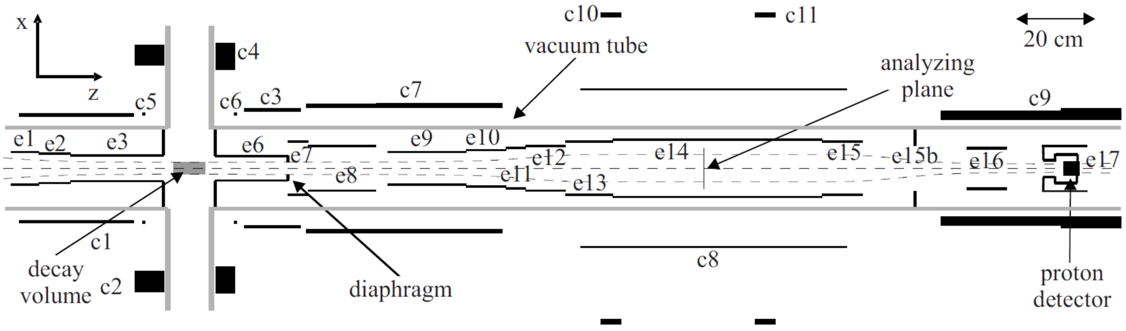

Figure 2.14: A sketch of the electromagnetic set-up of the aSPECT experiment at the FRM II. The magnet coils (c1−c11) surround the main vacuum system. The electrodes (e1−e17) are installed inside the vacuum system. The analyzing plane is a local magnetic field maximum; it is not made of any material. We note that the figure is rotated by 90 °. For details see the following chapter. Figure taken from Ref. [33].

transversal momentum was transformed into longitudinal momentum. The proton energy was then measured by means of a superimposed electric field. The result was

$$a = -0.1054(55), \tag{2.132}$$

with a 5 % relative error, similar to Stratowa *et al.* both in value and precision. Some of the weaknesses of the experiment were incomplete energy transfer from transverse to longitudinal motion, and violation of the adiabatic conditions.

First Measurements with aSPECT at the FRM II

First measurements of the parameter a with the aSPECT spectrometer were carried out at the particle physics beam MEPHISTO at the Forschungsneutronenquelle Heinz Maier-Leibnitz (FRM II) in Munich by Baeßler *et al.* [33]. The set-up is schematically shown in Fig. 2.14. The aSPECT experiment [46, 47] is a proton spectrometer, similar to Byrne *et al.* in approach but designed to correct some of its weaknesses. In short, aSPECT is a retardation spectrometer which measures the proton recoil spectrum by counting decay protons that overcome an electrostatic barrier, U_{A}. For details on the aSPECT spectrometer see the following chapters.

In our first beam time during 2005/2006 we studied the properties of the spectrometer [33, 49]. The most serious problem turned out to be situation- and time-dependent behavior of the background, cf. Fig. 2.15. For data sets, in which an unexpected proton-like peak is visible in pulse height spectra with $U_{\mathrm{A}} = 800\,\mathrm{V}$, the extracted value of a is shifted to more negative values, as can be seen from Fig. 2.15b[39]. From those data sets in which a background problem was not obvious, we could extract a value of a, but we could not quantify the background correction nor its uncertainty (see also page 56 under “Penning Traps and Penning Discharge” and Sec. 5.3).

To sum up, the present best experiments have an uncertainty of $\Delta a/a = 5\,\%$ and since the late 1970s there is no substantial improvement. The measurements of Grigor’ev *et al.*,

---

[39] Please note that Fig. 2.15b slightly differs from Fig. (4.6) in Ref. [49], as these are not the final results of the data analysis.

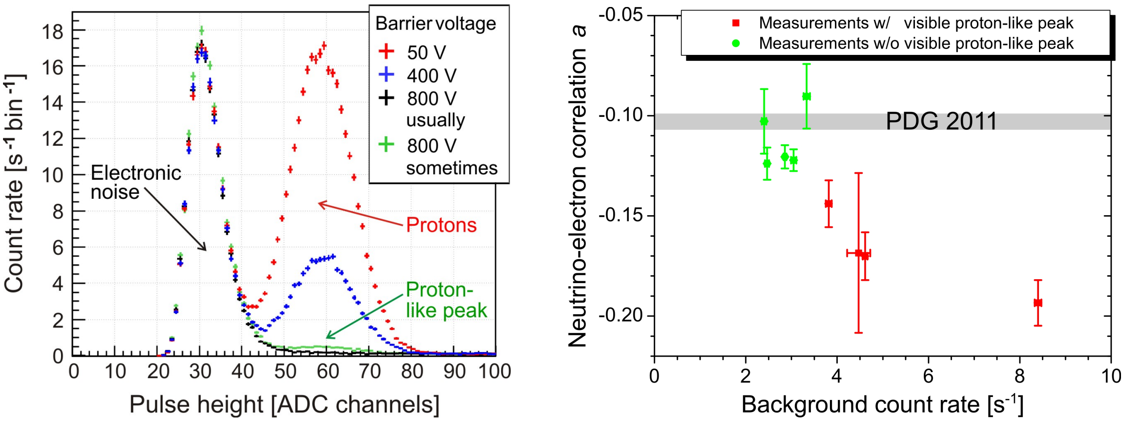

(a) (b)

Figure 2.15: (a) Pulse height spectra measured at the FRM II with a silicon PIN diode set at a potential of -30 kV. With increasing barrier voltage the count rate in the proton peak (right peak) decreases whereas the electronic noise (left peak) is not influenced. The background is measured at $U_A = 800\,\mathrm{V}$. (b) Extracted value of the angular correlation coefficient a versus background count rate. For data sets, in which an unexpected proton-like peak is visible in pulse height spectra with $U_A = 800\,\mathrm{V}$, as shown in (a), the extracted value of a is shifted to more negative values. Error bars show statistical errors only. For comparison, the gray bar represents the Particle Data Group's (PDG) 2011 average [10].

Stratowa *et al.*, and Byrne *et al.* yield a world average of [10]:

$$a = -0.103(4). \tag{2.133}$$

Here, the Particle Data Group does not use the data from [161] for their average as Mostovoi calculates a from its measurement of $\lambda = g_A/g_V$. Figure 2.16 shows the weighted average from the PDG 2011 review.

2.4.2 Upcoming Experiments

As discussed earlier in Chap. 1 there is strong motivation to improve the uncertainty in the neutrino-electron correlation coefficient a to less than 1 %. Two major, funded experiments, based in the United States are currently attempting to do this: aCORN [98, 162] at the National Institute of Standards and Technology (NIST) and Nab [99, 163] at the new Spallation Neutron Source (SNS) in Oak Ridge, Tennesse.

The aCORN Experiment at NIST

The aCORN experiment [98, 162] uses a new method first proposed by Yerozolimsky and Mostovoy [164, 165]. A sketch of the spectrometer is shown in Fig. 2.17a. Decay electrons and protons are detected in coincidence. The electron energy and the TOF between electron and proton detection will be measured, to discriminate between two groups of protons, as shown in the top of Fig. 2.17b. Group II (protons first emitted in the same direction as the electrons towards the electron detector) will be slower than the other group I (protons emitted in direction of the proton detector opposite the electron detector). The method relies on the construction of an asymmetry that directly yields a without

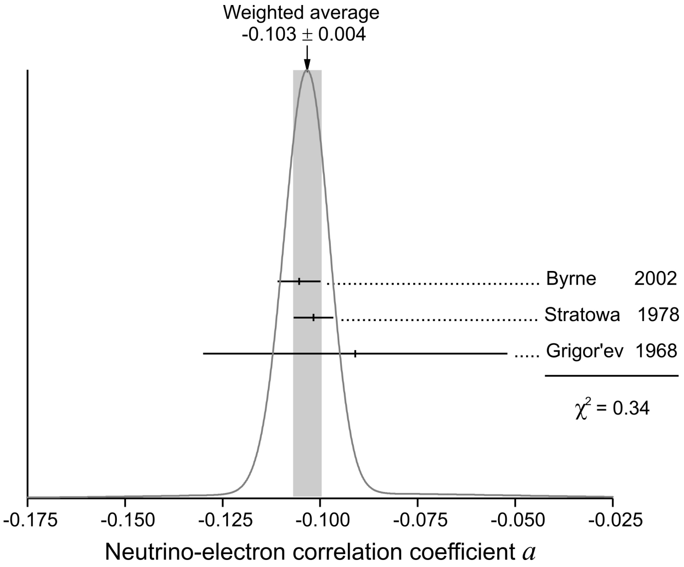

Figure 2.16: World average of the neutrino-electron correlation coefficient a from the PDG 2011 review [10].

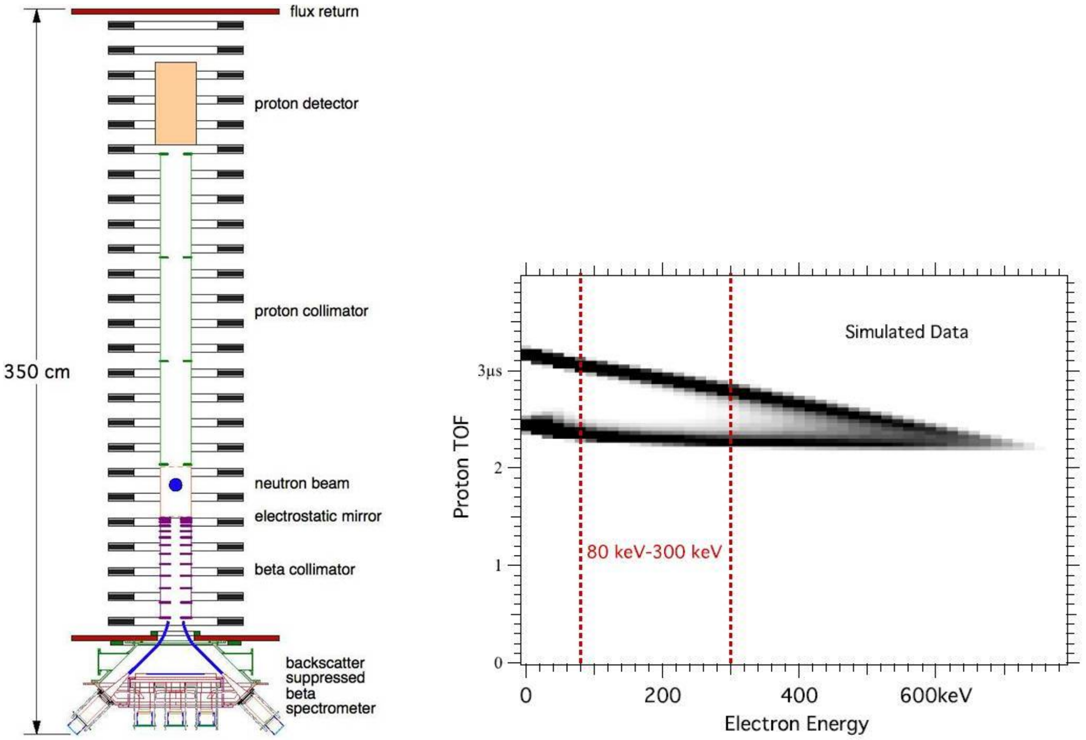

(a) (b)

Figure 2.17: (a) A sketch of the aCORN apparatus. (b) Measurement principle of aCORN: MC simulation of the proton TOF versus the electron energy. The two groups I (lower branch) and II (upper branch) are well separated for electron energies below 300 keV. Figures taken from Refs. [22, 98]

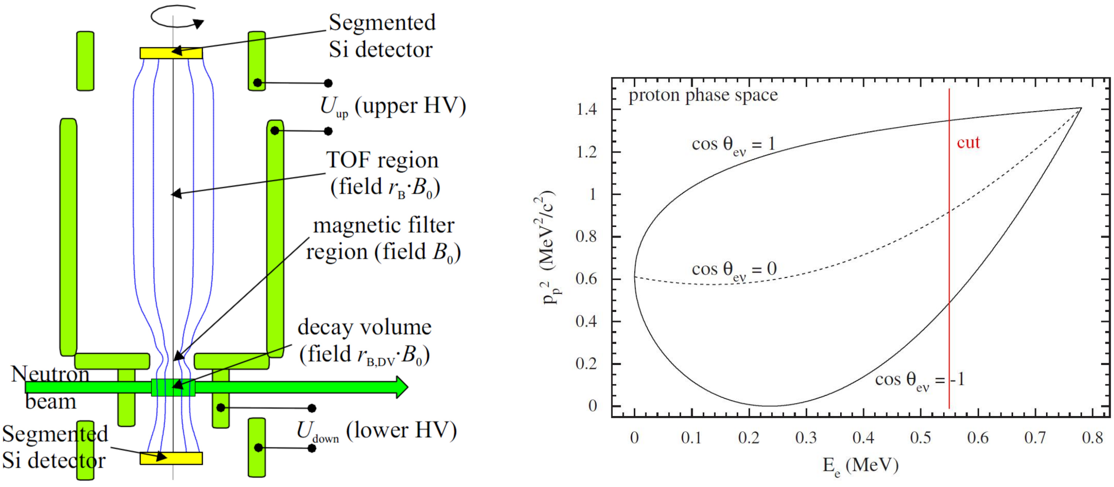

(a) (b)

Figure 2.18: (a) A sketch of the set-up of an asymmetric Nab spectrometer [163]. (b) Measurement principle of Nab: Proton phase space, in terms of p_p^2, as a function of electron kinetic energy. Figures taken from Refs. [99, 163]

requiring precise proton spectroscopy:

$$a(E_\mathrm{e}) = \frac{1}{v_\mathrm{e}} K(E_\mathrm{e}) \frac{N_\mathrm{I} - N_\mathrm{II}}{N_\mathrm{I} + N_\mathrm{II}}, \tag{2.134}$$

where $K(E_\mathrm{e})$ is a calculated instrumental constant, and N_I and N_II denote the number of events in group I and group II, respectively.

The apparatus was integrated and tested at the Indiana University Cyclotron Facility (IUCF) and then moved to the NIST Center for Research for the initial run. All systems work, but problems of high voltage discharges, due to crossed electric and magnetic fields, require a redesign of the proton focusing for low magnetic field [166]. The experiment hopes to obtain a relative uncertainty in a of 1 %.

The Nab Experiment at the SNS

The Nab experiment [99] is based on an observation made by Bowman [167]. The new asymmetric version of the instrument (for details see [163]) is conceptually shown in Fig. 2.18a. Decay electrons and protons are detected in coincidence. Similar to aCORN, the electron energy and the time between electron and proton detection, t_p, will be measured. The Nab method relies on the linear dependence of $\cos\theta_{\mathrm{e}\nu}$ on p_p^2 for a given electron momentum p_e (or kinetic energy E_e)[40]:

$$p_\mathrm{p}^2 = p_\mathrm{e}^2 + 2p_\mathrm{e}p_\nu \cos\theta_{\mathrm{e}\nu} + p_\nu^2. \tag{2.135}$$

Since p_ν depends almost only on E_e (or p_e), Eq. (2.135) reduces to a linear relation between $\cos\theta_{\mathrm{e}\nu}$ and p_p^2 for a fixed p_e; the mapping is graphically shown in the bottom of Fig. 2.18b. Hence, the parameter a is determined from the slopes of the $1/t_\mathrm{p}^2$ distributions for different values of E_e.

---

[40] Please note that E_e denotes, here, the electron kinetic energy.

The Nab Collaboration develops a novel electromagnetic spectrometer. The goal is to measure a and the Fierz interference term b in the same apparatus, with $\Delta a/a \approx 10^{-3}$ and $\Delta b \approx 3 \times 10^{-3}$.

In summary, the measurement of the neutrino-electron correlation coefficient a provides one of best avenues for an independent determination of λ. The prospects for a significantly improved value for a in the near future are promising.

Chapter 3

The *a*SPECT Experiment

The neutron decay spectrometer *a*SPECT [46, 47] has been designed to perform precise measurements of the neutrino-electron correlation coefficient a, by measuring the proton recoil spectrum in the decay of free, unpolarized neutrons. *a*SPECT is a retardation spectrometer which, in turn, measures the proton recoil spectrum by counting all decay protons that overcome an electrostatic barrier, U_{A}, similar to the experiment of Byrne *et al.* [41].

After a short introduction to the measurement principles, the electromagnetic set-up of the *a*SPECT spectrometer and its detection system will be presented in this chapter. The main emphasis of this thesis lies on the investigation of several different systematic effects. Hence, we also introduce the dominant uncertainties in the determination of a. More details on the electromagnetic set-up and the detection system are found in the theses of F. Ayala Guardia [53, 168] and M. Simson [52], respectively.

3.1 Measurement Principles

The *a*SPECT experiment is schematically shown in Fig. 3.1. Unpolarized, cold neutrons are coming from the left and pass through the decay volume (DV) where about 10^{-8} of the neutrons decay. The decay protons are guided by the strong magnetic field towards the analyzing plane (AP) and subsequently the proton detector on top of the spectrometer. Protons emitted in the negative z-direction are reflected by the electrostatic mirror on the bottom of the spectrometer, ensuring 100 % acceptance for decay protons. Therefore, the electrostatic mirror is held at a positive voltage $U_{\mathrm{M}} > T_{\mathrm{p,max}}$. In the AP, situated in the center of a 54 cm long cylindrical electrode, we apply a variable barrier voltage U_{A}. Only protons with sufficient kinetic energy can pass the potential barrier. These protons are accelerated by a high voltage of −15 kV and magnetically focused onto the detector where they are counted. The detector has to be held at a high negative potential to post-accelerate the protons to detectable energies and to ensure that they overcome the magnetic mirror (discussed in the following Sec. 3.1.1) right in front of the detector. The AP voltage U_{A} is varied between 0 and +800 V, to scan the proton spectrum shape, cf. Fig. 2.3. Measurements with $U_{\mathrm{A}} = 780\,\mathrm{V}$ serve to quantify the background. The magnetic field in the AP, B_{A}, is much lower than in the DV, B_0. Therefore, the momenta of the decay protons are aligned by the inverse magnetic mirror effect. Then the response of the spectrometer can be described by the so-called transmission function, introduced in Sec. 3.1.2. In between the DV and the AP a dipole electrode creates a transverse electric

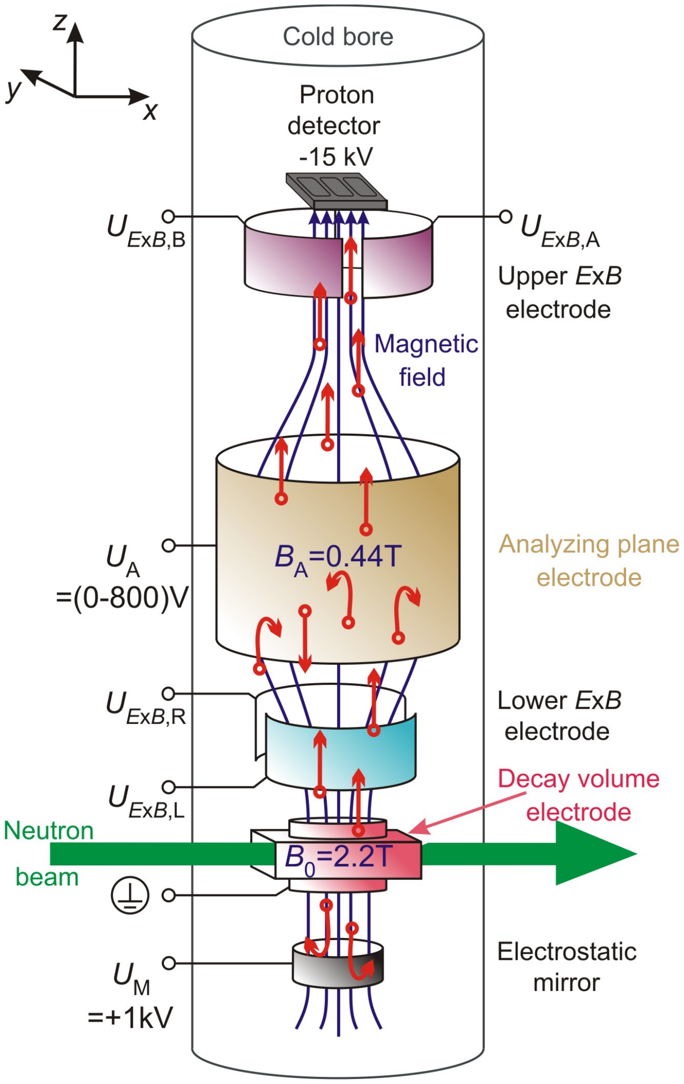

Figure 3.1: Scheme of the *a*SPECT experiment: Unpolarized, cold neutrons (green) pass through the decay volume (pink) where only a few neutrons decay. The decay protons (red) are guided by the strong magnetic field towards the analyzing plane (gold) and subsequently the proton detector (dark gray). The analyzing plane voltage U_A is varied between 0 and +800 V, to scan the proton spectrum shape, cf. Fig. 2.3. Protons emitted in the negative z-direction are reflected by the electrostatic mirror (black). Trapped protons are removed from the flux tube with the lower dipole electrode (turquoise). The upper dipole electrode (purple) serves to align the neutron beam on the detector.

field and hence a large $\mathbf{E}\times\mathbf{B}$. This is used to sweep out decay protons that would otherwise be trapped. In between the AP and the proton detector a second dipole electrode, rotated 90° in the vertical relative to the first one, serves to align the neutron beam on the detector.

3.1.1 Adiabatic Invariance and Magnetic Mirror Effect

Adiabatic Invariance

Adiabatic invariance, an approximate conservation law, is a general result for any dynamical system that can be described by a Hamiltonian $H(\mathbf{q}, \mathbf{p}, \lambda)$ and which follows periodic motion. Here, $\mathbf{q}$ and $\mathbf{p}$ denote the generalized coordinates and their canonically conjugate momenta, respectively, and $\lambda = \lambda(t)$ are the system's parameters. If λ is changed adiabatically, i.e., the timescale of changes in λ is much greater than the oscillation period, then the action integrals J_i

$$J_i(E, \lambda) = J_i(E(t), \lambda(t)) = \oint p_i dq_i, \quad i = 1, 2, 3, \tag{3.1}$$

are the adiabatic invariants of the system, where the contour integrals are taken at fixed total energy E and fixed value of λ.

Charged Particle Motion

In the *a*SPECT experiment, the decay products, electrons and protons, are moving in a static magnetic field, $\mathbf{B}$. The Lorentz force[1]

$$\mathbf{F}_{\mathrm{L}} = q\,(\mathbf{v} \times \mathbf{B}) \tag{3.2}$$

therefore forces the charged particles to move on circular orbits, i.e., to gyrate around a magnetic field line. Here, q and $\mathbf{v}$ are the charge and the velocity of the particle, respectively. The radius of gyration, r_{g}, is determined by equating the magnitude of the Lorentz force with the centripetal force

$$r_{\mathrm{g}} = \frac{mv_\perp}{eB}, \tag{3.3}$$

where the velocity component $v_\perp$ perpendicular to the magnetic field is given by

$$v^2 = v_{||}^2 + v_\perp^2. \tag{3.4}$$

Here, m is the particle's mass and $v_{||}$ is the velocity component parallel to the magnetic field. The maximum radius of gyration is achieved for particles emitted perpendicular to the magnetic field:

$$r_{\mathrm{g,max}} = \frac{mv_{\mathrm{max}}}{eB} = \frac{\sqrt{2mT_{\mathrm{max}}}}{eB}, \tag{3.5}$$

where v_{max} and T_{max} are the maximum velocity and kinetic energy of the particle, respectively. Assuming $B = B_0 = 2.2\,\mathrm{T}$ as in Fig. 3.1, the maximum radii of gyration are

$$r_{\mathrm{g,max}} \approx 1.80\,\mathrm{mm} \tag{3.6}$$

both for protons and electrons.

Adiabatic Invariants

Let us return to the adiabatic invariants. In the case of particle motion in an inhomogeneous magnetic field, the condition for adiabatic transport can be formulated as the requirement that the quantity ϵ, defined in [169] as:

$$\epsilon = \frac{2\pi p \cos\theta}{eB^2} \left| \frac{\partial B}{\partial z} \right|, \tag{3.7}$$

---

[1] Please note that we assume w.l.o.g. $c = 1$; see also our note on page 16 in Chap. 2.

is small ($\epsilon \ll 1$). Here p is the particle's momentum, θ its angle to the z-axis, and $\frac{\partial B}{\partial z}$ a small magnetic field gradient in z-direction. According to Ref. [170], then the adiabatic invariants are

$$B r_{\mathrm{g}}^2\,, \tag{3.8}$$

$$\frac{p_\perp^2}{B}\,, \qquad \text{and} \tag{3.9}$$

$$\gamma\mu\,, \tag{3.10}$$

where $p_\perp$ is the momentum component perpendicular to the magnetic field, $\gamma = \frac{1}{\sqrt{1-\beta^2}}$ is the relativistic factor, with the particle's velocity in units of the velocity of light, $\beta = \frac{v}{c}$, and

$$\mu = \frac{m v_\perp^2}{2\gamma B} = \frac{e\omega_B r_{\mathrm{g}}^2}{2} \tag{3.11}$$

is the orbital magnetic moment, with the Larmor frequency $\omega_B = \frac{eB}{\gamma m}$. By substituting Eq. (3.8) into Eq. (3.5) we get the maximum radius of gyration for any other strength B of the magnetic field

$$r_{\mathrm{g,max}}(B) = r_{\mathrm{g,max}}(B = 2.2\,\mathrm{T}) \cdot \sqrt{\frac{2.2\,\mathrm{T}}{B}}. \tag{3.12}$$

Magnetic Mirror Effect

Similarly, by substituting Eq. (3.9) into Eq. (3.4) we get

$$v_{||}^2(z) = v^2 - v_\perp^2(z) = v^2 - \frac{v_{\perp,0}^2}{B_0} \cdot B(z), \tag{3.13}$$

where $v_{\perp,0}$ and B_0 are the transverse velocity component and the strength of the magnetic field, respectively, at, e.g., the decay point $\mathbf{P}_0$, and $v_{||}(z)$, $v_\perp(z)$, and $B(z)$ are the longitudinal and transverse velocity components and the strength of the magnetic field, respectively, at any other point $\mathbf{P} = (x, y, z)$ of the particle's trajectory. Here, we assume that the dependence of both velocity and magnetic field on the coordinates x and y is negligible. Two cases must be considered:

Magnetic mirror effect: If a particle is moving towards an increasing magnetic field $B(z)$, its velocity component $v_{||}(z)$ parallel to the magnetic field decreases, becomes zero at a certain point, and finally changes its sign. The latter is equivalent to the reflection at a magnetic mirror. This effect can be used in magnetic bottles, where charged particles are trapped between two magnetic barriers.

Inverse magnetic mirror effect or magnetic adiabatic collimation: On the other hand, if a particle is moving towards a decreasing magnetic field $B(z)$, its velocity component $v_{||}(z)$ parallel to the magnetic field increases. This is equivalent to the alignment of the particle's momentum with the magnetic field.

In *a*SPECT, the decay protons are aligned in the AP by the inverse magnetic mirror effect. The electrostatic barrier U_{A} is only sensitive to the longitudinal momentum of the protons. Therefore, the inverse magnetic mirror effect serves to transfer almost the total proton momentum into longitudinal momentum without loss of momentum.

We note that the principle of magnetic adiabatic collimation was first applied in electron spectroscopy [169, 171, 172]. Starting in the mid 1980 s, this principle was successfully employed at Troitsk and Mainz in direct neutrino mass measurements via the endpoint of the tritium beta spectrum [153, 154]. The upgrade of the neutrino mass spectrometer, KATRIN [155], is based on the same principle [173, 174]. Currently, the WITCH experiment searches for exotic interactions by investigating the neutrino-electron correlation coefficient a in several allowed nuclear beta decays. For the measurement of the recoil energy spectrum, WITCH uses an electromagnetic retardation spectrometer with magnetic adiabatic collimation. As a first step, the recoil ions from the β^--decay of ^{124}In, stored in a Penning trap, have been investigated [175].

3.1.2 The Adiabatic Transmission Function

The aSPECT spectrometer has been designed such that all decay protons fulfill the condition for adiabatic transport. Therefore, the relative spatial changes of the magnetic and also electric field have to stay small during one particle gyration [174] (see also [176, 177]):

$$\Delta B/B \ll 1 \quad \text{and} \quad \Delta E/E \ll 1. \tag{3.14}$$

Then Eqs. (3.8) to (3.10) are still the adiabatic invariants of the system.

Similar to the proton's velocity, it is useful to decompose the proton kinetic energy T_p into longitudinal and transverse components, at any point $\mathbf{P}$ of the proton's trajectory:

$$T_{\mathrm{p},||}(z) = T_\mathrm{p}(z)\cos^2\theta(z) \quad \text{and} \tag{3.15}$$

$$T_{\mathrm{p},\perp}(z) = T_\mathrm{p}(z)\sin^2\theta(z). \tag{3.16}$$

Then we can rewrite the orbital magnetic moment Eq. (3.11) in terms of the proton kinetic energy[2]:

$$\mu(z) = \frac{m v_{\mathrm{p},\perp}^2(z)}{2B(z)} = \frac{T_{\mathrm{p},\perp}(z)}{B(z)} = \frac{T_\mathrm{p}(z)\sin^2\theta(z)}{B(z)}. \tag{3.17}$$

By substituting Eq. (3.10) into Eq. (3.17) we get the orbital magnetic moment at any point $\mathbf{P}$ of the proton's trajectory:

$$\mu = \frac{T_0 \sin^2\theta_0}{B_0} = \frac{T_\mathrm{p}(z)\sin^2\theta(z)}{B(z)}, \tag{3.18}$$

where T_0 and θ_0 are the proton kinetic energy and its polar angle, respectively, at the decay point $\mathbf{P}_0$. Solving Eq. (3.18) for $\sin^2\theta(z)$ yields:

$$\sin^2\theta(z) = \frac{B(z)}{B_0}\frac{T_0}{T_\mathrm{p}(z)}\sin^2\theta_0, \tag{3.19}$$

and subsequently for the longitudinal component Eq. (3.15) of the proton kinetic energy:

$$T_{||}^{\mathrm{ad}}(z) = T_\mathrm{p}(z)\cos^2\theta(z) = T_\mathrm{p}(z)\left(1-\sin^2\theta(z)\right) = T_\mathrm{p}(z) - \frac{B(z)}{B_0}T_0\sin^2\theta_0. \tag{3.20}$$

---

[2] Here and in the following, we assume w.l.o.g. $\gamma = 1$ because of the low energies of the protons.

Here, the superscript ad denotes “in adiabatic approximation”. For reasons of energy conservation

$$E_{\mathrm{p}} = T_{\mathrm{p}}(z) + V_{\mathrm{p}}(z) = T_0 = T_{\mathrm{p}}(z) + e\,(U(z) - U_0)\,, \tag{3.21}$$

where V_{p} is the potential energy of the proton, we can deduce the proton kinetic energy at any point **P**:

$$T_{\mathrm{p}}(z) = T_0 - e\,(U(z) - U_0)\,. \tag{3.22}$$

Substituting this into Eq. (3.20) yields:

$$T_{||}^{\mathrm{ad}}(z) = T_0 - e\,(U(z) - U_0) - \frac{B(z)}{B_0} T_0 \sin^2\theta_0. \tag{3.23}$$

A decay proton reaches the proton detector if and only if the adiabatic transmission condition

$$T_{||}^{\mathrm{ad}}(z) \overset{!}{>} 0 \tag{3.24}$$

is fulfilled for every point **P** along its trajectory. The other way round, if at some point $T_{||}^{\mathrm{ad}}(z) < 0$ then the proton will be reflected at this point. Therefore, an important design goal of *a*SPECT was that no proton with sufficient kinetic energy to overcome the electrostatic barrier can be reflected outside the AP, except for the electrostatic mirror.

Let us confine ourselves to the AP. Solving inequation (3.24) for T_0, where $T_{||}^{\mathrm{ad}}(z)$ is given by Eq. (3.23), yields:

$$T_0 > T_{\mathrm{tr}}(\theta_0) = e\,(U_{\mathrm{A}} - U_0)\left(1 - \frac{B_{\mathrm{A}}}{B_0}\sin^2\theta_0\right)^{-1}. \tag{3.25}$$

The adiabatic transmission energy, $T_{\mathrm{tr}}(\theta_0)$, is shown in Fig. 3.2. Hence, protons with

$$T_0 > T_{\mathrm{tr}}^{\max} = T_{\mathrm{tr}}(\theta_0 = \pm 90^\circ) = e\,(U_{\mathrm{A}} - U_0)\left(1 - \frac{B_{\mathrm{A}}}{B_0}\right)^{-1} \tag{3.26}$$

are transmitted through the potential barrier U_{A}, whereas protons with

$$T_0 < T_{\mathrm{tr}}^{\min} = T_{\mathrm{tr}}(\theta_0 = 0^\circ) = e\,(U_{\mathrm{A}} - U_0) \tag{3.27}$$

are reflected at the potential barrier and subsequently trapped between the AP and the electrostatic mirror, both independent of their (initial) polar angle. Solving inequation (3.24) for θ_0, in turn, yields that, for initial energies $T_{\mathrm{tr}}^{\min} < T_0 < T_{\mathrm{tr}}^{\max}$, protons can pass the potential barrier only if their (initial) polar angle goes below[3]

$$\theta_0 < \theta_{\mathrm{tr}}^{\max} = \arcsin\sqrt{\frac{B_0}{B_{\mathrm{A}}}\left(1 - \frac{e\,(U_{\mathrm{A}} - U_0)}{T_0}\right)}, \tag{3.28}$$

---

[3] Please note that, here, we need to consider only polar angles $\theta \in [0, 90^\circ]$ as protons emitted in the negative z-direction, i.e., with angles $\theta \in (90^\circ, 180^\circ]$, are reflected at the electrostatic mirror into angles $(180^\circ - \theta) \in [0, 90^\circ)$.

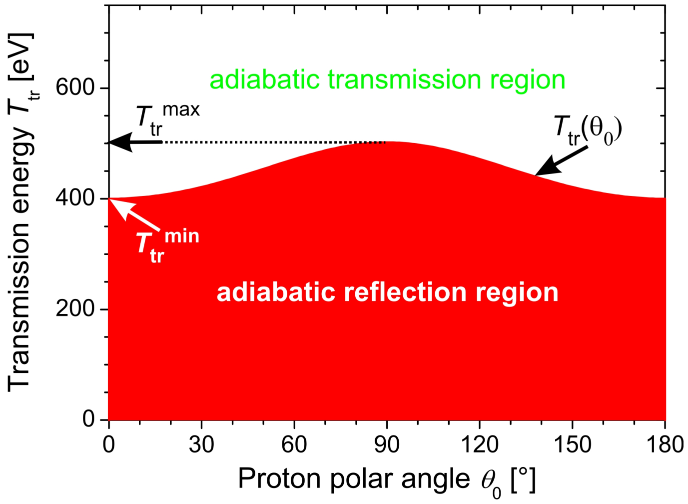

Figure 3.2: The adiabatic transmission energy Eq. (3.25) separates the reflection region (red) from the transmission region (white). In the adiabatic approximation, decay protons with an initial kinetic energy $T_0 > T_{\mathrm{tr}}(\theta_0)$ will be transmitted by the potential barrier U_{A}, whereas those with $T_0 < T_{\mathrm{tr}}(\theta_0)$ will be reflected. The transmission line $T_{\mathrm{tr}}(\theta_0)$ is shown for $U_{\mathrm{A}} - U_0 = 400\,\mathrm{V}$ and $B_{\mathrm{A}}/B_0 = 0.203$. We mention that, if the adiabatic transmission condition Eq. (3.24) is fulfilled for $\theta_0 = 90°$, it is fulfilled also for any other (initial) polar angle θ_0.

i.e., protons with an initial energy of $T_{\mathrm{tr}}^{\mathrm{min}} < T_0 < T_{\mathrm{tr}}^{\mathrm{max}}$ are transmitted through the potential barrier with a probability of[4]

$$\begin{aligned} w_{\mathrm{tr}}(T_0) &= \int_0^{\theta_{\mathrm{tr}}^{\mathrm{max}}} d\theta \sin\theta = \Big[-\cos\theta \Big]_0^{\theta_{\mathrm{tr}}^{\mathrm{max}}} = \left(1 - \sqrt{1 - \sin^2 \theta_{\mathrm{tr}}^{\mathrm{max}}}\right) \\ &= 1 - \sqrt{1 - \frac{B_0}{B_{\mathrm{A}}}\left(1 - \frac{e\,(U_{\mathrm{A}} - U_0)}{T_0}\right)}. \end{aligned} \tag{3.29}$$

Altogether, the probability that a proton with given definite kinetic energy T_0 can pass the AP is described by the transmission function:

$$F_{\mathrm{tr}}(T_0; U_{\mathrm{A}}) = \begin{cases} 0 & , \quad T_0 \leq T_{\mathrm{tr}}^{\mathrm{min}} \\ 1 - \sqrt{1 - \frac{B_0}{B_{\mathrm{A}}}\left(1 - \frac{e(U_{\mathrm{A}} - U_0)}{T_0}\right)} & , \quad T_{\mathrm{tr}}^{\mathrm{min}} < T_0 \leq T_{\mathrm{tr}}^{\mathrm{max}} \\ 1 & , \quad T_0 > T_{\mathrm{tr}}^{\mathrm{max}} \end{cases} . \tag{3.30}$$

In the ideal case, $B_{\mathrm{A}}/B_0 \longrightarrow 0$, the transmission function becomes a step function (see also Eqs. (3.26) and (3.27)). We have chosen $B_{\mathrm{A}}/B_0 = 0.203$ as a reasonable compromise between size and resolution of the spectrometer. In this case, deviations from the adiabatic approximation can be neglected [47]. The transmission function is shown in Fig. 3.3, together with the proton recoil spectrum with the recommended value for $a = -0.103$ [10].

---

[4] Please note that the proton recoil spectrum Eq. (2.43) depends neither on the proton's azimuthal nor polar angle; the latter because we are investigating unpolarized neutrons. We therefore can derive the transmission probability by integration over only the polar angle θ.

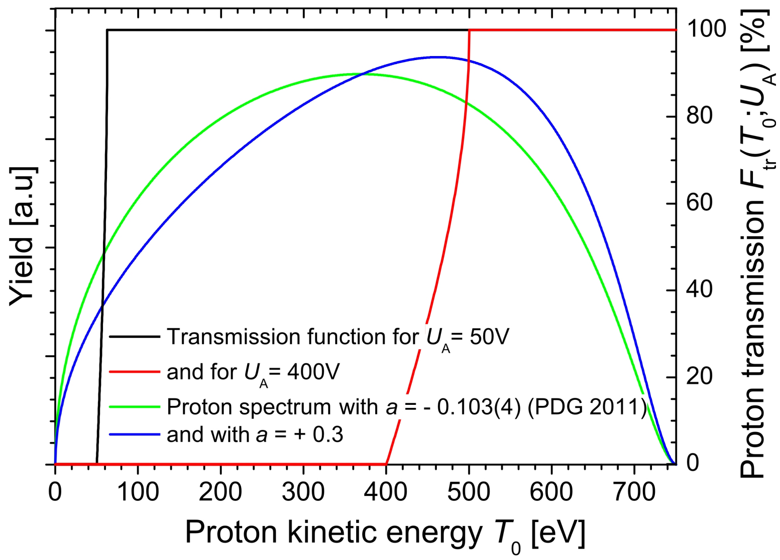

Figure 3.3: The black and red line indicate the transmission function for protons in unpolarized neutron decay, for $B_A/B_0 = 0.203$ and $U_A - U_0 = 50\,\text{V}$ respectively $U_A - U_0 = 400\,\text{V}$. For elucidation, the green line shows the proton energy spectrum with the recommended value for $a = -0.103$ [10]. To demonstrate the sensitivity of the proton recoil spectrum on the neutrino-electron correlation coefficient a, the blue line shows the proton spectrum for a different value of a.

We mention that Eq. (3.30) depends only on the electrostatic potential and the magnetic field values in the DV and the AP. More precisely, in the adiabatic approximation, the transmission function depends only on the ratio of the magnetic fields in the AP and the DV,

$$r_B = B_A/B_0, \tag{3.31}$$

and the barrier voltage U_A; the latter as in our measurement the DV is grounded, i.e., $U_0 \equiv 0$. Only these two quantities have to be determined with high precision [46]. At all other points of the proton's trajectory, a rough knowledge of the electrostatic potential and the magnetic field is sufficient, provided that the adiabatic transmission condition Eq. (3.24) is fulfilled everywhere. Furthermore, the transmission function does not depend on the detector characteristics, as long as the detector just counts the decay protons which pass the AP.

3.1.3 Computation of a from the Proton Recoil Spectrum

In our experiment, the proton detector counts all decay protons that overcome the electrostatic barrier. The proton count rate at a given barrier voltage U_A can then be derived from Eq. (3.30):

$$N_p(U_A) = N_0 \int_0^{T_{p,\max}} dT\, F_{tr}\,(T; U_A)\, w_{p,C,\alpha}(T), \tag{3.32}$$

where $N_0 = N_p(U_A = 0\,\text{V})$ is the full proton decay rate. Figure 3.4 shows the proton count rate $N_p(U_A)$ for two different values of a to demonstrate the sensitivity of the integral

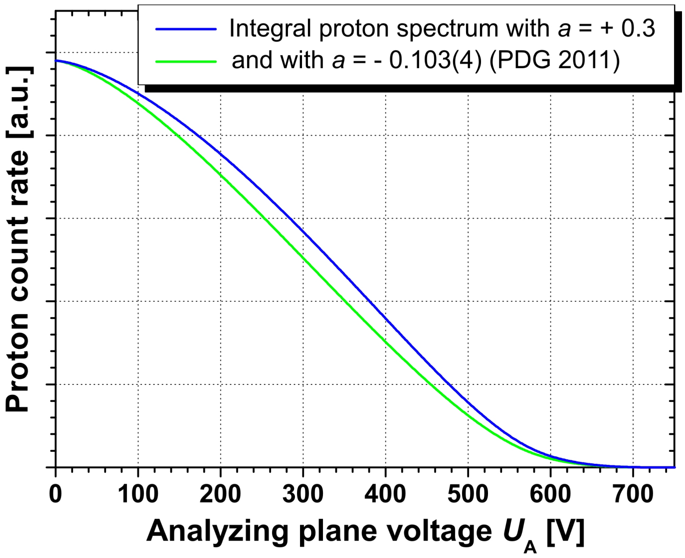

Figure 3.4: The theoretical integral proton spectrum Eq. (3.32) in neutron beta decay, for $B_\mathrm{A}/B_0 = 0.203$. The green line is the prediction from the SM with the recommended value for $a = -0.103$ [10], the blue line shows how a deviation from that ($a = +0.3$) would look like.

proton spectrum on the angular correlation coefficient a. We measure the proton count rate $N_\mathrm{p}(U_\mathrm{A})$ at different barrier voltages U_A and extract the neutrino-electron correlation coefficient a from a two parameter fit to $N_\mathrm{p}(U_\mathrm{A})$. The two fit parameters are N_0 and of course the angular correlation coefficient a. This is our standard method to determine a from the measured proton spectra.

In Ref. [46], the specific count rate ratio

$$r_\mathrm{h}(U_\mathrm{A}) = \frac{N_\mathrm{p}(U_\mathrm{A})}{N_0} \tag{3.33}$$

was considered and its sensitivity to a was demonstrated. If in Eq. (3.32) we now replace the proton recoil spectrum $w_{\mathrm{p,C},\alpha}(T)$ by Nachtmann's formula Eq. (2.38), $w_{\mathrm{p,[Nac68]}}$, we obtain for the count rate ratio

$$r_\mathrm{h}(U_\mathrm{A}) = \frac{\int_0^{T_\mathrm{p,max}} dT F_\mathrm{tr}(T;U_\mathrm{A}) g_1(T) + a \int_0^{T_\mathrm{p,max}} dT F_\mathrm{tr}(T;U_\mathrm{A}) g_2(T)}{\int_0^{T_\mathrm{p,max}} dT g_1(T) + a \int_0^{T_\mathrm{p,max}} dT g_2(T)}\,. \tag{3.34}$$

Solving Eq. (3.34) for a yields:

$$a = \frac{\int_0^{T_\mathrm{p,max}} dT F_\mathrm{tr}(T;U_\mathrm{A}) g_1(T) - r_\mathrm{h}(U_\mathrm{A}) \int_0^{T_\mathrm{p,max}} dT\, g_1(T)}{\int_0^{T_\mathrm{p,max}} dT F_\mathrm{tr}(T;U_\mathrm{A}) g_2(T) - r_\mathrm{h}(U_\mathrm{A}) \int_0^{T_\mathrm{p,max}} dT g_2(T)}\,. \tag{3.35}$$

Thus, the angular correlation coefficient a can also be determined from measurements of the decay rate ratio $r_\mathrm{h}(U_\mathrm{A})$ for different barrier voltages U_A. Then,

> **an absolute uncertainty of the potential barrier U_A of 7 mV and a relative uncertainty of the magnetic field ratio r_B of 1×10^{-4} would each correspond to a relative uncertainty in a of about 0.1 %,**

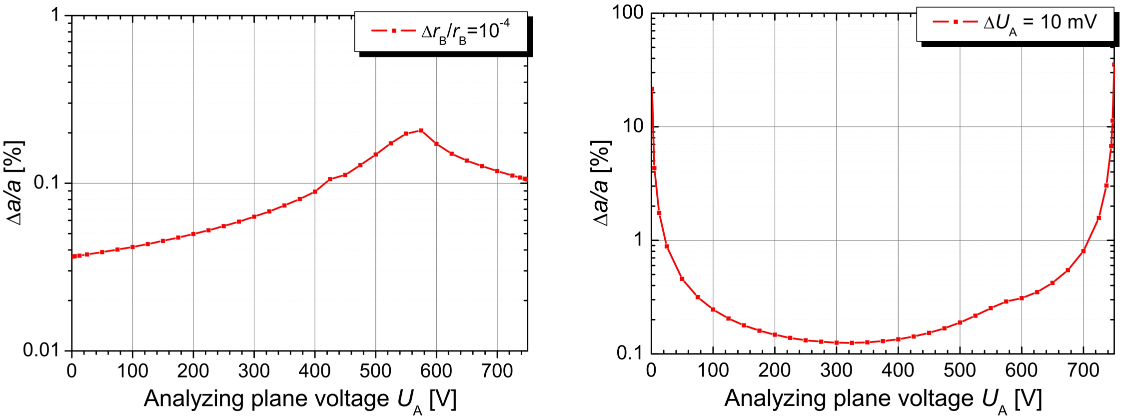

(a) (b)

Figure 3.5: Relative change of the angular correlation coefficient a for (a) a relative uncertainty of the magnetic field ratio r_{B} of 1×10^{-4} and (b) an absolute uncertainty of the potential barrier U_{A} of $10\,\mathrm{mV}$. Each value corresponds to a relative uncertainty in a of about $0.1\,\%$. We mention that the uncertainty in a strongly depends on the barrier voltage chosen. Input data for the simulation: $B_{\mathrm{A}}/B_0 = 0.203$ and $a = -0.103$ [10].

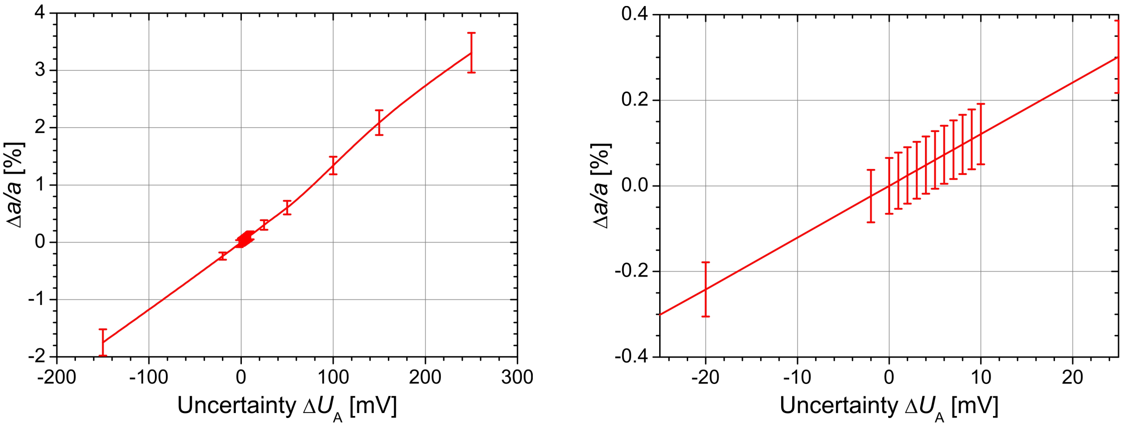

(a) Full view (b) Zoom

Figure 3.6: Relative change of the angular correlation coefficient a for (a) different uncertainties of the potential barrier U_{A}, for a special set of barrier voltages $U_{\mathrm{A}} = 50, 250, 400, 500, 600\,\mathrm{V}$. The (b) zoom to uncertainties in the order of $10\,\mathrm{mV}$ shows that an absolute uncertainty of the potential barrier U_{A} of $10\,\mathrm{mV}$ would correspond to a shift in a of $\Delta a/a = +0.12(5)\,\%$. Input data for the simulation: $B_{\mathrm{A}}/B_0 = 0.203$ and $a = -0.103$ [10]. The error bars, in the order of $0.05\,\%$, represent the error by fitting Eq. (3.32) to the simulated proton count rates only.

as can be seen from Fig. 3.5 (see also [46]). As one can also see in Fig. 3.5, the uncertainty in a strongly depends on the barrier voltage chosen. For measurements of the integral proton spectrum $N_{\mathrm{p}}(U_{\mathrm{A}})$, we therefore have to choose a suitable set of barrier voltages. An example for a special set of barrier voltages, $U_{\mathrm{A}} = 50, 250, 400, 500, 600\,\mathrm{V}$, is presented in Fig. 3.6. The figure shows the relative change in a for different uncertainties of the potential barrier.

Background, caused by positive ions coming from the decay region, may be efficiently reduced if measurements of the proton count rates $N_\mathrm{p}(U_\mathrm{A})$ are taken for U_A not less than $\approx 40\,\mathrm{V}$ (for details see Ref. [47] and also Secs. 3.4.3 and 4.2.4). Therefore, the decay rate ratio $r_\mathrm{h}(U_\mathrm{A})$ must be replaced by a decay rate ratio $r_\mathrm{h}^{50\,\mathrm{V}}(U_\mathrm{A})$ relative to the proton count rate $N_\mathrm{p}(U_\mathrm{A} = 50\,\mathrm{V})$. Analogous to Eq. (3.35), we then get a as a function of the transmission function:

$$a = \frac{\int_0^{T_\mathrm{p,max}} dT F_\mathrm{tr}(T;U_\mathrm{A}) g_1(T) - r_\mathrm{h}^{50\,\mathrm{V}}(U_\mathrm{A}) \int_0^{T_\mathrm{p,max}} dT F_\mathrm{tr}(T;50\,\mathrm{V}) g_1(T)}{\int_0^{T_\mathrm{p,max}} dT F_\mathrm{tr}(T;U_\mathrm{A}) g_2(T) - r_\mathrm{h}^{50\,\mathrm{V}}(U_\mathrm{A}) \int_0^{T_\mathrm{p,max}} dT F_\mathrm{tr}(T;50\,\mathrm{V}) g_2(T)} \,. \tag{3.36}$$

In contrast to our standard method, the last two methods are only used to study several different systematic effects.

In reality, deviations from adiabatic transport, proton scattering on residual gas molecules, and many other systematic effects may influence the transmission function and hence falsify the interpretation of the measured proton spectra. These issues will be discussed in Sec. 3.4.

3.2 The Retardation Spectrometer *a*SPECT

In fact, the electromagnetic set-up of the *a*SPECT spectrometer is much more complex than shown previously in Fig.3.1. A detailed sketch of the set-up is shown in Fig. 3.7. The high number of field shaping coils and electrodes follows from the requirement Eq. (3.14) that changes in the magnetic and electric fields are kept small. In this way, the adiabatic approximation can be used to calculate the proton's trajectories [47].

3.2.1 The Electrode System

The *a*SPECT spectrometer consists of a system of eighteen electrodes, denoted as e1 to e17,[5] placed inside the cold bore (vacuum) tube of the *a*SPECT magnet (for details see the following section). The design of the electrode system is shown in Fig. 3.7. All electrodes have cylindrical shape, but not all of them are axially symmetric, except for the DV electrode gr. The *a*SPECT electrodes were made of oxygen-free high thermal conductivity (OFHC) copper and electrolytically coated with $2\,\mu\mathrm{m}$ of silver[6] and then $1\,\mu\mathrm{m}$ of gold[7], except for the high-voltage electrodes e16 and e17. These two electrodes were made of stainless steel AISI-No. 316L (EN-norm 1.4404) and electropolished. The typical voltage settings are listed in Table 3.1. The electrostatic potential along the z-axis, for these settings, is shown in the bottom of Fig. 3.8.

The Decay Volume

The DV, shown in Fig. 3.9a, consists of three parts, denoted as e3, gr, and e6. All three parts are connected to ground to shield the DV from electric fields of the other electrodes. Accordingly the electrostatic potential within the DV is smaller than 1 mV, well within

---

[5] Please note that we use the (new) naming scheme of Ref. [53].

[6] The renewed and over-coated electrodes e3 to e6, e12, and e14 were coated with $10\,\mu\mathrm{m}$ of silver instead.

[7] Please note that in Refs. [34, 52] the layer thicknesses are misstated. In addition, we would like to stress that none of the electrodes was electropolished, except for the high voltage electrodes e16 and e17.

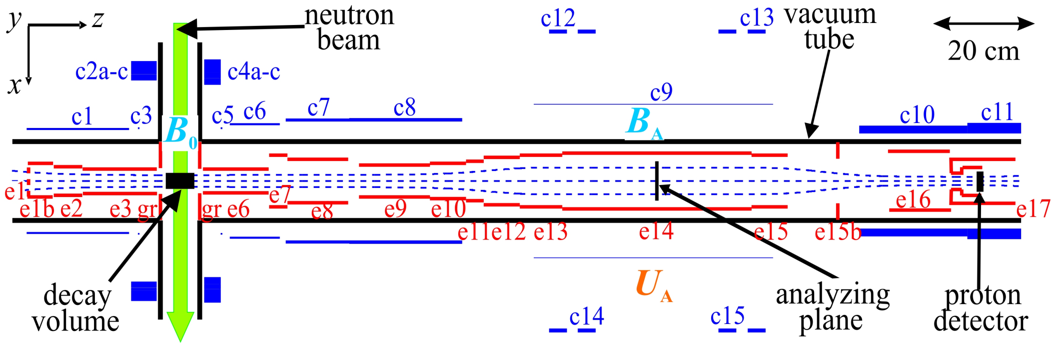

Figure 3.7: A sketch of the electromagnetic set-up of the *a*SPECT experiment at the ILL. The magnet coils (blue, c1−c15) surround the main vacuum system. The electrodes (red, e1−e17) are installed inside the vacuum system. The analyzing plane is a local magnetic field maximum; it is not made of any material. For comparison with the magnetic field and the electrostatic potential values in Fig. 3.8, the figure is rotated by 90°.

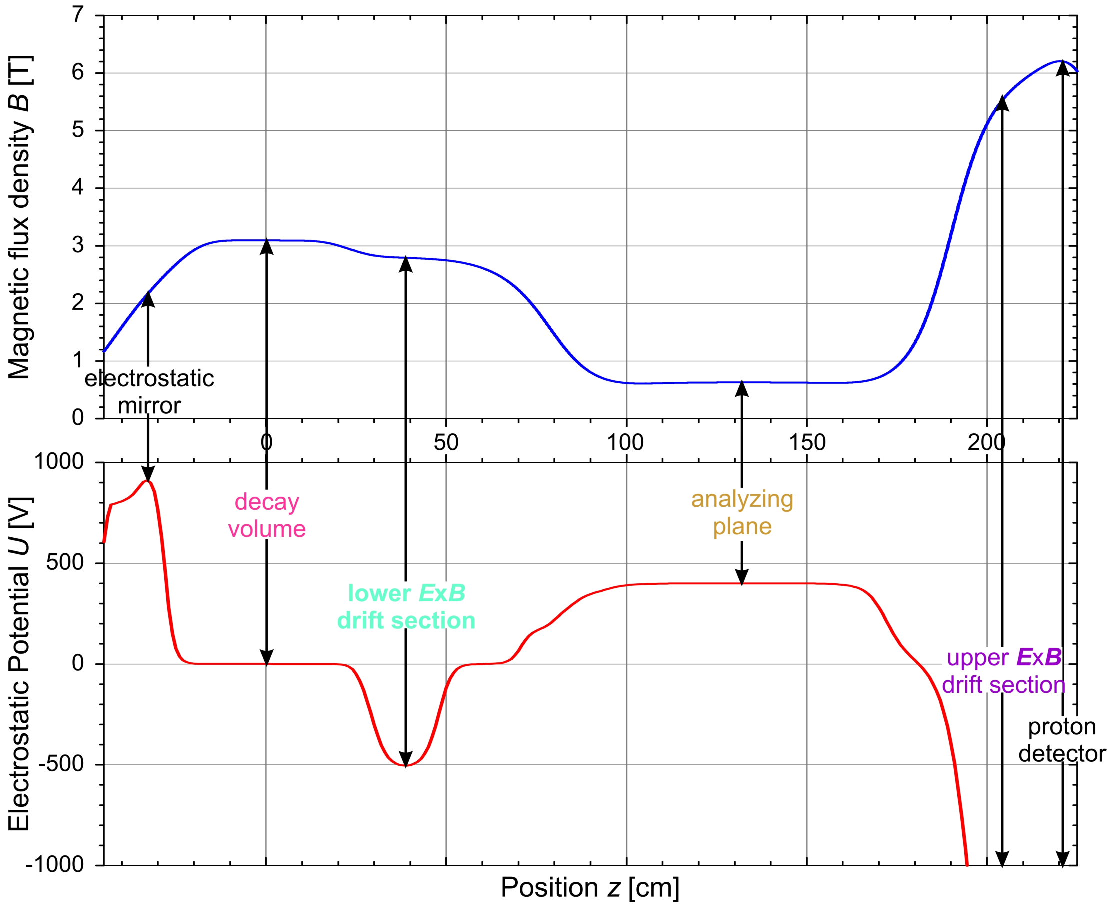

Figure 3.8: The values of (top) the magnetic field and (bottom) the electrostatic potential along the z-axis of the *a*SPECT spectrometer. The corresponding potentials of the electrodes e1 to e17 are listed in Table 3.1. Input data for the electromagnetic field calculations: $I_{\text{main}} = 100\,\text{A}$, $I_3 = 50\,\text{A}$, $I_5 = 21.4\,\text{A}$, $I_{12} = -I_{13} = 36.4\,\text{A}$, $I_{14} = I_{15} = 0$, $U_1 = U_{1\text{b}} = 800\,\text{V}$, $U_2 = 1000\,\text{V}$, $U_8 = -525\,\text{V}$, $U_\text{A} = 400\,\text{V}$, $U_{16} = -2\,\text{kV}$, and $U_{17} = -15\,\text{kV}$.

Table 3.1: Typical voltage settings of the *a*SPECT electrodes, denoted as e1 to e17.

El.no.	Voltage [V]	Comment
e1	800	electrostatic mirror (wire system)
e1b	800	electrostatic mirror (holder for wire system)
e2	1000 / 820	electrostatic mirror (quadrupole used as cylinder)
e3	grounded ($U_0 = 0$)	DV (bottom cylinder); wired individually (for tests)
gr	grounded ($U_0 = 0$)	DV electrode; wired individually (for tests)
e6	grounded ($U_0 = 0$)	DV (top cylinder); wired individually (for tests)
e7	grounded	same ground than DV; usable for systematic tests
e8	-50|-1000 or 0|-200	lower $\mathbf{E} \times \mathbf{B}$ drift, sides R and L (half cylinders)
e9	grounded	same than DV ground
e10	$0.435331 \times U_A$	variable
e11	$0.683960 \times U_A$	variable
e12	$0.892352 \times U_A$	variable
e13	$0.991040 \times U_A$	variable
e14	U_A	AP electrode (variable)
e15	$0.985094 \times U_A$	variable
e15b	grounded	same ground than spectrometer, not than DV
e16	-2|-2 or -3.7|-4.2×10^3	upper $\mathbf{E} \times \mathbf{B}$ drift, sides A and B (half cylinders)
e17	-10/-12/-15×10^3	detector HV

our tolerance of less than 10 mV. The neutron beam passes through the rectangular tunnel gr with a cross-section of $70 \times 110\,\mathrm{mm}^2$. The rectangular tunnel, in turn, has an opening on one side for vacuum pumping[8] (to the backside of the photograph). The decay protons are guided by the strong magnetic field B_0 towards the proton detector on top of the spectrometer (to the top of the photograph) or the mirror on the bottom, through two cylindrical openings on top and on bottom of the rectangular tunnel. Each of the two cylindrical openings is followed by a long cylinder, separated from it by a small gap[9].

The magnetic field lines connecting the DV and the proton detector define the so-called flux tube. For elucidation, the blue dashed lines in Fig. 3.7 show calculated field lines.

In comparison with our first beam time at the Forschungs-Neutronenquelle Heinz Maier-Leibnitz (FRM II) in Munich, Germany, several electrodes were changed in shape. The main reason was strong discharge phenomena as discussed in the following section.

---

[8] Please note that during our latest beam time at the ILL the opening was wrongly installed opposite to the turbo-molecular pump.

[9] Please note that in the first half (November/December 2007) of our latest beam time the cylindrical openings were separated from the long cylinders by means of two ceramics rings, with a smaller inner diameter than the DV electrodes e3, gr, and e6. These rings were removed just before the main phase of the data taking (April/Mai 2008), as it was found that in the first half of the beam time the proton count rates decreased with time. We are convinced that the two ceramics rings got charged by the decay protons and electrons and that the electric field distribution therefore exhibited a potential barrier above the neutron beam, comparable to the one shown in Fig. 6.21b.

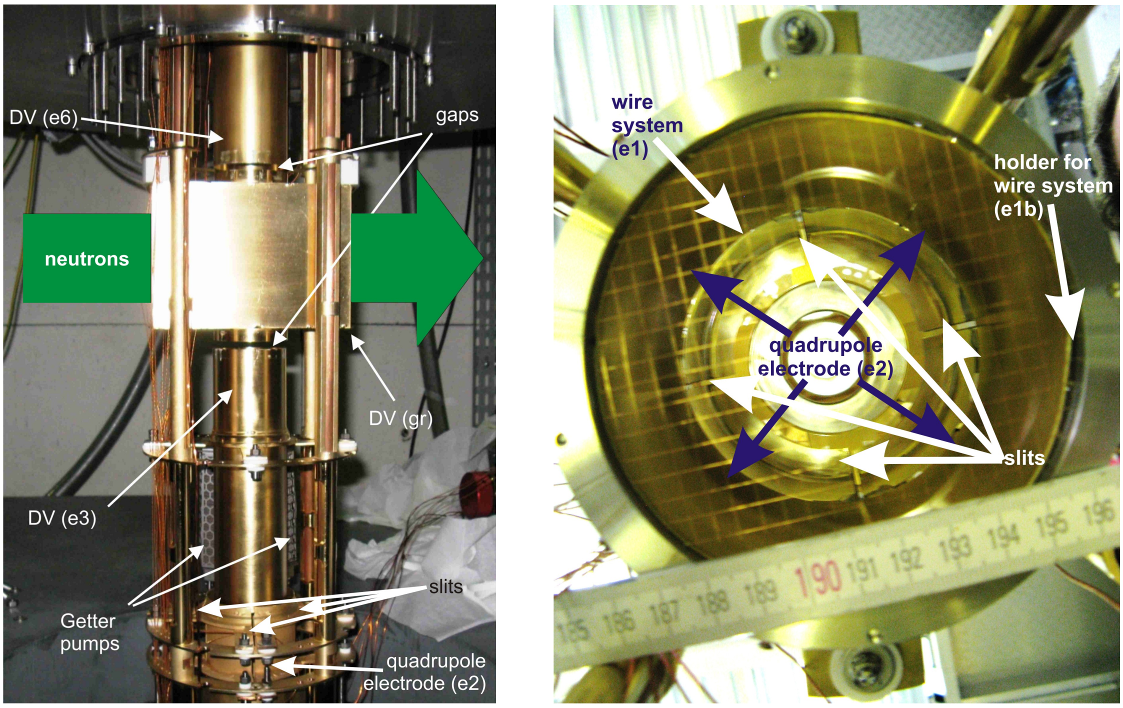

(a) (b)

Figure 3.9: Photographs of (a) the decay volume (DV) electrodes e3, gr, and e6 and (b) the electrostatic mirror electrodes e1, e1b, and e2. The photograph (a) also shows two of the four getter pumps to improve the vacuum conditions (discussed in Sec. 3.4.3) as well as the mirror electrode e2. See the text for details.

Penning Traps and Penning Discharge

In previous measurements with the *a*SPECT spectrometer, relatively strong discharge phenomena have been observed [33, 49] (see also page 38 under “First Measurements with *a*SPECT at the FRM II” and Sec. 5.3). These discharges could be due to field emission processes near the proton detector, where high electric field is present. Furthermore, the *a*SPECT electrode system contains several Penning traps [178, 179], both for electrons and for positive ions, as can be seen from Fig. 3.10. These traps, in turn, could also cause serious discharge processes. In order to understand these processes, the literature on the Penning discharge phenomenon was studied and a variety of calculations was performed to search for various traps, which could be responsible for the discharge and background processes observed.

In some respect, the Penning discharge is similar to the Townsend discharge, which occurs for relatively high gas pressure. Although both the vacuum breakdown and the Penning discharge are present even with very good vacuum conditions, the physics of the Penning discharge is completely different from that of the vacuum breakdown. The main difference is that the Penning discharge occurs only in the presence of magnetic field. It also requires stable charged particle trapping, mainly of electrons. In this process, trapped electrons can suffer ionization collisions with residual gas molecules even with a high vacuum in the order of 10^{-9} mbar. In addition, the positive ions, hitting the anode,

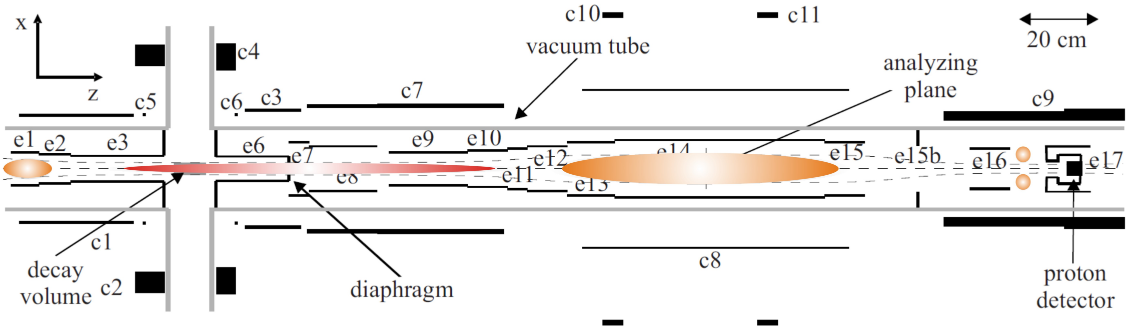

Figure 3.10: A sketch of the electromagnetic set-up of the *a*SPECT experiment at the FRM II. The orange and red regions show possible electron and positive ion traps, respectively, as discussed in the text. We note that the figure is rotated by 90°. Figure adapted from Ref. [33].

can produce more electrons by secondary emission.

A detailed comparison of the *a*SPECT discharge phenomena with those of other experiments, in particular the neutrino mass experiments of Mainz and KATRIN [180–183] (see also [184, 185]), has been performed and Penning traps in the *a*SPECT electrode system have been searched. Three main trapping regions have been found: in the bottom part of the spectrometer, at the AP, and near the proton detector. At the mirror electrode, a wire system was installed to prevent electron trapping (for details see the following section). At the detector, a different dipole electrode and a different detector electrode were installed and, simultaneously, the detector potential was decreased, all three to avoid the deep traps present in previous *a*SPECT measurements (see page 59 under "The Dipole Electrodes" for details). The Penning traps at the AP could not be changed, because these traps are absolutely necessary for the electric retardation method to measure the proton recoil spectrum. In addition, the traps at the AP are only a few hundred Volts deep.

Further details on the Penning traps and discharges can be found in Refs. [33, 47, 186]. For investigations of fake effects caused by Penning discharges, such as AP voltage dependent background, see also Ref. [50] and Sec. 5.3.

The Electrostatic Mirror

The electrostatic mirror, shown in Fig. 3.9b, also consists of three parts, denoted as e1, e1b, and e2. These three parts are typically held at positive potentials

$$U_1 = U_{1\mathrm{b}} = 800\,\mathrm{V} \quad \text{and} \quad U_2 = 1000\,\mathrm{V}, \tag{3.37}$$

to reflect all decay protons emitted in the negative z-direction.

The quadrupole electrode e2, in turn, consists of four quarter cylinders, denoted as parts M, N, P, and R (see also Fig. 3.18b), separated from each other by small slits. For measurements of the neutrino-electron correlation coefficient a, all four parts are powered by the same power supply; for tests with a calibration source (developed by M. Borg [34]), which can be flange-mounted to the bottom of the spectrometer, the four parts are powered individually. This allows us to shift the ion beam leaving the calibration source in the x-y-plane.

As discussed in the previous section, a wire system (e1) was installed at the mirror electrode e1b to prevent electron trapping. In order not to interfere with the calibration

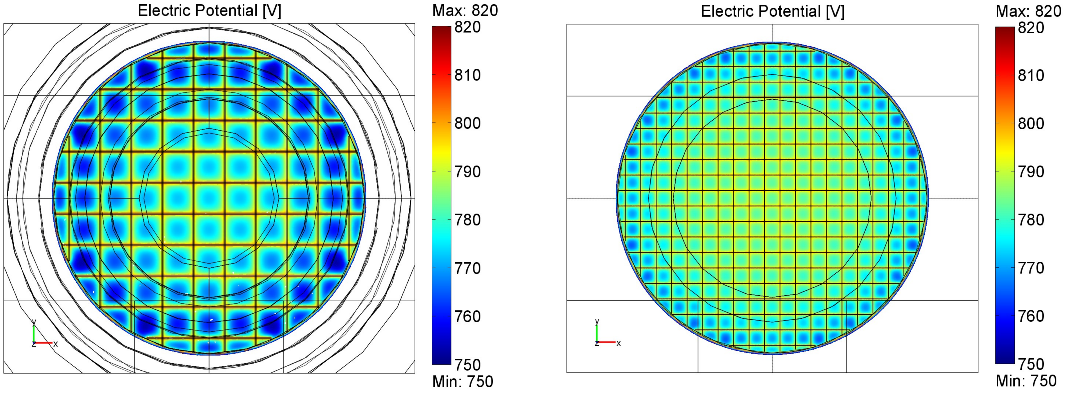

(a) (b)

Figure 3.11: Electrostatic potential in the x-y-plane of the wire system e1 for an OFHC wire (a) with a diameter of 500 μm and a wire distance of 10 mm and (b) with a diameter of 125 μm and a wire distance of 5 mm. Main input data for the electric field calculations (with COMSOL 3.2b Multiphysics): $U_1 = U_{1\mathrm{b}} = 800\,\mathrm{V}$ and $U_2 = 1000\,\mathrm{V}$. The comparison between (a) and (b) shows that a wire diameter and distance of 125 μm and 5 mm, respectively, ensure a rather homogeneous electric field distribution of at least 780 V over the entire flux tube. Here, the black lines represent the electrodes e1 to e16, the two heat shields for the detector electrode e17, as well as the vacuum tube.

source different wire diameters and distances were investigated. A wire diameter of 125 μm and a wire distance of 5 mm were chosen. This ensures a rather homogeneous electric field distribution of at least 780 V over the entire flux tube, as can be seen from Fig. 3.11.

The Analyzing Plane

The AP is situated in the center of the electrode e14, as shown in Fig. 3.7. The electrodes e10 to e15 are powered by the same power supply; the electrode e14 is connected directly to the power supply, whereas the electrodes e10 to e13 and e15 are connected by means of a resistor based voltage divider. This ensures that the potential in the center of the AP, for, e.g., $U_\mathrm{A} = 400\,\mathrm{V}$, is only by 2 mV smaller than at the surface of the electrode e14 and hence that the adiabatic transmission condition Eq. (3.24) is always fulfilled (as discussed in Sec. 3.2.2, cf. Eqs. (3.42) to (3.45)).

The Dipole Electrodes

In our measurement, two dipole electrodes, denoted as e8 and e16, are used. Each of the two dipole electrodes consists of two half cylinders, denoted as parts R and L respectively A and B, which may be held at different potentials. A different potential produces an electric field perpendicular to the magnetic field and this, in turn, a so-called $\mathbf{E} \times \mathbf{B}$ drift. In addition to their circular motion, the Lorentz force (see also Eq. (3.2) and Fn. 1)

$$\mathbf{F}_\mathrm{L} = q\,(\mathbf{E} + \mathbf{v} \times \mathbf{B}) \tag{3.38}$$

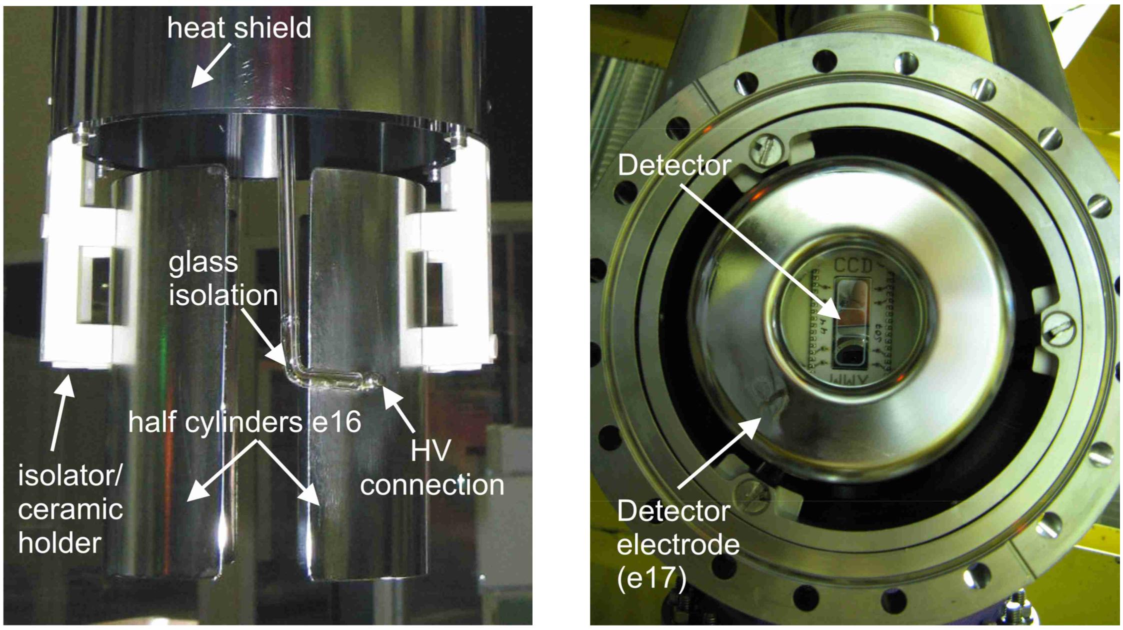

(a) (b)

Figure 3.12: Photographs of (a) the upper dipole electrode e16, sides A and B, and (b) the detector electrode e17. The photograph (a) also shows the heat shields to minimize the heat input from the detector electrode to the cold bore tube of the aSPECT magnet; the photograph (b) shows also the proton detector (see Sec. 3.3.1 for details).

forces the decay protons[10] to a drift perpendicular to both electric and magnetic field, with a drift velocity of

$$\mathbf{v}_{\mathrm{drift}} = \frac{\mathbf{E}\times\mathbf{B}}{B^2}. \tag{3.39}$$

The lower dipole electrode e8 is situated between the DV and the AP, as can be seen from Fig. 3.7. It serves to sweep out all decay protons that cannot pass the potential barrier and would otherwise be trapped between the electrostatic mirror and the AP. After several passages through the dipole electrode, these protons will be absorbed by the surface of an electrode or the cold bore tube, as the direction of drift is independent of the direction of flight. We mention that, with increasing potential difference between sides R and L, the trapping time of these protons decreases and consequently the systematic effect due to proton collisions with the residual gas molecules is reduced (discussed in Sec. 3.4.3).

The upper dipole electrode e16, shown in Fig. 3.12, is situated right in front of the proton detector (cf. Fig. 3.7). It causes a transverse drift which serves to align the neutron beam on the proton detector (see also Fig. 3.18b). The dipole electrode has to be held at a negative potential of at least −600 V to ensure that all decay protons that pass the potential barrier can also overcome the magnetic mirror right in front of the detector. As discussed earlier on page 56 under “Penning Traps and Penning Discharge”, the two parallel stainless steel plates (cf. Fig. 3.13) of the dipole electrode’s predecessor were

---

[10] Please note that the spatial displacement of charged particles moving in an $\mathbf{E}\times\mathbf{B}$ drift depends on the time they spend in the drift. Due to their higher energy but smaller mass the decay electrons pass far more quickly through an $\mathbf{E}\times\mathbf{B}$ drift. Therefore, the displacement of the decay electrons is negligible.

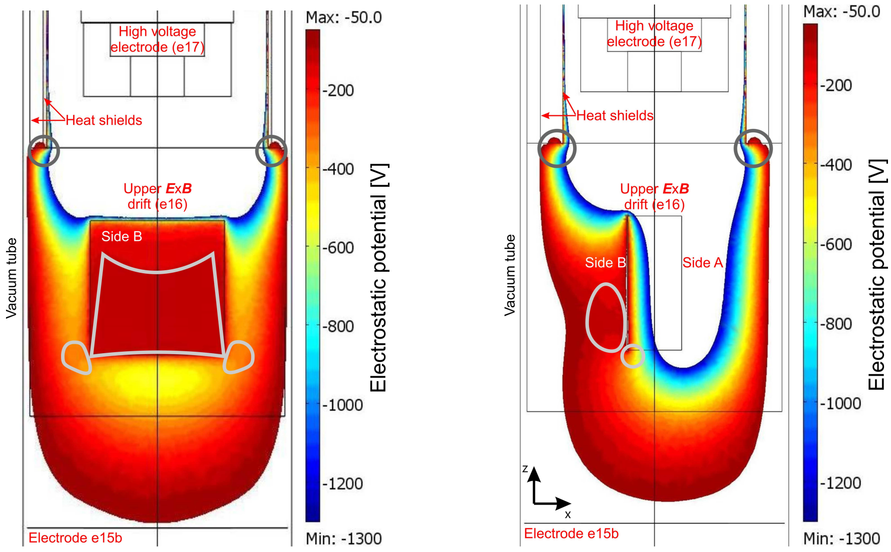

(a) (b)

Figure 3.13: Electrostatic potential of the upper dipole electrode e16 at the FRM II (a) in the y-z-plane for $x = -1.9\,\mathrm{cm}$ and (b) in the x-z-plane for $y = \pm 5\,\mathrm{cm}$. Main input data for the electric field calculations (with COMSOL 3.2b Multiphysics): $U_{16\mathrm{A}} = -4\,\mathrm{kV}$, $U_{16\mathrm{B}} = 0$, and $U_{17} = -30\,\mathrm{kV}$. The gray lines highlight potential Penning traps. We mention that the traps on the edge of the heat shields (dark gray) are always present, whereas those close to side B of the upper dipole electrode e16 (light gray) strongly depend on the voltage applied.

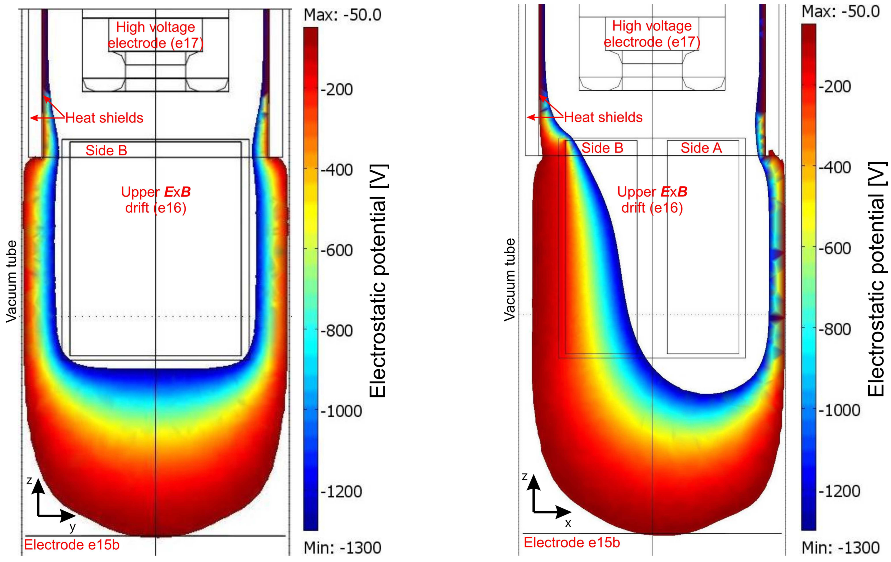

(a) (b)

Figure 3.14: Electrostatic potential of the upper dipole electrode e16 at the ILL (a) in the y-z-plane for $x = 0$ and (b) in the x-z-plane for $y = 0$. Main input data for the electric field calculations (with COMSOL 3.2b Multiphysics): $U_{16\mathrm{A}} = -4.2\,\mathrm{kV}$, $U_{16\mathrm{B}} = -0.2\,\mathrm{kV}$, and $U_{17} = -15\,\mathrm{kV}$. In the new design of the high voltage electrodes e16 and e17, the potential Penning traps shown in Fig. 3.13 are no longer present.

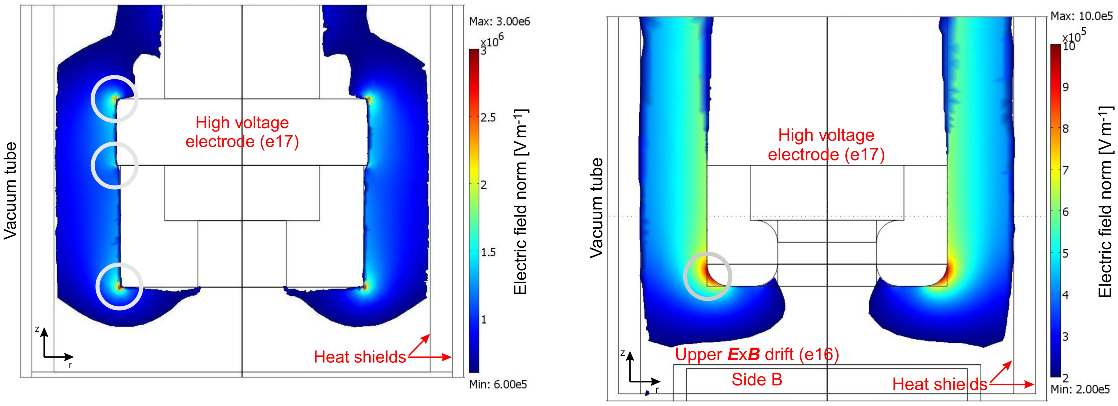

(a) (b)

Figure 3.15: Electric field strength of the detector high voltage electrode e17 in the r-z-plane (a) at the FRM II for $U_{17} = -30\,\mathrm{kV}$ and (b) at the ILL for $U_{17} = -15\,\mathrm{kV}$. To avoid electrical breakdown initiated by field emission, in the new design of the high voltage electrode e17, all edges (gray) were carefully rounded and electropolished (see also Fn. 11). The comparison between (a) and (b) shows that the electric field strength could be reduced by at least a factor of 3. Please note the different color ranges in (a) and (b). We note that, compared to all other electric field calculations with COMSOL 3.2b Multiphysics shown in this thesis, Figure (b) stems from a calculation with the new version COMSOL 3.5 [187].

replaced by two half cylinders. The comparison between Figs. 3.13 and 3.14 shows that, in the new design of the high voltage electrodes e16 and e17, the potential Penning traps shown in Fig. 3.13 are no longer present.

The High Voltage Electrode

As discussed earlier on page 56 under "Penning Traps and Penning Discharge" and in the previous section, also the detector high voltage electrode e17, shown in Fig. 3.12b, was changed in shape compared to our first beam time at the FRM II. The proton detector has to be shielded from radioactive background, mainly gamma's from the neutron apertures and from neighboring instruments. Therefore, the detector (described in Sec. 3.3.1) is surrounded by a stainless steel tube which has a massive cup on its bottom (see also Fig. 3.20b). To avoid electrical breakdowns, all edges of the tube were carefully rounded and electropolished[11], and the screws connecting the insulator and the preamplifier tube were covered with two semicircular, rounded, and electropolished pieces (see Fig. 3.20b for details). In combination with a reduced acceleration potential, U_{17}, the electric field strength could be reduced by at least a factor of 3, as can be seen from Fig. 3.15.

Details on the software used for axisymmetric magnetic and electric field calculations, with zonal harmonic expansion, as well as for relativistic charged particle tracking, with an 8th order Runge-Kutta method, are found in [47, 188–190] (see also [191–195]). For non-axially symmetric applications, as, e.g., the grid electrode e1, the quadrupole electrode e2,

---

[11] Please note that in the first half (November/December 2007) of our latest beam time parts of the surface have been scratched. The scratches were removed only by mechanical polishing.

the DV electrode gr, the lower and upper dipole electrodes e8 and e16, and the rounded detector cup, COMSOL 3.2b Multiphysics Electromagnetics Module was used [196].

3.2.2 The Superconducting Coil System

The *a*SPECT spectrometer consists of a system of eleven[12] superconducting coils, denoted as c1 to c11 (see also Fn. 5), placed inside a cylinder with a length of three meters and a diameter of seventy centimeters. The design of the (superconducting) coil system is shown in Fig. 3.7. The coil system and its magnetic field are axially symmetric. The *a*SPECT magnet generates a strong magnetic field which varies from 0.6 to 6 T along the symmetry axis, and down to 5 Gauss in a radial distance of five meters from the DV (see App. A for details), both at the design current of $I_\mathrm{main} = 100\,\mathrm{A}$.

The magnetic field of the *a*SPECT magnet came close to its design shape, but still the superconducting correction coils c3 and c5 and the normal conducting correction coils c12 and c13 were necessary to correct for small deviations both in the DV and the AP, respectively (for details see [168]). All superconducting coils are connected in series and operated in persistent mode[13], except for the correction coils c3 and c5. In this way, the ratios of the magnetic fields in the DV, the AP, and also at the height of the proton detector remain constant in time, independent of the applied current I_main. We mention that, in persistent mode, the values of the magnetic field B_0 and B_A in the DV and the AP, respectively, as well as the magnetic field ratio $r_\mathrm{B} = B_\mathrm{A}/B_0$ decrease very slowly with time. The latter as the correction coils are not operated in persistent mode, i.e., the magnetic field ratio r_B changes with time by [53]:

$$\frac{1}{r_\mathrm{B}}\frac{\partial r_\mathrm{B}}{\partial t} = -1.1 \times 10^{-4}\,\mathrm{year}^{-1}\,. \tag{3.40}$$

The magnetic field along the z-axis of the *a*SPECT spectrometer is shown in the top of Fig. 3.8. The coils c1 to c13 generate a very homogeneous magnetic field both in the DV and the AP, ensuring a relative accuracy of the magnetic field ratio r_B in the order of 1×10^{-4} (for details see Sec. 4.1.4 and Ref. [53]). In the region of the lower dipole electrode e8, the coil system produces also a rather homogeneous magnetic field. For this reason, we can apply a potential difference[14] of up to 3 kV between sides R and L without any significant influence on the adiabatic proton transport between the DV and the AP [47].

In the DV, the tiny correction coils c3 and c5 serve to adjust the shape of the magnetic field; they can provide a magnetic field of up to 1 % of the main field. We apply a slight magnetic field gradient there, with the field decreasing towards the proton detector, as shown in Fig. 3.16a. In this way, no protons can be trapped by the magnetic mirror effect between the DV and the electrostatic mirror, ensuring 100 % acceptance for decay protons.

In the AP, two pairs of (external) correction coils serve to adjust the shape of the magnetic field. The pair c12 and c13 is operated in anti-Helmholtz configuration to correct

---

[12] Please note that the coils c2a to c2c as well as c4a to c4c are interpreted as one superconducting coil, although they are manufactured in three parts each with a different cross-section of the windings.

[13] In persistent mode, the windings of a superconducting magnet are short-circuit with a piece of superconductor, a so-called persistent switch, as soon as the magnet has been energized. Then its windings become a closed superconducting loop and the power supply can be turned off. The great advantage of this method is the high stability of the magnetic field, independent of possible fluctuations of the power supply.

[14] Assuming that one side of the lower dipole electrode e8 is connected to ground.

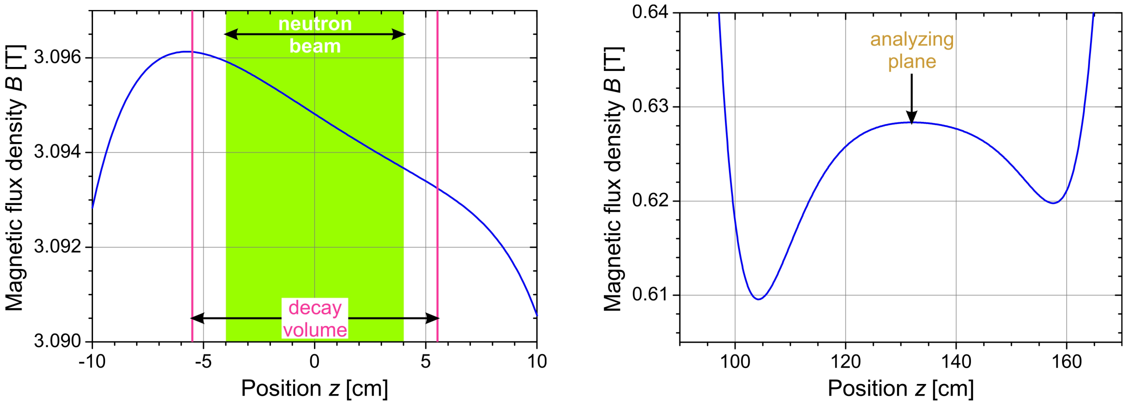

(a) (b)

Figure 3.16: The values of the magnetic field along the z-axis of the aSPECT spectrometer in (a) the decay volume (DV) and (b) the analyzing plane (AP). The slight magnetic field gradient in the DV ensured that no protons can be trapped by the magnetic mirror effect between the DV and the electrostatic mirror. Due to the local maximum in the AP the adiabatic transmission condition Eq. (3.24) is automatically fulfilled in the region close to the AP. Input data for the magnetic field calculation: $I_{\mathrm{main}} = 100\,\mathrm{A}$, $I_3 = 50\,\mathrm{A}$, $I_5 = 21.4\,\mathrm{A}$, $I_{12} = -I_{13} = 36.4\,\mathrm{A}$, $I_{14} = I_{15} = 0$.

for small deviations from the design shape; the pair c14 and c15 in Helmholtz configuration to change B_{A} by up to 1 %. In comparison with our first beam time at the FRM II, the coils c14 and c15 were added and subsequently the distance and the position of the coils c12 and c13 changed (compare with, e.g., Figs. 2.14 and 4.2). Changing B_{A} by 1 % allows us to quickly perform a statistically significant test of the above calculated transmission function Eq. (3.30), cf. Sec. 5.5.4. Therefore, the Helmholtz coils have to be placed symmetrically around the maximum of the electrostatic potential in the AP. Consequently, the anti-Helmholtz coils were mounted around the Helmholtz coils, as generally Helmholtz coils have a shorter distance. But, due to limited space, the anti-Helmholtz coils were installed at a distance of $\sqrt{2}R$ instead of the usual $\sqrt{3}R$, where R is the radius of the coils. The typical current settings are

$$I_{\mathrm{main}} = 70\,\mathrm{A},\ I_3 = 35\,\mathrm{A},\ I_5 = 15\,\mathrm{A},\ I_{12} = -I_{13} = 25.5\,\mathrm{A},\ \text{and}\ I_{14} = I_{15} = 0. \tag{3.41}$$

Figure 3.16b shows that the magnetic field exhibits a local maximum, B_{A}, in the AP, with a relative uncertainty in the order of 1×10^{-4}. In the region close to the AP, the electrostatic potential is nearly uniform. For, e.g., $U_{\mathrm{A}} = 400\,\mathrm{V}$, the potential in the region close to the AP is only by 2 mV smaller than in the center of the AP. If the magnetic field would have a minimum instead, the minimum therefore would have to be extremely flat to fulfill the adiabatic transmission condition Eq. (3.24). On the other hand, for our local maximum, we get

$$\begin{aligned} U_{\mathrm{A}} - U_0 &> U(z) - U_0 \quad \text{and} && (3.42)\\ B_0 - B(z)\sin^2(\theta_0) &> B_0 - B_{\mathrm{A}}\sin^2(\theta_0) && (3.43)\end{aligned}$$

in the region close to the AP, i.e.,

$$\frac{B_0 - B(z)\sin^2(\theta_0)}{B_0 - B_{\mathrm{A}}\sin^2(\theta_0)} > 1 > \frac{U(z) - U_0}{U_{\mathrm{A}} - U_0}. \tag{3.44}$$

Then the adiabatic transmission condition Eq. (3.24) is automatically fulfilled in the region close to the AP:

$$\begin{aligned}
T_{||}^{\mathrm{ad}}(z) &= T_{\mathrm{tr}}(\theta_0) - e\,(U(z) - U_0) - \frac{B(z)}{B_0} T_{\mathrm{tr}}(\theta_0)\sin^2(\theta_0) \\
&= \frac{e\,(U_{\mathrm{A}} - U_0)}{1 - \frac{B_{\mathrm{A}}}{B_0}\sin^2(\theta_0)} - e\,(U(z) - U_0) - \frac{B(z)}{B_0}\,\frac{e\,(U_{\mathrm{A}} - U_0)}{1 - \frac{B_{\mathrm{A}}}{B_0}\sin^2(\theta_0)}\sin^2(\theta_0) \\
&= e\,(U_{\mathrm{A}} - U_0)\,\frac{B_0 - B(z)\sin^2(\theta_0)}{B_0 - B_{\mathrm{A}}\sin^2(\theta_0)} - e\,(U(z) - U_0) \\
&\overset{(3.44)}{>} 0. \qquad (3.45)
\end{aligned}$$

In the detector region, the magnetic field is increased by about a factor of 2 compared to the DV, as can be seen from Fig. 3.8. The smaller cross-section of the flux tube therefore allows us to use a smaller proton detector. To ensure that no decay protons are reflected by the magnetic mirror effect, the protons are accelerated by the high negative potential of the electrodes e16 and e17. At the same time, the magnetic mirror effect significantly reduces the electron background (see also Sec. 3.4.4).

For the latest beam time, the *a*SPECT spectrometer had to move to the Institut Laue-Langevin (ILL) in Grenoble, France. In order not to disturb neighboring experiments, in particular the spin-echo spectrometer IN11, by the fringe field of the strong *a*SPECT magnet, a magnetic field return was built. The magnetic field return is shown in Fig. A.5 in App. A. It reduces the exterior magnetic field to less than 1 Gauss in a radial distance of five meters, as can be seen from Fig. A.6 in App. A. At the same time, the magnetic field return does not affect the homogeneity of the internal magnetic field, cf. Fig. A.7 in App. A. Details on the magnetic field return are found in App. A and in Ref. [1].

3.3 The Detection System

The *a*SPECT data acquisition (DAQ) consists of several parts: The proton detector, the signal processing electronics, and the DAQ computers and slow control. Details are found in Refs. [51, 52].

3.3.1 The Proton Detector

The main part of the *a*SPECT DAQ is the proton detector. In neutron beta decay, the proton is emitted with a maximum kinetic energy of only 751 eV. To obtain a signal well separated from the noise decay protons are usually post-accelerated onto the detector by at least −25 kV.

Our first measurements at the FRM II were performed with a silicon PIN diode with 25 strips, with a size of $25 \times 0.8\,\mathrm{mm}^2$ each, set at a potential of about −30 kV [33]. In such PIN diodes, the PN-structure of a normal diode is separated by an intrinsic layer to increase the active volume of the detector. However, the capacitive noise of such a detector is proportional to its active area. To implement a large detector surface, the detector therefore has to be divided into many single active areas with a separate readout for each area. But even with our high acceleration potential the proton signal was hardly separated from the noise of the system [49, 197] (see also Fig. 2.15a).

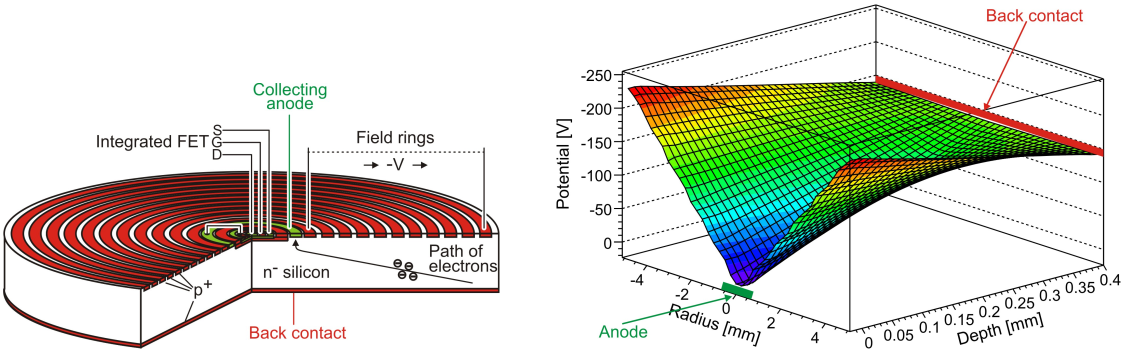

(a) (b)

Figure 3.17: Working principle of a silicon drift detector (SDD). (a) Schematic cross-section, taken from Refs. [51, 199]. (b) Calculation of the potential distribution inside a SDD detector with typical values. For better visibility of the valley, the axis of the potential is plotted inverted. Calculation taken from M. Simson [52]. Ionizing radiation enters the detector through the back contact. Free electrons created within the potential valley drift towards the central annular anode. The anode is connected to the gate (G) of the integrated FET which acts as a first amplification stage.

Repeated electrical breakdown during beam times triggered to go for a different solution. In our latest beam time at the ILL, we used a more sophisticated semiconductor detector. In our so-called silicon drift detector (SDD), supplied by PNSensor [198], the thermal noise is decoupled from the active area.

For more details on semiconductors and semiconductor detectors, the reader is referred to standard textbooks [199, 200].

Working Principle of a Silicon Drift Detector

The principle of a SDD was first proposed by Gatti and Rehak in 1984 [201] and is based on the sidewards depletion principle. It allows the full depletion of a large detector volume with a very small readout node. This greatly decreases the thermal noise compared to a conventional PIN diode.

Figure 3.17a shows a schematic cross-section of a SDD. The bulk material of the detector is n^- doped silicon[15], with a smooth p^+ layer on one side and concentric p^+ rings on the other side. The back contact is connected to a positive voltage, whereas the rings on the front side have different potentials. The n^- doped regions between these rings have a rather high resistivity and therefore act as a voltage divider. The corresponding potential valley is shown in Fig. 3.17b. Ionizing radiation enters the detector through the back contact. Free electrons created inside the potential valley drift towards the center of the front side where they are collected by a small n^+ doped anode.

The Detector Chip

In our experiment, three SDDs are used, implemented in a row on one silicon chip. Figure 3.18a shows the entrance side of the detector which is covered with a protective layer

---

[15] The superscript − refers to a faint degree of doping, whereas a + indicates a strong doping.

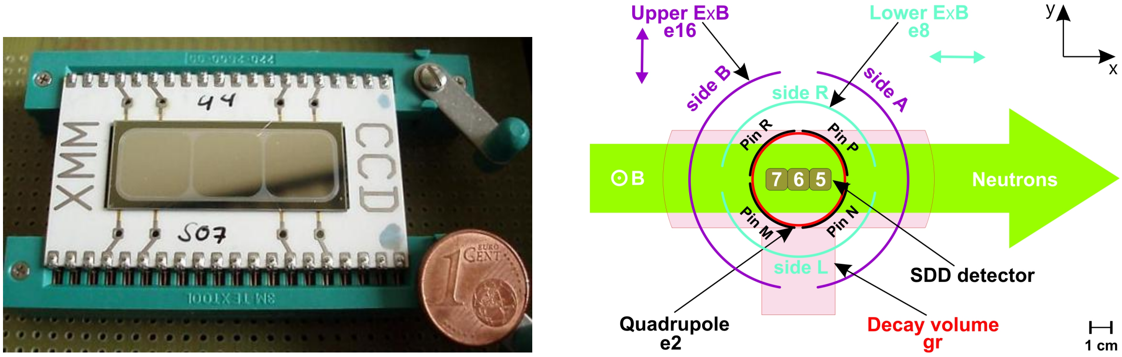

(a) (b)

Figure 3.18: Detector chip used at the ILL. (a) Photograph of the entrance side. Each of the three SDD pads has an active area of 100 mm^2. The chip is supplied on a special, ultra-high vacuum (UHV) suitable ceramics board. To establish an electrical contact wires are bonded between the chip and the board. The ceramics board is inserted in two commercially available 20 socket zero-insertion-force connectors which are not suitable for UHV. For use inside the spectrometer a special holder was designed [52]. (b) Sketch of the electromagnetic set-up. For better visibility, only non-axisymmetric electrodes are shown. Neutrons are coming from the left and pass through the decay volume (red), where only a few decay. The decay products are guided by the strong magnetic field towards the detector. The three detector pads, denoted by 5, 6, and 7, are aligned parallel to the neutron beam. Protons emitted in the negative z-direction are reflected by the electrostatic quadrupole (black). Trapped protons are removed from the flux tube with the lower dipole electrode (turquoise). The upper dipole electrode (purple) serves to align the neutron beam on the detector. Note that the electrodes are scaled to their projection by the magnetic field onto the detector.

of 30 nm of aluminum. Each of the three detector pads has an active area of 100 mm^2 in the form of a square with a side length of 10.3 mm and rounded corners with 2 mm radius. The total size of the chip is $34 \times 14 \times 0.45$ mm^3.

One specific feature of our SDD is that the first amplifying field-effect transistor (FET) is integrated directly onto the detector. This minimizes the cable length from the detector to the first amplification stage to nearly zero and hence decreases both the capacitive noise and the pick-up of external noise compared to conventional detectors. Another specific feature is that temperature sensors are implemented on the detector chip.

With the new proton detector, the acceleration potential could be reduced by a factor of 2 down to -15 kV [51, 52]. This solved the problem of frequent electrical breakdowns and, in combination with the redesign of several electrodes (see Sec. 3.2.1 for details), significantly improved the background conditions (discussed in Sec. 5.3). As can be seen from Fig. 3.19, the proton signal is sufficiently separated from the noise.

Mechanical Set-up

For our measurements, the detector has to be placed in the high magnetic field that guides and focuses the decay protons onto the detector. For reasons of maintenance, however, the detector should be rather easily accessible. Hence, we use a retractable system, in which the detector can be moved into and out of the magnet. The cold bore tube of the *a*SPECT

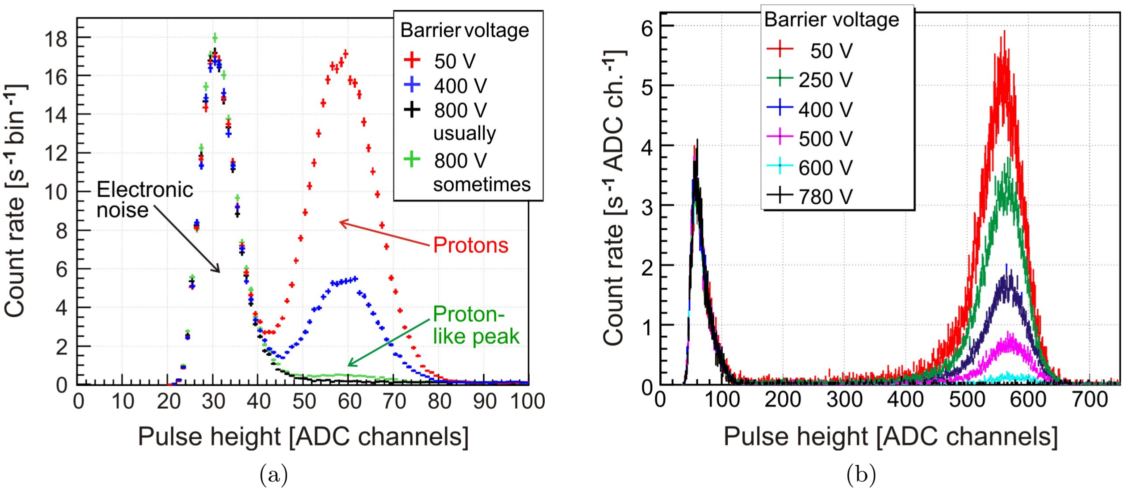

Figure 3.19: Pulse height spectra measured at (a) the FRM II with the silicon PIN diode set at a potential of −30 kV and (b) the ILL with the SDD detector set at −15 kV. With increasing barrier voltage the count rate in the proton peak (right peak) decreases whereas the electronic noise (left peak) is not influenced. The direct comparison shows that the noise could be sufficiently separated from the proton signals. The lower acceleration potential significantly improved the background conditions (proton-like peak).

magnet is separated from the detector vacuum by means of an ultra-high vacuum (UHV) gate valve. Thus the detector can be maintained without venting the cold bore tube.

Figure 3.20a shows the mechanical set-up of the detector. The mechanics can be divided into two parts: The lower part is on high voltage, whereas the upper part stays on ground potential. These two parts are electrically separated by a non-magnetic ceramics tube. The high voltage part, shown in Fig. 3.20b, consists of two nested tubes: The inner tube houses the preamplifier at atmospheric pressure. The outer tube surrounds the detector which is mounted outside the closed lower end of the inner tube. To shield the detector from radioactive background, mostly gamma's from the neutron apertures and from neighboring instruments, the tube has a massive stainless steel cup on the bottom.

The digital electronics is mounted on top of the spectrometer, inside an aluminum box for electrical shielding. The aluminum box, in turn, is situated inside a bigger perspex box for protection against high voltage. The cables which connect the analog and digital electronics are contained in an acrylic glass tube. To shield the cables against electrostatic noise they are surrounded by a stainless steel tube that is connected to the high voltage.

Two pressurized air tubes are used to cool the preamplifier board and the digital electronics inside the aluminum box, respectively. Since the air from the first tube escapes through the central cable tube no water can condense on the inside of the ceramics tube. The ceramics tube, in turn, is cooled passively by the surrounding cold bore walls. We note that water on the inside of the ceramics tube could cause electrical breakdowns.

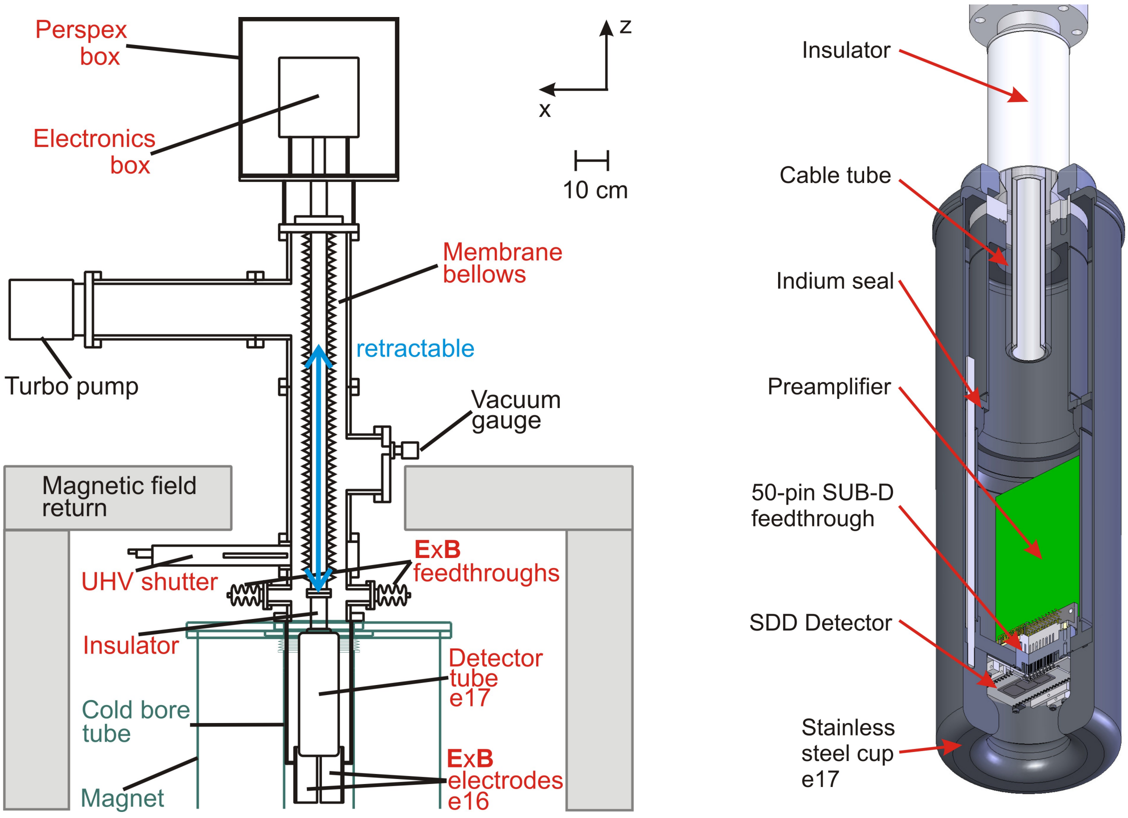

(a) (b)

Figure 3.20: (a) A detailed sketch of the mechanics with the detector inside the magnet. A membrane bellows is connected to the ground potential side of the insulator. It separates the inner tube at atmospheric pressure from the UHV inside the magnet and enables the movement of the detector. The digital electronics is mounted on top of the set-up inside an aluminum box. The upper $\mathbf{E} \times \mathbf{B}$ electrode is also inserted from the top. (b) A detailed sectional drawing of the high voltage part consisting of insulator, preamplifier tube, detector, and shielding cup, taken from [52]. The detector is directly connected to the preamplifier by a 50 pin UHV SUB-D feedthrough. The amplified signals are transferred by coaxial cables in the central tube to the aluminum box.

3.3.2 Signal Processing Electronics

Amplification Boards

The preamplifier board is directly connected to the detector feedthrough, as can be seen in Fig. 3.20b. In this way the shortest possible distance between detector and amplification is achieved, resulting in low electronic noise. This board also distributes the several voltages needed to operate the detector. In addition, a readout circuit for the temperature sensors on the detector chip is implemented on the preamplifier board.

The amplified signals are transferred to an adapter board inside the aluminum box on top of the spectrometer. This board shapes the signals and transfers them to the analog to digital converter (ADC). The raw signal shape consists of a steep rise followed by a long exponential decay. The shaper is mostly sensitive to the rise and shortens the pulse so that it can be further processed by the digital electronics. The adapter board also distributes

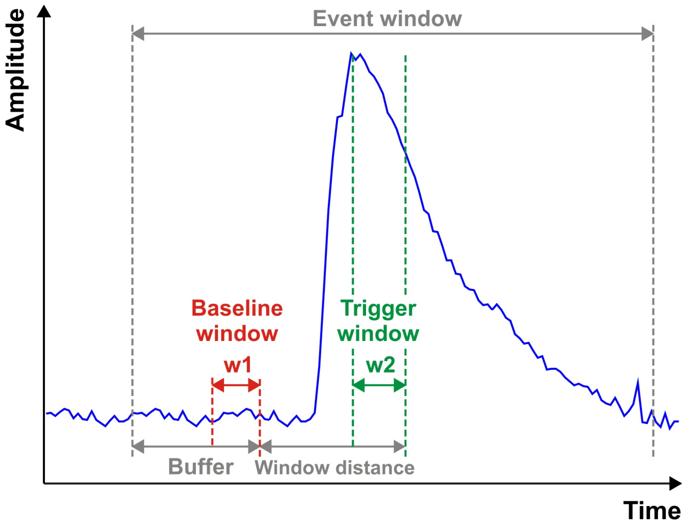

Figure 3.21: Illustration of the trigger algorithm. A typical proton event is shown in blue. The algorithm compares the level of the baseline to the signal height. Window w1 (red) is used to determine the baseline. If the mean value of window w2 (green) differs by more than a given threshold from the baseline, the trigger condition is fulfilled. Both windows are separated by the window distance. The exact stored region around the event is given by the length of the event window and the trigger buffer.

the voltages from the voltage divider board to the different parts of the electronics.

Digital Electronics and the Trigger Algorithm

The last part of the signal processing electronics is the sampling analog to digital converter (sADC) board, also mounted inside the aluminum box. The shaped signals are continuously digitized by a 12 bit ADC. Its sampling frequency is 20 MHz resulting in time bins with a width of 50 ns. This frequency offers a reasonable compromise between time resolution and data volume as the events typically have a length of about 5 μs.

Since there is no external trigger in our experiment the digitized signals are continuously sampled by field programmable gate arrays (FPGAs) and analyzed with respect to a trigger algorithm: The output signal of the ADC is continuously shifted through a register and discarded at the end if no pulse was detected. As shown in Fig. 3.21, the general algorithm is based on the comparison of two windows, denoted as w1 and w2, within the shift register. Window w1 is used to determine the baseline of the signal. The two windows are separated from each other by the window distance. If the mean values of the two windows differ by more than a given threshold, the trigger condition is fulfilled. To suppress triggers on noise an additional parameter, termed as delay, is introduced, so that the threshold condition has to be fulfilled several times in a row before a trigger decision is made. To record the entire pulse a certain amount of ADC values before the event, denoted as buffer, is stored. The total amount of stored ADC values is given by the length of the event window. Furthermore, a time stamp is added to the event.

The lengths of the event window, the two windows w1 and w2, and the trigger buffer as well as the delay can be set from the control program, whereas the window distance is fixed to 2^4 time bins (0.8 μs). During most of our measurements at the ILL, the event window was set to a length of 100 time bins (5 μs), both windows w1 and w2 to 2^4 time bins ($0.8\,\mu$s), the trigger buffer to 15 time bins ($0.75\,\mu$s), and the delay was set to 3.

If a trigger decision is made, the FPGA attaches a header[16] with additional information (heartbeat, slow-control, overflow, and ADC channel and size of the event) about the pulse. Then the event is sent to the DAQ computer, where it is stored for offline data analysis. The DAQ computer is set at ground potential. To operate the sADC board at the detector high voltage, the data is therefore transfered via a HOTLink interface[17] with optical fiber cable.

Readout Software and Instrument Control Set-up

When a measurement file is completed, the raw data is converted, i.e., decoded to a parseable data format by a C/C++ program. Since our data analysis software is based on ROOT[18] the decoding program creates a ROOT tree with all important information about every event from the raw data file[19]. In particular, for each event the program determines a baseline by the mean value of the first 15 ADC values and a preliminary pulse height by the maximum difference between the signal and its baseline. In addition, for each file the decoding program creates a pulse height histogram.

For our measurements, several voltages and other values have to be set and monitored. Thus we have used five personal computers (PCs) for data taking and instrument control: the DAQ PC (controls and reads the data from the sADC), the decode PC (decodes the data from the detector), the data server (used to store the data from the detector), the magnet control PC (reads the temperature sensors of the magnet and serves to set and monitor the high voltages on the detector and on one side of the upper $\mathbf{E} \times \mathbf{B}$ electrode), and the control PC (sets and reads the AP voltage, reads the neutron counter, controls the movement of the neutron shutter, writes several log files, and starts and stops the different operations performed by the other PCs). For control and readout of the different devices several LabVIEW[20] programs on the different PCs are used. The different PCs communicate with each other via DataSocket[21].

Further details on the detector, the signal processing electronics, simulations and investigations of detector properties, and the used programs can be found in Ref. [52].

3.4 Systematic Effects

The ultimate goal of the aSPECT experiment is to improve the uncertainty in the neutrino-electron correlation coefficient a to 0.3 % [47]. In order to meet this target figure, all systematic effects must be kept below $\Delta a/a = 0.1\,\%$. The dominant systematic effects are thoroughly discussed in Refs. [46, 47]. In this section, we will only summarize the main points.

---

[16] For details on the data structure see Refs. [52, 197].

[17] Interface to transfer data over long distances with serial links.

[18] Object oriented framework for large scale data analysis developed at CERN [202].

[19] For details on the structure of the ROOT tree see Ref. [52].

[20] Graphical programming environment developed by National Instruments (NI).

[21] Standard to transfer data via the network developed by NI.

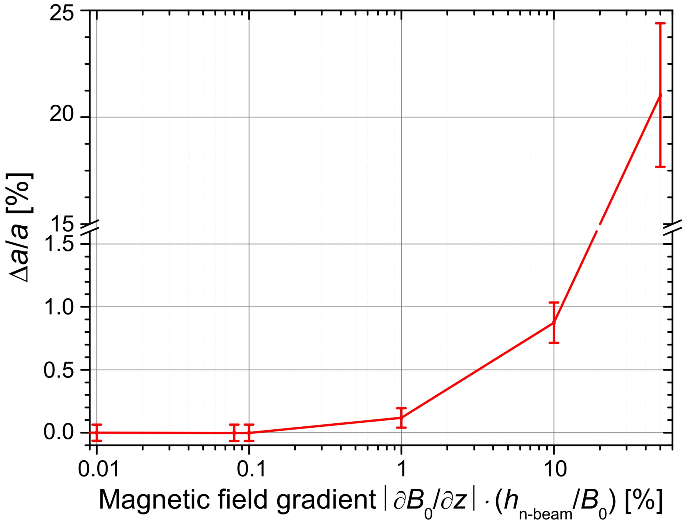

Figure 3.22: Relative change of the angular correlation coefficient a for different magnetic field gradients, $\partial B_0/\partial z$, in the decay volume (DV), assuming a uniform neutron beam density. For better visibility, the y-axis is broken at $\Delta a/a = 1.6\,\%$. An inhomogeneity of $(B_{\text{max}} - B_{\text{min}})\,/B_0 = 8\times10^{-4}$ over the full height, $h_{\text{n-beam}}$, of the neutron beam corresponds to a shift in a of $\Delta a/a = -0.001(50)\,\%$. Input data for the simulation (in INM approximation): $B_{\text{A}}/B_0 = 0.203$, $U_{\text{A}} = 50, 250, 400, 500, 600\,\text{V}$, and the recommended value for $a = -0.103$ [10]. The error bars, in the order of 0.05 %, represent the error by fitting Eq. (3.32) to the simulated proton count rates only.

3.4.1 The Adiabatic Transmission Function

As discussed earlier in Sec. 3.1.2, the transmission function Eq. (3.30) depends only on the ratio r_{B} of the magnetic fields in the AP and the DV and the barrier voltage U_{A}. As discussed further in Sec. 3.1.3 (see also Fig. 3.5), we have to know the magnetic field ratio r_{B} with a relative accuracy of 1×10^{-4} and the potential barrier U_{A} with an accuracy of better than 10 mV, in order to keep systematic uncertainties in a below $\Delta a/a = 0.3\,\%$.

In order to know the magnetic field ratio $r_{\text{B}} = B_{\text{A}}/B_0$ with a relative accuracy of $\Delta r_{\text{B}}/r_{\text{B}} = 1\times10^{-4}$, we have to know both the magnetic fields in the AP and the DV with a relative accuracy of $\Delta B_{\text{A}}/B_{\text{A}} = 1\times10^{-4}$ and $\Delta B_0/B_0 = 1\times10^{-4}$, respectively. Hence, a high temporal stability is required, as it was not yet possible to measure the magnetic field during data taking. First tests with a nuclear magnetic resonance (NMR) system with polarized ^{3}He (developed by F. Ayala Guardia [53]) have shown that the magnetic field ratio r_{B} is stable within $\Delta r_{\text{B}}/r_{\text{B}} = 0.1\times10^{-4}$ for 1 month (cf. Eq. (3.40)), well within our tolerance of 1×10^{-4}. We mention that in the upcoming measurements with aSPECT (see also Sec. 7.3) an improved NMR system with 1:1 acetone and ethanol mixture (developed by F. Ayala Guardia [53]) will be installed close to the DV and the AP.

However, the magnetic field in the DV exhibits a slight magnetic field gradient of $(\partial B_0/\partial z)\,/B_0 = -1\times10^{-4}\,\text{cm}^{-1}$,[22] as can be seen from Fig. 3.16a. This corresponds to an inhomogeneity of the magnetic field in the DV of $(B_{\text{max}} - B_{\text{min}})\,/B_0 = 8\times10^{-4}$ over the full height of the neutron beam (see Sec. 4.1.3 for details), out of our tolerance

---

[22] Please note that the figure slightly deviates from that given in Ref. [53], as the final analysis of the magnetic field measurements had not been completed at the time of this analysis.

of 1×10^{-4}. Consequently, we have to weight the transmission function Eq. (3.30) with the neutron beam density $n(\mathbf{P}_0)$. Figure 3.22 shows the relative change in a for different magnetic field gradients, assuming a uniform neutron beam density. The current magnetic field gradient of $(\partial B_0/\partial z)/B_0 = -1 \times 10^{-4}\,\mathrm{cm}^{-1}$ corresponds to a shift in a of

$$\Delta a/a = -0.001(50)\,\%. \tag{3.46}$$

Hence, the influence of the present magnetic field gradient on the neutrino-electron correlation coefficient a is negligible at the level of 0.1 %. Further investigations for different shapes of the neutron beam profile are found in Ref. [53].

According to our electric field calculations presented in Sec. 3.2.1, the electrostatic potential within the DV is smaller than 1 mV and its variations at the AP are smaller than 2 mV, both well within our tolerance of less than 10 mV. However, the following effects may influence the potential barrier U_{A}:

Negative space charges: The accumulation of negative space charges around the AP could change the electrostatic potential U_{A}. Experiences from similar experiments [41, 174, 203, 204] suggest that the accumulation rate is sufficiently small.

Work function differences: Work function differences of the different materials should cancel, as all electrodes are gold-plated and kept at the same temperature of about 70 K (of the cold bore tube of the aSPECT magnet), except for the high voltage electrodes e16 and e17. However, a variation of the work function of up to 250 meV was found in a cylindrical sample electrode at atmospheric pressure and room temperature, as can be seen from Fig. 6.1. The influence of possible variations of the work function within an electrode or between different electrodes is thoroughly discussed in Chap. 6.

Surface charges: Surface charges on a possible insulating surface layer of the electrodes could influence the electrostatic potential U_{A}. In Ref. [205] measurements of this effect due to external radiation are presented for different surfaces. Extrapolation of these results suggests that this effect is negligible.

In order to measure in situ the potential difference $U_{\mathrm{A}} - U_0$ between DV and AP, a monochromatic ion source is under development. Key requirements on the calibration source are:

- operation in a strong magnetic field and
- provision of charged particles with known energy and energy spread of about 10 meV.

A photo-electron source turned out not to fulfill these requirements [3]. First tests with a calibration source in which monoenergetic ^{4}He ions are produced are found in Ref. [34].

3.4.2 Non-Adiabatic Proton Motion

The aSPECT experiment was designed to eliminate the shortcomings of its predecessor [41] (see also page 37 under “The Measurement of Byrne *et al.* at the Institut Laue-Langevin”), in particular such that effects of to non-adiabatic proton motion are negligible [47]. As stated earlier in Sec. 3.1.2, in the adiabatic approximation, the orbital magnetic moment $\mu = T_{\mathrm{p},\perp}/B$ is constant and the transmission function can be calculated analytically.

Table 3.2: Relative change of the angular correlation coefficient a for different magnetic field values B_0. With decreasing magnetic field the non-adiabatic change of the orbital magnetic moment increases exponentially. For magnetic field values above $B_0 = 1.5\,\mathrm{T}$ the influence of non-adiabatic proton motion on a is negligible, while substantial for magnetic field values below $B_0 = 1\,\mathrm{T}$. Input data for the simulation [47]: magnetic field ratio $B_0/B_\mathrm{A} = 5$ and acceleration potential $|U_\mathrm{8R} - U_\mathrm{8L}| = 3\,\mathrm{kV}$ fixed (see also Fn. 14).

B_0 [T]	$\Delta a/a$ [%]
3	0.001
1.5	0.04
1.2	0.5
0.9	4
0.6	20

Our proton trajectory calculations showed that the value of μ in the AP is indeed close to its value at the decay point $\mathbf{P}_0$. In contrast, in regions with high electric and/or magnetic field gradient, e.g., at the lower dipole electrode e8, the value of μ oscillates with a period equal to the local gyration period; where the oscillation amplitude increases with the field gradients. Hence, the decay protons seem to remember their initial orbital magnetic moment when passing from one homogeneous field region to another [176] (here: from the DV to the AP). However, our trajectory calculations showed that breakdown of the adiabatic approximation sets an upper limit of 3 kV for the potential difference between sides R and L of the lower dipole electrode e8 (see also Fn. 14). With increasing acceleration potential the proton's gyration length and hence the deviation from the adiabatic approximation increase.

The effect of non-adiabatic proton motion is more severe for those decay protons that cannot pass the potential barrier and are subsequently trapped between the electrostatic mirror and the AP. These protons perform several axial oscillations between the electrostatic mirror and the AP, i.e., several passages through the lower dipole electrode e8, before they are removed from the flux tube with the dipole electrode. On the one hand, the non-adiabatic change of the orbital magnetic moment increases with the number of these oscillations [41]; on the other hand, the number of these oscillations decreases with increasing potential difference. For our upper limit of 3 kV for the potential difference (see also Fn. 14), the trapped protons perform less than five to six axial oscillations [47].

According to Ref. [177], the non-adiabatic change of the orbital magnetic moment increases exponentially with decreasing magnetic field. In Table 3.2 we list the relative change in the neutrino-electron correlation coefficient a for different values of the magnetic field B_0, for our upper limit of 3 kV for the potential difference (see also Fn. 14). For magnetic field values above $B_0 = 1.5\,\mathrm{T}$ the influence of non-adiabatic proton motion on a is negligible. To verify our calculations, measurements with different heights of the magnetic field were investigated (discussed in Sec. 5.5.5).

3.4.3 Residual Gas

A decay proton should reach the proton detector if and only if the adiabatic transmission condition Eq. 3.24 is fulfilled at the AP. On their way from the DV to the proton detector,

Table 3.3: Critical pressure values of elastic p-H_2 scattering for different acceleration potentials $|U_{8R} - U_{8L}|$ [47] (see also Fn. 14).

$\lvert U_{8R} - U_{8L}\rvert$ [kV]	p_{cr} [mbar]
3	5×10^{-8}
0.3	1×10^{-8}
0.03	1.4×10^{-9}

these protons may interact with residual gas molecules and hence change their energy and direction. Three cases must be considered:

- change of energy and direction due to elastic scattering,
- change of energy and direction due to inelastic scattering, and
- neutralization due to charge exchange processes.

The systematic effect due to these collisions is proportional to the residual gas density, i.e., for a fixed temperature (here: of about 70 K of the cold bore tube), to the gas pressure. Thus, we define p_{cr} as the critical value of the residual gas pressure[23] at which interactions introduce a systematic effect on a at the level of $\Delta a/a = 0.1\,\%$. In the following, we report the results of Monte Carlo (MC) simulations for the above mentioned three processes [47]:

Elastic scattering: Elastic scattering processes may change kinetic energy and pitch angle[24] of the decay protons. Two cases occur:

- trapped protons with $T_{tr}^{min} < T_0 < T_{tr}(\theta_0)$ can be transmitted through the AP,
- protons with $T_0 > T_{tr}(\theta_0)$ might be hindered to pass the potential barrier.

The scattering probability is proportional to the particle's path length. Thus, the first effect on the trapped protons is more important, as they perform several axial oscillations between the electrostatic mirror and the AP before they are removed from the flux tube with the lower dipole electrode e8. In Table 3.3 we list the critical pressure values of elastic p-H_2 scattering for different settings of the dipole electrode. With increasing potential difference the trapping time decreases and hence the critical pressure increases.

To verify our MC simulations, measurements with different settings of the lower dipole electrode e8 were investigated (discussed in Sec. 5.3.2).

Inelastic energy loss: Inelastic scattering processes may also change kinetic energy and pitch angle of the decay protons. Compared with elastic scattering processes, the change of the pitch angle is negligible [47] (see also [206–210]). The energy loss, in turn, is dominated by rotational and vibrational excitations. For inelastic scattering of protons on hydrogen, the energy loss due to vibrational excitations sets an upper limit of

$$p_{cr} = 4 \times 10^{-8}\,\text{mbar}. \tag{3.47}$$

---

[23] Please note that all figures in this section are based on a temperature of 60 K (see also [47]).

[24] Compared with the (initial) polar angle, the pitch angle denotes the angle between the proton's momentum and the magnetic field.

Table 3.4: Critical pressure values of charge exchange processes for different residual gases [47].

Gas	p_{cr} [mbar]
H_2	2×10^{-8}
Ar	1×10^{-8}
N_2	2×10^{-8}
O_2	4×10^{-8}
He	1×10^{-6}

For inelastic scattering of protons on other atoms and molecules, this has to be part of further investigations (by means of MC simulations).

Charge exchange: A decay proton may capture an electron from a residual gas molecule:

$$\mathrm{p} + \mathrm{M} \longrightarrow \mathrm{H} + \mathrm{M}^{+}. \tag{3.48}$$

The resulting positive ion will have very low energy. Thus, if the process takes place between the DV and the AP, no event will be detected. In Table 3.4 we list the critical pressure values for different residual gases.

Altogether, for a residual gas pressure of 10^{-8} mbar or better, the influence of interactions with residual gas molecules on the neutrino-electron correlation coefficient a is negligible at the level of 0.1 %. In comparison with our first beam time at the FRM II, four getter pumps[25] were installed directly on the electrode system to improve the vacuum conditions. Two of the four getter pumps are shown in Fig. 3.9a. In this way, the residual gas pressure was improved to at least[26] 8×10^{-9} mbar, i.e., by at least a factor of 2.5 compared to our first beam time at the FRM II [33].

3.4.4 Background

With regard to the background, we distinguish between:

Correlated background events: In neutron beta decay, the decay products, proton, electron, and anti-neutrino, are emitted simultaneously. In the aSPECT experiment, only protons and electrons can be detected. Decay electrons are detected only if they were emitted towards the proton detector and if they can overcome the electromagnetic mirror right in front of the detector. Due to their higher energy but smaller mass, the time-of-flight (TOF) of the electrons is about one thousands of the TOF of the decay protons. Thus, the detection time difference between correlated coincidence events may be estimated by the TOF of the proton. The minimum TOF of decay protons is about 5.2 μs[27], where the proton was emitted towards the

---

[25] To be specific, four SAES CapaciTorr D 400-2 DSK getter cartridges were installed. In order not to disturb the homogeneous magnetic field, the getter cartridges were chosen for their non-magnetic (relative permeability $\mu_{\mathrm{r}} \approx 1.011$), high performing St 172 (Zr-V-Fe) porous sintered getter material.

[26] In order not to disturb the homogeneous magnetic field, the cold cathode gauge was mounted on the bottom flange of the aSPECT spectrometer, at the far end of a 2 meters long, warm CF 40 tube.

[27] Please note that in Refs. [34, 52, 211] the minimum TOF is misstated. The minimum TOF at $U_{\mathrm{A}} = 0$ V was already corrected in Ref. [33] to 5.2 μs [47], for slightly different settings of the spectrometer.

proton detector, opposite to its correlated electron. Hence, for a dead time of the electronics smaller than the minimum TOF of the protons, i.e., $\tau_{\text{dead}} \leq 5.2\,\mu$s, all correlated proton events should be detected (for details see Sec. 5.2.1). Indeed, in our latest beam time at the ILL, a small fraction of the decay protons was lost due to a problem in the detector electronics (discussed in Sec. 5.4.1).

Uncorrelated background events: Positive ions coming from the residual gas or the electrodes, gamma radiation and high-energy electrons created by neutron capture and by cosmic rays cause uncorrelated background events. Obviously, the uncorrelated background can be subdivided into beam-related and environmental background. Although beam-related background is often a problem in neutron decay experiments, it is not treated differently in our data analysis (for details see Sec. 5.2.2), provided that the background does not depend on the barrier voltage. As mentioned earlier in Sec. 3.1, in our experiment, the background is measured at $U_{\text{A}} = 780\,\text{V}$. Further experimental studies are necessary to make sure that this method does not change the background to be measured, by, e.g., applying the barrier potential to different electrodes. Indeed, in our first beam time at the FRM II, the background count rate showed a dependence on the barrier voltage (see also page 56 under "Penning Traps and Penning Discharge" and Sec. 5.3.1).

3.4.5 Doppler Effect due to Neutron Motion

The motion of the decaying neutron also changes the observed energies and angles of the outgoing particles relative to the energies and angles in the center-of-mass system (CMS) of the neutron. The kinetic energy, T_{CMS}, and polar angle, θ_{CMS}, of the outgoing particles in the CMS system of the neutron change as follows:

$$T_{\text{LAB}} = T_{\text{CMS}} + \frac{m_{\text{p}}}{m_{\text{n}}} T_{\text{n}} + 2\sqrt{\frac{m_{\text{p}}}{m_{\text{n}}}}\sqrt{T_{\text{CMS}} T_{\text{n}}} \cos\theta_{\text{CMS}} \quad \text{and} \tag{3.49}$$

$$\theta_{\text{LAB}} = \arctan \frac{\sin\theta_{\text{CMS}}}{\cos\theta_{\text{CMS}} + \sqrt{\frac{m_{\text{p}}}{m_{\text{n}}}}\sqrt{\frac{T_{\text{n}}}{T_{\text{CMS}}}}}, \tag{3.50}$$

where T_{LAB} and θ_{LAB} are the kinetic energy and polar angle of the outgoing particles in the laboratory system, respectively, and T_{n} is the kinetic energy of the decaying neutron. This momentum change, in turn, may affect the transmission function Eq. (3.30).

Cold neutrons have an average kinetic energy of about $T_{\text{n}} = 4\,\text{meV}$. To get a feeling for the Doppler shift, we consider two examples:

$$(T_{\text{CMS}}; \theta_{\text{CMS}}) = (400\,\text{eV}; 0°) \longmapsto (T_{\text{LAB}}; \theta_{\text{LAB}}) = (402.54\,\text{eV}; 0°)\,, \tag{3.51}$$

$$(T_{\text{CMS}}; \theta_{\text{CMS}}) = (400\,\text{eV}; 30°) \longmapsto (T_{\text{LAB}}; \theta_{\text{LAB}}) = (402.20\,\text{eV}; 29.91°)\,. \tag{3.52}$$

These are both enormous energy and angle changes, especially in comparison with the required accuracy of 10 meV.

In *a*SPECT, this effect is strongly suppressed due to the transverse proton detection with respect to the neutron beam and its 4π acceptance (see also Sec. C.3). According to Eq. (3.49), protons emitted opposite to the neutron motion have a laboratory energy smaller than their CMS energy. We have therefore a large cancellation of Doppler effects. The impact of the Doppler effect on the neutrino-electron correlation coefficient a was calculated for a typical neutron velocity distribution and different settings of the barrier potential [47]. For $U_{\text{A}} < 500\,\text{V}$, the effect is smaller than 10^{-4}. Hence, we do not expect any essential systematic uncertainty from the Doppler effect.

3.4.6 Edge Effect

Depending on the size of the proton detector, the shape of the neutron beam profile (in the DV) may induce another systematic effect. The neutron beam profile is projected by the magnetic field onto the detector. The decay protons, in turn, are guided by the magnetic field towards the detector, gyrating around a magnetic field line. As shown in Fig. 3.23, at the edges of the detector, two cases occur:

- protons emitted outside the projected area can hit the detector and
- protons emitted within the projected area might miss the detector.

Depending on the shape of the neutron beam profile, two cases must be considered:

Uniform neutron beam profile: In the ideal case, the two above mentioned cases cancel, provided that the detection efficiency of the proton detector is uniform. We mention that the cancellation is independent of the proton's radius of gyration, as can be seen from Figs. 3.23a and 3.23b.

Non-uniform neutron beam profile: In reality, the neutron beam profile is more inhomogeneous. In this case, the probabilities for the two cases become different and dependent on the proton's radius of gyration, as can be seen from Figs. 3.23c and 3.23d. This leads to an energy dependent systematic effect, as the proton's radius of gyration depends on both its emission angle and energy (cf. Eq. (3.3)).

We note that for a given definite radius of gyration, any proton emitted in-between the two transition regions (see Figs. 3.23c and 3.23d) will hit the detector.

There are now two possibilities to eliminate or at least to minimize this effect:

- narrow the width of the neutron beam to the minimal width of the area in-between the two transition regions, i.e., to the width of the proton detector minus four times the maximum radius of gyration Eq. (3.5). For our typical current settings Eq. (3.41), this would correspond to a width of 7.4 mm, what in respect of statistics is not acceptable.
- optimize the neutron apertures to obtain a neutron beam profile as uniform as possible. We note that, if the neutron beam profile is not sufficiently homogeneous, its shape has to be known precisely.

MC simulations have to be used to correct this effect, as the projection of the neutron beam profile onto the detector is altered by both, the lower and upper, dipole electrodes. To verify our calculations, measurements with different shapes of the neutron beam profile were investigated (discussed in Sec. 5.5.6). The shape of each neutron beam profile was measured by copper foil activations in front and behind the *a*SPECT spectrometer (for details see Sec. 4.1.3).

3.4.7 Detection Efficiency

Even if a decay proton hits the detector it may stay undetected, due to the dead layer and the response function of the proton detector. The detection efficiency, i.e., the probability that a proton will be detected, depends on both its impact angle and energy. We note

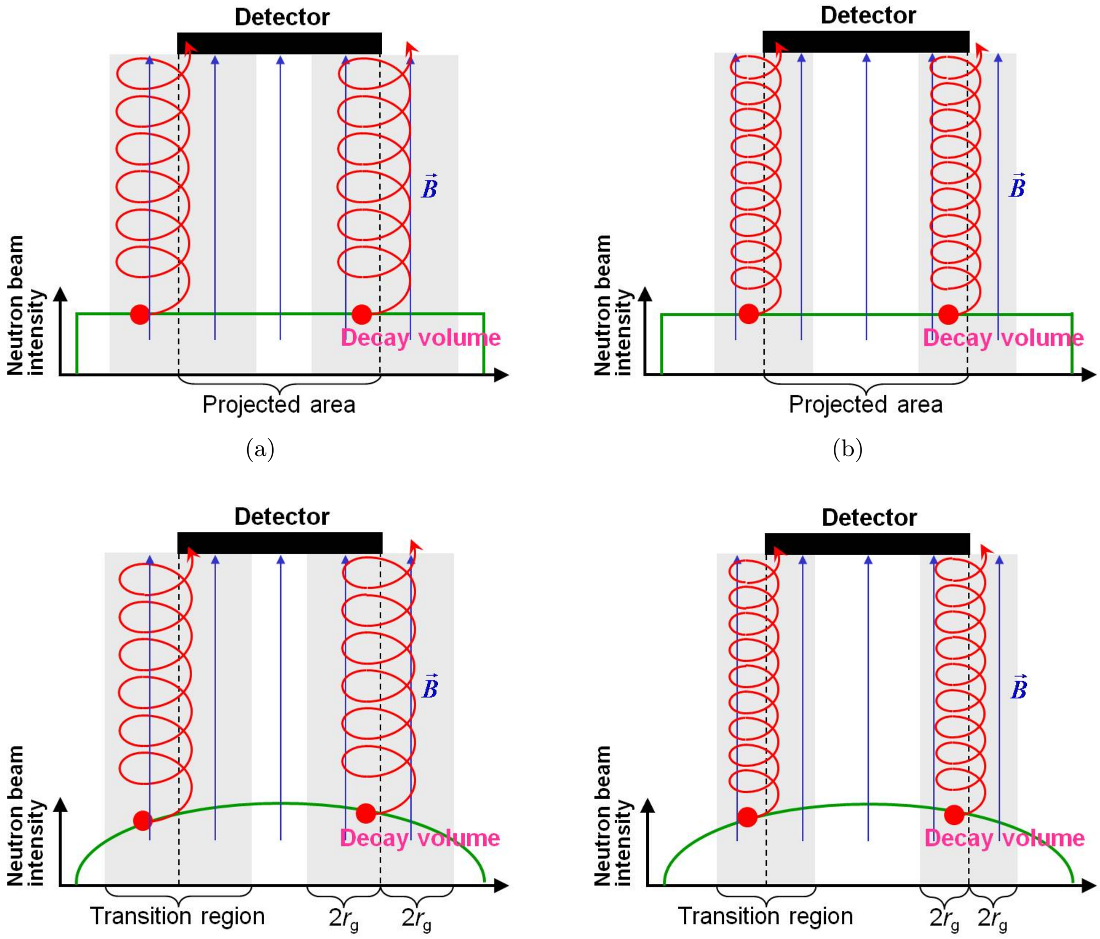

(a) (b)

(c) (d)

Figure 3.23: Illustration of the edge effect, for two different shapes of the neutron beam profile: (top) uniform profile and (bottom) non-uniform profile. At the edges of the proton detector, two cases occur: Protons emitted outside the projected area can hit the detector, whereas protons emitted within the projected area might miss the detector. The comparison between (a) and (b) shows that this two cases cancel, independent of the proton's radius of gyration; the comparison between (c) and (d) shows that the probabilities for the two cases become different and dependent on the proton's radius of gyration.

that the average detection efficiency is irrelevant to our data analysis, as it just reduces the count rates by a common factor.

The proton's impact energy is given by its emission energy $T_0 \in [0, T_{\mathrm{p,max}}]$ plus the acceleration potential $U_{17} \in [-15\,\mathrm{kV}, -10\,\mathrm{kV}]$, i.e., it will be close to the acceleration voltage. Hence, the energy-dependent detection efficiency can be written as

$$f_{\text{impact energy}} \propto 1 + c_1 \cdot T_0, \tag{3.53}$$

with a small constant c_1. For $|c_1| < 200\,\mathrm{ppm\,keV^{-1}}$, the influence of the energy-dependent detection efficiency on the neutrino-electron correlation coefficient a is negligible at the level of 0.1 % [47]. We note that reasons for an energy-dependent detection efficiency are

- backscattering in the dead layer of the proton detector (discussed below) and

- the threshold to distinguish between proton signals and the electronic noise (see also Sec. 5.4.1).

In the first case, a decay proton enters the detector, scatters several times inside the detector, before it leaves the detector again. After a rather short time of about 0.5 μs, the proton will hit the detector again, because of the electromagnetic set-up of aSPECT. This guarantees that at most one proton event is counted.

The angular-dependent detection efficiency, in turn, is dominated by backscattering in the dead layer of the proton detector and can therefore be written as

$$f_{\text{impact angle}} \propto 1 - \frac{c_2}{\cos\theta_{\text{p,det}}} \,, \tag{3.54}$$

where c_2 is a small constant and

$$\theta_{\text{p,det}} = \theta_{\text{p,det}}(T_0, \theta_0) = \arcsin\sqrt{\frac{B_{\text{det}}}{B_0} \cdot \frac{T_0 \sin^2\theta_0}{T_0 - e\,(U_{17} - U_0)}} \tag{3.55}$$

is the angle between the proton's momentum and the detector axis (cf. Eq. (3.18)). The maximum impact angle, $\theta_{\text{p,det}}(T_{\text{p,max}}, 90°)$, of decay protons is 18° at $U_{17} = -15\,\text{kV}$ up to 22° at $U_{17} = -10\,\text{kV}$. For $c_2 < 7 \times 10^{-3}$, the influence of the angular-dependent detection efficiency on the angular correlation coefficient a is negligible at the level of 0.1 % [47].

Investigations of the backscattering of decay protons are found in Ref. [52]. Figure 3.24 shows the probability of backscattering for different proton impact angles and energies [52]. The fraction of backscattered protons is about 1.0 % at $U_{17} = -15\,\text{kV}$ up to 1.8 % at $U_{17} = -10\,\text{kV}$ [52]. Here, we only present the possible influence of backscattering of decay protons on the neutrino-electron correlation coefficient a, derived from this data[28]:

$$\boxed{\Delta a/a < +0.22(16)\,\%} \tag{3.56}$$

In fact, a backscattered proton might loose enough energy in the active volume of the proton detector to be detected. Thus, Eq. (3.56) only sets an upper limit on the correction of the backscattering of decay protons.

For details on simulations[29] and investigations of detector properties the reader is referred to the thesis of M. Simson [52].

---

[28] Further input data for the MC simulation (in INM approximation, with Coulomb correction Eq. (2.56)): $B_0 = 2.177\,\text{T}$, $B_{\text{A}}/B_0 = 0.203$, $B_{\text{det}} = 4.340\,\text{T}$, $U_{\text{A}} = 50, 250, 400, 500, 600\,\text{V}$, $U_{17} = -15\,\text{kV}$, number of generated events $= 10^9$, and $a = -0.105$ (derived from $\lambda = -1.2701(25)$ [10]).

[29] The detector properties were simulated with the software package SRIM [212].

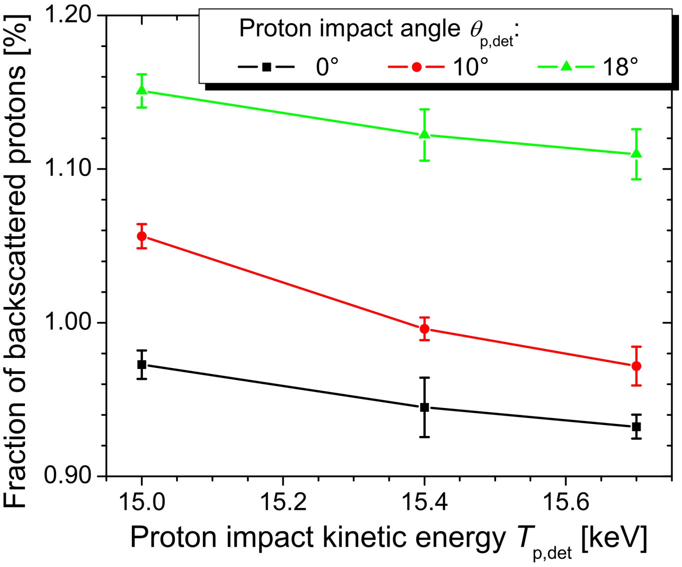

Figure 3.24: The probability of backscattering of decay protons for three different impact angles and energies. The fraction of backscattered protons is about 1.0 % at $U_{17} = -15\,\mathrm{kV}$ up to 1.8 % at $U_{17} = -10\,\mathrm{kV}$ [52]. 6×10^5 protons were simulated for each point. Data from Ref. [52].

Chapter 4

Measurements at the ILL

The aSPECT experiment was set up from November 2007 to June 2008 at the cold neutron beam facility PF1B of the Institut Laue-Langevin (ILL) high-flux reactor in Grenoble, France. The primary emphasis of this beam time has been put on the identification and investigation of possible systematic effects with sufficient statistical accuracy. This is because background instabilities due to particle trapping and the electronic noise level of the proton detector had prevented us from presenting a new value for the neutrino-electron correlation coefficient a from our first beam time at the Forschungs-Neutronenquelle Heinz Maier-Leibnitz (FRM II) in Munich, Germany [33, 49]. To avoid these problems, the proton detector was replaced by a silicon drift detector (SDD) at significantly reduced acceleration potential (discussed in Sec. 3.3.1), parts of the electrode system were redesigned (see Sec. 3.2.1 for details), and the ultra high vacuum (UHV) conditions were improved (for details see Sec. 3.4.3). As shown earlier in Fig. 3.19b (see Sec. 3.3.1), the electronic noise could be sufficiently separated from the proton signal. The secondary focus of this beam time was on the determination of a new value for the correlation coefficient a with a total relative error well below the present literature value of 4 % [10] (see also [40, 41] and Sec. 2.4).

In this chapter, we give a brief overview of our measurements during the beam time at the ILL. A detailed analysis of the measured data follows in Chap. 5. Details on detector and electronics tests, measurements of the neutron beam profile, and measurements of the magnetic field can be found in the theses of M. Simson [52], M. Borg [34], and F. Ayala Guardia [53], respectively.

4.1 Experimental Set-up at the ILL

Our experiment makes use of cold neutrons, i.e., neutrons with kinetic energies from $0.5\,\mu$eV to 0.025 eV (see also Fn. 38 in Chap. 2). Normally these neutrons are produced in a research reactor or by a spallation source. The Institut Laue-Langevin (ILL) is an international research center that operates the most intense neutron source in the world. The ILL's high-flux reactor is a fission reactor[1] with a thermal power of just 58.3 MW and

---

[1] When a nucleus of a ^{235}U target captures a neutron, it splits into two or more lighter nuclei, releasing kinetic energy of typically 200 MeV per fission, gamma radiation, and free neutrons. In a nuclear chain reaction, a portion of these neutrons is later captured by other fissile atoms and triggers further fission events, which in turn release more neutrons.

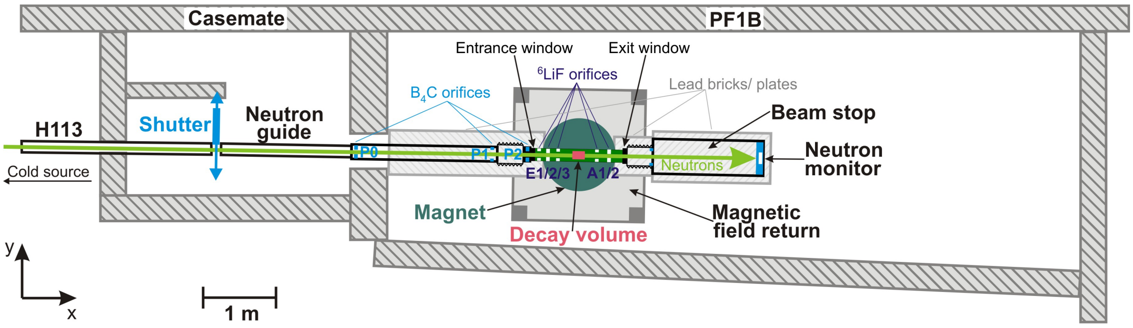

Figure 4.1: A sketch of the experimental set-up of the *a*SPECT experiment at the PF1b of the ILL. Unpolarized, cold neutrons (light green) are coming from the vertical liquid deuterium cold source (to the left of the scheme). Different equipment for neutron beam preparation, like velocity selector, polarizer, spin flipper, or chopper, can be installed inside the casemate. In our experiment, the neutrons are guided by an additional neutron guide (black). The beam is shaped by the collimation system, comprising of B_4C (turquoise) and ^{6}LiF (white) apertures. It flies through the *a*SPECT magnet (dark green) to a beam stop. The stability of the neutron beam intensity was continuously monitored with a ^{6}Li neutron counter at the end of the beam stop. In between the end of the guide H113 and our additional neutron guide a B_4C shutter was installed, which allows automated background measurements.

the most intense continuous neutron flux in the world:

$$\Phi = \int dv\, \Phi(v) = 1.5 \times 10^{15}\,\mathrm{cm}^{-2}\,\mathrm{s}^{-1}. \tag{4.1}$$

Its core comprises a single highly enriched ^{235}U fuel element cooled by heavy water. The fission neutrons are very high-energy neutrons, with velocities of about 20000 km s^{-1}. They are slowed down by the heavy water to thermal neutrons, with velocities of about 2200 m s^{-1}. This is still much too fast for nuclear and particle physics experiments, where the neutron decay rate is inversely proportional to the neutron's velocity. Hence, the thermal neutrons are further slowed down to the desired energy by one of two cold sources, i.e., 25 K liquid deuterium moderators near the reactor core. These cold neutrons have velocities of about 800 m s^{-1}. The neutrons are extracted from inside the reactor by neutron guides, which in turn distribute the neutrons to forty experimental areas (for research in materials science, biology, physics, and chemistry; as well for the production of radioisotopes for medical therapy and diagnosis), located up to 100 m from the reactor.

4.1.1 The Neutron Beam Facility PF1b of the ILL

The cold (polarized) neutron beam facility PF1b is installed at the vertical liquid deuterium cold source of the ILL, at the end position of the very intense ballistic supermirror[2] ($m = 2$) guide H113 [213]. The instrument layout is schematically shown in Fig. 4.1. The neutron guide H113 ends in a casemate, right in front of the experimental zone. The

---

[2] In contrast to a conventional, single layer nickel coated neutron guide ($m = 1$), a neutron supermirror consists of typically 100 double layers of nickel and titanium, of varying thickness. In this way, the critical angle of total reflection is increased by a factor of two or more ($m \geq 2$) and hence the transmission by up to a factor of four.

different equipment for neutron beam preparation, like focusing beam guides, neutron velocity selector, supermirror polarizer, spin flipper, or chopper, can be installed inside the casemate. The guide H113 offers a thermal equivalent neutron flux[3] of [214]

$$\Phi_{\mathrm{c}} = \int dv\, \Phi(v) \frac{v_0}{v} = 1.8 \times 10^{10}\,\mathrm{cm}^{-2}\,\mathrm{s}^{-1} \tag{4.2}$$

over a cross-section of $60 \times 200\,\mathrm{mm}^2$ [215], where $v_0 = 2200\,\mathrm{m\,s}^{-1}$ is the most probable velocity of a Maxwellian (thermal) spectrum at 300 K. We note that, in most nuclear and particle physics experiments, the capture flux Φ_{c} is more interesting than the particle flux Φ, as the detection efficiency of most neutron detectors is inversely proportional to the neutron's velocity. For cold neutrons, with $v < v_0$, the capture flux is higher than the particle flux.

Further characteristics of the instrument can be found in Ref. [215].

4.1.2 The Beam Line

Figure 4.1 shows a scheme of the experimental set-up of the *a*SPECT experiment at the instrument PF1b. Unpolarized, cold neutrons are guided (and shaped) by the beam line from the end of the neutron guide H113 to the spectrometer. The beam line comprises of

- an (additional) sintered boron carbide[4] (B_4C) shutter, which allows automated background measurements,
- an additional neutron guide with a cross-section of $50 \times 116\,\mathrm{mm}^2$, as *a*SPECT makes no use of additional equipment like velocity selector, polarizer, or chopper,
- three apertures from B_4C in the beam tube before the spectrometer,
- five apertures from isotopically enriched ^{6}LiF inside the spectrometer (see also Fn. 4), three before and two behind the decay volume (DV),
- a B_4C beam stop, with a small hole in the middle to allow some neutrons to pass through to
- a ^{6}Li neutron counter (see also Sec. 4.2.1) at the end of the beam stop, to continuously monitor the stability of the neutron beam intensity, and
- boron loaded rubber, in and outside the beam tube, followed by 5 to 10 cm of lead, for radiation protection.

Magnesium cast alloy (MgAl3Zn1) windows, with a thickness of 250 μm, were installed at both the entrance window and the exit window of the *a*SPECT magnet, in order to separate the rough vacua of the collimation system ($\approx 10^{-2}$ mbar) from the ultra-high vacuum (UHV) inside the spectrometer ($< 8 \times 10^{-9}$ mbar; see also Sec. 3.4.3). Figure 4.2 shows photographs of the experimental set-up at PF1b, with a view to both the entrance and the exit side of the *a*SPECT spectrometer.

---

[3] Also called the capture flux.

[4] Cold neutrons are easily absorbed by neutron capture in materials with a high neutron absorption cross-section. Most materials release primary gamma radiation, while others trigger secondary reactions, which in turn could produce fast neutrons. Inside the *a*SPECT spectrometer the use of isotopically enriched ^{6}LiF is preferable, as the production of gamma rays is suppressed by a factor of 10^{-4} compared to boron (^{10}B) and as most materials containing ^{10}B are not suitable for ultra high vacuum.

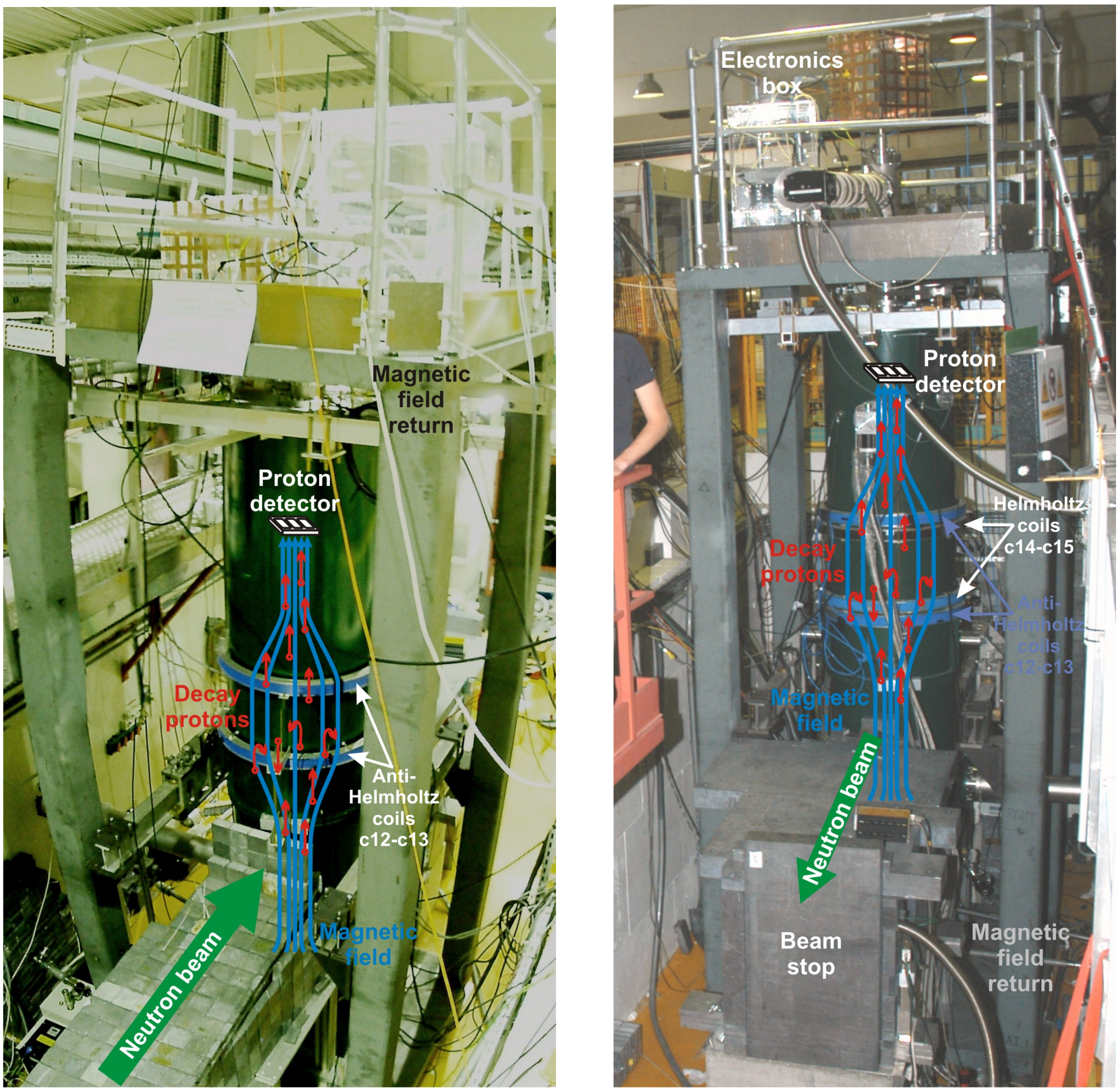

(a) (b)

Figure 4.2: Photographs of the experimental set-up of the *a*SPECT experiment at PF1b of the ILL. Figure (a) shows a view to the entrance side of the spectrometer, while Fig. (b) shows a view to its exit side. Unpolarized, cold neutrons (green) pass through the decay volume where only a few neutrons decay. The decay protons (red) are guided by the strong magnetic field (light blue) towards the analyzing plane (located between the Helmholtz coils c14 and c15 and not shown here) and subsequently the proton detector (white). *a*SPECT measures the proton recoil spectrum (see Fig. 2.3) by counting all decay protons that overcome an electrostatic barrier, applied in the analyzing plane. The photographs also show the magnetic field return, which serves to reduce the exterior magnetic field in order not to disturb neighboring experiments (for details see Chap. A). We note that the photo (a) was taken before the additional Helmholtz coils c14 and c15 were added (see also Sec. 3.2.2).

In the first half (November/December 2007) of our beam time at the ILL, the beam line with its collimation system and radiation protection was set-up, the superconducting magnet with its magnetic shielding (for details see Chap. A) and electrode system (described in Sec. 3.2.1) were installed, and the new SDD was tested as a proton detector (see Sec. 3.3.1 for details). The main phase of data taking took place in the second half (April/May 2008) of the beam time (discussed in Sec. 4.2.5 and Chap. 5). Further details on the beam line, the collimation system, and the alignment of the *a*SPECT spectrometer with respect to the neutron beam can be found in Refs. [34, 52].

The neutron beam was shaped by the additional neutron guide to a cross-section of $48 \times 72.5\,\mathrm{mm}^2$, measured by copper foil activation (for details see the following section and Ref. [34]) at the entrance of the *a*SPECT magnet. The thermal equivalent neutron flux was measured by gold foil activation at the exit flange to be

$$\Phi_{\mathrm{c}} = 6 \times 10^9\,\mathrm{cm}^{-2}\,\mathrm{s}^{-1} \tag{4.3}$$

over a cross-section of $54 \times 90\,\mathrm{mm}^2$. The beam profile was measured by copper foil activation.

4.1.3 Neutron Beam Profiles

As discussed earlier in Sec. 3.4.6, the neutron beam profile has to be sufficiently homogeneous or its shape has to be known precisely. To minimize the edge effect, the neutron apertures were optimized, by means of Monte Carlo (MC) simulations, to obtain a beam profile as uniform as possible. To verify our simulations [34], the neutron beam profile was measured by copper foil activation both in front of the entrance window and behind the exit window of the *a*SPECT spectrometer. For this purpose, thin foils (thickness $\approx 150\,\mu$m) of natural copper (composed of 69.15(15) % of ^{63}Cu and 30.85(15) % of ^{65}Cu) were irradiated by neutrons for about 80 min. Neutrons are captured by the two copper isotopes, ^{63}Cu and ^{65}Cu, and form the heavier isotopes ^{64}Cu and ^{66}Cu. The new isotopes are beta emitters which decay into the nickel and zinc isotopes ^{64}Ni or ^{64}Zn and ^{66}Zn, respectively. Here, the half-lifes are $\tau = 12.700(2)$ h for ^{64}Cu [216] and $\tau = 5.120(14)$ min for ^{66}Cu [217]. After a decay time of another 60 to 120 min, the two-dimensional neutron beam profiles were read out (see also [218]). For this purpose, the decay electrons, of almost only ^{64}Cu, were detected by a silicon PIN diode[5]. The silicon PIN diode was mounted to a robotic arm above the irradiated copper foils, which allowed to scan the copper foils in a grid pattern (for details see [34]). We mention that the overall spatial accuracy of our measured beam profiles is 1 mm, due to the uncertainties of the positioning both in the beam line and in the scanner.

Figure 4.3 shows the measured beam profiles in comparison with the simulated ones. After adaption of the input parameters for the MC simulation to the measured beam profiles a reasonable agreement was found. However, for the calculation of various systematic corrections, we need the neutron beam profile in the DV of *a*SPECT. At the time of our beam profile measurements, a measurement of the neutron beam profile directly in the DV was not feasible. Hence, we had to go for the simulated beam profiles in the DV instead. Therefore, the input parameters for the MC simulation were adjusted until the simulated beam profiles both in front and behind the spectrometer were consistent with the measured ones. We mention that, for the investigation of systematic effects, a cut at $x = 0$ is sufficient as the neutron beam profile varies only marginally over the depth, x, of the flux tube.

For systematic investigations of the edge effect (see Secs. 3.4.6 and 5.5.6 for details), measurements with two different reduced widths of the neutron beam were carried out.

---

[5] Normally, the neutron beam profile of an irradiated copper foil is read out after the transfer to an image plate. Unfortunately, the image plate scanner was damaged at the time of our beam profile measurements.

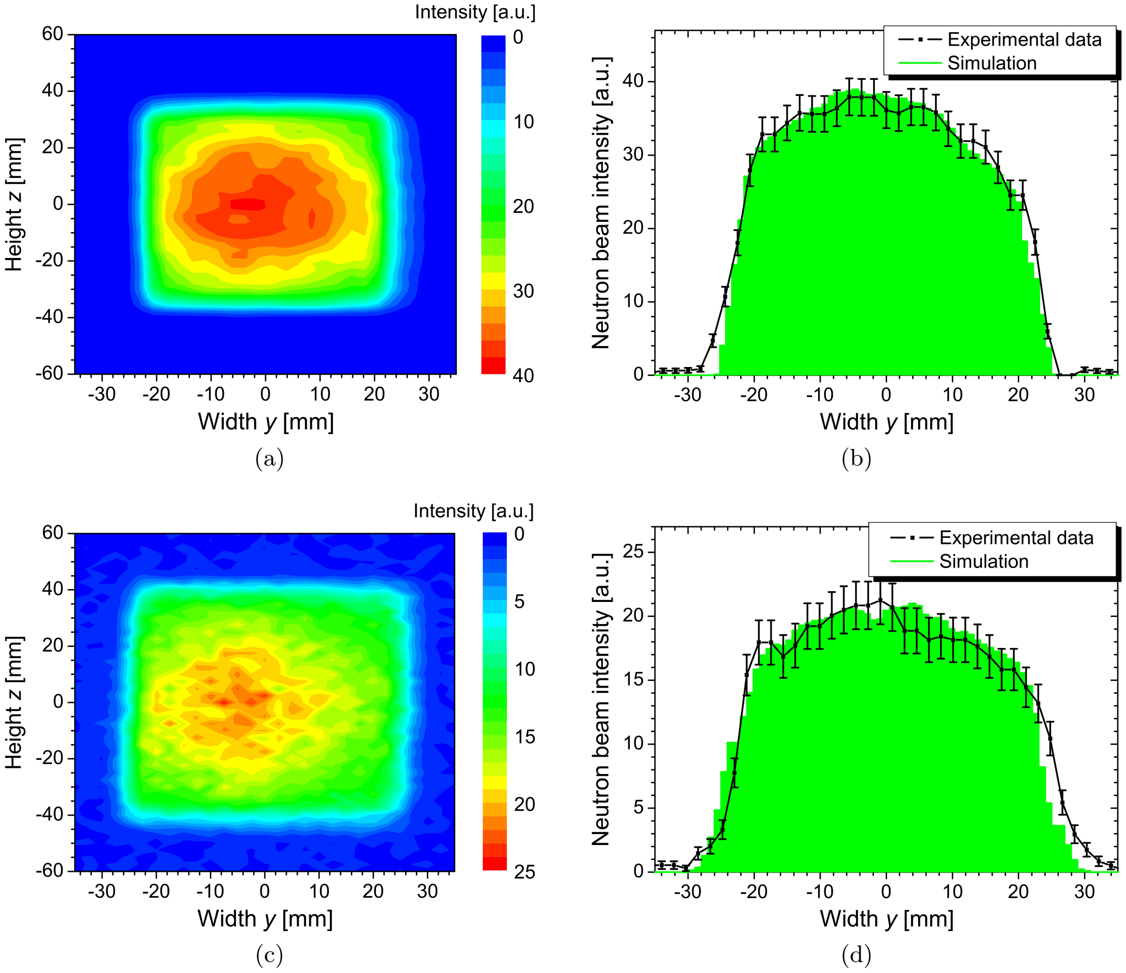

Figure 4.3: Neutron beam profiles measured by copper foil activation (top) in front of the entrance window and (bottom) behind the exit window of the *a*SPECT spectrometer. (a) and (c) show the two-dimensional, measured beam profiles; whereas (b) and (d) show horizontal cuts through the beam profiles (a) and (c), respectively, in comparison with the simulated beam profiles, at $z = 0$. Even though a reasonable agreement between the measured and the simulated beam profiles was found, the neutron beam profile in the DV was determined and subsequently smoothed both by bilinear interpolation of the measured beam profiles (a) and (c) (discussed also in Sec. 5.5.6). Error bars show statistical errors only.

For this purpose, an additional aperture was installed in front of the aperture P2, cf. Fig. 4.1. Figure 4.4 shows the neutron beam profiles for the 20 mm and the 5 mm wide aperture, respectively, both measured behind the exit window of *a*SPECT.

But even though a reasonable agreement between the measured and the simulated beam profiles was found, the poor quality of the simulated beam profiles is not adequate as input data for further MC simulations of, e.g., the edge effect. Hence, the two-dimensional, simulated beam profiles were smoothed by bilinear interpolation (described, e.g., in Ref. [90]). In the case of Fig. 4.3d, the agreement between the measured and the simulated beam profile is so poor that we had to determine the neutron beam profile in the DV by prior bilinear interpolation of the measured beam profiles in front of the entrance window and behind the exit window of the *a*SPECT magnet (discussed in Sec. 5.5.6).

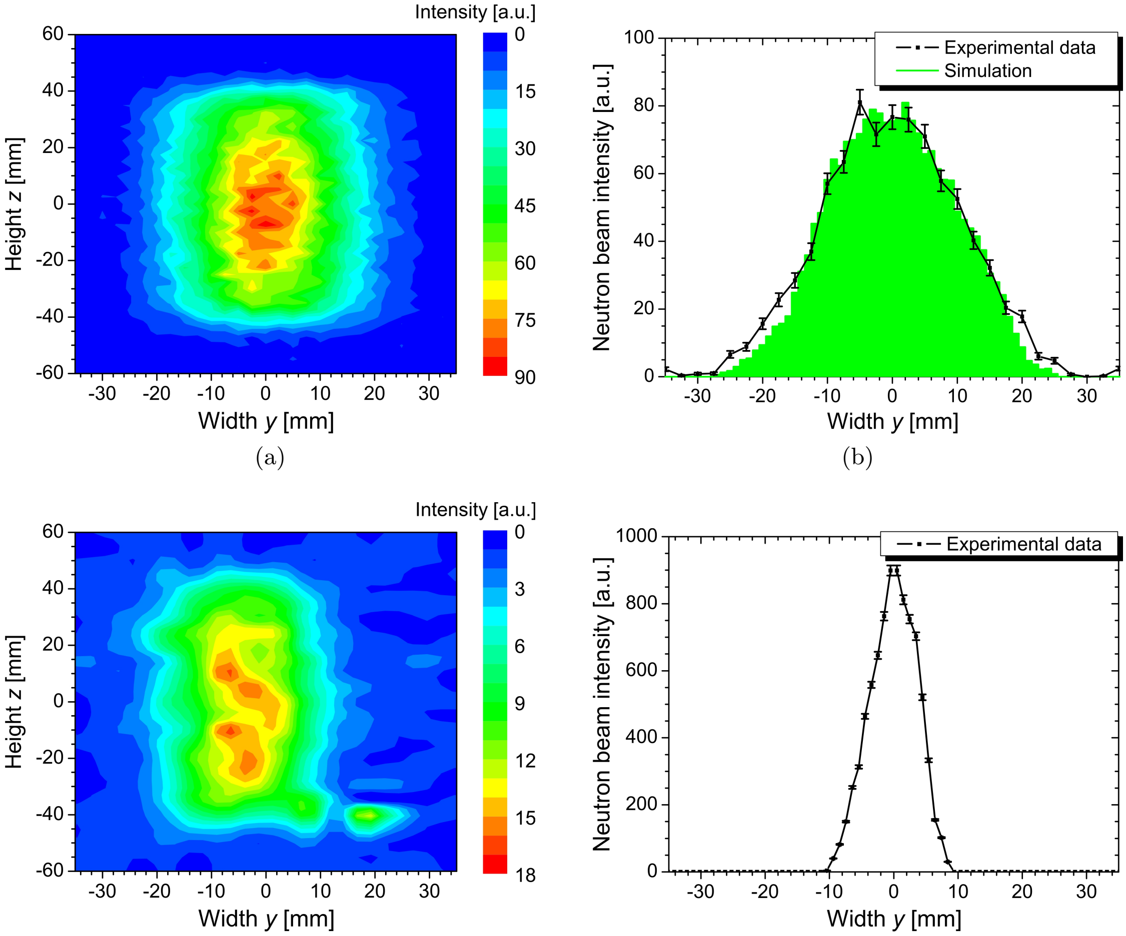

(a) (b)

(c) (d)

Figure 4.4: Neutron beam profiles measured by copper foil activation (top) for the 20 mm and (bottom) the 5 mm wide aperture. (a) and (c) show the two-dimensional, measured beam profiles; whereas (b) and (d) show horizontal cuts through the beam profiles (a) and (c), respectively, at $z = 0$. For comparison, Fig. (b) also shows the simulated beam profile. Even though a reasonable agreement between the measured and the simulated beam profiles was found, the neutron beam profile in the DV was smoothed by bilinear interpolation of the simulated beam profiles. Error bars show statistical errors only.

We note that the neutron beam profiles shown in Figs. 4.3a to 4.4d deviate from those presented in Refs. [34, 52, 53]. Owing to a coordinate system rotated by -90° in the x-y-plane the beam profiles were presented inversely. Therefore, the relationship $x = -y$ applies to the width of the neutron beam profile.

Further details on the simulations and measurements of the neutron beam profile can be found in Ref. [34].

4.1.4 Magnetic Field Profiles

As discussed earlier in Sec. 3.1.3, the magnetic field ratio $r_{\mathrm{B}} = B_{\mathrm{A}}/B_0$ has to be known with a relative accuracy of $\Delta r_{\mathrm{B}}/r_{\mathrm{B}} = 1 \times 10^{-4}$, in order to keep systematic uncertainties

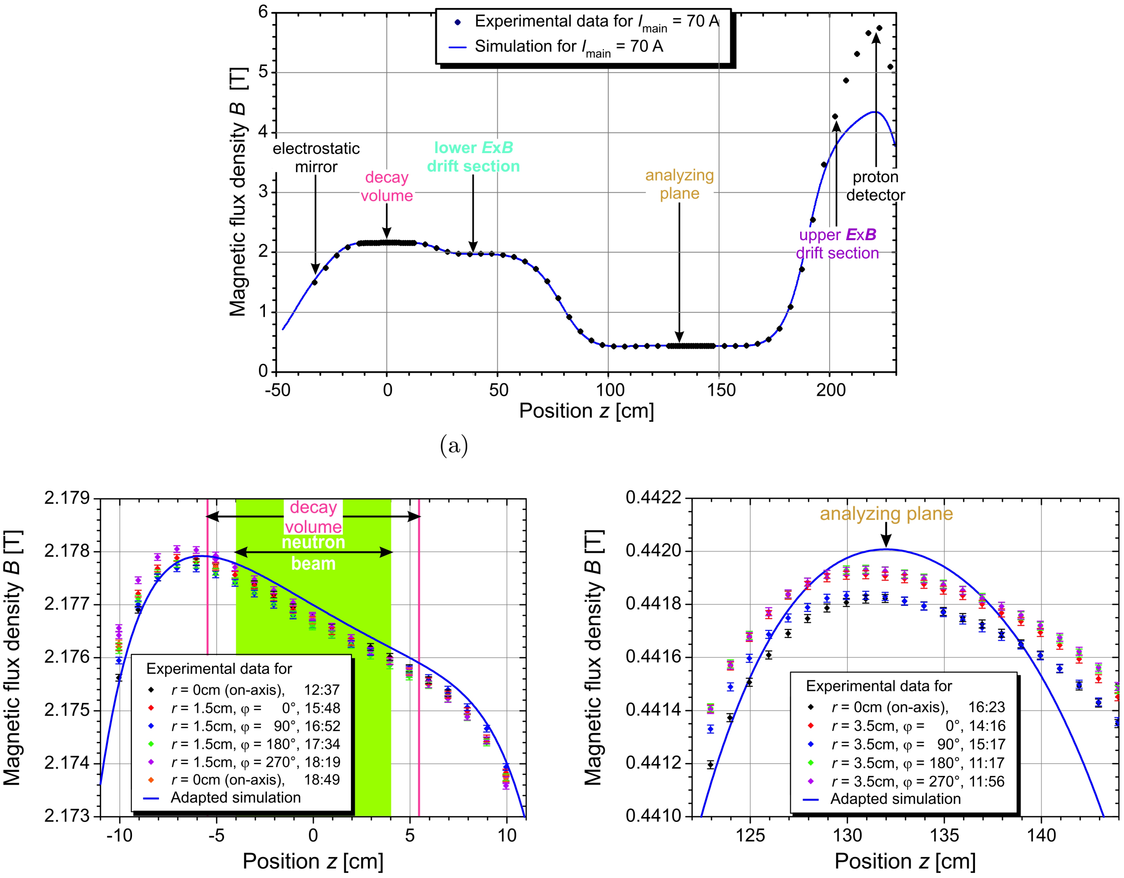

(a)

(b) (c)

Figure 4.5: The magnetic field profiles (a) along the z-axis, (b) in the decay volume (DV), and (c) in the analyzing plane (AP) of the aSPECT spectrometer. The black diamonds are measured on-axis, whereas the colored diamonds are measured off-axis at the edge of the flux tube. For comparison, the blue lines show the (adapted) simulated magnetic field profiles. See the text for details. The magnetic field profiles were measured (top) at $I_{\mathrm{main}} = 70\,\mathrm{A}$ and $I_3 = I_5 = I_{12} = \ldots = I_{15} = 0$ and (bottom) at $I_{\mathrm{main}} = 70\,\mathrm{A}$, $I_3 = 35\,\mathrm{A}$, $I_5 = 15\,\mathrm{A}$, $I_{12} = -I_{13} = 25.5\,\mathrm{A}$, and $I_{14} = I_{15} = 0$. The error bars represent the instability of the measurements, cf. Ref. [53].

in the neutrino-electron correlation coefficient a below $\Delta a/a = 0.1\,\%$. Therefore, we have to know the magnetic fields in the analyzing plane (AP) and in the DV with a relative accuracy of $\Delta B_{\mathrm{A}}/B_{\mathrm{A}} = 1\times10^{-4}$ and $\Delta B_0/B_0 = 1\times10^{-4}$, respectively (see also Sec. 3.4.1). To verify our calculations and to determine the magnetic field ratio r_{B}, the magnetic field was measured at the beam position, before and after[6] the beam time. The magnetic field was measured with a high accuracy, fully temperature compensated Hall probe[7], operated at room temperature. So in order to measure the magnetic field, the electrode system had to be removed and an inverted non-magnetic dewar had to be installed instead. The

---

[6] Shortly before the beam time, i.e., after the first magnetic field measurements at the beam position, the superconducting aSPECT magnet quenched, due to an interruption in the cooling water supply. To investigate the possible influence of the quench on the magnetic field ratio r_{B} or the magnetic field profile, the magnetic field was remeasured after the beam time. No difference was found between the measurements before and after the beam time [53].

[7] A Group3 Technologies miniature hall probe MPT-141 [219].

Table 4.1: The range of the magnetic field in the DV and the AP [53]. The inhomogeneity is out of our tolerance of 1×10^{-4}. See Sec. 3.4.1, Eq. (3.46), and the text for details.

Direction	$(B_{0,\mathrm{max}} - B_{0,\mathrm{min}})\,/B_0$	$(B_{\mathrm{A,max}} - B_{\mathrm{A,min}})\,/B_{\mathrm{A}}$
longitudinal	$7.4(4) \times 10^{-4}$	$0.3(5) \times 10^{-4}$
radial	$4(3) \times 10^{-4}$	$3(3) \times 10^{-4}$

results of the magnetic field measurements are shown in Fig. 4.5, in comparison with the (adapted) simulated magnetic field profiles.

Figure 4.5a shows the magnetic field profile along the z-axis for only $I_{\mathrm{main}} = 70\,\mathrm{A}$. The difference between the measured and the simulated magnetic field profile at the height of the HV electrodes e16A, e16B, and e17 is due to the fact that the calibration of the Hall probe is valid only up to 2.2 T. Figures 4.5b and 4.5c show a zoom to the DV and the AP, respectively. As mentioned earlier in Sec. 3.2.2, the correction coils c3, c5, c12, and c13 were necessary to correct for small deviations of the magnetic field from its design shape (see [168] for details). After adaption of the input parameters[8] for the magnetic field calculations to the measured magnetic field profiles a reasonable agreement was found. We note that the positions of the local maxima both in the DV and the AP are consistent with our calculations at the level of 0.5 cm. In particular, the positions of the local maxima of the magnetic field (simulated at $z = 132\,\mathrm{cm}$ and measured at $z \approx 131.5\,\mathrm{cm}$ [53]) and the electrostatic potential (simulated at $z = 132\,\mathrm{cm}$) in the AP differ only by about 0.5 cm, what automatically is compensated by the shrinkage of the electrode system by cooling down. Consequently, the adapted parameters, i.e., the fitted coil currents, served as input data for further MC simulations of, e.g., the edge effect.

The experimental data points off-axis were measured at the edge of the flux tube that connects the DV and the central detector pad[9]. For $I_{\mathrm{main}} = 70\,\mathrm{A}$ ($I_{\mathrm{main}} = 30\,\mathrm{A}$), the diagonal of this flux tube is $d \approx 2.6\,\mathrm{cm}$ ($d \approx 3.6\,\mathrm{cm}$) in the DV and $d \approx 5.8\,\mathrm{cm}$ ($d \approx 7.9\,\mathrm{cm}$) in the AP, taking account of the round edges of the detector pads (see Fig. 3.18). The measured magnetic field shows axially symmetry[10]. The range of the magnetic field values in the DV and in the AP

$$\frac{B_{0,\mathrm{max}} - B_{0,\mathrm{min}}}{B_0} \quad \text{and} \quad \frac{B_{\mathrm{A,max}} - B_{\mathrm{A,min}}}{B_{\mathrm{A}}} \tag{4.4}$$

is listed in Table 4.1 (see also [53]). From these magnetic field values, we obtain an average magnetic field ratio of[11] (cf. also Sec. 3.4.1 and Eq. (3.46))

$$r_{\mathrm{B}} = 0.20299(6), \tag{4.5}$$

with a relative error of 3×10^{-4} dominated by the accuracy of the Hall probe. In particular, the implemented calibration of the Hall probe is out of date. This yields a systematic error

---

[8] At the time of the analysis of several different systematic effects, the final analysis of the magnetic field measurements had not been completed. Hence, only the currents and not also the positions of the superconducting coils were fitted to the measured magnetic field profiles.

[9] For $I_{\mathrm{main}} = 70\,\mathrm{A}$, this flux tube also covers half of both the left and right detector pads.

[10] We suspect that the slightly different shape of the magnetic field in the AP for $\varphi = 90°$ represents the instability of the Hall probe [53].

[11] The error includes a scale factor of about 2/3, as generally we have to average over the on-axis and two off-axis measurements.

in the angular correlation coefficient a of

$$\boxed{\Delta a/a = \pm 0.26(10)\,\%} \tag{4.6}$$

Further details on the measurements of the magnetic field profile, the determination, stability, and reproducibility of the magnetic field ratio r_B, and the development of and first tests with an online nuclear magnetic resonance system can be found in Ref. [53].

4.2 Data Acquisition

The aSPECT data acquisition system (DAQ) was introduced in Sec. 3.3. In the following, we briefly discuss further details on the DAQ during our latest beam time at the ILL.

4.2.1 Neutron Beam Monitor

For a high-precision measurement of the neutrino-electron angular correlation coefficient a, for each measurement file the measured count rates have to be normalized to the number of (unpolarized, cold) neutrons that pass through the DV during the measurement time t (for details see Sec. 4.2.4). In the course of a beam time, this number may fluctuate due to changing conditions of the instrument set-up or the cold source (see Sec. 4.1), or a changing reactor power. The ^{6}Li neutron counter (introduced in Sec. 4.1.2) was therefore intended to continuously monitor the stability of the neutron beam intensity. The neutron counter showed fluctuations at a high level that was neither correlated to fluctuations in the reactor power nor in the measured proton count rates. It therefore makes little sense to normalize the measured proton count rates to the measured neutron count rates.

Details on the neutron counter performance can be found in Ref. [52].

4.2.2 Monitoring of the Barrier Potential

The voltage applied to the AP electrode e14 is provided by a custom-designed, high accuracy power supply[12] and monitored by a calibrated, precise multimeter[13]. The accuracy of the voltage settings is limited by the calibration of the multimeter to 4 mV. However, the stability and the reproducibility of the barrier voltage were both found at the level of 1 mV, i.e., much better than the calibration of the multimeter. This considerably simplifies the extraction of the neutrino-electron correlation coefficient a from the measured proton spectra (discussed in Sec. 5.2), as in the fit of the integral proton spectrum, for each barrier voltage, the average count rate can be used (see Secs. 5.2.2 and 5.2.3 for details). In addition, for each barrier voltage, the voltage selected at the power supply was used. But the true value of the voltage U_A differs from the selected one by up to 11 mV, as can be seen from Table 4.2. This introduces a shift in a of $\Delta a/a = -0.08(11)\,\%$ before and $\Delta a/a = -0.11(11)\,\%$ after correction for the multimeter's calibration. After additional correction for the penetration of electric field (see page 58 under "The Analyzing Plane"), this method introduces a shift in the angular correlation coefficient a of

$$\boxed{\Delta a/a = -0.09(11)\,\%} \tag{4.7}$$

Table 4.2: Typical voltage settings of the analyzing plane (AP) electrode e14. The four columns contain, from left to right, the voltage U_A selected at the power supply (see Fn. 12), its average value (avg) monitored by the precise multimeter (see Fn. 13), its average value after correction for the multimeter's calibration, and the corresponding electrostatic potential in the center of the AP.

U_A selected [V]	avg U_A monitored [V]	avg U_A corrected [V]	Potential in center of AP [V]
50	49.995	49.995	49.995
250	249.997	249.998	249.997
400	400.008	400.010	400.009
500	500.008	500.011	500.009
600	600.008	600.011	600.009

Details on the ramping and the stability of the barrier voltage can be found in Ref. [52].

4.2.3 Energy Calibration of the Proton Detector

As mentioned earlier in Sec. 3.3, for each measurement file the decoding program creates a pulse height histogram (in ADC channels), cf., e.g., Fig. 3.19b. Here, the pulse height is proportional to the particle energy deposited in the active layer of the SDD. To convert the pulse height into particle energy, our SDD was calibrated with ^{133}Ba before installation in the *a*SPECT spectrometer.

^{133}Ba disintegrates by electron capture to ^{133}Cs. The decay scheme is rather complicate, with several gamma transition, X-ray emission, and Auger escape lines [221, 222]. Figure 4.6 shows a calibration spectrum, recorded at room temperature, together with the fit to the K_α Auger escape, the K_α, and the K_β line. From the mean values of the Gaussian distributions, the following linear relationship between pulse height and particle energy at room temperature was derived:

$$\mathrm{ph} = \big(65.8\,(3)\ \mathrm{keV}^{-1} \cdot E_\mathrm{det} + (-4.4 \pm 8)\big)\ \mathrm{ADC\ channels}, \tag{4.8}$$

where ph is the detected pulse height and E_det is the energy detected by the SDD.

We note that the conversion factor of 65.8(3) keV^{-1} in Eq. (4.8) differs slightly from the result of our proton simulations of 63 keV^{-1} [52]. We are convinced that this difference is due to the different temperature of both measurements, as the proton spectra were recorded with the cooled SDD (see also [51]).

4.2.4 Measurement Sequence

As described earlier in Sec. 3.1.3, the neutrino-electron correlation coefficient a is derived from the proton spectrum shape, which, in turn, is measured by counting all decay protons that overcome the electrostatic barrier, U_A. During data taking, measurements with seven

---

[12] A FUG Elektronik high voltage power supply HCN 0,8M-800.

[13] Currently an Agilent Technologies 3458A digital multimeter.

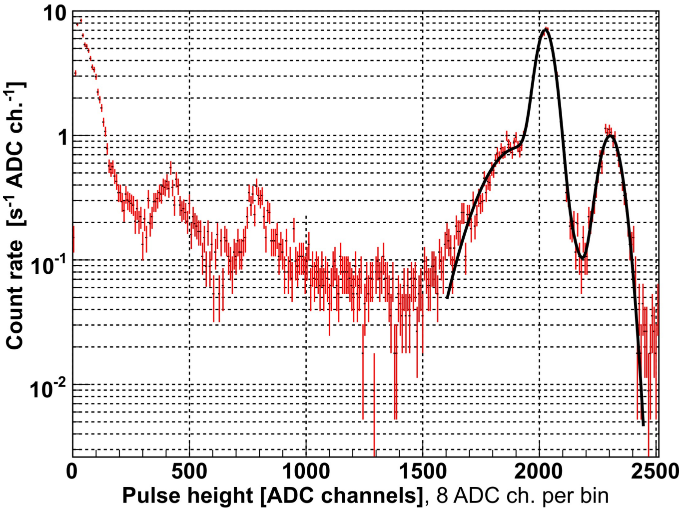

Figure 4.6: A calibration spectrum of our proton detector with ^{133}Ba, recorded at room temperature. The black line is the fit to the K_α Auger escape, the K_α, and the K_β line. At room temperature, the resolution of the detector is not sufficient to separate the single K_α and K_β lines. Thus, the K_α Auger escape, the K_α, and the K_β line were fitted with three superimposed Gaussian distributions with mean values $E_{\mathrm{Auger}} = 29.11(10)\,\mathrm{keV}$ [52] (see also [220]), $E_{\mathrm{K}_\alpha} = 30.85(10)\,\mathrm{keV}$, and $E_{\mathrm{K}_\beta} = 35.1(2)\,\mathrm{keV}$ [221]. Error bars show statistical errors only. Figure taken from Ref. [52].

different barrier voltages U_{A} were taken. In fact, measurements with only three different barrier voltages are required to

- quantify the background and
- determine the two fit parameters of the proton count rate Eq. (3.32), i.e., the full proton decay rate N_0 and the angular correlation coefficient a.

Measurements with $U_{\mathrm{A}} = 50\,\mathrm{V}$ were used to determine the full proton decay rate N_0 (see Secs. 3.1.3 and also 3.4.3), whereas measurements with $U_{\mathrm{A}} = 780\,\mathrm{V}$ served to quantify the background (see Secs. 3.1 and also 3.4.4). A further measurement with $U_{\mathrm{A}} \approx 400\,\mathrm{V}$ would provide the best statistical sensitivity to the angular correlation coefficient a [46]. However, to obtain a more precise knowledge of the proton spectrum shape and detailed information on the background, measurements with $U_{\mathrm{A}} = 0$, 50, 250, 400, 500, 600, and 780 V were carried out. In particular, measurements with $U_{\mathrm{A}} = 0\,\mathrm{V}$ were used to remove trapped particles. Typically, data taking cycles started with a measurement at $U_{\mathrm{A}} = 0\,\mathrm{V}$, followed by a measurement with $U_{\mathrm{A}} = 50\,\mathrm{V}$, then a measurement with an intermediate barrier voltage $U_{\mathrm{A}} = 250$, 400, 500, or 600 V, and finally a background measurement with $U_{\mathrm{A}} = 780\,\mathrm{V}$. After the background measurement, this cycle was repeated with a different intermediate barrier voltage. Every fifth cycle, the order of the measurements with $U_{\mathrm{A}} = 50\,\mathrm{V}$ and an intermediate barrier voltage were interchanged. For automated background measurements, each measurement, in turn, was subdivided into five neutron shutter statuses, i.e., (1) the neutron shutter was closed for 10 s, then (2) opening during 1.1 s,[14] (3) open for t s of measurement, then (4) closing during 0.6 s (see also Fn. 14), and finally (5) closed for another 10 s. Here, the measurement time t was different for every

---

[14] Please note that in Ref. [34] the times for opening and closing the neutron shutter are misstated.

barrier voltage, in order to optimize the measurement sequence for statistical sensitivity (see also [46]). Measurements with opened neutron shutter took $t = 10\,\mathrm{s}$ at $U_\mathrm{A} = 0\,\mathrm{V}$, $t = 40\,\mathrm{s}$ at $U_\mathrm{A} = 50\,\mathrm{V}$ and $780\,\mathrm{V}$, and $t = 120\,\mathrm{s}$ at $U_\mathrm{A} = 250$, 400, 500, and $600\,\mathrm{V}$. In this way, measurements with $U_\mathrm{A} = 50\,\mathrm{V}$ lasted 4/3 times as long as measurements with $U_\mathrm{A} = 250$, 400, 500, or $600\,\mathrm{V}$.

4.2.5 Investigation of Systematic Effects

Systematic effects, discussed thoroughly in Refs. [46, 47] and Sec. 3.4, were investigated experimentally. Here, we only summarize the essential measurements:

Additional neutron shutter: For automated background measurements, an additional neutron shutter was installed inside the casemate (see Sec. 4.1.2 for details).

Different settings of the lower dipole electrode: The lower dipole electrode e8 is used to sweep out all decay protons that cannot pass the potential barrier and would otherwise be trapped between the electrostatic mirror and the AP. To investigate particle trapping between the electrostatic mirror and the AP (see also Sec. 3.4.3 under “Elastic Scattering”), the potential barrier was set to $U_\mathrm{A} = 780\,\mathrm{V}$, so that no protons should be able to overcome the potential barrier, and the drift potential was reduced in several steps from $U_\mathrm{8R}|U_\mathrm{8L} = -50\,\mathrm{V}|-1000\,\mathrm{V}$ to $0\,\mathrm{V}|-2.5\,\mathrm{V}$ (discussed in Sec. 5.3.2).

Different settings of the upper dipole electrode: As discussed earlier on page 59 under “The Dipole Electrodes”, the upper dipole electrode e16 is used to align the neutron beam on the proton detector. Assuming a neutron beam profile symmetrical around its maximum (cf. Sec. 4.1.3), the edge effect is minimal, when the center of the neutron beam is aligned on the center of the detector. To determine the position of the high voltage electrode e17, and hence of the proton detector, relative to the rest of the electrode system and the magnetic field, and to study the edge effect, measurements at several different settings of the upper dipole electrode e16 were carried out. For details see Sec. 5.5.6.

Different ratio of the magnetic fields: The Helmholtz coils c14 and c15 were used to investigate the adiabatic transmission function Eq. (3.30). For $I_{14} = I_{15} = 50\,\mathrm{A}$, the magnetic field B_A in the AP and hence the magnetic field ratio $r_\mathrm{B} = B_\mathrm{A}/B_0$ change by about $+1\,\%$. This allows a quick and statistically significant test of the transmission function (discussed in Sec. 5.5.4).

Different height of the main magnetic field: During our beam time two different magnetic field values $B_0 = 0.933\,\mathrm{T}$ ($I_\mathrm{main} = 30\,\mathrm{A}$) and $B_0 = 2.177\,\mathrm{T}$ ($I_\mathrm{main} = 70\,\mathrm{A}$) were used (see Sec. 5.5.5), in order to study the influence of the non-adiabatic proton motion on the neutrino-electron correlation coefficient a (see also Secs. 3.4.2 and 5.4.4). We mention that with decreasing coil current I_main also the radii of gyration Eq. (3.3) increase and hence the edge effect changes (for details see Sec. 5.5.6).

Electrostatic mirror switched off: Due to the magnetic mirror effect (discussed on page 46 under “Magnetic Mirror Effect”) about $1\,\%$ of the decay protons, emitted in the negative z-direction, are reflected by the local magnetic field maximum below the neutron beam (see also Fig. 4.5b). To investigate the alignment between magnetic field and neutron beam, the proton count rates with and without electrostatic mirror were compared (see Sec. 5.5.2 for details).

Electric field gradient in the DV: As discussed in greater detail later in Sec. 6.4.3, work function inhomogeneities in the DV will lead to unexpected proton reflections from the DV. Approaches for this effect are presented in Sec. 6.4.4. Due to a lack of time, only different "Inverse electric field gradient[s]" were investigated during our beam time. For this a potential of a few volts was applied to the bottom and top cylinders e3 and e6 of the DV electrode, with opposite sign (for details see Sec. 5.3.3).

Second analyzing plane between DV and AP: To study possible background contributions of electrons, the lower dipole electrode e8 was used as a second analyzing plane (see also Sec. 3.4.4 under "Uncorrelated background events"). For this purpose, a positive potential of up to +1000 V was applied to sides R and L of the dipole electrode (see Sec. 5.3.1).

Different neutron beam profiles: As mentioned earlier in Sec. 4.1.3, measurements with three different widths of the neutron beam were carried out, in order to investigate the edge effect (see Secs. 3.4.6 and 5.5.6 for details).

Different trigger settings: To study the efficiency of our detection system, the windows w1 and w2, the delay, and the threshold (introduced on page 69 under "Digital Electronics and the Trigger Algorithm") were varied over a wide range. It was found that the measured count rate is independent of the trigger settings, provided that the window w1 is less than or equal 2^4 time bins ($0.8\,\mu$s). For details the reader is referred to Ref. [52].

Different post-acceleration voltages: During our beam time post-acceleration voltages from -10 to -15 kV were used, in order to investigate the detection efficiency of our proton detector. The influence of backscattering of decay protons on the angular correlation coefficient a was already discussed in Sec. 3.4.7 (see also [52]).

Chapter 5

Data Analysis

In the previous chapter, we discussed the measurements during our latest beam time at the Institut Laue-Langevin (ILL) in Grenoble, France. In this chapter, in turn, we present the detailed analysis of the measured data.

The raw data analysis was mostly carried out by M. Simson [52] and M. Borg [34]. To avoid a biased analysis, a blind data analysis was performed. Therefore the values of a extracted from the measured count rates were transformed by means of a linear function:

$$a_{\text{cheat}} = m \cdot a + b, \tag{5.1}$$

where the parameters m and b were selected so that the influence on the error bar of a is significantly small, i.e., $b/m \ll 1$. Both parameters were only known to me and two other persons not directly involved in the analysis. This made it impossible to push the extracted value of a towards or away from previously measured values, neither deliberately nor unconsciously. After the analysis was completed the figures were revealed to be[1]:

$$\begin{aligned} m &= 1.2477 \quad \text{and} \\ b &= -0.0008. \end{aligned} \tag{5.2}$$

Then the values of a were corrected according to Eq. (5.1).

The main emphasis of this thesis lies on the study of systematic effects. Exhaustive Monte Carlo (MC) simulations were performed to compute several systematic corrections. For details on the raw data analysis, the reader is referred to the theses of M. Simson [52] and M. Borg [34].

We note that the pictures and examples in this chapter stem from measurements at an acceleration potential of -15 kV, unless otherwise stated.

5.1 Data Fitting

As described earlier in Sec. 3.3.2, for every trigger an event as shown in Fig. 5.1 is stored. To extract the proton spectrum for one measurement run the pulse height of each event has to be determined. The simplest way to calculate the pulse height of an event is to determine its maximum and to subtract a fixed baseline from its maximum. The result of this method is denoted as h_{nf}. However, this method is insensitive to possible fluctuations

---

[1] Please note that in Ref. [52] the parameter b is misstated with positive sign.

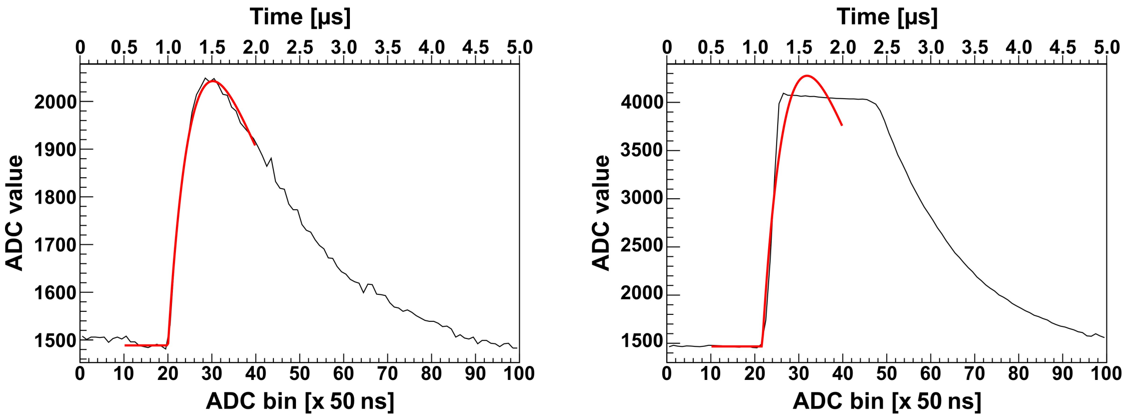

(a) (b)

Figure 5.1: Typical neutron decay events. (a) A proton event with its resulting fit (red line): $x_0 = 20.0(1)$, $y_0 = 1489(6)$, and $A = 29040(455)$. The corresponding pulse height is $h_{\text{fit}} = 554.0$ compared to $h_{\text{nf}} = 549.8$ from the "maximum−baseline" method. (b) An high energy electron or gamma event. The pulse is cut off by the maximum amplification of the electronics. In our analysis, such events are not fitted as the fitting routine gives nonsensical results (red line) due to the different pulse shape. See the text for details.

of the baseline. To avoid this problem, the baseline can be calculated separately for each event from the first 15 ADC bins. Nevertheless, the maximum of the pulse could be incorrectly determined due to, e.g., spikes from the electronic noise. Therefore, we concentrated on fitting the events.

5.1.1 The Fit Function

The pulse shape of a normal event can be described as a product of two exponential functions with different time constants [197]:

$$y_{\text{fit}}(x) = \begin{cases} y_0 & , \quad x \leq x_0 \\ y_0 + A\left(1 - e^{-\frac{x-x_0}{t_1}}\right)^p e^{-\frac{x-x_0}{t_2}} & , \quad x > x_0 \end{cases} . \tag{5.3}$$

Here, y_0 is the baseline, x_0 is the start point, t_1 and t_2 are the rise and decay time of the pulse, respectively, and A and p describe the height and the shape of the pulse, respectively. Table 5.1 presents the exact limits of the fit parameters[2]. The quantities t_1, t_2, and p are defined by the detector electronics and are therefore frozen in the fitting

---

[2] Please note that the fixed values of the parameters t_1 and p deviate from those given in Refs. [34, 52]. Owing to a misplaced bracket in the fitting routine the events were fitted to a function slightly different from Eq. (5.3):

$$y(x) = \begin{cases} y_0 & , \quad x \leq x_0 \\ y_0 + A\left(1 - \left(e^{-\frac{x-x_0}{t'_1}}\right)^{p'}\right)^1 e^{-\frac{x-x_0}{t_2}} & , \quad x > x_0 \end{cases} . \tag{5.4}$$

Therefore, the relationship $t_1 = t'_1/p'$ applies to the fit parameters.

Table 5.1: Limits of the used fit parameters. The time constants t_1 and t_2 and the parameter p are defined by the electronics and thus frozen in the fitting routine.

Parameter	Unit	Lower limit	Upper limit
y_0	ADC channels	800	2000
x_0	ADC bins ($\times 50\,\mathrm{ns}$)	13	23.5
t_1	ADC bins ($\times 50\,\mathrm{ns}$)	196.675	(frozen)
t_2	ADC bins ($\times 50\,\mathrm{ns}$)	10.47	(frozen)
p	÷	1	(frozen)
A	ADC channels	1	$2 \cdot 10^5$

Table 5.2: Overview of the different fit states. A reduced chi-squared $\chi^2/(h_{\mathrm{fit}} \cdot \mathrm{ndof}) < 0.00741$ indicates a good fit whereas $\chi^2/(h_{\mathrm{fit}} \cdot \mathrm{ndof}) \geq 0.00741$ indicates a poor fit to the model. Events with a bad χ^2 are sub-classified according to their pulse height, as electronic noise events have a $h_{\mathrm{fit}} < 80$. High energy events are not fitted as they are cut off by the maximum amplification of the electronics. Events where the fit did not converge or with a bad χ^2 are refitted with adapted fitting routines. See the text for details.

Status	Description
0	Normal events with good χ^2
1	Events with bad χ^2 and $h_{\mathrm{fit}} \geq 80$
2	Events with bad χ^2 and $h_{\mathrm{fit}} < 80$
3	High energy events
4	Fit failed
5	Refitted status 1 events
6	Refitted status 2 events
7	Events with different pulse shape

routine. The start point x_0 depends on the settings of the trigger algorithm and slightly on the pulse height. Thus it is not fully fixed in the fitting routine.

To obtain the pulse height of an event, function Eq. (5.3) is fitted to the pulse. The fit is limited to ADC bins 10 to 40, to significantly reduce the computing power and, consequently, the fitting time. The maximum point of the fit depends on the fit parameters as follows:

$$x_{\mathrm{max}} = x_0 + t_1 \left(\ln\left(t_1 + pt_2\right) - \ln t_1\right) \approx x_0 + 10.2 \text{ ADC bins}. \tag{5.5}$$

By substituting x_{max} into Eq. (5.3) we get the fitted pulse height, termed as h_{fit}:

$$h_{\mathrm{fit}} = y_{\mathrm{fit}}(x_{\mathrm{max}}) - y_0 = A \left(\frac{pt_2}{t_1 + pt_2}\right)^p \left(\frac{t_1}{t_1 + pt_2}\right)^{t_1/t_2} \approx A \cdot 0.019 \text{ ADC ch.}^{-1}. \tag{5.6}$$

5.1.2 Fit States

According to the result of their fit the events are classified into different categories. In Table 5.2 we list the different fit states.

Since high energy electrons and gammas are cut off by the limited maximum amplification of the electronics, the exact pulse height of these events cannot be reproduced by the fit. Thus only events with ADC values below 3500 before ADC bin 30 are fitted.

Events where the fit did converge are classified according to the reduced chi-squared. Since electronic noise events have a $h_{\text{fit}} < 80$, events with a bad $\chi^2/\left(h_{\text{fit}} \cdot \text{ndof}\right) \geq 0.00741$ are additionally classified according to their pulse height, where ndof is the number of degrees of freedom. To achieve the best possible separation between good and bad events the limits were chosen manually[3]. Two examples for fit states 0 and 3 are shown in Fig. 5.1.

Events where the fit did not converge are refitted with the improved fitting routine of ROOT. If the fit still does not converge, the pulse is rebinned, to even out short spikes in the electronic noise, and fitted again. In this way, practically all events can be fitted.

5.1.3 Refitted Events

Unfortunately, not all events are sorted correctly by the standard fitting routine. Especially in two cases valid proton events are sorted incorrectly into fit status 1 or 2:

Pile-up: When a second proton is detected immediately after the triggering one (before ADC bin 40) the fit does not work as the rising edge of the second proton changes the trailing edge of the triggering one. Top Fig. 5.2a shows a pile-up event.

Proton after electron: When a proton is triggered shortly after an high energy electron its baseline is changed by the exponentially decaying edge of the electron, which in turn is longer than one event window. Top Fig. 5.2b shows such an event.

To identify and separate the incorrectly sorted events from the correctly sorted ones the derivative of the event shape is calculated. Two examples are shown in the bottom Fig. 5.2. A steep rise in the signal corresponds to a significant peak in its derivative. From the number and position of those peaks the two above mentioned cases can be distinguished:

- Pile-up events have two peaks in their derivative, the first one around ADC bin 23 and the second one between ADC bin 25 and 40. Such events are refitted with the standard fit function Eq. (5.3), but the fit is limited to ADC bin 5 to $1\,\sigma$ before the second Gaussian peak. This method works well down to time differences of the two proton events of about $0.25\,\mu$s [52]. A comparison of the standard fit with the adapted fit is shown in Fig. 5.2a.

- Protons shortly after high energy electrons have one single peak before ADC bin 13.5 in their derivative, as they are triggered later than normal events. Those events are refitted with an adapted fit function:

  $$y_{\text{PaE}}(x) = y_{\text{fit}}(x) + e^{p_1 x + x_1} - 1, \tag{5.7}$$

  where y_{fit} is the standard fit function Eq. (5.3). The quantities p_1 and x_1 describe the exponentially decaying edge of the electron. To improve the knowledge of the changing baseline the fit is limited to ADC bin 1 to 35. We mention that the pulse height of such events is also given by Eq. (5.6). A comparison of the standard fit with the adapted fit is shown in Fig. 5.2b.

---

[3] Usually, a reduced chi-squared near 1.0 means that within the error bars one has a good fit to the model. In our case, this rule of thumb is not valid as we assigned an error bar of 20 to each ADC value.

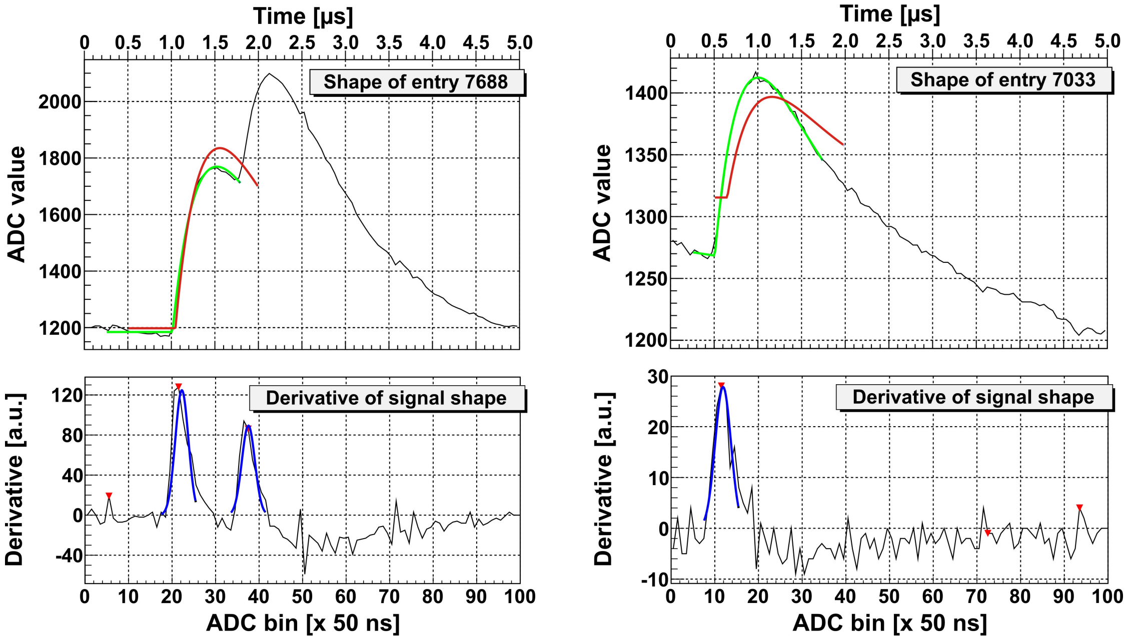

(a) $h_{\text{fit}} = 584.8$ compared to $h_{\text{nf}} = 906.2$

(b) $h_{\text{fit}} = 151.5$ compared to $h_{\text{nf}} = 115.9$

Figure 5.2: Valid proton events which were sorted incorrectly into fit status 1. Figure (a) shows a pile-up event, whereas Fig. (b) shows a proton shortly after an high energy electron. Top: The results of the standard fit and the adapted fit are shown in red and green, respectively. According to the result of the adapted fit the events are assigned fit status 5. Bottom: To separate these events from the correctly sorted ones the derivative of the event shape is calculated. A steep rise in the signal corresponds to a significant peak in its derivative. From the number and position of those peaks the two cases (a) and (b) can be distinguished. The positions of possible peaks are marked with red triangles. The Gaussian fits to the relevant peak candidates are shown in blue.

Some valid proton events, which were incorrectly sorted into fit status 1, do not fall into the above mentioned two categories. These events have a slightly different pulse shape: The rising edge is not as steep as for the normal events and thus the maximum is shifted to higher ADC bins. Such events are refitted with the standard fit function Eq. (5.3), but with different fit limits. To focus on the falling edge the fit is limited to ADC bins 30 to 90. Additionally, the upper limit of the start point is extended to ADC bin 25.

The results of the fit are written to a ROOT tree for further analysis. More examples and details on the structure of the fit tree can be found in Ref. [52].

Figure 5.3 shows a comparison of fitted with non-fitted pulse height spectra. Obviously the data fitting improves the separation between the proton signal and the electronic noise.

5.2 Extraction of a from the Proton Spectra

From the fitted pulse height spectra (see Fig. 5.3) we now can extract the value of the neutrino-electron correlation coefficient a. Before that, the count rate of each measurement file has to be corrected for the dead time of the electronics. Then the background,

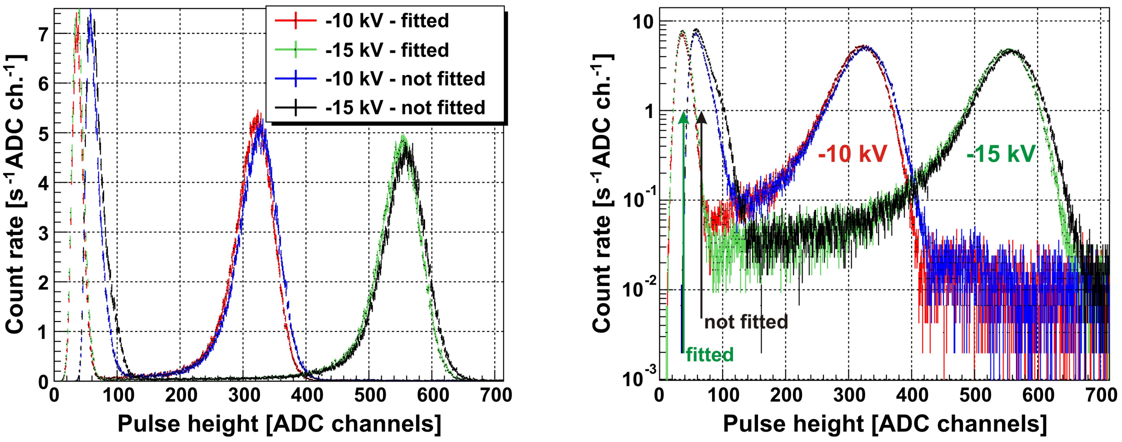

(a) (b)

Figure 5.3: Typical pulse height spectra for one detector pad from 15_05_08/rampHV for -10 and -15 kV acceleration potential in (a) linear and (b) logarithmic representation. Fitted pulse height spectra are shown in red and green, non-fitted ones in blue and black. With increasing acceleration potential the proton peak (right peak) is shifted to higher ADC channels whereas the electronic noise (left peak) is almost not influenced. For both potentials, the noise peak is shifted to lower ADC channels for the fitted spectra whereas the proton peak remains almost the same. The fit evens out spikes from the electronic noise on the proton events. Thus the proton peak is slightly shifted to lower ADC channels for the fitted spectra. Error bars show statistical errors only.

measured at 780 V barrier voltage, has to be subtracted. For each barrier voltage, the proton count rate has to be determined from the background subtracted pulse height spectra by integration over the pulse height. To finally obtain the angular correlation coefficient a, function Eq. (3.32) has to be fitted to the integral proton spectrum. In addition, several different corrections have to be applied.

5.2.1 Dead Time Correction

As described earlier in Sec. 3.3.2, for every trigger an event with a length of normally $5\,\mu$s is stored (see Fig. 5.1). During this time no other event can be registered, apart from pile-up events. In the case of a pile-up event, the fitting routine ensures that only the first proton is counted, as can be seen from Fig. 5.2a. Due to the processing time of the electronics of $0.2\,\mu$s, the next registered event has a minimum time difference to the preceding one of $5.2\,\mu$s. This defines a so-called non-extendable [223] dead time, τ_{dead}, which causes a reduction of the proton count rate, $N_{\mathrm{p}}(U_{\mathrm{A}})$. The measured proton count rate, $N_{\mathrm{p,meas}}(U_{\mathrm{A}})$, then depends on the total count rate

$$N_{\mathrm{total}}(U_{\mathrm{A}}) = N_{\mathrm{p}}(U_{\mathrm{A}}) + N_{\mathrm{e}} + N_{\mathrm{noise}} \tag{5.8}$$

as follows:

$$N_{\mathrm{p,meas}}(U_{\mathrm{A}}) = N_{\mathrm{p}}(U_{\mathrm{A}})\left(1 - N_{\mathrm{total}}(U_{\mathrm{A}}) \cdot \tau_{\mathrm{dead}}\right), \tag{5.9}$$

where $N_{\mathrm{e}} = N_{\mathrm{e}}(U_{17})$ and N_{noise} are the electron and electronic noise count rates, respectively. The actual proton count rate may be estimated by [223]:

$$\boxed{N_{\mathrm{p,corr}}(U_{\mathrm{A}}) = \frac{N_{\mathrm{p,meas}}(U_{\mathrm{A}})}{1-N_{\mathrm{total,meas}}(U_{\mathrm{A}})\cdot\tau_{\mathrm{dead}}}} \tag{5.10}$$

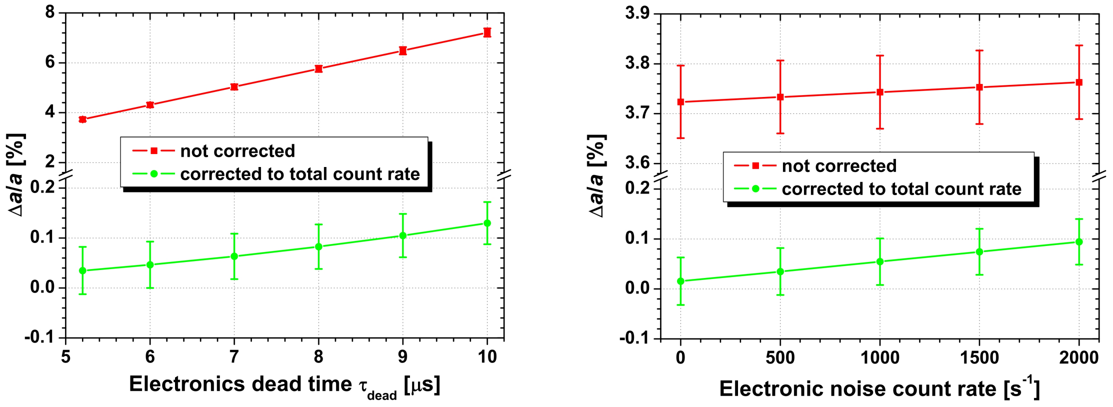

(a) (b)

Figure 5.4: Relative change of the angular correlation coefficient a for (a) different dead times of the electronics and (b) different electronic noise count rates, before (red) and after (green) correction for the dead time by Eq. (5.10). For better visibility, the y-axis is broken at $\Delta a/a = 0.22$. The dead time correction is the better, the shorter the electronics dead time and the lower the electronic noise count rate are. Input data for the simulation (with Nachtmann's formula Eq. (2.38)): $N_0 = 490\,\mathrm{s}^{-1}$, $U_\mathrm{A} = 50, 250, 400, 500, 600\,\mathrm{V}$, $U_{17} = -15\,\mathrm{kV}$, $N_\mathrm{noise} = 500\,\mathrm{s}^{-1}$ (a), $\tau_\mathrm{dead} = 5.2\,\mu\mathrm{s}$ (b), and $a = -0.103$ [10]. The error bars, in the order of 0.05 % after correction for the dead time, represent the error by fitting Eq. (3.32) to the simulated proton count rates only.

where

$$N_\mathrm{total,meas}(U_\mathrm{A}) = N_\mathrm{p,meas}(U_\mathrm{A}) + N_\mathrm{e,meas} + N_\mathrm{noise,meas} \tag{5.11}$$

is the total measured count rate. Here, $N_\mathrm{e,meas}$ and $N_\mathrm{noise,meas}$ are the measured electron and electronic noise count rates, respectively. The measured count rates $N_\mathrm{e,meas}$ and $N_\mathrm{noise,meas}$ depend on the total count rate $N_\mathrm{total}(U_\mathrm{A})$ in the same way as Eq. (5.9). Because of the quite high count rate on one detector pad, the dead time correction has a significant impact on the extracted value of the angular correlation coefficient a. Figure 5.4a shows the relative change of the angular correlation coefficient a for different dead times of the electronics, before and after correction for the dead time by Eq. (5.10). Assuming a full proton decay rate of $N_0 = 490\,\mathrm{s}^{-1}$, an electronic noise count rate of $N_\mathrm{noise} = 500\,\mathrm{s}^{-1}$, and an electronics dead time of $\tau_\mathrm{dead} = 5.2\,\mu\mathrm{s}$, the proton count rate loss at $U_{17} = -15\,\mathrm{kV}$ would be approximately 0.54 %[4] for $U_\mathrm{A} = 50\,\mathrm{V}$ down to 0.3 % for $U_\mathrm{A} = 600\,\mathrm{V}$. This would correspond to a relative shift of the angular correlation coefficient a of +3.7 % (see also Fn. 4) before and of

$$\Delta a/a = +0.035(50)\,\% \tag{5.12}$$

after correction for the dead time. We mention that during our latest beam time at the ILL the electronic noise count rate usually was around $(250 - 950)\,\mathrm{s}^{-1}$; during the hottest

---

[4] Please note that the figures deviate from those given in Refs. [34, 52, 53], in which neither the electron nor the electronic noise count rate were taken into account. In our example, the proton count rate loss would be $2.5\,\mathrm{s}^{-1}$ at $U_\mathrm{A} = 50\,\mathrm{V}$, two times higher than stated in Refs. [34, 52, 53].

days it reached in excess of $1450\,\mathrm{s}^{-1}$. Actually, one would not expect a shift of the angular correlation coefficient a after correction for the dead time. At first order, Eq. (5.10) is a good estimation for the actual proton count rate $N_{\mathrm{p}}(U_{\mathrm{A}})$, as follows from Eqs. (5.9) and (5.10):

$$
\begin{aligned}
\Delta N_{\mathrm{p}}(U_{\mathrm{A}}) &= N_{\mathrm{p}}(U_{\mathrm{A}}) - N_{\mathrm{p,corr}}(U_{\mathrm{A}}) \\
&= \frac{N_{\mathrm{p,meas}}(U_{\mathrm{A}})}{1 - N_{\mathrm{total}}(U_{\mathrm{A}}) \cdot \tau_{\mathrm{dead}}} - \frac{N_{\mathrm{p,meas}}(U_{\mathrm{A}})}{1 - N_{\mathrm{total,meas}}(U_{\mathrm{A}}) \cdot \tau_{\mathrm{dead}}} \\
&= \frac{N_{\mathrm{p}}(U_{\mathrm{A}})\,(1 - N_{\mathrm{total}}(U_{\mathrm{A}}) \cdot \tau_{\mathrm{dead}})\,[N_{\mathrm{total}}(U_{\mathrm{A}}) \cdot \tau_{\mathrm{dead}} - N_{\mathrm{total,meas}}(U_{\mathrm{A}}) \cdot \tau_{\mathrm{dead}}]}{(1 - N_{\mathrm{total}}(U_{\mathrm{A}}) \cdot \tau_{\mathrm{dead}})\,(1 - N_{\mathrm{total,meas}}(U_{\mathrm{A}}) \cdot \tau_{\mathrm{dead}})} \\
&= N_{\mathrm{p}}(U_{\mathrm{A}}) \frac{N_{\mathrm{total}}(U_{\mathrm{A}})\,(N_{\mathrm{total}}(U_{\mathrm{A}}) \cdot \tau_{\mathrm{dead}}) \cdot \tau_{\mathrm{dead}}}{(1 - N_{\mathrm{total,meas}}(U_{\mathrm{A}}) \cdot \tau_{\mathrm{dead}})} \\
&= N_{\mathrm{p}}(U_{\mathrm{A}}) N_{\mathrm{total}}^{2}(U_{\mathrm{A}}) \cdot \tau_{\mathrm{dead}}^{2} \\
&\quad \times \left[1 + N_{\mathrm{total}}(U_{\mathrm{A}})\,(1 - N_{\mathrm{total}}(U_{\mathrm{A}}) \cdot \tau_{\mathrm{dead}}) \cdot \tau_{\mathrm{dead}} + \mathcal{O}\left(\tau_{\mathrm{dead}}^{2}\right)\right] \\
&= N_{\mathrm{p}}(U_{\mathrm{A}}) N_{\mathrm{total}}^{2}(U_{\mathrm{A}}) \cdot \tau_{\mathrm{dead}}^{2} \left[1 + N_{\mathrm{total}}(U_{\mathrm{A}}) \cdot \tau_{\mathrm{dead}} + \mathcal{O}\left(\tau_{\mathrm{dead}}^{2}\right)\right] \\
&= N_{\mathrm{p}}(U_{\mathrm{A}}) \left[\left(N_{\mathrm{p}}^{2}(U_{\mathrm{A}}) + 2N_{\mathrm{p}}(U_{\mathrm{A}})N_{\mathrm{e}} + 2N_{\mathrm{p}}(U_{\mathrm{A}})N_{\mathrm{noise}}\right) \cdot \tau_{\mathrm{dead}}^{2} + \mathcal{O}\left(\tau_{\mathrm{dead}}^{2}\right)\right] \\
&\approx N_{\mathrm{p}}^{2}(U_{\mathrm{A}}) \cdot \mathcal{O}\left(\tau_{\mathrm{dead}}^{2}\right).
\end{aligned}
\tag{5.13}
$$

But according to Eq. (5.13), the relative error due to the dead time correction, $\Delta N_{\mathrm{p}}(U_{\mathrm{A}})/N_{\mathrm{p}}(U_{\mathrm{A}})$, is proportional to both τ_{dead}^{2} and $N_{\mathrm{p}}(U_{\mathrm{A}})\,[N_{\mathrm{p}}(U_{\mathrm{A}}) + 2N_{\mathrm{e}} + 2N_{\mathrm{noise}}]$. Consequently, the correction for the dead time is the better, the shorter the electronics dead time is, as shown in Fig. 5.4a. In addition, the dead time correction is the better, the lower the electronic noise count rate is, as can be seen from Fig. 5.4b. In our example, the correlation coefficient a would be shifted by $\Delta a/a = +0.015(50)\,\%$ even without electronic noise. However, the electronic noise count rate has a minor impact on the extracted value for the neutrino-electron correlation coefficient a than the electronics dead time. To minimize the remaining shift of the correlation coefficient a after correction for the dead time, one has to choose the event length as short as possible and to reduce the noise as much as possible.

As mentioned above, the secondary focus of our latest beam time at the ILL was on the determination of a new value for a with a total relative error well below $4\,\%$. Thus, the change of the angular correlation coefficient a by the dead time can be sufficiently corrected, i.e., to $\Delta a/a < 0.1\%$, as long as the dead time is precisely known. Figure 5.5 illustrates the influence of a wrongly corrected dead time on the extracted value of the angular correlation coefficient a. In our example, the neutrino-electron correlation coefficient a would be shifted by

$$\boxed{\Delta a/a = \left({}^{+0.18}_{-0.11} \pm 0.05\right)\,\%} \tag{5.14}$$

(see also Fn. 4) if the actual dead time $\tau_{\mathrm{dead}} = 5.2\,\mu\mathrm{s}$ would be unknown by $\pm 0.2\,\mu\mathrm{s}$.

In Eqs. (5.9) and (5.10) it is assumed that the events are occurring randomly, i.e., obey Poisson statistics. But free neutron decay is a three-body decay in which the decay products, proton, electron, and anti-neutrino, are emitted simultaneously. In our experiment, only protons and electrons can be detected. If the electrostatic mirror is switched off, decay protons are detected only if they were emitted towards the detector or if they

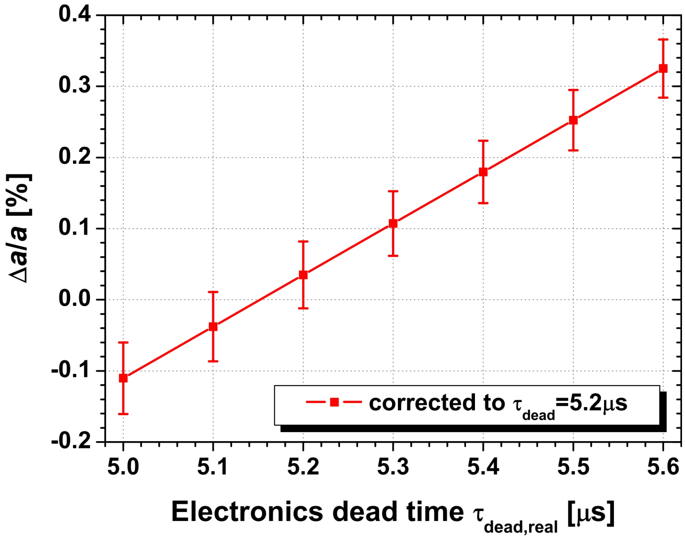

Figure 5.5: Relative change of the angular correlation coefficient a for a wrongly corrected dead time. If the actual dead time $\tau_{\text{dead}} = 5.2\,\mu\text{s}$ would be unknown by $\pm 0.2\,\mu\text{s}$, the neutrino-electron correlation coefficient a would be shifted by ${}^{+0.18\%}_{-0.11\%}$ (see also Fn. 4). Input data for the simulation (with Nachtmann's formula Eq. (2.38)): $N_0 = 490\,\text{s}^{-1}$, $U_{\text{A}} = 50, 250, 400, 500, 600\,\text{V}$, $U_{17} = -15\,\text{kV}$, $N_{\text{noise}} = 500\,\text{s}^{-1}$, and $a = -0.103$ [10]. The error bars, in the order of 0.05 %, represent the error by fitting Eq. (3.32) to the simulated proton count rates only.

were reflected by the magnetic mirror in the DV (see Fig. 3.16a), else all decay protons are detected. Decay electrons are detected only if they were emitted towards the proton detector and if they can overcome the electromagnetic mirror right in front of the detector. Here, we neglect effects regarding backscattering of electrons inside the spectrometer (discussed in Sec. 5.4.2). Due to different emission momenta and particle masses, the time-of-flight (TOF) of the decay electrons is about one thousands of the TOF of the decay protons. Therefore, the detection time difference between correlated coincidence events may be estimated by the TOF of the proton. The minimum TOF of decay protons is about $5.3\,\mu\text{s}$ for $U_{\text{A}} = 50\,\text{V}$ (see Dalitz plot[5] 5.6a and also Fn. 27 in Chap. 3) up to $8.2\,\mu\text{s}$ for $U_{\text{A}} = 600\,\text{V}$, where the proton was emitted towards the proton detector, opposite to its correlated electron as can be seen from Fig. 5.7. If we exclude backscattering of electrons from the bottom of the spectrometer (discussed in Sec. 5.4.2), these protons will not be detected in coincidence with the electron from the same decay. The minimum TOF of decay protons detected in coincidence with their correlated electron is about $7.2\,\mu\text{s}$ for $U_{\text{A}} = 50\,\text{V}$ (see Fig. 5.6b) up to $10.0\,\mu\text{s}$ for $U_{\text{A}} = 600\,\text{V}$, where the proton was emitted towards the electrostatic mirror, opposite to its correlated electron. Altogether, we can assume that the events obey Poisson statistics, provided the dead time of the electronics is smaller than the minimum TOF of the decay protons, i.e., $\tau_{\text{dead}} \leq 5.2\,\mu\text{s}$.

---

[5] In high-energy physics, a Dalitz plot originally is a scatterplot of the squared invariant mass of a subset of the particles emitted in a three-body decay, versus the squared invariant mass of another subset.

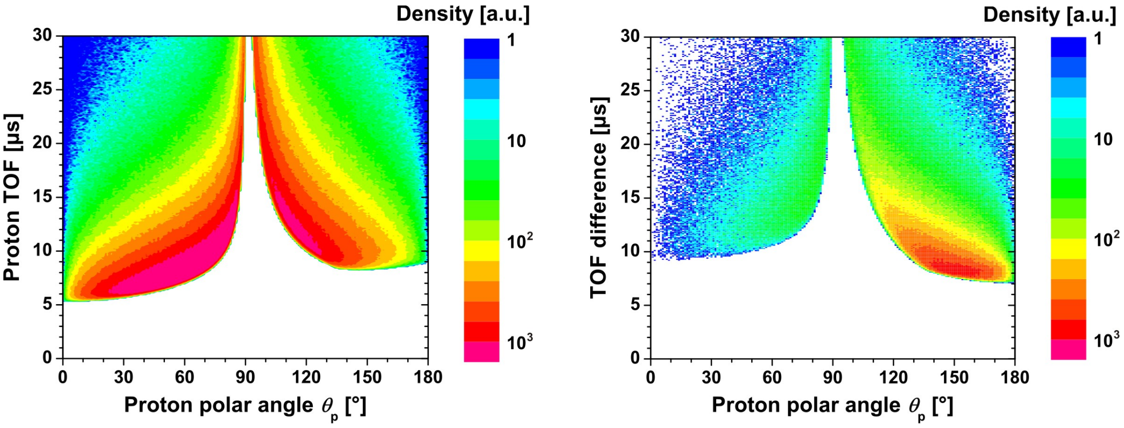

(a)

(b)

Figure 5.6: Dalitz plot distribution of proton time-of-flight (TOF) and polar emission angle, for (a) protons not detected in coincidence with their correlated electron and (b) correlated coincidence events. If we neglect effects regarding backscattering of electrons (discussed in Sec. 5.4.2), a maximum of 13.1 % of the decay electrons can be detected in coincidence with their correlated proton (see Sec. 5.4.2). Since the TOF of the electrons is about one thousands of the TOF of the protons, the detection time difference between correlated coincidence events may be estimated by the TOF of the proton. The minimum TOF of decay protons is about 5.2 μs for (a) and 7.1 μs for (b). Input data for the MC simulation (in INM approximation): $U_1 = U_{1\mathrm{b}} = 800\,\mathrm{V}$, $U_2 = 1000\,\mathrm{V}$, $U_8 = -525\,\mathrm{V}$, $U_\mathrm{A} = 0\,\mathrm{V}$, $U_{16} = -2\,\mathrm{kV}$, $U_{17} = -15\,\mathrm{kV}$, number of generated events = 10^7, and $a = -0.105$ (derived from $\lambda = -1.2701(25)$ [10]). Except for the settings of the lower dipole electrode, the input data correspond to the data set 19_05_08/night. Here, we neglect the spatial separation of protons and electrons achieved by both, the lower and upper, dipole electrodes.

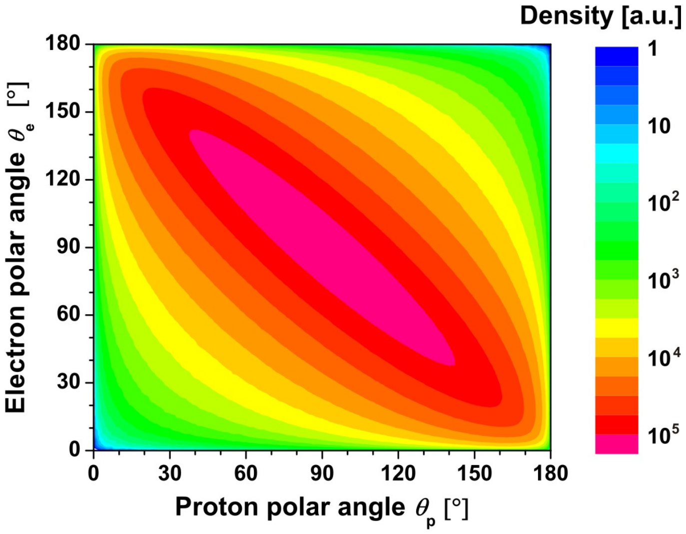

Figure 5.7: Dalitz plot distribution of electron and proton polar emission angles. If the proton is emitted towards the proton detector ($\theta_p = 0°$) or towards the electrostatic mirror ($\theta_p = 180°$) the electron tends to be emitted opposite. Input data for the MC simulation (in INM approximation): Number of generated events = 10^9 and $a = -0.105$ (derived from $\lambda = -1.2701(25)$ [10]).

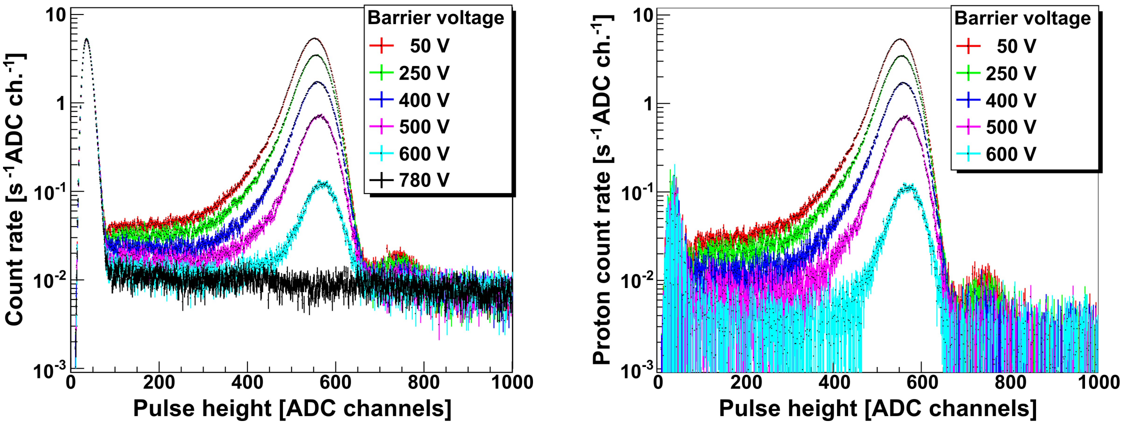

(a) (b)

Figure 5.8: Subtraction of the background from the pulse height spectra: (a) Typical pulse height spectra for one detector pad from 19_05_08/night for different barrier voltages, determined by adding all measurements with the same barrier voltage. With increasing barrier voltage the count rate in the proton peak (right peak) decreases whereas the electronic noise (left peak) is not influenced. (b) Pure proton pulse height spectra, obtained by subtracting the background measured at $U_{\mathrm{A}} = 780\,\mathrm{V}$ from the measurements at lower barrier voltages. The tiny peak centered around ADC channel 750 is an artifact of the detector (for details see the text and Refs. [34, 52]). Error bars show statistical errors only.

5.2.2 Background Correction

Figure 5.8a shows typical pulse height spectra for different barrier voltages. The left peak below ADC channel 100 is due to electronic noise, whereas the right peak centered around ADC channel 550 is due to protons. For systematic studies on the electronic noise [52], the trigger settings are normally chosen in such a way that some noise is recorded. The count rate in the proton peak decreases as the barrier voltage is ramped up and vanishes at $U_{\mathrm{A}} = 780\,\mathrm{V}$; the latter as the endpoint of the proton recoil spectrum is at about 751 eV. For $U_{\mathrm{A}} = 780\,\mathrm{V}$ it can be clearly seen, that the electrons and gammas constitute an almost constant distribution over the entire visible part of the pulse height spectra. With increasing barrier voltage less protons can pass the AP, but with higher kinetic energy. Therefore, the maximum of the proton peak rises slightly from ADC channel 552 for $U_{\mathrm{A}} = 50\,\mathrm{V}$ to ADC channel 567 for $U_{\mathrm{A}} = 600\,\mathrm{V}$. The tiny peak centered around ADC channel 750 was not expected and has been carefully investigated. It is an artifact of the detector, probably caused by a slightly higher amplification on a small spot of the detector [34, 52].

The background is measured at $U_{\mathrm{A}} = 780\,\mathrm{V}$. The pure proton count rate is obtained by subtracting the background from measurements at lower barrier voltages. There are two different approaches to subtract the background:

Closest: From each single measurement the count rate of the closest background measurement in time is subtracted.

Averages: For each barrier voltage, the average count rate is calculated by adding all measurements with the respective voltage. Then the average background count rate is subtracted from the count rates at lower voltages. The result is shown in Fig. 5.8b.

The first method has the advantage of correcting short-term fluctuations in the count rate. However, it is difficult not to introduce a systematic effect: If some background measurements are used more often than others, the errors become correlated and different weighting of the measurements will be necessary. Although the background is measured regularly every fourth file, some measurements had to be excluded because of malfunctions of the DAQ system. Moreover, no short-term fluctuations in the background count rate were found in a detailed analysis of the background (see Sec. 5.3 for details). For both these reasons, the second method, the subtraction of averages, was chosen for further analysis.

5.2.3 Integration of the Count Rate

For each barrier voltage, the proton count rate has to be determined from the background subtracted pulse height spectra, as shown in Fig. 5.8b. For this purpose, the count rates are integrated over the pulse height, namely within certain limits. Normally, the lower integration limit is set as close as possible to the electronic noise at ADC channel 80, whereas the upper integration limit is set significantly above the proton peak at ADC channel 1200. Obviously, the integration includes the tiny peak centered around ADC channel 750, as the events in that peak have normal pulse shapes and as the count rate in the tiny peak behaves exactly the same as in the main proton peak.

Figure 5.9 shows the corresponding integral proton spectrum, together with the prediction from the Standard Model with the recommended value for the neutrino-electron correlation coefficient $a = -0.103$ [10]. To obtain the angular correlation coefficient a, function Eq. (3.32) is fitted to the integral proton spectrum, where $w_{\mathrm{p,C},\alpha}(T)$ is given by Eq. (2.43)[6]. The fit parameters are the full proton decay rate N_0 and of course the angular correlation coefficient a. Finally, several different corrections have to be applied, as discussed in the following sections.

5.3 Background

As mentioned earlier on page 38 under “First Measurements with aSPECT at the FRM II” (see also page 56 under “Penning Traps and Penning Discharge”), in our first beam time at the Forschungsneutronenquelle Heinz Maier-Leibnitz (FRM II), situation- and time-dependent behavior of the background was the main problem [33, 49] (see also Fig. 2.15). To considerably improve the background conditions, the proton detector was replaced by a silicon drift detector (SDD) at significantly reduced acceleration potential (see Sec. 3.3.1 for details), parts of the electrode system were redesigned (discussed in Sec. 3.2.1), and the ultra high vacuum (UHV) conditions were improved (see Sec. 3.4.3).

5.3.1 Dependence on the Barrier Potential

In our first beam at the FRM II, the background count rate without neutron beam at $U_\mathrm{A} = 780\,\mathrm{V}$ was higher than that at $U_\mathrm{A} = 50\,\mathrm{V}$ by about 3 Hz [33, 49], as can be seen from Fig. 5.10. If the actual background count rate would be unknown by this amount,

---

[6] Please note that the fit function was incorrectly described in Refs. [34, 49, 52, 197].

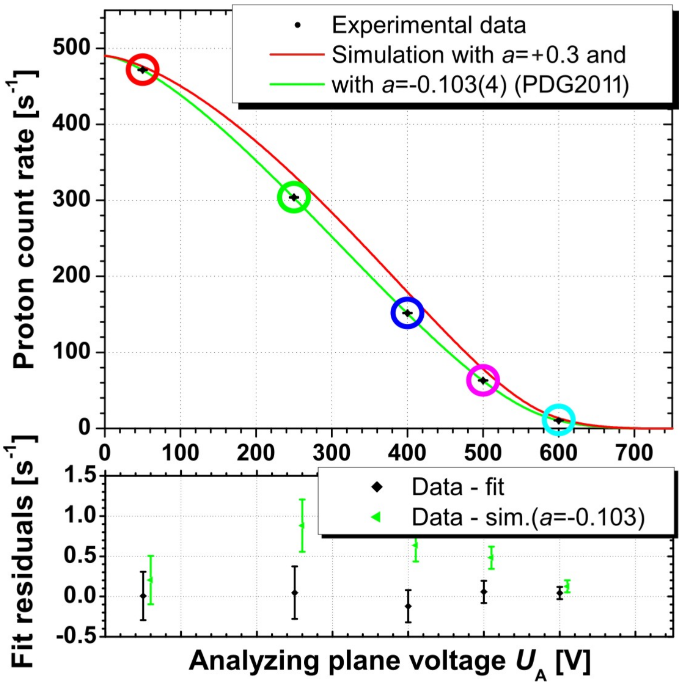

Figure 5.9: Top: Integral proton spectrum after only subtraction of the background, corresponding to Fig. 5.8b. The green line is the prediction from the SM with the recommended value for $a = -0.103$ [10], the red line shows how a deviation from that would look like. Bottom: The black diamonds are the fit residuals. For better distinction, the green triangles are shifted by $+10\,\mathrm{V}$. They represent the difference between the experimental data and a simulation with $a = -0.103$. Further input data for the simulation: $N_0 = 490\,\mathrm{s}^{-1}$ and $B_{\mathrm{A}}/B_0 = 0.203$. Error bars show statistical errors only, and do not include the uncertainty of the recommended value for a.

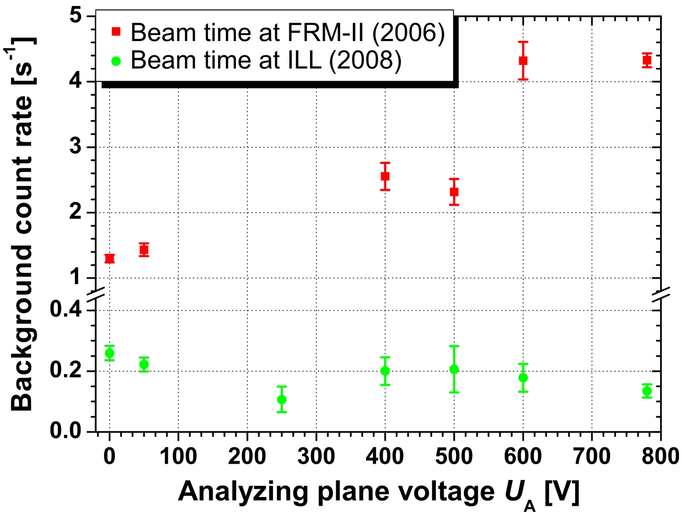

Figure 5.10: Background count rate without neutron beam versus barrier voltage U_{A}. In this case, the background count rate does not include the contribution of decay electrons. The red squares stem from the worst data set 2604N of our first beam time at the FRM II [33, 49], whereas the green circles stem from 20_05_08/lunch (shutter status 5) of our latest beam time at the ILL. The comparison between the red and the green data points shows that, for our latest beam time at the ILL, the barrier voltage dependent background could be effectively suppressed by about an order of magnitude. However, this still corresponds to a shift in a at the level of $-1\,\%$ (see also [34]).

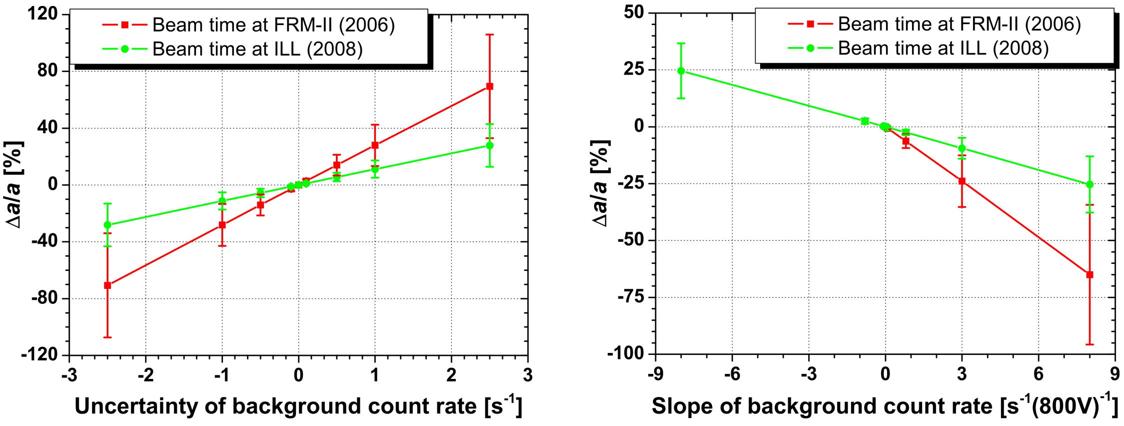

(a) (b)

Figure 5.11: Relative change of the angular correlation coefficient a for (a) different uncertainties and (b) different slopes of the background count rate. The comparison between our first beam time at the FRM II (red squares) and our latest beam time at the ILL (green circles) shows that the dependence of a both on the uncertainty and the slope of the background count rate decreases already with increasing full proton decay rate N_0, by about a factor of 2.3. We note that, for a further beam time, we have to know the background count rate with an accuracy of 10 mHz, in order to keep systematic uncertainties in a below $\Delta a/a = 0.1\,\%$. In the case of a linear relationship between the barrier voltage U_A and the background count rate instead, we have to know the slope with an accuracy of $40\,\mu\mathrm{Hz\,V^{-1}}$. Input data for the simulation: $B_\mathrm{A}/B_0 = 0.2028$, $U_\mathrm{A} = 50, 100, 150, 200, 250, 300, 350, 400, 450, 500, 550, 600\,\mathrm{V}$ for our beam time at the FRM II [33] respectively $B_\mathrm{A}/B_0 = 0.203$, $U_\mathrm{A} = 50, 250, 400, 500, 600\,\mathrm{V}$ for our beam time at the ILL, and the recommended value for $a = -0.103$ [10]. The error bars represent the error by fitting Eq. (3.32) to the simulated proton count rates only.

the neutrino-electron correlation coefficient a would be shifted by $\Delta a/a \approx -80\,\%$, as can be seen from Fig. 5.11a (see also Fig. 2.15b). Assuming a linear relationship between the barrier voltage U_A and the background count rate instead, a would be shifted by $\Delta a/a \approx -25\,\%$, cf. Fig. 5.11b. This fact prevented us from presenting a new value for the angular correlation coefficient a from this beam time.

In addition to the improvements mentioned above, for our latest beam time at the ILL, an additional neutron shutter was installed inside the casemate (see Sec. 4.1.2 for details). While this shutter has no direct influence on the background conditions, it allows for detailed studies of the background for closed neutron shutter, i.e., without neutron beam (e.g., in shutter status 1; defined in Sec. 4.2.4) and also shortly after measurements with neutron beam (in shutter status 5, see also Fig. 5.13). As can also be seen from Fig. 5.10, the AP voltage dependent background without neutron beam could be effectively suppressed by about an order of magnitude. But if we would not correct for the measured AP voltage dependent background, the neutrino-electron correlation coefficient a would still be shifted by $\Delta a/a \approx -2\,\%$; assuming an uncertainty of the background count rate of $0.2\,\mathrm{s^{-1}}$ (cf. Fig. 5.11a).

We would like to emphasize, that, for a further beam time, we have to know the background count rate with an accuracy of 10 mHz, in order to keep systematic uncertainties in a below $\Delta a/a = 0.1\,\%$ (cf. Fig. 5.11a). It is also for this reason that we have carefully examined the background for shutter statuses 1 and 5, i.e., for closed neutron shutter

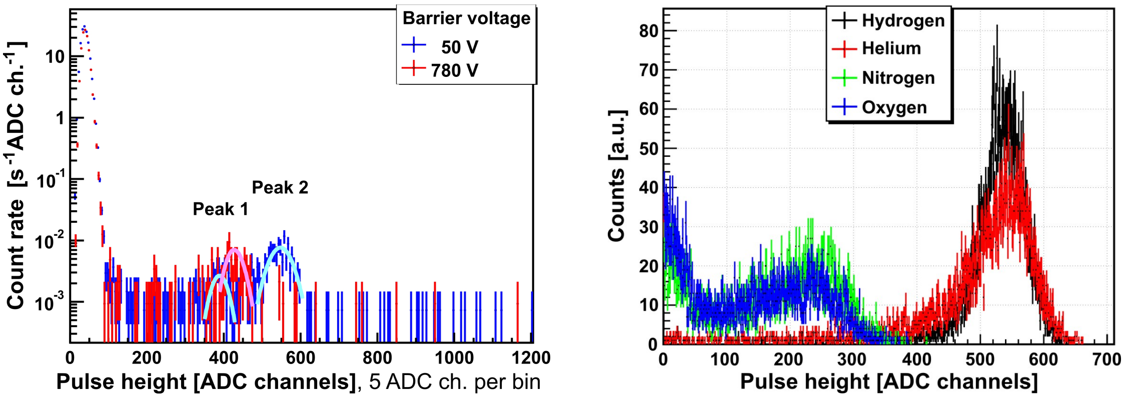

(a) (b)

Figure 5.12: (a) Typical pulse height spectra for one detector pad after measurements with neutron beam (in shutter status 5). The one to two tiny peaks are visible only in logarithmic representation after adding all measurements with the same barrier voltage. The light blue and pink lines are Gaussian fits to these peaks for $U_A = 50\,\mathrm{V}$ and 780 V, respectively. (b) Simulated pulse height spectra for different residual gas ions, with an impact angle and kinetic energy of 0° and 15 keV, respectively. Figure taken from Ref. [52]. The comparison between (b) and (a) shows that the simulation results are inconclusive [52]. For details see the text. Error bars show statistical errors only.

before and after a measurement with neutron beam, respectively. This allows us to distinguish between background caused by the neutron beam, the neutron decay products, or by other sources like field emission near the proton detector (for details see page 56 under “Penning Traps and Penning Discharge”). In contrast to our first beam time at the FRM II (cf. the “proton-like peak” in Fig. 2.15a), only a small background contribution was found. As can be seen from Fig. 5.12a, this contribution is visible only in logarithmic representation after adding all measurements with the same barrier voltage. Depending on the barrier voltage, one to two tiny peaks appear in the pulse height spectra for shutter status 5. A detailed analysis of both peaks revealed [34]:

Peak 1 (centered around ADC channel 400): The first peak is visible both before and after measurements with neutron beam (shutter statuses 1 and 5), for both −10 kV and −15 kV acceleration potential, and for all barrier voltages. Its maximum and intensity both rise slightly with increasing barrier voltage, but its count rate fluctuates randomly.

We believe that this background contribution is strongly correlated to the electron trap at the AP, i.e., the trap between the lower dipole electrode e8 and the high voltage electrodes e16 and e17 (see also Fig. 3.10).

Peak 2 (centered around ADC channel 550): The second peak is at the same position as the proton peak (cf., e.g., Fig. 5.8b). In contrast to peak 1, it appears only after measurements with neutron beam (shutter status 5), for −15 kV acceleration potential, for $U_A = 0\,\mathrm{V}$ and 50 V, its intensity decreases from $U_A = 0\,\mathrm{V}$ to 50 V, and its count rate decreases exponentially with a time constant of 2 to 3 s. As discussed in the following section, this peak also appears randomly when the neutron shutter is open (shutter status 3); then its count rate fluctuates non-statistically.

> We believe that this background contribution is strongly correlated to trapped electrons, which in turn may ionize residual gas molecules and/or interact with trapped decay protons.

In Ref. [34] it was derived that background peak 1 yields a shift in the neutrino-electron correlation coefficient a of

$$\boxed{\Delta a/a = 1.14(30)\,\%} \tag{5.15}$$

while peak 2 corresponds to a shift in a of

$$\boxed{\Delta a/a = -2.07(31)\,\%} \tag{5.16}$$

To further identify the types of ions involved in this background contribution, pulse height spectra for possible contributors have been simulated (see also Fn. 29 in Chap. 3). The comparison between Figs. 5.12b and 5.12a shows that the simulation results are inconclusive [52]. Peak 2 might be caused by protons or helium ions, whereas heavier residual gas ions, like oxygen and nitrogen, are expected below peak 1. An explanation for peak 1 could possibly be protons with a lower impact energy of about 12 keV. However, such protons must be produced at a potential of about -3 kV, i.e., near the high voltage electrodes e16 or e17.

5.3.2 Dependence on the Lower Dipole Potential

As mentioned earlier on page 59 under "The Dipole Electrodes" (see also Sec. 3.4.3 under "Elastic Scattering"), the lower dipole electrode e8 serves to remove all decay protons and positive ions with too low energy to overcome the potential barrier and that would otherwise be trapped between the electrostatic mirror and the AP (see also Fig. 3.10). To investigate the efficiency of the lower dipole electrode, the temporal evolution of the background count rate was examined for different settings of the electrode. For this purpose, the potential barrier was set to $U_{\mathrm{A}} = 780\,\mathrm{V}$ and the drift potential was reduced in several steps from $U_{8\mathrm{R}}|U_{8\mathrm{L}} = -50\,\mathrm{V}|-1000\,\mathrm{V}$ to $0\,\mathrm{V}|-2.5\,\mathrm{V}$.

Figure 5.13 shows a comparison of the temporal evolution of the background count rate for two different settings of the lower dipole electrode. Before the neutron shutter is opened, we only observe some counts of the environmental background (for details see Sec. 3.4.4 under "Uncorrelated background"), independent of the drift potential. But as soon as the shutter is opened, decay protons get trapped for the lowest potential difference of 2.5 V. Then the count rate starts to fluctuate non-statistically and does not stop to fluctuate even after the shutter is closed again. For a drift potential of $U_{8\mathrm{R}}|U_{8\mathrm{L}} = 0\,\mathrm{V}|-200\,\mathrm{V}$ instead, the count rate is stable as long as the neutron shutter is open and drops back to the environmental background count rate immediately after the shutter is closed again.

We note that for the lowest drift potential of $U_{8\mathrm{R}}|U_{8\mathrm{L}} = 0\,\mathrm{V}|-2.5\,\mathrm{V}$, an additional peak centered around ADC channel 230 is visible in the pulse height spectra for shutter status 5 [34]. The additional peak might be caused by heavier residual gas ions, like oxygen or nitrogen (cf. Fig. 5.12b), but it can be effectively suppressed by the typical potential difference of 200 V.

To further investigate possible background contributions from electrons, the lower dipole electrode was used as a second analyzing plane. More precisely, a positive potential

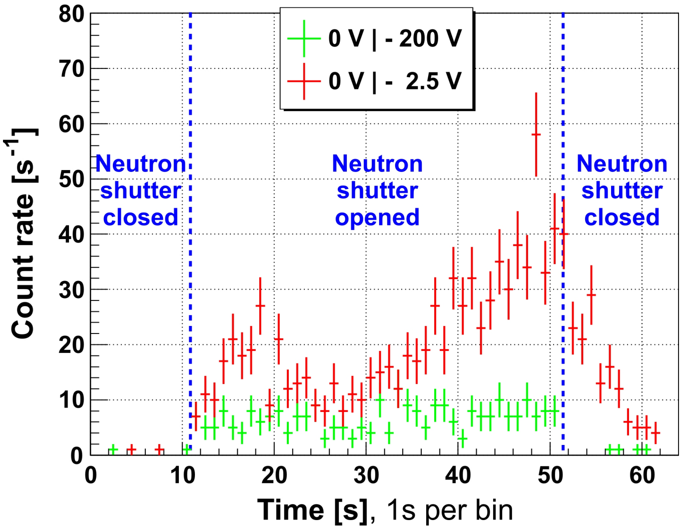

Figure 5.13: The temporal evolution of the background count rate measured at $U_{\mathrm{A}} = 780\,\mathrm{V}$ for two different settings of the lower dipole electrode e8, from 19_05_08/lExB. For elucidation, the dashed blue lines show when the neutron shutter was opened and later closed again. The comparison between the red and the green data points shows the efficiency of the lower dipole electrode in the emptying of the possible positive ion trap between electrostatic mirror and analyzing plane (cf. Fig. 3.10). Error bars show statistical errors only.

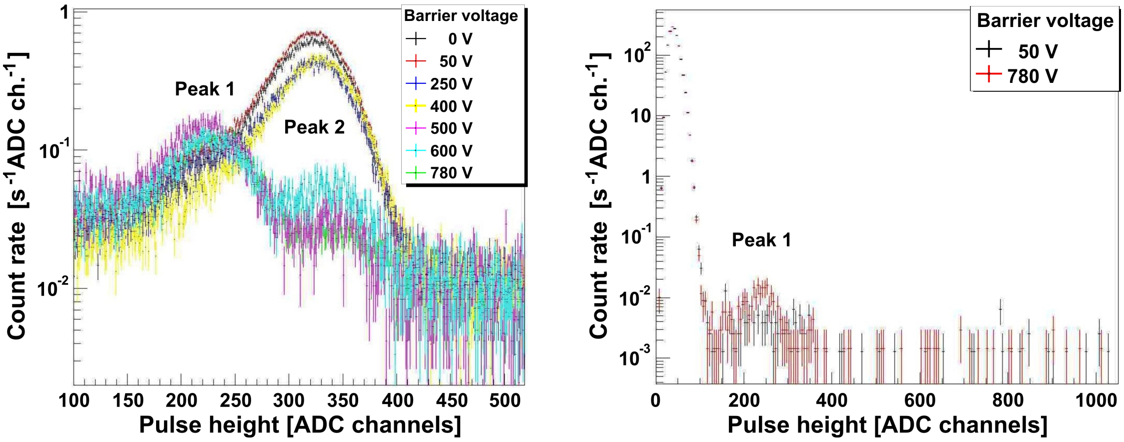

(a) Shutter status 3 (b) Shutter status 5

Figure 5.14: Pulse height spectra for one detector pad from 03_05_08/lExB_p1kV for a second analyzing plane. For this investigation a positive potential of +1000 V was applied to both sides of the lower dipole electrode e8. Depending on the barrier voltage U_{A}, one to two peaks appear in the pulse height spectra for (a) measurements with neutron beam, while only one tiny peak appears (b) after measurements with neutron beam. We note that in the case of (a) the background count rate includes the contribution of decay electrons. In comparison with Fig. 5.12, these spectra stem from measurements at an acceleration potential of $-10\,\mathrm{kV}$ and therefore both background peaks are shifted to lower ADC channels. But in contrast to Fig. 5.12a and Sec. 5.3.1, for measurements with neutron beam, the second peak is visible for all barrier voltages. Error bars show statistical errors only.

of +1000 V was applied to sides R and L of the dipole electrode, in order to prevent all decay protons from reaching the AP. Figure 5.14 shows the corresponding pulse height spectra for different barrier voltages U_A. Again, one to two peaks appear in the pulse height spectra for measurements with neutron beam, while only one tiny peak appears after measurements with neutron beam. In contrast to Sec. 5.3.1, for measurements with neutron beam, the second peak is visible for all barrier voltages. In this case, the derived shift in the angular correlation coefficient a Eq. (5.16) would be wrong. However, we must also note that these pulse height spectra were recorded at a time when the count rates were fluctuating non-statistically[7] and with manually switching of the electrostatic mirror only. Hence, we should not jump to conclusions until there is evidence that the second background peak is present for all barrier voltages. And since the second peak is at the same position as the proton peak, we strongly recommend to repeat this measurement in a further beam time, but with automated switching of the electrostatic mirror. Where possible, the second analyzing plane should be applied to different electrodes both below and above the AP electrode e14.

5.3.3 Trapping of Decay Protons

As discussed in greater detail later in Sec. 6.4.3, work function inhomogeneities in the DV could lead to trapping of decay protons between the DV and the electrostatic mirror. Approaches to eliminate and/or to handle this effect are presented in Sec. 6.4.4. Due to a lack of time during our latest beam time at the ILL, we could only study different “Inverse electric field gradient[s]”. For the investigation of electric field gradients, a potential of a few volts is applied to the bottom and top cylinders e3 and e6 of the DV electrode, with opposite sign. Only in the case of a positive gradient, decay protons may be trapped between the DV and the electrostatic mirror, whereas in the case of a negative gradient, the protons remain unaffected. In the event of work function inhomogeneities, described by a positive electric field gradient, a superimposed negative gradient should reduce the trapping conditions. To be specific, with increasing negative electric field gradient the proton count rate should increase, until the work function inhomogeneities are compensated.

Figure 5.15 shows the short-term evolution of the proton count rates for two different settings of the DV electrodes e3 and e6. Absolutely unexpected the proton count rates, both for $U_\mathrm{A} = 0\,\mathrm{V}$ and 50 V, decrease with increasing negative electric field gradient. Obviously, these measurements were performed at a time when the count rates were fluctuating non-statistically (cf. Fn. 7). However, the count rate losses of several Hz (cf. Table 5.3) are so large that another effect seem to be in play. In the event that the electrical connections of the electrodes e3 and e6 have been changed by mistake, the count rate losses might at least partly be explained by an additional electric mirror above the DV, as can be seen from Table 5.3. It is very likely that we investigated different “Definite electric mirror[s] above the DV” (cf. Sec. 6.4.4) instead of “Inverse electric field gradient[s]”. Hence, we recommend to repeat this measurement in a further beam time.

---

[7] At the beginning of our latest beam time at the ILL, the count rates were fluctuating non-statistically. We identified and fixed problems with a power supply for side R of the lower dipole electrode e8, several ground loops, and the electrical connections of the electrode system.

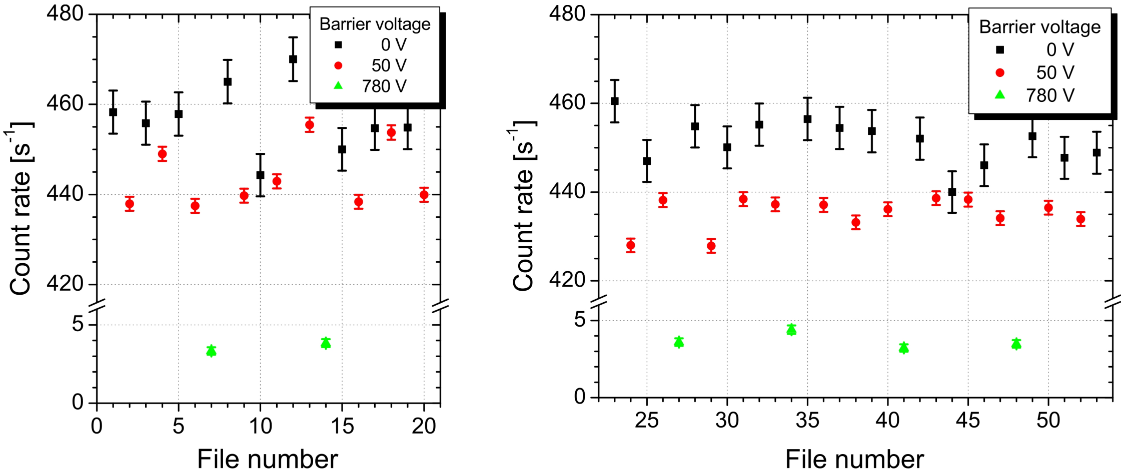

(a) $U_3 = -U_6 = 1\,\mathrm{V}$ (b) $U_3 = -U_6 = 2\,\mathrm{V}$

Figure 5.15: Influence of an electric field gradient in the decay volume (DV) on the proton count rates from 23_04_08/DV_gradient_evs100 for different barrier voltages $U_\mathrm{A} = 0, 50, 780\,\mathrm{V}$. For this investigation a potential of a few volts (a) $U_3 = -U_6 = 1\,\mathrm{V}$ respectively (b) $U_3 = -U_6 = 2\,\mathrm{V}$ was applied to the bottom and top cylinders e3 and e6 of the DV electrode. In comparison with the top of Fig. 5.9, these count rates stem from a measurement at an acceleration potential of $-10\,\mathrm{kV}$ and are therefore lower by about 15 to 20 Hz. Unfortunately, the measurement results are inconclusive (see also Fn. 7); see the text and Table 5.3 for details. Error bars show statistical errors only.

Table 5.3: Influence of an electric field gradient $\partial U_0/\partial z$ in the decay volume (DV) on the proton count rate for $U_\mathrm{A} = 50\,\mathrm{V}$, corresponding to Fig. 5.15 and Eq. (6.19). For this purpose a potential of a few volts, $U_3 = -U_6$, was applied to the DV electrodes e3 and e6. In the event of work function inhomogeneities in the DV, the count rates should increase with the superimposed external electric field, by a few Hz (cf. the fourth column). This is not the case. Hence, we assume that the electrical connections of the electrodes e3 and e6 have been changed by mistake. The comparison between the third and the last column shows that this might at least partly explain the count rate losses by an additional electric mirror above the DV, corresponding to Eq. (3.30). Input data for the calculation (with Nachtmann's formula Eq. (2.38)): $B_0 = 2.177\,\mathrm{T}$, $B_\mathrm{A}/B_0 = 0.203$, and the recommended value for $a = -0.103$ [10]. The following abbreviations appear: avg (average value) and CPS (count rate or counts per second).

$U_3 = -U_6$ [V]	avg $\partial U_0/\partial z$ [mV cm^{-1}]	avg CPS measured [s^{-1}]	CPS due to electric field gradient [s^{-1}]	CPS due to electric mirror above DV [s^{-1}]
0	0	448.0 ± 1.0	448.0	448.0
-1	25	440.3 ± 1.4	446.8	441.6
-2	50	431.5 ± 1.0	444.9	427.6

5.3.4 Trapping of Decay Electrons

Due to the slight magnetic field gradient $(\partial B_0/\partial z)/B_0 = -1 \times 10^{-4}\,\mathrm{cm}^{-1}$ in the DV, a small fraction of decay protons and electrons, emitted in the negative z-direction with (initial) polar angle 90°< θ_0 <92°, is reflected by the magnetic mirror just below the DV (see Fig. 4.5b). While all protons can overcome the magnetic mirror right in front of the proton detector (see Fig. 4.5a), only about 13.1 % of the electrons will reach the detector (for details see Sec. 5.4.2). In particular, decay electrons with (initial) polar angles 88°< θ_0 <92° will be reflected both on the magnetic mirror just below the DV and right in front of the proton detector.

Assuming a uniform neutron beam density, a fraction of about[8]

$$\begin{aligned} 1 \quad & - \quad \frac{1}{\int_{\mathbf{P}_0} d\mathbf{P}_0} \int_{\mathbf{P}_0} d\mathbf{P}_0 w_{\mathrm{tr}}(T_0;\mathbf{P}_0) \\ & \overset{(3.29)}{=} \quad \frac{1}{\int_{z_0} dz_0} \int_{z_0} dz_0 \sqrt{1 - \frac{B_0 - z_0 \cdot 9.25 \times 10^{-5} \cdot B_0}{B_0 + 6 \cdot 9.25 \times 10^{-5} \cdot B_0}} \\ & = \quad \frac{1}{\int_{-4}^{4} dz_0} \int_{-4}^{4} dz_0 \sqrt{\frac{(z_0+6) \cdot 9.25 \times 10^{-5}}{1 + 6 \cdot 9.25 \times 10^{-5}}} = \frac{1}{8} \frac{\sqrt{92.5} \times 10^{-3}}{\sqrt{1 + 6 \cdot 9.25 \times 10^{-5}}} \int_{2}^{10} dz_0 \sqrt{z_0} \\ & = \quad \frac{\sqrt{92.5}}{8} \frac{10^{-3}}{\sqrt{1 + 6 \cdot 9.25 \times 10^{-5}}} \left[\frac{2}{3} z_0^{3/2} \right]_2^{10} \\ & = \quad \frac{\sqrt{92.5}}{12} \frac{10^{-3}}{\sqrt{1 + 6 \cdot 9.25 \times 10^{-5}}} \left(10^{3/2} - 2^{3/2} \right) \qquad (5.17) \\ & \approx \quad 2.3\,\% \end{aligned}$$

of all decay electrons will therefore be trapped between the DV and the upper dipole electrode e16. Here, $\mathbf{P}_0 = (x_0, y_0, z_0)$ denotes the decay point and B_0 is the average magnetic field in the DV (see also Sec. 4.1.4). For a full proton decay rate of $N_0 = 490\,\mathrm{s}^{-1}$ this corresponds to about 12 Hz. These electrons perform lots of axial oscillations between the DV and the upper dipole electrode before they have lost their total energy by means of inelastic scattering on residual gas molecules and/or synchrotron radiation. The latter process can take up to 1 s [224], assuming a constant magnetic field of 1 T. For a residual gas pressure of 1×10^{-9} mbar, one such trapped decay electron would produce background of about 10 Hz [224]. The exact background count rate depends on its storage time.

In Ref. [47] (see also Sec. 3.4.4 under "Uncorrelated background events") it is assumed that this background contribution does not depend on the barrier voltage and can therefore be measured at $U_\mathrm{A} = 780\,\mathrm{V}$. Indeed these electrons spend most of their time at their both turning points, i.e., around the DV and below the upper dipole electrode. Hence, it is less than likely that these electrons interact with residual gas molecules in the AP, in which case this background contribution would depend on the barrier voltage.

To further investigate this systematic effect, we recommend measurements with different magnetic field gradients, in a further beam time. In particular, we propose a measurement with a positive magnetic field gradient, i.e., with a magnetic mirror above the DV, so that no decay electrons can be trapped above the DV. We note that this investigation is not independent of possible work function inhomogeneities in the DV (discussed in Sec. 6.4.4 under "Definite magnetic mirror above the DV").

A detailed analysis of the (measured) background conditions can be found in Ref. [34] (see also [52]).

---

[8] In our measurement, we expect a fraction of only about $2.10 \pm 0.01(\mathrm{stat})^{+0.04}_{-0.01}(\mathrm{sys})\,\%$, cf. Eq. (5.52).

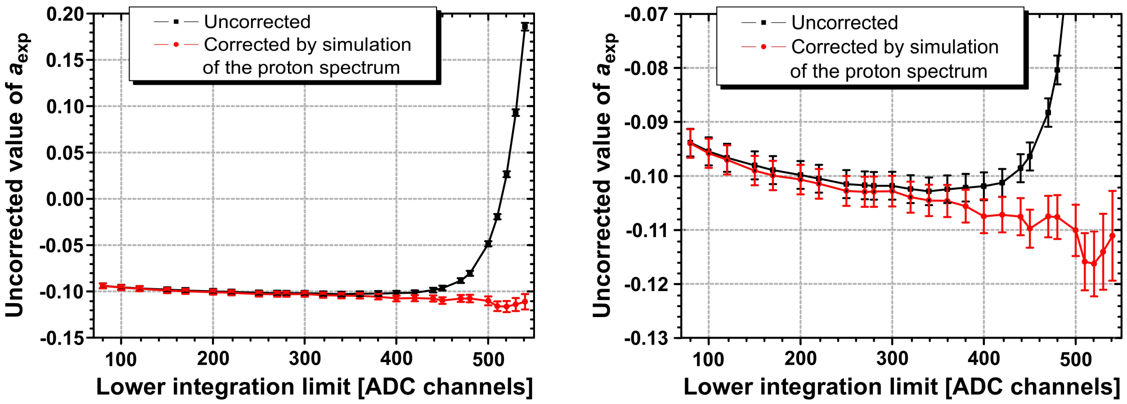

(a) Full view (b) Zoom

Figure 5.16: The uncorrected value a_{exp} of the angular correlation coefficient a for (a) different lower integration limits, for one detector pad from 16_05_08/night. The (b) zoom to values $a_{\mathrm{exp}} = -0.1 \pm 0.03$ shows that, for lower integration limits higher than 400 ADC channels, the steep rise of a_{exp} disappears after correction by simulation of the proton recoil spectrum, whereas the flat slope, for lower integration limits smaller than 340 ADC channels, remains unaffected. The error bars show statistical errors only and are strongly correlated, as each data point stems from the same measurement run. Figures taken from Ref. [52].

5.4 Unexpected Systematic Effects

As mentioned earlier in Chap. 4, the primary focus of our latest beam time at the ILL was on the identification and investigation of possible systematic effects as discussed in Sec. 3.4 (see also Sec. 4.2.5). However, among other unexpected systematic effects, we identified and fixed a problem in the detector electronics. In this (see also Sec. 6.4.3) and the following Sec. 5.5, we discuss the unexpected and "expected" systematics, respectively.

We note that the values given in this and the following Sec. 5.5 for the neutrino-electron correlation coefficient a are for comparison purposes only. We would like to stress that these values do not represent a final value for a, as they are corrected only for the dead time of the electronics Eq. (5.10) and the blind analysis Eqs. (5.1) and (5.2).

5.4.1 Dependence of a on the Lower Integration Limit

During the data analysis, both the upper and the lower integration limit were investigated and a rather strong dependence of the angular correlation coefficient a on the lower integration limit was found. From a lower integration limit of 80 to 340 ADC channels, the uncorrected value for a decreases by

$$\Delta a_{\mathrm{exp}}/a_{\mathrm{exp}} = (-9.6 \pm 4.7)\,\% \tag{5.18}$$

from $a_{\mathrm{exp}} = -0.094(3)$ to $a_{\mathrm{exp}} = -0.103(3)$, as can be seen from Fig. 5.16. For lower integration limits higher than 400 ADC channels, the value for a_{exp} increases steeply towards positive values. In the latter area, the strong increase of a_{exp} can be explained by the electric retardation method of aSPECT and can therefore be corrected by simulations (for details see [52] and also Fn. 29 in Chap. 3): As already mentioned in Sec. 5.2.2, with increasing barrier voltage U_A less protons can overcome the AP, but with higher kinetic energy. Thus, for a fixed lower integration limit for all barrier voltages, one cuts away more counts for the lower than for the higher voltages, as can be seen from Fig. 5.8.

Figure 5.16 also shows that, for lower integration limits higher than 340 ADC channels, the steep rise of a_exp disappears after correction by simulation of the proton recoil spectrum. However, for lower integration limits smaller than 340 ADC channels, the flat slope remains unaffected. Obviously, the remaining dependence must be caused by a completely different systematic effect, as will be discussed in the following sections. We note that, for a lower integration limit of 80 ADC channels, the correction is only

$$\boxed{\Delta a/a = 0.13(9)\,\%} \tag{5.19}$$

with a relative error of 70 % dominated by simulation statistics [52].

For a fixed lower integration limit, no such dependence of the angular correlation coefficient a on the upper integration limit was found, even if the upper integration limits falls below the tiny peak centered around ADC channel 750 (see Fig. 5.8).

Details on the selection of upper and lower integration limit can be found in Ref. [34] (see also [52]).

Correlated Events

To further investigate the dependence of the neutrino-electron correlation coefficient a on the lower integration limit, we analyzed our measurement data for possible anomalies. This revealed a time-dependent loss mechanism of decay protons shortly after high-energy electrons [52]. Figure 5.17a shows pulse height spectra of events after high-energy electrons, sorted according to their time difference to the high-energy electron. For pulse-heights below ADC channel 200,

- there are almost no events less than 8 μs after a high-energy electron,
- while obviously “additional” events between 8 and 15 μs after a high-energy electron.

Thus, we probably lose decay protons with low pulse height and short time difference to the electron, as described in the following section.

As discussed earlier in Sec. 5.2.1, the detection time difference between correlated coincidence events may be estimated by the TOF of the proton. The minimum TOF of decay protons is about 5.3 μs for $U_\mathrm{A} = 50\,\mathrm{V}$ (see also Fn. 27 in Chap. 3) up to 8.2 μs for $U_\mathrm{A} = 600\,\mathrm{V}$, where the correlated electron was emitted towards the electrostatic mirror. If we neglect effects regarding backscattering of electrons (discussed in Sec. 5.4.2), these protons will not be detected in coincidence with the electron from the same decay. The minimum TOF of decay protons detected in coincidence with the correlated electron is about 7.2 μs for $U_\mathrm{A} = 50\,\mathrm{V}$ up to 10.0 μs for $U_\mathrm{A} = 600\,\mathrm{V}$. Thus, for $U_\mathrm{A} \geq 500\,\mathrm{V}$, we cannot lose decay protons, as can also be seen from Fig. 5.17b. Hence, the loss rate strongly depends on the barrier voltage U_A, what, in turn, has a major impact on the angular correlation coefficient a.

However, the question remains whether both above mentioned effects can explain the observed shift Eq. (5.18) in the uncorrected value for a. As can be seen from Fig. 5.18, the energy distribution of only correlated coincidence events is shifted to lower proton kinetic

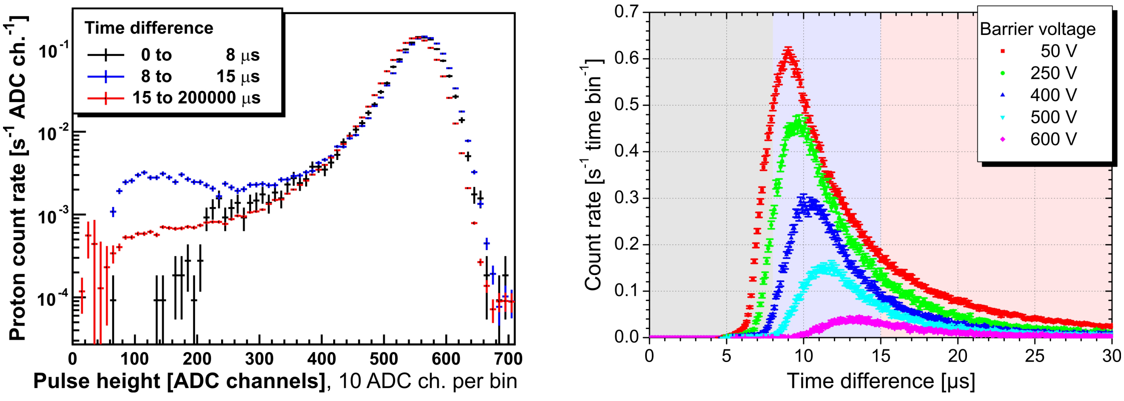

(a) (b)

Figure 5.17: (a) Background subtracted pulse height spectra of events after high-energy electrons from 20_05_08/night for $U_A = 50\,\mathrm{V}$. According to their time difference to the electron, the events were sorted into three different categories. Apparently, we lose decay protons with low pulse height (ADC channels < 200) and short time difference to the electron (black points). We note that the spectra were normalized to the count rate between ADC channels 500 and 600. (b) Typical (detection) time difference spectra from 18_05_08/night for different barrier voltages U_A. With increasing barrier voltage the count rate decreases whereas the minimal TOF increases. The colorful highlighted areas correspond to the three different categories from (a). For $U_A \geq 500\,\mathrm{V}$, we cannot lose decay protons, as their minimal TOF is greater than $8\,\mu$s. Thus, the loss rate strongly depends on the barrier voltage. Error bars show statistical errors only.

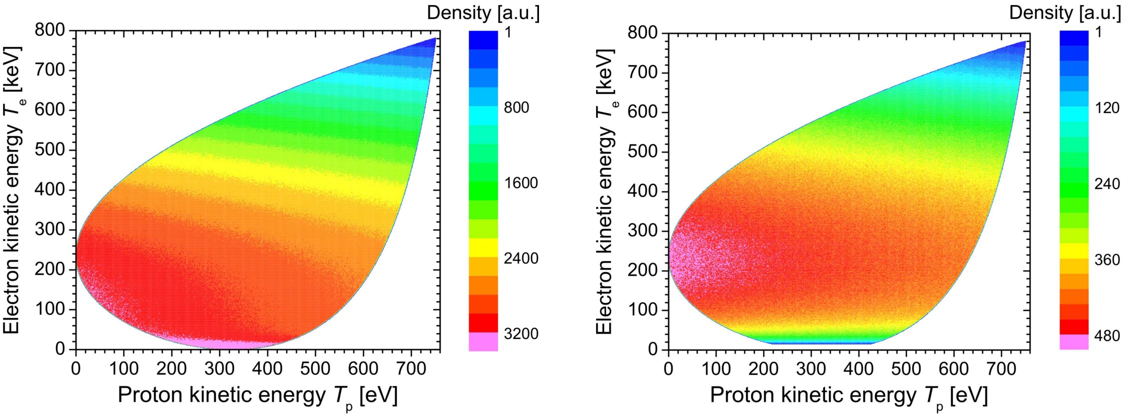

(a) (b)

Figure 5.18: Dalitz plot distribution of electron and proton kinetic energy, for (a) protons not detected in coincidence with their correlated electron and (b) correlated coincidence events. Please note the different contour scales. If we neglect effects regarding backscattering of electrons (discussed in Sec. 5.4.2), a maximum of 13.1 % of the decay electrons can be detected in coincidence with their correlated proton (see Sec. 5.4.2). Input data for the MC simulation (in INM approximation): Number of generated events = 10^9 and $a = -0.105$ (derived from $\lambda = -1.2701(25)$ [10]).

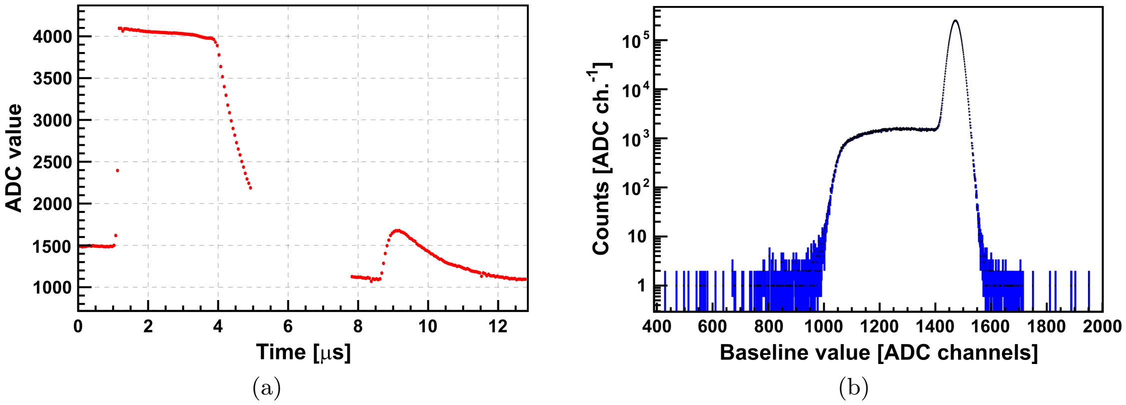

(a) (b)

Figure 5.19: (a) A proton event shortly after an high-energy electron. The first (electron) event saturates the detector electronics and is therefore cut off by the maximum amplification of the electronics. After the first (electron) event the baseline drops down to around 1100 ADC channels. The next (proton) event therefore has a lower and changing baseline. We note that the red data points show the ADC values of two consecutive events, where the values between the two events are not recorded. (b) Typical baseline value distribution for one measurement file. Most events have a baseline of (1490 ± 20) ADC channels, whereas events shortly after high-energy electrons have a lower baseline of down to 1000 ADC channels. Error bars show statistical errors only.

energies. Analysis of only correlated coincidence events (Fig. 5.18b) would therefore lead to $a = +0.546$, whereas analysis of only protons not detected in coincidence with their correlated electron (Fig. 5.18a) would lead to $a = -0.237$. Hence, the observed shift Eq. (5.18) is realistic.

Baseline Shifts

Our analysis revealed that the trigger efficiency is reduced after high-energy electrons [52], what at least partly explains the unexpected proton losses less than 8 μs after high-energy electrons.

As mentioned earlier in Sec. 5.1.3, the pulse of an high-energy electron is longer than one event window (5 μs). For a proton shortly after an high-energy electron, it is therefore probable that the proton will sit on the decaying edge of the electron, as shown in the top of Fig. 5.2b. In most cases, the baseline of such a proton is changed by the exponentially decaying edge of the electron, as can be seen in Fig. 5.19a (see also Fig. 5.2b). Figure 5.19b shows that most events have a baseline of (1490±20) ADC channels, whereas events shortly after high-energy electrons have a lower baseline of down to 1000 ADC channels.

The pulse heights of the measured events can be corrected with the adapted fit (described in Sec. 5.1.3). However, the shifts of the baseline already influence the data acquisition by means of the trigger algorithm (described on page 69 under "Digital Electronics and the Trigger Algorithm"): On the decaying edge of an high-energy electron, the value of the (baseline) window w1 is shifted to higher values compared to the true baseline value at the position of trigger window w2. If the shift of the (baseline) window w1 is too high, events with a rather low pulse height will be lost. In other words, the trigger efficiency is reduced after high-energy electrons.

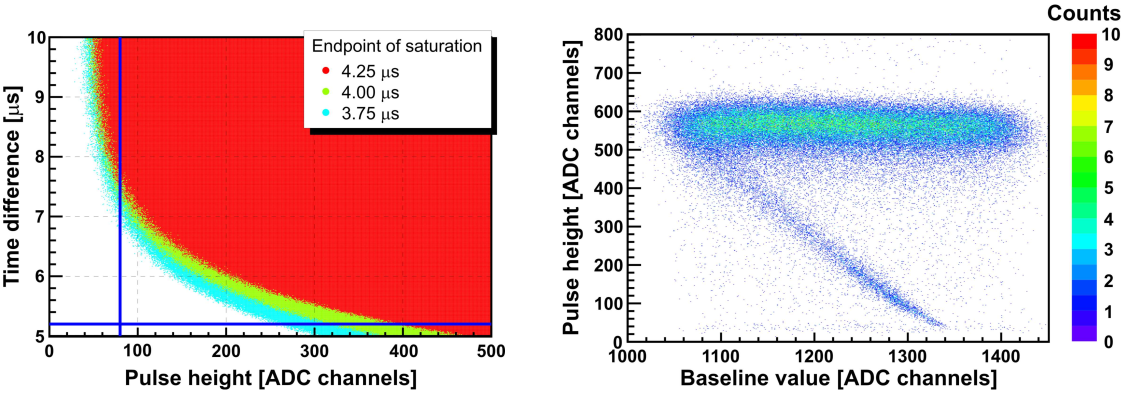

(a) (b)

Figure 5.20: (a) The reduced trigger ranges after high-energy electrons for a baseline lowered to 1000 ADC channels and different endpoints of the saturation. The scatter plots show that the trigger efficiency decreases with later endpoint of the saturation. For elucidation, the horizontal and the vertical blue line indicate the dead time of the electronics ($5.2\,\mu$s), i.e., the minimal time difference to the electron, and the usually used lower integration limit (80 ADC channels), respectively. Figure taken from Ref. [52]. (b) Typical relationship between the pulse height of protons after high-energy electrons and the lowered baseline value, for one measurement file with $U_{\mathrm{A}} = 50\,\mathrm{V}$. The broad (turquoise) band shows the distribution of the proton events with a lowered baseline (see also Fig. 5.19b), whereas the thin diagonal (blue) branch reveals the "additional" events between 8 and $15\,\mu$s after high-energy electrons (see also Fig. 5.17a).

To reproduce the proton losses less than $8\,\mu$s after high-energy electrons, the reduced trigger efficiency was investigated by means of MC simulations [52]. For this purpose electron-proton coincidence events were generated and subsequently analyzed with the trigger algorithm described on page 69 under "Digital Electronics and the Trigger Algorithm". To determine the reduced trigger range, the pulse height of the proton, its time difference to the electron, the endpoint of the saturation, and the lowered baseline value were varied. For example, Fig. 5.20a shows the reduced trigger ranges for a baseline lowered to 1000 ADC channels and different endpoints of the saturation. As expected, the trigger efficiency decreases with later endpoint of the saturation.

In Ref. [34] it was derived that the reduced trigger efficiency after high-energy electrons corresponds to a shift in the neutrino-electron correlation coefficient a of

$$\boxed{\Delta a/a \approx 0.2\,\%} \tag{5.20}$$

This is far too little to explain the observed shift Eq. (5.18) in the uncorrected value for a. Therefore the strong dependence of the angular correlation coefficient a on the lower integration limit must be caused by a different systematic effect, as described in the following section.

We mention that further conclusions were drawn from scatter plots, showing the relationship between the pulse height of protons after high-energy electrons and the lowered baseline value. Figure 5.20b shows such a scatter plot. As expected, the broad (turquoise) band shows the distribution of the proton events with a lowered baseline. However, the figure also reveals a thin diagonal (blue) branch, from normal pulse heights at around ADC channel 1050 down to almost zero pulse height at around ADC channel 1350. This branch corresponds to the “additional” events between 8 and 15 μs after high-energy electrons, already observed in Fig. 5.17a (see also the previous section).

We note that the trigger efficiency issue can be easily solved by an optimized pulse shaping, in a further beam time.

Saturation of the Preamplifier

Figure 5.20b revealed that the “additional” events between 8 and 15 μs after high-energy electrons are not distributed randomly but lie on a thin diagonal branch. In particular, a slightly lowered baseline already leads to a strongly reduced pulse height. Further investigations showed that the “additional” events appear only after high-energy electrons which saturate the detector electronics for at least about 3 μs [52]. We are convinced that this effect is due to a saturation of the preamplifier after very high-energy events.

The principle of this saturation effect is shown in Fig. 5.21. As explained earlier on page 68 under “Amplification Boards”, the raw signal shape consists of a steep rise ($\tau_{\text{rise}} \approx 25\,\text{ns}$)[9] followed by a long exponential decay ($\tau_{\text{decay}} \approx 150\,\mu\text{s}$, see also Fn. 9). In the case of a double event, a second event shortly after the first one will therefore sit on the decaying edge of the first event. Hence, if an high-energy electron deposits so much energy in the detector that the preamplifier comes close to its maximum amplification, a proton shortly after the electron will drive the preamplifier into saturation. Consequently, the proton peak is cut off. Then, the shaper differentiates and integrates the amplified signal. The shaper is mostly sensitive to the rising edge of the signal and shortens the pulse. And since the height of the pulse after the shaper is proportional to the change in pulse height before the shaper, the proton peak will ultimately have a lower pulse height after the shaper. We note that the cut-off (of high-energy events) seen in the pulse shapes (see Fig. 5.1b) is due to a saturation of the shaper (see Fig. 6.27 in Ref. [52]).

To confirm our suspicion that the saturation of the preamplifier causes the reduced pulse height of the “additional” events and, at the same time, to reproduce this saturation effect, the detector electronics was tested in several steps [52]. For this purpose, the proton detector has been replaced by a waveform generator. A high, electron-like pulse followed by a low, proton-like pulse were generated with a waveform generator, fed through the entire electronics chain, and subsequently analyzed with the trigger algorithm described on page 69 under “Digital Electronics and the Trigger Algorithm”. To reproduce the saturation effect, the amplitude of the electron-like pulse and its time difference to the proton-like pulse were varied.

For example, Fig. 5.22 shows pulse height spectra for two different amplitudes of the electron-like pulse and several different time differences between the electron-like and the proton-like pulse. In contrast to, e.g., Fig. 5.8a the “left” peak below ADC channel 100, due to electronic noise, is missing. Since the detector was disconnected from the electronics, the noise level was much lower than usual and hence no noise was triggered this time. Spectra for a time difference lower than the lowest one shown do not contain any proton-like counts, due to the reduced trigger efficiency after high-energy electrons (see the previous section for details). As expected, the saturation of the preamplifier shifts the proton-like peaks to lower pulse heights. With decreasing time difference to the electron-like pulse the maximum of the proton-like peaks drops to lower pulse heights. Furthermore, with increasing amplitude of the electron-like pulse the proton-like peaks are shifted to even

---

[9] Please note that in Ref. [34] both the typical rise and the approximate decay time are misstated.

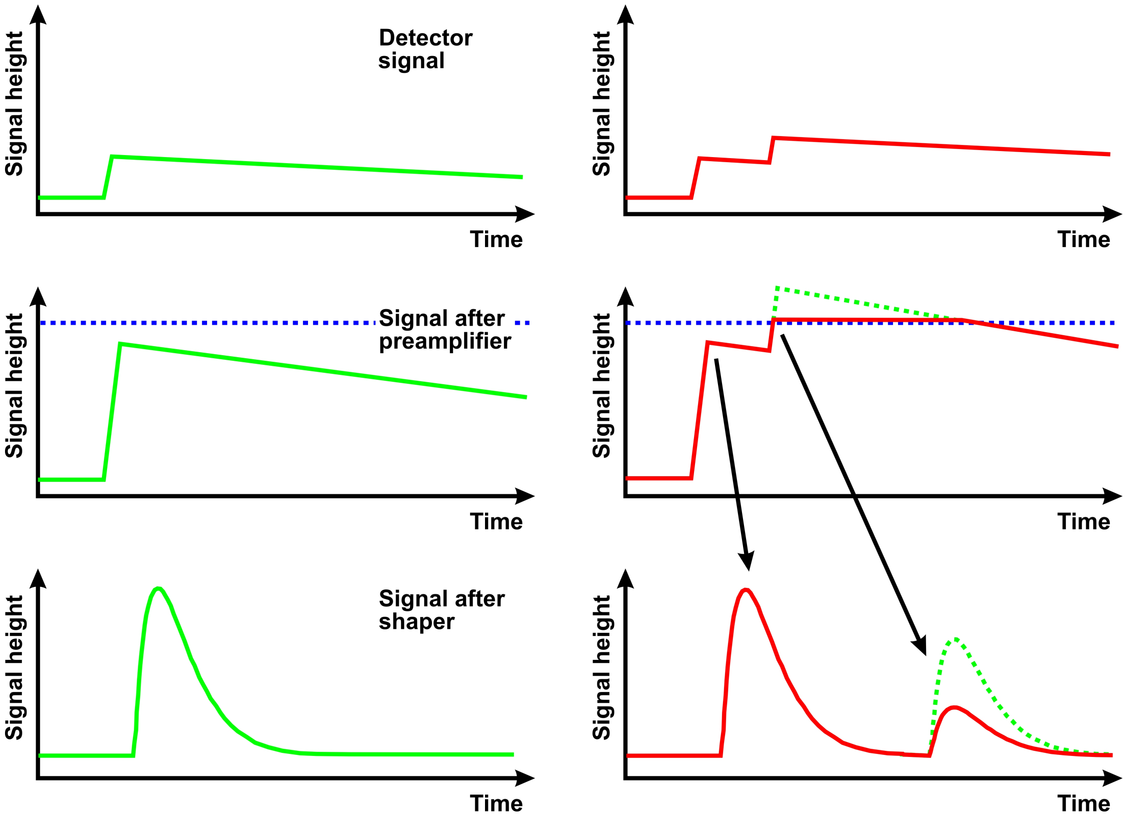

(a) (b)

Figure 5.21: Illustration of the signal processing for (a) a single event and (b) two consecutive events, where the second event drives the preamplifier into saturation. The figures show, from top to bottom, how (top) a signal from the detector is (middle) amplified by the preamplifier, then (bottom) shaped by the adapter board, and finally (not shown here) digitized by the ADC (see page 68 for details). Assuming a first event deposits so much energy in the detector that the preamplifier comes close to its maximum amplification (blue, dashed), a second event shortly after the first one will drive the preamplifier into saturation. Therefore, the second peak (green, dashed) is cut off and, consequently, will have a reduced (red, solid) pulse height after the shaper. Illustration adapted from Ref. [52].

lower pulse heights and the minimum time difference to trigger a proton-like pulse increases. We mention that, in our real measurement, proton-like counts below ADC channel 80 are superimposed on the electronic noise. However, lowering the lower integration limit would not provide additional information about the angular correlation coefficient a, because of fluctuations in the electronic noise.

In Ref. [52] it was derived that a decay electron has to deposit a minimum energy of

$$T_{\mathrm{e,deposit}}^{\mathrm{sat}} \geq 400(20)\,\mathrm{keV} \tag{5.21}$$

in the proton detector in order to saturate the preamplifier (see also Eq. (4.8)), with a relative error of 5 % dominated by the difficulty to determine to start point of the saturation effect. To determine which (with regard to their impact angle and energy) and how

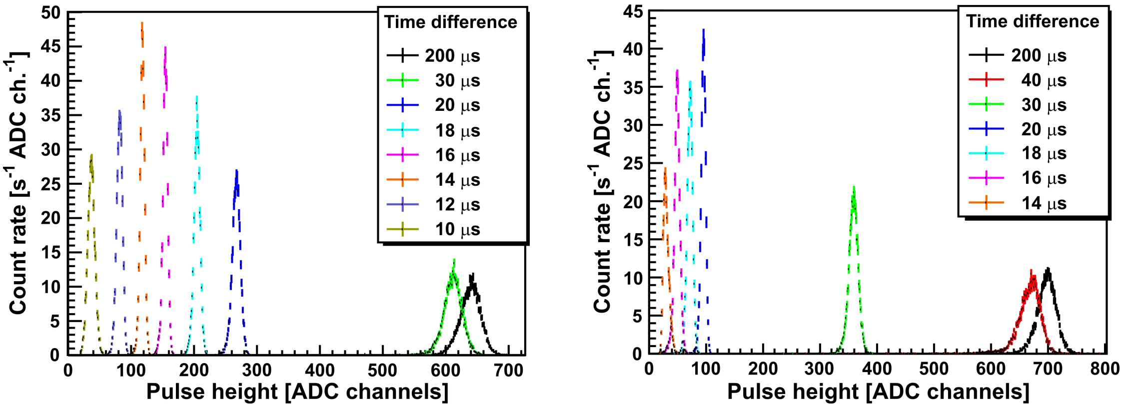

(a) Amplitude 220 mV (b) Amplitude 240 mV

Figure 5.22: Pulse height spectra for two different amplitudes (in mV) of the electron-like pulse and several different time differences between the electron-like and the proton-like pulse. With decreasing time difference the maximum of the proton-like peaks drops to lower pulse heights. The comparison between (a) and (b) shows that, with increasing amplitude of the electron-like pulse, the proton-like peaks are shifted to even lower pulse heights and the minimum time difference to trigger a proton-like pulse increases. For better distinction, only a selection of pulse height spectra is shown. Error bars show statistical errors only. Figures taken from Ref. [52].

many decay electrons can deposit more than 400 keV inside the detector, the backscattering of electrons was investigated by means of MC simulations[10] [52]. The simulations have shown that only a fraction of the high-energy electrons is stopped inside the proton detector. Figure 5.23a shows the fraction of electrons that deposit more than 400 keV inside the detector, for different impact angles and energies. According to this, only about 12.6 % of the decay electrons that reach the proton detector deposit more than 400 keV inside the detector (see also Fig. 5.18b). If we neglect effects regarding backscattering of electrons (discussed in Sec. 5.4.2), a maximum of 13.1 % of the decay electrons can be detected in coincidence with their correlated proton (see Sec. 5.4.2). Therefore, not more than about 1.66 % of all decay protons are affected by the saturation effect. However, the relationship Eq. (5.21) might change as soon as the waveform generator is replaced by the proton detector again.

In addition, Figure 5.23b shows that the dead time of the detector might rise up to about 50 μs after electrons that deposit more than 750 keV inside the detector. However, during our latest beam time, we observed "additional" events only less than 20 μs after high-energy electrons [225] (see also page 116 under "Correlated Events"). But on the other hand, it is unlikely that such high-energy electrons are stopped inside the proton detector [52, 225].

We note that the preamplifier saturation issue can be easily solved by reducing the amplification of the preamplifier down to about 40 %, in a further beam time.

Details on the problem in the detector electronics, simulations of electron-proton coincidence events as well as electron energy deposition inside the proton detector (see also

---

[10] The backscattering of electrons was simulated with CASINO [226]. The CASINO v2.42 program is a Monte Carlo simulation of electron trajectory in solid specially designed for low beam interaction in a bulk and thin foil [227, 228].

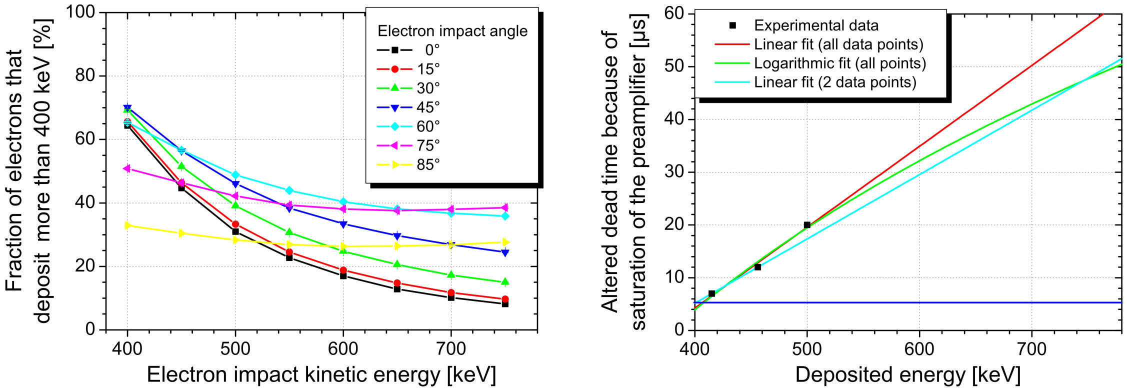

(a) (b)

Figure 5.23: (a) The fraction of electrons that deposit more than 400 keV inside the proton detector, for different impact angles and energies. With increasing impact kinetic energy this fraction decreases. Altogether, only about 12.6 % of the decay electrons that reach the detector deposit more than 400 keV inside the proton detector and hence not more than about 1.66 % of all decay protons are affected by the saturation effect. (b) Change of the dead time due to the saturation of the preamplifier. With increasing impact kinetic energy the minimum time difference to trigger a proton pulse and hence the dead time increase (see also Fig. 5.22). The colored lines are different fits to the measured data points, except for the blue one. See the following section for details. For elucidation, the horizontal blue line indicates the actual dead time of the electronics (5.2 μs). Data from Ref. [225].

Fn. 10), and tests of the detector electronics can be found in Ref. [52] (see also [34]).

Correction for the Saturation Effect

At first sight, it might be thought that it is easy to correct for the saturation effect, by simply introducing an artificially increased dead time, τ_{art} (see later in Fig. 5.25a). With regard to counting statistics, we cannot select τ_{art} such that we cut away all protons detected in coincidence with the electron from the same decay. Rather, we must determine a minimal artificial dead time, so that the uncertainty in the respective shift in a is small compared to the statistical accuracy. However, the amount of protons detected in coincidence with their correlated electron strongly depends on the spatial separation of electron and proton. The spatial separation, in turn, depends on the settings of all three, the lower and the upper dipole electrodes as well as the height of the main magnetic field (cf. Sec. 5.5.6). That is why, if we introduce an artificially increased dead time, we have to correct for the proton count rate reduction by calculating the proton and electron trajectories (by means of MC simulations). However, in addition to the saturation effect, our data analysis revealed that a fraction of the decay electrons is backscattered from the bottom of the aSPECT spectrometer (for details see the following section). Unfortunately, a fraction of these electrons will be detected in coincidence with the proton from the same decay. Therefore, if we introduce an artificially increased dead time, we also have to correct for their correlated protons. Consequently, we can instead also reproduce the observed shift in the neutrino-electron correlation coefficient a with MC simulations.

Figure 5.24a shows the flow chart of the MC simulation to reproduce both the satura-

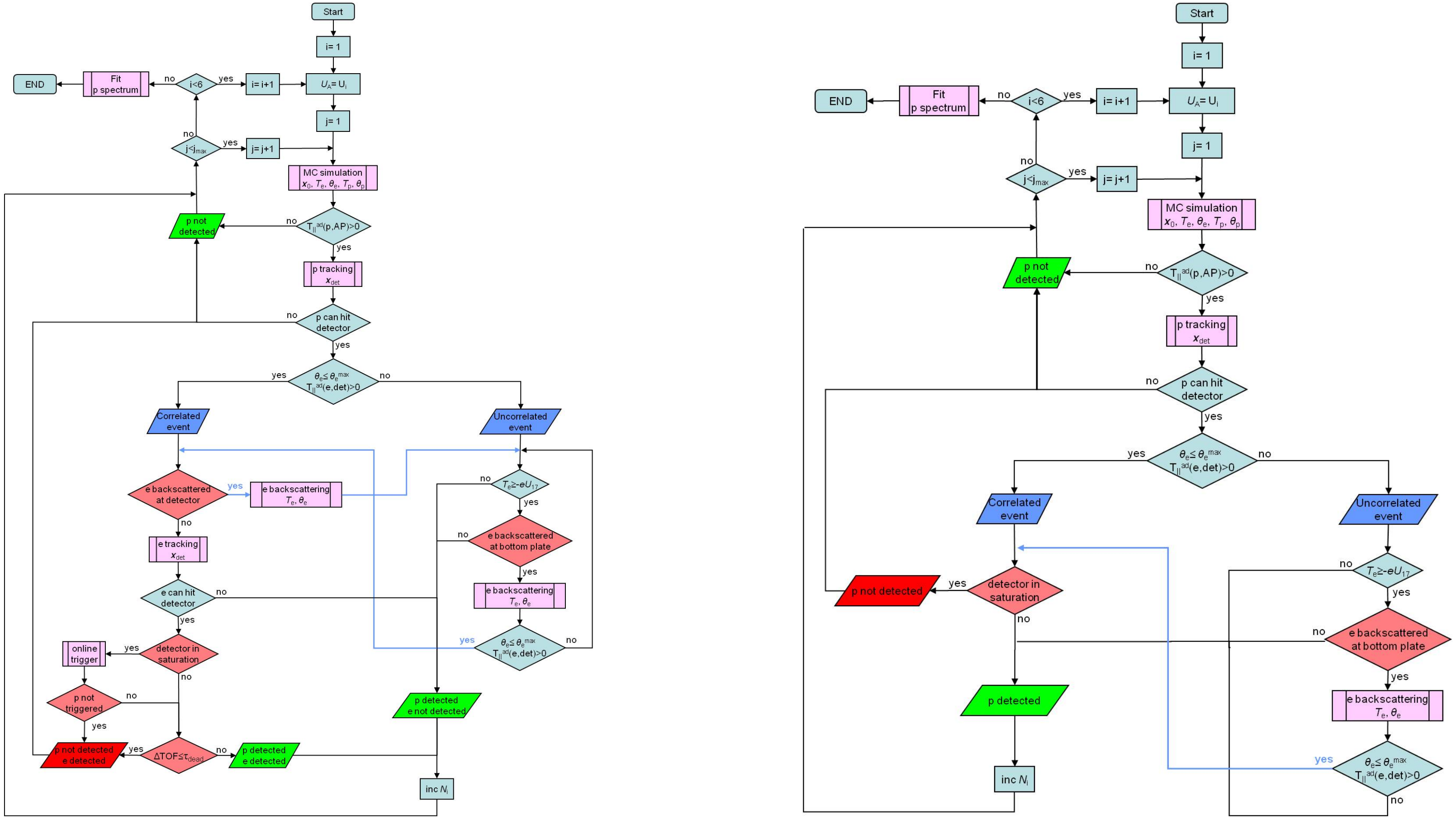

(a) Complete description

(b) Simplified model

Figure 5.24: Flow chart of the MC simulation to reproduce the saturation effect. (a) Complete description of both the saturation of the preamplifier and the electron backscattering inside the *a*SPECT spectrometer. (b) Simplified model to describe both just mentioned effects. We decided to go for model (b), as too many input parameters for the saturation effect could only be determined with large uncertainties [52]. The red highlighted rhombuses and parallelograms indicate decisions and output in connection with the saturation effect.

tion effect and the backscattering of decay electrons inside the spectrometer. With regard to the saturation effect, there are far too many input parameters for the MC simulation which could only be determined with large uncertainties. In particular, there is no correction matrix that describes the relationship between electron impact energy and angle and the energy deposited by the electron in the proton detector (see the previous section and also [52]). Hence, we decided to go for a simplified MC simulation instead, as shown in Fig. 5.24b. In addition, as in the case of our MC Simulations of the edge effect (see also page 161 under "Correction for the Edge Effect"), we decided to derive the impact of the saturation effect on the angular correlation coefficient a from combined MC simulations, where

- MC simulations in (2D) axially symmetric fields serve to determine the dependence of a on the single parameters of the saturation of the preamplifier and
- MC simulations in (3D) non-axially symmetric electric fields serve to determine the dependence of a on the saturation effect for different settings of the spectrometer, i.e., the spatial separation of decay protons and electrons (see later in Table 5.6).

Here, the data from Fig. 5.23 are used as input for the MC simulations. We mention that the impact of the backscattering of decay electrons from the bottom of the spectrometer on a (in combination with the saturation effect) was determined separately (discussed in greater detail in Sec. 5.4.2).

For our standard settings (cf. Table 3.1), but in 2D axially symmetric electric fields, i.e., $U_8 = -525\,\mathrm{V}$ and $U_{16} = -2\,\mathrm{kV}$, the saturation of the preamplifier yields a shift in the neutrino-electron correlation coefficient a of

$$\Delta a/a = \left(-27.28^{+2.14}_{-0.00}\right)\,\%, \tag{5.22}$$

where the error reflects the uncertainty in fixing the relationship between the dead time of the proton detector after an high-energy electron and the energy deposited by the electron in the detector, cf. Fig. 5.23b.

As mentioned in the previous section, in contrast to Fig. 5.23b, we observed "additional" events only less than 20 μs after high-energy electrons. From our 2D MC simulations for different fixed dead times of the proton detector after an high-energy electron, we expect an error in the shift in a of

$$\Delta\left(\Delta a/a\right) = \left(+3.31^{+0.34}_{-1.21}\right)\,\%, \tag{5.23}$$

in agreement with the error identified above in Eq. (5.22).

In addition, as also stated in the previous section, the minimum energy to saturate the preamplifier Eq. (5.21) could only be derived with a relative error of 5 %. From our 2D MC simulations for different fixed minimum energies, we expect an additional uncertainty in the shift in a of

$$\Delta\left(\Delta a/a\right) = \pm 1.44\,\%. \tag{5.24}$$

For our standard settings, but in 3D non-axially symmetric electric fields, i.e., $U_{8\mathrm{R}} = -50\,\mathrm{V}$, $U_{8\mathrm{L}} = -1000\,\mathrm{V}$, and $U_{16\mathrm{A}} = U_{16\mathrm{B}} = -2\,\mathrm{kV}$, the saturation effect yields a shift in the angular correlation coefficient a of

$$\Delta a/a = \left(-17.54 \pm 3.77\right)\,\%, \tag{5.25}$$

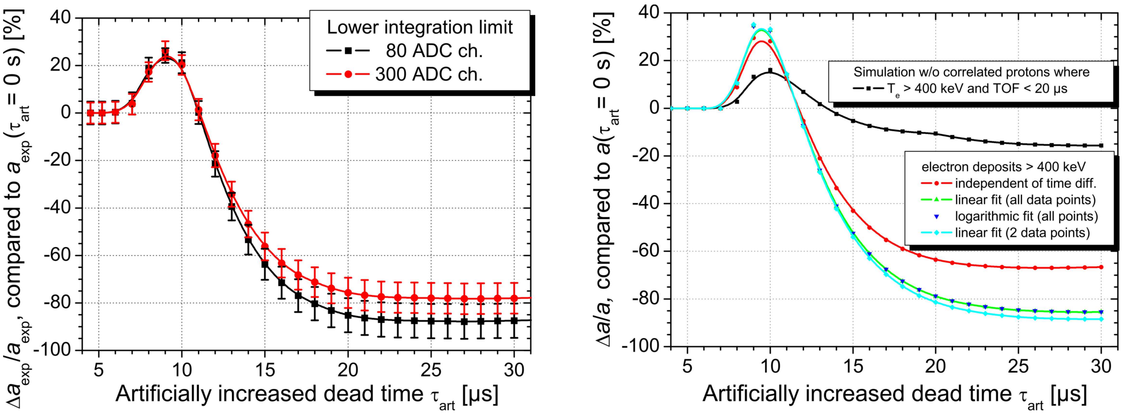

(a) Experimental data (b) 2D MC simulation

Figure 5.25: Relative change of the angular correlation coefficient a for an artificially increased dead time, τ_{art}: (a) Relative change of the uncorrected value, a_{exp}, for a from 19_05_08/night for two different lower integration limits. The error bars show statistical errors only and are strongly correlated, as each data point stems from the same measurement run. (b) Relative change of a for different input parameters for the MC simulation, according to the previous section and Fig. 5.23. Obviously, the linear fit to only two (turquoise) instead of all three (green) data points in Fig. 5.23 has little influence on a, while a logarithmic (blue) instead of the linear fit has no influence on a. See the text for details. Input data for the MC simulation (in INM approximation): $B_0 = 2.177\,\mathrm{T}$, $B_{\mathrm{A}}/B_0 = 0.203$, $U_1 = U_{1\mathrm{b}} = 800\,\mathrm{V}$, $U_2 = 1000\,\mathrm{V}$, $U_8 = -525\,\mathrm{V}$, $U_{\mathrm{A}} = 50, 250, 400, 500, 600\,\mathrm{V}$, $U_{16} = -2\,\mathrm{kV}$, $U_{17} = -15\,\mathrm{kV}$, number of generated events $= 10^7$, and the recommended value for $a = -0.105$ (derived from $\lambda = -1.2701(25)$ [10]). Except for the settings of the lower dipole electrode (e8), the input data correspond to the data set 19_05_08/night.

with a relative error of 21.5 % dominated by simulation statistics (number of generated events $= 6 \times 10^6$). Compared to Eq. (5.22), this corresponds to a reduction of the shift in a due to the spatial separation of decay protons and electrons of

$$\Delta\left(\Delta a/a\right) = \left(+9.54^{+3.77}_{-4.34}\right)\,\%. \tag{5.26}$$

Altogether, the comparison with our calculations in 2D axially symmetric fields results in a shift in the neutrino-electron correlation coefficient a due to the saturation effect of

$$\Delta a/a = \left(-17.54^{+5.23}_{-4.21}\right)\,\%. \tag{5.27}$$

However, Eq. (5.27) only takes into consideration the change of the dead time of the proton detector after high-energy electrons, but it does not include the shift of the proton peaks to lower pulse heights as shown in Fig. 5.22. For this reason, Eq. (5.27) can only serve to correct the experimental values, a_{exp}, for a for a lower integration limit of 0 ADC channels. Unfortunately, due to fluctuations in the electronic noise, we cannot lower the lower integration limit to below ADC channel 80. With regard to the saturation effect, it would not be very serious to, e.g., linearly extrapolate the uncorrected values a_{exp} for a from ADC channel 80 to 0.

On the other hand, we still can investigate the experimental values a_{exp} for a for an artificially increased dead time. Figure 5.25 shows the influence of an artificially increased dead time on the experimental value for a in comparison with the expected values from our 2D MC simulations. Obviously, the functional dependence of the relative shift in a depends on the chosen lower integration limit and particularly on the input parameters for the MC simulation. If we use the data from Fig. 5.23 as input for the MC simulations, then the functional dependence is very similar to the measurement. We note that the deviation from simulation to measurement between $\tau_{\text{art}} = 5$ and $15\,\mu$s is dominated by the poor agreement between the measured and the simulated TOF spectra, cf. Fig. 5.26 (for details see the following section). In addition, the real deviation for $\tau_{\text{art}} = 30\,\mu$s is different from Fig. 5.25b, because of the spatial separation of decay protons and electrons Eq. (5.26).

From the measurements (cf. Fig. 5.25a), we extract an absolute shift in a due to an artificial dead time $\tau_{\text{art}} = 30\,\mu$s of

$$\Delta a_{\text{exp}} = \begin{cases} -0.0809(49) & \text{for} \quad \text{a lower integration limit of 80 ADC ch.} \\ -0.0772(49) & \text{for} \quad \text{a lower integration limit of 300 ADC ch.} \end{cases} \tag{5.28}$$

whereas an absolute shift in a of

$$\Delta a = -0.0881(14) \tag{5.29}$$

from our 2D MC simulations (cf. Fig. 5.25b). The latter has to be corrected for the spatial separation of decay protons and electrons by

$$\Delta a = +0.0100^{+0.0040}_{-0.0046}, \tag{5.30}$$

cf. Eq. (5.26). All three together, we have to correct Eq. (5.27) for the shift of the proton peaks to lower pulse heights by

$$\Delta a/a = \begin{cases} \left(-2.66^{+6.16}_{-6.53}\right)\,\% & \text{for} \quad \text{a lower integration limit of 80 ADC ch.} \\ \left(+0.86^{+6.16}_{-6.53}\right)\,\% & \text{for} \quad \text{a lower integration limit of 300 ADC ch.} \end{cases} \tag{5.31}$$

After correction, we derive a shift in the neutrino-electron correlation coefficient a due to the saturation of the preamplifier of

$$\boxed{\Delta a/a = \begin{cases} \left(-20.20^{+8.08}_{-7.77}\right)\,\% & \text{for} \quad \text{a lower integration limit of 80 ADC ch.} \\ \left(-16.68^{+8.37}_{-8.37}\right)\,\% & \text{for} \quad \text{a lower integration limit of 300 ADC ch.} \end{cases} \quad (5.32)}$$

Strictly speaking, we can only set upper limits on the correction of the problem in the detector electronics, which are too high to determine a new value for the neutrino-electron correlation coefficient a, with a total relative error below the present literature value of 4 % [10], from our latest beam time at the ILL.

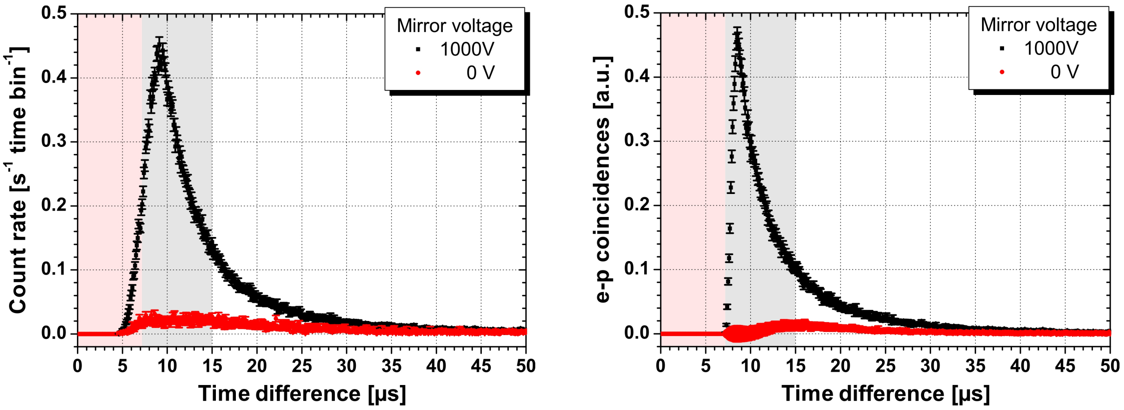

(a) Measurement (b) Simulation

Figure 5.26: (a) Typical (detection) time difference spectra from 18_05_08/morning and 09_05_08/MirrorOff for $U_{\mathrm{A}} = 50\,\mathrm{V}$, with and without electrostatic mirror, respectively. Without electrostatic mirror, only the small fraction of decay protons emitted with angles $0 \leq \theta_0 < 92^\circ$ is detected in coincidence with their correlated electron, cf. Fig. 5.6b. In comparison with Fig. 5.17b, these spectra stem from measurements at a drift potential of $U_{16\mathrm{A}}|U_{16\mathrm{B}} = -4.2\,\mathrm{kV}|-0.2\,\mathrm{kV}$. Due to the increased spatial separation of decay protons and electrons, their peak height is therefore reduced. (b) Simulated TOF spectra with and without electrostatic mirror, corresponding to the data sets 18_05_08/morning and 09_05_08/MirrorOff, respectively. Input data for the MC Simulation (in INM approximation): $B_0 = 2.177\,\mathrm{T}$, $B_{\mathrm{A}}/B_0 = 0.203$, $U_1 = U_{1\mathrm{b}} = 800\,\mathrm{V}$, $U_2 = 1000\,\mathrm{V}$, $U_{8\mathrm{R}} = -50\,\mathrm{V}$, $U_{8\mathrm{L}} = -1000\,\mathrm{V}$, $U_{\mathrm{A}} = 50\,\mathrm{V}$, $U_{16\mathrm{A}} = -4.2\,\mathrm{kV}$, $U_{16\mathrm{B}} = -0.2\,\mathrm{kV}$, $U_{17} = -15\,\mathrm{kV}$, number of generated events $= 2 \times 10^6$, and $a = -0.105$ (derived from $\lambda = -1.2701(25)$ [10]), or, in the case of measurements without electrostatic mirror: $U_1 = U_{1\mathrm{b}} = U_2 \equiv 0$ and $U_{17} = -10\,\mathrm{kV}$. The colorful highlighted areas indicate those areas with poor (red) or moderate (gray) agreement between the measured time difference and the simulated TOF spectra. See the text for details. Error bars show statistical errors only.

5.4.2 Backscattering of Decay Electrons Inside the Spectrometer

As we have seen in the previous section (cf. Fig. 5.25), the credibility of our correction for the saturation effect strongly depends on the simulated proton (and electron) TOF spectra. Figure 5.26 shows measured time difference spectra in comparison with the expected TOF spectra from our MC simulations for two different settings of the electrostatic mirror. As one can see, the simulated TOF spectra show only poor to moderate agreement with the measured ones. In particular, the measured spectra exhibit coincidence events also between the actual dead time ($5.2\,\mu$s) of the proton detector and the minimum TOF ($7.1\,\mu$s) of protons detected in coincidence with the electron from the same decay. Due to the problem in the detector electronics, by contrast, we would expect a count rate loss less than $20\,\mu$s after high-energy electrons (for details see the previous section).

In our measurement, in contrast to the simulation, we cannot decide which proton belongs to which electron. Therefore, the measured time difference spectra also include random coincidence events. Figure 5.27a shows the influence of random coincidence events on the TOF spectra. Obviously, random coincidence events cannot explain the “additional” coincidence events less than $7.2\,\mu$s after an electron.

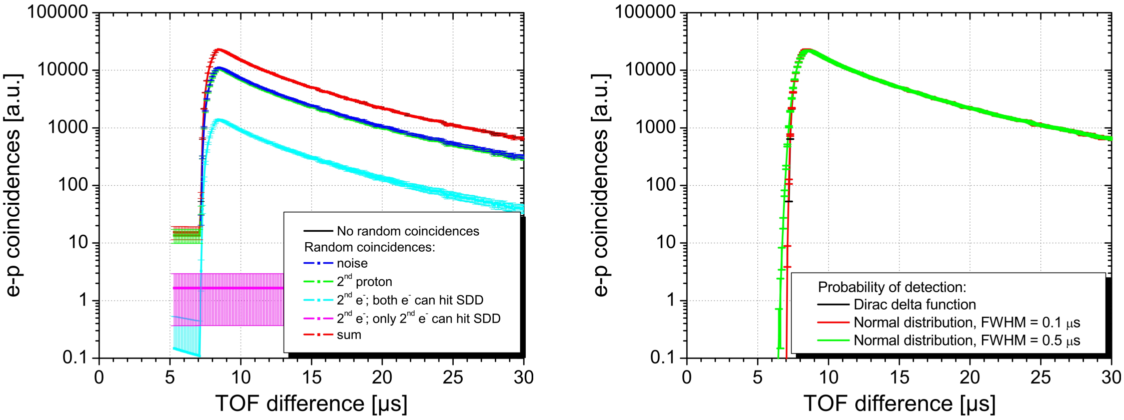

(a) Random coincidences

(b) Gaussian broadening

Figure 5.27: Influence of (a) random coincidence events and (b) a Gaussian broadening due to, e.g. electronic noise on the TOF spectra for $U_\mathrm{A} = 50\,\mathrm{V}$. None of the both effects can explain the deviation from measurement to simulation shown in Fig. 5.26. Input data for the MC Simulation (in INM approximation): $B_0 = 2.177\,\mathrm{T}$, $B_\mathrm{A}/B_0 = 0.203$, $U_1 = U_{1\mathrm{b}} = 800\,\mathrm{V}$, $U_2 = 1000\,\mathrm{V}$, $U_8 = -525\,\mathrm{V}$, $U_{16} = -2\,\mathrm{kV}$, $U_{17} = -15\,\mathrm{kV}$, number of generated events $= 10^8$, and $a = -0.105$ (derived from $\lambda = -1.2701(25)$ [10]). Error bars show statistical errors only.

On the other hand, a Gaussian broadening due to, e.g. electronic noise can explain a minor broadening of the measured time difference spectra, but also not the deviation from simulation to measurement between 5.2 and 7.2 μs, as can be seen from Fig. 5.27b.

In addition, our data analysis has revealed that about

$$r_{\mathrm{e,p}} \overset{\mathrm{def}}{=} \frac{N_\mathrm{e}}{N_0} \approx 20\,\% \tag{5.33}$$

of the decay electrons $(97.45(8)\,\mathrm{s}^{-1}$ for the measurement run 16_05_08/night) are detected in our experiment. In principle decay electrons are detected if and only if they were emitted towards the proton detector and if they can overcome the electromagnetic mirror right in front of the detector (cf. Fig. 3.8). To be specific: decay electrons, emitted towards the proton detector, with kinetic energies less than 15 keV (cf. Fig 5.18) are reflected by the detector potential towards the electrostatic mirror, while electrons with (initial) polar angles of more than 45 ° (see also Fig. 5.28b) are reflected by the magnetic mirror right in front of the detector. Therefore, we expect that only about[11]

$$r_{\mathrm{e,p}} = 13.1\,\% \tag{5.34}$$

of the decay electrons are detected in our experiment. This is far too little to explain the observed fraction Eq. (5.33). We note that the fraction of electrons detected in coincidence with the proton from the same decay is even smaller due to the spatial separation of decay electrons and protons.

As stated earlier on page 120 under “Saturation of the Preamplifier”, not more than 1.66 % of all decay protons are affected by the saturation effect. Assuming that the full

---

[11] Please note that in Refs. [34, 52, 197] the fraction is misstated.

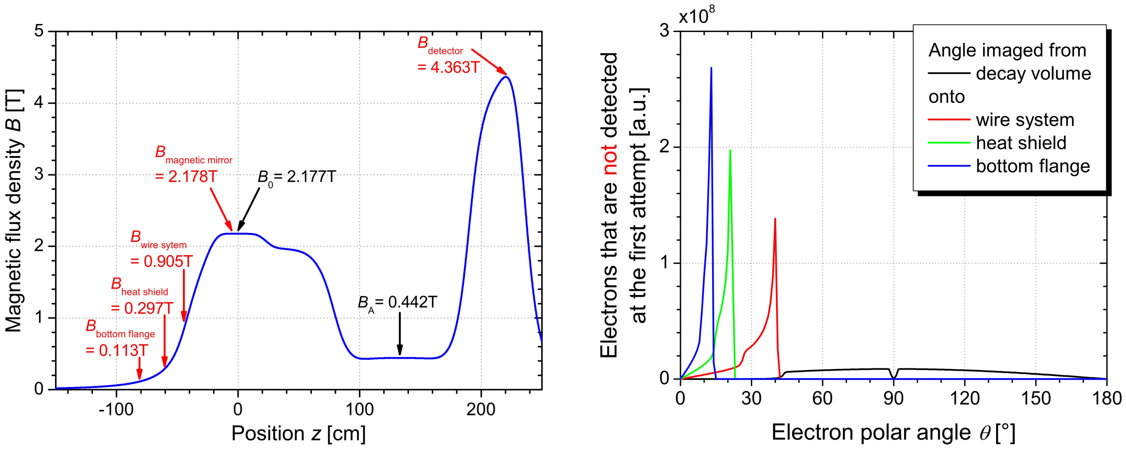

(a) (b)

Figure 5.28: (a) The values of the magnetic field along the z-axis of the aSPECT spectrometer, see Fig. 3.8 for details. Potential places where the decay electrons can be reflected or might be backscattered are additionally highlighted. (b) Angular distribution of those decay electrons that are not detected by the proton detector at the first attempt. From the DV towards the bottom flange, the magnetic field drops down by about a factor of 20. Therefore, from the wire system towards the bottom flange, the maximum incident angle of the electrons is reduced from about 42° to 15°.

proton decay rate N_0 would be reduced by this amount, the observed fraction $r_{\mathrm{e,p}}$ would be increased to only about 13.3 %. This is not enough to explain the observed fraction Eq. (5.33).

On the other hand, backscattering of decay electrons inside the aSPECT spectrometer might explain the observed fraction Eq. (5.33), as shown in the following section. We mention that, compared to Eq. (5.34), only a fraction of about 85 % of all decay electrons might be backscattered, because of the trapping of decay electrons with (initial) polar angles $88° < \theta_0 < 92°$ between both the magnetic mirror just below the DV and right in front of the proton detector (for details see Sec. 5.3.4).

Backscattering from the Bottom of the Spectrometer

As explained above, decay electrons not detected at the first attempt were either emitted towards the electrostatic mirror or reflected towards the electrostatic mirror. Therefore, it is very likely that decay electrons are backscattered from the bottom of the aSPECT spectrometer. There, the electrons can be either backscattered from the wire system (e1), the heat shield(s)[12], or the bottom flange of the spectrometer.

Figure 5.28a shows that, from the DV towards the bottom flange of the spectrometer, the magnetic field drops down by about a factor of 20. For this and geometrical reasons, about 5 % of the decay electrons can hit the wire system, 50 % the heat shield, and 50 %

---

[12] In total, three heat shields were installed between the electrode system and the bottom flange of the spectrometer, to minimize the heat input from the environment to the cold bore tube of the aSPECT magnet. The heat shields are arranged one behind the other. For the power supply of the electrodes e1 to e15b as well as the getter pumps (cf. Fig. 3.9a and also Fn. 25 in Chap. 3), all three heat shields have a cabling hole in their center.

the bottom flange of the spectrometer. Here, the total sum of more than 100 % allows for the possibility that decay electrons are transmitted through the thin (diameter of 125 μm) wires of the wire system. In addition, from the wire system towards the bottom flange, the maximum incident angle of the decay electrons is reduced from about 42° to 15°, as can be seen from Fig. 5.28b.

The backscattering of decay electrons from the bottom of the *a*SPECT spectrometer was investigated with the program CASINO [227, 228] (see also Fn. 10). As input data for the CASINO simulations we have chosen:

Wire system: 125 μm thin bulk of cooper,

Heat shield(s): composed of

1. 1 mm thick substrate of copper,
2. interlayer with 2 μm of silver, and
3. surface coating with 1 μm of gold.

Bottom flange: $>$ 1 mm thick bulk of stainless steel[13].

In contrast to SRIM (cf. Fn. 29 in Chap. 3), CASINO allows only the simulation of one electron energy and incident angle at a time. As can be seen from Fig. 5.29, the penetration depth and hence also the backscatter probability strongly depend on the electron incident energy and angle. Therefore, a matrix of electron incident energies and angles was investigated.

Figure 5.30 shows the results of our CASINO simulations. Obviously, the backscatter probability varies between 14 and 50 %, depending on the incindent energy and angle. However, only a fraction of the backscattered electrons can pass the magnetic mirror below the DV, then overcome the electromagnetic mirror right in front of the proton detector, and finally be detected by the proton detector (cf. Fig. 5.28a).

We mention that our results are in good "agreement" with those presented in Ref. [229] (cf. also [32]), using the ETRAN [230] electron transport code instead. Like in Ref. [229], the energy distribution, $\rho(X)$, of backscattered electrons (see Figs. 5.30b, 5.30d, and 5.30f) could be modeled by a function:

$$\rho(X) = B_0 \exp\left(-\frac{(X-P)^2}{B_1(B_2+X)(B_3-X)}\right), \tag{5.35}$$

where X is the ratio of backscattered energy to incident energy and the parameter P represents the peak of the distribution. The fit parameters P, B_0, B_1, B_2, and B_3 were found to vary with both incident energy and angle. For the MC simulations of the saturation effect, we therefore decided to go for a more simplified model, i.e., by linear interpolation between $(X_0, \rho_0) = (0, 0)$, $(X_1, \rho_1) = (P, \rho(P))$, and $(X_2, \rho_2) = (1, 0)$.

As stated above, decay electrons can also be transmitted through the thin wires of the wire system. Although, the corresponding results of our CASINO simulations are not shown here, they are included in the MC simulations of the saturation effect.

In contrast to more sophisticated programs like, e.g., GEANT4 [231] (see also [232, 233]), CASINO provides no information on the distribution of polar angle, θ_{back}, of

---

[13] The bottom flange is manufactured from stainless steel AISI-No. 316L (EN-norm 1.4404), i.e., it is composed of 17 % Cr, 12 % Ni, 2 % Mo, $<$ 0.08 % C, $<$ 1 % Si, $<$ 2 % Mn, $<$ 0.045 % P, and $<$ 0.03 % S.

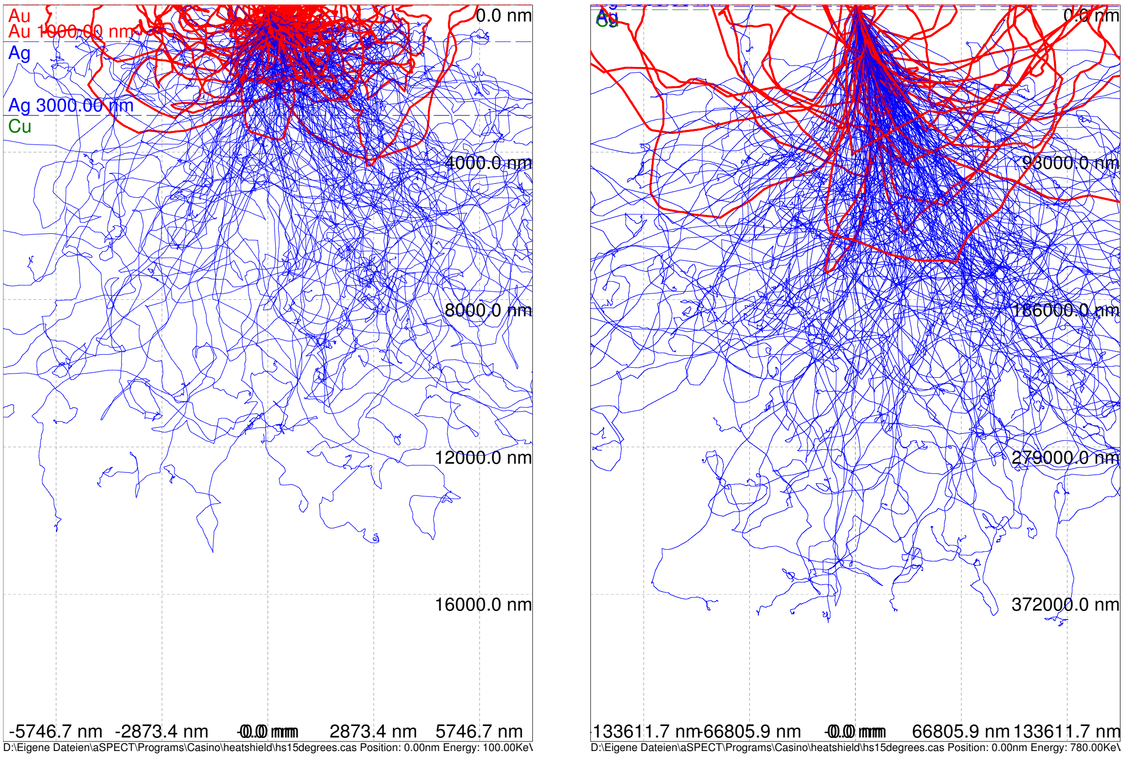

(a) $T_{\text{inc}} = 100\,\text{keV}$ and $\theta_{\text{inc}} = 15\,^\circ$

(b) $T_{\text{inc}} = 780\,\text{keV}$ and $\theta_{\text{inc}} = 15\,^\circ$

Figure 5.29: CASINO simulations of electron trajectories inside an heat shield, with the upper edge as incident surface, for an incident angle of 15 ° and two different incident energies: (a) of 100 keV and (b) of 780 keV. The blue trajectories correspond to electrons which deposit all energy inside the heat shield, whereas the red ones represent electrons which are backscattered from the heat shield. With increasing incident energy the penetration depth increases and therefore the backscatter probability decreases. Please note the different axes ranges in (a) and (b).

backscattered electrons. In Ref. [229], for the case of backscattering from a plastic scintillator, it has been found that this distribution can be well-represented by a parabola with a peak at 135°:

$$\kappa(\theta_{\text{back}}) = 1 - \frac{(\theta_{\text{back}} - 135^\circ)^2}{2025}, \tag{5.36}$$

where θ_{back} is measured with respect to the incident normal, i.e., $\theta_{\text{back}} = 180\,^\circ$ corresponds to backscatter perpendicular to the surface. If this were the true representation of the distribution, we would expect that in our experiment a fraction of

$$r_{\text{back}} = 1.3\,\% \tag{5.37}$$

of all decay electrons is detected additionally to Eq. (5.34). This is too little to explain the observed fraction Eq. (5.33). Hence, we developed our own model to describe the distribution:

$$\kappa(\theta_{\text{back}}) = \begin{cases} 1 - \frac{|\theta_{\text{back}}+\theta_{\text{inc}}|^{2-\theta_{\text{inc}}/90^\circ}}{|90^\circ+\theta_{\text{inc}}|^{2-\theta_{\text{inc}}/90^\circ}} & \text{for} \quad \theta_{\text{back}} > -\theta_{\text{inc}} \\ 1 - \frac{|\theta_{\text{back}}+\theta_{\text{inc}}|^{2-\theta_{\text{inc}}/90^\circ}}{|-90^\circ+\theta_{\text{inc}}|^{2-\theta_{\text{inc}}/90^\circ}} & \text{for} \quad \theta_{\text{back}} < -\theta_{\text{inc}} \end{cases}, \tag{5.38}$$

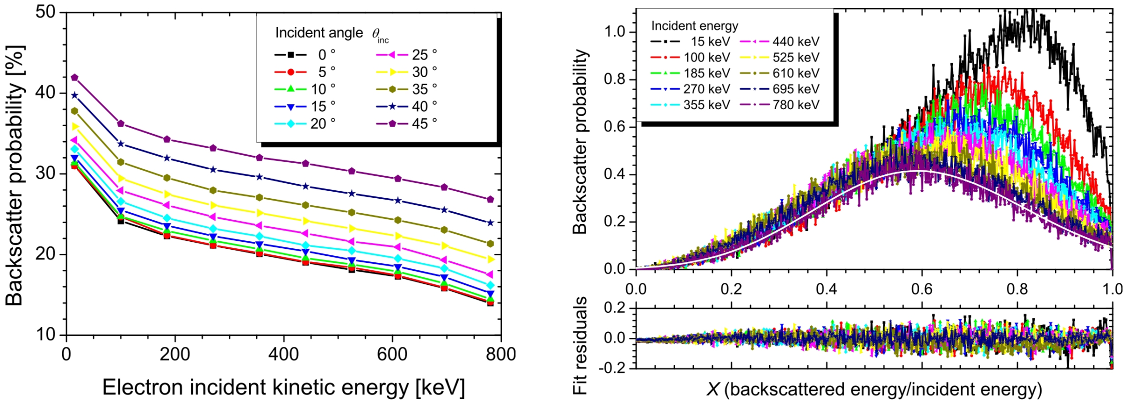

(a) Wire system (b) Wire system

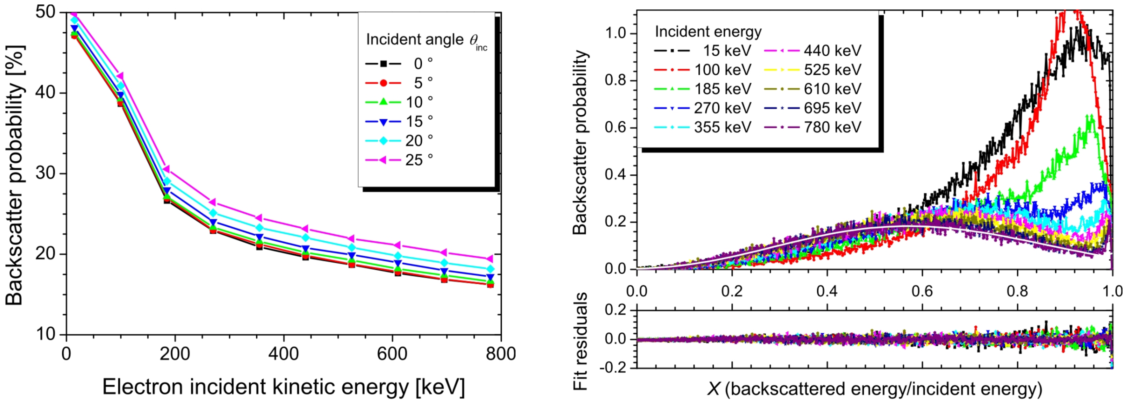

(c) Heat shield (d) Heat shield

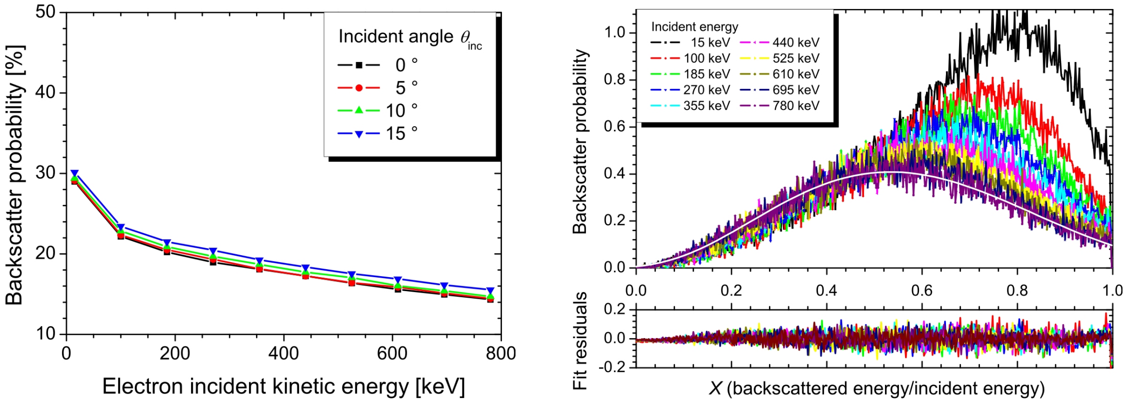

(e) Bottom flange (f) Bottom flange

Figure 5.30: Backscatter probability from the bottom of the *a*SPECT spectrometer for different incident energies and angles. (a), (c), and (e) show the backscatter probability from the wire system, the heat shield(s), and the bottom flange, respectively, as a function of the electron incident angle, while (b), (d), and (f) present the energy distribution Eq. (5.35) of backscattered electrons for an incident angle of 15 °. The fit residuals indicate that our results are in good “agreement” with those presented in Ref. [229].

where θ_{inc} denotes the incident polar angle. Here, $-90\,^\circ < \theta_{\text{back}} < 90\,^\circ$ is measured with respect to the z-axis of the spectrometer, i.e., $\theta_{\text{back}} = 0\,^\circ$ corresponds to backscatter

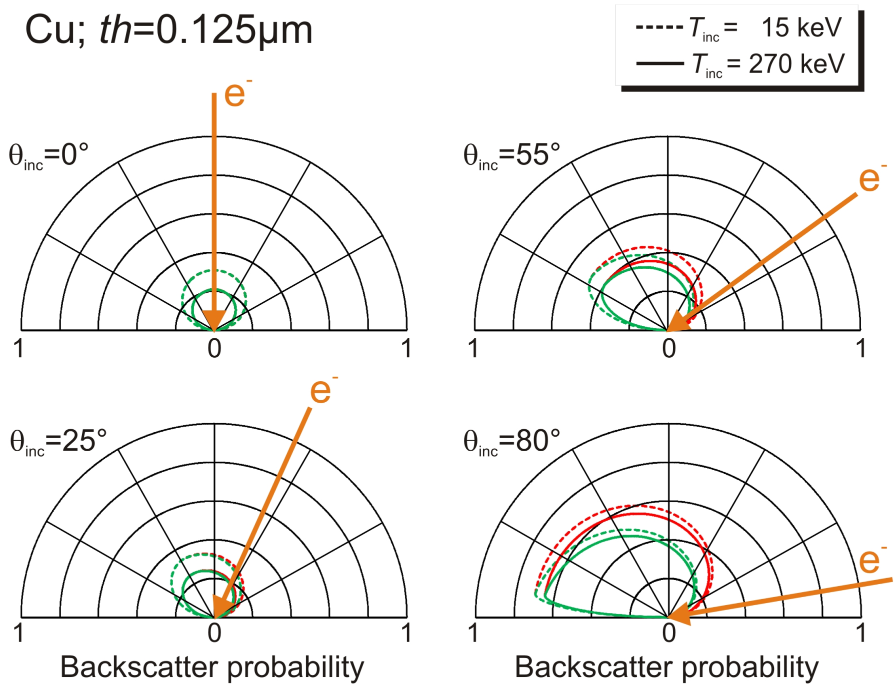

Figure 5.31: Angular distribution of backscattered electrons from copper for different incident energies and angles. The green lines correspond to our own model Eq. (5.38), while the red lines represent a slightly different angular distribution. Namely, a distribution in which the exponents in Eq. (5.38) have been replaced by 2. The model is based on measurements of backscattered electrons from copper, silver, and gold [234].

perpendicular to the surface. We note that our model, shown in Fig. 5.31, is based on measurements of backscattered electrons from aluminum, copper, silver, and gold [234].

Figure 5.32 shows the energy and angular distributions of backscattered electrons from the bottom of the spectrometer, but now based on our model Eq. (5.38). For this model, we expect that in our experiment a fraction of

$$\boxed{r_{\mathrm{back}} = \left(4.24^{+3.12}_{-1.52}\right)\,\%} \tag{5.39}$$

of all decay electrons is detected additionally to Eq. (5.34), in moderate agreement with the observed fraction Eq. (5.33). Here, the error stems from the uncertainty in the polar angle θ_{back} of backscattered electrons. We note that, apart from Eq. (5.38), several different models were investigated. We further note that our investigation did not include the possibility that backscattered electrons, not detected at the second attempt, might be again backscattered from the bottom of the spectrometer, but then into angles $\theta_{\mathrm{back}} \approx 0°$ and therefore be detected at the third attempt. In this context it has to be mentioned, that in total about 21.9 % of all decay electrons might be reflected from the bottom of the *a*SPECT spectrometer, whereas only $\left(7.0^{+4.3}_{-0.0}\right)\,\%$ can also overcome the magnetic mirror below the DV.

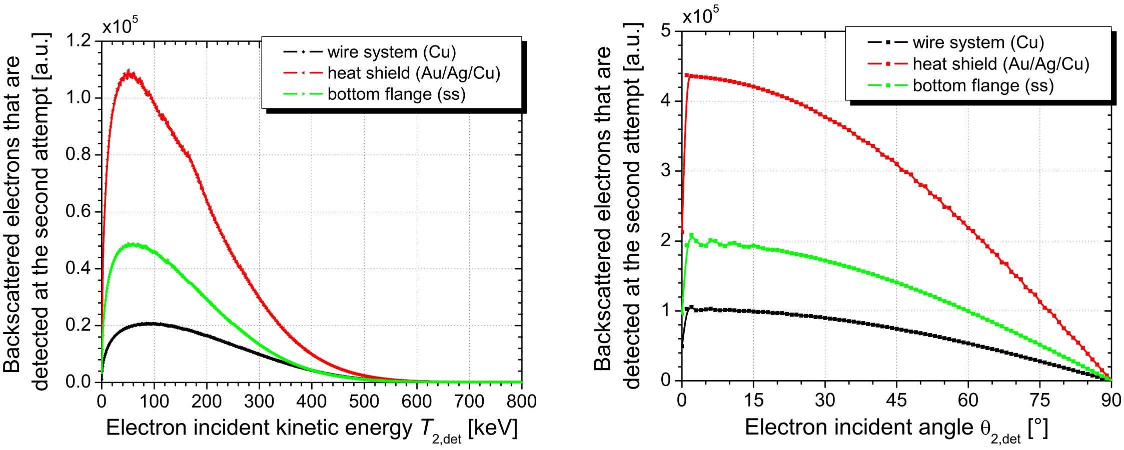

(a) (b)

Figure 5.32: (a) Energy and (b) angular distributions of backscattered electrons which are detected by the proton detector at the second attempt, according to Figs. 5.28b, 5.30, and Eq. (5.38). From the wire system towards the bottom flange, the magnetic field drops down (cf. Fig. 5.28a). Therefore, about 1:4:2 electrons are backscattered from the wire system, the heat shield(s), or the bottom flange of the spectrometer, respectively.

Influence on the Measured Time-of-Flight Spectra

Figure 5.33 shows the measured time difference spectra, previously shown in Fig. 5.26, but now in comparison with the simulated TOF spectra considering both the backscattering of decay electrons from the bottom of the *a*SPECT spectrometer and the saturation of the preamplifier (for details see page 123 under “Correction for the Saturation Effect”). In the case of measurements without electrostatic mirror, the backscattering of decay electrons can resolve the deviation from simulation to measurement completely. In contrast, in the case of measurements with electrostatic mirror, the backscattering of decay electrons can only partly explain the deviation from simulation to measurement. We note that, in the case of measurements without electrostatic mirror, the TOF spectra of backscattered electrons were scaled down by a multiplication factor of 1/3, in order to fit the measured time difference spectra. This takes into account the spatial separation of decay protons and electrons achieved by both, the lower and the upper, dipole electrodes. In the case of measurements with electrostatic mirror, the TOF spectra of backscattered electrons were subsequently scaled down by a multiplication factor of only 1/2 (see also [34]), as in these measurements the upper dipole electrode was used as a cylindrical electrode instead.

As one can see from Fig. 5.6b, TOF differences of less than $9\,\mu$s can be clearly assigned to decay protons emitted towards the electrostatic mirror, with (initial) polar angles greater than 130 °. Therefore, possible causes for the remaining deviation are:

- proton reflections from the DV due to a charging of the collimation system (investigated in Sec. 5.4.4) or
- a violation of the condition for adiabatic transport due to an enhanced energy transfer from transverse to longitudinal motion (discussed in Sec. 5.4.3).

Since coincidence events additionally to the backscattered electrons did not show up in measurements without electrostatic mirror, proton reflections from the DV can be ruled

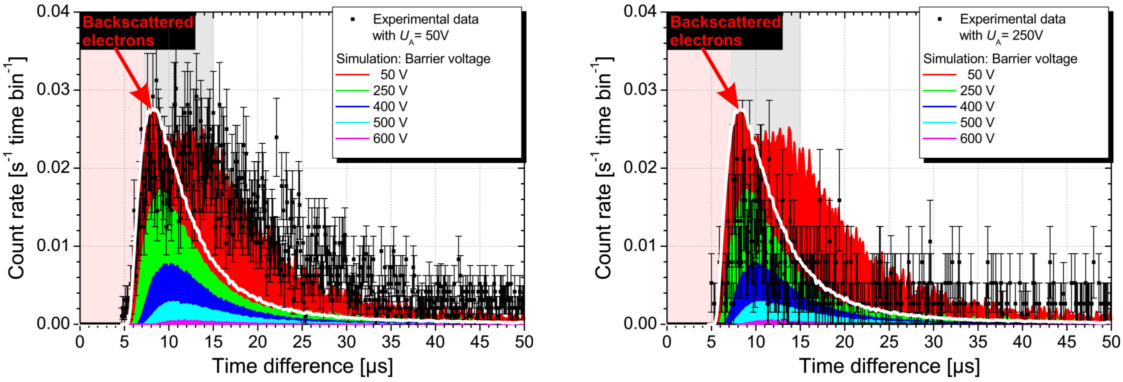

(a) $U_{\mathrm{A}} = 50\,\mathrm{V}$ (b) $U_{\mathrm{A}} = 250\,\mathrm{V}$

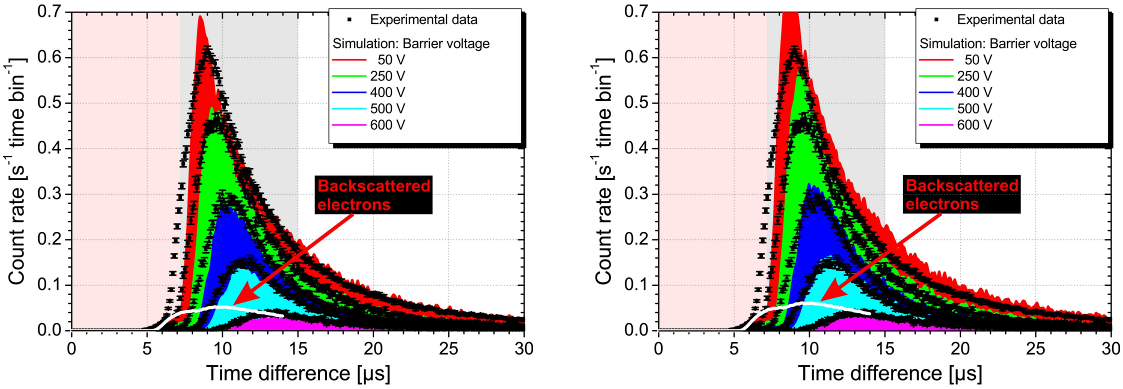

(c) Scaled to exponential decay at $U_{\mathrm{A}} = 50\,\mathrm{V}$ (d) Scaled to $U_{\mathrm{A}} = 500\,\mathrm{V}$

Figure 5.33: Time difference spectra considering both the backscattering of decay electrons from the bottom of the aSPECT spectrometer and the saturation of the preamplifier. (a) and (b) correspond to the data set 09_05_08/MirrorOff, while (c) and (d) correspond to the data set 18_05_08/morning, see Fig. 5.26 for details. Only in the case of measurements without electrostatic mirror, the backscattering of decay electrons can resolve the deviation from simulation to measurement completely. The comparison between (c) and (d) shows that different scales, because of, e.g., the saturation effect, can at least minimize the deviation from simulation to measurement. See the text for details. Error bars show statistical errors only.

out as main explanation for the deviation from simulation to measurement. Hence, we suggest to decrease the electrostatic mirror potential, in a further beam time.

Correction for the Backscattering of Decay Electrons

From our 3D MC simulations of the saturation effect (for details see page 123 under "Correction for the Saturation Effect"), we determine a shift in the neutrino-electron correlation coefficient a due to the backscattering of decay electrons from the bottom of the aSPECT spectrometer of

$$\boxed{\Delta a/a = (-0.38 \pm 3.46)\,\%} \tag{5.40}$$

where the relative error is dominated by simulation statistics (number of generated events $= 6 \times 10^6$). We note that, strictly speaking, this is an additional shift in a due to the saturation effect.

Table 5.4: Proton count rates from 17_05_08/night2 and 18_05_08/night respectively 20_05_08/lunch and 20_05_08/night (after correction for the different magnetic field ratio, cf. Sec. 5.5.4) for our typical mirror settings $U_2 = 1000\,\mathrm{V}$ respectively $U_2 = 820\,\mathrm{V}$. For comparison, the third, fifth, and seventh column represent the expected count rates from our MC simulations. We note that the simulated count rates were normalized to the measured proton count rate for $U_2 = 820\,\mathrm{V}$ and $U_\mathrm{A} = 50\,\mathrm{V}$. See the text for details. Input data for the MC simulation (in INM approximation): $B_0 = 2.177\,\mathrm{T}$, $B_\mathrm{A}/B_0 = 0.203$, $U_1 = U_\mathrm{1b} = 800\,\mathrm{V}$, $U_\mathrm{8R} = -50\,\mathrm{V}$, $U_\mathrm{8L} = -1000\,\mathrm{V}$, $U_\mathrm{16A} = U_\mathrm{16B} = -2\,\mathrm{kV}$, $U_{17} = -15\,\mathrm{kV}$, number of generated events $= 6 \times 10^6$ (for each mirror voltage), and $a = -0.105$ (derived from $\lambda = -1.2701(25)$ [10]). The following abbreviations appear: avg (average value) and CPS (count rate or counts per second).

	$U_2 = 1000\,\mathrm{V}$		$U_2 = 820\,\mathrm{V}$			
U_A [V]	avg CPS measured [s^{-1}]	CPS simulated [s^{-1}]	avg CPS measured [s^{-1}]	CPS simulated [s^{-1}]	ΔCPS measured [s^{-1}]	ΔCPS simulated [s^{-1}]
50	469.60(33)	467.25(35)	467.15(29)	467.15(35)	−2.46(44)	−0.10(49)
250	302.31(29)	300.45(28)	300.59(29)	300.34(28)	−1.72(41)	−0.11(40)
400	151.01(23)	149.91(20)	149.78(21)	149.77(20)	−1.23(31)	−0.14(28)
500	62.42(15)	62.10(13)	61.63(13)	62.11(13)	−0.78(20)	0.01(18)
600	10.43 (9)	10.33 (5)	10.27 (8)	10.32 (5)	−0.16(12)	−0.01 (7)

5.4.3 Dependence of a on the Electrostatic Mirror Potential

During our latest beam time, the mirror potential U_2 was reduced from 1000 V to 820 V. The data analysis has revealed that with decreasing mirror potential

- the proton count rates drop down by up to $2.46(44)\,\mathrm{s}^{-1}$ for $U_\mathrm{A} = 50\,\mathrm{V}$, as can be seen from Table 5.4, and
- the uncorrected value for the angular correlation coefficient a is reduced by

  $$\Delta a_\mathrm{exp}/a_\mathrm{exp} = (-4.55 \pm 2.63)\,\% \tag{5.41}$$

  from $a_\mathrm{exp} = -0.0978(29)$ to $a_\mathrm{exp} = -0.1025(28)$.

Non-Adiabatic Proton Motion

From our MC simulations, we expect far less reduced $\left(\mathcal{O}\left(0.1\,\mathrm{s}^{-1}\right)\right)$ proton count rates, as can be seen from Table 5.4, but also a smaller shift in a of

$$\boxed{\Delta a/a = (-0.55 \pm 3.40)\,\%} \tag{5.42}$$

Here, the error is dominated by simulation statistics (number of generated events $= 6 \times 10^6$, for each mirror voltage). We believe that this shift is due to an enhanced energy transfer from transverse to longitudinal motion for $U_2 = 1000\,\mathrm{V}$: Decay protons emitted in the negative z-direction are reflected by the electrostatic mirror at the latest at $z = -298.5\,\mathrm{mm}$ for $U_2 = 1000\,\mathrm{V}$ whereas at $z = -318.5\,\mathrm{mm}$ for $U_2 = 820\,\mathrm{V}$.

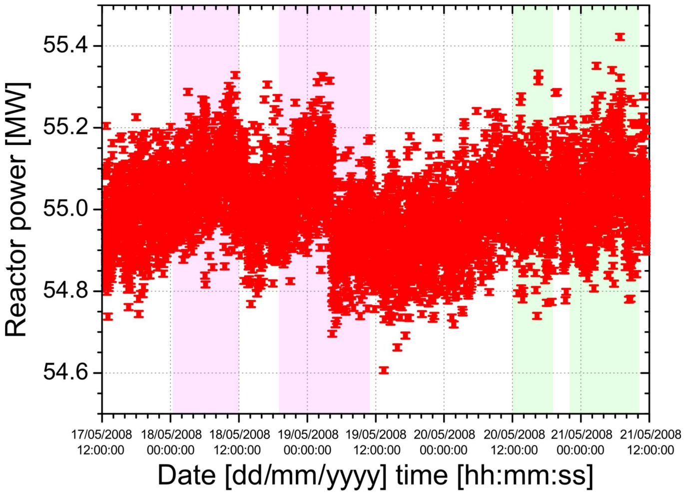

Figure 5.34: Reactor power as measured from the ILL. The colorful highlighted areas correspond to the measurement runs 17_05_08/night2 and 18_05_08/night with $U_2 = 1000\,\mathrm{V}$ (red) respectively 20_05_08/lunch and 20_05_08/night with $U_2 = 820\,\mathrm{V}$ (green). For different measurement runs, the reactor power changes by $\pm 0.18\,\%$ (mean value).

However, this is far too little to explain the observed shift Eq. (5.41) or the count rate losses for $U_2 = 820\,\mathrm{V}$. The latter could be explained by a reduced reactor power during our measurements with $U_2 = 820\,\mathrm{V}$. As can be seen from Fig. 5.34, a change in the reactor power of $\pm 0.18\,\%$ (mean value) for different measurement runs is realistic. A reduction in that order would correspond to a decrease of the proton count rate of about $1\,\mathrm{s}^{-1}$ for $U_\mathrm{A} = 50\,\mathrm{V}$. This is still too little to explain the observed count rate loss of up to $2.46(44)\,\mathrm{s}^{-1}$ for $U_\mathrm{A} = 50\,\mathrm{V}$.

Penning Discharges in the Bottom of the Spectrometer

On the other hand, it is also possible that the supposed count rate loss for $U_2 = 820\,\mathrm{V}$ is actually a rise in the AP dependent background for $U_2 = 1000\,\mathrm{V}$. The electric field distribution exhibits a saddle point at the electrostatic mirror. Our electric field calculations (see also Fig. 3.11 and our note on page 62) have shown that with increasing mirror potential the saddle point is shifted from $z = -364\,\mathrm{mm}$ to $z = -330.5\,\mathrm{mm}$. At the same time, its potential is increased from about 800 to $911.5\,\mathrm{V}$, while the potential at height of the wire system (e1), of at least $782.5\,\mathrm{V}$ over the entire flux tube, remains unaffected (see also Fig. 3.11). Hence, for $U_2 = 1000\,\mathrm{V}$, the potential at the saddle point might be too high to prevent Penning discharges in the bottom part of the *a*SPECT spectrometer [235] (see also page 56 under "Penning Traps and Penning Discharge"). For $U_\mathrm{A} \geq 726\,\mathrm{V}$, only a part of this background contribution can pass the AP, because of the electric retardation method of *a*SPECT. Thus, neither a background measurement with $U_\mathrm{A} = 780\,\mathrm{V}$ (discussed in Sec. 5.2.2) nor measurements with closed neutron shutter (for details see Sec. 5.3.1) are sufficient to determine such a background contribution. Ultimately, the proton count rates are larger by this background contribution. Figure 5.35 gives an impression of how such a background contribution could depend on the barrier voltage U_A. In comparison with Fig. 5.11 the observed shift Eq. (5.41) is realistic. Assuming that the additional background contribution would be as large as shown in Fig. 5.35 (green

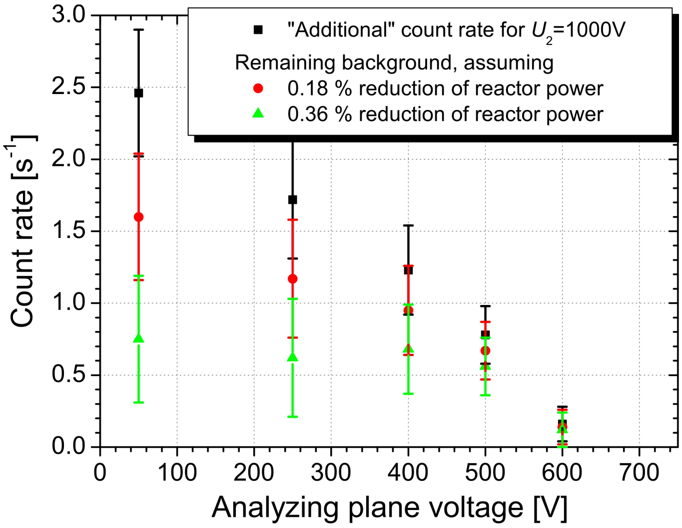

Figure 5.35: "Additional" count rate for $U_2 = 1000\,\mathrm{V}$ compared to $U_2 = 820\,\mathrm{V}$ versus barrier voltage U_A, before (black) and after correction (red) for a reduction of the reactor power corresponding to Fig. 5.34. For comparison, the green triangles show the remaining count rates after double correction for the reduction of the reactor power. We mention that such a reduction reflects the possible influence of a charging of the collimation system (discussed in the following section). Input data for the correction: $B_\mathrm{A}/B_0 = 0.203$ and $a = -0.103$ [10]. Error bars show statistical errors only.

triangles), the neutrino-electron correlation coefficient a would be shifted by

$$\boxed{\Delta a/a = (+8.50 \pm 4.03)\,\%} \tag{5.43}$$

with a relative error of 47 % dominated by counting statistics.

We note that the non-adiabatic proton motion issue can be easily solved by

- electrically decoupling the wire system from its holding electrode (e1b) and subsequently
- swapping the mirror voltages U_1 and U_2, to, e.g., $U_1 = 800\,\mathrm{V}$, $U_{1\mathrm{b}} = 860\,\mathrm{V}$, and $U_2 \leq 400\,\mathrm{V}$,

in a further beam time. Our electric field calculations suggest that, then, decay protons emitted in the negative z-direction are reflected at the latest at $z \leq -371\,\mathrm{mm}$. At the same time, the saddle point is shifted to $z \leq -406\,\mathrm{mm}$ and its potential is reduced to less than 815.5 V. A more sophisticated analysis will be part of further investigations (by means of MC simulations). However, the question remains whether the observed shift Eq. (5.41) was mainly due to Penning discharges in the bottom part of the spectrometer. Hence, we strongly recommend to further investigate this systematic effect, in a further beam time. In particular, we propose background measurements with different barrier voltages $U_\mathrm{A} = U_\mathrm{back} > T_\mathrm{p,max}$ and measurements with different mirror potentials $U_1 \sim U_\mathrm{back}$. To obtain meaningful results from these measurements, we highly recommend to improve the stability of the neutron beam monitor (discussed in Sec. 4.2.1); in order to normalize the measured proton count rates to the measured neutron count rates.

5.4.4 Charging of the Collimation System

In addition, our data analysis revealed that for

Measurements in November/December 2007: the proton count rates decreased with time (cf. Fn. 9 in Chap. 3). We are convinced that the two ceramics rings (previously used to electrically decouple the long DV cylinders e3 and e6 from the DV electrode gr) got charged by the decay protons and electrons, what may have had the effect of proton reflections from the DV (discussed in Sec. 6.4.3).

Measurements with a reduced width of the neutron beam: (see also Sec. 5.5.6)

20 mm wide aperture:

- less than 30 % of the measurements show a contribution (> 0 counts for shutter status 5, i.e., when the neutron shutter is closed for 10 s) to background peak 1, compared to up to 75 % for the standard beam width [34]. And less than 15 % of the measurements show a contribution to background peak 2, compared to up to 65 % for the standard beam width [34].
- the proton count rate drops down by $-11.03(9)\,\%$ from $471.5(3)\,\mathrm{s}^{-1}$ (16_05_08/night) to $419.5(3)\,\mathrm{s}^{-1}$ (15_05_08/night), while the electron count rate remains unaffected ($97.52(8)\,\mathrm{s}^{-1}$ for the measurement run 15_05_08/night versus $97.45(8)\,\mathrm{s}^{-1}$ for 16_05_08/night).

5 mm wide aperture: the uncorrected value for the neutrino-electron correlation coefficient a decreases by

$$\Delta a_{\mathrm{exp}}/a_{\mathrm{exp}} = (-33.93 \pm 7.00)\,\% \tag{5.44}$$

from $a_{\mathrm{exp}} = -0.1014(40)$ (20_04_08/night) to $a_{\mathrm{exp}} = -0.1358(48)$ (16_04_08/night). From our MC simulations of the edge effect (see Sec. 5.5.6 for details), we expect a shift in a at the level of $-10\,\%$. But after considering the saturation of the preamplifier (discussed on page 123 under “Correction for the Saturation Effect”), we expect a shift in a at the level of $-40\,\%$, in agreement with the observed shift Eq. (5.44) (cf. also Fn. 7).

Measurements with a reduced height of the main magnetic field: cf. Sec. 4.2.5

- the slope of the background count rate (cf. Fig. 5.10) increases by a factor of about 2, for both background peak 1 and peak 2 [34].
- the uncorrected value for the angular correlation coefficient a increases by

$$\Delta a_{\mathrm{exp}}/a_{\mathrm{exp}} = (+31.97 \pm 4.16)\,\% \tag{5.45}$$

from $a_{\mathrm{exp}} = -0.1025(28)$ for $B_0 = 2.177\,\mathrm{T}$ to $a_{\mathrm{exp}} = -0.0697(38)$ for $B_0 = 0.933\,\mathrm{T}$ (21_05_08/night). From our MC simulations (for details see Secs. 5.5.5 and 5.5.6), we expect a shift in a at the level of -5 to $-20\,\%$. Compared with the observed shift Eq. (5.45), this is a shift in the wrong direction.

On the basis of our experiences from November/December 2007 and our measurements with a reduced width of the neutron beam respectively a reduced height of the main magnetic field, we suspect that the collimation system, shown in Fig. 5.36, got charged

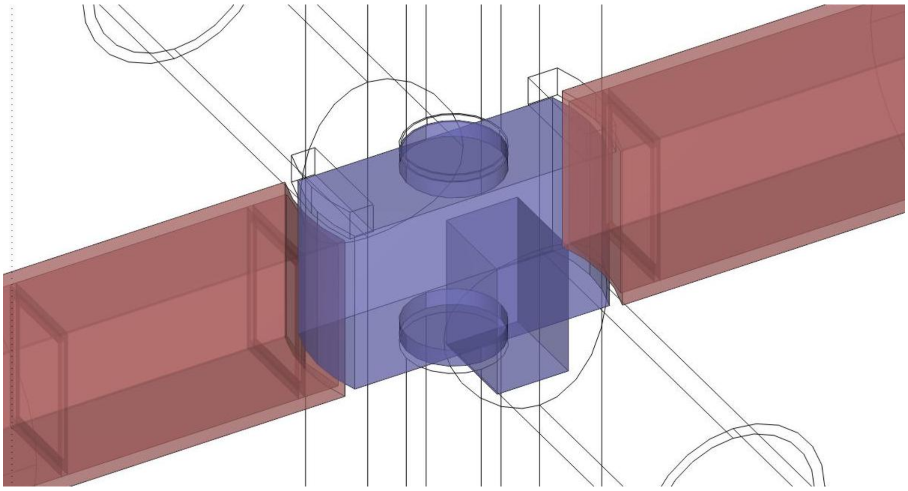

Figure 5.36: A sketch of the collimation system inside the spectrometer. The ruby highlighted parts show the ^{6}LiF orifices E2, E3, and A1 (cf. Fig. 4.1) and the boron loaded glass before and behind the decay volume (DV), while the pastel blue rectangular tunnel shows the DV electrode gr with an opening on one side for vacuum pumping (cf. also Fn. 8 in Chap. 3). Neutrons are coming from the left and are guided and shaped by the collimation system through the aSPECT magnet to a beam stop (to the right of the scheme; not shown here). We suspect that the collimation system got charged by the decay electrons and protons, cf.Fig. 5.37.

by the decay electrons and protons. We note that with increasing width of the additional aperture (cf. Sec. 4.1.3) not only the width of the neutron beam inside the DV decreases by about a factor of 2 or 3 from about 54 to 36 or 18 mm, but also the total neutron flux[14] decreases by about a factor of 1.5 or 4.5, for the 20 or 5 mm wide aperture, respectively.

Similar experiences of the PERKEO II collaboration suggest a charging at the level of 100 V [236]. Figure 5.37 gives an impression of how such a charging of the collimation system may have changed the electric field distribution inside the DV, which is usually grounded. For example, we assumed an asymmetrical charging of the collimation system, i.e., a potential of -150 V for the three ^{6}LiF orifices E1, E2, and E3 (see Fig. 4.1) and the boron loaded glass before the DV, while -50 V for the two ^{6}LiF orifices A1 and A2 (see also Fig. 4.1) and the boron loaded glass behind the DV. This has two consequences:

- the electric field distribution exhibits a saddle point in the DV (see Fig. 5.37a), i.e., a local minimum in the y-z-plane (see Fig. 5.37b). Thus decay protons may be reflected from both the top and the bottom end of the DV electrode gr and finally trapped inside the DV. We note that, for the bottom half of the neutron beam, also decay electrons emitted almost perpendicular to the magnetic field may be reflected from the local electric field minimum in the DV. This, in turn, is at least a partial explanation for the constant electron count rate independent of the neutron beam width. Inside the DV the electric field gradient $\partial U_0/\partial z$ is around $-125\,\mathrm{mV\,cm^{-1}}$ for $z < 0$ and $+125\,\mathrm{mV\,cm^{-1}}$ for $z \geq 0$. The latter corresponds to a shift in a of

$$\Delta a/a = (+21.82 \pm 1.95)\,\%, \tag{5.46}$$

---

[14] To be precise: The measured neutron flux, assuming that the peak value remains unaffected. For comparison, in Ref. [34] it was derived that the calculated neutron flux decreases by about a factor of 1.85 in the case of the 20 mm wide aperture.

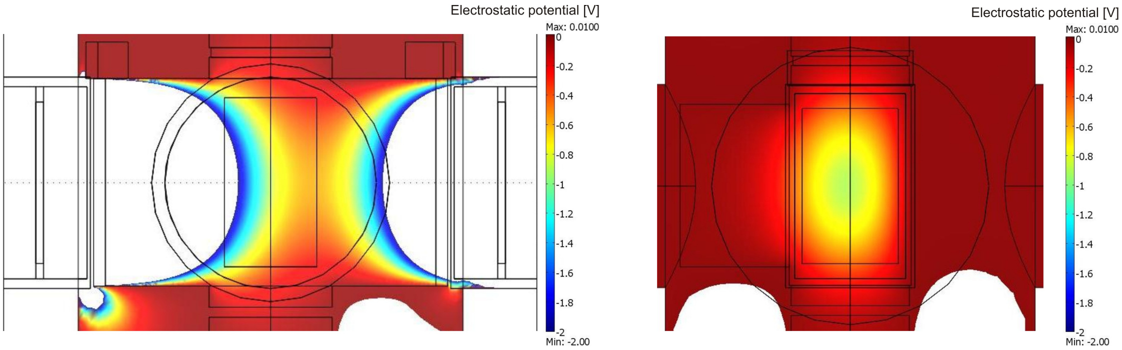

(a) x-z plane (b) y-z plane

Figure 5.37: Influence of a possible charging of the collimation system on the electric potential in the decay volume (DV) (a) in the x-z-plane for $y = 0$ and (b) in the y-z-plane for $x = 0$. In our measurement, it is assumed that the DV is grounded, but in this event, the real potential inside the DV drops down to up to $-2\,\mathrm{V}$. See the text for details. Here, the black lines represent the DV electrodes e3, gr, and e6, the ^{6}LiF orifices E3 and A1 (cf. Fig. 4.1), and the boron loaded glass before and behind the DV.

according to Fig. 6.23 in Chap. 6. This is still too little to explain the observed shift Eq. (5.45). But in addition, the electric field gradient $\partial U_0/\partial z \approx -125\,\mathrm{mV\,cm^{-1}}$ for $z < 0$ can lead to a violation of the condition for adiabatic transport. Therefore, the angular correlation coefficient a would be shifted to even more positive values. This could be part of further investigations (by means of MC simulations). We note that, depending on the real electric field distribution, an electric field parallel to the neutron beam could help to sweep out decay protons that would otherwise be trapped.

- the real potential inside the DV drops down from nearly zero to up to $-2\,\mathrm{V}$. Assuming an overall decreased electrostatic potential in the DV of $U_0 = -1\,\mathrm{V}$, i.e., $\Delta(U_\mathrm{A} - U_0) = +1\,\mathrm{V}$, the angular correlation coefficient a would be shifted by

$$\Delta a/a = (+12.40 \pm 1.53)\,\%, \tag{5.47}$$

according to Fig. 3.6. This alone is too little to explain the observed shift Eq. (5.45). We mention that with a reduced height of the main magnetic field also the drift perpendicular to both the electric and the magnetic field increases (cf. Eq. (3.39)). From our MC simulations, we expect a drift at the height of the proton detector of

$$\Delta x = \begin{cases} -5\,(4)\ \mathrm{mm} \ , & \text{for } B_0 = 0.933\,\mathrm{T} \\ -2\,(2)\ \mathrm{mm} \ , & \text{for } B_0 = 2.177\,\mathrm{T} \end{cases} \tag{5.48}$$

$$\Delta y = \begin{cases} (-1.5 \pm 4.5)\ \mathrm{mm} \ , & \text{for } B_0 = 0.933\,\mathrm{T} \\ 0\,(2)\ \mathrm{mm} \ , & \text{for } B_0 = 2.177\,\mathrm{T} \end{cases} \tag{5.49}$$

for our standard drift potentials $U_\mathrm{8R}|U_\mathrm{8L} = -50\,\mathrm{V}|{-1000}\,\mathrm{V}$ and $U_\mathrm{16A} = U_\mathrm{16B} = -2\,\mathrm{kV}$. We note that the "uncertainties" are dominated by simulation statistics (number of generated events $= 2 \times 10^5$, for each height of the main magnetic field) and, for $B_0 = 0.933\,\mathrm{T}$, additionally by the enhanced drift for protons emitted almost perpendicular to the magnetic field (cf. Fig. 5.47). With a reduced height of the main magnetic field, depending on the real electric field distribution, the volume projected onto the detector could therefore exhibit an even lower electrostatic potential.

On the other hand, our experiences from November/December 2007 rather suggest a positive potential for the collimation system. But then, an overall increased electrostatic potential in the DV of, e.g., $U_0 = +1\,\mathrm{V}$, would yield a shift in a of $\Delta a/a = (-12.40 \pm 1.54)\,\%$, in contradiction to the observed shift Eq. (5.45). However, for a charging of the collimation system, the real electric field distribution inside the DV is hard to predict. Therefore, we have chosen a more conservative estimate of the error in the neutrino-electron correlation coefficient a of

$$\boxed{\Delta a/a = (+18.85 \pm 12.4)\,\%} \tag{5.50}$$

Here, the shift stems from proton reflections[15] from the DV, while the error stems from the overall altered electrostatic potential U_0, cf. Eq. (5.47).

We note that the charging of the collimation system issue can be easily solved by surface coating with, e.g., aluminum or titanium, in a further beam time. However, the work function differences both between the collimation system and the proposed surface coating as well as between the surface coating and the gold-plated surfaces of our electrode system should still be investigated (cf. also Chap. 6). Hence, we strongly recommend to repeat both the tests with a reduced width of the neutron beam and with a reduced height of the main magnetic field in a further beam time. In particular, we propose measurements with several different widths of the neutron beam profile and at least three different heights of the main magnetic field. Given the changes in the mirror potentials proposed in the previous section, we also suggest to re-examine the influence of non-adiabatic proton motion (discussed in Sec. 3.4.2) on a (by means of MC simulations).

5.5 Investigations of Systematic Effects

During our latest beam time, several different systematic effects were investigated experimentally (see also Sec. 4.2.5). Here, we present the results of their analysis, primarily with regard to their impact on the neutrino-electron correlation coefficient a.

5.5.1 Electrostatic Mirror Potential

As mentioned earlier in Sec. 3.1 (see also page 57 under “The Electrostatic Mirror”), the electrostatic mirror is held at a positive voltage $U_\mathrm{M} > T_{\mathrm{p,max}}$, in order to reflect all decay protons emitted in the negative z-direction. To verify that our two typical voltage settings (see Table 3.1) of the electrostatic mirror electrodes e1, e1b, and e2 are sufficient for this purpose, the mirror potential was reduced in several steps from $U_1(= U_{1\mathrm{b}})|U_2 = 1080\,\mathrm{V}|1100\,\mathrm{V}$ to $0\,\mathrm{V}|0\,\mathrm{V}$.

Our electric field calculations (see also Fig. 3.11 and our note on page 62) have shown that a mirror potential of $U_1|U_2 = 760\,\mathrm{V}|780\,\mathrm{V}$ already ensures a rather homogeneous electric field distribution of at least 760 V (740 V at the height of the wire system e1) over the entire flux tube. The measurements have confirmed that a potential of $U_1|U_2 = 760\,\mathrm{V}|780\,\mathrm{V}$ guarantees 100 % acceptance for decay protons, as can be seen from Table 5.5.

---

[15] Please note that mostly the top half of the neutron beam is affected by the proton reflections and therefore the angular correlation coefficient a is only shifted by $\Delta a/a = (+18.85 \pm 1.63)\,\%$, compared to Eq. (5.46).

Table 5.5: Proton count rates from 14_05_08/mirror and 14_05_08/mirror_rate for different settings of the electrostatic mirror electrodes e1, e1b, and e2, for $U_\mathrm{A} = 50\,\mathrm{V}$. A potential of $U_1|U_2 = 760\,\mathrm{V}|780\,\mathrm{V}$ already ensures that all decay protons emitted in the negative z-direction will be reflected by the electrostatic mirror. In comparison with the top of Fig. 5.9, these count rates stem from measurements at an acceleration potential of $-10\,\mathrm{kV}$ and are therefore lower by about 15 to 20 Hz.

$U_1 = U_{1\mathrm{b}}$ [V]	U_2 [V]	Proton count rate [s^{-1}]	Comment
1080	1100	452.40(92)	
800	1000	449.98(20)	typical voltage setting
850	900	450.60(92)	
800	820	not measured	typical voltage setting
760	780	451.10(92)	
0	0	228.58(12)	

Given the changes in the mirror potentials proposed in Sec. 5.4.3, we recommend to repeat this measurement in a further beam time.

5.5.2 Magnetic Mirror Effect in the Decay Volume

As discussed earlier in Sec. 5.3.4, a small fraction, δ, of all decay protons, emitted in the negative z-direction, is reflected by the local magnetic field maximum just below the DV (see Fig. 4.5b). From the measurements both of the neutron beam (presented in Sec. 4.1.3) and the magnetic field profiles (see Sec. 4.1.4 for details), this fraction can be calculated.

Count Rate Ratio With and Without Electrostatic Mirror

In our experiment, the fraction δ cannot be measured directly, but indirectly via the proton count rates with and without electrostatic mirror:

$$\frac{N_\mathrm{p}(U_\mathrm{A} = 0\,\mathrm{V}; U_\mathrm{M} = 0\,\mathrm{V})}{N_\mathrm{p}(U_\mathrm{A} = 0\,\mathrm{V}; U_\mathrm{M} > T_{\mathrm{p,max}})} = \frac{N_0(0.5+\delta)}{N_0} = 0.5 + \delta\,. \tag{5.51}$$

In the first order, the count rate ratio Eq. (5.51) does not depend on the drift potentials $U_{8\mathrm{R}}|U_{8\mathrm{L}}$ and $U_{16\mathrm{A}}|U_{16\mathrm{B}}$. Hence, the count rate ratio can be calculated by computing the proton's trajectories only in (2D) axially symmetric electric and magnetic fields (see also our note on page 62). From our MC simulations, we expect a count rate ratio of

$$\frac{N_\mathrm{p}(U_\mathrm{A}; U_1 = U_2 = 0\,\mathrm{V})}{N_\mathrm{p}(U_\mathrm{A}; U_1|U_2 = 800\,\mathrm{V}|1000\,\mathrm{V})} = \begin{cases} 51.052 \pm 0.004(\mathrm{stat})^{+0.018}_{-0.006}(\mathrm{sys})\,\%\,, & \text{for } U_\mathrm{A} = 0\,\mathrm{V} \\ 51.048 \pm 0.003(\mathrm{stat})^{+0.018}_{-0.005}(\mathrm{sys})\,\%\,, & \text{for } U_\mathrm{A} = 50\,\mathrm{V} \end{cases} \tag{5.52}$$

Here, the systematic error stems from the poor quality of the simulated beam profiles (discussed in Sec. 4.1.3) and the uncertainty in the exact position (including the rotation angle in the x-y-plane) of the proton detector relative to the neutron beam (determined in Sec. 5.5.6), cf. Fig. 5.38a.

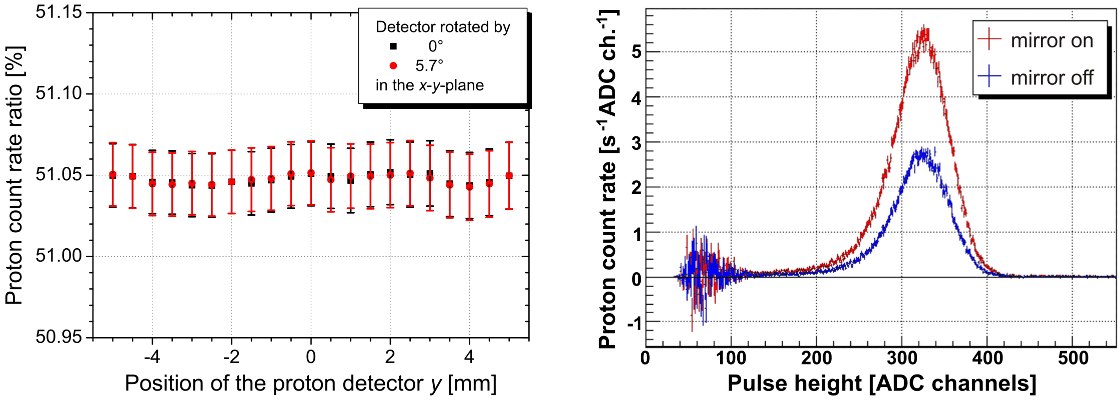

(a) (b)

Figure 5.38: (a) Proton count rate ratio with and without electrostatic mirror for different positions of the proton detector (for details see Sec. 5.5.6). We note that the neutron beam profile varies only marginally over the depth of the flux tube (cf. Sec. 4.1.3). Input data for the MC simulation (in INM approximation): $B_0 = 2.177\,\mathrm{T}$, $B_\mathrm{A}/B_0 = 0.203$, $U_1 = U_{1\mathrm{b}} = 800\,\mathrm{V}$, $U_2 = 1000\,\mathrm{V}$, $U_8 = -525\,\mathrm{V}$, $U_\mathrm{A} = 50\,\mathrm{V}$, $U_{16} = -2.2\,\mathrm{kV}$, $U_{17} = -10\,\mathrm{kV}$, number of generated events $= 10^8$, and $a = -0.105$ (derived from $\lambda = -1.2701(25)$ [10]). Except for the settings of the lower dipole electrode (e8), the input data correspond to the data set 14_05_08/mirror_rate. The error bars show statistical errors only and are strongly correlated, as each point stems from the same MC simulation. (b) Background subtracted pulse height spectra from 14_05_08/mirror_rate with (red) and without (blue) electrostatic mirror for $U_\mathrm{A} = 50\,\mathrm{V}$. In comparison with Fig. 5.8b, both spectra stem from measurements at an acceleration potential of $-10\,\mathrm{kV}$ and therefore the proton peak is shifted to lower ADC channels (see also Fig. 5.3). The error bars show statistical errors only.

To investigate the alignment between the magnetic field and the neutron beam, the proton count rates with and without electrostatic mirror were compared. From the measurements, shown in Fig. 5.38b (see also Table 5.5), we derive a count rate ratio of

$$\frac{N_\mathrm{p}(50\,\mathrm{V}; U_1 = U_2 = 0\,\mathrm{V})}{N_\mathrm{p}(50\,\mathrm{V}; U_1|U_2 = 800\,\mathrm{V}|1000\,\mathrm{V})} = 50.80(3)\,\%. \tag{5.53}$$

The result is 5.2 standard deviations from our expectation Eq. (5.52). According to Fn. 8 in Chap. 4, a slightly different magnetic field profile (see Fig. 4.5b) might at least partly explain this deviation, but would rather suggest an even higher count rate ratio.

With increasing barrier voltage U_A the slope of the transmission function Eq. (3.30) increases. Therefore, less protons with polar emission angles around 90 degrees can pass the AP (see also Fig. 3.2). Ultimately, the count rate ratio decreases down to nearly 50 % for $U_\mathrm{A} = 600\,\mathrm{V}$, as can be seen in Fig. 5.39 (green triangles). Unfortunately, the measured count rate ratios are in poor agreement with the predicted values from our MC simulations. Even computing the proton's trajectories in (3D) non-axially symmetric electric fields cannot improve the poor agreement, as can also be seen from Fig. 5.39. We are convinced that this is attributed to non-statistically fluctuating count rates during these measurements (cf. Fn. 7 and also Fig. 5.15).

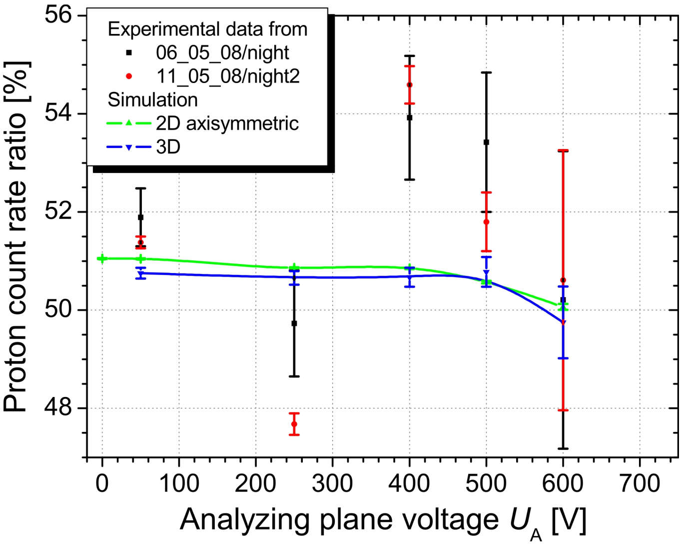

Figure 5.39: Proton count rate ratio with and without (count rates from 09_05_08/MirrorOff) electrostatic mirror versus barrier voltage U_A. The black squares and red circles stem from measurements performed at a time when the count rates were fluctuating non-statistically (cf. Fn. 7). For comparison, the triangles show the expected ratios from our MC simulations, where the blue ones also consider the drift potentials of both, the lower and the upper, dipole electrodes. Input data for the MC simulations (in INM approximation): $B_0 = 2.177\,\mathrm{T}$, $B_\mathrm{A}/B_0 = 0.203$, $U_1 = U_{1\mathrm{b}} = 800\,\mathrm{V}$, $U_2 = 1000\,\mathrm{V}$, $U_{8\mathrm{R}} = -50\,\mathrm{V}$, $U_{8\mathrm{L}} = -1000\,\mathrm{V}$, $U_{16\mathrm{A}} = -4.2\,\mathrm{V}$, $U_{16\mathrm{B}} = -0.2\,\mathrm{kV}$, $U_{17} = -10\,\mathrm{kV}$, number of generated events $= 6 \times 10^6$ (for each AP voltage), and $a = -0.105$ (derived from $\lambda = -1.2701(25)$ [10]); or, in the case of our computations in (2D) axially symmetric electric fields: $U_8 = -525\,\mathrm{V}$, $U_{16} = -2.2\,\mathrm{kV}$, and number of generated events $= 10^8$ (for each AP voltage). Error bars show statistical errors only.

Conclusions for a Charging of the Collimation System

Let us assume that the full proton decay rate N_0 is reduced by a factor x while the proton count rate without electrostatic mirror is only reduced by a factor $y = t \cdot x$, with a parameter $0 \leq t \leq 1$. Then, the count rate ratio for $U_\mathrm{A} = 50\,\mathrm{V}$ changes to about

$$\frac{0.5106 \cdot (0.9619 \cdot N_0) - y \cdot (0.9619 \cdot N_0)}{(0.9619 \cdot N_0) - x \cdot (0.9619 \cdot N_0)} = \frac{0.5106 - t \cdot x}{1 - x} \overset{!}{=} 0.508. \tag{5.54}$$

Solving Eq. (5.54) for x yields:

$$x = \frac{0.0026}{t - 0.508} \overset{!}{>} 0, \tag{5.55}$$

and therefore $t > 50.8\,\%$. However, during our latest beam time, we observed the effects of the saturation of the preamplifier (discussed on page 120) only less than $20\,\mu\mathrm{s}$ after high-energy electrons. According to Fig. 5.6, the saturation effect can therefore be ruled out as main explanation for the deviation from simulation to measurement.

On the other hand, a charging of the collimation system (discussed in Sec. 5.4.4) can lead to unexpected proton reflections from the DV (see also Sec. 6.4.3). The protons affected may be trapped between the DV and the electrostatic mirror, what, in turn, will lead to a reduction of the proton count rate. This mostly affects the protons emitted almost

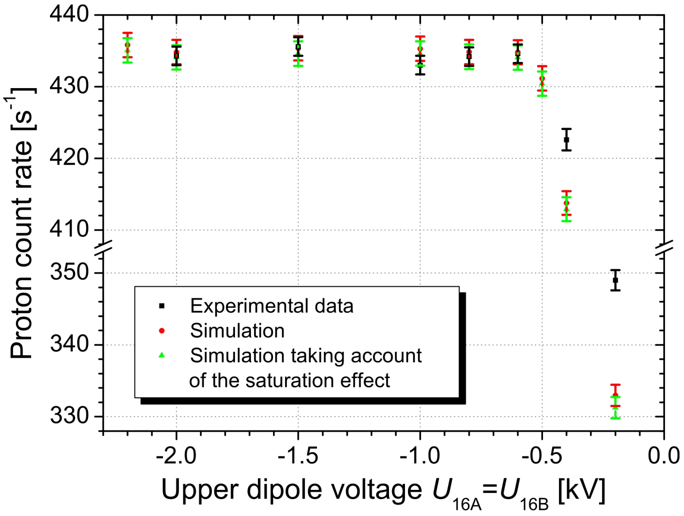

Figure 5.40: Proton count rates from 20_04_08/trans for different upper dipole voltages $U_{16\mathrm{A}} = U_{16\mathrm{B}}$. For better visibility, the y-axis is broken at $353\,\mathrm{s}^{-1}$. Because of the lack of background measurements with $U_\mathrm{A} = 780\,\mathrm{V}$, the background count rate was estimated to be $3.5\,\mathrm{s}^{-1}$. In comparison with the top of Fig. 5.8b, these count rates stem from measurements at an acceleration potential of $-10\,\mathrm{kV}$ and, additionally, an increased length of trigger window w2 of 2^5 time bins, and are therefore lower by about 30 Hz. For comparison, the red circles show the expected count rates from our MC simulations. For $|U_{16\mathrm{A}}| < 0.6\,\mathrm{kV}$, the measured proton count rates do not fit the simulated count rates (cf. also Fn. 7), even after taking account of the saturation of the preamplifier (green triangles). We note that the simulated count rates were normalized to the measured proton count rates for $|U_{16\mathrm{A}}| \geq 0.6\,\mathrm{kV}$. Input data for the MC simulations (in INM approximation): $B_0 = 2.177\,\mathrm{T}$, $B_\mathrm{A}/B_0 = 0.203$, $U_1 = U_{1\mathrm{b}} = 800\,\mathrm{V}$, $U_2 = 1000\,\mathrm{V}$, $U_{8\mathrm{R}} = -50\,\mathrm{V}$, $U_{8\mathrm{L}} = -1000\,\mathrm{V}$, $U_\mathrm{A} = 50\,\mathrm{V}$, $U_{17} = -10\,\mathrm{kV}$, number of generated events $= 5 \times 10^5$ (for each dipole voltage), and $a = -0.105$ (derived from $\lambda = -1.2701(25)$ [10]). Error bars show statistical errors only.

perpendicular to the magnetic field (cf. Figs. 3.2 and 6.22), what speaks for $t \gg 50.8\,\%$. We mention that solving Eq. (5.54) for y, in turn, yields

$$y = 0.0026 + 0.508 \cdot x \overset{!}{\leq} x, \tag{5.56}$$

and hence

$$\boxed{x \geq 0.53\,\%} \tag{5.57}$$

In comparison with Table 5.3 this is quite realistic.

In summary, measurements with and without electrostatic mirror have to be repeated in a further beam time. Again (cf. Sec. 5.4.3), we recommend to improve the stability of the neutron beam monitor.

5.5.3 Magnetic Mirror Effect in Front of the Proton Detector

As mentioned earlier on page 59, the upper dipole electrode e16 also ensures that all decay protons that pass the potential barrier can overcome the magnetic mirror right in front of the proton detector (see Fig. 4.5a). To verify that our typical voltage settings (see also Table 3.1) of the upper dipole electrodes e16A and e16B are sufficient for this purpose, the dipole potential was enlarged in several steps from $U_{16\mathrm{A}} = U_{16\mathrm{B}} = -200\,\mathrm{V}$ to -2000 V.

Our electric field calculations (see Fig. 3.8 and our note on page 62) have shown that a dipole potential of $U_{16\mathrm{A}} \approx -600\,\mathrm{V}$ already guarantees 100 % acceptance of decay protons. Our measurements have confirmed that a potential of $U_{16\mathrm{A}} = -600\,\mathrm{V}$ ensures that all decay protons concerned also overcome the magnetic mirror in front of the detector, as can be seen from Fig. 5.40.

But for $|U_{16\mathrm{A}}| < 600\,\mathrm{V}$, the measured proton count rates do not match the simulated count rates, even after considering the saturation of the preamplifier (discussed on page 120 under “Correction for the Saturation Effect”). We note that these measurements were performed at a time when the count rates were fluctuating non-statistically (cf. Fn. 7). It is therefore very difficult to decide what is the major cause of

- increased proton count rates for $|U_{16\mathrm{A}}| < 600\,\mathrm{V}$ or possibly
- reduced proton count rates for $|U_{16\mathrm{A}}| \geq 600\,\mathrm{V}$.

To summarize, possible causes include:

- non-statistically fluctuating count rates (see Fig. 5.15),
- the increased length of trigger window w2, from usually 2^4 to 2^5 time bins (see page 69 under “Digital Electronics and the Trigger Algorithm”). The comparison with Table 5.5 shows that a loss rate at the level of 10 Hz for $U_{\mathrm{A}} = 50\,V$ is realistic.
- the saturation of the preamplifier; owing to Fig. 5.40 this is almost excluded,
- an enhanced energy transfer from transverse to longitudinal motion for $U_2 = 1000\,\mathrm{V}$ (discussed on page 137 under “Non-Adiabatic Proton Motion”). This mainly affects the protons with large emission angles to the magnetic field axis (cf. Fn. 3 in Chap. 3). Hence, it will lead to an increase of the proton count rates for $|U_{16\mathrm{A}}| < 600\,\mathrm{V}$, while the proton count rates for $|U_{16\mathrm{A}}| \geq 600\,\mathrm{V}$ remain unaffected.
- a possible charging of the collimation system. According to the previous section, this mostly affects the protons emitted almost perpendicular to the magnetic field. Therefore, it will lead to a reduction of the proton count rates for $|U_{16\mathrm{A}}| \geq 600\,\mathrm{V}$, while leave the proton count rates for $|U_{16\mathrm{A}}| < 600\,\mathrm{V}$ nearly unaffected.

Hence, for measurements with $|U_{16\mathrm{A}}| \leq 1000\,\mathrm{V}$ and $|U_{16\mathrm{B}}| \leq 1000\,\mathrm{V}$, we propose to repeat this test in a further beam time.

5.5.4 Ratio of the Magnetic Fields

To test the calculated transmission function Eq. (3.30), the ratio of the magnetic fields in the AP and the DV, $r_{\mathrm{B}} = B_{\mathrm{A}}/B_0$, was changed (see Secs. 3.2.2 and 4.2.5 for details) by

$$\Delta r_{\mathrm{B}}/r_{\mathrm{B}} = 0.94(21)\,\% \tag{5.58}$$

from the standard ratio $r_{\mathrm{B}} = 0.2030(3)$ to $r_{\mathrm{B}} = 0.2049(3)$ [53]. Unfortunately, with a relative error of 22 % dominated by the accuracy of the Hall probe (discussed in Sec. 4.1.4). From our simulations, we expect a shift in the angular correlation coefficient a of

$$\Delta a/a = (-8.65 \pm 1.46^{+1.41}_{-1.39})\,\%, \tag{5.59}$$

if Eq. (3.32) would be fitted to the integral proton spectrum by using the standard ratio $r_{\mathrm{B}} = 0.203$. Here, the first error stems from fitting Eq. (3.32) to the simulated proton count rates and the latter one from the uncertainty in the magnetic field ratios. From the measured proton count rates (20_05_08/night), we determine a value for a of

$$a_{\mathrm{exp}} = \begin{cases} -0.1029(34)\ , & \text{for } F_{\mathrm{tr}}(T; U_{\mathrm{A}}, r_{\mathrm{B}} = 0.2049) \text{ in Eq. (3.32)} \\ -0.1141(34)\ , & \text{for } F_{\mathrm{tr}}(T; U_{\mathrm{A}}, r_{\mathrm{B}} = 0.203\ \ ) \text{ in Eq. (3.32)} \end{cases} \tag{5.60}$$

This corresponds to a shift in the neutrino-electron correlation coefficient a of

$$\Delta a_{\mathrm{exp}}/a_{\mathrm{exp}} = (-10.89 \pm 4.93)\,\%, \tag{5.61}$$

in agreement with the expected value Eq. (5.59) from our simulations. We note that another measurement at the same day (20_05_08/lunch), but with the standard ratio $r_{\mathrm{B}} = 0.203$ instead, leads to $a_{\mathrm{exp}} = -0.1020(45)$. This is also consistent with Eq. (5.60).

But obviously our statistics was too low to draw further conclusions concerning an angular-dependent detection efficiency of the aSPECT spectrometer:

> Let us assume that protons emitted almost perpendicular to the magnetic field will either not reach the proton detector or will not be counted by the detector. To be specific: The proton count rate is reduced by protons with an (initial) polar angle $90° \geq \theta_0 > \theta_{\mathrm{acc}}^{\mathrm{max}} \sim 90°$ (cf. also Fn. 3 in Chap. 3), where $\theta_{\mathrm{acc}}^{\mathrm{max}}$ denotes the maximum polar angle accepted. With increasing barrier voltage U_{A} the slope of the transmission function Eq. (3.30) increases and therefore the relative count rate loss decreases (see also Fig. 3.4). Thus, with decreasing maximum angle accepted $\theta_{\mathrm{acc}}^{\mathrm{max}}$ the angular correlation coefficient a is shifted to more positive values, as can be seen in Fig. 5.41. This shift slightly depends on the ratio of the magnetic fields $r_{\mathrm{B}} = B_{\mathrm{A}}/B_0$, as can also be seen from Fig. 5.41. Hence, high-precision measurements with different magnetic field ratios might reveal a possible angular-dependent detection efficiency of our spectrometer.

Hence, we suggest to repeat this measurement in a future (high-precision) beam time; if possible, with different and more radically changed magnetic field ratios. We recommend at the same time to improve the stability of the neutron beam monitor (see also Sec. 5.4.3).

5.5.5 Height of the Main Magnetic Field

To study the influence of the non-adiabatic proton motion (discussed in Sec. 3.4.2; see also Sec. 5.4.3) on the neutrino-electron correlation coefficient a, measurements with two different heights of the main magnetic field were performed. As mentioned earlier in Sec. 5.4.4, with decreasing main magnetic field the uncorrected value for the angular correlation coefficient a increases by

$$\Delta a_{\mathrm{exp}}/a_{\mathrm{exp}} = (+31.97 \pm 4.16)\,\% \tag{5.62}$$

from $a_{\mathrm{exp}} = -0.1025(28)$ for $B_0 = 2.177\,\mathrm{T}$ to $a_{\mathrm{exp}} = -0.0697(38)$ for $B_0 = 0.933\,\mathrm{T}$ (21_05_08/night). From the MC simulations [47], we expect a much smaller shift in a of[16]

$$0.5\,\% \ll \Delta a/a < 4\,\%, \tag{5.63}$$

---

[16] Please note that in Refs. [34, 53] the shift in a was greatly underestimated with $|\Delta a/a| > 0.4\,\%$.

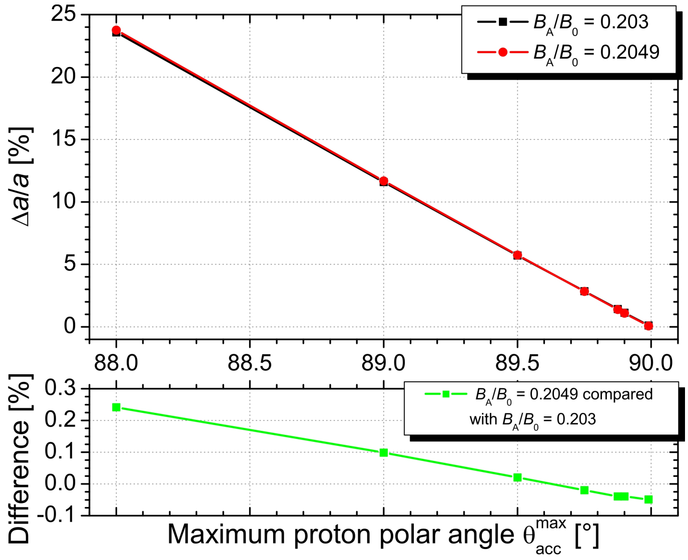

Figure 5.41: Top: Relative change of the angular correlation coefficient a for different maximum polar angles accepted $\theta_{\text{acc}}^{\text{max}}$ (for details see the text). With decreasing maximum angle accepted $\theta_{\text{acc}}^{\text{max}}$ the angular correlation coefficient a is shifted to more positive values. The comparison between the black squares ($B_{\text{A}}/B_0 = 0.203$) and the red circles ($B_{\text{A}}/B_0 = 0.2049$) shows that the shift slightly depends on the ratio of the magnetic fields $r_{\text{B}} = B_{\text{A}}/B_0$. Bottom: For elucidation, the green squares show the difference between the red circles and the black squares. Input data for the simulation: $U_{\text{A}} = 50, 250, 400, 500, 600\,\text{V}$ and the recommended value for $a = -0.103$ [10].

cf. Table 3.2. This is far too little to explain the observed shift Eq. (5.62).

On the other hand, with decreasing main magnetic field the proton's radius of gyration increases (cf. Eq. (3.3)) and hence both transition regions shown in Fig. 3.23 get wider. Therefore, the impact of the edge effect (described in Sec. 3.4.6) on the angular correlation coefficient a increases. However, from our MC simulations of the edge effect (see the following section), we expect a shift in a of

$$\Delta a/a = -22.82(97)\,\%, \tag{5.64}$$

cf. Table 5.7. Compared with the observed shift Eq. (5.62), this is a shift in the wrong direction.

Even computing the proton's trajectories in (3D) non-axially symmetric electric fields cannot improve the poor agreement, but at least reveal a possible underestimation of the change in a due to non-adiabatic proton motion. From our 3D MC simulations, we expect a shift in a of only

$$\Delta a/a = (-7.03 \pm 3.83)\,\%. \tag{5.65}$$

We note that with decreasing main magnetic field the proton's drift increases (cf. Eqs. (5.48) and (5.49); see also Table 5.6) and hence the spatial separation of decay protons and electrons on the proton detector increases. Therefore, the saturation effect of the detector electronics (discussed on page 120 under "Saturation of the Preamplifier") is reduced. Altogether, the comparison with our calculations in 2D axially symmetric fields Eq. (5.64) results in a shift in the angular correlation coefficient a due to non-adiabatic proton motion of

$$\boxed{\Delta a/a = (+15.79 \pm 3.96)\,\%} \tag{5.66}$$

with a relative error of 25 % dominated by simulation statistics (number of generated events $= 6 \times 10^6$ for $B_0 = 2.177\,\mathrm{T}$ and 12×10^6 for $B_0 = 0.933\,\mathrm{T}$). Compared with Eq. (5.63), this is much higher than expected [47].

We mention that the figures in Table 4.1 (from Ref. [47]) are based on a potential difference of $|U_{8\mathrm{R}} - U_{8\mathrm{L}}| = 3\,\mathrm{kV}$ (see also Fn. 14 in Chap. 3). Thus, it is unclear whether the expected shift in a from Ref. [47] for $B_0 = 2.177\,\mathrm{T}$ of

$$0.001\,\% < \Delta a/a < 0.04\,\% \tag{5.67}$$

also underestimates the actual impact of non-adiabatic proton motion on a. Hence, we strongly recommend to re-examine the influence of non-adiabatic proton motion on a (by means of MC simulations). In addition, we suggest to repeat this test with at least three different heights of the main magnetic field, in a further beam time.

5.5.6 Edge Effect

To determine the correction for the edge effect (introduced in Sec. 3.4.6), measurements with three different widths of the neutron beam profile (see also Secs. 4.1.3 and 4.2.5) were performed. As explained earlier (in Sec. 3.4.6), the edge effect strongly depends on the shape of the neutron beam profile and hence also on the exact position of the proton detector relative to the rest of the electrode system and the magnetic field. The high voltage electrode e17 (surrounding the detector) is mounted to a long arm[17], cf. Fig. 3.20a. Therefore, a deflection of the long arm out of the magnetic field axis by a few tenth of a degree can lead to a displacement of the proton detector in the x-y-plane of several millimeters. We note that a deflection of the superconducting coil system (fixed relative to the DV) out of the symmetry axis of the electrode system has the same effect. This is not considered in the present thesis, but could be part of further investigations (by means of MC simulations). Consequently, for each width of the neutron beam profile, we first aligned the "center" of the neutron beam on the detector. Therefore, we compared the proton count rates for several different settings of both the lower and the upper dipole electrodes e8 and e16, respectively.

The rotation angle of the proton detector in the x-y-plane, ϕ_{det}, was measured to be

$$\boxed{\phi_{\mathrm{det}} = 5.7(5)\,^\circ} \tag{5.68}$$

Fig. 5.42 suggests that this rotation corresponds to a widening of the projected area (see Fig. 3.23), by about 10 % (cf. Fig. 5.45). Actually, the figure also shows how a shift of $-3\,\mathrm{mm}$ in both the x- and the y-direction would look like.

Determination of the Position of the Proton Detector

According to Eq. (3.39) (see also Fig. 5.47)

- the lower dipole electrode e8 mainly[18] causes a drift of the decay protons in x-direction, i.e., parallel to the neutron beam, whereas

---

[17] The distance between the center of rotation and the proton detector is about 1.4 meters.

[18] To be precise, the dipole electrodes cause a transvection (shear mapping) of the flux tube, as can also be seen from Fig. 5.47.

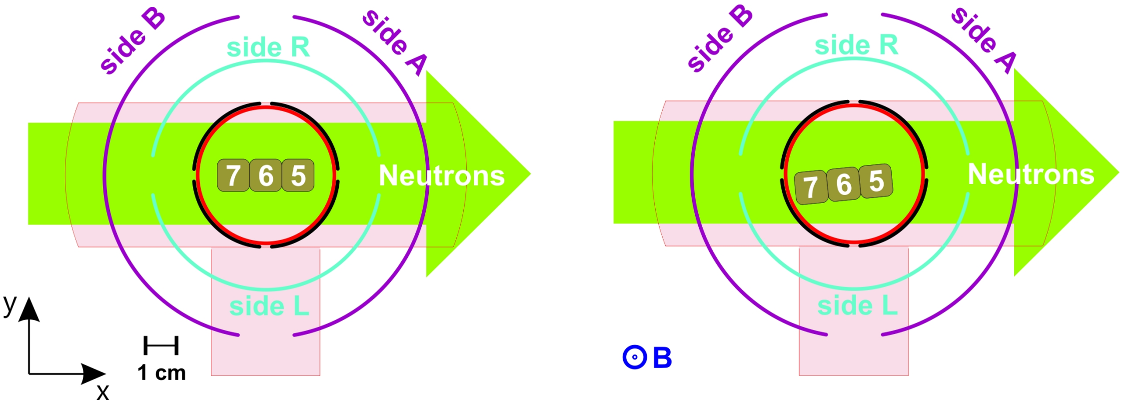

(a) $x = y = 0$ and $\phi_{\mathrm{det}} = 0^\circ$ (b) $x = y = -3\,\mathrm{mm}$ and $\phi_{\mathrm{det}} = 5.7^\circ$

Figure 5.42: A sketch of the electromagnetic set-up, see Fig. 3.18b for details. The comparison between (a) and (b) shows the effect of both a rotation and a shift of the proton detector by, e.g., $\Delta\phi_{\mathrm{det}} = 5.7^\circ$ and $\Delta x_{\mathrm{det}} = \Delta y_{\mathrm{det}} = -3\,\mathrm{mm}$, respectively.

- the upper dipole electrode e16 mainly (cf. Fn. 18) causes a drift in y-direction, i.e., perpendicular to the neutron beam.

Therefore, the displacement of the proton detector in x- and y-direction was determined separately by measurements with different lower and upper dipole voltages, respectively.

From the measurements with an additional aperture, shown in Fig. 5.43, we derive a displacement of the proton detector in y-direction of

$$\Delta y_{\mathrm{det}} = -3.5(5)\,\mathrm{mm} \tag{5.69}$$

The same result was obtained for a measurement with the 20 mm wide aperture but $U_{\mathrm{A}} = 400\,\mathrm{V}$.

We would like to emphasize that our data analysis revealed that the poor quality (cf. Figs. 4.4 and 4.3) of the simulated neutron beam profiles (from Ref. [34]) was not adequate to describe the measured proton count rates. Therefore, the simulated neutron beam profiles were smoothed by bilinear interpolation (see also Sec. 4.1.3). In particular, for the full width of the neutron beam, the simulated neutron beam profile results in a displacement of only $\Delta y_{\mathrm{det}} = -1.5(5)\,\mathrm{mm}$, even after smoothing of the beam profile, as can be seen from Figs. 5.44a and 5.44b. Even though the input parameters for the MC simulation were adapted to the measured beam profiles (cf. Ref. [34]), this deviation from Eq. (5.69) cannot be explained by the overall spatial accuracy of our measured beam profiles of 1 mm (for details see Sec. 4.1.3). Hence, for the full width of the neutron beam, the neutron beam profile in the DV was determined by bilinear interpolation of the measured beam profiles in front of the entrance window (see Fig. 4.3a) and behind the exit window (see Fig. 4.3c) of the aSPECT magnet instead. This yields a displacement of $\Delta y_{\mathrm{det}} = -3.0(5)\,\mathrm{mm}$, in agreement with Eq. (5.69). For comparison, the extrapolation of the measured beam profile behind the exit window, shown in Fig. 5.44c, results in a displacement of $\Delta y_{\mathrm{det}} = -3.5(5)\,\mathrm{mm}$, as can be seen from Fig. 5.44d. For our analysis, we therefore use the extrapolated neutron beam profile. We note that the saturation of the preamplifier (discussed on page 120) has only minor impact on Figs. 5.43 to 5.46.

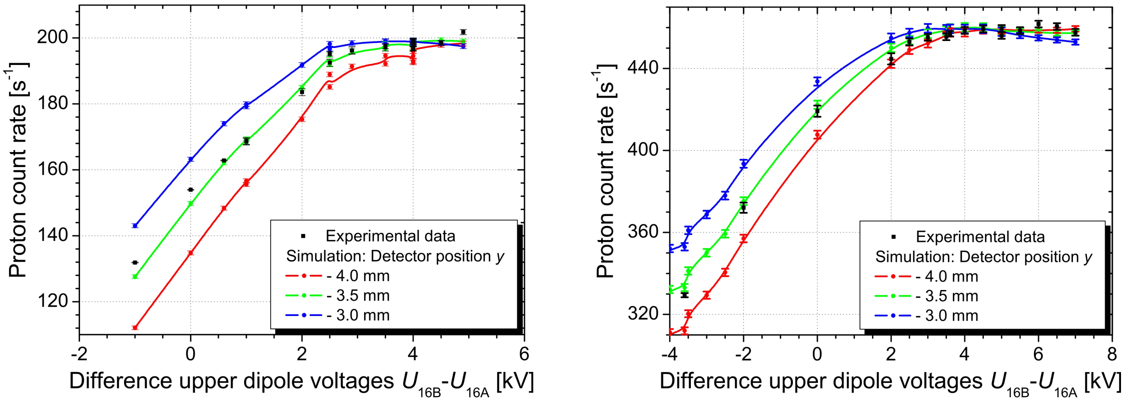

(a) 5 mm wide aperture

(b) 20 mm wide aperture

Figure 5.43: Proton count rates (a) from 17_04_08/uExB with the 5 mm wide aperture and (b) from 16_05_08/uExB2 with the 20 mm wide aperture for different upper dipole drifts $U_{16\mathrm{A}}|U_{16\mathrm{B}}$. The colored circles show the expected count rates from our MC simulations for different positions of the proton detector. Input data for the MC simulations (in INM approximation): $B_0 = 2.177\,\mathrm{T}$, $B_\mathrm{A}/B_0 = 0.203$, $U_1 = U_{1\mathrm{b}} = 800\,\mathrm{V}$, $U_2 = 1000\,\mathrm{V}$, $U_{8\mathrm{R}} = -50\,\mathrm{V}$, $U_{8\mathrm{L}} = -1000\,\mathrm{V}$, $U_\mathrm{A} = 50\,\mathrm{V}$, $U_{17} = -10\,\mathrm{kV}$, number of generated events $= 5 \times 10^5$ (for each dipole voltage), and $a = -0.105$ (derived from $\lambda = -1.2701(25)$ [10]), or, in the case of measurements with the 20 mm wide aperture: $U_1 = U_{1\mathrm{b}} = 800\,\mathrm{V}$, $U_2 = 820\,\mathrm{V}$, $U_{8\mathrm{R}} = 0\,\mathrm{V}$, $U_{8\mathrm{L}} = -200\,\mathrm{V}$, $U_\mathrm{A} = 50\,\mathrm{V}$, $U_{17} = -15\,\mathrm{kV}$. Error bars show statistical errors only.

As mentioned above, the rotation angle ϕ_det of the proton detector was measured. In the case of Figs. 5.43, 5.44, and also 5.46, this has no influence on the determination of the position of the proton detector. In contrast to a measurement with a reduced height of the main magnetic field, as can be seen from Fig. 5.45. This measurement yields a displacement of $\Delta y_\mathrm{det} = -3.0(5)\,\mathrm{mm}$, also in agreement with Eq. (5.69) (cf. also Sec. 5.4.4). Taken together, we determine the displacement of the proton detector in y-direction to

$$\boxed{\Delta y_\mathrm{det} = (-3.5 \pm 1.0)\,\mathrm{mm}} \tag{5.70}$$

As mentioned earlier in Sec. 4.1.3, the neutron beam profile varies only slightly over the depth, x, of the flux tube. But, with increasing drift potential $U_{8\mathrm{R}}|U_{8\mathrm{L}}$ the left and/or the right detector pad will step out from or into the shadow of the electrode system. Hence, the displacement of the detector in x-direction can only be determined from the proton count rates in an outer detector pad, i.e., in detector channel 5 or 7. From the measurements with several different settings of the lower dipole electrode e8, shown in Fig. 5.46, we derive a displacement of the proton detector in x-direction of

$$\boxed{\Delta x_\mathrm{det} = -3(1)\,\mathrm{mm}} \tag{5.71}$$

Here, the uncertainty also considers that these measurements were performed at a time when the count rates were fluctuating non-statistically (cf. Fn. 7).

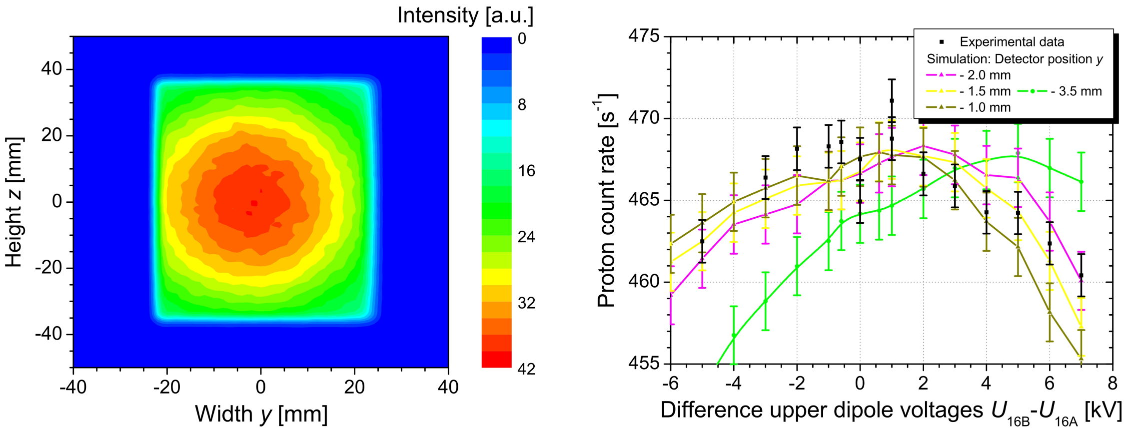

(a) Simulated neutron beam profile (b) Simulated neutron beam profile

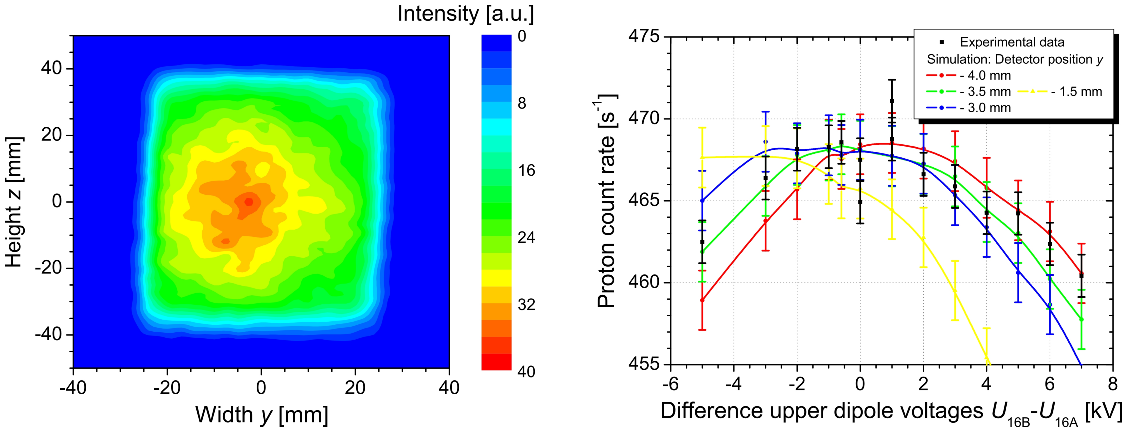

(c) Profile measured behind the exit window (d) Profile measured behind the exit window

Figure 5.44: Uncertainty in the position of the proton detector due to the knowledge of the neutron beam profile, (a) and (b) for the simulated beam profile and (c) and (d) for the neutron beam profile measured behind the exit flange. (a) and (c) show the neutron beam profiles, while (b) and (d) show the proton count rates from 17_05_08/uExB_fullbeam for different upper dipole drifts $U_{16\mathrm{A}}|U_{16\mathrm{B}}$. The colored circles show the expected count rates from our MC simulations for different positions of the proton detector. See the text for details. Input data for the MC simulations (in INM approximation): $B_0 = 2.177\,\mathrm{T}$, $B_\mathrm{A}/B_0 = 0.203$, $U_1 = U_{1\mathrm{b}} = 800\,\mathrm{V}$, $U_2 = 820\,\mathrm{V}$, $U_{8\mathrm{R}} = 0\,\mathrm{V}$, $U_{8\mathrm{L}} = -200\,\mathrm{V}$, $U_\mathrm{A} = 50\,\mathrm{V}$, $U_{17} = -15\,\mathrm{kV}$, number of generated events $= 5 \times 10^5$ (for each dipole voltage), and $a = -0.105$ (derived from $\lambda = -1.2701(25)$ [10]). Error bars show statistical errors only.

Dependence of the Drift on the Proton's Momentum

In addition to the drift potentials $U_{8\mathrm{R}}|U_{8\mathrm{L}}$ and $U_{16\mathrm{A}}|U_{16\mathrm{B}}$, the proton's drift also depends on its flight time through the dipole electrodes. The flight time, in turn, depends on the proton's velocity component $v_{||}$ parallel to the magnetic field. Therefore, the proton's drift caused by the dipole electrodes e8 and e16 depends on both the proton (initial) kinetic energy, T_0, and its polar angle, θ_0. However, in the case of the upper dipole electrode, the decay protons are additionally post-accelerated by the high negative potential of the detector electrode e17. For, e.g., $U_{16\mathrm{A}} = U_{16\mathrm{B}} = -2\,\mathrm{kV}$ and $U_{17} = -15\,\mathrm{kV}$, the acceleration

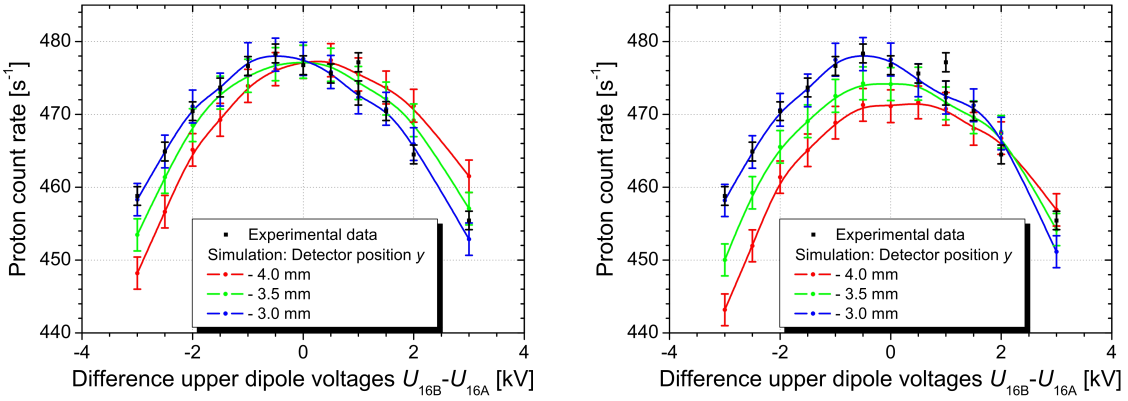

(a) $B_0 = 0.933\,\mathrm{T}$, $\phi_{\mathrm{det}} = 0\,^\circ$ (b) $B_0 = 0.933\,\mathrm{T}$, $\phi_{\mathrm{det}} = 5.7\,^\circ$

Figure 5.45: Uncertainty in the position of the proton detector due to its rotation angle, (a) for $\phi_{\mathrm{det}} = 0\,^\circ$ and (b) for $\phi_{\mathrm{det}} = 5.7\,^\circ$. (a) and (b) show the proton count rates from 22_05_08/uExB for different upper dipole drifts $U_{16\mathrm{A}}|U_{16\mathrm{B}}$. The colored circles show the expected count rates from our MC simulations for different positions of the proton detector. See the text for details. Input data for the MC simulations (in INM approximation): $B_0 = 0.933\,\mathrm{T}$, $B_\mathrm{A}/B_0 = 0.203$, $U_1 = U_{1\mathrm{b}} = 800\,\mathrm{V}$, $U_2 = 820\,\mathrm{V}$, $U_{8\mathrm{R}} = -50\,\mathrm{V}$, $U_{8\mathrm{L}} = -1000\,\mathrm{V}$, $U_\mathrm{A} = 50\,\mathrm{V}$, $U_{17} = -15\,\mathrm{kV}$, number of generated events $= 5 \times 10^5$ (for each dipole voltage), and $a = -0.105$ (derived from $\lambda = -1.2701(25)$ [10]). Error bars show statistical errors only.

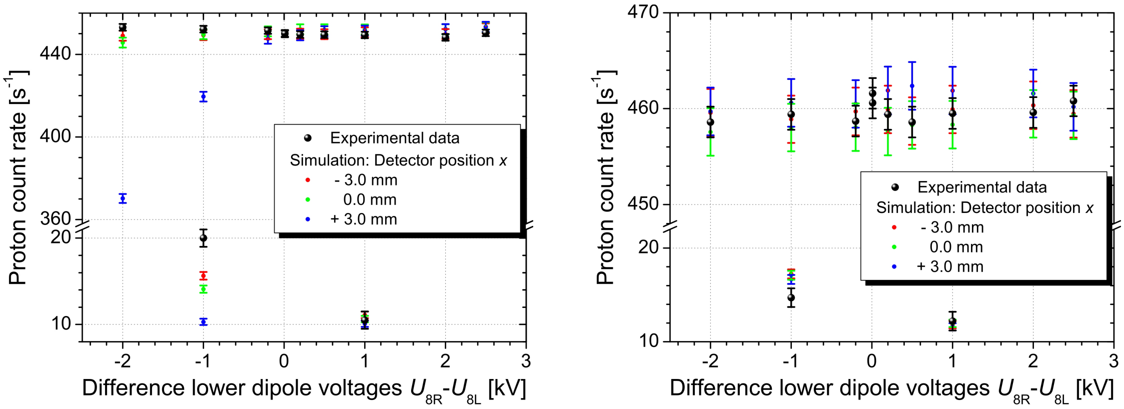

(a) Detector channel 5 (b) Detector channel 6

Figure 5.46: Proton count rates from 07_05_08/lExB for different lower dipole drifts $U_{8\mathrm{R}}|U_{8\mathrm{L}}$, (a) for an outer detector pad and (b) for the central detector pad. The count rates $< 20\,\mathrm{s}^{-1}$ correspond to measurements with positive voltages $U_{8\mathrm{R}}$, $U_{8\mathrm{L}} > 0$. Thus, for better visibility, the y-axis is broken at $21\,\mathrm{s}^{-1}$. The colored circles show the expected count rates from our MC simulations for different positions of the proton detector. Input data for the MC simulations (in INM approximation): $B_0 = 2.177\,\mathrm{T}$, $B_\mathrm{A}/B_0 = 0.203$, $U_1 = U_{1\mathrm{b}} = 800\,\mathrm{V}$, $U_2 = 1000\,\mathrm{V}$, $U_\mathrm{A} = 50\,\mathrm{V}$, $U_{16\mathrm{A}} = -4.2\,\mathrm{kV}$, $U_{16\mathrm{B}} = -0.2\,\mathrm{kV}$, $U_{17} = -10\,\mathrm{kV}$, number of generated events $= 5 \times 10^5$ (for each dipole voltage), and $a = -0.105$ (derived from $\lambda = -1.2701(25)$ [10]). Error bars show statistical errors only.

potential drops from about $-1.35\,\mathrm{kV}$ at the bottom edge to $-6.7\,\mathrm{kV}$ at the top edge of the upper dipole electrode. In addition, the magnetic field at height of the upper dipole electrode is higher by about a factor of 1.8 compared to the lower dipole electrode and hence the drift velocity Eq. (3.39) is reduced by about a factor of 0.55. Therefore, in the case of the upper dipole electrode, we expect a suppressed angular and a strongly suppressed energy dependence of the proton's drift.

Figure 5.47 shows the dependence of the drift on both the proton kinetic energy and its polar angle for two different settings of the *a*SPECT spectrometer. Obviously, the drift is enhanced for both protons emitted with low kinetic energy and/or almost perpendicular to the magnetic field. Moreover, the figure confirms our expectation that, in the case of the upper dipole electrode, both the energy and the angular dependence are suppressed.

However, compared to Eq. (5.70), both the energy and the angular dependence of the proton's drift are in the same order of magnitude as the uncertainty in the position of the proton detector. In view of the low simulation statistics in the case of computing the proton's trajectories in (3D) non-axially symmetric electric fields, we go for calculations in (2D) axially symmetric electric and magnetic fields (see also Sec. 5.5.2). Then, additional 3D MC simulations serve to

- determine the mean proton drift in dependence of the settings of the spectrometer, in order to correct the calculations in 2D axially symmetric fields for the proton's drift, and
- cross-check our combined simulations (i.e., compute the proton's trajectories in 2D axially symmetric fields and "add" the mean proton drift).

From our 3D MC simulations, we determine the mean proton drifts presented in Table 5.6.

For a precision measurement of the neutrino-electron correlation coefficient a, i.e, a measurement with at least optimized pulse shaping and reduced amplification of the preamplifier (cf. Sec. 5.4.1) in a further beam time, we strongly recommend to additionally integrate the slight energy and angular dependencies (see Fig. 5.47) of the proton drift into the combined simulations. This, however, requires improved determinations of the neutron beam profile(s) and also the position of the proton detector relative to the rest of the electrode system and the magnetic field.

Dependence of a on the Position of the Proton Detector

As explained above, calculations in 2D axially symmetric fields serve to determine the influence of the edge effect on the neutrino-electron correlation coefficient a. Figure 5.48 shows the results of our 2D MC simulations for measurements with the standard settings of the *a*SPECT spectrometer, reduced widths of the neutron beam as well as a reduced height of the main magnetic field.

The comparison between Figs. 5.48a to 5.48c shows the strong dependence of the edge effect on the shape of the neutron beam profile. With increasing width of the neutron beam, the impact of the edge effect on the angular correlation coefficient a decreases: The strong dependence of the shift in a on the exact position of the proton detector drops down from $\Delta a/a \in (-10.5\,\%, +2.5\,\%)$ for the 5 mm wide aperture to $\Delta a/a \in (-2.2\,\%, +1\,\%)$ for the full width of the neutron beam. Thus, also the magnitude of the shift in a decreases.

In addition, the comparison between Figs. 5.48c and 5.48d shows the dependence of the edge effect on the width of both transition regions (see Fig. 3.23). With decreasing height of the main magnetic field the proton's radius of gyration Eq. (3.3) increases and

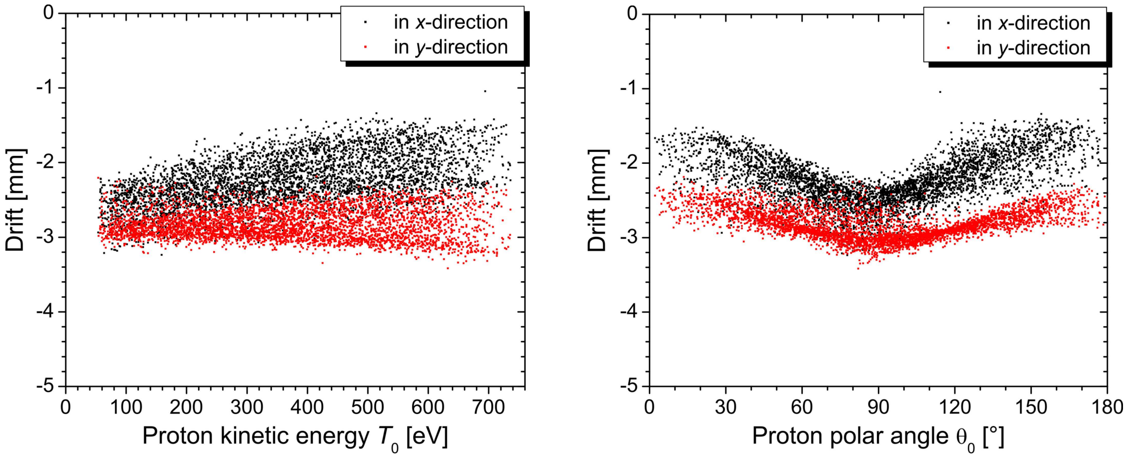

(a) $B_0 = 2.177\,\mathrm{T}$ (b) $B_0 = 2.177\,\mathrm{T}$

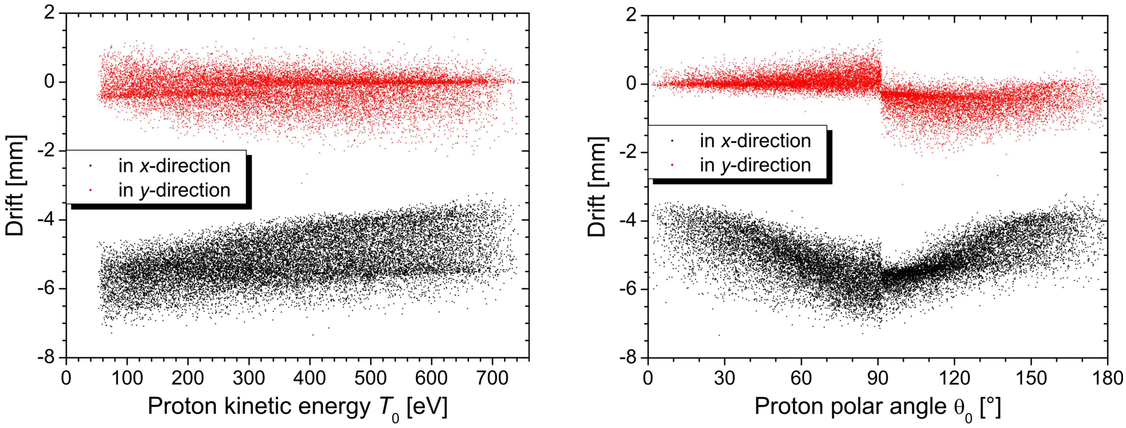

(c) $B_0 = 0.933\,\mathrm{T}$ (d) $B_0 = 0.933\,\mathrm{T}$

Figure 5.47: Drift of the decay protons in the x-y-plane for different settings of the aSPECT spectrometer: (a) and (b) for $I_{\text{main}} = 70\,A$ and $U_{16\mathrm{A}}|U_{16\mathrm{B}} = -4.2\,\mathrm{kV}|{-0.2}\,\mathrm{kV}$, and (c) and (d) for $I_{\text{main}} = 30\,A$ and $U_{16\mathrm{A}} = U_{16\mathrm{B}} = -2\,\mathrm{kV}$. (a) and (c) show the energy dependence of the proton drift, while (b) and (d) present the angular dependence. We note that the lower dipole electrode e8 mainly causes a drift of the decay protons in x-direction, while the upper dipole electrode e16 causes a drift in y-direction. Further input data for the MC simulations (in INM approximation): $B_\mathrm{A}/B_0 = 0.203$, $U_1 = U_{1\mathrm{b}} = 800\,\mathrm{V}$, $U_2 = 820\,\mathrm{V}$, $U_{8\mathrm{R}}|U_{8\mathrm{L}} = -50\,\mathrm{V}|{-1000}\,\mathrm{V}$, $U_\mathrm{A} = 50\,\mathrm{V}$, $U_{17} = -15\,\mathrm{kV}$, number of generated events $= 2 \times 10^6$ (for each setting), and $a = -0.105$ (derived from $\lambda = -1.2701(25)$ [10]). For better visibility, we only show 2×10^4 events.

hence the transition regions get wider. Therefore, the shift in a increases dramatically, compared to measurements with the standard height of the main magnetic field. Moreover, the impact of the edge effect further depends on the rotation angle ϕ_{det} of the proton detector in the x-y-plane. This also reflects the dependence of the edge effect on the width of the transition regions, as the rotation angle Eq. (5.68) corresponds to a widening of the projected area (see also Fig. 3.23) by about 10 %.

For comparison, Fig. 5.49 shows the influence of the edge effect on a for the full width of the neutron beam but the simulated beam profile instead. The comparison to Figs. 5.48c and 5.48d emphasizes the necessity of a precise knowledge of the neutron beam profile

Table 5.6: Mean proton drift $(\Delta x, \Delta y)$ for several different settings of the *a*SPECT spectrometer. See the text for details.

I_{main} [A]	U_1 [V]	U_2 [V]	$U_{8\mathrm{R}}$ [V]	$U_{8\mathrm{L}}$ [V]	$U_{16\mathrm{A}}$ [kV]	$U_{16\mathrm{B}}$ [kV]	U_{17} [kV]	Δx [mm]	Δy [mm]	Measurement run
30	800	820	0	-200	-2	-2	-15	-1.25 ± 3.75	-1.5 ± 4.5	22_05_08/night
30	800	820	-50	-1000	-2	-2	-15	-5 ± 4	-1.5 ± 4.5	21_05_08/night, 22_05_08/teatime
70	0	0	-50	-1000	-4.2	-0.2	-10	-2.5 ± 2	-3 ± 1.5	21_04_08/night
70	800	820	0	-200	-2	-2	-15	-0.75 ± 1.25	0 ± 1.5	15_05_08/night
70	800	820	0	-200	-3.7	-4.3	-15	-0.5 ± 2.5	0.5 ± 2	16_05_08/night
70	800	820	-50	-1000	-2	-2	-15	-2 ± 2	0 ± 2	19_05_08/night_2, 20_05_08/lunch, 20_05_08/night, 21_05_08/morning
70	800	1000	0	-10	-2	-2	-15	0 ± 2	0 ± 1.5	19_05_08/lExB
70	800	1000	0	-100	-4.2	-0.2	-10	-0.25 ± 2.75	-3 ± 2	23_04_08/night
70	800	1000	0	-200	-4.2	-0.2	-10	-0.2 ± 2.75	-3 ± 3	12_05_08/night
70	800	1000	0	-2000	-4.2	-0.2	-10	-3.5 ± 2.5	-3 ± 3	24_04_08/night
70	800	1000	-50	-1000	-2	-2	-9	-2 ± 2	0 ± 2	16_04_08/night
70	800	1000	-50	-1000	-2	-2	-10	-2 ± 2	0 ± 2	20_04_08/night, 14_05_08/night
70	800	1000	-50	-1000	-2	-2	-12	-2 ± 2	0 ± 2	27_04_08/night, 28_04_08/night
70	800	1000	-50	-1000	-2	-2	-15	-2 ± 2	0 ± 2	17_05_08/night2, 18_05_08/night, 19_05_08/night_1
70	800	1000	-50	-1000	-3.7	-4.3	-15	-2 ± 2	0.25 ± 2.25	17_05_08/night
70	800	1000	-50	-1000	-4.2	-0.2	-10	-2.25 ± 2.25	-3 ± 3	17_04_08/night, 18_04_08/night, 19_04_08/night, 22_04_08/night, 25_04_08/night2, 06_05_08/night, 11_05_08/night2, 13_05_08/night2
70	800	1000	-50	-1000	-4.2	-0.2	-15	-2.25 ± 2.25	-3 ± 3	18_05_08/morning

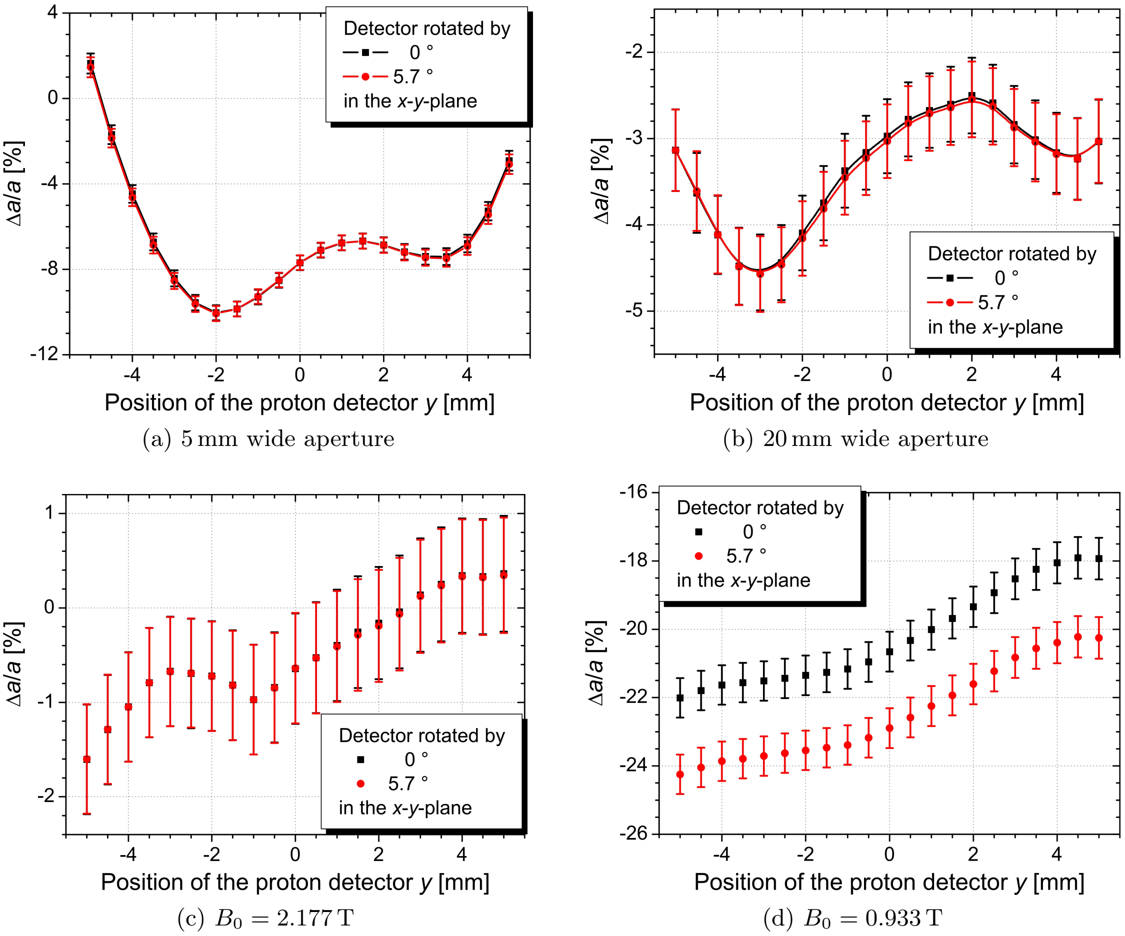

(a) 5 mm wide aperture (b) 20 mm wide aperture

(c) $B_0 = 2.177\,\mathrm{T}$ (d) $B_0 = 0.933\,\mathrm{T}$

Figure 5.48: Relative change of the angular correlation coefficient a for different positions and rotation angles of the proton detector, (a) for the 5 mm wide aperture (17_04_08/night), (b) for the 20 mm wide aperture (14_05_08/night), (c) for the full width of the neutron beam (20_05_08/night), and (d) for the full width of the neutron beam but a reduced height of the main magnetic field (21_05_08/night). With increasing width of the neutron beam the impact of the edge effect on a decreases, whereas with decreasing height of the main magnetic field the shift in a increases dramatically. See the text and Table 5.6 for details. The error bars show statistical errors only and are strongly correlated, as each point stems from the same MC simulation (number of generated events = 10^8).

in the DV. Hence, we strongly recommend improved measurements of the neutron beam profile(s) directly in the DV and subsequent analysis of the measured beam profiles by means of the image plate scanner (cf. also Fn. 5 in Chap. 4), in a further beam time.

Dependence of a on the Location on the Proton Detector

Further measurements at a low-energy, low-flux proton accelerator for detector tests (PAFF) [237, 238] revealed that the pulse height of the protons and hence the position of the proton peak changes over the detector [52]. Figure 5.50 shows that the average pulse height of the protons is reduced close to the edges of the detector. At present, it is still unclear whether this effect is restricted to a small area around the point investigated with

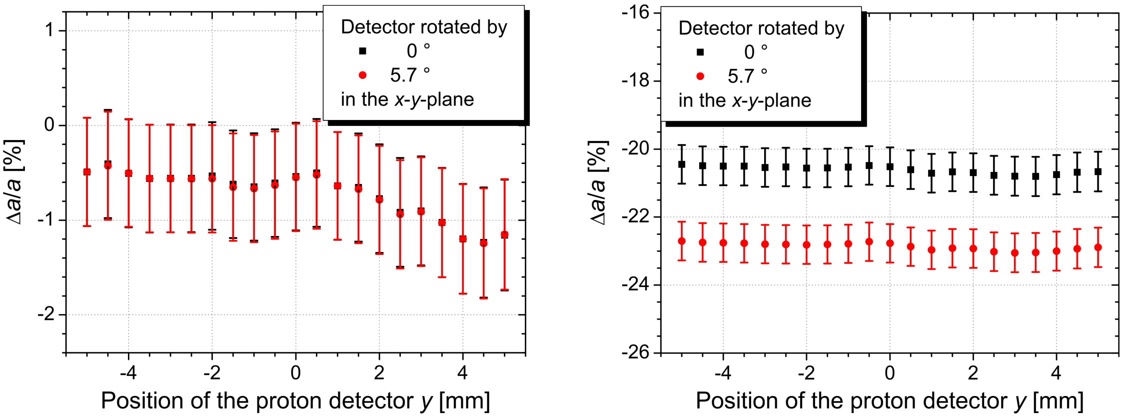

(a) $B_0 = 2.177\,\mathrm{T}$ (b) $B_0 = 0.933\,\mathrm{T}$

Figure 5.49: Uncertainty in the angular correlation coefficient a due to the knowledge of the neutron beam profile. (a) and (b) show the relative change of a for different positions and rotation angles of the proton detector. Compared to Figs. 5.48c and 5.48d, these figures show the influence of the edge effect on a for the simulated instead of the measured beam profile. See the text and Figs. 5.44 and 5.48 for details. The error bars show statistical errors only and are strongly correlated, as each point stems from the same MC simulation (number of generated events = 10^8).

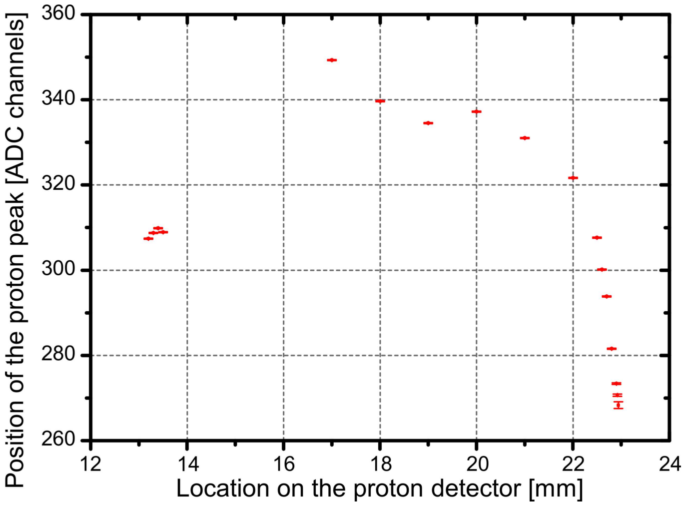

Figure 5.50: Change of the position of the proton peak over the detector. Figure taken from Ref. [52].

PAFF. For details the reader is referred to Ref. [52].

With regard to the dependence of the neutrino-electron correlation coefficient a on the lower integration limit (discussed in Sec. 5.4.1), the spatial distribution of the edge effect over the detector was investigated. For this purpose, the detector was divided into twenty 0.5 mm wide stripes parallel to the neutron beam. Then, the influence of the edge effect on a was calculated separately for each stripe. Figure 5.51 shows the results of our 2D MC simulations for measurements with a reduced widths of the neutron beam as well as the standard settings of our spectrometer. Again, the impact of the edge effect on a strongly depends on the position of a single stripe. In the case of the 5 mm wide aperture,

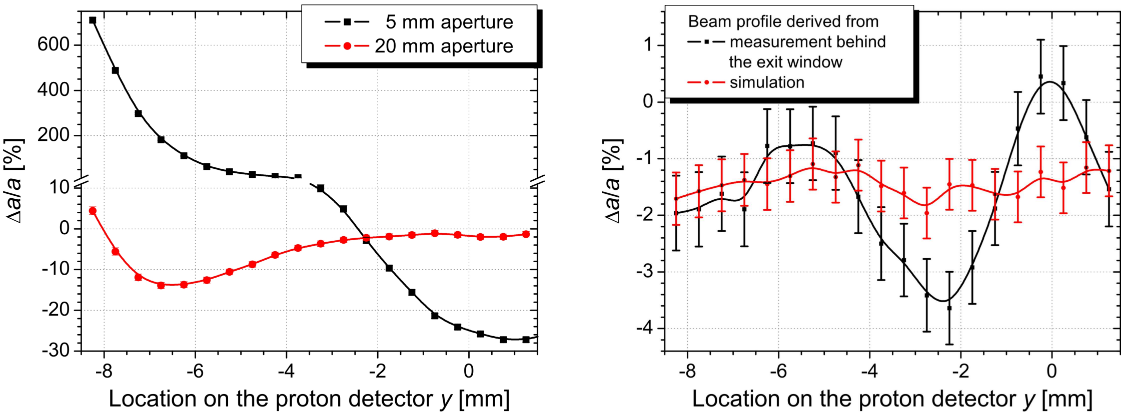

(a) Additional aperture (b) Full width

Figure 5.51: Relative change of the angular correlation coefficient a for different locations on the proton detector, (a) for the 5 mm and the 20 mm wide aperture and (b) for the full width of the neutron beam. The figures show the spatial distribution of the edge effect over the width of the proton detector. See the text and Figs. 5.48 and 5.49 for details. Number of generated events $= 4 \times 10^8$ for the 5 mm wide aperture, 8×10^8 for the 20 mm wide aperture, 16×10^8 for the full width of the neutron beam, and 32×10^8 for the full width of the neutron beam but the simulated instead of the measured beam profile. Error bars show statistical errors only.

the shift in a reaches in excess of $\Delta a/a \approx 700\,\%$, compared to $\Delta a/a = -6.86(39)\,\%$ over the entire detector (from Fig. 5.48a). However, for the full width of the neutron beam, the dependence of a on the location on the proton detector ($\mathcal{O}\,(1\,\%)$) cannot explain the observed shift Eq. (5.19) in the order of $-10\,\%$, cf. Fig. 5.51b.

We note that Fig. 5.51b additionally emphasizes the necessity of a more uniform neutron beam profile. For the rather flat, simulated neutron beam profile (Fig. 5.44a compared to 5.44c), the shift in the angular correlation coefficient a is almost constant over the proton detector.

Correction for the Edge Effect

As explained in the previous sections, the impact of the edge effect on the neutrino-electron correlation coefficient a is derived from combined MC simulations, where

- MC simulations in (2D) axially symmetric fields serve to determine the dependence of a on the position of the proton detector, cf. Fig. 5.48, and
- MC simulations in (3D) non-axially symmetric electric fields serve to determine the mean proton drift in dependence of the settings of the spectrometer, cf. Fig. 5.47 and Table 5.6.

Table 5.7 presents the results of our combined MC simulations in comparison with the uncorrected values, a_{exp}, for the angular correlation coefficient a. Obviously, the observed shifts, $\Delta a_{\mathrm{exp}}/a_{\mathrm{exp}}$, in the angular correlation coefficient a are in poor or no agreement with the predicted values, $\Delta a/a$, from our MC simulations. In particular,

Table 5.7: Relative change of the angular correlation coefficient a for different settings of the aSPECT spectrometer, see Table 5.6 for details. The third column gives the uncorrected values a_{exp} for a. The fourth and fifth column list the observed changes of a_{exp} in comparison with the expected values from our MC simulations of the edge effect. See the text for details.

Measurement run	Δy [mm]	a_{exp}	$\Delta a_{\text{exp}}/a_{\text{exp}}$ [%]	$\Delta a/a$, simulated [%]	Test	Comment
21_05_08/night	0	-0.0697(38)			$B_0 = 0.933\,\text{T}$	
20_05_08/lunch, 20_05_08/night	0	-0.1025(28)	31.97 ± 4.16	$-22.82 \pm 0.91^{+0.35}_{-0.00}$	vs. $B_0 = 2.177\,\text{T}$	
15_05_08/night	0	-0.1092(31)			20 mm aperture	different
20_05_08/lunch, 20_05_08/night	0	-0.1025(28)	-6.58 ± 4.22	$-3.67 \pm 0.74^{+1.37}_{-0.09}$	vs. full width	lower $\mathbf{E} \times \mathbf{B}$
18_05_08/morning	-3	-0.0978(37)			full width,	
17_05_08/night2, 18_05_08/night	0	-0.0978(29)	0.00 ± 4.80	$-0.06 \pm 0.81^{+0.52}_{-0.00}$	upper $\mathbf{E} \times \mathbf{B}$	
14_05_08/night	0	-0.1118(46)			20 mm aperture	different U_{17};
27_04_08/night, 28_04_08/night	0	-0.1050(33)	-6.53 ± 5.49	$-3.67 \pm 0.74^{+1.37}_{-0.09}$	vs. full width	cf. also Fn. 7
13_05_08/night2	-3	-0.1003(43)			20 mm aperture,	
14_05_08/night	0	-0.1118(46)	10.29 ± 5.33	$1.20 \pm 0.59^{+0.37}_{-1.41}$	upper $\mathbf{E} \times \mathbf{B}$	cf. also Fn. 7
13_05_08/night2	-3	-0.1003(43)			20 mm aperture	
22_04_08/night, 25_04_08/night	-3	-0.1014(22)	1.06 ± 4.74	$-2.36 \pm 0.73^{+0.09}_{-0.61}$	vs. full width	cf. also Fn. 7
17_04_08/night	-3	-0.1433(64)			5 mm aperture	
18_04_08/night, 19_04_08/night	-3	-0.1084(28)	-32.23 ± 6.83	$-7.58 \pm 0.71^{+1.07}_{-1.38}$	vs. full width	cf. also Fn. 7
16_04_08/night	0	-0.1358(48)			5 mm aperture,	different U_{17};
17_04_08/night	-3	-0.1433(64)	5.23 ± 5.40	$1.51 \pm 0.48^{+3.37}_{-1.30}$	upper $\mathbf{E} \times \mathbf{B}$	cf. also Fn. 7
16_04_08/night	0	-0.1358(48)			5 mm aperture	different U_{17};
20_04_08/night	0	-0.1014(40)	-33.93 ± 7.09	$-6.02 \pm 0.72^{+4.86}_{-2.22}$	vs. full width	cf. also Fn. 7

- in the case of measurements with a reduced height of the main magnetic field, by a factor of 3/7, the uncorrected value for a is shifted to more positive values while the simulations predict a shift to more negative values, and
- in the case of measurements with an additional 5 mm wide aperture, i.e., a neutron beam profile reduced in width by about a factor of 3, the uncorrected value for a is shifted to much more negative values than predicted by the simulations.

As stated in the previous Sec. 5.4, our data analysis revealed three major problems in the aSPECT spectrometer:

- a saturation effect of the detector electronics shortly after high-energy electrons (for details see Sec. 5.4.1). For measurements with a reduced height of the main magnetic field, this effect is reduced, because of an increased spatial separation of decay protons and electrons on the proton detector (cf. Sec. 5.5.5).
- a possible charging of the collimation system (see Secs. 5.4.4 and also 5.5.2). As already mentioned, for a strongly reduced width of the neutron beam, this effect is suppressed.
- possible Penning discharges in the bottom of the spectrometer (discussed in Sec. 5.4.3). For the strongly reduced width of the neutron beam, the total neutron flux decreases by about a factor of 4.5 (cf. Fn. 14). Then also the full electron decay rate is reduced by about a factor of 4.5 and hence the effect of Penning discharges in the bottom of the spectrometer is reduced.

and in the case of a reduced height of the main magnetic field, additionally,

- an enhanced violation of the condition for adiabatic transport (discussed in Sec. 5.5.5).

Hence, the measurements with a strongly reduced width of the neutron beam are dominated by the saturation of the preamplifier. Thus, it is possible to estimate the impact of the saturation effect on the angular correlation coefficient a from the observed shift in a in comparison to the predicted value from our MC simulations. This comparison results in a shift of the neutrino-electron correlation coefficient a due to the saturation of the preamplifier of

$$\boxed{\Delta a/a = (-26.27 \pm 4.95^{+1.31}_{-2.49})\,\%} \tag{5.72}$$

in agreement with our correction for the saturation effect Eq. (5.32). Here, the relative error of 19 % is dominated by counting statistics. Further 3D MC simulations, considering the saturation effect, confirmed a shift in the angular correlation coefficient a due to the saturation of the preamplifier of

$$\Delta a/a = -28.92(31)\,\%. \tag{5.73}$$

We note that the opposite sign of the shift in a, in the case of measurements with a reduced height of the main magnetic field, was already discussed in Sec. 5.5.5 (see also Secs. 5.4.3 and 5.4.4).

Finally, to correct for the edge effect, we have to subtract the respective shift in a due to the edge effect, shown in Fig. 5.48, from the uncorrected values, a_{exp}, for a. For our

Table 5.8: The uncorrected values, a_exp, for a for measurements with the full width of the neutron beam.

Measurement run	r_B	U_2 [V]	$U_{8\mathrm{R}}$ [V]	$U_{8\mathrm{L}}$ [V]	$U_{16\mathrm{A}}$ [kV]	$U_{16\mathrm{B}}$ [kV]	a_exp
16_05_08/night	0.203	820	0	-200	-3.7	-4.3	-0.0953(27)
17_05_08/night2	0.203	1000	-50	-1000	-2	-2	-0.0960(48)
18_05_08/morning	0.203	1000	-50	-1000	-4.2	-0.2	-0.0978(37)
18_05_08/night	0.203	1000	-50	-1000	-2	-2	-0.0996(32)
19_05_08/lExB	0.203	1000	0	-10	-2	-2	-0.0921(51)[a]
19_05_08/night	0.203	1000/820	-50	-1000	-2	-2	-0.0991(34)
20_05_08/lunch	0.203	820	-50	-1000	-2	-2	-0.1020(45)
20_05_08/night	0.2049	820	-50	-1000	-2	-2	-0.1029(34)

[a] The uncorrected value a_exp for a was determined by the "maximum−baseline method" instead of from the fitted pulse height spectra (for details see Sec. 5.1). On average, the data fitting shifts such results to more negative values, by $\Delta a_\mathrm{exp}/a_\mathrm{exp} = (-2.01 \pm 2.00)\,\%$.

standard settings (cf. Table 3.1), the edge effect yields a shift in the neutrino-electron correlation coefficient a of

$$\boxed{\Delta a/a = (-1.474 \pm 0.145^{+0.100}_{-0.490})\,\%} \tag{5.74}$$

cf. Fig. 5.48c. Here, the first error stems from the simulation statistics (number of generated events $= 16 \times 10^8$) and the latter one from the uncertainty in the position of the proton detector relative to the rest of the electrode system and the magnetic field.

As a note on the performance of our MC simulations: the simulation of only 1×10^8 events yields to a shift in a of, e.g., $\Delta a/a = -0.79(58)\,\%$, in moderate agreement with Eq. (5.74). Hence, for further investigations of the edge effect, we strongly recommend to increase the simulation statistics (by means of MC simulations on a computer cluster). In addition, we suggest to repeat all investigations concerning the edge effect, in a further beam time.

5.6 The Antineutrino-Electron Correlation Coefficient a

5.6.1 Analysis

As explained at the beginning of this chapter, the data analysis was performed blinded. After the data analysis was completed, the data was unblinded. Table 5.8 presents the uncorrected values, a_exp, for a for measurements with the full width of the neutron beam and from a time when the count rates were not fluctuating non-statistically (cf. Fn. 7). The values for the neutrino-electron correlation coefficient a given in Table 5.8 are corrected only for the blind analysis Eqs. (5.1) and (5.2), the dead time of the electronics Eq. (5.10), and the AP voltage dependent background (for details see Sec. 5.3.1). Those corrections for systematic effects determined in this thesis are not yet included. Therefore, the quoted uncertainties on a represent only the statistical errors.

The scatter between the individual measurement runs was investigated earlier in Sec. 5.4.3. In contrast to Sec. 5.4.3, the uncorrected value a_{exp} for a from the measurement run 16_05_08/night is shifted to more positive values. We believe that this is the result of the reduced drift potential (cf. Sec. 5.3.2), from $U_{8\mathrm{R}}|U_{8\mathrm{L}} = -50\,\mathrm{V}|-1000\,\mathrm{V}$ to $0\,\mathrm{V}|-200\,\mathrm{V}$. But we should not jump to conclusions, as also the drift potential $U_{16\mathrm{A}}|U_{16\mathrm{B}}$ and the mirror potential U_2 were changed. Indeed, the uncorrected value a_{exp} for a from the measurement run 19_05_08/lExB, for which the drift potential was drastically reduced to $U_{8\mathrm{R}}|U_{8\mathrm{L}} = 0\,\mathrm{V}|-10\,\mathrm{V}$, is shifted to even more positive values.

5.6.2 Corrections

In Table 5.9 we list all systematic effects on the neutrino electron-correlation coefficient a, together with the respective corrections and uncertainties. In addition, we give a **preliminary** value for the total uncertainty on a.

Table 5.9: Corrections and uncertainties on the antineutrino-electron angular correlation coefficient a. See the text for details.

Effect on the angular correlation coefficient a	Relative correction [%]	Relative error [%]	Relative error (MC) [%]	Reference
Theoretical corrections				
Coulomb correction[a]	-6.86			
Higher-order Coulomb[a]	-0.26			
Recoil correction[a]	0.09		0.07	see also [74]
Radiative correction[a]	≈ 2.98			[74] and (2.43)
Weak magnetism		$^{+0.02}_{-0.01}$		from [74]
Fit of MC data[b]		< 0.05		
Transmission function				
B field gradient	-0.001		0.05	(3.46)
B field ratio r_{B}		0.26	0.1	(4.6) (see also [53])
Barrier voltage U_{A}	-0.09		0.11	(4.7)
Non-adiabatic motion[c]	0.014	$^{+0.013}_{-0.026}$		(5.67) (see also [47])
Mirror potential[d]	-0.55	$^{+3.48}_{-3.25}$		(5.42)
Charging collimation	23.23	$^{+22.23}_{-16.33}$		(5.50)
Background				
Dependence on U_{A}[e]	≈ -1	0.2		from [34]
Background peak 1	-1.14	0.3		[34] and (5.15)

---

[a] Theoretical correction already included in the fit function.

[b] Correction already taken into account in the data analysis.

[c] Derived from Table 4.1 by numerical interpolation, with $\Delta a/a = 75.52 \cdot \exp(-3.952\,\mathrm{T}^{-1} \cdot B_0)$.

[d] Correction only applicable for $U_2 = 1000\,\mathrm{V}$ compared to $U_2 = 820\,\mathrm{V}$.

[e] Correction already included in the raw data analysis.

Effect on the angular correlation coefficient a	Relative correction [%]	Relative error [%]	Relative error (MC) [%]	Reference
Background peak 2	2.07	0.31		[34] and (5.16)
Penning Discharges[d]	≈ 9.29	$^{+5.04}_{-4.61}$		(5.43)
Detector efficiency				
Proton backscattering	< 0.22		0.16	(3.56) (see also [52])
Electronic noise	0.035		0.05	(5.12)
Dead time	< 4[e]	0.145		[34, 52], (5.12), (5.14)
Lower integration limit[e]	0.13		0.09	[52] and (5.19)
Trigger efficiency	≈ 0.2			Ref. [34] and (5.20)
Preamplifier saturation[f]	-16.81	$^{+6.00}_{-5.05}$		(5.32)
Electron backscattering	-0.38	$^{+3.56}_{-3.32}$		(5.40)
Edge effect[g]	-1.45	$^{+0.18}_{-0.49}$		(5.74)
WF inhomogeneity				
in the AP		0.37	0.07	(6.9)
in the DV		0.24	0.05	(6.10)
Proton reflections	0.03	$^{+0.03}_{-0.32}$	0.08	(6.27)
Absolute WF values		$^{+1.01}_{-0.99}$	0.13	(6.9),(6.10),(6.27),(6.28)
Systematics, included	≈ -0.93		0.09	
Systematics, excluded	≈ 5.93	$^{+23.38}_{-17.43}$	0.28	please note Fn. f
Systematics, excluded[d]	≈ 14.68	$^{+24.17}_{-18.32}$	0.28	please note Fn. f
Statistics		1.4		from [34]

5.6.3 Result

As quoted earlier on page 127, we could only set upper limits on the correction of the problem in the detector electronics, which are too high to determine a meaningful result from our latest beam time at the ILL. Therefore, our collaboration decided to stop the data analysis without giving a final or even preliminary value for the antineutrino-electron angular correlation coefficient a.

From the measurement runs 20_05_08/lunch and 20_05_08/night, e.g., we could extract a preliminary value for the angular correlation coefficient a of

$$a^{\text{prel}} = -0.1085 \pm 0.0028(\text{stat})^{+0.0179}_{-0.0240}(\text{sys}), \tag{5.75}$$

similar to Stratowa *et al.* and Byrne *et al.*, but less accurate. However, I merely mention it as a personal example.

---

[f] Correction only applicable for a lower integration limit of 80 ADC channels.

[g] Correction only applicable for the full width of the neutron beam, $I_{\text{main}} = 70\,\text{A}$, and $U_{16} = -2\,\text{kV}$.

Chapter 6

Investigations of the Patch Effect

In our measurement, the potential difference between decay volume (DV) and analyzing plane (AP), $U_A - U_0$, has to be known precisely to determine the transmission function, Eq. (3.30). In order to keep systematic uncertainties in the neutrino-electron correlation coefficient a well below the design accuracy of aSPECT, which is $\Delta a/a = 0.3\,\%$, we have to know the potential barrier U_A ($U_0 \equiv 0$) with an accuracy of better than 10 mV, cf. Sec. 3.1.3. The voltage applied to the AP electrode e14 is monitored by a precise multimeter, currently an Agilent 3458A. The accuracy of the voltage settings is better than 5 mV, limited by the calibration of the multimeter. However, a variation of the work function within an electrode or between different electrodes would render the potential difference $U_A - U_0$ uncertain despite the multimeter measurement. Indeed, a variation of up to 250 meV over a distance of several cm was found in a cylindrical sample electrode at atmospheric pressure and room temperature[1], shown in Fig. 6.1. Assuming the potential barrier U_A were measured incorrectly by this amount, the extracted value for a would be wrong by 3.2(1) %, cf. Sec. 3.1.3. Therefore, surface coatings and/or treatments for the inner surfaces of our electrode system, which do not show this spatial variation, have to be found. We suspect that the impurity of our gold surface caused the problem[2]. Sputter coated gold surfaces or different surface materials are reported to give better results [205, 239–241].

To investigate this effect, further measurements with a Kelvin Probe are ongoing. These measurements are conducted at the University of Virginia in Charlottesville, USA. After a short introduction to the Kelvin technique, we will present the current status of our study. Based on the results of our investigations with the Kelvin Probe, we will determine the impact of the patch effect on the angular correlation coefficient a. More details on the measurements with the Kelvin Probe can be found in the theses of R. Hodges [242] and S. McGovern [243].

---

[1] This investigation was performed in cooperation with Prof. I. Baikie from KP Technologies Inc. in Wick, Scotland, using a custom-designed Kelvin probe similar to the one discussed in Ref. [239]. Details of the specific Kelvin probe and details about the investigation will be published soon.

[2] E.g., traces of Ca, Ni, Al, Si, Ti, Mg, Na, C, and O were found using a scanning electron microscope (SEM) together with an energy dispersive X-ray (EDX) analysis. The measurement was taken in cooperation with Dr. J. Huth from the Max Planck Institute for Chemistry in Mainz, Germany.

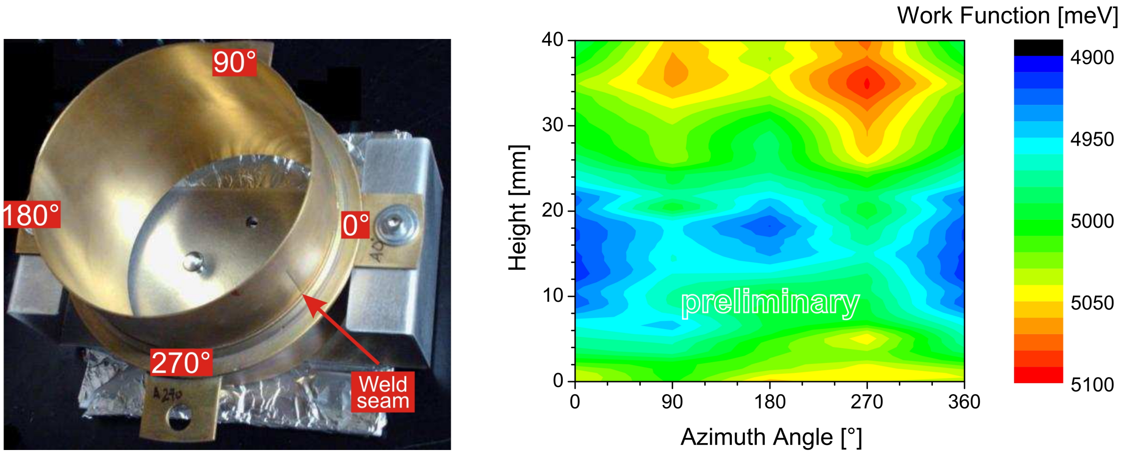

(a) (b)

Figure 6.1: Cylindrical sample electrode. The electrode was made of OFHC copper and was electrolytically coated with 2 μm of silver and then 1 μm of gold. (a) Morphological image. For circumference measurements, the electrode was held by an aluminum sample holder which was then mounted onto a rotational platform. Photograph courtesy of R. Hodges [242]. (b) Kelvin Probe scan[1]. Work function (WF) topography with 10 meV contour graduations: avg WF 4991 meV, RMS WF 44.5 meV, PTP WF 178.9 meV. R. Hodges measured the electrode at University of Virginia, after it had been measured by Prof. I. Baikie, and found a PTP WF value of about 250 meV [242].

6.1 Introduction

The work function (WF) is the minimal energy required to extract one electron from the surface of a conducting material to a point outside the metal with zero kinetic energy. The WF is continuous across the interior of the material, however at the surface the electron energy is influenced by the exact state of the surface, e.g., type orientation and direction of the outer atoms and molecules. Thus different crystallographic orientations of the same material may have different WF, see Table 6.1. As the electron has to move through the surface region, its energy is influenced by the optical, electric, and mechanical characteristics of this region. Hence, the WF is modified by absorbed or evaporated layers [245, 246], surface reconstruction, surface charging, oxide layer imperfections, surface and bulk contamination, etc. The WF may vary over the surface of a polycrystalline material due to regions of different crystal orientation and over the surface of an alloy or compound due to non-uniform segregation of the elements [247]. Such differences in WF over regions of a surface cause the so-called patch effect.

6.1.1 Surface Analysis

The WF is an extremely sensitive indicator of surface condition and can therefore be employed in many detection-based scenarios. Examples include WF/topography variations which occur in, e.g., adsorption, biotechnology, charge analysis, coatings, corrosion, nanotechnology, semiconductors, solar cells, surface contamination, surface chemistry, and surface photo-voltaic. Scanning probe microscopy (SPM) covers several related technologies for imaging and measuring surfaces on the nanometer scale. SPM technologies share

Table 6.1: Electron work function (WF) of selected elements from the CRC Handbook of Chemistry and Physics [244]. As can be seen in the second column, the WF usually differs for each face of a mono-crystalline sample. Since the WF is dependent on the cleanliness of the surface, measurements reported in the literature often cover a considerable range. The third column contains selected values for the WF which may be regarded as typical values for a reasonably clean surface. Values in parentheses are only approximate. In the fourth column, the method of measurement is indicated for each value. The following abbreviations are used: polycr (polycrystalline sample), PE (photoelectric effect), and CPD (contact potential difference).

Element	Plane	WF [meV]	Method	Element	Plane	WF [meV]	Method
Ag	100	4640	PE	Fe	100	4670	PE
	110	4520	PE		111	4810	PE
	111	4740	PE	Mg	polycr	3660	PE
Al	100	4200	PE	Na	polycr	2360	PE
	110	4060	PE	Ni	100	5220	PE
	111	4260	PE		110	5040	PE
Au	100	5470	PE		111	5350	PE
	110	5370	PE	Pt	polycr	5640	PE
	111	5310	PE		100	5840	PE
Be	polycr	4980	PE		111	5930	PE
C	polycr	(5000)	CPD		320	5220	PE
Ca	polycr	2870	PE		331	5120	PE
Cr	polycr	4500	PE	Rh	polycr	4980	PE
Cu	100	5100	PE	Si	n	4850	CPD
	110	4480	PE		p 100	(4910)	CPD
	111	4940	PE		p 111	4600	PE
	112	4530	PE	Ti	polycr	4330	PE

the concept of scanning an extremely sharp tip (3-50 nm radius of curvature) across the object surface. The most commonly used SPM techniques are:

Atomic Force Microscopy (AFM): measures the interaction force between the tip and surface.

Scanning Tunneling Microscopy (STM): measures a weak electrical current flowing between tip and sample as they are held a very distance apart.

In the present thesis, a Kelvin Probe (KP) was used to measure the WF of primarily gold- and platinum-plated samples. Although not as well known as other surface analysis techniques, the KP has undergone a dramatic renaissance over the last few years. The KP is a non-invasive technique, yet it is extremely sensitive to changes in the top-most atomic layers, such as those caused by deposition, absorption, corrosion, and atomic displacement.

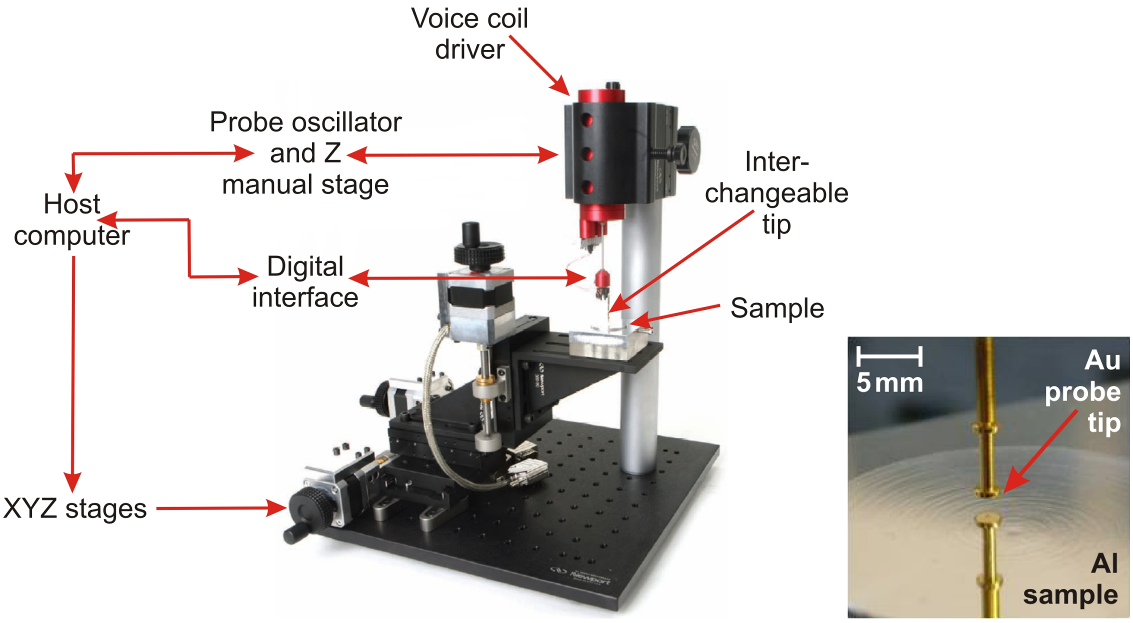

(a) (b)

Figure 6.2: (a) Main components of the computer (PC) controlled ambient Scanning Kelvin Probe system SKP5050 [250]. The PC houses the digital oscillator (which powers the voice coil actuator), data acquisition system, and motorized (x, y, z) stage controller. The signal is derived from a low-noise, high-gain current to voltage (I/V) converter mounted close to the tip. (b) Gold probe tip measuring a reflective aluminum sample. Photograph courtesy of S. McGovern [243].

6.2 Operation of the Kelvin Probe

The Kelvin Probe is a non-contact, non-destructive vibrating capacitor device which measures the WF difference between a conducting specimen and a vibrating probe tip, as shown in Fig. 6.2b. The KP measures the average WF of the sample under the probe tip without the bias toward low WF patches characteristic of photo and field emission. The particular KP at University of Virginia used for these measurements is a custom-designed ambient Scanning Kelvin Probe (SKP) system [242, 243], similar to the one shown in Fig. 6.2a. The probe tip used is a gold disk electrode of diameter 2 mm, shown in Fig. 6.2b, which is scanned above the sample surface using a computer controlled (x, y, z) scanning system. This allows the measurement of the WF, with a resolution of $(1-3)$ meV [248][3], to be spatially resolved across the surface. A general description of the probe operation can be found in Ref. [249] and more details in its operating manual [248]. Here, we will only give a brief description.

6.2.1 Theory

The series of schematic diagrams on the following page illustrate the principles of local WF measurement using a KP. In Figure 6.3a, the KP tip has a Fermi level, E_{Tip}, which differs from that of the sample, E_{S}. The difference in Fermi levels also implies a difference in the WF, Φ. If an external electrical contact is made between probe tip and sample, the

---

[3] In the case of a 50 μm tip, the WF resolution is $(5-10)$ meV only.

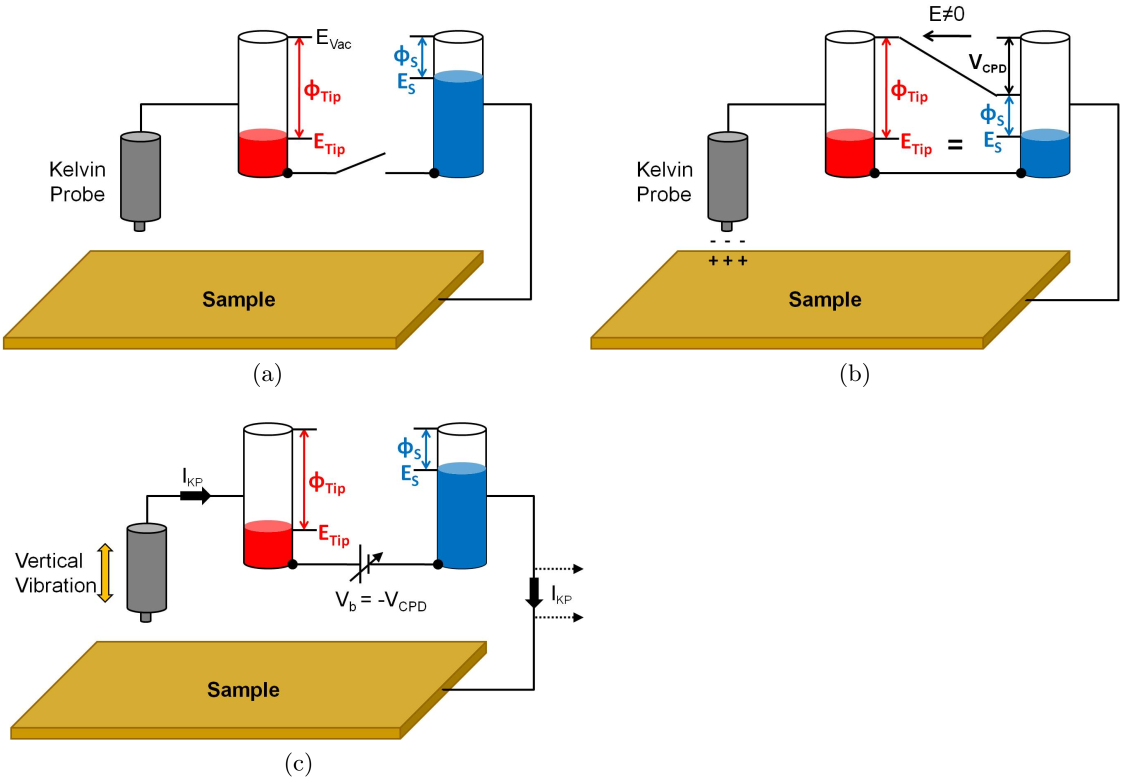

Figure 6.3: Electron energy level diagrams of two conducting specimens, Tip and Sample (S), (a) without contact, (b) with external electrical contact, and (c) with inclusion of the backing potential V_{b}. Φ_{Tip} and Φ_{S} are the work functions of the materials, and E_{Tip} and E_{S} represent their Fermi levels. In (b) the surface charge is related to the contact potential difference, V_{CPD}, through $Q = V_{\mathrm{CPD}} C_{\mathrm{KP}}$, where C_{KP} is the Kelvin probe capacitance. If tip and sample are connected by the external emf, V_{b}, and vibrated, then the current $I_{\mathrm{KP}} = dQ/dt = (V_{\mathrm{CPD}} + V_{\mathrm{b}})\, dC_{\mathrm{KP}}/dt$ flows.

Fermi levels equalize, resulting in the generation of an electrical charge on the respective surfaces, as shown in Fig. 6.3b. This surface charge gives rise to a potential difference, termed the contact potential difference (CPD), V_{CPD}, which relates to the difference in WF, $\Delta\Phi = \Phi_{\mathrm{S}} - \Phi_{\mathrm{Tip}}$, such that:

$$V_{\mathrm{CPD}} = \frac{1}{e}\Delta\Phi, \tag{6.1}$$

If a variable backing potential, V_{b}, is included in the external circuit, as shown in Fig. 6.3c, then the surface charge will become zero at the unique point where:

$$V_{\mathrm{b}} = -V_{\mathrm{CPD}}. \tag{6.2}$$

The KP deduces the point of zero charge by vibrating the probe tip in a vertical plane perpendicular to the sample surface and measuring the AC current flow, I_{KP}, that results if a surface charge, Q, exists:

$$I_{\mathrm{KP}}(t) = \frac{d}{dt}Q(t). \tag{6.3}$$

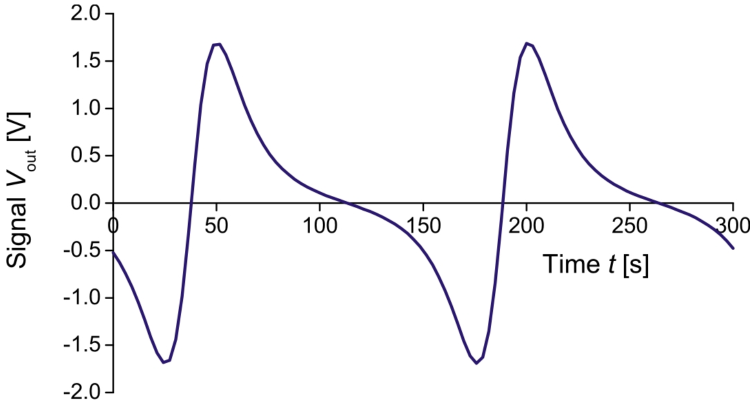

Figure 6.4: Typical Kelvin Probe output signal. As the probe oscillates above the sample the voltage change is recorded. The periodic signal Eq. (6.8) is shown with the modulation index set to $\epsilon = 0.7$.

The surface charge is related to the CPD and the external emf, V_{b}, through

$$Q(t) = (V_{\mathrm{CPD}} + V_{\mathrm{b}})C_{\mathrm{KP}}(t), \tag{6.4}$$

where C_{KP} is the KP capacitance. If probe tip and sample are assumed to have parallel-plate geometry, then the KP capacitance is given by

$$C_{\mathrm{KP}}(t) = \epsilon_0 \frac{A}{d(t)}, \tag{6.5}$$

where ϵ_0 is the dielectric constant, A is the area of the capacitor, and d is the separation distance of the plates. As the probe tip is oscillated above the sample surface, the separation distance can be written as

$$d(t) = d_0 + d_1 \sin(\omega t), \tag{6.6}$$

where d_0 is the distance at rest between probe tip and sample, d_1 is the amplitude of oscillation, and ω is the angular frequency of vibration. By substituting ϵ for d_1/d_0, termed the modulation index, and C_0 for $\epsilon_0 A/d_0$ in Eq. (6.5) we get

$$C_{\mathrm{KP}}(t) = \frac{C_0}{1 + \epsilon \sin(\omega t)}. \tag{6.7}$$

We successively substitute the result into Eqs. (6.4) and (6.3) to get the voltage change, given by the Ohm's law, $V_{\mathrm{out}}(t) = I_{\mathrm{KP}}(t)R$:

$$\begin{aligned} V_{\mathrm{out}}(t) &= -\left(V_{\mathrm{CPD}} + V_{\mathrm{b}}\right) RC_0\omega\epsilon \frac{\cos(\omega t)}{(1+\epsilon\sin(\omega t))^2} \\ &= \left(V_{\mathrm{CPD}} + V_{\mathrm{b}}\right) RC_0\omega\epsilon \frac{\sin(\omega t + \theta)}{(1+\epsilon\sin(\omega t))^2}, \end{aligned} \tag{6.8}$$

where R is the I/V converter feedback resistance and θ is the phase angle. A typical KP output signal is shown in Fig. 6.4. When the peak-to-peak voltage, V_{PTP}, is equal to zero, then the WF difference is simply equal and opposite to V_{b}, see also Eq. (6.1).

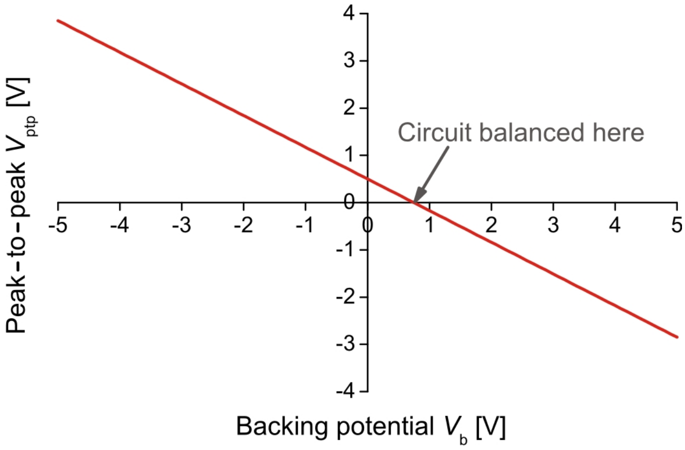

Figure 6.5: Peak-to-peak voltage V_{PTP} versus backing potential V_{b}. As can be seen from Eq. (6.8) this is a straight line. The slope is termed the Gradient and the intersection with the V_{b}-axis defines the measured work function value.

6.2.2 The “off-null” Technique

Traditional phase sensitive methods utilize a lock-in amplifier to detect the null output condition. However, these methods have the disadvantage that at the balanced point, the signal-to-noise ratio (SNR) reaches a minimum and the noise creates an offset voltage. A better method is to set the backing potential V_{b} to a range of voltages around the balanced point and then extrapolate to the null signal condition, as shown in Fig. 6.5, thus working to a high SNR. In this way, changes in V_{CPD} can be determined to sub-mV resolution. This “off-null” detection method was invented by Prof. I. Baikie [251].

6.2.3 Work Function Measurement

Since KP measurements can only detect the CPD, actual WF measurements are only possible through calibration. In other words, the KP needs to be calibrated against a surface with known WF. The challenge in this respect is that under ambient conditions it is hard to generate a surface with a defined WF. Hence KP measurements are more reliable in vacuum, where a well-defined surface can more reproducibly be generated and controlled. In *a*SPECT, we only have to know precisely the potential difference between DV and AP, $U_{\mathrm{A}} - U_0$, to determine the transmission function, Eq. (3.30). Therefore, the calibration against a surface with known WF can be trade off for a SKP which moves between DV and AP and measures the WF difference between the respective electrode surfaces and the vibrating probe tip.

Within this thesis, an ambient SKP was used to measure the WF difference between the samples and the probe tip. The WF measurements were performed at atmospheric pressure and room temperature. Preliminary calibration and experimentation of the SKP followed the instructions given in the operating manual [248]. WF measurements are prone to difficulties caused by stray charges, parasitic capacitance effects (discussed in Ref. [249]), and external mechanical vibrations. Stray charges were reduced by grounding the system to a common potential, except for the samples and the probe tip. External mechanical vibrations were reduced by weighing down the SKP stage with lead bricks.

6.2.4 Reference Sample

In Ref. [252] an error deduction method was suggested to eliminate the influence of space charge on the performance of the KP by introducing a reference sample. As mentioned above, this method is also valid to cancel the error due to changes in the WF of the probe. The particular KP used for these measurements was delivered with a reference sample with associated SKP topography. It is a polished aluminum substrate, half of the surface is gold-plated. The reference sample was characterized in Ref. [242]. A WF difference of 1404 meV to the theoretical difference of about 1400 meV was found[4]. In Ref. [243] the performance of a reference sample was tested[5]. A linear slide was introduced which moves back and forth between sample and reference sample. The probe tip remained at the same place and measurements, of one point on each surface, were taken for several hours. Unexpectedly, it has been found that the difference in WF values was not constant in time. We suspect that the surfaces are effected in different ways over time. Primarily, the target of our investigation is WF variation. In this regard, comparison of the standard deviation (RMS) on the WF for different samples is independent of the average WF value of a single sample. Consequently, further use of a reference sample was eliminated.

6.3 Samples, Data, and Results

The present thesis focused on the investigation of primarily gold and platinum coated oxygen-free high thermal conductivity (OFHC) copper samples, although others have been characterized. Table B.1 in App. B presents a summary of the samples studied to date including details of the substrates, surface treatments, and coatings[6]. The deposition method mainly used was electrolytically coating, although samples were fabricated by electro-chemical coating and physical vapor deposition (PVD), i.e., namely sputtering. Altogether, 58 samples were manufactured for measurement with the SKP, from what 17 samples remain to be scanned[7]. Another 18 samples are in preparation for sputtering. The majority of the samples were coated off-site and then shipped to the University of Virginia. Except for the glass substrate, the samples were $50 \times 50\,\mathrm{mm}^2$ by 1 mm in size. This size was chosen since it fitted with the SKP (x, y) translation of $50 \times 50\,\mathrm{mm}^2$ in the standard version. The samples were studied individually.

6.3.1 Details of the Samples

The samples chosen for study reflect the various possible materials for the electrodes, their surface treatments, and coatings to be used in *a*SPECT. The previous electrodes were made of OFHC copper and electrolytically coated with $2\,\mu$m of silver[8] and then $1\,\mu$m of gold. In order to keep systematic uncertainties in the angular correlation coefficient a well below 0.3 %, additionally, the residual gas pressure has to be $\leq 10^{-8}$ mbar and we have to know the size of the magnetic field B_0 in the DV (≈ 2.2 T) and B_{A} in the AP (≈ 0.44 T) with a relative accuracy of 10^{-4} (for details see Sec. 3.1.3 and Fig. 3.5). Suitable candidates for the substrate material are therefore ultra-high vacuum (UHV)

---

[4] The polishing process increases the rate of oxidation which decreases the WF of aluminum from 4200 meV (cf. Tab. 6.1) to about 4000 meV [205, 253].

[5] In Ref. [243] sample Cu25 (cf. Sec. 6.3) was used as a reference sample for its twin Cu26 instead.

[6] Details of the samples coated in the USA can be found in Refs. [242, 243].

[7] Unfortunately, the KP scans could not be finished within the Master's thesis of S. McGovern.

[8] The renewed and over-coated electrodes e3 – e6, e12, and e14 were coated with $10\,\mu$m of silver instead.

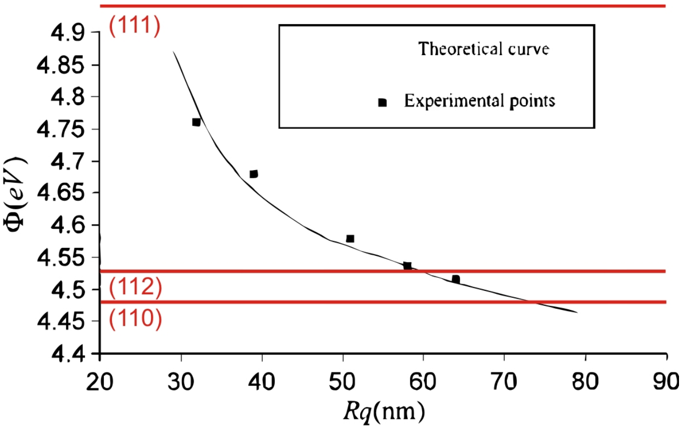

Figure 6.6: Work function (WF) Φ versus surface roughness (SR) Rq of copper, theoretical curve and experimental results. The WF of copper decreases with increasing SR. Figure taken from Ref. [254]. Different crystallographic orientations are emphasized in red for comparison only.

compatible, non-magnetic, and resistant to chemical reactions, such as OFHC copper, titanium, glass, silicon, and sapphire[9]. Candidates for the surface coating are additionally conductive, such as gold, platinum, ruthenium, and graphite[10]. Diffusion of copper in gold can be prevented by depositing an interlayer between the toplayer and the OFHC copper substrate. The various intermediate layers were chosen from adhesion, conductivity, and smoothness considerations. In our application, the standard interlayer, nickel, is excluded as nickel is ferromagnetic.

In addition, materials must be free of cracks and crevices which can trap cleaning solvents and become a source of virtual vacuum leaks later on. The (unpolished) copper and titanium substrates have a surface roughness (SR) better then 210 and 400 nm R_a (arithmetic average roughness value) plus 2.5 and 5.5 μm R_max (maximum roughness depth), respectively (for details see Table 6.5). With smaller SR, the coating adhesion but also the wear rate increase. In Ref. [254] it was reported that the WF of copper decreases with increasing SR, as shown in Fig. 6.6. We note that in Ref. [254] all samples were annealed to eliminate the effect of deformation from polishing on the WF. In order to increase the coating adhesion and, simultaneously, avoid an anisotropic WF, polishing techniques were investigated. Where possible, the substrate surface was polished (mechanically and/or by hand) to a mirror finish, as shown in Fig. 6.7a. Thereby non-magnetic polishing compounds and buffing wheels have been used only.

The electrodes used previously in *a*SPECT had a cylindrical shape, as shown in Fig. 6.1a, with the exception of the DV electrode gr. The pipes used were formed by rolling OFHC copper plates and welding the seam. To get an idea, whether and if so how the fabrication alters the metal's crystal lattice and/or WF, processing techniques were

---

[9] p-type 100 silicon wafers coated with 1 μm of titanium and then 0.1 and 0.2 μm of platinum, respectively, were investigated in Ref. [243]. Sapphire wafers were not yet studied.

[10] In Ref. [205] graphite coating was used to reduce charging inside the beam tube. Attempts to coat the inner surfaces of our electrode system with colloidal graphite failed. The graphite did not adhere to the surface. Even preheating the substrate and/or drying in the oven for up to one hour could not stabilize the adhesion. In contrast, Electrodag E graphite was successfully tested on thin copper and stainless steel foil sheets in Ref. [242]. R. Hodges found PTP WF values of less than 10 meV for single traces.

investigated. In a first step, copper plates were chopped and subsequently connected again (by means of welding or brazing), as shown in Fig. 6.12a. The cold forming may require additional normalizing with subsequent stress relieve annealing. This could be part of further investigations.

Most of the samples were doubly manufactured, i.e., twins of the same substrate, surface treatment, and coating (method, material, and layer thickness) were produced. Samples Cu1, Cu2, Cu7, Cu8, Cu21, Cu22, Ti1, and Ti2 were manufactured at a time when the ion source at University of Mainz, normally used to clean the substrate surface before sputtering, was inoperative. To get an impression, how important the cleaning process is, only samples Cu1, Cu8, Cu21, and Ti2 were cleaned with isopropyl alcohol before sputtering. Thus, these sputtered samples are no real twins. In addition, there was one processing technique which could not be studied. Samples Cu5 and Cu6 cannot be scanned as a tracking error occurs due to the weld seam. Besides, there is one surface coating which will not be studied. This is a titanium nitride (TiN) coating on copper. The sputtering on samples Cu39 to Cu42 failed, especially sample Cu39 fell down during the sputtering process. The company suspects that either the temperature of the substrate [255] or remnants of the polishing compound [256] caused the problem. To get an idea, how well an electrolytically coating adheres to the TiN, sample Cu41 was then nickel-plated. As expected, the nickel does not adhere to the TiN surface.

6.3.2 Kelvin Probe Data

Two types of data were taken, namely **spatial** and **temporal**:

- For temporal measurements, the probe tip remained at the same place and measurements were taken for several hours typically. In earlier runs an enigmatic long-term drift of about $(0.5 - 1.0)\,\mathrm{meV\,min}^{-1}$ was observed, independent of the sample material [242]. In Ref. [243] it has been found that this long-term drift was mainly due to relative humidity and temperature fluctuations[11].

- For spatial scans, a raster of points was taken. The KP moves 50 steps of 0.4 mm per step in y, holding x constant, then moves 1.6 mm in x and steps back along the y-direction for 10 steps[12]. The whole raster therefore took data of 500 pts and covered a 14.4 mm by 19.6 mm rectangular area[13]. To avoid edge effects, we did not scan closer than 5 mm to the edges of the samples. At each position the CPD between probe tip and sample was measured once[14]. It took approximately 1 h to complete one scan. It is claimed that in the majority of measurements, this trade-off

---

[11] The KP in Ref. [242] exhibited large noise caused by vibrations of the wires leading from the probe tip amplifier to the housing of the drive shaft. This additional noise prevented R. Hodges from observing the influence of relative humidity and temperature fluctuations on the drift.

[12] According to the instruction manual [248], one translation step of the stepper motor corresponds to 400 nm. The scan parameter were set to 4000 and 1000 translation steps in x and y, respectively. This corresponds to the specified steps of 1.6 mm and 0.4 mm in x- and y-direction, respectively. Later, it was found that one motor step corresponds to (631 ± 10) nm instead [257]. Consequently, all x- and y-axis scalings would have to be multiplied by about a factor of 1.6, and therefore, e.g., the scans would have covered a $22.7 \times 30.9\,\mathrm{mm}^2$ area instead.

[13] Later high-resolution scans took data of 2500 pts and covered a $19.6 \times 19.6\,\mathrm{mm}^2$ area. In such cases, the KP moves 50 steps of 0.4 mm per step in x instead. Please see also Fn. 12.

[14] In Ref. [240] at each position the CPD was measured 11 times and averaged. As of August 2010, the KP Technologies proprietary software does not allow for averaging at each point of a scan.

between signal averaging, raster size, and measurement duration was sufficient to keep the drift to under $(3-5)\,\mathrm{meV}$ [258].

In Table 6.2 we list all the samples studied with spatial scans. The WF topographies were all recorded with the same SKP measurement parameters. In particular, the tracking was set to keep the gradient at (300 ± 5) a.u. for each measurement point, i.e., the separation distance in Eq. (6.6) at $d_0 \approx 0.5\,\mathrm{mm}$, with the exception of samples Cu53 and Cu54. However, the standard deviation of the gradient values (RMS Grad) reached in excess of 40 a.u., see also Secs. 6.3.3 and 6.3.6. To reduce the influence of surface charges on the measured WF value, the samples were prepared for measurement exclusively with compressed air dusting[15]. In some cases there are two or even three sets of data of the same day for one sample. These were taken on the same area of the sample, so that we averaged over the sets, as indicated in the last column.

Table 6.2: Summary of Kelvin Probe scans. Samples Cu5 and Cu6 cannot be scanned as a tracking error occurs due to the weld seam. Samples Cu24, Cu35 to Cu38, Cu43 to Cu46, Cu55 to Cu58, and Ti9 to Ti12 remain to be scanned. All other samples are in preparation as stated in Table B.1. See text and Table B.1 for details. The first column gives the name of the sample. The second and third column list the gradient (Grad) tracking data. The fourth to sixth column list the work function (WF) data. And the last column gives a short comment, if appropriate. The following abbreviations appear: avg (average value), RMS (standard deviation), and PTP (peak-to-peak value).

Ref.no.	avg Grad [a.u.]	RMS Grad [a.u.]	PTP WF [meV]	avg WF [meV]	RMS WF [meV]	Comment
Cu25	301.5	22.2	49.0	311.0	6.6	avg of 3 scans
Cu26	301.1	20.4	54.0	280.0	9.0	avg of 2 scans
Cu12	301.0	21.4	54.0	35.5	10.9	
Cu11	301.0	21.2	86.0	31.3	14.2	
Cu20	301.2	21.0	107.0	136.7	14.3	
Cu4	301.3	17.8	64.0	-11.0	14.7	
Cu23	301.0	16.3	66.0	82.9	15.0	
Cu32	305.0	64.7	80.0	13.5	16.2	
Cu34	301.4	25.3	98.0	-186.6	18.0	
Cu29	301.5	21.6	100.0	-45.2	18.0	
Cu33	306.0	38.2	98.0	13.5	20.7	
Cu3	301.4	20.7	129.0	-91.3	21.2	
Cu30	301.4	22.4	212.0	-60.5	21.2	
Cu13	301.0	18.1	134.0	-21.7	21.7	
Cu27	302.0	23.5	106.0	294.7	22.4	
Cu9	301.1	20.2	148.0	-192.9	25.7	

---

[15] In Ref. [243] it has been found that ethyl alcohol wipes are the most effective cleaning technique, since they removed visible contaminants, left by compressed air, without obvious damage to the sample surface. In later measurements with alcohol cleaning, the sample was covered and allowed to regain WF value stability overnight before SKP measurement.

Ref.no.	avg Grad [a.u.]	RMS Grad [a.u.]	PTP WF [meV]	avg WF [meV]	RMS WF [meV]	Comment
Cu14	300.6	15.8	153.0	-83.1	26.8	
Cu18	302.1	24.3	228.0	23.0	33.5	
Cu31	301.0	18.2	164.0	-77.2	37.3	
Cu15	301.0	17.7	191.0	67.4	39.6	
Cu1					$\approx$ 40	data from [259]
Cu16	301.4	22.8	263.0	257.9	41.0	
Cu19	301.0	20.5	196.0	36.8	42.8	
Cu7	302.0	24.7	281.3	227.7	46.7	avg of 3 scans
Cu54	259	55	$\approx$ 233	-4	48	data from [257]
Cu8	301.5	24.0	291.5	6.5	51.5	avg of 2 scans
Cu10	300.8	17.6	206.0	-70.8	53.2	
Cu17	302.0	22.8	257.0	110.6	56.8	
Cu53	254.7	27.4	$\approx$ 195	-74.3	58.3	avg 3 scans [257]
Cu21	301.0	23.0	278.0	-75.0	63.0	
Cu28	301.9	22.2	248.0	166.3	65.3	
Cu2					$\approx$ 70	data from [259]
Cu22			$\approx$ 200			data from [243]
Ti1	301.0	20.0	185.5	-56.5	32.0	
Ti2	293.0	37.5	202.0	8.0	36.5	
Glass1	301.0	16.8	79.0	19.1	8.8	avg of 3 scans
Glass2	301.0	12.5	109.5	103.5	17.1	avg of 2 scans

The present investigation showed that a platinized sample (Cu25) achieved the lowest standard deviation of the WF values over all the points measured over its surface (RMS WF)[16]. The sample, shown in Fig. 6.7a, was made of OFHC copper, hand-polished to a mirror finish, and electrolytically coated with 10 μm of silver and then 0.2 μm of platinum[17]. Although the peak-to-peak spread (PTP WF) is in excess of 10 meV, the RMS WF value is 6.6 meV, see also Figs. 6.7b, 6.7c, and 6.8a. The RMS WF value of its twin, sample Cu26, was only a few meV higher at 9.0 meV.

6.3.3 Gradient Tracking Error

In Ref. [243] an algorithmic error in the KP Technology Ltd. proprietary software was identified: The gradient tracking is deficient.

---

[16] Since the scans are stepped in 0.4 mm steps in y-direction and the probe size is 2 mm, each value recorded is not uncorrelated with the next, and this complicates the interpretation of the RMS of the whole data set. To get an idea of the significance of this correlation, in Ref. [240] the RMS has been calculated for a reduced set of data points. It has been found that these values were not dissimilar to the RMS of the full data set, and so to the required precision, we can use the RMS of the full data set.

[17] Please note that in Ref. [243] the thickness of the platinum layer is misstated.

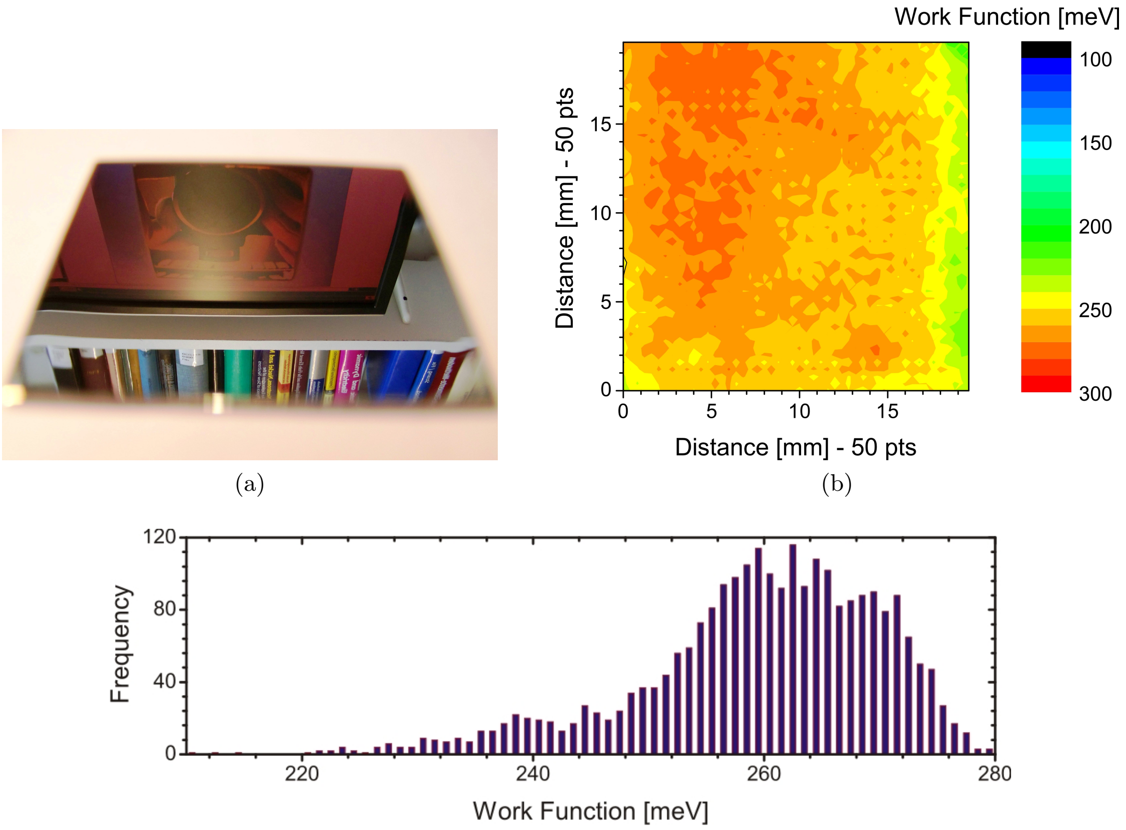

(a) (b)

(c)

Figure 6.7: Sample Cu25 (best result). The sample was made of OFHC copper, hand-polished to a mirror finish, and electrolytically coated with 10 μm of silver and then 0.2 μm of platinum. (a) Morphological image. (b) Work function (WF) topography with 10 meV contour graduations. Color scheme applied for comparison with the cylindrical sample electrode shown in Fig. 6.1b. (c) WF Histogram. Different Kelvin Probe scan than what appears in Table 6.2. Scan with 2500 pts over 5 hours: RMS WF 10.6 meV, PTP WF 71.0 meV, cf. Table 6.3 (February 2010).

When the KP moves from one point to the next, in general, the separation distance d_0 will change, due to variations in surface height, and the gradient will be altered. Actually it was thought that the tracking adjusts to hold the gradient at the chosen value, equivalent to holding the probe tip-to-sample distance d_0 constant. For spatial scans, the probe is moved laterally over the sample surface and, instead of first finding the preset gradient, the measurement is taken at the current gradient. Only after the WF measurement the tracking of the targeted gradient value is completed. Keeping the step size small reduces how much the separation distance d_0 can change and accordingly how much the gradient can fluctuate. Indeed, removing the effect by post-processing the data would not be a straightforward procedure. For smooth surfaces, the influence of the gradient fluctuation on the measured WF topographies is small and at the level of the signal noise, as can be seen in Fig. 6.8, along $y = 2$ and $y = 16$. With increasing SR the gradient fluctuations increase and may affect the WF topographies. Altogether, the SKP still provides meaningful data, although the gradient tracking error becomes a limiting factor for precision.

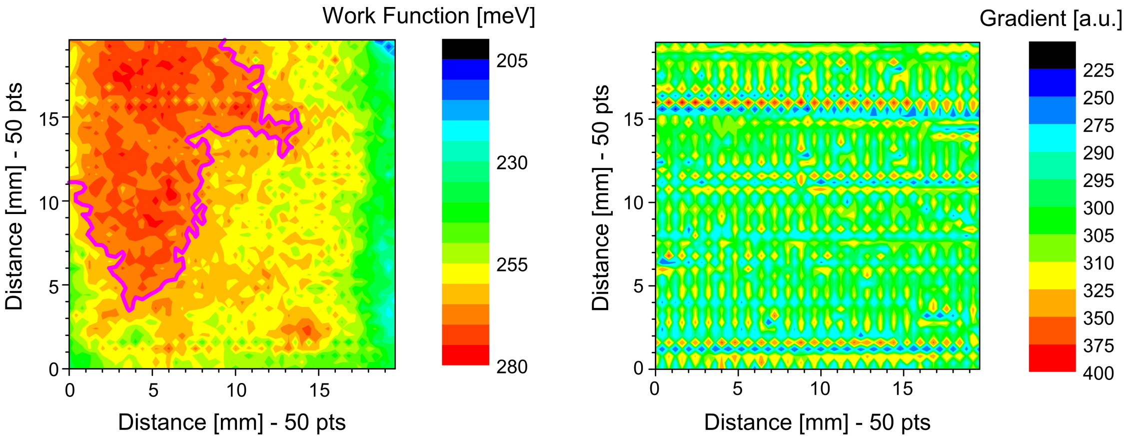

(a) (b)

Figure 6.8: Sample Cu25 (best result), see Fig. 6.7 for details. (a) Work function topography with 5 meV contour graduations. The pink contour line is shown to emphasize the temporal stability of Kelvin Probe (KP) scans over a week, cf. Fig. 6.9. (b) Gradient topography with **non-equidistantly** contour graduations. Scan with 2500 pts over 5 hours. The tracking was set to keep the gradient at (300 ± 5) a.u. for each measurement point. The comparison with (a) shows how the noise in the KP, e.g., the gradient fluctuation (tracking error) along $y = 2$ and $y = 16$, becomes a limiting factor for precision.

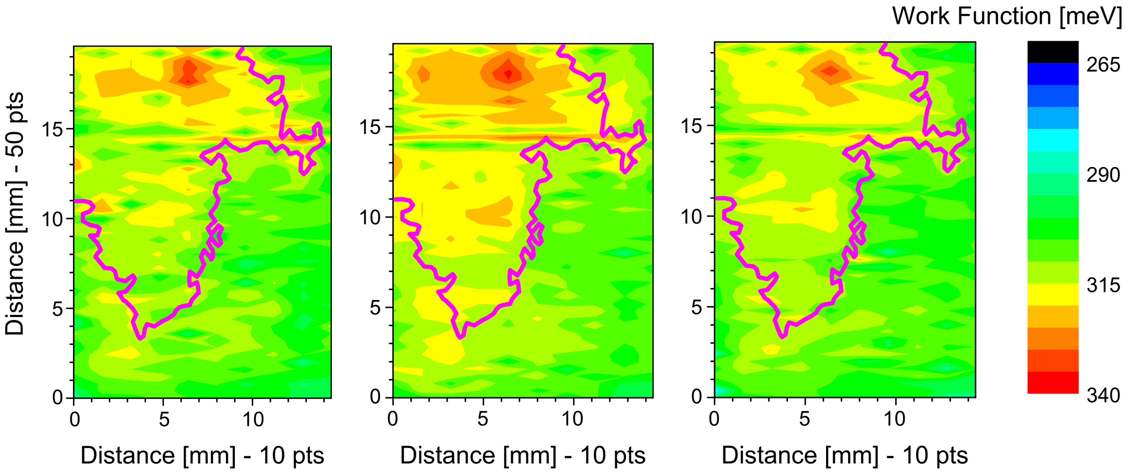

(a) (b) (c)

Figure 6.9: Sample Cu25 (best result), see Fig. 6.7 for details. Temporal stability of the Kelvin Probe scans over one day. The work function topographies, with 5 meV contour graduations, were recorded on (a) January 28, 2010 at 9:50 pm, (b) January 29, 2010 at 0:13 am, and (c) January 29, 2010 at 1:59 pm. Scans with 500 pts over 1 hour. The pink contour line is shown to additionally highlight the temporal stability over a week, cf. Fig. 6.8a recorded on February 4, 2010 at 10:38 am. The comparison between (a)−(c) and Fig. 6.8a shows that the absolute values of the measured WF change, due to the drift described on page 176 under "temporal measurements", whereas the WF topographies are comparable.

Table 6.3: Temporal stability of Kelvin probe scans over months and over a day. For these scans, a raster of 500 points was taken, except for the latest measurements of Cu12 and Cu25. The first column gives the name of the sample. The second column includes the measurement dates. The third and fourth column list the gradient (Grad) tracking data. The fifth to eight column list the work function (WF) data. And the last column gives a short comment, if appropriate. The following abbreviations appear: avg (average value), RMS (standard deviation), and PTP (peak-to-peak value).

Ref.no.	Date	avg Grad [a.u.]	RMS Grad [a.u.]	PTP WF [meV]	avg WF [meV]	RMS WF [meV]	Δ avg WF [meV]	Comment
Cu3	Aug 09	301.4	20.7	129.0	-91.3	21.2		
	Jan 10				-11.4	21.5	80	data from [243]
	Jan 10				-12.8	24.0		data from [243]
Cu10	Aug 09	300.8	17.6	206.0	-70.8	53.2		
	Jan 10				-58.4	36.2	12	data from [243]
	Jan 10				-34.5	33.8		data from [243]
Cu11	Aug 09	301.0	21.2	86.0	31.3	14.2		
	Jan 10	301.1	22.5	66.0	-30.6	11.3	-62	
	Jan 10	300.7	19.2	51.0	-32.7	9.3		
Cu12	Aug 09	301.0	21.4	54.0	35.5	10.9		
	Jan 10	300.9	25.9	129.0	-51.8	17.5	-87	
	Jan 10	301.0	26.2	119.0	-65.0	11.7		
	May 10	301.0	21.0	75.0	-61.0	11.8	4	2500 pts
Cu20	Aug 09	301.2	21.0	107.0	136.7	14.3		
	Jan 10				160.6	16.0	24	data from [243]
	Jan 10				163.6	15.7		data from [243]
Cu25	Jan 10	302.0	22.4	44.0	310.0	7.0		
	Jan 10	301.6	22.9	46.0	312.9	6.5		
	Jan 10	301.0	21.4	56.0	210.0	6.3		
	Feb 10	301.0	19.0	71.0	259.0	10.6	-51	2500 pts

In addition, Fig. 6.8b shows a stripiness in the direction in which the SKP is stepped to take data, i.e, along the y-direction. The stripy effect is seen in all gradient data and is caused by mechanical hysteresis. The stepper motor has some backslash, i.e., the separation distance d_0 changes depending on the direction of motion, and hence the gradient alternates between higher and lower values. This effect, without present peaks, was also observed in Ref. [240].

6.3.4 Temporal Stability

In Table 6.3 we list all the samples studied in at least two different months and at least twice one day. As mentioned earlier in Sec. 6.2.3, these measurement data were taken in

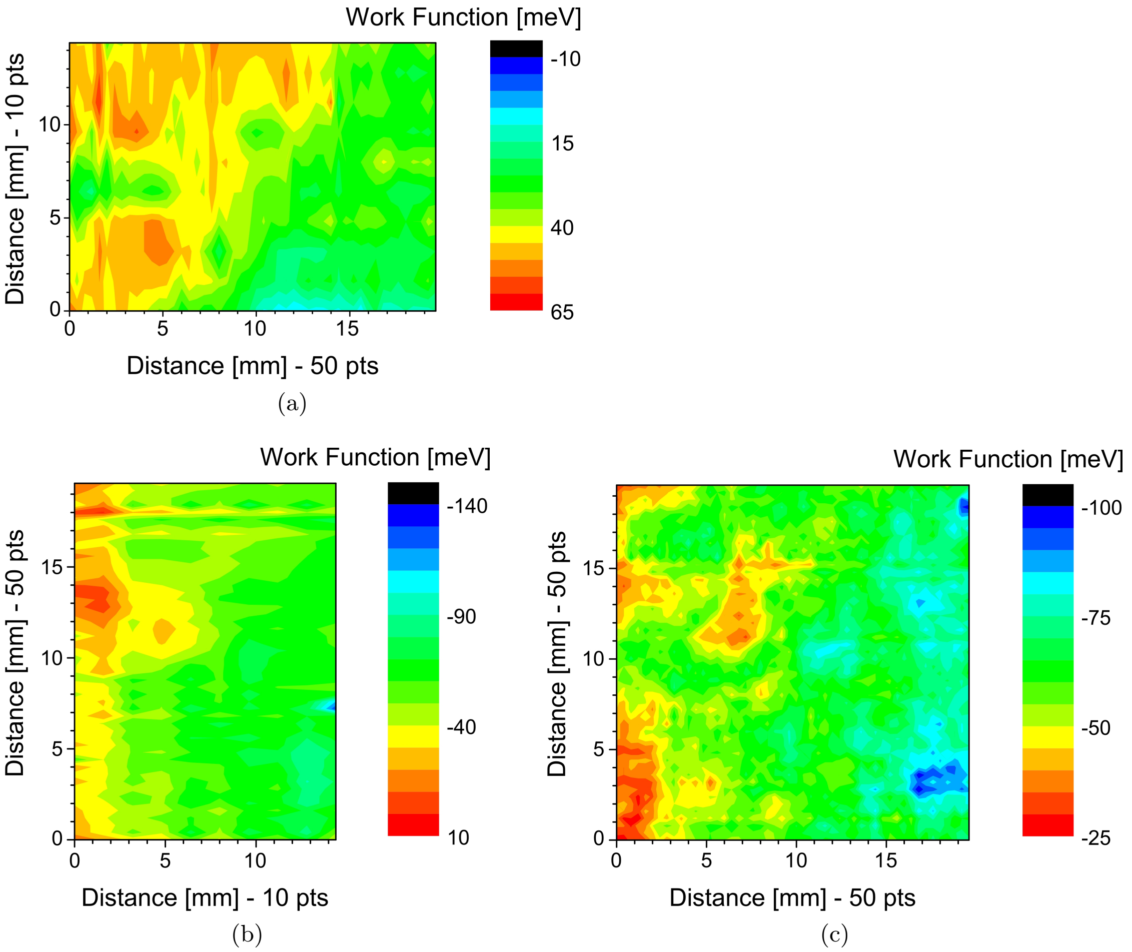

(a)

(b)

(c)

Figure 6.10: Sample Cu12 (best gold-plated result). The sample was made of OFHC copper, hand-polished to a mirror finish, and electrolytically coated with 10 μm of silver and then 1 μm of gold. Temporal stability of the Kelvin Probe (KP) scans over months. The work function (WF) topographies, with 5 (10 in (b)) meV contour graduations, were recorded in (a) August 2009, (b) January 2010, and (c) May 2010. The KP scan (a) was rotated by -90° as we cannot exclude the possibility that the sample was scanned in a different orientation than (b) and (c). Scans with 500 (2500 in (c)) pts over 1 (5) hour(s). The comparison between (a)−(c) shows that the absolute values of the measured WF change, due to the drift described on page 176 under "temporal measurements", whereas the WF topographies are comparable. Please note the different contour scales.

the open laboratory and not in the isolated glove box discussed in Ref. [243]. The average values of the measured WF (avg WF) change, due to the drift described on page 176 under "temporal measurements". The RMS WF values, however, remain stable to about ±3.0 meV or less, with the exception of sample Cu10. The reasons for the high temporal stability of the KP scans are on the one hand the reproducibility of the SKP and on the other hand the storage stability of noble metals under standard laboratory conditions.

Figures 6.9 and 6.10 illustrate the temporal stability of the KP scans over one day and over eight months, respectively. The WF topographies are comparable.

We note that sample Cu12 (best gold-plated result) was measured by Prof. I. Baikie in Scotland in Spring 2010, after and before it had been measured at University of Virginia in

Table 6.4: Reproducibility of those Kelvin probe samples which were produced at least twice. As input for our comparison we have used the measurement data from Table 6.2. For details on the samples see App. B. The first column gives the name of the samples. The second column specifies the respective manufacturer. The third and fourth column list the work function (WF) data. The fifth and sixth column specify the coating, listed from substrate surface to outer surface. The last column gives a short comment, if appropriate. All abbreviations are standard nomenclature for chemical elements. In addition, the following abbreviation is used: RMS (standard deviation).

Ref.no.	Co.	avg RMS WF [meV]	RMS RMS WF [meV]	1^{st} layer [μm]	2^{nd} layer [μm]	Comment
Cu3-Cu4	Adler	17.8	4.6	Ag 10	Au 1	polished mechanically
Cu9-Cu10	Adler	39.5	19.4	Ag 10	Au 2	
Cu11-Cu12	Adler	12.6	2.3	Ag 10	Au 1	
Cu13-Cu14	Adler	24.3	3.6	Ag 10	Au 5	
Cu32-Cu33	Adler	18.5	3.2	Ag 10	Au 1	brazed seam
Cu15-Cu17	Gierich	45.8	9.6	Ag 10	Au 2	
Cu18-Cu20	Gierich	30.2	14.5	White bronze 1	Pt 1	
Cu25-Cu26	Sigrist	7.8	1.8	Ag 10	Pt 0.2	
Cu27-Cu28	Sigrist	43.9	30.3	Ag 10	Au 2	
Cu53-Cu54	Sigrist	53.2	7.3	Ag 10	Pt 0.2	
Cu25-Cu26 &Cu53-Cu54	Sigrist		26.6	Ag 10	Pt 0.2	

Winter 2009 and Spring 2010, respectively. Despite differences in scan parameters, Prof. I. Baikie confirmed the results of the SKP measurements in Virginia. In particular, Prof. I. Baikie found a RMS WF value of 10.8 meV [243]. At University of Virginia, an averaged RMS WF value of 13.0 meV was found; where the average over four measurements includes one measurement of 10.9 meV. This shows that the SKP used for our investigation is close to the sensitivity of the establihed equipment used by the founder of KP Technology Inc.

6.3.5 Reproducibility of the Samples

As mentioned earlier in Sec. 6.3.1, most of the samples were doubly manufactured. In some cases even triplets or a quadruplet of the same substrate, surface treatment, and coating were produced. More precisely, the quadruplet (Cu25, Cu26, Cu53, and Cu54) consists of two pairs of twins manufactured in February 2009 (Cu25 and Cu26) respectively August 2010 (Cu53 and Cu54). In Table 6.4 we list all the samples produced at least twice. The RMS WF values of seven out of ten twins (triplets) are reproducible to about ±10 meV or less. Unfortunately, there is no obvious explanation why half of the twins (triplets) exceed ±5 meV.

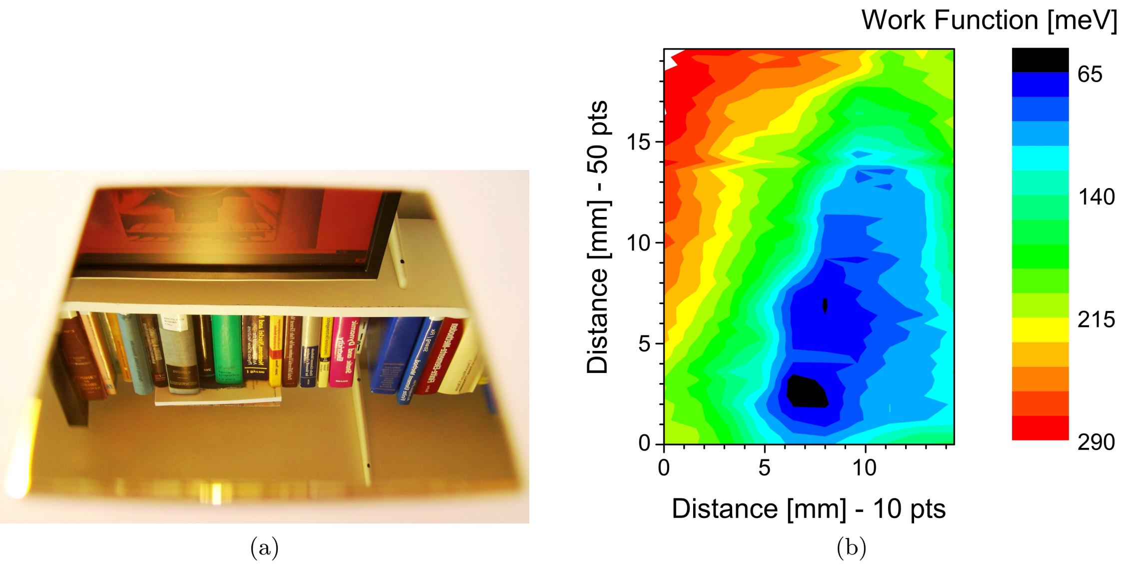

(a) (b)

Figure 6.11: Sample Cu28 (worst result). The sample was made of OFHC copper, hand-polished to a mirror finish, and electrolytically coated with 10 μm of silver and then 2 μm of gold. (a) Morphological image. (b) Work function (WF) topography with 15 meV contour graduations. Scan with 500 pts over 1 hour: RMS WF 65.3 meV, PTP WF 248.0 meV. The sample lacks of the desirable homogeneity in WF, even though it was polished and coated by the same company as the best sample (Cu25). The large fluctuations in WF cannot be explained by the noise of the Kelvin Probe, either (avg Gradient 301.9 a.u., RMS Gradient 22.2 a.u.). In the photograph (a), neither scratches nor irregularities are visible to the naked eye, and not even its twin, sample Cu27, shows such fluctuations.

Figure 6.11 shows, for example, a morphological image of sample Cu28 in comparison with its WF topography. Even though the sample was polished and coated by the same company as the best sample (Cu25), it achieved the highest RMS WF value. Its large fluctuations in WF cannot be explained by the noise of the Kelvin Probe, either. In the Photograph 6.11a, neither scratches nor irregularities are visible to the naked eye, and not even its twin, sample Cu27, shows such fluctuations.

To better understand the bad result of sample Cu28 and to see whether the manufacturer of samples Cu25 to Cu28 can reproduce the high quality of samples Cu25 and Cu26, we ordered twins of Cu25 and Cu26 as well as of Cu27 and Cu28. So far, only samples Cu53 and Cu54 (twins of Cu25 and Cu26) have been investigated, cf. Fn. 7. The RMS WF values of the new twins are reproducible to ±7.3 meV, but the quadruplet exceeds ±25 meV. Possible explanations for the bad reproducibility of the pairs of twins are the poor quality of the polishing (see also the following section) of the new twins and the fact that the new samples were stored in zip lock bags for about nine months. In the latter case, the samples might have been corroded by means of perspiration [260] (see also Sec. 6.3.6). On the other hand, no impurities were found using a SEM analysis [257].

However, the manufacturer of the best gold-plated result is able to reproduce the high quality of sample Cu12. In comparison with samples Cu3, Cu4, Cu11, Cu32, and Cu33 the RMS WF values are reproducible to ±3.3 meV, independent of different processing techniques and/or surface treatments.

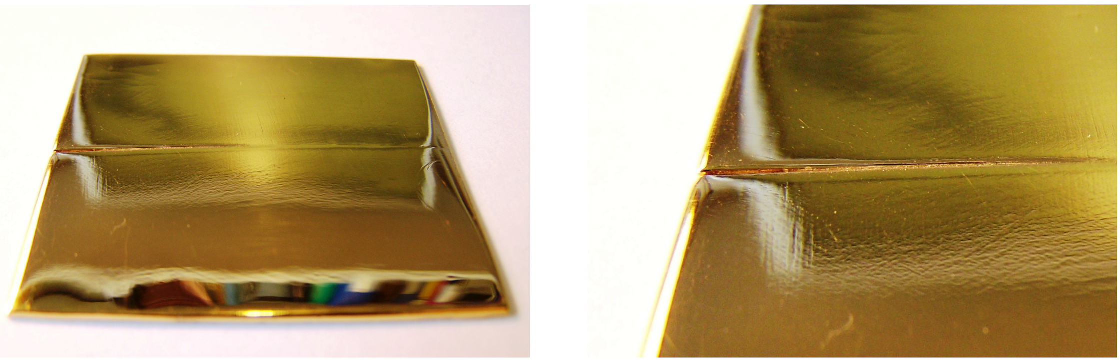

(a) Full picture (b) Zoom

Figure 6.12: Sample Cu33 (brazed seam). The sample was made of OFHC copper, chopped and subsequently connected again by means of brazing, polished mechanically and then by hand, and finally electrolytically coated with 10 μm of silver and then 1 μm of gold. (a) Morphological image. (b) Zoom to the brazed seam. Owing to the mechanical polishing the sample could not be polished to a mirror finish anymore. Nevertheless, it shows a reasonable homogeneity in WF: RMS WF 20.7 meV, PTP WF 98.0 meV. However, the imperfect coating along the brazed seam is prone to chemical reactions later on.

6.3.6 Surface Conditions

Processing Techniques

As discussed earlier in Sec. 6.3.1 processing techniques were investigated. Namely, the chopping and subsequently brazing of OFHC copper substrates. Figure 6.12 shows a photograph of sample Cu33. The sample was chopped and subsequently connected again by means of brazing, polished mechanically and then by hand, and finally electrolytically coated. Owing to the mechanical polishing the sample could not be polished to a mirror finish anymore. Nevertheless, it shows a reasonable homogeneity in WF. Additionally, the RMS WF values of the twins Cu32 and Cu33 are reproducible to ±3.2 meV, cf. Table 6.4. In comparison with the twins Cu3 and Cu4 (neither chopped nor polished by hand), the chopping and subsequently brazing seem not to have an influence on the good quality of the samples. However, the imperfect coating along the brazed seam is prone to chemical reactions, can trap cleaning solvents, and can become a source of virtual vacuum leaks later on. We also note that the brazed seam of samples Cu 32 and Cu33 is responsible for their high RMS grad values.

Surface Treatment

To increase the coating adhesion and, simultaneously, avoid an anisotropic WF, polishing techniques were investigated. Where possible, the substrate surface was polished mechanically and/or by hand. Figures 6.7a, 6.11a, and 6.12 show examples for hand-polished and mechanically polished samples. Our investigation revealed that first mechanically polishing excluded polishing to a mirror finish, even after subsequently hand-polishing. The comparison of the twins Cu11 and Cu12 (hand-polished to a mirror finish) with the twins Cu3 and Cu4 (mechanically polished) shows that the polishing seems to have an

Table 6.5: Surface roughness (SR) of Kelvin Probe samples. For the hand-polished samples, the SR profiles were taken twice, once parallel and a second time perpendicular to the direction of the polishing. The first column gives the name of the sample. The second column specifies the perthometer parameters L_t (traversing length) and hence L_c (cut-off; $L_c = 0.8\,\text{mm}$ for $L_t = 5.6\,\text{mm}$ respectively $L_c = 0.25\,\text{mm}$ for $L_t = 1.75\,\text{mm}$). The third to fifth column list the perthometer data parallel to the polishing direction; the sixth to eighth column perpendicular to the direction of polishing. The last column gives a short comment, if appropriate. All abbreviations are standard nomenclature for chemical elements. In addition, the following abbreviations are used: R_a (roughness average), R_{max} (maximum roughness depth), and P_c (peak count); see also Fig. 6.13a.

Ref.no.	L_t [mm]	min R_a [nm]	R_{max} [μm]	Pc [cm^{-1}]	max R_a [nm]	R_{max} [μm]	Pc [cm^{-1}]	Comment
CuRef	5.60	209	2.3	5.0				not polished, one scan only
Cu41	1.75	301	1.8	64.0	340	2.3	40.0	coated w/ TiN & Ni, average of 3 scans
Cu39	1.75	12	0.1	0.0	27	2.0	0.0	coated with TiN, average of 3 scans
Cu40	5.60	89	1.0	0.0	116	1.9	5.0	coated with TiN
Cu42	5.60	37	1.5	0.0	44	2.0	0.0	coated with TiN
Cu47	5.60	71	1.6	0.0	240	5.6	2.5	
Cu48	5.60	47	0.8	0.0	159	2.5	0.0	
Cu49	5.60	14	<0.1	0.0	49	0.7	0.0	
Cu50	5.60	72	1.5	2.5	174	2.7	2.5	
Cu51	5.60	14	0.3	0.0	46	0.3	0.0	
Cu52	5.60	11	0.1	0.0	89	1.7	2.5	
Cu57	5.60	55	1.0	0.0	82	0.9	0.0	
Cu58	5.60	19	0.4	0.0	51	0.4	0.0	
TiRef	5.60	436	5.2	85.0				not polished, one scan only
Ti3	5.60	123	1.4	2.5	326	7.3	7.5	coated with TiN
Ti4	5.60	174	1.5	5.0	208	3.4	2.5	coated with TiN
Ti5	5.60	217	2.5	2.5	241	5.5	2.5	coated with TiN
Ti6	5.60	148	2.8	0.0	244	2.9	5.0	coated with TiN
Ti7	5.60	194	3.3	5.0	208	1.8	5.0	
Ti8	5.60	159	1.9	2.5	161	1.6	0.0	

influence on the high quality of the samples Cu11 and Cu12: The RMS WF values decrease from (17.8 ± 4.6) meV to (12.6 ± 2.3) meV, i.e., by about 5 meV, possibly due to the hand-polishing. We note that the SR and hence the polishing of the samples determine the precision of our WF measurements, as discussed in Sec. 6.3.3 (see also Fig. 6.8).

In Table 6.5 we list all the samples studied with a Mahr perthometer H1, a surface measuring instrument. We note that this is a destructive technique as the perthometer leaves 5 mm long scratches on the sample surface. Figures 6.13 and 6.14 show examples for SR profile measurements; the perthometer principles and parameters[18] are illustrated in Fig. 6.13a (see also [261]). We note that the investigations with the perthometer started in the final phase of this thesis. Hence, measurement data exist only for the hand-polished samples Cu39 to Cu 42 (coated with TiN), Cu47 to Cu52, Cu57 and Cu58, Ti3 to Ti6 (coated with TiN), and Ti7 and Ti8, as well as for the two (not polished) reference samples CuRef and TiRef.

As stated earlier in Sec. 6.3.1, the unpolished copper and titanium substrates have a SR better then 210 and 400 nm R_a plus 2.5 and 5.5 μm R_max, respectively. Thanks to the hand-polishing, the SR of the samples was much improved, although the titanium samples remain far inferior to the copper samples. The present investigation showed that a sputter coated sample (Cu39) achieved the lowest SR values. The sample was made of OFHC copper, hand-polished to a mirror-finish, and sputter coated with 0.8 μm of titanium nitride. Although the R_max value is in excess of 2 μm, the R_a value is (20.0 ± 7.5) nm. The R_a value of the only hand-polished sample Cu51 was only a few nm higher at (30.0 ± 22.6) nm. We note that the measured SR values strongly depend on the orientation of the perthometer relative to the polishing direction, cf. Table 6.5 and Figures 6.13 and 6.14. For further investigations, we therefore recommend to turn the substrate by 90° after each polishing step. On average, the R_a values of the copper samples were improved to (74.6 ± 64.4) nm before and (49.4 ± 38.5) nm after sputter coating; the R_a values of the titanium samples were improved to (180.5 ± 24.4) nm before and (211.0 ± 63.6) nm after sputter coating. Unfortunately, a direct comparison with the respective WF values is not possible.

Layer Thickness

As mentioned earlier, the WF may vary over the surface of an alloy due to non-uniform segregation of the elements [247]. Plated surfaces may also show corrosion in perspiration or in sulfur dioxide-containing atmospheres. In Ref. [260] the important influence of intermediate layers on the corrosion behavior of platinized samples was investigated, excerpts shown in Fig. 6.15. To ensure that the surface coatings provide entire coverage, and to prevent corrosion and alloy formation on the sample surfaces, various metal combinations and layer thicknesses[19] were investigated. We note that the SR and hence the WF may

---

[18] The traversing length L_t is the overall length traveled by the stylus when acquiring the traced profile. Pre-travel and post-travel are required for phase correct filtering. The values of the surface parameters are determined over the evaluation length L_n, which comprises five consecutive sampling lengths L_i. The single roughness depth R_zi is the vertical distance between the highest peak and the deepest valley within a sampling length. The maximum roughness depth R_max is the largest single roughness depth. The roughness average R_a is the arithmetic average of the absolute values of the roughness profile ordinates. The peak count P_c is the number of roughness profile elements per cm which consecutively intersect the specified upper and lower profile section levels c_1 and c_2, respectively. In addition, the cut-off of a profile filter, L_c, determines which wavelengths belong to roughness and which ones to waviness; see also [261]

[19] In some cases, e.g., in the case of titanium nitride, the layer thickness is limited by the manufacturing process.

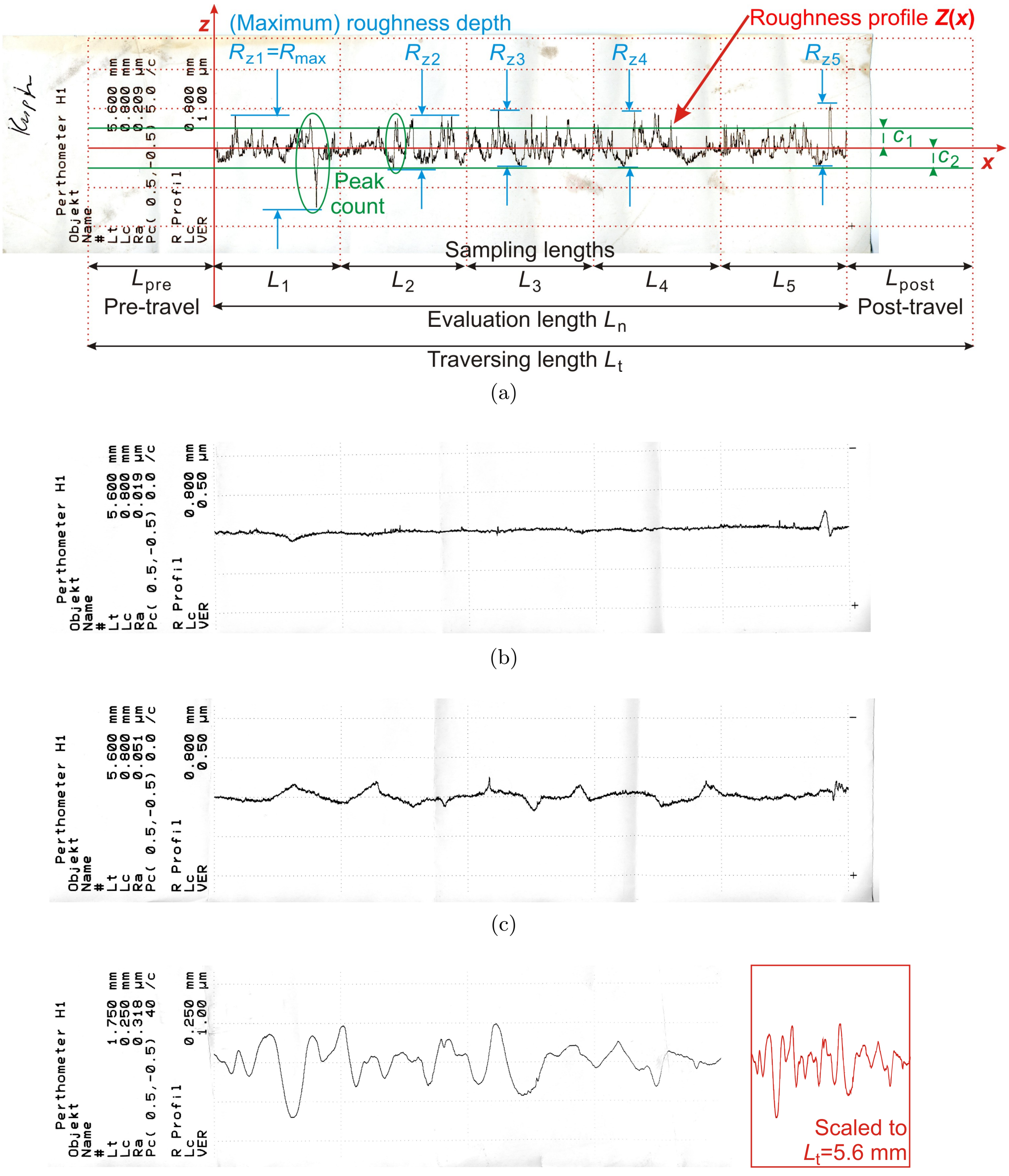

(a)

(b)

(c)

(d)

Figure 6.13: Surface roughness (SR) profiles $Z(x)$ of copper samples. (a) Not polished (CuRef), (b) and (c) hand-polished to a mirror finish (Cu58), and (d) finally sputter coated with $0.8\,\mu$m of titanium nitride (TiN) and then electrolytically coated with $1\,\mu$m of nickel (Cu41). Please note the different x- and y-scales of the SR profiles. Samples Cu41 and Cu58 were analyzed (b) parallel and (c) and (d) perpendicular to the polishing direction. Thanks to the hand-polishing, the SR was improved by a factor of about 11 (4) parallel (perpendicular) to the polishing direction; the peak count, P_c, was also reduced to zero. The higher SR in (c) in comparison with (b) is due to the ripple formation in polishing; the even higher SR in (d) in comparison with (a) to (c) is due to the miserable adhesion of Ni on TiN. The perthometer principles are illustrated in (a); its parameters are introduced in Fn. 18

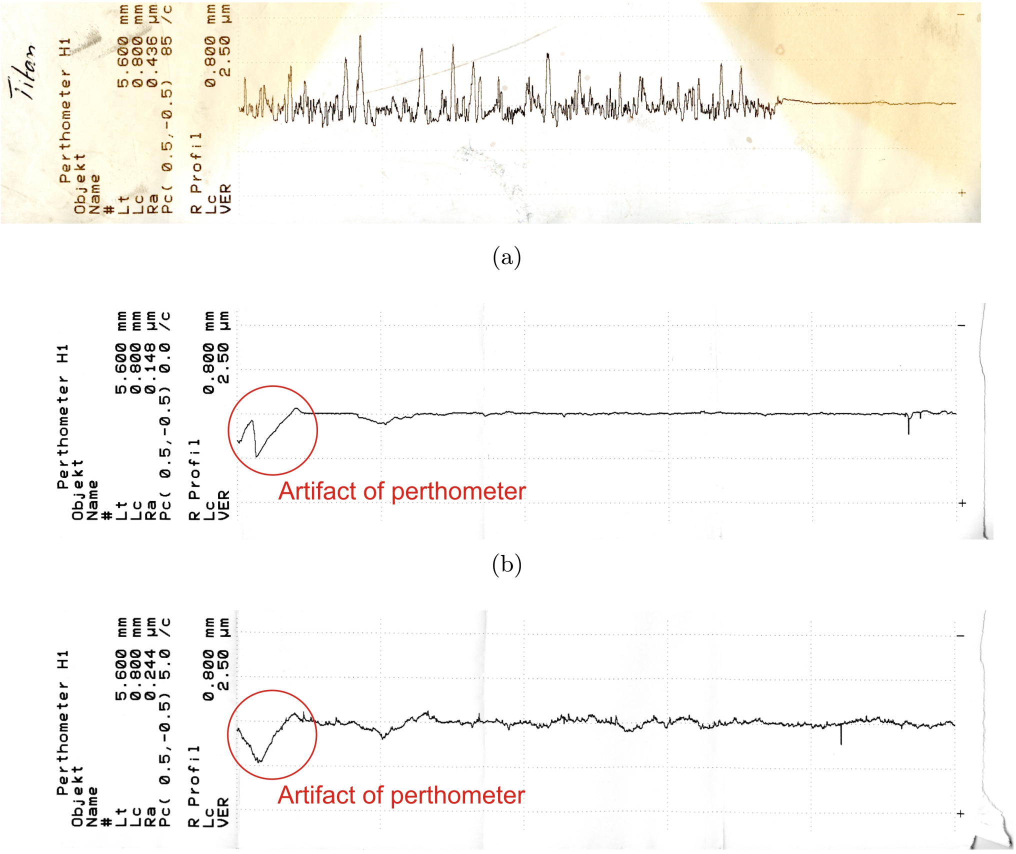

(a)

(b)

(c)

Figure 6.14: Surface roughness (SR) profiles of titanium samples. (a) Not polished (TiRef), and (b) and (c) hand-polished to a mirror finish (Ti6). The SR profile of sample Ti6 was taken twice, (b) once parallel and a second time (c) perpendicular to the polishing direction. Thanks to the hand-polishing, the SR was improved by a factor of about 3 (2) parallel (perpendicular) to the direction of the polishing; the peak count, P_c, was also reduced to zero (by a factor of 17). The higher SR in (c) in comparison with (b) is due to the ripple formation in polishing.

depend on the thickness of the deposited layers [262]. In Refs. [263, 264] is has been found that the SR increases monotonically with the thickness (of platinum and gold thin films deposited on silicon and glass substrate). In contrast, in Ref. [265] it has been found that the SR exhibits a minimum at a certain layer thickness (of silver deposited on glass substrate). We further note that the degradation under thermal annealing may influence the SR [263, 266, 267]. According to Table 6.4 the WF might exhibit a minimum at a layer thickness of 2 μm of gold; but we do not have enough data to support this hypothesis. However, the present investigation showed that a layer combination of 10 μm of silver and then 1 μm of gold achieved the lowest and most reproducible RMS WF values.

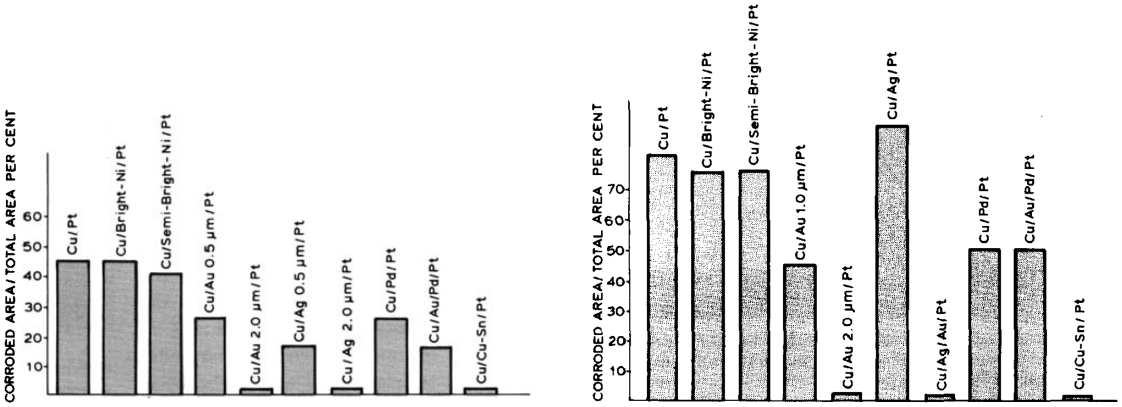

(a) Artificial perspiration (b) Sulfur dioxide-containing atmosphere

Figure 6.15: The corrosion behavior of plated samples, for various metal combinations, obtained after (a) 48 hours in artificial perspiration and (b) 5 cycles in sulfur dioxide-containing atmospheres. The summary of corrosion data (a) showed the benefit of imposing a thin layer of gold, silver, or copper-tin between the platinum coating and the copper substrate. Similar results were obtained after 48 hours salt spray test. Corrosion data (b) showed some similarities with (a), although a silver intermediate layer was not as effective unless overlaid with gold. Figures taken from Ref. [260].

6.3.7 Sputtered Gold and SEM Analysis

Sputter coated gold surfaces are reported to give better WF results [240]. Hence, we have investigated sputtered surfaces, for various metal combinations. We note that these investigations started in a later phase of this thesis. At that time, the ion source at University of Mainz, normally used to clean the substrate surface before sputtering, was inoperative. To get an idea, how important the cleaning process is, only half of the copper samples were cleaned with isopropyl alcohol before sputtering.

So far, only 8 sputtered samples were analyzed. The sputtered copper samples were made of OFHC copper, hand-polished to a mirror finish, and sputter coated with 2 μm of silver and then 0.2 μm of gold. Figure 6.16 shows WF topographies of copper samples Cu7 and Cu8, where only sample Cu8 was cleaned with isopropyl alcohol. Both samples lack the desirable homogeneity in WF. They show a gradual increase in WF from left to right, only interrupted by sharp peaks, and independent of the cleaning process. Possible explanations for the poor quality of the sputtered surfaces are an insufficient adhesion, because of the missing cleaning with the ion source, and the orientation of the sputter head relative to the sample surface. Indeed, compressed air dusting later destroyed half of the coating of sample Cu7.

The question, why our sputtered samples lack the desirable quality, was investigated using a scanning electron microscope (SEM) together with an energy dispersive X-ray (EDX) analysis[20]. Figure 6.17 shows SEM images of copper sample Cu22, for different magnifications. The defects (depression, chunks) shown in Fig. 6.17 lead to large fluctuations in the WF (PTP WF 200 meV). For further investigations, we therefore recommend to shield the sputter head in such a way that meteor-like impacts cannot destroy the WF homogeneity any more.

---

[20] These measurements were taken in cooperation with R. White, the lab manager of the Nano Materials Characterization Facility (NMCF) at the University of Virginia.

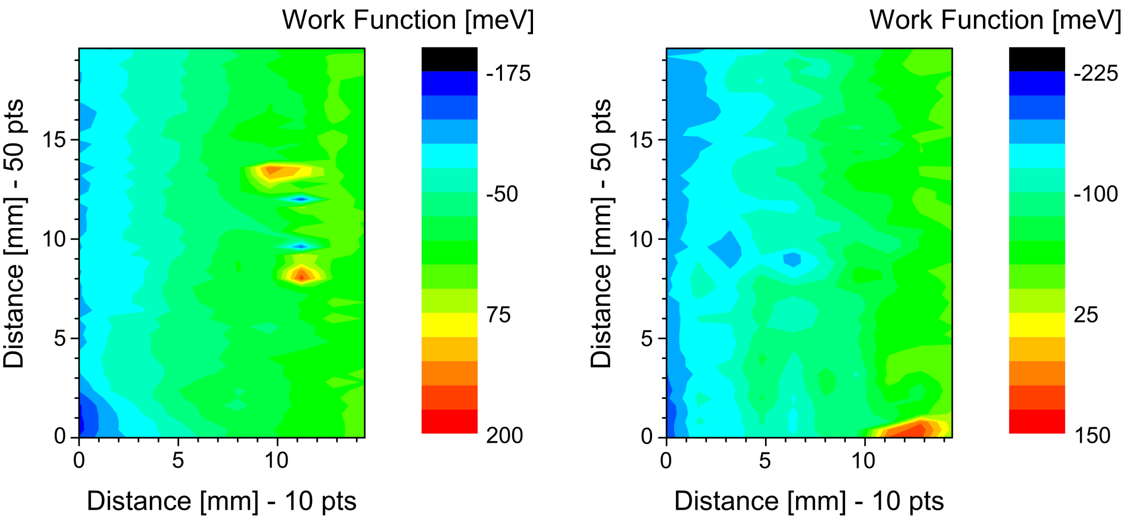

(a) Not cleaned (b) Cleaned with isopropyl alcohol

Figure 6.16: Samples Cu7 and Cu8 (sputtered gold). The samples were made of OFHC copper, hand-polished to a mirror finish, and sputter coated with 2 μm of silver and then 0.2 μm of gold. Work function (WF) topographies, with 25 meV contour graduations, of (a) sample Cu7 not cleaned and (b) sample Cu8 cleaned with isopropyl alcohol. The samples show a gradual increase in WF from left to right, only interrupted by sharp peaks, and independent of the cleaning process. One reason for this might be an insufficient adhesion, due to the missing cleaning with the ion source. Indeed, compressed air dusting later destroyed half of the coating of sample Cu7.

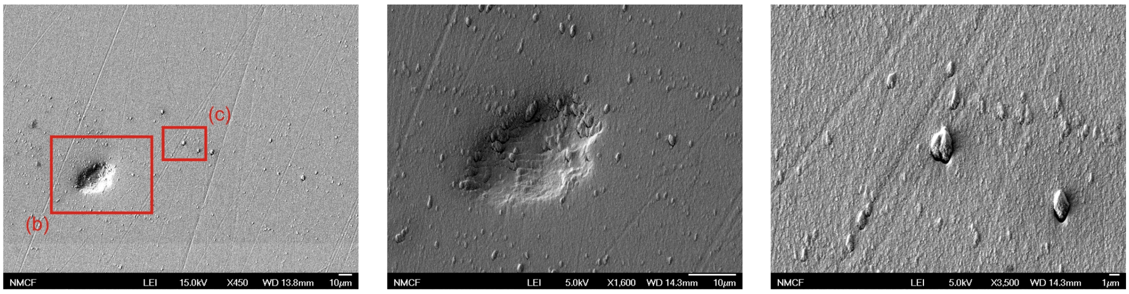

(a) Magnification factor 450x (b) Magnification factor 1600x (c) Magnification factor 3500x

Figure 6.17: Sample Cu22 (sputtered gold). The sample was made of OFHC copper, hand-polished to a mirror finish, and sputter coated with 2 μm of silver and then 0.2 μm of gold, but not cleaned with isopropyl alcohol before sputtering. (a) Surface at low magnification. (b) Surface at higher magnification, showing depression. (c) Surface at high magnification, examining chunks. These defects lead to large fluctuations in the work function (PTP WF 200 meV). SEM images courtesy of S. McGovern [243]

In general, the copper and titanium substrates were far inferior to electrolytically coated samples and achieved RMS WF values of 32 meV or more. However, both glass samples showed reasonable WF values. The sputtered silver sample achieved a RMS WF value of 8.8 meV, competitive with the electrolytically coated samples. The sputtered gold sample was a few meV higher at 17.1 meV. We suspect that the lower SR and the higher cleanliness of the glass substrates favored lower WF values.

6.4 Influence of the Patch Effect on a

As discussed earlier in Sec. 3.1.3, the potential difference between DV and AP, $U_{\mathrm{A}} - U_0$, has to be known precisely to determine the transmission function Eq. (3.30) and subsequently the neutrino-electron correlation coefficient a. However, a variation of the WF within an electrode or between different electrodes could render the potential difference $U_{\mathrm{A}} - U_0$. Hence, we have to study the influence of our measured WF values on the transmission function Eq. (3.30). We consider two different scenarios:

Present thesis: The (present) inner surfaces of our electrode system are best described by the cylindrical sample electrode shown in Fig. 6.1a and samples Cu3, Cu4, Cu32, and Cu33. In average, the PTP WF of these samples is (133.3 ± 70.2) meV. On the one hand, it is very likely that the cylindrical sample electrode overestimates the WF inhomogeneities, as the DV and AP electrodes e3−e6 and e14 were renewed respectively over-coated for our latest beam time (see also Fn. 8). On the other hand, the samples Cu3, Cu4, Cu32, and Cu33 might underestimate the WF inhomogeneities, as our electrodes have an unfolded surface of up to $440 \times 540\,\mathrm{mm}^2$, whereas our samples were only $50 \times 50\,\mathrm{mm}^2$ in surface. Altogether, we assume WF inhomogeneities of 150 meV over patches with a surface of $40 \times 40\,\mathrm{mm}^2$.

Further investigations: The present investigation showed that a platinized sample (Cu25) achieved the lowest PTP WF value of 49.0 meV, cf. Table 6.2. Hence, we assume WF inhomogeneities of 50 meV over patches with a surface of $20 \times 20\,\mathrm{mm}^2$.

Figures 6.18 to 6.21 show the possible influence of the patch effect on the electric field distributions in the AP and in the DV, respectively.

6.4.1 Patch Effect in the Analyzing Plane

Assuming that the DV is grounded ($U_0 \equiv 0$), we have to know the potential barrier U_{A} with an accuracy of better than 10 mV, in order to keep systematic uncertainties in a below $\Delta a/a = 0.1\,\%$ (for details see Sec. 3.1.3 and Fig. 3.6). Indeed, a variation of the WF within the AP electrode e14 could render the electric field distribution. Figure 6.18 shows the influence of one patch on the electric potential in the AP. Only in the case of the present thesis, the electrostatic potential exceeds $U_{\mathrm{A}} + 10\,\mathrm{mV}$ on the right detector pad. The left and central detector pads are almost not affected by the WF inhomogeneities. For the central detector pad, the field inhomogeneity is in excess of 10 mV only on the right boundary.

In case of Fig. 6.18, the electric field calculations showed that the field inhomogeneity

- averaged over the central detector pad is around 5 mV for the present situation, what corresponds to a shift in a of $\Delta a/a = +0.06(5)\,\%$,
- over the central detector pad is less than 1.1 mV for further investigations, which yields a shift in a of $\Delta a/a = +0.01(5)\,\%$. Similar results were obtained for the left and right detector pads. The electric field inhomogeneity averaged over the right detector pad is around 3 mV, what corresponds to a shift in a of $+0.04(5)\,\%$. However, for the left detector pad, the field inhomogeneity is less than 0.02 mV, which yields a shift in a of less than $0.01(5)\,\%$.

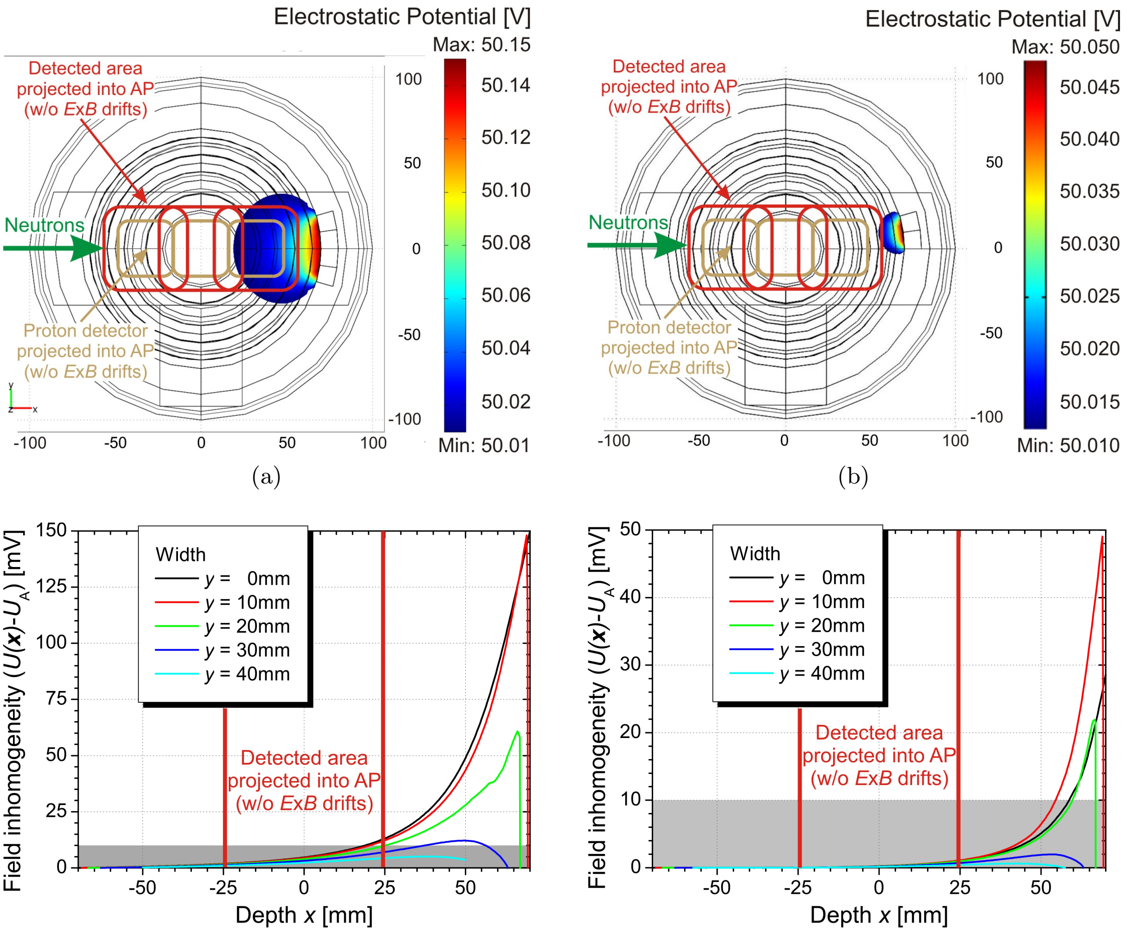

(a) (b)

(c) (d)

Figure 6.18: Influence of work function (WF) inhomogeneities on the electric potential in the analyzing plane (AP) at $z = 1.32\,\mathrm{m}$, for (a) and (c) the present thesis and (b) and (d) further investigations, with $U_{\mathrm{A}} = 50\,\mathrm{V}$. We mention that almost the same results were obtained for, e.g., $U_{\mathrm{A}} = 400\,\mathrm{V}$. (a) and (b) show the electric field distribution. Only in the case of the present thesis (a), the electrostatic potential exceeds 50.01 V on the right detector pad. Please note the different contour scales. The left and central detector pads are almost not affected by the WF inhomogeneities. Here, the black lines represent the electrodes e1 to e16, the two heat shields for the detector electrode e17, as well as the vacuum tube. (c) and (d) show the electric field inhomogeneity, $U(\mathbf{x}) - U_{\mathrm{A}}$, after deduction of the barrier voltage U_{A}, for 4 different widths y. For the central detector pad, the field inhomogeneity is in excess of 10 mV only in the case (c) and on the right boundary. The gray bar represents the 10 mV boundary. Please note the different y-scales. For elucidation, the golden frames show a projection of the (proton) detector chip into the AP; the red frames (lines) include two gyration radii on each side (for $B_0 = 2.177\,\mathrm{T}$). Here, we neglect the spatial displacement of both the detector chip and by the lower and upper dipole electrodes.

We note that Fig. 6.18 is only an example for both possible patches in the AP and the influence of the patch effect on the angular correlation coefficient a. Figure 6.19 shows further examples for the influence of the patch effect on the electric field distribution in the AP. In both cases, all three detector pads are affected by the WF inhomogeneities. The electric field inhomogeneity is in excess of 10 mV over the entire detector chip. In the

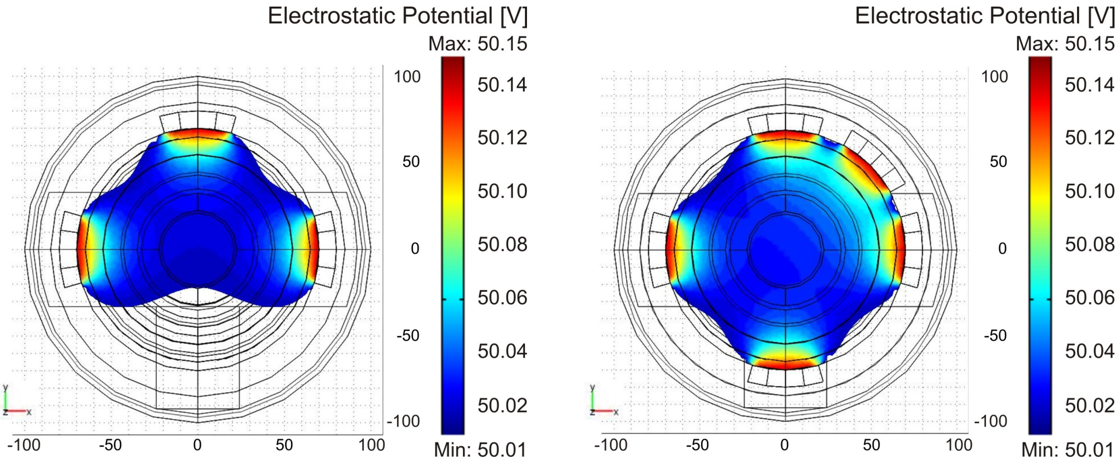

(a) (b)

Figure 6.19: Influence of work function inhomogeneities on the electric potential in the analyzing plane (AP) at $z = 1.32\,\mathrm{m}$, for the present thesis. With (a) 3 patches, the electric field inhomogeneity is already in excess of 10 mV over the entire detector chip; with (b) 5 patches, the field inhomogeneity averaged over the central detector pad is around 27 mV, what corresponds to a shift in a of $\Delta a/a = +0.37(7)\,\%$. The (present) inner surface of the AP electrode is best described by (b), where the five patches correspond to one brazed seam of the AP cylinder and four welding points for the supporting arms of the AP. Here, the black lines represent the electrodes e1 to e16, the two heat shields for the detector electrode e17, as well as the vacuum tube.

case of 5 patches (Fig. 6.19b), the field inhomogeneity averaged over the central detector pad is around 27 mV, what corresponds to a shift in a of

$$\Delta a/a = +0.37(7)\,\%. \tag{6.9}$$

We note that the (present) inner surface of the AP electrode is best described by Fig. 6.19b. Thus, for the present thesis, the influence of the patch effect in the AP on the neutrino-electron correlation coefficient a is negligible at the level of 1 %. However, for further investigations, the influence of the patch effect in the AP on a is negligible at the level of 0.1 %, as electric field calculations of, e.g., 8 patches in the AP show.

6.4.2 Patch Effect in the Decay Volume

In our measurement, the DV is grounded. We therefore can assume that $U_0 \equiv 0$. On the other hand, a variation of the WF within the DV electrode gr could render the electric field distribution. Figure 6.20 shows the influence of one patch on the electric potential in the DV. Only in the case of the present thesis, the electrostatic potential exceeds 10 mV, but almost over the entire cross-section of the neutron beam. However, for further investigations, the electrostatic potential is well below 10 mV.

In the case of Fig. 6.20, the electric field calculations showed that the field inhomogeneity averaged over the the central detector pad

- is around 20 mV for the present situation, what corresponds to a shift in a of

$$\Delta a/a = -0.24(5)\,\%, \tag{6.10}$$

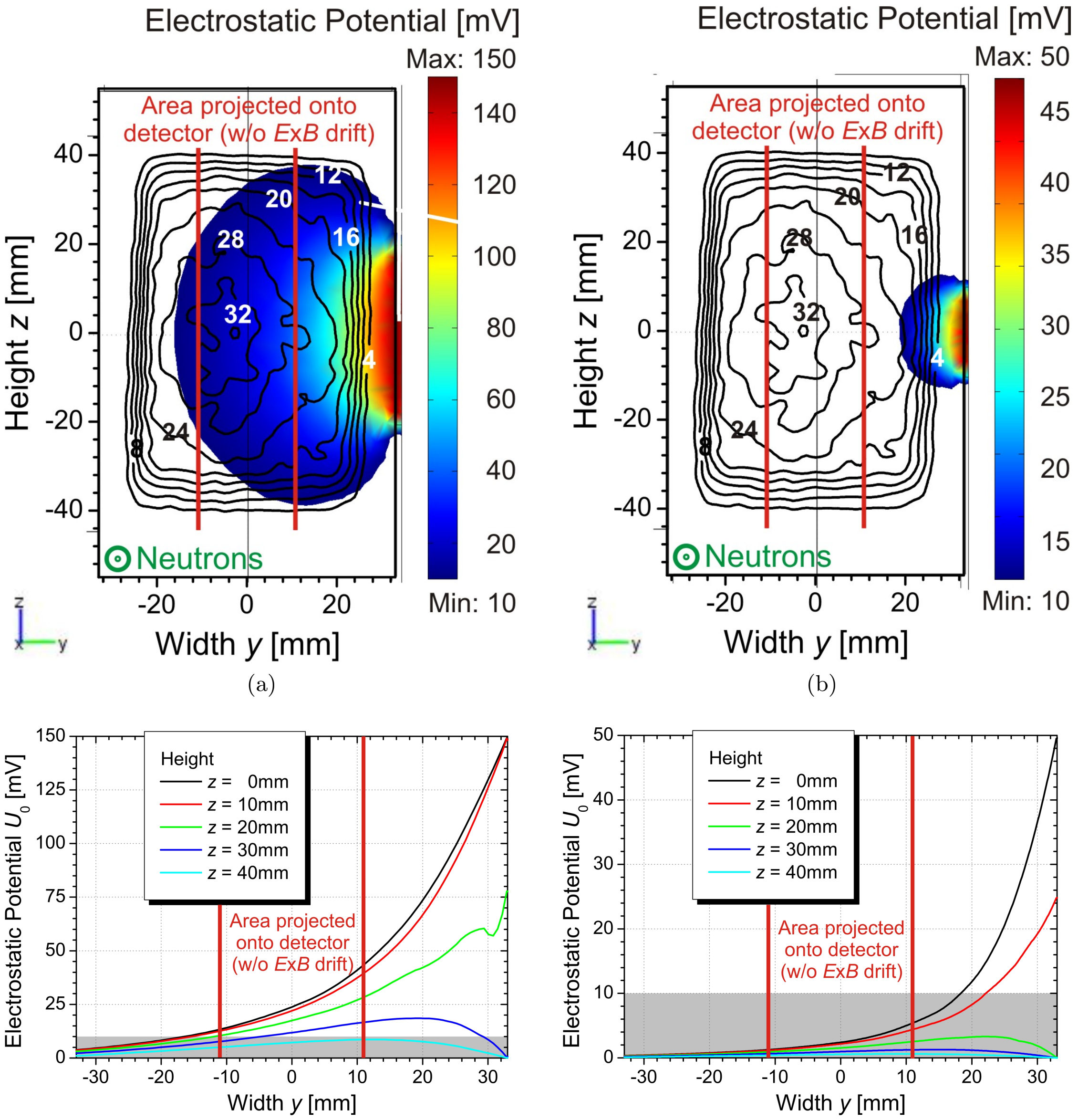

(a)

(b)

(c)

(d)

Figure 6.20: Influence of work function inhomogeneities on the electric potential in the decay volume (DV) at $x = 0$, for (a) and (c) the present thesis and (b) and (d) further investigations, with $U_0 \equiv 0\,\mathrm{V}$. (a) and (b) show the electric field distribution. Only in the case of the present thesis (a), the electrostatic potential exceeds 10 mV, but almost over the entire cross-section of the neutron beam. Please note the different contour scales. For comparison, the black contour lines indicate the neutron beam profile. (c) and (d) show the electrostatic potential, for 4 different heights z. In the case (c), the electrostatic potential exceeds 10 mV over the entire width of the (proton) detector, for all 4 heights. However, in the case (d), the electrostatic potential is well below 10 mV. The gray bar represents the 10 mV boundary. Please note the different y-scales. For elucidation, the red lines show a projection of the detector into the DV, including two gyration radii on each side (for $B_0 = 2.177\,\mathrm{T}$). Here, we neglect the spatial displacement of both the detector chip and by the lower and upper dipole electrodes.

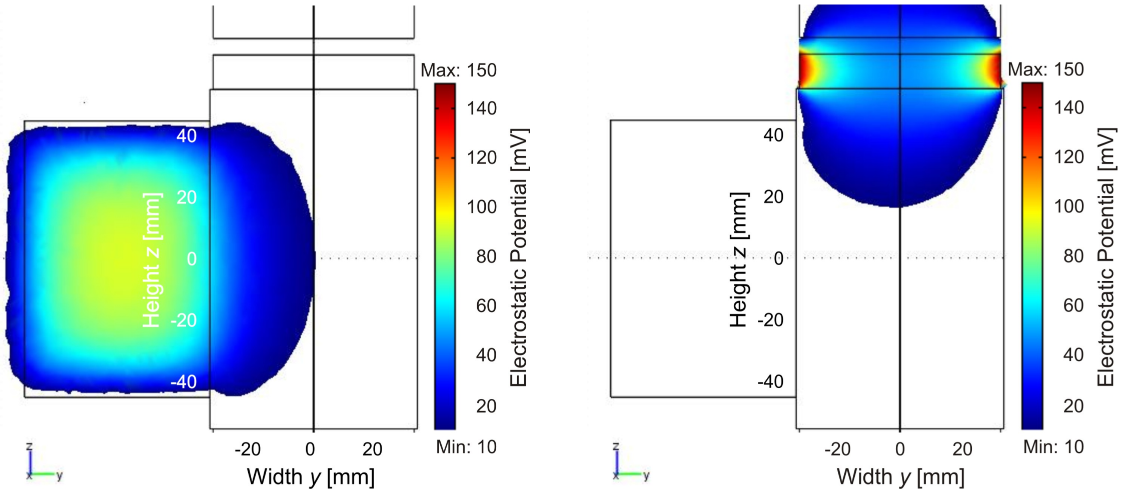

(a) (b)

Figure 6.21: Influence of work function (WF) inhomogeneities on the electric potential in the decay volume (DV) at (a) $x = 0$ and (b) $x = -11$ mm, for the present thesis. With a variation of the WF over (a) the rear side part (of the side port) of the DV electrode gr, the electrostatic potential exceeds 10 mV over almost the left half of the neutron beam; with a variation of the WF over (b) the upper ring of the DV electrode gr, the electric potential exceeds 10 mV only over the top quarter of the neutron beam. However, in the case of (b), decay protons may be trapped between the DV and the electrostatic mirror, as the electric field distribution exhibits a potential barrier above the neutron beam, of up to 105 mV at the edges of the detector chip. Such a variation of the WF reflects the possible influence of the brazed seam on top of the DV electrode gr. See the text for details. Here, the black lines represent the DV electrodes gr and e6.

Similar results were obtained for the left and right detector pads. The electric field inhomogeneity averaged over an outer detector pad is around 15 mV, which yields a shift in a of $-0.18(5)\,\%$.

- is around 2 mV for further investigations, what corresponds to a shift in a of

$$\Delta a/a = -0.02(5)\,\%. \tag{6.11}$$

Similar results were obtained for the left and right detector pads. The electric field inhomogeneity averaged over an outer detector pad is around 1.5 mV, which yields a shift in a of less than -0.02(5) %.

As in the case of the AP, Fig. 6.20 is only an example for both possible patches in the DV and the influence of the patch effect on the angular correlation coefficient a. Figure 6.21 shows additional examples for the influence of the patch effect on the electric field distribution in the DV. In both cases, only a part of the neutron beam is affected by the WF inhomogeneities. Thus, Eq. 6.10 sets an upper limit for the influence of the patch effect in the DV on the angular correlation coefficient a.

However, in the case of Fig. 6.21b, the electric field distribution exhibits a potential barrier above the neutron beam, of up to 105 mV at the edges of the detector chip. We mention that such a variation of the WF reflects the possible influence of the brazed seam on top of the DV electrode gr. As a result, decay protons may be reflected at the potentail barrier and subsequently trapped between the DV and the electrostatic mirror. Similarly, in the case of Figs. 6.20a to 6.21a, the electric field distribution exhibits a potential barrier in the DV, at, e.g., $z = 0$. Depending on their initial momentum, protons emitted below this potential barrier (at negative z-positions) may be reflected at the maximum and trapped between the DV and the electrostatic mirror. This, in turn, will lead to unexpected background due to interactions of the trapped protons with the residual gas and/or other decay products. For the same reason, local magnetic field maxima in the DV must be avoided. For protons emitted above the potential barrier (at positive z-positions), the condition for adiabatic transport may be violated, also depending on their initial momentum. Both effects will lead to a distortion of the adiabatic transmission function Eq. (3.30). Hence, the influence of the patch effect in the DV on the neutrino-electron correlation coefficient a is not negligible.

6.4.3 Unexpected Proton Reflections and Influence on a

In Refs. [5, 33, 46, 47, 50] we did not consider possible proton reflections from the DV. To incorporate the patch effect and hence the proton reflections into the transmission function Eq.(3.30), we make the following Ansatz:

> **WF inhomogeneities in the DV are described by an electric field gradient $\partial U_0/\partial z > 0$, between the decay point and the potential barrier.**

This electric field gradient will be superimposed on the slight magnetic field gradient $\partial B_0/\partial z < 0$ in the DV, cf. Sec. 3.2.2. The slight magnetic field gradient, in turn, causes a slow and adiabatic momentum transfer from transverse to longitudinal motion. On their way from the decay point $\mathbf{P_0}$ to the potential barrier $\mathbf{P}_{\mathrm{DV}}$, the polar angle of the protons will therefore have changed from its initial value θ_0, i.e., $|90°-\theta_0|$ will have increased. Thus, the magnetic field gradient weakens the influence of the patch effect. In the following, we neglect the possible effect of non-adiabatic proton motion. This could be part of further investigations (by means of MC simulations).

The potential barrier in the DV, caused by the patch effect, acts as an electric mirror. For a given definite kinetic energy T_0 only protons with sufficient longitudinal momentum can overcome this electric mirror. In the adiabatic approximation, the condition for transmission through the potential barrier can be written as (cf. Eqs. (3.23) and (3.24)):

$$T_{||}^{\mathrm{ad}}(\mathbf{P}_{\mathrm{DV}}) = T_0 - e\left(\left(U_0 + \frac{\partial U_0}{\partial z}\Delta z\right) - U_0\right) - \frac{B_0 + \frac{\partial B_0}{\partial z}\Delta z}{B_0} T_0 \sin^2\theta_0 \overset{!}{>} 0, \tag{6.12}$$

where $\Delta z = z(\mathbf{P}_{\mathrm{DV}}) - z(\mathbf{P_0}) > 0$. Solving inequation (6.12) for T_0 yields:

$$T_0 > T_{\mathrm{tr,DV}}(\theta_0) = e\frac{\partial U_0}{\partial z}\Delta z\left(1 - \frac{B_0 + \frac{\partial B_0}{\partial z}\Delta z}{B_0}\sin^2\theta_0\right)^{-1}. \tag{6.13}$$

Hence, protons with[21]

$$\begin{aligned} T_0 &> T_{\mathrm{tr,DV}}^{\max} = T_{\mathrm{tr,DV}}(\theta_0 = \pm 90^\circ) \qquad (6.14) \\ &= e\frac{\partial U_0}{\partial z}\Delta z \left(1 - \frac{B_0 + \frac{\partial B_0}{\partial z}\Delta z}{B_0}\right)^{-1} = -e\frac{\partial U_0}{\partial z} B_0 \left(\frac{\partial B_0}{\partial z}\right)^{-1} = \mathcal{O}(100\,\mathrm{eV}) \end{aligned}$$

are transmitted through the potential barrier, whereas protons with

$$T_0 < T_{\mathrm{tr,DV}}^{\min} = T_{\mathrm{tr,DV}}(\theta_0 = 0^\circ) = e\frac{\partial U_0}{\partial z}\Delta z = \mathcal{O}(10\,\mathrm{meV}) \qquad (6.15)$$

are reflected at the potential barrier and subsequently trapped, both independent of their (initial) polar angle. Solving inequation (6.12) for θ_0, in turn, yields that, for initial energies $T_{\mathrm{tr,DV}}^{\min} < T_0 < T_{\mathrm{tr,DV}}^{\max}$, protons can pass the potential barrier only if their (initial) polar angle goes below (see also Fn. 3 in Chap. 3)

$$\theta_0 < \theta_{\mathrm{tr,DV}}^{\max} = \arcsin\sqrt{\frac{B_0}{B_0 + \frac{\partial B_0}{\partial z}\Delta z}\left(1 - \frac{e\frac{\partial U_0}{\partial z}\Delta z}{T_0}\right)}, \qquad (6.16)$$

i.e., protons with an initial energy of $T_{\mathrm{tr,DV}}^{\min} < T_0 < T_{\mathrm{tr,DV}}^{\max}$ are transmitted through the potential barrier with a probability of (see also Fn. 4 in Chap. 3)

$$\begin{aligned} w_{\mathrm{tr,DV}}(T_0) &= \int_0^{\theta_{\mathrm{tr,DV}}^{\max}} d\theta \sin\theta = \Big[-\cos\theta\Big]_0^{\theta_{\mathrm{tr,DV}}^{\max}} = \left(1 - \sqrt{1 - \sin^2\theta_{\mathrm{tr,DV}}^{\max}}\right) \\ &= 1 - \sqrt{1 - \frac{B_0}{B_0 + \frac{\partial B_0}{\partial z}\Delta z}\left(1 - \frac{e\frac{\partial U_0}{\partial z}\Delta z}{T_0}\right)}. \qquad (6.17) \end{aligned}$$

Thus, the proton reflections in the DV are described by the transmission function:

$$F_{\mathrm{tr,DV}}(T_0) = \begin{cases} 0 & , \quad T_0 \leq T_{\mathrm{tr,DV}}^{\min} \\ 1 - \sqrt{1 - \frac{B_0}{B_0 + \frac{\partial B_0}{\partial z}\Delta z}\left(1 - \frac{e\frac{\partial U_0}{\partial z}\Delta z}{T_0}\right)} & , \quad T_{\mathrm{tr,DV}}^{\min} < T_0 \leq T_{\mathrm{tr,DV}}^{\max} \\ 1 & , \quad T_0 > T_{\mathrm{tr,DV}}^{\max} \end{cases} . \qquad (6.18)$$

To finally calculate the influence of the proton reflections on the angular correlation coefficient a, we have to convolve the transmission functions Eq. (3.30) with Eq. (6.18). Depending on the relative figures of $T_{\mathrm{tr,DV}}^{\min}$, $T_{\mathrm{tr}}^{\min}$, $T_{\mathrm{tr,DV}}^{\max}$, and $T_{\mathrm{tr}}^{\max}$, the transmission functions can intersect or not. If, however, the two transmission functions have no common point of intersection, the convolution is one of the two transmission functions Eq. (3.30) or Eq. (6.18). Altogether, the patch effect in the DV can be described by the transmission

---

[21] The orders shown in Eqs. (6.15) and (6.15) are based on the assumptions that $\partial U_0/\partial z = \mathcal{O}(10\,\mathrm{mV\,cm^{-1}})$, $(\partial B_0/\partial z)/B_0 = \mathcal{O}(1 \times 10^{-4}\,\mathrm{cm^{-1}})$, and $\Delta z = \mathcal{O}(1\,\mathrm{cm})$.

function:

$$F_{\mathrm{tr,PE}}(T_0) = \begin{cases} 0 & , \quad T_0 \leq T_{\mathrm{tr,PE}}^{\mathrm{min}} \\ 1 - \sqrt{1 - \frac{B_0}{B_\mathrm{A}}\left(1 - \frac{eU_\mathrm{A}}{T_0}\right)} & , \quad T_{\mathrm{tr,PE}}^{\mathrm{min}} < T_0 \leq T_{\mathrm{tr,PE}}^{\mathrm{inter}} \\ 1 - \sqrt{1 - \frac{B_0}{B_0 + \frac{\partial B_0}{\partial z}\Delta z}\left(1 - \frac{e\frac{\partial U_0}{\partial z}\Delta z}{T_0}\right)} & , \quad T_{\mathrm{tr,PE}}^{\mathrm{inter}} < T_0 \leq T_{\mathrm{tr,PE}}^{\mathrm{max}} \\ 1 & , \quad T_0 > T_{\mathrm{tr,PE}}^{\mathrm{max}} \end{cases} , \tag{6.19}$$

where

$$T_{\mathrm{tr,PE}}^{\mathrm{min}} = \mathrm{Max}\left(T_{\mathrm{tr}}^{\mathrm{min}}; T_{\mathrm{tr,DV}}^{\mathrm{min}}\right) \quad \text{and} \tag{6.20}$$

$$T_{\mathrm{tr,PE}}^{\mathrm{max}} = \mathrm{Min}\Big(T_{\mathrm{p,max}}; \mathrm{Max}\left(T_{\mathrm{tr}}^{\mathrm{max}}; T_{\mathrm{tr,DV}}^{\mathrm{max}}\right)\Big). \tag{6.21}$$

The point of intersection, if existent, is located at the intersection of the second and third line of Eq. (6.19), i.e.,

$$T_{\mathrm{tr,PE}}^{\mathrm{inter}} = \begin{cases} T_{\mathrm{tr,PE}}^{\mathrm{max}} & , \quad T_{\mathrm{tr,PE}}^{\mathrm{min}} < T_{\mathrm{tr}}^{\mathrm{min}} \text{ and } T_{\mathrm{tr,PE}}^{\mathrm{max}} < T_{\mathrm{tr}}^{\mathrm{max}} \\ \frac{eU_\mathrm{A}\left(B_0 + \frac{\partial B_0}{\partial z}\Delta z\right) - e\frac{\partial U_0}{\partial z}\Delta z B_\mathrm{A}}{B_0 + \frac{\partial B_0}{\partial z}\Delta z - B_\mathrm{A}} & , \quad \text{otherwise} \\ T_{\mathrm{tr,PE}}^{\mathrm{min}} & , \quad T_{\mathrm{tr}}^{\mathrm{min}} < T_{\mathrm{tr,PE}}^{\mathrm{min}} \text{ and } T_{\mathrm{tr}}^{\mathrm{max}} < T_{\mathrm{tr,PE}}^{\mathrm{max}} \end{cases} . \tag{6.22}$$

We note that the transmission function Eq. (6.19) reduces to the familiar expression Eq. (3.30) if $T_{\mathrm{tr,PE}}^{\mathrm{min}} < T_{\mathrm{tr}}^{\mathrm{min}}$ and $T_{\mathrm{tr,PE}}^{\mathrm{max}} < T_{\mathrm{tr}}^{\mathrm{max}}$, i.e., in the case of high AP voltages ($U_\mathrm{A} \geq 250\,\mathrm{V}$) and/or small WF inhomogeneities, as shown in Fig. 6.22b. We further note that the transmission function will not reach 100 % any more if $T_{\mathrm{tr,DV}}^{\mathrm{max}} > T_{\mathrm{p,max}}$, i.e., in the case of large WF inhomogeneities, as shown in Figs. 6.22a and 6.22b.

Figure 6.22 shows the influence of the proton reflections on the transmission function. The figure shows that the slight magnetic field gradient $\partial B_0/\partial z < 0$ in the decay volume dramatically reduces the influence of the patch effect. In addition, Fig. 6.23 shows the influence of the patch effect on the angular correlation coefficient a. The higher the WF inhomogeneities $\partial U_0/\partial z$ are, the worse the systematic error in a is. For electric field gradients $\partial U_0/\partial z > 100\,\mathrm{mV\,cm^{-1}}$, the systematic error even exceeds 18 %.

In order to calculate the systematic error in a for the present thesis, we first have to determine the size of the WF inhomogeneities $\partial U_0/\partial z$ over the central detector pad. In Table 6.6 we list the electric field gradients $\partial U_0/\partial z$ for the two extreme cases shown in Fig. 6.20a and 6.21b. In the case of Fig. 6.20a the electric field distribution exhibits a maximum at $z = 0$; in the case of Fig. 6.21b at $z = +6\,\mathrm{cm}$. In the direction of the neutron beam the electric field gradients are nearly independent of the depth x. The closer one gets in y-direction to the maximum, the higher the electric field gradients and the shorter their height expansion L_z get.

Next, we have to weight the electric field gradients with the neutron beam distribution. W.l.o.g. we assume a uniform neutron beam distribution over the central detector

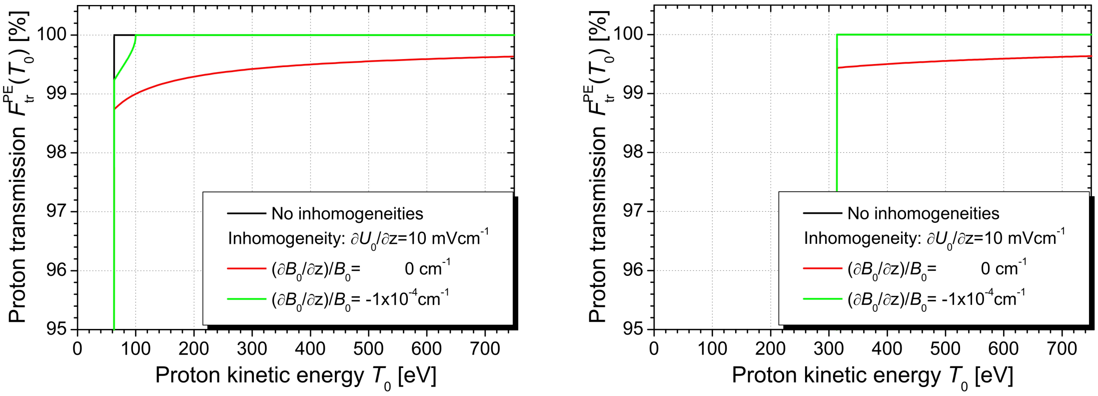

(a) (b)

Figure 6.22: Influence of work function inhomogeneities on the transmission function, for two different analyzing plane (AP) voltages: (a) $U_\mathrm{A} = 50\,\mathrm{V}$ and (b) $U_\mathrm{A} = 250\,\mathrm{V}$, with $\Delta z = 1\,\mathrm{cm}$, $B_0 = 2.177\,\mathrm{T}$, and $B_\mathrm{A}/B_0 = 0.203$. For better visibility, the y-axis is enlarged to $(95 - 100)\,\%$. The comparison between the green and red lines shows that the slight magnetic field gradient $\partial B_0/\partial z < 0$ in the decay volume dramatically reduces the influence of the patch effect. We mention that for high AP voltages ($U_\mathrm{A} \geq 250\,\mathrm{V}$) the transmission function Eq. (6.19) reduces to the familiar expression Eq. (3.30), shown in black, depending on the size of the magnetic field gradient $\partial B_0/\partial z$.

pad. Then, the systematic errors in a are approximated with the averaged electric field gradients. A more sophisticated analysis will be part of further investigations (by means of MC simulations).

In the case of Fig. 6.20a, only the top half of the neutron beam is affected by the proton reflections. Thus, for positive z values, we have to weight the electric field gradients with 0. In the event that L_z does not cover the whole bottom part of the neutron beam, we have to redefine the electric field gradient over the uncovered part of the neutron beam:

$$\begin{aligned}\frac{\partial U_0}{\partial z} \quad &\longmapsto \quad \frac{\partial U_0}{\partial z} L_z \left\langle \frac{1}{z} \right\rangle = \frac{\partial U_0}{\partial z} L_z \frac{1}{\int_{L_0-L_z}^{L_0} dz z} \int_{L_0-L_z}^{L_0} dz \frac{1}{z} \\ &= \frac{\partial U_0}{\partial z} L_z \frac{1}{\frac{1}{2}\left[z^2\right]_{L_0-L_z}^{L_0}} \Big[\ln z\Big]_{L_0-L_z}^{L_0} = \frac{\partial U_0}{\partial z} \frac{2}{2L_0 - L_z} \ln \frac{L_0}{L_0 - L_z},\end{aligned} \tag{6.23}$$

where L_0 denotes the distance between the lower edge of the neutron beam and the maximum of the electric field (here: $z = 0$, i.e., $L_0 \approx 4\,\mathrm{cm}$). Thus, for $L_z < L_0$, we have to weight the electric field gradients with

$$\frac{1}{L_0}\left((L_0 - L_z) \frac{2}{2L_0 - L_z} \ln \frac{L_0}{L_0 - L_z} + L_z \right). \tag{6.24}$$

This method gets an average electric field gradient of $\partial U_0/\partial z = (2.2 \pm 2.9)\,\mathrm{mV\,cm^{-1}}$. Together with our magnetic field gradient of $\left(\partial B_0/\partial z\right)/B_0 = -1 \times 10^{-4}\,\mathrm{cm^{-1}}$ (see also Fn. 22 in Chap. 3) this corresponds to a systematic error in a of

$$\Delta a/a = (0^{+0.04}_{-0.00} \pm 0.04)\,\%. \tag{6.25}$$

Here, the first error stems from the uncertainty in the electric field gradient and the latter one from the respective errors shown in Fig. 6.23.

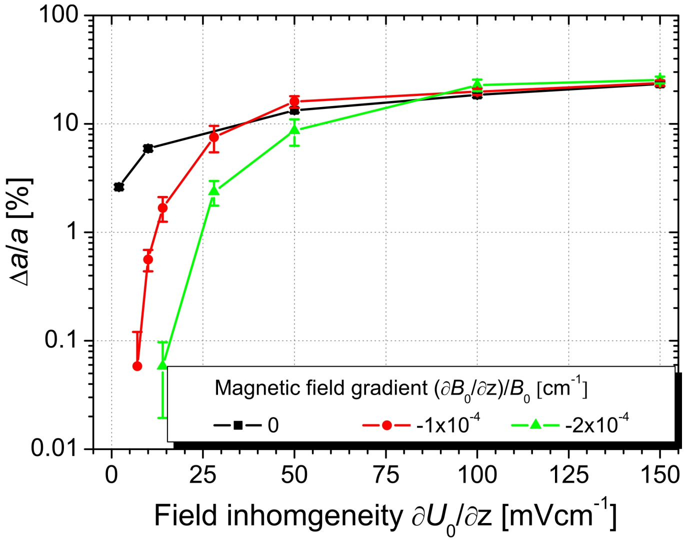

Figure 6.23: Relative change of the angular correlation coefficient a for different work function (WF) inhomogeneities in the DV, described by an electric field gradient $\partial U_0/\partial z > 0$. The higher the WF inhomogeneities $\partial U_0/\partial z$ are, the worse the systematic error in a is. For electric field gradients $\partial U_0/\partial z > 100\,\mathrm{mV\,cm^{-1}}$, the systematic error even exceeds 18 %. The comparison between the green, red, and black line shows that the slight magnetic field gradient $\partial B_0/\partial z < 0$ in the decay volume dramatically reduces the influence of the patch effect. Input data for the calculation (with Nachtmann's Formula Eq. (2.38)): $\Delta z = 1\,\mathrm{cm}$, $B_0 = 2.177\,\mathrm{T}$, $B_\mathrm{A}/B_0 = 0.203$, $U_\mathrm{A} = 50, 250, 400, 500, 600\,\mathrm{V}$, and the recommended value for $a = -0.103$ [10].

In the case of Fig. 6.21b, the electric field gradient stretches only over $L_z \leq 6\,\mathrm{cm}$, i.e., over positive z values. In the event that L_z does not cover the whole top part of the neutron beam, we have to weight the electric field gradients with Eq. (6.24) (here: $L_0 = 6\,\mathrm{cm}$). For negative z values, we have to weight the electric field gradients with

$$L_z \frac{1}{\int_{L_0-L_\mathrm{max}}^{L_0} dz z} \int_{L_0-L_\mathrm{max}}^{L_0} dz \frac{1}{z} = \frac{2L_z}{2L_0L_\mathrm{max} - L_\mathrm{max}^2} \ln \frac{L_0}{L_0 - L_\mathrm{max}}, \tag{6.26}$$

where L_max denotes the distance between $z = 0$ and the maximum of the electric field (here: $z = +6\,\mathrm{cm}$, i.e., $L_\mathrm{max} \approx 6\,\mathrm{cm}$ and $L_0 \approx 10\,\mathrm{cm}$). This way we get an average electric field gradient of $\partial U_0/\partial z = (4.6 \pm 3.6)\,\mathrm{mV\,cm^{-1}}$, which yields a systematic error in a of

$$\Delta a/a = (+0.03^{+0.32}_{-0.03} \pm 0.08)\,\%. \tag{6.27}$$

Thus, for the present thesis, the influence of the patch effect in the DV on the neutrino-electron correlation coefficient a is negligible at the level of 1 %. However, the effect of possible proton trapping between the DV and the mirror electrode, in the order of $0.1\,\mathrm{s^{-1}}$ for a full proton decay rate of $N_0 = 490\,\mathrm{s^{-1}}$, requires further investigations (by means of MC simulations). However, for further investigations, the influence of the patch effect in the DV on a is negligible at the level of 0.1 %. In the case of Fig. 6.21b, but with a variation of the WF of only 50 mV, we get an average electric field gradient of $\partial U_0/\partial z = (1.5 \pm 1.2)\,\mathrm{mV\,cm^{-1}}$. This corresponds to a systematic error in a of only $\Delta a/a = (0.00^{+0.01}_{-0.00} \pm 0.02)\,\%$.

Table 6.6: Work function (WF) inhomogeneities in the DV, described by an electric field gradient $\partial U_0/\partial z$. Here, we consider the two extreme cases shown in Fig. 6.20a (columns 2 to 5) and 6.21b (columns 6 to 9). In the case of Fig. 6.20a the electric field distribution exhibits a maximum at $z = 0$; in the case of Fig. 6.21b at $z = +6\,\text{cm}$. The electric field gradients stretch over L_z in height from this maxima. In the direction of the neutron beam we only list the three values $x = 0, \pm 11\,\text{mm}$, as the electric field gradients are nearly independent of the depth x. The closer one gets in y-direction to the maximum, the higher the WF inhomogeneities and the shorter the height expansions L_z get.

	Patch (see Fig. 6.20a)				Ring (see Fig. 6.21b)			
Depth	$x = 0$		$x = \pm 11$ mm		$x = 0$		$x = \pm 11$ mm	
Width y [mm]	$\partial U_0/\partial z$ [mV cm^{-1}]	L_z [cm]	$\partial U_0/\partial z$ [mV cm^{-1}]	L_z [cm]	$\partial U_0/\partial z$ [mV cm^{-1}]	L_z [cm]	$\partial U_0/\partial z$ [mV cm^{-1}]	L_z [cm]
-20	1.5	4.0	1.3	4.0	9.2	6.0	10.0	6.0
-15	2.0	4.0	1.8	4.0	8.3	6.0	8.3	6.0
-10	2.5	4.0	2.3	4.0	8.3	6.0	8.3	6.0
-5	3.5	4.0	3.1	4.0	7.9	6.0	8.3	6.0
0	4.3	4.0	3.8	4.0	7.9	6.0	8.3	6.0
5	6.6	3.5	6.0	3.5	7.9	6.0	8.3	6.0
10	9.1	3.5	8.9	3.5	7.9	6.0	8.3	6.0
15	12.9	3.5	11.4	3.5	8.3	6.0	8.3	6.0
20	22.0	2.5	18.3	3.5	8.3	6.0	9.2	6.0
25	38.5	2.0	37.0	2.0	43.0	2.0	42.5	2.0
30	120.0	1.0	100.0	0.5	110.0	1.0	260.0	0.5

In summary, for the present thesis, the patch effect introduces an unexpected systematic error to the angular correlation coefficient a of

$$\boxed{\Delta a/a = (+0.03^{+1.93}_{-1.64} \pm 0.18)\,\%} \tag{6.28}$$

consisting of:

- Proton reflections in the DV: $(+0.03^{+0.32}_{-0.03} \pm 0.08)\,\%$, from Eq. (6.27),
- Inhomogeneity of the WF in the AP: ±0.37(7) %, from Eq. (6.9),
- Inhomogeneity of the WF in the DV: ±0.24(5) %, from Eq. (6.10), and
- Absolute WF values in the DV and the AP: ±1.00(13) %,
  assuming that the absolute WF values in the DV and the AP would differ by about 75 mV. This would describe, e.g., different aging processes of the DV and the AP electrode as observed for the cylindrical sample electrode shown in Fig. 6.1a.

We note that the sign of three of the errors is unknown since we do not know the sign of the WF inhomogeneities, except for the proton reflections.

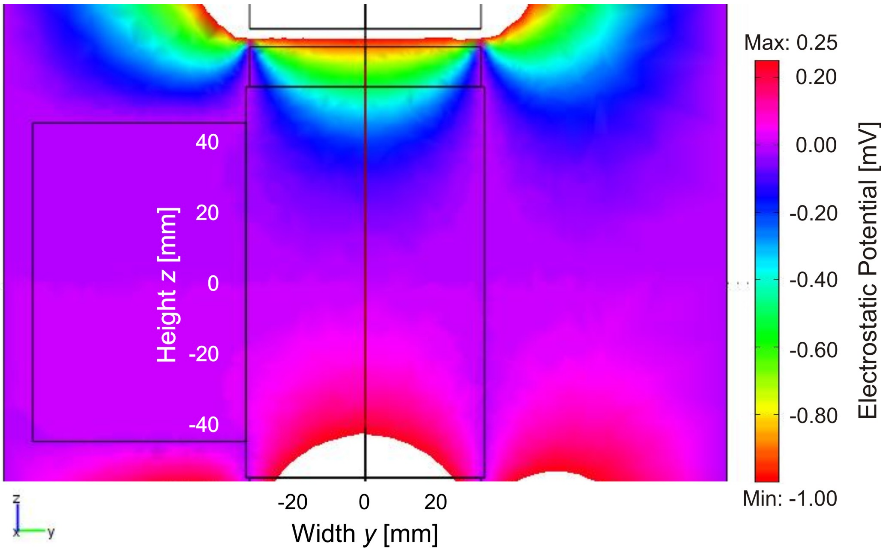

Figure 6.24: Electric field distribution in the decay volume (DV) for ±2 V on the bottom and top cylinders e3 and e6 of the DV electrode, respectively, with 20 mV contour graduations. With this setting we can eliminate both local electric field maxima in and above the DV. Inside the DV the electric field gradient is not less than $25\,\mathrm{mV\,cm^{-1}}$; at the top end of the DV electrode it is up to $350\,\mathrm{mV\,cm^{-1}}$. Here, the black lines represent the DV electrodes gr and e6.

6.4.4 Approaches for the Unexpected Proton Reflections

As discussed in the previous section, there are possibilities to reduce the influence of the patch effect on the neutrino-electron correlation coefficient a. Here, we only list approaches to eliminate local electric field maxima in the DV and/or to handle the unexpected proton reflections:

Slight magnetic field gradient: The slight magnetic field gradient in the DV causes a slow and adiabatic momentum transfer from transverse to longitudinal motion. Thus, it weakens the influence of the patch effect on a, as shown in Fig. 6.23. We therefore have to investigate the impact of various magnetic field gradients on a as well as on the proton count rates, in a further beam time. As stated in the previous section, the transmission function Eq. (6.19) reduces to the familiar expression Eq. (3.30) in the case of high AP voltages ($U_\mathrm{A} \geq 250\,\mathrm{V}$), as shown in Fig. 6.22b. As a first step, it is sufficient to only study the proton count rates at AP voltages $U_\mathrm{A} = 50\,\mathrm{V}$ and $U_\mathrm{A} = 250\,\mathrm{V}$ for different magnetic field gradients. On the other hand, a too large increase of the magnetic field gradient in the DV goes hand in hand with the violation of the condition for adiabatic transport. Thus, it is to be hoped that the proton count rates stabilize at a reasonable size of the magnetic field gradient.

Inverse electric field gradient: Protons may be trapped between the DV and the electric mirror only in the event of a positive electric field gradient in the DV or an electric field maximum above the DV. Consequently, it suggests itself to turn the electric field gradient in opposite direction, by means of a superimposed external electric field. The simplest way is to apply a potential of a few Volts to the bottom and

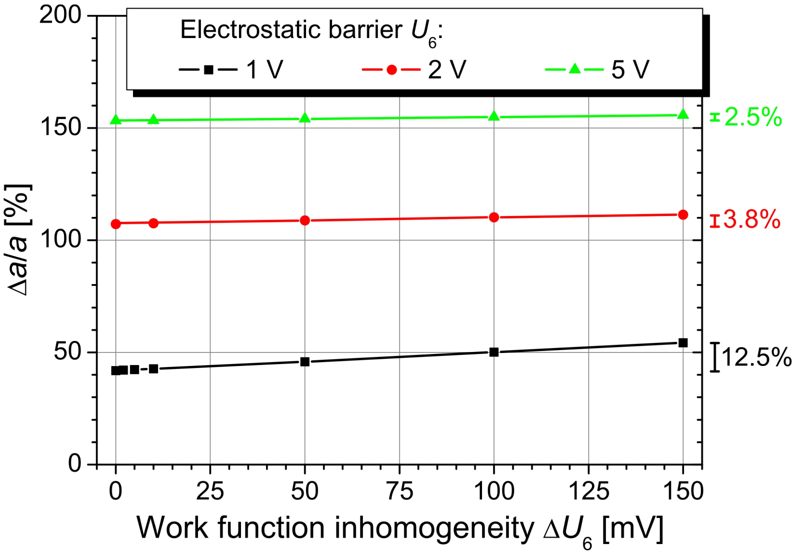

Figure 6.25: Relative change of the angular correlation coefficient a for different work function (WF) inhomogeneities, ΔU_6, in the top cylinder e6 of the DV electrode. The higher the electrostatic barrier U_6 is, the higher the systematic change in a is. But, the comparison between the green, red, and black line shows that the electrostatic barrier U_6 dramatically reduces the sensitivity of this change on the patch effect. For WF inhomogeneities $\Delta U_6 \leq 10\,\mathrm{mV}$, the sensitivity is only in the order of permille. Input data for the calculation (with Nachtmann's Formula Eq. (2.38)): $B_0 = 2.177\,\mathrm{T}$, $B_\mathrm{A}/B_0 = 0.203$, $U_\mathrm{A} = 50, 250, 400, 500, 600\,\mathrm{V}$, and the recommended value for $a = -0.103$ [10].

top cylinders e3 and e6 of the DV electrode, with opposite sign. Figure 6.24 shows the influence of ±2 V on the electric field distribution in the DV. With this setting we can eliminate both local electric field maxima in and above the DV. Inside the DV the electric field gradient $\partial U_0/\partial z$ is not less than $25\,\mathrm{mV\,cm^{-1}}$; at the top end of the DV electrode it is up to $350\,\mathrm{mV\,cm^{-1}}$. Compared with Figs. 6.20, 6.21, and Table 6.6 these gradients might already be too strong. As in the first approach, we have to study the influence of different electric field gradients on a as well as on the proton count rates, in a further beam time. We mention that one such first test in our latest beam time at the Institut Laue-Langevin (ILL) was inconclusive, due to non-statistical fluctuations of the count rates (for details see Sec. 5.3.3). As in the case of the magnetic field gradient, a too large increase of the electric field gradient is accompanied with the violation of the condition for adiabatic transport.

Definite electric mirror above the DV: Instead of compensating local electric field maxima, we can introduce a small but known potential barrier above the DV. For instance, we can apply a potential of a few Volts to the top cylinder e6 of the DV electrode. This causes a systematic but correctable change in a of several 10 %, as can be seen from Fig. 6.25. Fortunately, the sensitivity of this change on WF inhomogeneities is only in the order of permille. A great disadvantage of this method is that the potential barrier will be located at around $z = +13\,\mathrm{cm}$, depending on the settings of the lower $\mathbf{E}\times\mathbf{B}$ electrode e8, far above the DV. At this height, neither the magnetic nor the electric field will be as homogeneous as in the DV or the AP. Thus, we have to analyze whether the potential barrier can be described by a transmission function similar to the familiar one Eq. (3.30) or Eq. (6.19). This will be part of further investigations (by means of MC simulations).

Definite magnetic mirror above the DV: Instead of a potential barrier above the DV, we can introduce a small but known magnetic mirror (cf. also the measurement principles of PERC in App. C.1). For instance, we can inverse the magnetic field gradient so that we shift the local magnetic field maximum from $z = -6\,\mathrm{cm}$ at present to, e.g., $z = +6\,\mathrm{cm}$. A great advantage of this method is that the magnetic mirror will be located at a rather homogeneous magnetic field. However, we have to find a setting of the correction coils c3 and c5 which compensates the proton trapping due to variations of the WF and simultaneously does not violate the condition for adiabatic transport. This has to be part of further investigations (by means of MC simulations).

We note that in the last two proposals we must pay attention to the trapped protons. Possible ways to clean the proton trap between mirror electrode and potential barrier or magnetic mirror are:

- introducing a further $\mathbf{E} \times \mathbf{B}$ electrode between DV and electric mirror. For instance, the quadrupole electrode e2 may be connected like an $\mathbf{E} \times \mathbf{B}$ electrode. The great disadvantage of this method is that the magnetic field at height of the quadrupole lacks the desirable homogeneity. A violation of the condition for adiabatic transport may be the result.
- periodical switching on and off of the electric mirror, or
- measurements in which the electric mirror is switched off completely.

6.5 Summary and Outlook

In order to keep systematic uncertainties in the neutrino-electron correlation coefficient a below $\Delta a/a = 0.1\,\%$, the potential difference between DV and AP has to be known precisely. Indeed, a variation of the WF within an electrode or between different electrodes could render this potential difference. Hence, we investigated experimentally the patch effect and theoretically its impact on a.

6.5.1 Investigations of the Patch Effect and Influence on a

The present investigation showed that a platinized sample (Cu25) achieved the lowest WF values: RMS WF 6.6 meV and PTP WF 49.0 meV. The WF values of its twin (Cu26) were only a few meV higher at RMS WF 9.0 meV and PTP WF 54.0 meV. Although the RMS WF value of sample Cu25 was stable to ±2.2 meV over months, the manufacturer of this sample was not able to reproduce its good quality. However, a gold-plated sample (Cu12) achieved the lowest and most reproducible WF values: RMS WF 10.9 meV, PTP WF 54.0 meV, stable to ±3.0 meV over at least 9 months, and reproducible to ±3.3 meV, independent of different processing techniques and/or surface treatments. Our investigations with the SKP have shown that coating adhesion and SR both have a significant influence on the measured WF values. In particular, our analysis suggests that hand-polishing to a mirror finish decreases the RMS WF values by about 5 meV.

Platinum has the highest polycrystalline WF value, as shown in Table 6.1, nearly 200 meV greater than the highest mono-crystalline WF value of gold. Low WF values, in turn, are prone to oxidation. This would speak for platinum as outer surface coating, without experimental proof. However, the WF data presented in this thesis are not clearly in favor of platinum or gold. With regard to the reproducibility of the samples, we suggest gold as outer surface coating for the upcoming measurements with aSPECT.

Nevertheless, a few questions remain:

- Whether and if so to which electrode size the present results can be upscaled?
- Why could the sample with the lowest WF values not be reproduced?
- Whether and if so how would rolling or bending alter the WF?
- Whether and if so how much could an UHV compatible SKP improve the measured WF values? (e.g., in comparison with Ref. [240])

Therefore, for further investigations, we suggest to not only scan the samples with the SKP but also

- study the SR, the coating composition, and the sample surface by means of a perthometer respectively a SEM together with an EDX analysis, and
- superimpose the SR, SEM, and EDX results on the measured WF data,

in order to draw significant conclusions.

For the latest beam time, we have shown that the patch effect introduces an unexpected systematic error to the angular correlation coefficient a of

$$\Delta a/a = (+0.03^{+1.93}_{-1.64} \pm 0.18)\,\%, \tag{6.29}$$

caused by proton reflections in the DV, WF inhomogeneities in the AP, WF inhomogeneities in the DV, and different absolute WF values in the DV and the AP. However, for an improved electrode system we expect that the influence of the patch effect on a is negligible at the level of 0.1 %.

6.5.2 Improvements for a Further Beam Time

Based on our investigations with the SKP, we suggest, for further beam times:

- avoid welding and brazing, if not possible prefer brazing, otherwise plugging into each other or screwing,
- favor flat shapes over cylinders for the electrodes, e.g., construct the AP electrode, shaped as a regular polygon, out of small plates,
- polish the substrates at least by hand to a mirror finish, turn the substrates by 90° after each polishing step,
- clean the surfaces thoroughly from remnants of the polishing compound,

and in particular for the upcoming measurements:

- re-open the right side of the DV electrode gr, to reduce the influence of WF inhomogeneities as shown in Fig. 6.20 on a and simultaneously increase the pumping speed,
- increase the volume of the DV and subsequently the distance between the neutron beam and the inner surfaces of the DV electrode gr,
- use a layer combination of first $10\,\mu$m of silver and then $1\,\mu$m of gold.

We mention that there are a plenty of reasons for an in-situ measurement of the WF, by means of an UHV SKP periodically switching between DV and AP:

- different absolute WF values in the DV and the AP,
- adsorption of residual gas on the inner surfaces of the electrodes,
- aging processes of the electrodes, and many more.

6.5.3 Upcoming Measurements with *a*SPECT

Currently, the *a*SPECT experiment is set up at the PF1B of the ILL. With measurements in the June/July and the September/October 2011 cycle, we aim to improve the uncertainty in a to 1 %, well below the present literature value of 4 % [10].

For this purpose, the DV electrodes e3, gr, and e6 were already renewed. In view of the short time till the beam time, spare parts for the DV electrode gr were produced to be analyzed with the SKP. So far, the two spare parts T1 and T2 (plates, $55 \times 110\,\mathrm{mm}^2$ in surface) were analyzed. The SR analysis yielded R_a values of 48(19) nm and 40(19) nm, respectively [268]. With the SKP, RMS WF values of (28.8 ± 11.1) meV and (33.0 ± 4.7) meV, respectively, were achieved [257]. Both values are comparable with but inferior to our samples Cu3, Cu4, Cu11, Cu12, Cu32, and Cu33. Thus, we expect that the impact of the patch effect on the angular correlation coefficient a is negligible at the level of 0.1 %, except for different absolute WF values in the DV and the AP.

Chapter 7

Summary and Outlook

The retardation spectrometer *a*SPECT [46, 47] has been built to perform precise measurements of the antineutrino-electron angular correlation coefficient a, by measuring the proton recoil spectrum in the decay of free, unpolarized neutrons. A precise measurement of a can be used to study the Standard Model of elementary particles and fields as swell to search for evidence of possible extensions to it, like right-handed currents or scalar and tensor interactions, cf. Secs. 2.2 and 2.3.

7.1 Statistical and Systematic Limits

In this thesis the latest measurement with the *a*SPECT spectrometer at the Institut Laue-Langevin (ILL) in Grenoble, France (2007-2008), is described. The primary focus of this beam time was on the identification and investigation of possible systematic effects. The overall aim of the *a*SPECT experiment is to improve the accuracy of the neutrino-electron correlation coefficient a by more than one order of magnitude in comparison to previous measurements [40, 41]. In the latest beam time a statistical accuracy of about 2 % per 24 hours measurement time was reached.

Compared with our first beam time at the Forschungs-Neutronenquelle Heinz Maier-Leibnitz in Munich, Germany (2005-2006) [33], the major improvements for this beam time were a new proton detector, the redesign of several electrodes (cf. Sec. 3.2.1), and improved ultra high vacuum. For the first time, a silicon drift detector was used [52]. This detector has a much better separation of signal and noise. With the new detector, the acceleration potential could be significantly reduced and therefore the problem of frequent electrical breakdowns be solved [34].

During the data analysis several different systematic effects were investigated. Exhaustive Monte Carlo simulations were performed to compute a variety of systematic corrections, cf. Sec. 5.5. However, the data analysis revealed a problem in the detector electronics which caused a significant systematic error. Unfortunately, this effect was discovered only after the beam time. Despite our best efforts, we could only set upper limits on the correction of the problem, which are too high to determine a meaningful result from our latest beam time at the ILL, cf. Sec. 5.4.1.

Apart from the problem in the detector electronics, the dominant systematic uncertainties on the neutrino-electron correlation coefficient a are a possible charging of the collimation system, potential Penning discharges in the bottom of the spectrometer, and a violation of the condition for adiabatic transport, cf. Secs. 5.4.3 and 5.4.4.

7.2 Improvements for a Further Beam Time

Thanks to the knowledge of the systematic effects gained in this thesis and the theses of M. Simson [52], M. Borg [34], and F. Ayala Guardia [53], we are now able to improve the aSPECT spectrometer to perform a 1 % measurement of a in a further beam time at the ILL (see the next section). The following measures to improve the spectrometer have been proposed (for details see Chaps. 5 and 6):

- reduce the amplification of the current preamplifier down to about 40 % or switch to, e.g., a logarithmic preamplifier instead, in order to prevent the saturation of the preamplifier after high-energy electrons, cf. Sec. 5.4.1.
- optimize the pulse shaping, to remove the undershoot of the baseline after high-energy electrons, cf. Sec. 5.4.1.
- implement a stabilized cooling system for the detector electronics, to improve both the level and the stability of the electronic noise, cf. Sec. 5.2.1.
- switch to a detector mechanics (see Fig. 3.20a) movable in the x-y-plane, for a better determination of the position of the proton detector relative to the rest of the electrode system and the magnetic field, cf. Sec. 5.5.6.
- further improve the vacuum conditions by means of, e.g., an additional external getter pump, in order to reduce the probability of rest gas ionization and hence also the amount of uncorrelated background.
- re-open the right side of the decay volume (DV) electrode gr, to increase the pumping speed and simultaneously reduce the influence of work function (WF) inhomogeneities on a, cf. Sec. 6.4.2.
- reduce the electrostatic mirror potential, to prevent both a violation of the condition for adiabatic transport and Penning discharges in the bottom part of the spectrometer, cf. Sec. 5.4.3. Therefore, electrically decouple the wire system (e1) from its holding electrode (e1b).
- coat the surfaces of the collimation system with, e.g., aluminum or titanium, in order to prevent a charging of the collimation system, cf. 5.4.4.
- increase the volume of the DV and subsequently the distance between the neutron beam and the inner surfaces of the DV electrode gr, to reduce the influence of WF inhomogeneities on a, cf. Sec.6.4.2.
- re-polish and subsequently re-coat the inner surfaces of the analyzing plane (AP) electrode e14, in order to reduce the influence of WF inhomogeneities on a, cf. Sec.6.4.1.
- measure the neutron beam profile(s) directly in the DV and improve their quality by means of the image plate scanner, to reduce the uncertainty in the correction for the edge effect, cf. Sec. 5.5.6.
- improve the stability of the neutron beam monitor (cf. Sec. 4.2.1), in order to normalize the measured proton count rates to the measured neutron count rates.

- implement an automated switching of the electrostatic mirror, to, e.g., perform measurements with a second analyzing plane below and above the AP electrode e14, cf. Sec. 5.3.2.
- install the nuclear magnetic resonance system developed by F. Ayala Guardia [53], in order to monitor the stability of the magnetic field ratio r_{B}, of the magnetic fields in the AP and the DV, during data taking.
- re-examine the influence of non-adiabatic proton motion (by means of MC simulations), in particular with regard to the height of the main magnetic field, cf. Sec. 5.5.5.
- additionally integrate the slight energy and angular dependencies (see Fig. 5.47) of the proton drift into the combined simulations of the edge effect, cf. Sec. 5.5.6.
- increase the simulation statistics (by means of MC simulations on a computer cluster), to reduce the uncertainty in the correction for the edge effect, cf. Sec. 5.5.6.
- develop an ultra-high vacuum compatible scanning Kelvin probe, periodically switching between DV and AP, in order to monitor the WF values in the DV and the AP during data taking, cf. Sec. 6.5.2.
- develop a monochromatic ion source to measure in situ the potential difference between DV and AP, cf. Sec. 3.4.1.

7.3 Upcoming Measurements with *a*SPECT

Currently, the *a*SPECT experiment is set up at the PF1B of the ILL. With measurements in the June/July and the September/October 2011 cycle, we aim to improve the uncertainty in a to 1 %, well below the present literature value of 4 % [10]. Further emphasis lies on the study of systematic effects. In particular, we will investigate the remaining trapped particle background, in order to continue improving the *a*SPECT spectrometer to permit a measurement of a with its design accuracy of 0.3 %, in a future beam time.

At the same time, we prepare a first measurement of the proton asymmetry parameter C with the *a*SPECT spectrometer, derived from the proton recoil spectrum in decays of polarized neutron. So far, the first and only measurement of $C = -0.2377(26)$ has been performed with the PERKEO II spectrometer [86, 269]. We aim to improve the uncertainty in C from currently 1.1 % to the 0.1 % accuracy level [48].

All these investigations will also help to prepare high-precision measurements of angular correlations in neutron beta decay with the new beam facility PERC[1], cf. Sec. 7.4 and App. C.

7.4 The Future with PERC

The new beam station PERC [104], a clean, bright, and versatile source of neutron decay products, is designed to improve the sensitivity of neutron decay studies by one order of magnitude. In this way, several symmetry tests based on neutron beta decay data become competitive [6]. The charged decay products are collected by a strong longitudinal

---

[1] Acronym for Proton and Electron Radiation Channel.

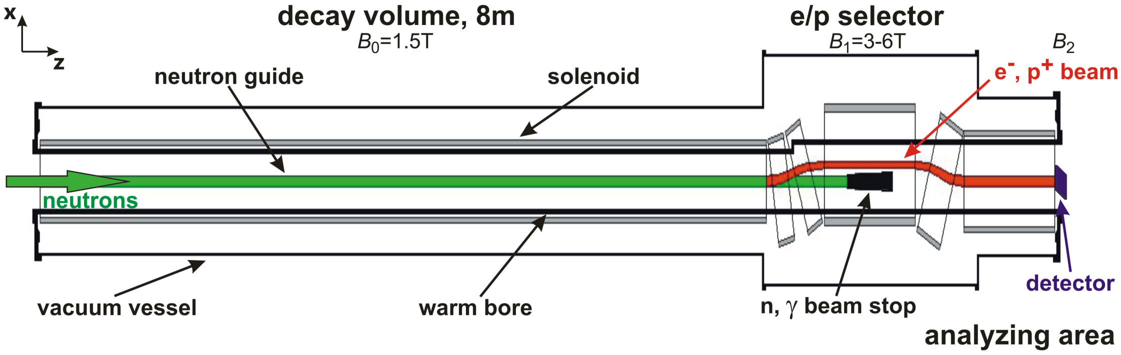

Figure 7.1: Scheme of the new facility PERC [270]: Cold neutrons (green) pass through the decay volume where only a small fraction decays. The decay products (red) are guided by the strong magnetic field towards the detector (blue). The superconducting coils are drawn in grey. The equipment for neutron beam preparation, like velocity selector, polarizer, spin flipper, or chopper, is located in front of the instrument (to the left of the scheme) and not shown here. For details see [104]. Figure taken from Ref. [7].

magnetic field of 1.5 T directly from inside a neutron guide, as can be seen in Fig. 7.1. This combination provides the highest phase space density of decay products. A magnetic mirror at 6 T serves to perform precise cuts in phase space, reducing related systematic errors. Systematic errors related to electron spectroscopy have been shown to be on the level of 10^{-4}, more than 10 times better than that achieved today [104].

PERC is under development by an international collaboration with the Universities of Heidelberg and Mainz, the Technische Universität München, the Institut Laue-Langevin in Grenoble, and the Vienna University of Technology. The instrument will be set up at a new position of the beam facility MEPHISTO of the Forschungs-Neutronenquelle Heinz Maier-Leibnitz in Munich, Germany.

Depending on the decay parameters studied, the analysis of the decay electrons and protons will be performed with specialized detectors. For protons, PERC will feed a charged particle spectrometer, for instance an adapted spectrometer which is based on our *a*SPECT spectrometer. The knowledge of the systematic effects gained in this thesis (see Sec. 5 for details) and the investigations of the patch effect (discussed in Sec. 6) will help to achieve the aimed uncertainties in the correlation coefficients a and C. For details see App. C and Ref. [7].

Appendix A

Design of an Anti-Magnetic Screen

This Appendix deals with the design of an anti-magnetic screen for the superconducting retardation spectrometer *a*SPECT using COMSOL Multiphysics Electromagnetics Module. COMSOL 3.2b was used to model and optimize the anti-magnetic screen to obtain a design that reduces the exterior magnetic field by a factor of about 10, that does not affect the internal magnetic field and its homogeneity, and that makes sure that the additional forces onto the magnet are non-destructive.

The anti-magnetic screen has already been presented in my publication [1]. I am going to closely follow the description therein and will update the experimental results.

A.1 The Shielding Problem

As explained earlier in Sec. 3.2.2, the spectrometer *a*SPECT consists of a system of eleven (cf. Fn. 12 in Chap. 3) superconducting coils placed inside a cylinder with a length of three meters and a diameter of seventy centimeters (cf. Figs. 3.7 and A.5). The coil system and its magnetic field are axially symmetric. The magnet generates a strong magnetic field which varies from 0.6 to 6 T along the symmetry axis (see Figs. 3.8 and 4.5), and down to 5 Gauss in a radial distance of five meters from the decay volume (DV) (see later in Fig. A.6).

For the latest beam time, the spectrometer *a*SPECT had to move to the Institut Laue-Langevin (ILL) in Grenoble, France. So as not to disturb other experiments by its strong magnetic stray field, an anti-magnetic screen was built that, as a first condition, has to lower the exterior magnetic field to less than 1 Gauss in a radial distance of 5 m, i.e., by a factor of about 10.

Magnets can be screened by either active or passive shielding. Active shielding refers to using a second magnet wound in the opposite direction of the main magnet. However, active shielding works very well only if the second magnet is of substantial larger diameter than the main magnet. In case of the *a*SPECT magnet, with coil diameters up to 60 cm (see Fig. 3.7), an active shield would need too much space.

A passive shield, made of ferromagnetic materials, must have large magnetization. This creates a substantial magnetic field inside the spectrometer and accordingly additional forces onto the coils. On the other hand, the *a*SPECT experiment depends strongly on the condition that the inhomogeneity of the magnetic field in the DV and in the analyzing plane (AP) (see Figs. 3.16 and 4.5) does not exceed 10^{-4}. Thus, an additional requirement of the design is that 2) the disturbance of the magnetic field caused by the shield does not affect the internal magnetic field and its homogeneity.

The manufacturer of the *a*SPECT magnet, Cryogenics Ltd., agrees to the anti-magnetic screen only if the electromagnetic forces onto the coils do not change their sign and if the relative changes are small. Therefore, a further requirement of the design is that 3) the additional forces onto the coils are non-destructive in this sense. Obviously, conditions 1) and 3) are contradictory terms for the strength of the shield.

Figure A.5 shows the spectrometer *a*SPECT inside of the anti-magnetic screen. Let's suppose, the spectrometer is not connected to the antimagnetic screen, and that we could neglect the gravitational forces, then the magnet would hang in the air only if he is already placed at a location that nulls the forces onto the coils. Otherwise, if the magnet is displaced, e.g. just a little bit moved towards a pillar, he will be attracted towards this pillar. Consequently, the final requirement of the design is that 4) the magnet has to be adjusted inside the shield.

A.2 Axially Symmetric Shielding

We have begun the design of a passive shield with 2D simulations in axial symmetry.

The magnetic field at any point in space due to a current loop can be obtained using the law of Biot Savart, integrated over a circular current loop [170], i.e. by numerical integration of analytical formulas. Consequently, we proved first that our semi-analytical calculations of the magnetic field and a shield of linear permeability are in agreement with COMSOL. For this comparison, the spectrometer *a*SPECT was enclosed by a cylinder with a length of 400 cm and a diameter of 190 cm with a lid on top and on bottom, both with a thickness of 10 cm, what corresponds to a mass of 20 tons.

Ferromagnetic materials have non-linear permeability, described by a so called B-H-curve. The shape of this curve, especially the initial permeability, the maximal permeability and the saturation, are strongly correlated with the special kind of the magnetic material (construction steel, transformer steel, mumetal, etc.), and depend on the thickness and the pretreatment of the material. Thus, the 2D modeling was completed by simulations of different materials of non-linear permeability. In these simulations the shield factor (defined as the ratio of the magnetic fields in radial direction without and with shield) reached a constant value from a radial distance of 5 m on, as expected for physical reasons. Figure A.1 shows a simulation for an axially symmetric model in COMSOL. In this design the spectrometer *a*SPECT is enclosed by a cylinder as described above, made of the special steel grade RTM3.

Although such designs would provide big enough shield factor (up to about 60 for RTM3), they make the support of the spectrometer very difficult. On the other hand, for a box instead of the cylinder we expect a lower but still sufficient large shield factor. Thus, availability and price of ferromagnetic materials suggest to using a box instead of the cylinder, i.e. a non-axially symmetric design what required a 3D simulation to be done (see the following section).

As mentioned above, a shield made of ferromagnetic materials creates additional forces onto the coils. Hence, the requirements 3) and 4) demand a minimum size on a passive shield, what required electromagnetic force calculations to be done simultaneously (for details see Sec. A.4).

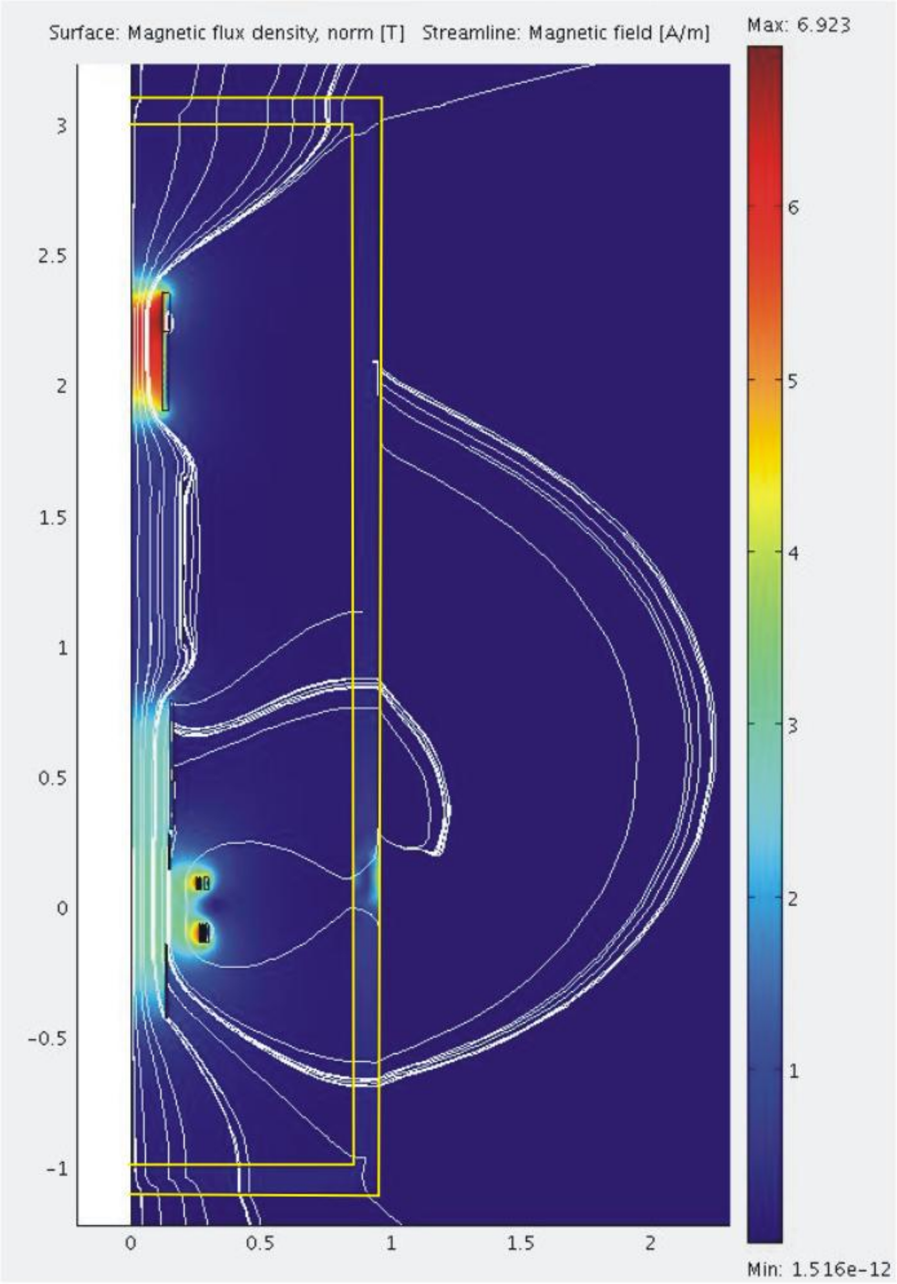

Figure A.1: The magnetic field for a 2D shield made of RTM3. The boundary of the shield is drawn in yellow. Figure taken from Ref. [1].

A.3 Non-axially Symmetric Shielding

We continued the design of a passive shield with 3D simulations, in the application modes that use either the magnetic vector potential **A** or the magnetic scalar potential V_m.

The conditions 1) – 4) require a fine mesh in radial direction (at least up to 10 m), close to the z-axis, in the DV, in the AP and inside the coils, at the same time. This requirement is equivalent to a fine mesh in the whole space and so nearly impossible. In order to refine the mesh in our regions of interest we simulated only an eighth of the

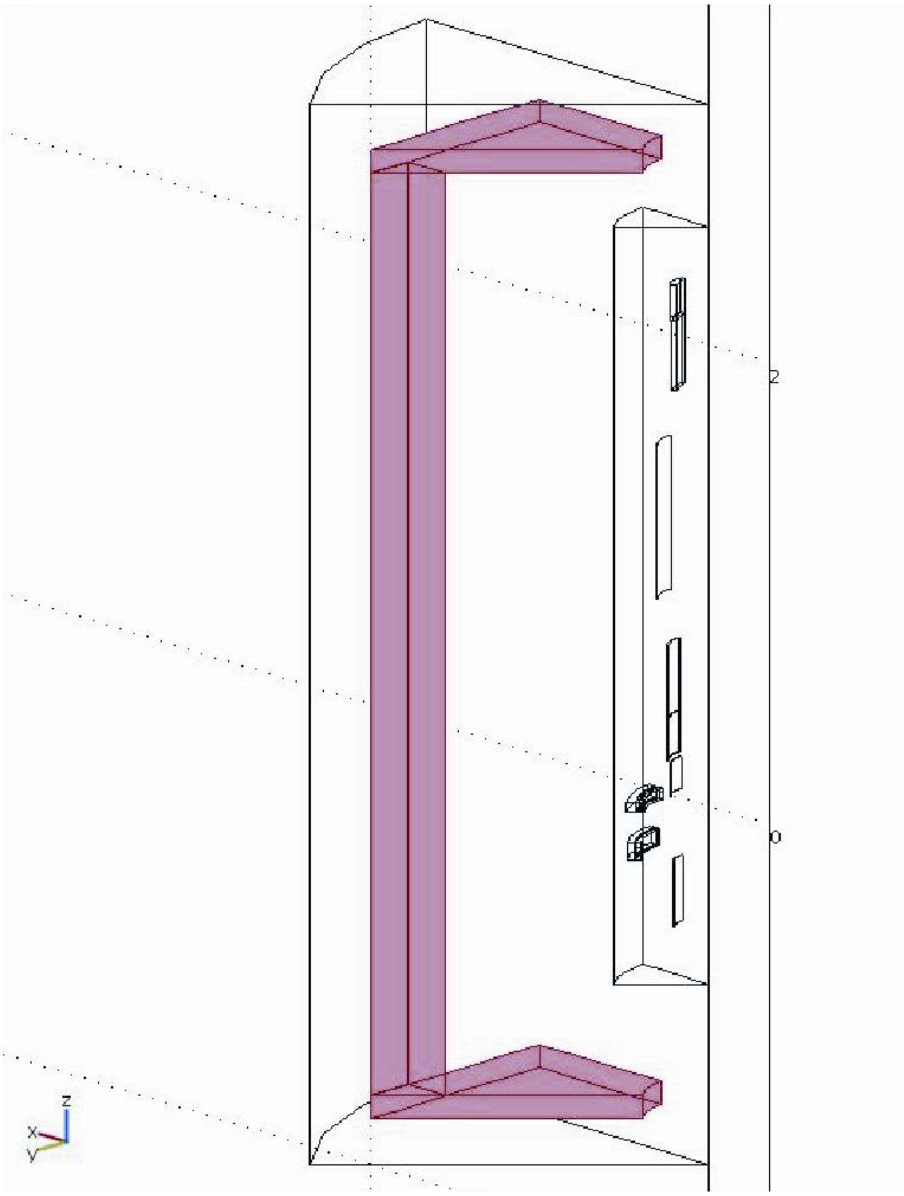

Figure A.2: The final design for passive shielding. A combination of both construction steel (plates) and ARMCO iron (pillar) provides a sufficient reduction of the exterior magnetic field without considerable effect on the internal magnetic field and its homogeneity, as can be seen from Fig. A.4. Figure taken from Ref. [1].

geometry taking advantage of the symmetry of the shield (see Fig. A.2 and also A.5). That way, the radial direction turns into two boundaries and the z-axis into an edge of the geometry, and the volume of the coils is reduced considerably. Furthermore, for this purpose we have to use "magnetic insulation" $\mathbf{n} \times \mathbf{A} = \mathbf{0}$ as boundary condition on the symmetry planes.

The 3D simulations of axially symmetric shields were in agreement with the corresponding 2D modeling results, as well. Thus, we have finished the design with 3D simulations of non-linear materials. We modeled a series of shields with the following geometry and variable parameters: A frame with 2 plates of variable cross-section and thickness,

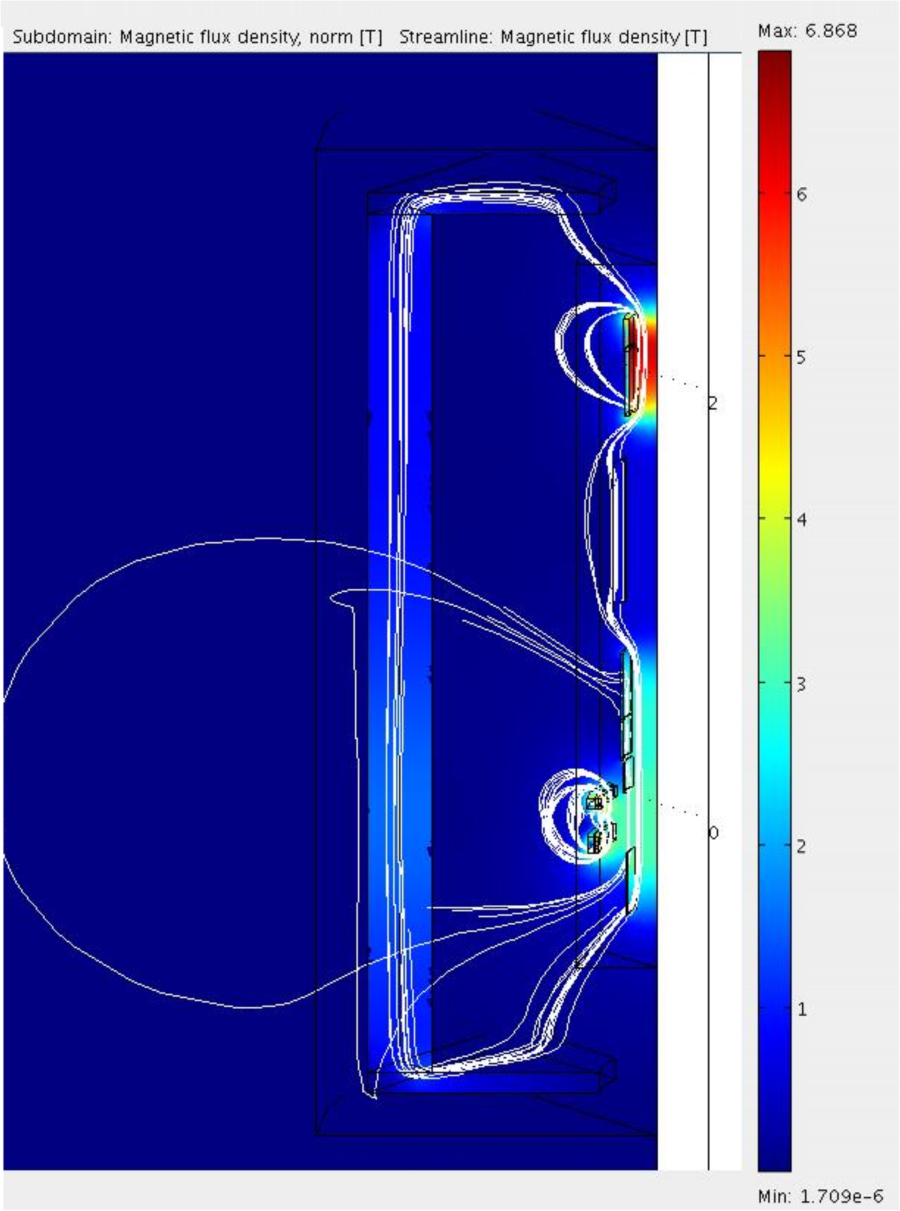

Figure A.3: The magnetic field in the symmetry plane that cuts through a pillar of the anti-magnetic screen for the model in Fig. A.2. Figure taken from Ref. [1].

with a hole of variable diameter at the center, and $n \cdot 4$ pillars between the plates, in their corners, each quartet of variable cross-section and length. Figures A.2 and A.3 show a simulation for a non-axially symmetric model in COMSOL. In this final design the magnet is enclosed by a combination of construction steel S235JRG2 (2 plates each of volume $180 \times 180 \times 10\,\mathrm{cm}^2$ and with a hole of a diameter of 50 cm) and ARMCO iron (4 pillars each of volume $20 \times 20 \times 400\,\mathrm{cm}^2$), what corresponds to a mass of 10 tons. This combination of different materials was chosen only because of availability of materials. The subdomain plot in Fig. A.3 illustrates already the saturation effect ($B_{\mathrm{sat}}^{\mathrm{ARMCO}} = 2.13\,\mathrm{T}$) in highmagnetic field environments, what explains the impracticalness of high-permeability materials like transformer steel or mumetal in case of the spectrometer *a*SPECT, also. In summary, this design meets the requirement to reduce the exterior magnetic field by a

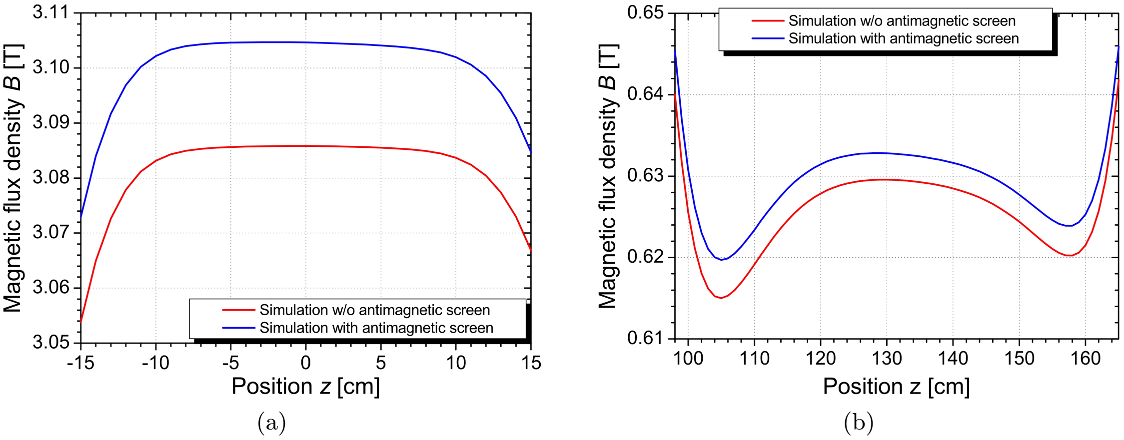

(a) (b)

Figure A.4: Expected influence on the internal magnetic field: The magnetic field on the z-axis (a) in the DV and (b) in the AP for the model in Fig. A.2, without (red line) and with anti-magnetic screen (blue line).

shield factor of 8.2 from a radial distance of 10 m on, and can be compared to a shield factor of about 30 for a cylinder as described in Sec. A.2 made of ARMCO iron. Moreover, the influence on the internal magnetic field is quite small, i.e. the shape and the homogeneity of the magnetic field in the DV and in the AP remain unaffected, only the ratio of the magnetic fields in these regions changes (cf. Fig. A.4).

A.4 Electromagnetic Force Calculation

The 3D simulations of a passive shield were accompanied by electromagnetic force calculations, in the application mode that uses the magnetic scalar potential V_m.

The additional force onto a coil in the external magnetic field $\mathbf{B}_\mathrm{ext}$ caused by the shield is result from subdomain integration to

$$\mathbf{F}_V = \int_V dV\, \mathbf{J} \times \mathbf{B}_\mathrm{ext}\,, \tag{A.1}$$

where V denotes the volume of the coil and $\mathbf{J}$ its current density [170].

Table A.1 shows a simulation of the electromagnetic forces onto an eighth of the aSPECT coils (denoted by c1 − c11 as in Fig. 3.7), where $F_r = \sqrt{F_x^2 + F_y^2}$ and $\varphi = \arcsin F_y/F_r$. As one can see from the total sum of additional forces ΔF_z, the magnet is already placed at a location that nulls the additional forces caused by the shield. Moreover, none of the forces changes its sign and the relative changes are quite small, both as desired (except for the already small radial forces onto the coils c2c and c4c). Besides, by displacement of the anti-magnetic screen relative to the aSPECT magnet, we calculated the gradient of the additional forces to about 300 N per 1 cm displacement of the magnet along the z-axis.

Without shield, the total sum of forces F_z onto the coils has to be zero, in contradiction to a calculated sum of 1 kN, cf. Table A.1. The angle φ of the radial forces is 22.5°, as

Table A.1: The electromagnetic forces onto an eighth of the coils without shield (F_r and F_z w/o shield) and the additional forces caused by the anti-magnetic screen (ΔF_r and ΔF_z) for the model in Fig. A.2. Data taken from Ref. [1].

coil	F_r (kN) w/o shield	φ (°)	F_z (kN) w/o shield	ΔF_r (kN)	ΔF_z (kN)
c1	65	22.5	15	0.5	-0.02
c2a	143	22.5	17	0.5	-0.03
c2b	61	22.5	10	0.3	-0.02
c2c	6	22.5	53	-1.4	-0.10
c4a	100	22.5	-10	0.3	-0.02
c4b	73	22.5	-11	0.3	-0.02
c4c	0.3	16.8	-44	1.2	-0.09
c6	44	22.5	-4	0.2	-0.01
c7	66	22.5	2	0.4	-0.02
c8	109	22.5	-26	0.7	-0.05
c9	16	22.5	0.03	0.3	0
c10	379	22.4	104	1.6	0.20
c11	256	22.5	-105	1.6	0.20
$\sum$			1		0

expected (except for c4c, where small errors of the small components F_x and F_y can explain a deviation of about 6°). However, errors of that order are tolerable.

A.5 Experimental Results

On the basis of the electromagnetic force calculations the spectrometer aSPECT was centered inside the anti-magnetic screen (see Fig. A.5). For that purpose, the magnet was hanged on a crane and separated from its suspension to the anti-magnetic screen meanwhile the magnetic field was ramped up very slowly. The obtained unstable position of equilibrium deviates from the calculations by only 1 cm along the z-axis, a deviation that corresponds to a small force of 300 N.

Moreover, we verified the simulations by measuring the reduction of the exterior magnetic field by a factor of about 7 (in a radial distance of 5.6 m from the DV), as can be seen in Fig. A.6.

The last step was to prove the simulations by measuring the internal magnetic field on and close to the z-axis with our Hall probe (cf. Fn. 7 in Chap. 4). Figure A.7 shows a measurement along the z-axis of the spectrometer. In the AP, the experimental data points perfectly match the expected values from our simulations. In the DV, by contrast, the experimental data points exceed the expected values from our simulations. However, both the shape and the homogeneity of the magnetic field in the DV remain unaffected, while only the ratio of the magnetic fields in the DV and the AP changes. We believe that the minor deviation can be attributed to the moderate knowledge of the B-H-curves.

Figure A.5: Setup of the spectrometer *a*SPECT inside the anti-magnetic screen, a combination of construction steel (plates of cross-section $180 \times 180 \times 10\,\mathrm{cm}^2$ and thickness 10 cm) and ARMCO iron (pillars of cross-section $20 \times 20 \times 10\,\mathrm{cm}^2$ and length 400 cm). The shield provides a sufficient reduction of the exterior magnetic field (cf. Fig. A.6). Photograph taken from Ref. [1].

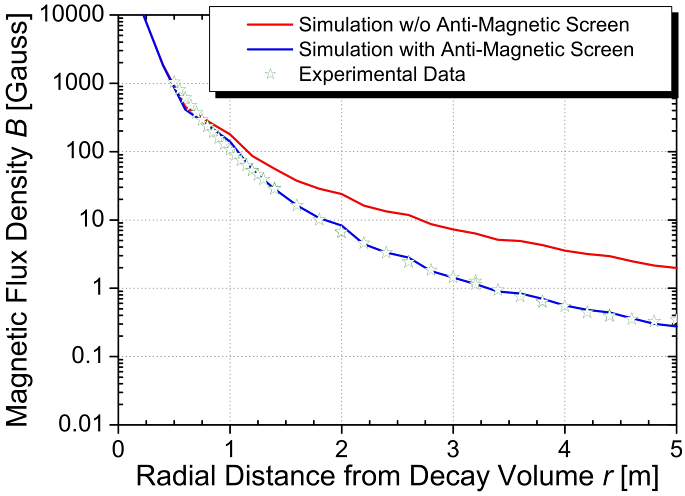

Figure A.6: Influence on the exterior magnetic field: The magnetic field in radial direction for the model in Fig. A.2, without (red) and with anti-magnetic screen (blue line). The green stars indicate a measurement between two pillars of the anti-magnetic screen.

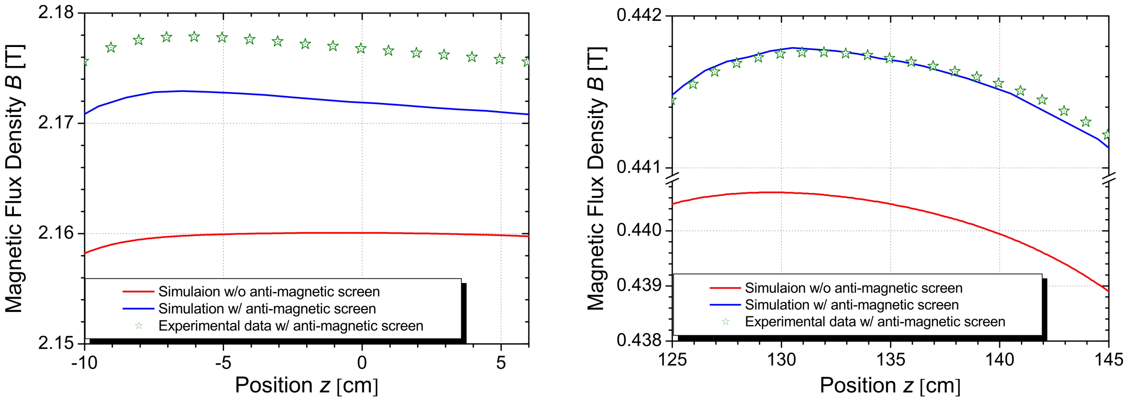

(a) (b)

Figure A.7: Influence on the internal magnetic field: The magnetic field on the z-axis (a) in the DV and (b) in the AP for the model in Fig. A.2, without (red line) and with anti-magnetic screen (blue line). The green stars indicate a measurement along the z-axis of the spectrometer.

Appendix B

Details of the Kelvin Probe Samples

Table B.1 presents a summary of the samples studied to date, to be scanned, or in preparation, including details of the substrates, surface treatments, and coatings. The first column gives the name of the sample, i.e., the common abbreviation for the substrate plus a serial number. The second column specifies the substrate type. The third and fourth column indicate if the substrate was subjected to welding or brazing in the mechanical workshop (MW) at the University of Mainz. The fifth and sixth column list the method of polishing along with the respective manufacturer. The seventh to eleventh column specify the coating, listed from substrate surface to outer surface, along with the respective manufacturer. The last column gives a short comment, if appropriate. All abbreviations are standard nomenclature for chemical elements, except OFHC Cu (oxygen-free high thermal conductivity copper), WB (white bronze), and IPA (isopropyl alcohol). In addition, the following abbreviations are used: PC (polishing compound), BW (buffing wheel), Sp (Physical Vapor Deposition, i.e., sputtering), EP (electroplating, i.e., galvanically), and EC (electroplating, i.e., electro-chemical). The remaining abbreviations stand for the various manufacturers, i.e., MVG (Metallveredelungs GmbH in Wiesbaden, Germany), AG (Adler Galvano GmbH in Mainz, Germany), GG (Galvanotechnik Gierich GmbH in Neuss, Germany), SMV (Sigrist Metallveredelung GmbH in Pforzheim, Germany), TL (Dr. Thorsten Lauer at the University of Mainz), and ECG (EC EuropCoating GmbH in Hohenlockstedt, Germany).

Table B.1: Details of the Kelvin Probe samples studied, to be scanned, or in preparation.

Ref.no.	Substrate	Welding method	Co.	Polishing method	Co.	Coat. techn.	1^{st} layer [μm]	Co.	2^{nd} layer [μm]	Co.	Comment
Cu1	OFHC Cu			PC green rouge	MVG	Sp[a]	Ag 2	TL	24C Au 0.2	TL	cleaned w/ IPA
Cu2	OFHC Cu			PC green rouge	MVG	Sp[a]	Ag 2	TL	24C Au 0.2	TL	
Cu3	OFHC Cu			nylon fleece	MW	EP	Ag 10	AG	24C Au 1	AG	
Cu4	OFHC Cu			nylon fleece	MW	EP	Ag 10	AG	24C Au 1	AG	
Cu5	OFHC Cu	OFHC Cu, cont. seam	MW	nylon fleece	MW	EP	Ag 10	AG	24C Au 1	AG	cannot be scanned
Cu6	OFHC Cu	OFHC Cu, cont. seam	MW	nylon fleece	MW	EP	Ag 10	AG	24C Au 1	AG	cannot be scanned
Cu7	OFHC Cu			PC talcum	AG	Sp[a]	Ag 2	TL	24C Au 0.2	TL	
Cu8	OFHC Cu			PC talcum	AG	Sp[a]	Ag 2	TL	24C Au 0.2	TL	cleaned w/ IPA
Cu9	OFHC Cu			PC talcum	AG	EP	Ag 10	AG	24C Au 2	AG	
Cu10	OFHC Cu			PC talcum	AG	EP	Ag 10	AG	24C Au 2	AG	
Cu11	OFHC Cu			PC talcum	AG	EP	Ag 10	AG	24C Au 1	AG	
Cu12	OFHC Cu			PC talcum	AG	EP	Ag 10	AG	24C Au 1	AG	
Cu13	OFHC Cu			PC talcum	AG	EP	Ag 10	AG	24C Au 5	AG	
Cu14	OFHC Cu			PC talcum	AG	EP	Ag 10	AG	24C Au 5	AG	
Cu15	OFHC Cu			PC blue, BW	GG	EP	Ag 10	GG	24C Au 2	GG	0.3 % Co
Cu16	OFHC Cu			PC blue, BW	GG	EP	Ag 10	GG	24C Au 2	GG	0.3 % Co
Cu17	OFHC Cu			PC blue, BW	GG	EP	Ag 10	GG	24C Au 2	GG	0.3 % Co
Cu18	OFHC Cu			PC blue, BW	GG	EP	WB 1	GG	Pt 1	GG	
Cu19	OFHC Cu			PC blue, BW	GG	EP	WB 1	GG	Pt 1	GG	
Cu20	OFHC Cu			PC blue, BW	GG	EP	WB 1	GG	Pt 1	GG	

---

[a] Only one side of the substrate was sputter coated.

Ref.no.	Substrate	Brazing		Polishing		Coat.	1st layer		2nd layer		Comment
		method	Co.	method	Co.	techn.	[μm]	Co.	[μm]	Co.	
Cu21	OFHC Cu			PC white, Inlett	SMV	Sp[a]	Ag 2	TL	24C Au 0.2	TL	cleaned w/ IPA
Cu22	OFHC Cu			PC white, Inlett	SMV	Sp[a]	Ag 2	TL	24C Au 0.2	TL	
Cu23	OFHC Cu			PC white, Inlett	SMV	EP	Ag 10	SMV	Rh 0.2	SMV	
Cu24	OFHC Cu			PC white, Inlett	SMV	EP	Ag 10	SMV	Rh 0.2	SMV	to be scanned
Cu25	OFHC Cu			PC white, Inlett	SMV	EP	Ag 10	SMV	Pt 0.2	SMV	
Cu26	OFHC Cu			PC white, Inlett	SMV	EP	Ag 10	SMV	Pt 0.2	SMV	
Cu27	OFHC Cu			PC white, Inlett	SMV	EP	Ag 10	SMV	24C Au 2	SMV	
Cu28	OFHC Cu			PC white, Inlett	SMV	EP	Ag 10	SMV	24C Au 2	SMV	
						EC	Ni 1	AG			1st layer electro-
Cu29	OFHC Cu			manually	AG	EP			24C Au 2	AG	chemical, magnetic
Cu30	OFHC Cu			manually	AG	EP	Ni 1	AG	24C Au 2	AG	magnetic
Cu31	OFHC Cu			manually	AG	EP	Ni 10	AG	24C Au 2	AG	magnetic
		Cd-free Ag,		nylon fleece	MW						
Cu32	OFHC Cu	cont. seam	MW	PC talcum	AG	EP	Ag 10	AG	24C Au 1	AG	
		Cd-free Ag,		nylon fleece	MW						
Cu33	OFHC Cu	cont. seam	MW	PC talcum	AG	EP	Ag 10	AG	24C Au 1	AG	
		Cd-free Ag,		nylon fleece	MW						
Cu34	OFHC Cu	cont. seam	MW	PC talcum	AG						
		Cd-free Ag,									
Cu35	OFHC Cu	cont. seam	MW	PC talcum	AG	EP	Ag 10	AG	24C Au 1	AG	to be scanned
		Cd-free Ag,									
Cu36	OFHC Cu	cont. seam	MW	PC talcum	AG	EP	Ag 10	AG	24C Au 1	AG	to be scanned

Ref.no.	Substrate	Brazing		Polishing		Coat.	1st layer		2nd layer		Comment
		method	Co.	method	Co.	techn.	[μm]	Co.	[μm]	Co.	
Cu37	OFHC Cu	Cd-free Ag, 2 capillary joints	MW	PC talcum	AG	EP	Ag 10	AG	24C Au 1	AG	to be scanned
Cu38	OFHC Cu	Cd-free Ag, 2 capillary joints	MW	PC talcum	AG	EP	Ag 10	AG	24C Au 1	AG	to be scanned
Cu39	OFHC Cu			PC	AG	Sp	TiN 0.8	ECG			1st layer failed
Cu40	OFHC Cu			PC	AG	Sp	TiN 0.8	ECG	24C Au 0.2	TL	1st layer failed, 2nd layer projected
Cu41	OFHC Cu			PC	AG	Sp	TiN 0.8	ECG	Ni 1	AG	1st layer failed, 2nd layer non-adhere
Cu42	OFHC Cu			PC	AG	Sp	TiN 0.8	ECG	24C Au 0.2	TL	1st layer failed, 2nd layer projected
Cu43	OFHC Cu			PC	AG	Sp	TiN 0.8	ECG	23.5C Au 0.1	ECG	2 % Ni, magnetic, to be scanned
Cu44	OFHC Cu			PC	AG	Sp	TiN 0.8	ECG	23.5C Au 0.1	ECG	2 % Ni, magnetic, to be scanned
Cu45	OFHC Cu			PC	AG	Sp	TiN 0.8	ECG	23.5C Au 0.1	ECG	2 % Ni, magnetic, to be scanned
Cu46	OFHC Cu			PC	AG	Sp	TiN 0.8	ECG	23.5C Au 0.1	ECG	2 % Ni, magnetic, to be scanned
Cu47	OFHC Cu			PC	AG	Sp	Ag 10	TL	24C Au 1	TL	coating projected
Cu48	OFHC Cu			PC	AG	Sp	Ag 10	TL	24C Au 1	TL	coating projected
Cu49	OFHC Cu			PC	AG	Sp	Ag 2	TL	24C Au 0.2	TL	coating projected
Cu50	OFHC Cu			PC	AG	Sp	Ag 2	TL	24C Au 0.2	TL	coating projected

Ref.no.	Substrate	Brazing		Polishing		Coat.	1st layer		2nd layer		Comment
		method	Co.	method	Co.	techn.	[μm]	Co.	[μm]	Co.	
Cu51	OFHC Cu			PC	AG	Sp	Cr 2	TL	24C Au 0.2	TL	coating projected
Cu52	OFHC Cu			PC	AG	Sp	Cr 2	TL	24C Au 0.2	TL	coating projected
Cu53	OFHC Cu			manually	SMV	EP	Ag 10	SMV	Pt 0.2	SMV	
Cu54	OFHC Cu			manually	SMV	EP	Ag 10	SMV	Pt 0.2	SMV	
Cu55	OFHC Cu			manually	SMV	EP	Ag 10	SMV	24C Au 1	SMV	to be scanned
Cu56	OFHC Cu			manually	SMV	EP	Ag 10	SMV	24C Au 1	SMV	to be scanned
Cu57	OFHC Cu			manually	SMV	EP	Ag 10	SMV	24C Au 2	SMV	to be scanned
Cu58	OFHC Cu			manually	SMV	EP	Ag 10	SMV	24C Au 2	SMV	to be scanned
Cu59	OFHC Cu			PC	AG	Sp	TiW 2	TL	24C Au 0.2	TL	coating projected
Cu60	OFHC Cu			PC	AG	Sp	TiW 2	TL	24C Au 0.2	TL	coating projected
Ti1	Ti grade 1					Sp[a]	24C Au 0.2	TL			
Ti2	Ti grade 1					Sp[a]	24C Au 0.2	TL			cleaned w/ IPA
Ti3	Ti grade 1			PC talcum	AG	Sp	TiN 0.8	ECG	24C Au 0.2	TL	2nd layer projected
Ti4	Ti grade 1			PC talcum	AG	Sp	TiN 0.8	ECG	24C Au 0.2	TL	2nd layer projected
Ti5	Ti grade 1			PC talcum	AG	Sp	TiN 0.8	ECG	24C Au 0.2	TL	2nd layer projected
Ti6	Ti grade 1			PC talcum	AG	Sp	TiN 0.8	ECG	24C Au 0.2	TL	2nd layer projected
Ti7	Ti grade 1			PC	AG	Sp	24C Au 0.2	TL			coating projected
Ti8	Ti grade 1			PC	AG	Sp	24C Au 0.2	TL			coating projected
Ti9	Ti grade 1			PC	AG	Sp	TiN 0.8	ECG	23.5C Au 0.1	ECG	2 % Ni, magnetic, to be scanned
Ti10	Ti grade 1			PC	AG	Sp	TiN 0.8	ECG	23.5C Au 0.1	ECG	2 % Ni, magnetic, to be scanned

Ref.no.	Substrate	Brazing method	Co.	Polishing method	Co.	Coat. techn.	1^{st} layer [μm]	Co.	2^{nd} layer [μm]	Co.	Comment
Ti11	Ti grade 1			PC	AG	Sp	TiN 0.8	ECG	23.5C Au 0.1	ECG	2 % Ni, magnetic, to be scanned
Ti12	Ti grade 1			PC	AG	Sp	TiN 0.8	ECG	23.5C Au 0.1	ECG	2 % Ni, magnetic, to be scanned
Glass1	glass					Sp[a]	Ag 0.2	TL			
Glass2	glass					Sp[a]	Au 0.2	TL			
Glass3	glass					Sp	Au 0.2	TL			coating projected
Glass4	glass					Sp	Au 0.2	TL			coating projected

Appendix C

The New Facility PERC

The Proton and Electron Radiation Channel (PERC) is a new type of beam station for the measurement of angular correlations in the beta decay of free neutrons. In contrast to existing neutron decay spectrometers, PERC is a user instrument which delivers at its exit not neutrons but an intense beam of decay electrons and protons, under well defined and precisely variable conditions. Depending on the observable to be investigated, different secondary spectrometers can be used, for instance an adapted proton spectrometer which is based on our aSPECT spectrometer. Thus, with PERC, we can measure the shapes and magnitudes of electron or proton energy spectra from polarized or unpolarized neutron decay, in pulsed or continuous neutron beam mode, with or without electron spin analysis. Many quantities can be derived from such spectra, some for the first time [7, 104].

After a short description of its measurement principles, we will present the uncertainties and systematics of PERC. We note that the achievable accuracies of the correlation coefficients a and C depend heavily on the systematic uncertainties in the spectroscopy of decay protons, which have not yet been completely analyzed, cf. Sec. C.3.

PERC has already been presented in my publication [7]. I am going to closely follow the description therein and will update some details on proton spectroscopy.

C.1 Measurement Principles and Instrument

PERC is a beam station, which delivers at its exit neutron decay products. The set-up is schematically shown in Fig. 7.1 and in Refs. [7, 104]; its design principles are thoroughly discussed in Ref. [104]. Here, we will only summarize the essential parts: Cold neutrons pass through an 8 meters long neutron guide, with a cross section of $6 \times 6\,\mathrm{cm}^2$, where about 10^6 neutrons decay per second and per meter of guide. The neutron guide is surrounded by a superconducting solenoid ($B_0 = 1.5\,\mathrm{T}$) of equal length. Decay electrons and protons are guided by the strong longitudinal magnetic field towards the electron/proton (e/p) detection system, i.e., detectors specialized for certain tasks. This combination provides the highest phase space density of decay products. At the end of the neutron guide, the decay products can be separated from the neutron beam by means of bending coils. In the e/p selector, the decay products pass a region of strongly enhanced magnetic field $B_1 > B_0$ ($B_1 = 3 - 6\,\mathrm{T}$) before they reach the detector (at, e.g., $B_2 = 0.5\,\mathrm{T}$). The field B_1 acts as a magnetic mirror and transmits only the fraction $(1 - \cos\theta_\mathrm{C})/2$ ($\approx B_0/4B_1$, for $B_0 < B_1$) of all decay products, namely those emitted upstream under angles $\theta_0 \leq \theta_\mathrm{C} = \arcsin\sqrt{B_0/B_1}$ to the $z-$axis. Field variations $B(z)$ must be slow enough such that the

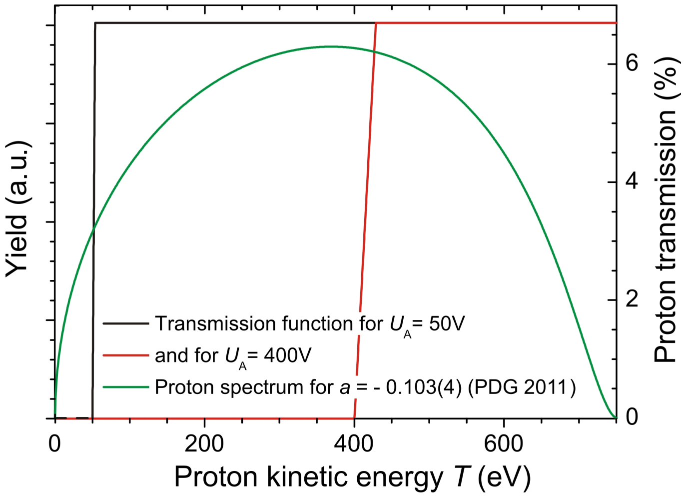

Figure C.1: The black and red line indicate the transmission function of PERC for protons in unpolarized neutron decay (preliminary), for $B_1 = 6\,\mathrm{T}$ and aSPECT as detection system, with $B_2 = B_\mathrm{A} = 0.4\,\mathrm{T}$ and $U_\mathrm{A} = 50\,\mathrm{V}$ respectively $U_\mathrm{A} = 400\,\mathrm{V}$. For elucidation, the green line shows the proton recoil spectrum with the recommended value for $a = -0.103$ [10].

decay electrons and protons are transported adiabatically. Then, the magnetic transport no longer depends on the energy of the decay products.

C.2 Measurement Uncertainties and Systematics

The magnetic mirror serves to limit the phase space precisely, reducing related systematic errors. Systematic errors related to electron spectroscopy have been shown to be on the level of 10^{-4}, more than 10 times better than that achieved today [104]. There is one exception related to the knowledge of the neutron beam polarization, where presently the error is on the 10^{-3} level [44]. Techniques for the polarization of a roughly monochromatic ($\Delta\lambda/\lambda \approx 10\,\%$) cold neutron beam will be improved towards the 10^{-4} level.

Further details on the sensitivity and the applications of PERC may be found in [104]. For details on the neutron beam preparation and the polarization analysis we refer to [271–273], respectively.

C.3 Dominant Uncertainties in the Analysis of Protons

Depending on the decay parameters studied with PERC, the analysis of the decay electrons and protons will be performed with specialized detectors. As far as electrons are concerned, this can be done with an energy sensitive detector. For protons, PERC will feed a charged particle spectrometer, for instance an adapted spectrometer which can partially be based on the aSPECT detection system. The most important associated systematic uncertainties for aSPECT as detection system for PERC are:

Homogeneity of the magnetic field: In the adiabatic approximation, the transmission function as shown in Fig. C.1 can be calculated analytically:

$$F_{\mathrm{tr}}^{\mathrm{PERC}}(T_0;U_\mathrm{A}) \;=\; \frac{1}{2}\begin{cases} 0 & ,\ \text{if}\quad T_0 \leq eU_\mathrm{A} \\ 1-\sqrt{1-\frac{B_0}{B_2}\left(1-\frac{eU_\mathrm{A}}{T_0}\right)} & ,\ \text{if}\quad \mathit{otherwise} \\ 1-\sqrt{1-\frac{B_0}{B_1}} & ,\ \text{if}\quad T_0 \geq \frac{eU_\mathrm{A}}{1-B_2/B_1} \end{cases}, \tag{C.1}$$

where U_A is the barrier voltage of aSPECT. Our initial calculations indicate that the magnetic fields B_0, B_1, and $B_2 = B_\mathrm{A}$ must be controlled at the level of $\Delta B_0/B_0 < 1\,\%$, $\Delta B_1/B_1 = 1 \times 10^{-4}$, and $\Delta B_2/B_2 = 1 \times 10^{-4}$, respectively, in order to keep $\Delta a/a < 0.1\,\%$. The condition $\Delta B_0/B_0 < 1\,\%$ can be fullfilled in pulsed neutron beam mode. Then, the decay products will be counted in the detector only while the neutron pulse is fully contained within the central, homogeneous part of the magnetic field. The magnetic field calculations show that the condition $\Delta B_1/B_1 = 1 \times 10^{-4}$ is fulfilled within the flux of neutron decay products [7]. For aSPECT, it has been shown that $\Delta B_2/B_2$ is on the level of 10^{-4} [53].

Homogeneity of the electric field: Our first estimates demonstrate that the electric potential between the decay volume, the e/p selector, and the electrostatic barrier will have to be known with an accuracy of better than 10 mV, comparable to aSPECT and Nab [99, 163].

Doppler effect due to neutron motion: Unlike in aSPECT or Nab, the Doppler effect is not negligible as the neutron beam is collinear to the detection system. For a Gaussian neutron spectrum, preliminary estimates show that the mean neutron energy has to be known with a precision of better than 10^{-2}, whereas the uncertainty in width of the spectrum is negligible [274]. An approximately Gaussian neutron spectrum can be obtained, e.g., by a neutron velocity selector.

Adiabaticity of the proton motion: For the determination of the neutrino-electron correlation coefficient a, adiabatic transport must be guaranteed between the decay volume and the electrostatic barrier. Equation (3.7) is a first estimate for the adiabaticity of the proton motion. The magnetic field calculations show that adiabatic transport is guaranteed along the particle trajectories [7]. We note that electric fields are not considered in this ansatz.

Residual gas: Simulations for aSPECT and Nab [163] have demonstrated that changes in the extracted value of a are tolerable if the residual gas pressure can be reduced to 10^{-8} mbar independent of the type of gas, and negligible if the pressure can be reduced to 10^{-9} mbar.

Particle trapping: Surface potential variations in the order of 100 mV have been found in electrodes prepared within the aSPECT project, cf. Ref. [33] and Sec. 6. Such variations can lead to local field extrema within the decay volume, the e/p selector, or the electrostatic barrier, and can therefore give rise to potential penning traps. For the same reason, local magnetic field minima must be avoided.

All these systematic effects are on the simulation agenda, and will be analyzed in due course. Measures to reduce and to precisely control systematic errors, like an online nuclear magnetic resonance system for monitoring of the magnetic field with 10^{-4} accuracy [53] or investigations of the patch effect with surface potential variations < 10 mV (see Sec. 6 and Ref. [243]), have already been initiated.

Bibliography

[1] G. Konrad et al., Design of an Anti-Magnetic Screen for the Neutron Decay Spectrometer *a*SPECT, in *Proceedings of the European Comsol Conference, Grenoble, 2007*, pp. 241–245, 2007, `http://www.comsol.com/papers/3276/`. (Cited on pages vii, 64, 213, 215, 216, 217, 219, and 220.)

[2] Report for the TRAPSPEC JRA-11 in EURONS on task T-J11-1 (Simulations and calculations), `http://www.gsi.de/documents/DOC-2009-Mar-290-19.pdf`, 2008. (Cited on page vii.)

[3] Report for the TRAPSPEC JRA-11 in EURONS on task T-J11-8 (Neutron decay retardation spectrometer), `http://www.gsi.de/documents/DOC-2009-Mar-290-26.pdf`, 2008. (Cited on pages vii and 72.)

[4] Measurement of the Proton Spectrum in free Neutron Decay, ILL Experimental Report, 2009. (Cited on page vii.)

[5] G. Konrad et al., *Nucl. Phys. A* **827**, 529c (2009). (Cited on pages vii, 4, and 197.)

[6] G. Konrad, W. Heil, S. Baessler, D. Počanić, and F. Glück, Impact of Neutron Decay Experiments on Non-Standard Model Physics, in *Proceedings of the 5th International Conference Beyond 2010, Cape Town, South Africa*, edited by H. V. Klapdor-Kleingrothaus, I. V. Krivosheina, and R. Viollier, pp. 660–672, World Scientific, Singapore, 2011, arXiv:1007.3027v2 [nucl-ex]. (Cited on pages vii, 2, 5, 28, and 211.)

[7] G. Konrad et al., *J. Phys.: Conf. Series* (2011), accepted. (Cited on pages vii, 212, 229, and 231.)

[8] J. Chadwick, *Nature* **129**, 312 (1932). (Cited on page 1.)

[9] *Nobel Lectures, Physics 1922-1941*, Elsevier Publishing Company, Amsterdam, 1965. (Cited on page 1.)

[10] Nakamura K. *et al.* (Particle Data Group), *J. Phys. G: Nucl. Part. Phys.* **37**, 075021 (2010), and 2011 partial update for the 2012 edition (`http://pdg.lbl.go`). (Cited on pages 1, 2, 3, 4, 6, 8, 14, 15, 16, 17, 18, 21, 22, 23, 24, 25, 26, 29, 34, 39, 40, 49, 50, 51, 52, 71, 79, 81, 101, 103, 104, 106, 107, 108, 113, 117, 126, 127, 128, 129, 137, 139, 145, 146, 147, 150, 153, 154, 155, 157, 201, 204, 207, 211, and 230.)

[11] S. L. Glashow, *Nucl. Phys.* **22**, 579 (1961). (Cited on page 1.)

[12] P. W. Higgs, *Phys. Rev. Lett.* **13**, 508 (1964). (Cited on pages 1 and 6.)

[13] A. Salam and J. C. Ward, *Physics Letters* **13**, 168 (1964). (Cited on page 1.)

[14] S. Weinberg, *Phys. Rev. Lett.* **19**, 1264 (1967). (Cited on page 1.)

[15] A. Salam, *Elementary Particle Physics: Relativistic Groups and Analyticity, Eighth Nobel Symposium, Stockholm*, p. 367, Almquvist and Wiksell, 1968. (Cited on page 1.)

[16] F. J. Hasert et al., *Phys. Lett. B* **46**, 138 (1973). (Cited on page 1.)

[17] N. Severijns, M. Beck, and O. Naviliat-Čunčić, *Rev. Mod. Phys.* **78**, 991 (2006). (Cited on pages 2, 5, 20, 28, 29, and 33.)

[18] H. Abele, *Prog. Part. Nucl. Phys.* **60**, 1 (2008). (Cited on pages 2, 3, 4, 5, and 23.)

[19] D. Dubbers and M. G. Schmidt, *Rev. Mod. Phys.* (2011), in print. (Cited on pages 2, 3, 5, 13, 23, and 26.)

[20] P. Herczeg, *Prog. Part. Nucl. Phys.* **46**, 413 (2001). (Cited on pages 2 and 5.)

[21] M. J. Ramsey-Musolf and S. Su, *Phys. Rev.* **456**, 1 (2008). (Cited on page 2.)

[22] J. S. Nico, *J. Phys. G: Nucl. Part. Phys.* **36**, 104001 (2009). (Cited on pages 2, 3, 5, 23, and 40.)

[23] T. Soldner et al., editors, *Proceedings of the International Workshop on Particle Physics with Slow Neutrons, Grenoble, France, 2008*, Nucl. Instr. and Meth. A **611**, 2009. (Cited on pages 2 and 23.)

[24] J. D. Jackson, S. B. Treiman, and H. W. Wyld, *Phys. Rev.* **106**, 517 (1957). (Cited on pages 2, 10, and 11.)

[25] N. Cabibbo, *Phys. Rev. Lett.* **10**, 531 (1963). (Cited on pages 2 and 8.)

[26] M. Kobayashi and T. Maskawa, *Prog. Theor. Phys.* **49**, 652 (1973). (Cited on pages 2 and 8.)

[27] F. Glück, J. Joó, and J. Last, *Nucl. Phys. A* **593**, 125 (1995). (Cited on pages 2, 9, 10, 11, 12, 13, 15, 20, 21, and 31.)

[28] F. Glück, *Phys. Lett. B* **376**, 25 (1996). (Cited on pages 2 and 12.)

[29] J. Liu et al., *Phys. Rev. Lett.* **105**, 181803 (2010),
see also PRL 105 219903 (errat). (Cited on pages 3, 4, and 23.)

[30] H. Abele, *Nucl. Instr. and Meth. A* **611**, 193 (2009). (Cited on pages 3, 23, and 28.)

[31] D. Mund, *Messung der Betaasymmetrie A im Neutronenzerfall*, PhD thesis, Ruprecht-Karls-Universität Heidelberg, 2006. (Cited on pages 3 and 23.)

[32] H. Mest, *Measurement of the β-Asymmetry in the Decay of Free Polarized Neutrons with the Spectrometer PERKEO III*, PhD thesis, Ruperto-Carola University of Heidelberg, 2011. (Cited on pages 3, 4, 21, 23, and 131.)

[33] S. Baessler et al., *Eur. Phys. J. A* **38**, 17 (2008). (Cited on pages 3, 4, 38, 56, 57, 64, 75, 81, 106, 107, 108, 197, 209, and 231.)

[34] M. Borg, *The Electron Antineutrino Angular Correlation Coefficient a in Free Neutron Decay: Testing the Standard Model with the aSPECT-Spectrometer*, PhD thesis, Johannes Gutenberg-Universität Mainz, 2011. (Cited on pages 3, 4, 53, 57, 72, 75, 81, 85, 87, 92, 95, 96, 101, 105, 106, 107, 109, 110, 114, 116, 119, 120, 123, 129, 135, 140, 141, 149, 152, 165, 166, 209, and 210.)

[35] W. J. Marciano and A. Sirlin, *Phys. Rev. Lett.* **96**, 032002 (2006). (Cited on pages 3 and 13.)

[36] A. Czarnecki, W. J. Marciano, and A. Sirlin, *Phys. Rev. D* **70**, 093006 (2004). (Cited on pages 3, 13, and 25.)

[37] P. Bopp et al., *Phys. Rev. Lett.* **56**, 919 (1986). (Cited on pages 3 and 4.)

[38] B. G. Erozolimsky et al., *Phys. Lett. B* **412**, 240 (1997).

[39] P. Liaud et al., *Nucl. Phys. A* **612**, 53 (1997). (Cited on pages 3 and 4.)

[40] C. Stratowa, R. Dobrozemsky, and P. Weinzierl, *Phys. Rev. D* **18**, 3970 (1978). (Cited on pages 3, 4, 36, 37, 81, and 209.)

[41] J. Byrne et al., *J. Phys. G: Nucl. Part. Phys.* **28**, 1325 (2002). (Cited on pages 3, 4, 37, 43, 72, 73, 81, and 209.)

[42] H. Abele et al., *Phys. Lett. B* **407**, 212 (1997). (Cited on page 4.)

[43] H. Abele et al., *Phys. Rev. Lett.* **88**, 211801 (2002). (Cited on pages 4 and 27.)

[44] M. Kreuz et al., *Nucl. Instr. and Meth. A* **547**, 583 (2005). (Cited on pages 3 and 230.)

[45] S. Gardner and C. Zhang, *Phys. Rev. Lett.* **86**, 5666 (2001). (Cited on page 3.)

[46] O. Zimmer et al., *Nucl. Instr. and Meth. A* **440**, 548 (2000). (Cited on pages 3, 38, 43, 50, 51, 52, 70, 92, 93, 197, and 209.)

[47] F. Glück et al., *Eur. Phys. J. A* **23**, 135 (2005). (Cited on pages 3, 4, 38, 43, 49, 53, 57, 61, 62, 70, 72, 73, 74, 75, 76, 78, 79, 93, 114, 149, 151, 165, 197, and 209.)

[48] O. Zimmer, private communication, 2010, see also: `http://gepris.dfg.de/gepris/OCTOPUS/;jsessionid=5CEA2AFD3040D036E9433144DAEEAF54?module=gepris&task=showDetail&context=projekt&id=167643526`. (Cited on pages 3, 4, 24, and 211.)

[49] R. Muñoz Horta, *First measurements of the aSPECT spectrometer.*, PhD thesis, Johannes Gutenberg-Universität Mainz, 2011. (Cited on pages 4, 26, 38, 56, 64, 81, 106, and 107.)

[50] M. Simson et al., *Nucl. Instr. and Meth. A* **611**, 203 (2009), in *Proceedings of the International Workshop on Particle Physics with Slow Neutrons, Grenoble, 2008*, `arXiv:0811.3851v1`. (Cited on pages 4, 57, and 197.)

[51] M. Simson et al., *Nucl. Instr. and Meth. A* **581**, 772 (2007). (Cited on pages 4, 64, 65, 66, and 91.)

[52] M. Simson, *Measurement of the electron antineutrino angular correlation coefficient a with the neutron decay spectrometer aSPECT*, PhD thesis, Technische Universität München, 2010. (Cited on pages 4, 43, 53, 64, 65, 66, 68, 70, 75, 79, 80, 81, 85, 87, 90, 91, 92, 94, 95, 96, 98, 99, 101, 105, 106, 109, 110, 114, 115, 116, 118, 119, 120, 121, 122, 123, 124, 125, 129, 159, 160, 166, 209, and 210.)

[53] F. Ayala Guardia, *Calibration of the retardation spectrometer aSPECT*, PhD thesis, Johannes Gutenberg-Universität Mainz, 2011, in progress. (Cited on pages 4, 43, 53, 62, 71, 72, 81, 87, 88, 89, 90, 101, 148, 149, 165, 210, 211, and 231.)

[54] J. Byrne, *Neutrons, Nuclei and Matter: An Exploration of the Physics of Slow Neutrons*, Institute of Physics Publ., Bristol, 1995. (Cited on page 5.)

[55] F. Halzen and A. D. Martin, *Quarks and Leptons: An Introductory Course in Modern Particle Physics*, volume 1, Wiley, 1st edition, 1984. (Cited on page 5.)

[56] P. Renton, *Electroweak interactions: an introduction to the physics of quarks and leptons*, Cambridge University Press, Cambridge, 1990.

[57] W. N. Cottingham and D. A. Greenwood, *An Introduction to the Standard Model of Particle Physics*, Cambridge University Press, Cambridge, 2nd edition, 2007. (Cited on pages 5 and 8.)

[58] V. M. Abazov et al., *Phys. Rev. Lett.* **104**, 061804 (2010). (Cited on page 6.)

[59] T. D. Lee and C. N. Yang, *Phys. Rev.* **104**, 254 (1956). (Cited on pages 7, 9, and 10.)

[60] C. S. Wu et al., *Phys. Rev.* **105**, 1413 (1957). (Cited on page 7.)

[61] E. Fermi, *Zeitschrift für Physik* **88**, 161 (1934). (Cited on page 7.)

[62] G. Gamow and E. Teller, *Phys. Rev.* **49**, 895 (1936). (Cited on pages 7 and 10.)

[63] G. Sudarshan and R. Marshak, *Phys. Rev.* **109**, 1860 (1958). (Cited on page 7.)

[64] R. Feynman and M. Gell-Mann, *Phys. Rev.* **109**, 193 (1958). (Cited on page 7.)

[65] J. D. Jackson, S. B. Treiman, and H. W. Wyld, *Nucl. Phys.* **4**, 206 (1957). (Cited on pages 10 and 11.)

[66] H. P. Mumm et al., (2011), arXiv:1104.2778v2 [nucl-ex]. (Cited on page 11.)

[67] T. Soldner et al., *Phys. Lett. B* **581**, 49 (2004). (Cited on page 11.)

[68] A. Kozela et al., *Phys. Rev. Lett.* **102**, 172301 (2009). (Cited on pages 11 and 13.)

[69] A. Kozela et al., *Acta Physica Polonica B* **42**, 789 (2011). (Cited on pages 11 and 13.)

[70] D. H. Wilkinson, *Nucl. Phys. A* **377**, 474 (1982). (Cited on pages 13, 16, 17, and 31.)

[71] I. S. Towner and J. C. Hardy, *Phys. Rev. C* **77**, 025501 (2008). (Cited on page 13.)

[72] H. Abele et al., *Eur. Phys. J. C* **33**, 1 (2004). (Cited on page 13.)

[73] A. Sirlin, *Phys. Rev.* **164**, 1767 (1967). (Cited on pages 13 and 17.)

[74] F. Glück, *Phys. Rev. D* **47**, 2840 (1993). (Cited on pages 13, 15, 16, 17, 31, and 165.)

[75] I. S. Towner and J. C. Hardy, *Rev. Part. Phys.* **73**, 046301 (2010). (Cited on pages 13, 25, and 31.)

[76] J. C. Hardy and I. S. Towner, *Phys. Rev. C* **79**, 055502 (2009). (Cited on pages 13, 20, 22, 25, 28, 30, 31, and 32.)

[77] O. Nachtmann, *Z. Phys.* **215**, 505 (1968), please note a correction of a sign error in Eq. (4.5), found by C. Habeck, PhD Thesis, University of Sussex, 1997. (Cited on page 14.)

[78] C. Habeck, PhD thesis, University of Sussex, 1997. (Cited on page 14.)

[79] P. G. Dawber et al., *Nucl. Instr. and Meth. A* **440**, 543 (2000). (Cited on page 14.)

[80] S. Baessler, *Die Betaasymmetrie im Zerfall des freien Neutrons*, PhD thesis, Ruprecht-Karls-Universität Heidelberg, 1996. (Cited on page 16.)

[81] B. Povh et al., *Teilchen und Kerne*, Springer, Berlin, Heidelberg, 2004. (Cited on page 16.)

[82] J. Pati and A. Salam, *Phys. Rev. D* **10**, 275 (1974). (Cited on page 21.)

[83] R. Mohapatra and J. Pati, *Phys. Rev. D* **11**, 566 (1975). (Cited on page 21.)

[84] M. A. Bég, *Phys. Rev. Lett.* **38**, 1252 (1977). (Cited on page 21.)

[85] J. Döhner, *Der Beta-Zerfall freier Neutronen und rechtshändige Ströme*, PhD thesis, Ruprecht-Karls-Universität Heidelberg, 1990. (Cited on page 21.)

[86] M. Schumann, *Measurement of Neutrino and Proton Asymmetry in the Decay of polarized Neutrons*, PhD thesis, Ruperto-Carola University of Heidelberg, 2007. (Cited on pages 21 and 211.)

[87] Y. Zhang et al., *Phys. Rev. D* **76**, 091301 (2007). (Cited on pages 21 and 30.)

[88] C. A. Baker and other, *Phys. Rev. Lett.* **97**, 131801 (2006). (Cited on page 21.)

[89] W. T. Eadie et al., *Statistical Methods in Experimental Physics*, North-Holland Publishing Co., 1971. (Cited on page 22.)

[90] W. H. Press et al., *Numerical Recipes: The Art of Scientific Computing*, Cambridge University Press, 3rd edition, 2007, Sec. 15.6. (Cited on pages 22 and 86.)

[91] V. F. Ezhov et al., *Nucl. Instr. and Meth. A* **611**, 167 (2009). (Cited on pages 23 and 24.)

[92] V. F. Ezhov, Neutron lifetime measuring using magnetic trap, in *Proceedings of the 7th International UCN Workshop "Ultracold and Cold Neutrons. Physics and Sources."*, 2009. (Cited on page 23.)

[93] A. P. Serebrov et al., *Phys. Lett. B* **605**, 72 (2005). (Cited on pages 23 and 24.)

[94] A. Pichlmaier et al., *Phys. Lett. B* **693**, 221 (2010). (Cited on page 23.)

[95] C. Amsler et al., *Phys. Lett. B* **667**, 1 (2008), and 2009 partial update for the 2010 edition. (Cited on page 23.)

[96] R. W. Pattie et al., *Phys. Rev. Lett.* **102**, 01231 (2009). (Cited on page 23.)

[97] H. Abele, private communication, 2010. (Cited on page 23.)

[98] F. E. Wietfeldt et al., *Nucl. Instr. and Meth. A* **611**, 207 (2009). (Cited on pages 23, 39, and 40.)

[99] D. Počanić et al., *Nucl. Instr. and Meth. A* **611**, 211 (2009). (Cited on pages 23, 39, 41, and 231.)

[100] K. P. Hickerson, The Fierz Interference Term in Beta Decay Spectrum of Ultracold Neutrons, in *UCN Workshop, November 6-7 2009, Santa Fe, New Mexico*, 2009, `http://neutron.physics.ncsu.edu/UCN_Workshop_09/Hickerson_SantaFe_2009.pdf`. (Cited on page 23.)

[101] B. Märkisch et al., *Nucl. Instr. and Meth. A* **611**, 216 (2009). (Cited on page 23.)

[102] B. Plaster et al., *Nucl. Instr. and Meth. A* **595**, 587 (2008). (Cited on page 23.)

[103] R. Alarcon et al., The abBA Experiment proposal, 2007, `http://nab.phys.virginia.edu/ABBA_proposal_2007.pdf`. (Cited on pages 23 and 24.)

[104] D. Dubbers et al., *Nucl. Instr. and Meth. A* **596**, 238 (2008),
for an extended version, see arXiv:0709.4440v1 [nucl-ex]. (Cited on pages 23, 211, 212, 229, and 230.)

[105] W. S. Wilburn et al., *Rev. Mex. Fís.* **55**, 119 (2009). (Cited on page 24.)

[106] R. Alarcon et al., PANDA @ SNS proposal, 2008, `http://research.physics.lsa.umich.edu/chupp/panda/PANDA@SNS.pdf`. (Cited on page 24.)

[107] M. Dewey et al., *Nucl. Instr. and Meth. A* **611**, 189 (2009). (Cited on page 24.)

[108] H. M. Shimizu, in *Proceedings of the 7th International UCN Workshop, Saint Petersburg, Russia*, 2009, `http://cns.pnpi.spb.ru/ucn/articles/Shimizu.pdf`. (Cited on page 24.)

[109] S. Arzumanov et al., *Nucl. Instr. and Meth. A* **611**, 186 (2009). (Cited on page 24.)

[110] A. P. Serebrov, in *Proceedings of the 7th International UCN Workshop, Saint Petersburg, Russia*, 2009, `http://cns.pnpi.spb.ru/ucn/articles/Serebrov3.pdf`. (Cited on page 24.)

[111] P. L. Walstron et al., *Nucl. Instr. and Meth. A* **599**, 82 (2009). (Cited on page 24.)

[112] S. Materne et al., *Nucl. Instr. and Meth. A* **611**, 176 (2009).

[113] K. K. H. Leung and O. Zimmer, *Nucl. Instr. and Meth. A* **611**, 181 (2009).

[114] C. M. O'Shaughnessy et al., *Nucl. Instr. and Meth. A* **611**, 171 (2009). (Cited on page 24.)

[115] Y. A. Mostovoĭ and A. Frank, *J. Exp. and Theor. Phys. Lett.* **24**, 38 (1976), Translated from. (Cited on page 24.)

[116] J. C. Hardy and I. S. Towner, *Phys. Rev. C* **71**, 055501 (2005). (Cited on pages 25 and 31.)

[117] G. A. Miller and A. Schwenk, *Phys. Rev. C* **78**, 035501 (2008). (Cited on page 25.)

[118] G. A. Miller and A. Schwenk, arXiv:0910.2790, 2009.

[119] N. Auerbach, *Phys. Rev. C* **79**, 035502 (2009).

[120] H. Liang, N. Van Giai, and J. Meng, *Phys. Rev. C* **79**, 064316 (2009). (Cited on page 25.)

[121] O. Naviliat-Čunčić and N. Severijns, *Phys. Rev. Lett.* **102**, 142302 (2009). (Cited on page 26.)

[122] D. Počanić et al., *Phys. Rev. Lett.* **93**, 181803 (2004). (Cited on page 26.)

[123] A. P. Serebrov et al., *Zh. Éksp. Teor. Fiz.* **113**, 1963 (1998). (Cited on pages 26 and 27.)

[124] A. P. Serebrov et al., *J. Exp. and Theor. Phys.* **86**, 1074 (1998). (Cited on pages 26 and 27.)

[125] M. Schumann et al., *Phys. Rev. Lett.* **99**, 191803 (2007). (Cited on page 27.)

[126] A. I. Boothroyd, J. Markey, and P. Vogel, *Phys. Rev. C* **29**, 603 (1984). (Cited on page 28.)

[127] J. Camps, *Search for right-handed currents and tensor type interactions in the beta decay of polarised nuclei*, PhD thesis, Kath. Univ. Leuven, 1997. (Cited on pages 28 and 30.)

[128] N. Severijns et al., *Hyperfine Interact.* **129**, 223 (2000). (Cited on pages 28 and 30.)

[129] F. Wauters et al., *Phys. Rev. C* **80**, 062501 (2009), arXiv:0901.0081v2 [nucl-ex]. (Cited on page 28.)

[130] F. Wauters et al., *Phys. Rev. C* **82**, 055502 (2010), arXiv:1005.5034v1 [nucl-ex]. (Cited on page 28.)

[131] S. Profumo, M. J. Ramsey-Musolf, and S. Tulin, *Phys. Rev. D* **75**, 075017 (2007). (Cited on pages 28 and 34.)

[132] M. Schumann, Precision measurements in neutron decay, in *Proceedings of the XLIInd Rencontres de Moriond - Electroweak Interactions and Unified Theories, March 10-17 2007, La Thuile, Italy*, 2007, `arXiv:0705.3769v2[hep-ph]`. (Cited on page 28.)

[133] G. Barenboim et al., *Phys. Rev. D* **55**, 4213 (1997). (Cited on page 30.)

[134] R. P. MacDonald et al., *Phys. Rev. D* **78**, 032010 (2008). (Cited on pages 29 and 30.)

[135] M. Czakon, J. Gluza, and M. Zrałek, *Phys. Lett. B* **458**, 355 (1999). (Cited on page 30.)

[136] V. M. Abazov et al., *Phys. Rev. Lett.* **100**, 031804 (2008). (Cited on pages 29 and 30.)

[137] N. Severijns et al., *Nucl. Phys. A* **629**, 429c (1998). (Cited on page 29.)

[138] N. Severijns et al., *Phys. Rev. C* **78**, 055501 (2008). (Cited on page 31.)

[139] J. C. Hardy and I. S. Towner, *Nucl. Phys. A* **254**, 221 (1975). (Cited on page 32.)

[140] H. Klapdor-Kleingrothaus, I. Krivosheina, and R. Viollier, editors, *Physics Beyond the Standard Model of Particles, Cosmology and Astrophysics: Proceedings of the Fifth International Conference Beyond 2010*, World Scientific, Singapore, 2011. (Cited on page 33.)

[141] C. A. Gagliardi, R. Tribble, and N. J. Williams, *Phys. Rev. D* **72**, 073002 (2005). (Cited on page 34.)

[142] V. Cirigliano, private communication to D. Počanić, 2009. (Cited on page 34.)

[143] M. Bychkov et al., *Phys. Rev. Lett.* **103**, 051802 (2009). (Cited on page 34.)

[144] P. Herczeg, private communication to D. Počanić, 2004. (Cited on page 34.)

[145] `http://pibeta.phys.virginia.edu/`. (Cited on page 34.)

[146] `http://pen.phys.virginia.edu/`. (Cited on page 34.)

[147] M. Doi, T. Kotani, and E. Takasugi, *Prog. Theor. Phys. Suppl.* **83**, 1 (1985). (Cited on pages 34 and 35.)

[148] H. Päs et al., *Phys. Lett. B* **453**, 194 (1999). (Cited on pages 34 and 35.)

[149] R. Mohapatra and A. Y. Smirnov, *Annu. Rev. Nucl. Part. Sci.* **56**, 569 (2006). (Cited on page 34.)

[150] J. Hirsch, H. V. Klapdor-Kleingrothaus, and O. Panella, *Phys. Lett. B* **374**, 7 (1996). (Cited on page 35.)

[151] H. V. Klapdor-Kleingrothaus and I. V. Krivosheina, *Modern Phys. Lett. A* **21**, 1547 (2006). (Cited on page 35.)

[152] T. M. Ito and G. Prezeau, *Phys. Rev. Lett.* **94**, 161802 (2005). (Cited on page 35.)

[153] V. M. Lobashev et al., *Nucl. Phys. A* **719**, C153 (2003). (Cited on pages 35 and 47.)

[154] C. Kraus et al., *Eur. Phys. J. C* **40**, 447 (2005). (Cited on pages 35 and 47.)

[155] J. Angrik et al., *FZKA Scientific Report* **7090** (2004), `http://bibliothek.fzk.de/zb/berichte/FZKA7090.pdf`. (Cited on pages 35 and 47.)

[156] E. Komatsu et al., *Astrophys. J. Suppl. Ser.* **180**, 330 (2009). (Cited on page 35.)

[157] M. Tegmark et al., *Phys. Rev. D* **69**, 103501 (2004). (Cited on page 35.)

[158] V. K. Grigor'ev et al., *Sov. J. Nucl. Phys.* **6**, 239 (1968). (Cited on page 36.)

[159] J. Byrne, *J. Res. Natl. Inst. Stand. Technol.* **110**, 395 (2005). (Cited on page 37.)

[160] J. Byrne et al., *Europhys. Lett.* **33**, 187 (1996). (Cited on page 37.)

[161] Y. A. Mostovoĭ et al., *Phys. Atomic Nucl.* **64**, 1955 (2001), Translated from YAF 64 2040. (Cited on page 39.)

[162] F. E. Wietfeldt et al., *Nucl. Instr. and Meth. A* **545**, 181 (2005). (Cited on page 39.)

[163] R. Alarcon et al., Nab proposal update and funding request, 2010, `http://nab.phys.virginia.edu/nab_doe_fund_prop.pdf`. (Cited on pages 39, 41, and 231.)

[164] B. Yerozolimsky et al., (2004), `arXiv:nucl-ex/0401014`. (Cited on page 39.)

[165] S. Balashov and Y. Mostovoy, (1994), Preprint IAE-5718/2, Russian Research Center Kurchatov Institute, Moscow. (Cited on page 39.)

[166] G. Jones, aCORN: 'a' CORrelation in Neutron Decay, in *Proceedings of the 8th International UCN Workshop "Ultracold and Cold Neutrons. Physics and Sources."*, 2011. (Cited on page 41.)

[167] J. Bowman, *J. Res. Natl. Inst. Stand. Technol.* **110**, 407 (2005). (Cited on page 41.)

[168] F. Ayala Guardia, First Tests of the neutron decay spectrometer aSPECT, Master's thesis, Johannes Gutenberg-Universität Mainz, 2005. (Cited on pages 43, 62, and 89.)

[169] P. Kruit and F. H. Read, *J. Phys. E* **16**, 313 (1983). (Cited on pages 45 and 47.)

[170] J. D. Jackson, *Classical Electrodynamics*, John Wiley & Sons, 3rd edition, 1975. (Cited on pages 46, 214, and 218.)

[171] T. Hsu and J. L. Hirshfield, *Rev. Sci. Instrum.* **47**, 236 (1976). (Cited on page 47.)

[172] G. Beamson, H. Q. Porter, and D. W. Turner, *J. Phys. E* **13**, 64 (1980). (Cited on page 47.)

[173] V. M. Lobashev and P. E. Spivak, *Nucl. Instr. and Meth. A* **240**, 305 (1985). (Cited on page 47.)

[174] A. Picard et al., *Nucl. Instr. and Meth. B* **63**, 345 (1992). (Cited on pages 47 and 72.)

[175] M. Beck et al., *Eur. Phys. J. A* **47**, 45 (2011). (Cited on page 47.)

[176] T. G. Northrop, *The Adiabatic Motion of Charged Particles*, Interscience Publ., 1963. (Cited on pages 47 and 73.)

[177] R. Dendy, editor, *Plasma Physics: An Introductional Course*, Cambridge University Press, 1993. (Cited on pages 47 and 73.)

[178] F. M. Penning, *Physica (Utrecht)* **3**, 873 (1936). (Cited on page 56.)

[179] H. G. Dehmelt, *Adv. At. Mol. Phys.* **3**, 53 (1967). (Cited on page 56.)

[180] B. Müller, Umbau des Mainzer Neutrinomassenxperiments und Untergrunduntersuchungen im Hinblick auf KATRIN, Master's thesis, Johannes Gutenberg-Universität Mainz, 2002. (Cited on page 57.)

[181] F. M. Fränkle, Erste Messungen der elektromagnetischen Eigenschaften des KATRIN Vorspektrometers, Master's thesis, Universität Karlsruhe (IEKP), 2006.

[182] K. A. Hugenberg, Design of the electrode system for the KATRIN main spectrometer, Master's thesis, Westfälische Wilhelms-Universität Münster, 2008.

[183] F. Habermehl for the KATRIN Collaboration, *J. Phys.: Conf. Series* **120**, 052301 (2008). (Cited on page 57.)

[184] K. Valerius, *Spectrometer-related background processes and their suppression in the KATRIN experiment*, PhD thesis, Westfälische Wilhelms-Universität Münster, 2009. (Cited on page 57.)

[185] F. M. Fränkle, *Background Investigations of the KATRIN Pre-Spectrometer*, PhD thesis, KIT/IEKP, 2010. (Cited on page 57.)

[186] F. Glück, *The Penning discharge*, to be published. (Cited on page 57.)

[187] J. Erhart, private communication, 2011. (Cited on page 61.)

[188] F. Glück, *Axisymmetric electric field calculation with zonal harmonic expansion*, to be published in PIER. (Cited on page 61.)

[189] F. Glück, *Axisymmetric magnetic field calculation with zonal harmonic expansion*, to be published in PIER.

[190] F. Glück, *Relativistic charged particle tracking with 8th order Runge-Kutta method*, to be published in PIER. (Cited on page 61.)

[191] F. Glück, *Axisymmetric electric field calculation with BEM and with zonal harmonic expansion*, http://project8.physics.ucsb.edu/twiki/pub/Main/KatrinEgun/BoundaryElementMethod.pdf, 2007. (Cited on page 61.)

[192] T. J. Corona, Tools for Electromagnetic Field Simulation in the KATRIN Experiment, Master's thesis, Massachusetts Institute of Technology, 2009.

[193] F. Glück, *Axisymmetric electric field calculation with charge density method*, to be published.

[194] F. Glück, *Axisymmetric magnetic field calculation with Legendre polynomials and elliptic integrals*, to be published.

[195] F. Glück, *Axisymmetric coil design for homogeneous magnetic field*, to be published. (Cited on page 61.)

[196] http://www.comsol.com/. (Cited on page 62.)

[197] G. Petzoldt, *Measurement of the electron-antineutrino angular correlation coefficient a in neutron beta decay with the spectrometer aSPECT*, PhD thesis, Technische Universität München, 2007. (Cited on pages 64, 70, 96, 106, and 129.)

[198] PNSensor GmbH, http://www.pnsensor.de. (Cited on page 65.)

[199] G. Lutz, *Semiconductor Radiation Detectors*, Springer, Berlin, Heidelberg, New York, 1st edition, 2007, http://dx.doi.org/10.1007/978-3-540-71679-2. (Cited on page 65.)

[200] G. F. Knoll, *Radiation detection and measurement*, Wiley, Hoboken, 4th edition, 2010. (Cited on page 65.)

[201] E. Gatti and P. Rehak, *Nucl. Instr. and Meth. A* **225**, 608 (1984). (Cited on page 65.)

[202] R. Brun and F. Rademakers, *Nucl. Instr. and Meth. A* **389**, 81 (1997), http://root.cern.ch. (Cited on page 70.)

[203] H. Backe et al., *Phys. Scr. T.* **22**, 98 (1988). (Cited on page 72.)

[204] C. Weinheimer et al., *Phys. Lett. B* **460**, 219 (1999). (Cited on page 72.)

[205] R. Dobrozemsky, *Nucl. Instr. and Meth.* **118**, 1 (1974). (Cited on pages 72, 167, 174, and 175.)

[206] C. F. Giese and W. R. Gentry, *Phys. Rev. A* **10**, 2156 (1974). (Cited on page 74.)

[207] R. Schinke, *Chem. Phys.* **24**, 379 (1977).

[208] H. Krüger and R. Schrinke, *J. Chem. Phys.* **66**, 5087 (1977).

[209] G. Niedner et al., *J. Chem. Phys.* **87**, 2685 (1987).

[210] D. Dhuicq and C. Benoit, *J. Phys. B* **24**, 3599 (1991). (Cited on page 74.)

[211] R. Muñoz Horta, in *Proceedings of the XIV International Seminar on Interaction of Neutrons with Nuclei, Dubna, 2007*, 2007. (Cited on page 75.)

[212] J. F. Ziegler et al., SRIM - The Stopping and Range of Ions in Matter. Computer Program, `http://www.srim.org`, 2008. (Cited on page 79.)

[213] H. Häse et al., *Nucl. Instr. and Meth. A* **458**, 453 (2002). (Cited on page 82.)

[214] H. Abele et al., *Nucl. Instr. and Meth. A* **562**, 407 (2006). (Cited on page 83.)

[215] `http://www.ill.eu/instruments-support/instruments-groups/instruments/pf1b/characteristics/`. (Cited on page 83.)

[216] B. Singh, *Nucl. Data Sheets* **108**, 197 (2007). (Cited on page 85.)

[217] E. Browne and J. K. Tuli, *Nucl. Data Sheets* **111**, 1093 (2010). (Cited on page 85.)

[218] J. Krempel, Optimierung und Durchführung einer Beta-Asymmetriemessung im Zerfall polarisierter Neutronen, Master's thesis, Ruprecht-Karls-Universität Heidelberg, 2004. (Cited on page 85.)

[219] Group3 Technology Ltd., `http://www.group3technology.com/dlarea/docs/MPT-141%20spec.pdf`. (Cited on page 88.)

[220] S. J. B. Reed and N. G. Ware, *J. Phys. E* **5**, 582 (1972). (Cited on page 92.)

[221] J. A. Bearden, *Rev. Mod. Phys.* **39**, 78 (1967). (Cited on pages 91 and 92.)

[222] R. G. Helmer and C. van der Leun, *Nucl. Instr. and Meth. A* **450**, 35 (2000). (Cited on page 91.)

[223] W. R. Leo, *Techniques for Nuclear and Particle Physics Experiments*, Springer-Verlag, Berlin, Heidelberg, New York, 2nd edition, 1994. (Cited on page 100.)

[224] F. Glück, private communication, 2010. (Cited on page 114.)

[225] M. Simson, private communication, 2010. (Cited on pages 122 and 123.)

[226] D. Drouin et al., CASINO - monte CArlo SImulation of electroN trajectory in sOlids, Computer program. `http://www.gel.usherbrooke.ca/casino`, 2001, please note that the new 3D version v3.2 is available since August 05, 2011. (Cited on page 122.)

[227] D. Drouin et al., *Scanning* **29**, 92 (2007). (Cited on pages 122 and 131.)

[228] P. Hovington et al., *Scanning* **19**, 1 (1997), `10.1002/sca.4950190101`. (Cited on pages 122 and 131.)

[229] F. E. Wietfeldt et al., *Nucl. Instr. and Meth. A* **538**, 574 (2005). (Cited on pages 131, 132, and 133.)

[230] S. M. Seltzer, *Int. J. Appl. Radiat. Isot.* **42**, 917 (1991). (Cited on page 131.)

[231] GEANT4 - a toolkit for the simulation of the passage of particles through matter, Computer program. `http://geant4.cern.ch/`. (Cited on page 131.)

[232] S. Agostinelli et al., *Nucl. Instr. and Meth. A* **506**, 250 (2003). (Cited on page 131.)

[233] J. Allison et al., *IEEE Transactions on Nuclear Science* **53**, 270 (2006). (Cited on page 131.)

[234] H. Kanter, *Annalen der Physik* **20**, 144 (1957). (Cited on page 134.)

[235] F. Glück, private communication, 2008. (Cited on page 138.)

[236] B. Märkisch, private communication to T. Soldner, 2010. (Cited on page 141.)

[237] A. R. Müller et al., *Nucl. Instr. and Meth. A* **582**, 395 (2007). (Cited on page 159.)

[238] A. R. Müller, *Characterization of solid deuterium as a source material for ultracold neutrons (UCN) and development of a detector concept for the detection of protons from the neutron decay*, PhD thesis, Technische Universität München, 2008. (Cited on page 159.)

[239] I. Baikie and P. Estrup, *Rev. Sci. Instrum.* **69**, 3902 (1998). (Cited on page 167.)

[240] N. A. Robertson et al., *Class. Quantum Grav.* **23**, 2665 (2006). (Cited on pages 176, 178, 181, 190, and 206.)

[241] S. E. Pollack, S. Schlamminger, and J. H. Gundlach, *Phys. Rev. Lett.* **101**, 071101 (2008). (Cited on page 167.)

[242] R. Hodges, *Application of a Scanning Kelvin Probe to Measure Local Surface Potential Inhomogeneities*, Bachelor's thesis, University of Virginia, 2009. (Cited on pages 167, 168, 170, 174, 175, and 176.)

[243] S. McGovern, On the Determination of Surface Potential Variations with a Kelvin Probe, Master's thesis, University of Virginia, 2010. (Cited on pages 167, 170, 174, 175, 176, 177, 178, 181, 182, 183, 191, and 231.)

[244] W. M. Haynes, editor, *CRC Handbook of Chemistry and Physics*, CRC Press Inc., 91st edition, 2010. (Cited on page 169.)

[245] F. Rossi and G. I. Opat, **25**, 1349 (1992). (Cited on page 168.)

[246] D. Sauer and M. Stuve, Changes in Work Function of Pt(111), `http://www.mcallister.com/papers/stuve.html`., 1994. (Cited on page 168.)

[247] J. Camp, T. W. Darling, and R. E. Brown, *J. Appl. Phys.* **71**, 783 (1992). (Cited on pages 168 and 187.)

[248] KP Technology Ltd., Ambient Scanning Kelvin Probe Manual. (Cited on pages 170, 173, and 176.)

[249] I. D. Baikie, *Old Principles, New Techniques: A Novel UHV Kelvin Probe and its Application in the Study of Semiconductor Surfaces.*, PhD thesis, University of Twente, 1988, ISBN 90-9002444-1. (Cited on pages 170 and 173.)

[250] `http://www.kelvinprobe.info/technique-pccontrol.htm`. (Cited on page 170.)

[251] I. Baikie, *Rev. Sci. Instrum.* **62**, 1326 (1991). (Cited on page 173.)

[252] G.-N. Luo, K. Yamaguchi, T. Terai, and M. Yamawaki, *Rev. Sci. Instrum.* **72**, 2350 (2001). (Cited on page 174.)

[253] I. Baikie, private communication to R. Hodges, 2008. (Cited on page 174.)

[254] W. Li and D. Y. Li, *J. Chem. Phys.* **122**, 064708 (2005). (Cited on page 175.)

[255] M. Dressend, private communication, 2010. (Cited on page 176.)

[256] H. Diettrich, private communication, 2010. (Cited on page 176.)

[257] S. Baessler, private communication, 2011. (Cited on pages 176, 178, 184, and 207.)

[258] I. Baikie, private communication to S. McGovern, 2009. (Cited on page 177.)

[259] S. McGovern, private communication, 2010. (Cited on page 178.)

[260] M. Baumgärtner and C. J. Raub, *Platinum Metals Rev.* **29**, 155 (1985). (Cited on pages 184, 187, and 190.)

[261] `http://www.universalmeasurement.com/MahrFederalFinish.pdf`. (Cited on page 187.)

[262] M. Zanker, private communication, 2010. (Cited on page 189.)

[263] S. L. Firebaugh, K. F. Jensen, and M. A. Schmidt, *JMEMS* **7**, 128 (1998). (Cited on page 189.)

[264] L. L. Melo et al., *Journal of Metastable and Nanocrystalline Materials* **20-21**, 623 (2004). (Cited on page 189.)

[265] R. Petrović et al., *J. Sci. Instrum.* **66**, 483 (2001). (Cited on page 189.)

[266] A. W. Groenland, *Degradation of processes of platinum thin films on a silicon nitride surface*, Bachelor's thesis, University of Twente, 2004. (Cited on page 189.)

[267] W. Chen et al., *Appl. Phys. Lett.* **97**, 211107 (2010). (Cited on page 189.)

[268] M. Beck, private communication, 2011. (Cited on page 207.)

[269] M. Schumann et al., *Phys. Rev. Lett.* **100**, 151801 (2008), arXiv:0712.2442 [hep-ph]. (Cited on page 211.)

[270] M. Horvath, private communication, 2011. (Cited on page 212.)

[271] C. Gösselsberger et al., *Physics Procedia* (2011), accepted,
see also: Badurek G, Gösselsberger C and Jericha E, *Physica B* **406** 2458 (2011). (Cited on page 230.)

[272] C. Gösselsberger et al., (2011), submitted to J. Phys.: Conf. Series.

[273] C. Klauser et al., (2011), submitted to J. Phys.: Conf. Series. (Cited on page 230.)

[274] A. Senft, *Calculations on Proton Transmission for PERC*, Project work, Technische Universität München, 2010. (Cited on page 231.)

Erklärung

Hiermit versichere ich, dass ich die vorliegende Arbeit selbstständig verfasst und keine anderen als die von mir angegebenen Quellen und Hilfsmittel verwendet habe.
Die Arbeit ist in dieser oder ähnlicher Form noch nicht als Prüfungsarbeit eingereicht worden.

Mainz, im August 2011

Gertrud Emilie Konrad

Acknowledgments

I would like to take this opportunity to express my heartfelt thanks to all those who have contributed to the success of this work.

Curriculum Vitæ

Birthday	April 2nd, 1977
Birthplace	Worms, Germany
Since 01/2011	Project assistant at the Institute of Atomic and Subatomic Physics of the Vienna University of Technology
Since 01/2006	PhD student at the Johannes Gutenberg-University of Mainz
2003 - 2005	Student in physics at the Johannes Gutenberg-University of Mainz
10/2003	Diploma in mathematics at the Johannes Gutenberg-University of Mainz Title: “Eigenwertcharakterisierung und Lösungsgeometrie bei semilinearen gewöhnlichen Differentialgleichungen höherer Ordnung” (“Characterization of eigenvalues and geometry of solutions to semilinear differential equations of higher order”)
10/1999	Prediploma in mathematics at the Johannes Gutenberg-University of Mainz
1996 - 2003	Student in mathematics, physics and computer science at the Johannes Gutenberg-University of Mainz
06/1996	Abitur at the Eleonoren-Gymnasium of Worms
1987 - 1996	High school Eleonoren-Gymnasium of Worms
1983 - 1987	Primary school Otto Hahn-Schule of Westhofen